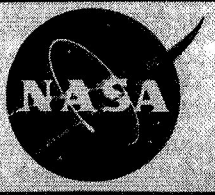
NASA Conference Publication 3341

19th Space Simulation Conference Cost Effective Testing for the 21st Century

Proceedings of a conference held at
the Radisson Plaza Lord Baltimore
Baltimore, Maryland
October 29-31, 1996



NASA Conference Publication 3341

19th Space Simulation Conference Cost Effective Testing for the 21st Century

Compiled by
Joseph L. Stecher
NASA Goddard Space Flight Center
Greenbelt, Maryland

Sponsored by
National Aeronautics and Space Administration
Institute of Environmental Sciences
American Institute for Aeronautics and Astronautics
American Society for Testing and Materials
Canadian Space Agency



National Aeronautics
and Space Administration

Goddard Space Flight Center
Greenbelt, Maryland 20771

1997

This publication is available from the NASA Center for AeroSpace Information,
800 Elkridge Landing Road, Linthicum Heights, MD 21090-2934, (301) 621-0390.

FOREWARD

The Nineteenth Space Simulation Conference, held at the Radisson Plaza Lord Baltimore Hotel in Baltimore, Maryland from October 28 through 31, 1996, was hosted by the Institute of Environmental Sciences (IES) and was supported by the American Institute of Aeronautics and Astronautics (AIAA), the American Society for Testing and Materials (ASTM), the National Aeronautics and Space Administration (NASA), and the Canadian Space Agency (CSA).

These proceedings attest to the scope of the conference; papers were presented on topics as diverse as shuttle payload contamination effects, simulating Martian environment for testing, to state-of-the-art 6-axis hydraulic shaker testing system. A good cross section of the international aerospace community took advantage of the opportunity to get together, to share their experiences, and to participate in the technical sessions. The two invited keynote speakers were Lieutenant General Malcolm O'Neill (USA, Ret.), past Director of BMDO, and Mr. Thomas Coughlin, Space Programs Manager at the Johns Hopkins University Applied Physics Laboratory. Their most informative and thought provoking talks were on cost effective testing approaches in Defense Department programs for the 21st Century and what part testing plays in the faster, better, cheaper approach for the NEAR and APL programs, respectively. The preceding tutorial and the tour of the Garber Facility of the Air and Space Museum rounded out a comprehensive conference contributing to the knowledge base vital to cost effective testing for successful missions into the 21st Century.

Special thanks are due to the Technical Program Chair, Alda Simpson and her Committee for their success in selecting the papers and planning the program. I wish to express my gratitude also to John Campbell (Meeting Manager), Tom Hollingsworth (Facilities Chair), and Joseph Stecher III (Publication Chair), for their effectiveness and professional performance. Our host society (IES and its Executive Director, Janet Ehmann), and sponsoring agencies (AIAA, ASTM, NASA, and CSA) are gratefully acknowledged. The Johns Hopkins University Applied Physics Laboratory provided the program and NASA published the Proceedings. Their kind generosity helped make this conference possible and the active participation of registrants made it a success.

Harold Fox
General Chair

COMMITTEES FOR
19TH SPACE SIMULATION CONFERENCE

MEETING MANAGEMENT COMMITTEE

General Chairman:	Harold G. Fox The Johns Hopkins University Applied Physics Laboratory
Technical Program:	Alda Simpson, NASA Goddard Space Flight Center
IES Meeting Chair:	John D. Campbell, Consultant
Publication Chairman:	Joseph L. Stecher III, NASA Goddard Space Flight Center
IES Executive Director:	Janet A. Ehmann, Institute of Environmental Sciences
Facilities Chairman:	Russell T. Hollingsworth, Consultant
Tutorial Co-Chair:	Al E. Armstrong, Consultant
Tutorial Co-Chair:	John N. Packard, Management Technology–NSI

TECHNICAL PROGRAM COMMITTEE

Greg Proulx, Hughes Aircraft Company
John W. Harrell, Jet Propulsion Laboratory
John Hazen, Boeing Defense and Space Group
Robert G. Moss, Space Systems Loral
Peter W. Brinkmann, ESA/ESTEC
Patric F. Neary, TRW
Bill O. Wilkinson, The Johns Hopkins University Applied Physics Laboratory
Michael Bietler, Martin Marietta Astro Space, East Windsor
Dr. Rolf Mamen, Canadian Space Agency

JOINT POLICY COMMITTEE

IES

John D. Campbell, Consultant
Joseph L. Stecher III, NASA Goddard Space Flight Center

ASTM

Robert G. Moss, Space Systems Loral

AIAA

John W. Harrell, Jet Propulsion Laboratory

CONTENTS

SESSION 1A: MATERIALS /CONTAMINATION

STS Contamination Effects Orbiter Payload Bay and Mated Payloads 1-1
D. W. Bartelson and R. Manning

GSFC Space Simulation Laboratory Contamination Philosophy:
Efficient Space Simulation Chamber Cleaning Techniques 23-2
J. A. Roman, G. F. Stitt, and F. R. Roman

Verification of the Baking Efficiency Using Micro-VCM Test Data 41-3
A. Zwaal

Investigation of Non-volatile Residue (NVR) Plate Results 51-4
R. S. Lange and W. J. Mitchell

Reduction of Calcofluor in Solithane Conformal Coatings of Printed Wiring Boards 59-5
Lt. M. K. Miller

Midcourse Space Experiment Molecular Contamination Modeling Predictions
for Early Orbital Operations 67-6
D. M. Silver, R. C. Benson, M. T. Boies, J. S. Dyer, R. E. Erlandson, G. E. Galica, B. D. Green, D. F. Hall, J. C. Lesho, T. E. Phillips, O. M. Oy, and B. E. Wood

SESSION 2: THERMAL VACUUM TESTING

Mars Pathfinder Spacecraft, Lander, and Rover Testing in Simulated Deep
Space and Mars Surface Environments 79-7
K. R. Johnson

SWAS Spacecraft T/V Test, Unique Chamber Tests Systems Actuation 99-8
J. L. Dunn

MSX Spacecraft Thermal Vaccum Testing 103-9
J. A. Krein and D. S. Mehoke

Solar Thermal Vacuum Testing of the Mars Global Surveyor Spacecraft 119-10
W. N. Breeden II and G. D. Chambers

NEAR Spacecraft Thermal Vacuum Testing 129-11
C. J. Ercol and S. J. Krein

SESSION 3: DYNAMIC TESTING

Mechanical Testing of the NEAR Spacecraft 141
D. F. Persons

†Launch Vibroacoustics Simulation and Validation of Transmitting Antennas of Telecommunications Satellites 161
M. Fornesi, L. Trittoni, P. C. Marucchi-Chierro, and M. Milano

Acceleration Testing–A Better, Faster, Cheaper Alternative for Strength Qualification Testing 163
C. F. Mattiello

A Method for Implementing Force-Limited Vibration Control 173
D. B. Worth

Structural Evaluation of TOPAZ II–The Russian Space-based Nuclear Reactor 187
E. D. Schaefer and J. M. Lacy

SESSION 4: DYNAMIC TESTING (con't.)

†Modal Testing of the Midcourse Space Experiment (MSX) Spacecraft 193
T. M. Betenbaugh and R. L. Tomkiewicz

Evaluating the Vibroacoustic Response of Honeycomb Panels 195
E. D. Schaefer

†A Near Perfect Spin Balance (Measurement in Chaos) 205
R. A. Luntz

Holddown Interface Load Cells, A Validation Tool 207
G. Slagter, B. Winter, and H. Cruijssen

Simulation of the Zero-Gravity Environment for Dynamic Testing of Structures 219
D. A. Kienholz

SESSION 5A: SPECIAL TOPICS

End-to-End System Test and Optical Performance Evaluation for the Solar and Heliospheric Observatory (SOHO) Ultraviolet Coronagraph Spectrometer (UVCS) 231
P. A. Carosso, L. D. Gardner, M. Jhabvala, and P. Nicolosi

Magnetic Test Performance Capabilities at the Goddard Space Flight Center as Applied to the Global Geospace Science Initiative 251
D. R. Mitchell

† *abstract only*

SESSION 5A: SPECIAL TOPICS (con't.)

INTESPACE from 1970 to Present Day 263 -24
J. L. Marce', J. F. Imbert, and J. C. Pasquet

SESSION 5B: SPECIAL TOPICS (con't.)

Laboratory Simulation of Hypervelocity Debris 277 -25
R. Roybal, J. Shively, C. Stein, and P. Tolmak

Assessing Meteoroid and Space Debris Risks 287 -26
A. L. Lee

SESSION 6A: MATERIAL DEGRADATION IN ORBIT

A Comparison of Atomic Oxygen Degradation in Low Earth Orbit and in a Plasma Etcher 295 -27
J. A. Townsend and G. Park

Combined Effects of Fluxes of Atomic Oxygen and Electrons on Chemical Reactions with Polymeric Materials 305 -28
J. Shively, T. King, C. Miglionico, R. Robertson, S. Davis, C. Stein, W. Wilson, and J. Baird

SESSION 6B: MATERIAL DEGRADATION IN ORBIT (con't.)

The Oxidation of Refractory Elements and Compounds in an Atomic Oxygen Environment 315 -29
M. M. Opeka, R. A. Rapp, and M. Wuttig

†Oxygen and VUV Irradiation of Polymers: Atomic Force Microscopy (AFM) and Complementary Studies 333 -30
E. Grossman, Y. Noter, and Y. Lifshitz

SESSION 7A: NEW APPROACHES AND FACILITIES I

Thermal Systems Upgrade of the Space Environment Simulation Test Chamber 335 -31
A. B. Desai

Graphic Three-Axes Presentation of Residual Gas Analyzer Data 355 -32
K. Johnson and A. G. Levi

New Generation Deployment Rigs for Solar Arrays 363 -33
A. P. Eggers, R. Kaal, H. J. Cruijssen, and R. F. Kolthof

† *abstract only*

SESSION 7B: NEW APPROACHES AND FACILITIES I

†The GSFC 6-Axis Hydraulic Shaker System 371-34
D. J. Hershfeld

Upgrade of a 10-foot Diameter by 15-foot Long Thermal Vacuum Chamber 373-35
A. T. Webb, J. Sushon, and L. McCrary

Air Coupled Ultrasonic C-Scan (AIRSCAN) for Nondestructive Inspection 387-36
R. W. A. van der Ven and H. Bolks

SESSION 8A: NEW APPROACHES AND FACILITIES II

†Low-Pressure Measurement Performance of Capacitance Diaphragm Gages 401-37
A. P. Miller and R. W. Hyland

Video-Aided Inspection of Solar Arrays 403-38
D. van der Vegt, F. H. Naber, and H. J. Cruijssen

SESSION 8B: NEW APPROACHES AND FACILITIES II

Ambient Pressure Thermal Cycling Test Facility for Solar Panels 415-39
J. Ch. Geerse and J. H. Mertens

Electron Omni-Directional Irradiator System for Space Package Testing 421-40
V. G. Adams and W. J. Chappas

†New Facility for Extreme Ultraviolet and X-ray Testing 429
A. Cucchiaro, I. Domken, P. Jamotton, I. Tychon, and J.P. Tock

† *abstract only*

51-18

031429

069341

24

STS CONTAMINATION EFFECTS
ORBITER PAYLOAD BAY AND MATED PAYLOADS

A FOCUS ON GROUND NON-VOLATILE RESIDUE MEASUREMENTS USING WIPE AND RINSE SAMPLING TECHNIQUES

Donald W. Bartelson
Materials & Processes
Contamination Control Engineering
Operations Support Group
Brown & Root
Launch Operations Services
Cape Canaveral Air Station, Fl

Roland Manning
M&P Engineering
Ball Aerospace (BASG)
Boulder, CO

ABSTRACT

An observation was made during the STS 45 Mission in which the SSBUV payload experienced optical degradation (optical reflectance measurements shorter than 250 nm) due to molecular contamination in the interior instrument package, specifically the surface of the diffuser and depolarizer optics. This contamination was subsequently identified to be primarily aliphatic hydrocarbons, followed by esters and then dimethyl silicones. Several contamination control Technical Interchange Meetings (TIM) were held at Kennedy Space Center (KSC) and Johnson Space Center (JSC) to discuss the SSBUV experience and implement investigative action. This paper presents the results of some of those activities, all of which were supported by the Contamination Control Working Group chaired by NASA Headquarters Code Q.

While orbiter Non-Volatile Residue (NVR) requirements are not established, our measurements have shown that NVR rates during a typical Space Transportation System (STS) mission are well within the most stringent NVR requirements stated in SN-C-0005C and MIL-STD-1246, i.e., <1.0 ug/cm^2. The data in this report revealed Payload Bay (PLB) mission values in the range of 0.19 to 0.40 ug/cm^2 for pre-flight and 0.14 to 0.20 ug/cm^2 for post-flight.

In evaluating the results of this study and citing other studies of similar interest, the author concludes that significant molecular contamination found on individual payloads is most likely self-induced. The evidence suggests localized source and re-deposition behavior rather than a widespread phenomena induced by the orbiters' Thermal Control System (TCS) materials to create any significant payload contamination effects. Further reduction of NVR contamination could possibly be achieved by careful selection of payload materials, functional considerations and advertising of critical contamination concerns to affect more favorable manifest assignments, ground processing activities/upgrades and on-orbit avoidance maneuvers.

INTRODUCTION

There has always been a keen interest expressed by the STS Payload Community in the molecular deposition of a contaminant onto sensitive payload optics and other components.

Contamination is a process where material is transported from one location to another. It is very important to understand the inherent dichotomy of this process when your concerns are centered towards maximum life-expectancy and operational effectiveness of a payload. Outgassing characteristics of materials alone does not predispose the event of a critical surface contamination event. Outgassing is a potential source of contamination in the form of deposition and molecular column density. Outgassing species must, in fact deposit on a surface for contamination to occur. As a payload designer, your objectives are to either minimize (or eliminate) the quantity of source materials or to physically block the critical surface from the source material so it cannot re-deposit via scattering, direct path or return flux mechanisms.

THE STS 45 SPARK

An observation was made during the STS-45 Mission in which the SSBUV payload experienced optical degradation (optical reflectance measurements shorter than 250 nm) due to molecular contamination in the interior instrument package, specifically the surface of the diffuser and depolarizer optics (1 & 2). This contamination was subsequently identified, in quantitative perspective, to be primarily aliphatic hydrocarbons, esters and dimethyl silicones (3 & 4). The exact source of the contaminants are as yet unknown, and quite possibly, may never be determined. Analysis at KSC (and at BASG) indicate that the overwhelming contaminant, around 50% of most samples, is hydrocarbons. These materials can be found in the composite make-up of the orbiter and are generally introduced during ground processing. They can also be found in the materials composition of almost every payload and/or introduced during payload processing. Hydrocarbon contamination is certainly ubiquitous.

To understand and identify the possible mechanism and source of the STS-45 SSBUV contamination event, the SSBUV instrument was sent to BASG for examination. Surface samples, taken with wipers composed of 45% polyester and 55% cellulose, dampened with a mixture of methyl chloroform and ethanol, showed a general pattern of largely aliphatic hydrocarbon oils, mixed esters, including aromatic substituted esters (such as Benzoflex 50), phthalate plasticizers, and dimethyl silicones. (3) Interior surfaces revealed NVR values ranging from 0.02 to 0.50 mg/0.1m^2 and 0. 18 to 1.6 mg/0.1m^2 on exterior surfaces. Likewise, samples of STS 45 PLB (bay 9 liner) and a ATLAS Igloo flight MLI blanket samples were also sent to BASG for evaluation. These results are shown below and reflect total mass deposition, i.e., NVR and particlulate.

Sample	NVR, mg 0.1m^2	IR Analysis
Bay 9 liner, front	0.9	HC, nitrate, ester/amide and 10% MP silicone
Bay 9 liner, back	0.8	MP silicone and 5% ester
Bay 9 liner, front	0.6	HC, ester and about 10% MP Silicone
Bay 9 liner, back	1.3	MP silicone and about 5% ester
ATLAS Igloo MLI blanket	4.4	MP silicone and 10- 15% amide/esters

Qualitative analysis did not identify the presence of a benzoate-like contaminant or methyl silicones. In fact as shown in this report, an aromatic-substituted ester, like benzoate, was not found in any of the PLB or Payload wipe or rinse samples on 8 STS missions.

BACKGROUND

In an effort to minimize the molecular off-gassing of materials selected for the space environment, NASA has imposed off-gassing specifications for the orbiter and payloads. This initial screening process provides an effective first measure in the minimization of molecular deposition onto payload surfaces.

Beyond this careful materials selection process, there are other parameters to consider when your goal is to achieve specific cleanliness levels on a payload. Some of these parameters involve ground-induced contamination onto payloads and orbiter surfaces, payload element self/cross contamination, orbiter in-flight orientations and operations, payload dynamics and payload design considerations including material source selection and vent paths pointed normal to the direction of motion and to critical surfaces. Many of these parameters can associate synergistically to induce the observed contamination.

In addition to the materials selection criteria, NASA has also imposed facility (ground processing) NVR deposition rates of 1.0 mg/0.1m^2/month (about 1100 ng /cm^2/ month) in the Orbiter Processing Facility (OPF) high bays and Payload Changeout Rooms (PCR) at launch pads 39A & B. Facility NVR data for the OPF high bays and PCR shows an average rate of 0.22 mg/0. 1 m^2/mo. for the OPF high bays and 0.30 mg/0. 1 m^2/mo. in the PCR's. Reference Table 1. Payload-sponsored pre-flight ground contamination measurements of the IOCM payload were performed at PAD A during STS-44 processing. A "Remove Before Flight Cover" was evaluated for NVR and showed a rate of about 0.16 mg/0.1 m^2/mo. The NVR was identified as an aliphatic hydrocarbon. (5)

Several Contamination Control Technical Interchange Meetings (TIM) were held at KSC and JSC to discuss the SSBUV experience. While lively discussions were held and pertinent data presented, a consensus to the cause and subsequent corrective action was not reached. In pursuit of an answer and to protect future SSBUV objectives, action items were assigned and new procedures/methods to monitor and control contamination were suggested. This report presents part of that follow-up endeavor and consolidates two different tasks, both supported by the Contamination Control Working Group chaired by NASA Headquarters Code Q, with complementary objectives. Our goals in performing these tasks were to evaluate the quantitative and qualitative impact of STS NVR.

The first task was authorized by KSAR KS0083 and implements PLB surface wipes of 6 STS missions on three different orbiters and includes both pre-flight and post-flight measurements. While all samples were evaluated quantitatively, only significant residues, i.e., >0.1 mg/0.1 m^2, were assessed qualitatively. Task discipline was documented in the *Payload Bay NVR Assessment Plan*, written by Contamination Control Engineering, Materials and Processes, Lockheed Martin Space Operations, dated January 1993. The plan presented basic instructions for both sampling and analysis protocol.

The second task involved a rinse and vacuum method, developed by Ball Aerospace, Boulder, CO., to determine surface NVR. This technique was used very successfully and has several advantages over the wiper technique. The NVR assessment by solvent rinse was requested by the SSBUV Program Office and authorized by OMRSD requirements for SSBUV Program flights, STS Missions 56, 62 and 66. The SSBUV NVR rinse assessment also sampled payload surfaces in addition to PLB surfaces.

In addition to both a quantitative and qualitative assessment, other mission parameters are also presented to ascertain any consequential influences; i.e., flight orbital attitudes and orientation, mission cleanliness levels and ground induced NVR rates. Reference table 2.

Mission Profiles & NVR Results

PLB Cleanliness Levels & Facility NVR

STS	OV & Flight	Mission Dates	PLB Clean Level	Facility NVR(2)		Event	PLB Wiper Non-Painted Surfaces (3)	PLB Rinse All Samples (4)	PL Rinse Results All Samples (4)
56	103/16	4/08-17 93	Standard (1)	OPF	0.25	Pre	0.18	0.69	1.08
				PCR	0.15	Post	0.29	0.50	0.45
55	102/14	4/26 - 5/06/93	Standard	OPF	0.44	Pre	0.32	NA (6)	NA (6)
				PCR	0.78	Post	0.17	NA	NA
57	105/4	6/21 - 7/01/93	Standard	OPF	0.34	Pre	0.10	NA	NA
				PCR	<01	Post	0.10	NA	NA
51	103/17	9/12-22 93	Standard	OPF	0.13	Pre	0.26	NA	NA
				PCR	<01	Post	0.10	NA	NA
58	102/15	10/18-11/01/93	Standard	OPF	0.16	Pre	0.10	NA	NA
				PCR	0.17	Post	0.10	NA	NA
61	105/5	12/2-13/93	Highly Sensitive	OPF	0.13	Pre	0.19	NA	NA
				PCR	0.21	Post	0.10	NA	NA
62	102/16	3/4-18/94	Standard (1)	OPF	<0.1	Pre	NA (5)	0.95	0.89
				PCR	<0-1	Post	NA	0.50	0.61
66	104/13	11/3-14/94	Standard	OPF	0.21	Pre	NA	0.78	0.95
				PCR	0.76	Post	NA	0.55	0.27
Avg				OPF	0.22	Pre	0.19	0.81	0.97
				PCR	0.30	Post	0.14	0.52	0.44

1 Although this mission was processed as a Standard cleanliness level, a complete PLB vacuum and solvent wipedown was performed as an optional service. Surface cleanliness was evaluated at the Standard Level.

2 These are mission event flow values; the facility values were correlated with the same dates that the orbiter was present in the facility (OPF and PCR). As a rule of thumb, the orbiter was in residence in the OPF for approximately 3 months while length of residence in the PCR was 1 month. Units are mg/0.1 m^2/mo.

3 Refer to tables 4 & 5 for further information. Units are mg/0.1 m^2

4 Refer to tables 6 & 7 for further information. Units are mg/0.1 m^2

5 Wipe sampling was not performed for STS missions 62 and 66

6 Rinse sampling was not performed for STS missions 55, 57, 51, 58 or 61

TABLE 1

Mission Profiles & NVR Results

Atomic Oxygen & UV Influences On PLB Contamination

STS #	Alt	Velocity Vector @ 10 deg (1)	Velocity Vector @ 70 deg (2)	Sun Exposure (3)	Event	PLB Wiper Non-painted Surface (4)	PLB Rinse All Samples (5)	PL Rinse All Samples (5)	Relative AO Exposure (6)	Relative UV Exposure (6)	AO & UV Overall Relative Aggressive-ness (7)
56	160	4	24	51	Pre Post	0.18 0.29	0.69 0.50	1.08 0.45	6	6	6
55	160	4	56	35	Pre Post	0.32 0.17	NA (9) NA	NA (9) NA	4	8	7
57	250	5	33	86	Pre Post	0.10 0.10	NA NA	NA NA	7	1	5
51	160	45	59	53	Pre Post	0.26 0.10	NA NA	NA NA	1	5	3
58	153	16	18	67	Pre Post	0.10 0.10	NA NA	NA NA	3	3	2
61	310	4	16	42	Pre Post	0.19 0.10	NA NA	NA NA	8	7	8
62	160	33	44	64	Pre Post	NA(8) NA	0.95 0.50	0.89 0.61	2	4	1
66	164	4	32	82	Pre Post	NA NA	0.78 0.55	0.95 0.27	5	2	4

1 & 2 Velocity vector line-of-sight durations (hours) are computed for 10-degree and 70-degree half-cone angles about the Orbiter -Z body axis.

3 Sun exposure durations (hours) are defined whenever the Sun rises above the Orbiter X-Y plane.

4 Refer to table 4 for further information. Units are mg/0.1 m^2

5 Refer to table 6 for further information. Units are mg/0.1 m^2

6 The numerical value represents the relative (to the other missions) placement of that mission to the severity (ranked where 1 is most severe and 8 is least severe) of AO or UV exposure.

7 The lower the value the more severe are the expected synergistic "consequences" of AO and UV.

8 Wipe sampling was not performed for STS missions 62 and 66

9 Rinse sampling was not performed for STS missions 55, 57, 51, 58 or 61

TABLE 2

TEST METHODOLOGY

Wiper Analysis & Sampling

The technique used in this study is a modified draft-ASTM procedure adapted to the specific requirements of this task. The procedure is described in KSCWA-01 and titled " Standard Method for Determination of NVR from Clean Room Wipes". A brief summary of the method follows.

Certified (soxhlet extracted with IPA and then sonically-agitated with 3/1 TCE/EtOH) polyester wipers are used to take wipe samples of selected surfaces. After sampling, each individual wiper is immersed in 100 mls 3/1 TCE/EtOH and ultrasonically agitated. The solute is then vacuum filtered and allowed to evaporate to a low volume at ambient temperature in a HEPA filtered hood. The remaining solute is then placed in an oven at 35 degrees Celsius for 30 minutes. (Several low volume rinses are performed during the filtration and transfer steps). The residue is then weighed and reported as mg/0.1 m^2. To ensure the most complete recovery of NVR obtainable, multiple extraction's were performed until the extraction process yielded less than or equal to the initial certified value of the wiper. In order to establish a methodology background level, eight blank wipers (pre-cleaned) were submitted for quantitative analysis. All eight wipers reported results of 0.01 mg or less per wiper *(6)*. An analytical balance with a 0.01 mg readability was used. Therefore, the limits of detection were established at 0.1 mg/wiper, taking into account any uncertainty in the fifth decimal place. Upon completion of the gravimetric analysis, the residue was sent to the NASA Microchemical Analysis Laboratory (KSC) for qualitative assessment.

Orbiter sampling was performed using polyethylene gloves and certified TCE/EtOH solvent dispensed from a certified 250 ml teflon flip-top bottle. Wipers were stored/packaged in aluminum foil. To match pre-flight and post flight sample locations, coordinates and photographs were taken. The wipers were lightly dampened with certified solvent and then used to uniformly wipe a known area. The wiper was then folded, with wiped surface folded inward, and placed in an aluminum foil wrap for transportation to the lab. Figure 1 shows the wiper technique during STS 51 operations at PAD B.

Rinse Analysis and Sampling

Using pre-certified equipment and materials, IPA is dispensed onto the target surface and then retrieved into a vacuum powered stainless steel sampler. The intent is to apply the rinse solvent until 50 mls of solvent is recovered over approximately a 0.05 m^2 surface area. Experimentation has shown that it takes 60-80 mls of applied solvent to collect the required 50 mls. After sampling, the NVR samplers were taken to the NASA Microchemical Analysis Laboratory. For each sampler, the retrieved solvent is poured from the sampler into a pre-certified, numbered beaker. The sampler is rinsed out with approximately 20 mls of certified IPA and added to the beaker. The beaker is then placed on a hot plate (100 +/- 5 degrees Celsius) and allowed to evaporate to approximately 1 ml. A pre-certified weighing mirror (3/8 " X 1" stainless steel) is then removed from a desiccator, weighed (to 5 places) and placed on a second hot plate maintained at 60 degrees Celsius. The solute in the beaker is then quantitatively transferred to the mirror on the second hot plate.

The beaker is rinsed with approximately 1 ml of IPA and added to the mirror surface. The mirror is placed back onto the first hot plate for 5 minutes at 100 degrees Celsius and then into the desiccator for 15 minutes minimum, prior to weighing. After weighing, IR analysis is performed on the residue directly from the mirror surface. This technique uses reflection-absorption spectrometry (a double pass through a thin film on a reflective metallic surface) on a stainless steel coupon for assessing both qualitative and quantitative infrared data of molecular contamination. (7) Sampling technique differences are shown in Table 3. Figure 2 shows the rinse technique during STS 56 operations in OV-103, OPF high bay III.



Figure 1- Wiper Samples Being Taken During STS 51 Operations

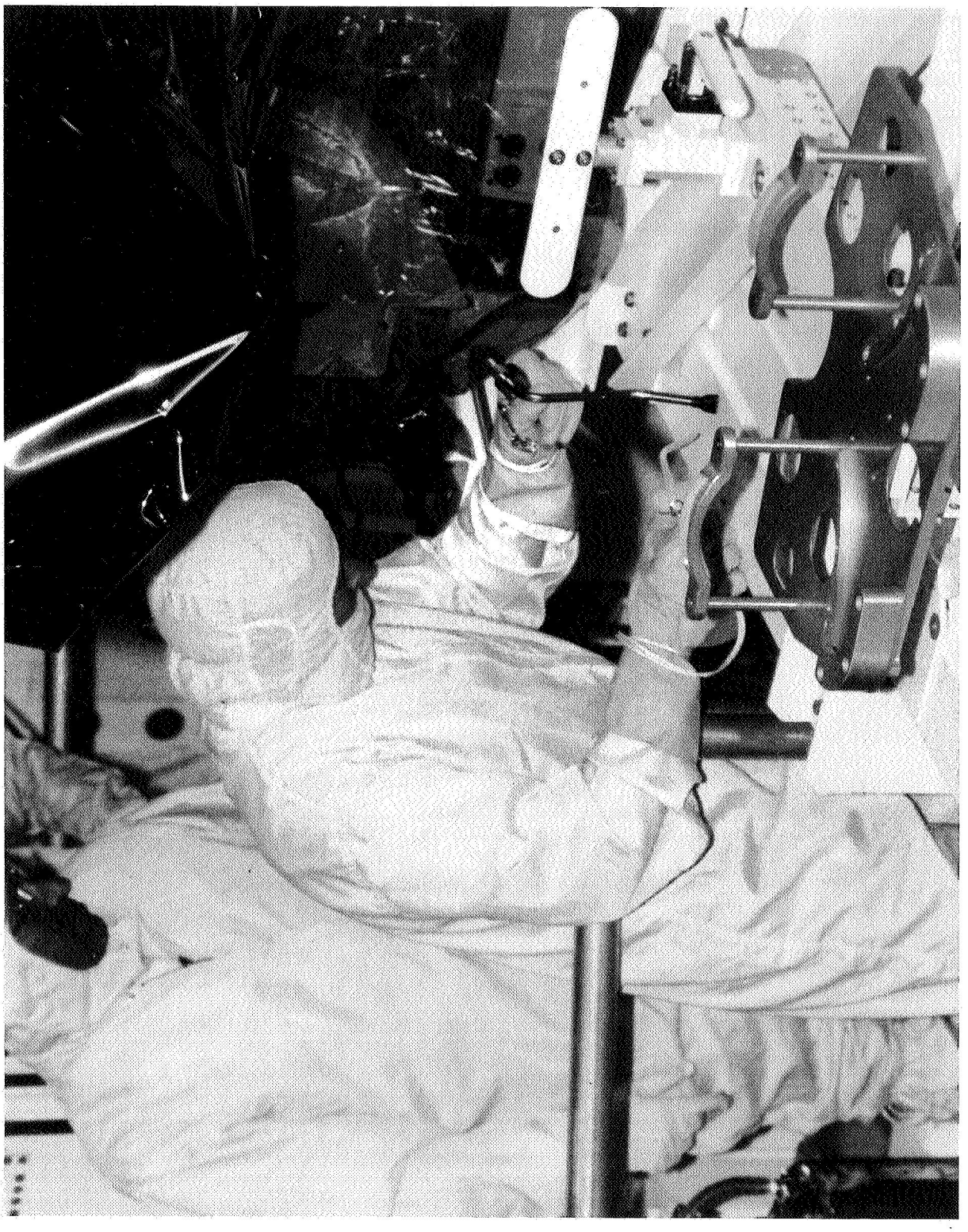


Figure 2 - Rinse Samples Being Taken During STS 56 Operations

Characteristic	Wiper Technique	Rinse Technique
Solvent System	TCE/EtOH	IPA
Filtration	Yes	No
Transfer Media	Polyester Wiper	None
Solvent Evaporation Temperature	Ambient/35C	100C/60C

Characteristics of Sampling Techniques

TABLE 3

PAYLOAD BAY CLEANING

During OPF orbiter processing, a time period of about 65-90 days, the PLB is vacuumed about every 3 days. Solvent wiping is minimal and performed if vacuum techniques are not successful in removing an observed contaminant.

For STANDARD Level missions, the closeout PLB cleaning operations involve an inspection at 5-10 feet with an approximate illumination level of 50 ft-candles. This inspection also occurs (in the appropriate area) if a payload is installed during the OPF processing flow. If contamination is observed under these conditions, vacuuming, and solvent wiping, if required, is performed. The solvent system used is 75/25 IPA/DI water. This procedure was implemented on STS missions 55, 57, 51 and 58.

For HIGHLY SENSITIVE Level missions, the closeout PLB cleaning operations involve a thorough PLB vacuuming and solvent wipedown of all accessible surfaces at a distance of 6-18 inches with an approximate illumination level of 100 ft-candles. (PLB areas are cleaned incrementally if payload installations occur during the OPF processing flow). Normally, the solvent system used is also 75/25 IPA/DI water. This procedure was performed at the PCR for STS-61.

Additionally, a modified Standard cleaning process was performed in the OPF for STS-61 including a UV light inspection. The UV evaluation showed nominal results. For STS missions 56, 62 and 66, the inspection criteria was STANDARD but cleaning protocol was performed according to Highly Sensitive requirements. Also, the solvent system used was 60/40 IPA/freon, a more aggressive solvent for organic/silicone contaminants.

RESULTS AND DISCUSSION

The data presented in this study were taken directly from NASA and BASG analysis reports and reformatted for presentation. The raw data presentation is extensive with detail showing results of each mission and not included in this paper. The data is available upon request and can be obtained by contacting the author.

Sampling Methodologies

Due to the inherent differences between the two sampling methodologies, an examination and interpretation of the results should include unique considerations of each method.

The rinse technique was intrusive to TCS blankets and PLB liner, the wiper technique was not. This was observed with the rinse and vacuum extraction of intrinsic phenyl methyl (PM) silicone from the TCS beta cloth materials. PM silicone was not found in any of the wiper sampling results. The wiper technique proved to be a better method for the discovery of surface contaminants on porous substrates without sub-surface material matrix complications. In this situation, the solvent stream and vacuum action used in the rinse method was sufficient to penetrate the teflon-coated TCS surface into the fibrous substrate and extract the inherent phenyl methyl silicone.

The solvent systems used were different and consequently targeted materials and contaminants with varying degrees of solvency. The wiper solvent (TCE/EtOH) was more aggressive toward silicones than the rinse solvent (IPA) chosen by Ball Aerospace. IPA is most effective at removing surface contamination without getting gross interference from the inherent beta-cloth MP silicone.

The wiper solvent was also more aggressive toward urethanes as evident in the results of the painted-surface samples. However, the TCE/EtOH solvent was still considered acceptable for the wiper technique since FTIR analysis is capable of detecting both functionality's in a single spectrum. Signature absorption peaks for silicones are defined at 1265, 1080, 1024 and 800 reciprocal centimeters, representing the interaction of silicon with the methyl groups and oxygen. Aromatic silicones are characterized by aromatic peaks around 3000 reciprocal centimeters. A reference urethane paint was used as a baseline for the presence of urethane, which gave characteristic peaks at around 1730, 1660 and 1560 reciprocal centimeters. It is noted that at higher levels of NVR (for example, in the wiper samples of STS-56), the urethane presence could mask trace amounts of silicones. However, at lower NVR's and minor amounts of silicone (as seen in STS 61), silicone was detected.

The background contaminant characteristics of the rinse technique proved to be "cleaner" than in the wiper technique. This is mostly due to the intermediate use of the polyester wiper in taking the wipe samples. While additional contaminants were introduced as an intrinsic component of the wiper technique, the background levels were very low, i.e., the average background NVR value for the prepared wipers was 0.14 mg/100 mls. In accordance to the analysis procedure, a wiper was pre-cleaned to a NVR level of less than 0.3 mg/100 mls or approximately 3 ppm prior to use. Further, upon receipt of the wiper after taking a PLB sample, the NVR extraction process was repeated until a single extraction event yielded < 0.3 mg/l00 mls. This technique returned us to approximately the NVR baseline of the wiper. The results of each extraction were added until this end point requirement was reached and became our NVR yield for that sample.

Another difference between the two sampling methodologies is found in the analytical approach for acquiring the mass residue. The wiper solute is filtered whereas the rinse solute is not. In almost all cases, the actual NVR reported in the Ball rinse reports includes both NVR and particulate.

Several sampling events showed significant particulate percentages approaching 50% of the reported NVR. While this revelation introduces another contaminant source not specifically addressed in this report i.e., particulate contamination, it does tend to lesson the impact of the reported NVR rinse values and provides an inflated (worse case) contaminant condition.

Wiper Results

This study is a measure of surface NVR, and more specifically, NVR which has achieved physical and chemical separation from its initial state and origin through elevated temperature and/or pressure differentials to molecularly condense onto another surface. Successful extraction techniques in which intrinsic material is pulled by contact transfer is not considered valid NVR of significance. For the wiper technique, the non-painted surfaces were shown to be a more reliable source to determine vapor-deposited NVR. These data reveal NVR amounts well within the STS Program maximum target value of 1.0 mg/0.1 m^2. As shown in table 4, the average value for all 6 missions was 0.19 mg/0.1 m^2 at pre-flight and 0.14 mg/0.1 m^2 at post-flight. These values indicate a 1) relative insignificance between pre and post flight sampling events and from the techniques background value of approximately 0.1 mg/0.1 ^{m2} and 2) supporting evidence of a relatively benign Low Earth Orbit (LEO) NVR contamination environment.

Payload Bay Wipe Samples
Quantitative Results Summary
Average Values (mg/0.1 m^2)

Mission/Orbiter	Pre-Flight		Post-Flight	
	All Samples	Non-Painted Samples	All Samples	Non-Painted Samples
57/105	1.29	0.10	0.13	<0.10
61/105	0.76	0.19	<0.10	<0.10
56/103	2.16	0.18	0.65	0.29
51/103	2.62	0.26	<0.10	<0.10
55/102	2.24	0.32	1.04	0.17
58/102	0.45	<0.10	<0.10	<0.10
Average	1.59	0.19	0.35	0.14
% Difference (1)			78% Decrease	26% Decrease

1. This value represents the average percent difference between the pre-flight NVR value and the post-flight NVR value.

TABLE 4

In reviewing the qualitative data of all 6 missions, the only silicone found was a dimethyl silicone contaminant seen intermittently during the pre-flight phase of STS-61 processing. The silicone was found to be in trace amounts and the least significant species in each of the 4 STS-61 samples. R. Manning also mentions a methyl silicone in the rinse results for STS-56 on painted PLB surfaces. A composite analysis presentation of contaminants and likely sources are shown in table 5.

Payload Bay
Wiper Samples
Qualitative Results Summary

Residue	Mission Discovered	Possible Source
Polyester	57, 61, 56, 51, 55, 58	Wiper
DOP	57, 5 1	Wiper
Urethane	57,61,56,51,55,58	Paint
Olefin	57, 61, 56, 55,58	Polyethylene gloves
Silicone, dimethyl	61 (pre-flight)	Unknown
Olefin	61	Polyethylene Squeeze Bottle
Hydrocarbon (HC)	61, 56, 51, 58	Unknown
Soap, Stearate	56, 55, 58	Unknown
Alkyd resin	51, 55	Wiper
Nitrate	57, 61, 55, 58	Unknown

1. Urethane was an overwhelming component of almost all painted surface samples.
2. Polyester, DOP and alkyd resins were components originating from the wipers.
3. The olemide and olefins were also components found in background samples in trace amounts.
4. The remaining contaminants were found in very small (trace) quantities and were present occasionally.

TABLE 5

While the urethane component was the dominant NVR species (originating from the PLB painted surfaces; Chemglaze A276), many of the other "contaminants" included chemical functionality's also found in the blanks. Those contaminants outstanding are nitrates in STS 55, 5 7, 5 8 and 61, and a stearate-type soap in STS 55, 56 and 58. Generally, stearic acid (and their derivatives) lead all other fatty acids in industrial use, primarily as a dispersing agent and accelerator activator in rubber products and in soaps. Even though these contaminants were identified, they were found in trace amounts, probably less than 0. 1 mg/0.1 m^2. Present in almost all mission sample sets was the omnipresent HC and ester. Together with the hydrocarbons, the ubiquitous ester functionality, (especially the phthalates), are transferred from the air, packaging materials, manufacturing or even from impure cleaning solutions.

Except for the STS-56 forward bulkhead result, all TCS samples were less than 0.32 mg/0.1 m^2 with an average value of 0. 17 mg/0.1 m^2. Within this data set, all contaminants observed were also seen in the background samples. The STS-56 pre-flight forward bulkhead TCS NVR was 1.86 mg/0.1 m^2 and identified as DOP. The validity of this result as a likely PLB surface contaminant is questionable because of its unique and solitary occurrence.

There is evidence that the ester is also found in the background (wiper) and most importantly, a rinse sample taken on an adjacent TCS blanket did not reveal evidence of any phthalate ester.

The German D-2 payload flown on STS-55 revealed several contamination problems, discovered during pre-flight operations. Reference NASA test reports MCB 0150-93 and MCB 0210-93. These analysis, requested by the payload, showed a possible epoxy resin on the Gauss camera star sensor lens and a dimethyl silicone on the Gauss camera convex mirror. Subsequently, additional sampling was performed at PAD A of several D-2 face panels revealing significant amounts of a dimethyl silicone, hydrocarbons and an amide. Reference MCB 0261-93. In addition, PLB surfaces were also sampled. These results did not show any silicone materials or any other contaminant beyond the background NVR of the technique.

Rinse Results

On the average mission, as determined by this study and collaborated by the wipe sample results, the corrected pre-flight and post-flight PLB/Payload rinse samples were found to be all less than 1.0 mg/0.1m^2 . Reference table 6. The background NVR levels for the rinse method were <0.3 mg/100 mls for STS-56 sampling and < 0.1 mg/100 mls for STS missions 62 and 66. The rinse data results are formally documented in Ball Aerospace Memo's V3020 93.129 for STS 56, V3020 94.100 for STS 62 and V3020 95.129 for STS 66.

Rinse Samples

Qualitative Results Summary

Payload

Residue	Mission	Possible Source
HC (Aliphatic)	56, 62, 66	Unknown
Soap, organic acid salt	56 (Multiple Payloads)	Unknown
Ester (include. Phthalate)	56, 62, 66	Handling Contaminants
Amide?	56, 62, 66	Handling Contaminants
Polyether	66 (SSBUV)	Unknown
Urethane	56, 62, 66	Paint
Nitrate	56, 66 (SSBUV)	Unknown
Methyl Phenyl Silicone	56, 62, 66	Insulation Blankets, TCS
(Dimethyl ?) Silicone	66 (ERPCL)	Unknown

Payload Bay

Residue	Mission	Possible Source
Hydrocarbons	56, 62, 66	Unknown
Ester (include acetate)	56, 62, 66	Unknown, possibly Beta-cloth
Soap, organic acid	56	Unknown
Dimethyl Silicone	56	Unknown
Amide	56, 62,66	
Nitrate	56, 62	Unknown
Urethane	56, 62, 66	Paint
Polyether	62	Braycote 601, Icephobic coating for PLB Door seal
Methyl Phenyl Silicone	56, 62, 66	Insulation Blankets, TCS

TABLE 6

FTIR identification of the rinse residues for all 3 missions, i.e. STS-56, 62 and 66, showed more similarities than differences, with the predominant contaminants (excluding paint) consisting of hydrocarbon oil, mixed amides and esters - all common atmospheric contaminants. Other intermittent contaminants, found in trace quantities and in the wiper analysis, were nitrates and acid salts. Some contaminants were unique to a particular mission, e.g., the hand-type soap on STS 56 and the alkyd on OAST in STS 62. Reference table 7.

Rinse Samples
Payloads & Payload Bay
Quantitative results Summary
Average Values (mg/0.1m^2)

	Pre-Flight				Post-Flight			
Mission & Orbiter	**Payload All Samples**	**Payload Non-Painted Samples**	**PLB All Samples**	**PLB Non-Painted Samples**	**Payload All Samples**	**Payload Non-Painted Samples**	**PLB All Samples**	**PLB Non-Painted Samples**
56/103	1.08	0.40	0.69	0.68	0.45	0.32	0.50	0.41
% Difference					58% Decrease	20% Decrease	28% Decrease	40% Decrease
62/102	0.89	0.73	0.95	1.02	0.61	0.55	0.50	0.29
% Difference					31% Decrease	25% Decrease	47% Decrease	72% Decrease
66/104 (Include. ITEPC) (2)	0.95 1.63	0.85 1.61	0.78	0.48	0.27 0.31	0.27 0.32	0.55	0.28
% Difference					72% Decrease	68% Decrease	29% Decrease	42% Decrease
Average	**0.97**	**0.66**	**0.81**	**0.73**	**0.44**	**0.38**	**0.52**	**0.33**
% Difference					55% Decrease	42% Decrease	36% Decrease	55% Decrease

1. This value describes the percent difference between the pre-flight value and the post-flight value.

2. The ITEPC NVR value was significantly higher, i.e., 7.74 mg, than the other samples. This data point was discarded in determining mission averages.

TABLE 7

The only silicones actually identified were the MP silicones removed from the TCS, an intrinsic component and expected response due to the extraction method used, a dimethyl silicone on STS-56 PLB surfaces and a methyl silicone on the STS 66 ERPCL payload. Rinse samples also show surface particles not discernible with the wipe method results. External SSBUV NVR's were consistently lower than the overall average and are considered more accurate than the average sample since they contained no background contribution from paint or oil.

The shuttle PLB environment always proved to be at or below acceptable limits, i.e., < 1.0 mg/0.1 m^2, with most NVR levels on both payload and PLB surfaces improving as a result of flight.

STS-56 Rinse Highlights

Particulate contamination was significant, with some portion of the weight of each sample due to lint and dust particles. The exception was the SSBUV instrument samples which contained very few particles. The SSBUV modules were kept covered with llumalloy plastic film during open- bay operations. The SSBUV post-flight samples were also the lowest in weight (0.16-0.24 mg/0.1m^2) of all the samples. The exterior residues were common in composition with the general orbiter bay contamination. No contamination was detected above the paint background from either the pre- or post flight door interior samples. The prevailing composition of the contaminants; e.g., paraffinic HC oil, soap, and esters, are common except for perhaps the soap. Only traces of silicone were observed, and seemed to be limited to bay samples, i.e., longeron sils and the radiator (adhesive type). Remember that none of the wiper samples showed the presence of silicones, even though the TCE/EtOH solvent is more aggressive towards silicone than IPA. (It is also important to remember that if silicones were present in the wiper samples in trace amounts, the urethane component could possibly mask the silicone characteristics). PLB samples did show trace methyl silicones in both the pre-flight and post-flight data sets taken from painted surfaces. There was only a slight decrease shift in NVR from pre to post flight with silicones still present in the post flight samples. Evidently, the LEO environment was not able to totally oxidize/polymerize the silicone. The surfaces remained virtually unchanged.

As part of the SSBUV pre-flight preparations protocol, a contamination bake-out (10 days at 80 degrees C at 1.0 X 10^{-7} torr) procedure is performed. Reference GSFC procedure TP 41019.001. During the bake-out of some of the SSBUV components, a 25 square foot section of beta-cloth liner material was also included. (8) The chamber was monitored using TQCM's and cold fingers for analysis of offgassed materials. Quantitative analysis showed 0.3 mg of condensed material and FTIR analysis indicated hydrocarbons and dimethyl silicone. (The results didn't reveal phenyl methyl silicone, an intrinsic component of the liner material).

STS 62 Rinse Highlights

Most of the contamination found was identified as consisting of hydrocarbon oil, esters and amides and showed a general improvement from pre-flight to post-flight. Exceptions were 1) SSBUV and 2) LDCE. The SSBUV increase is not surprising since the pre-flight samples were so low, i.e., 0.08 mg/0.1 m^2. The LDCE increase is due primarily to the extraction of more MP silicone from the TCS fabric.

A significant portion of the weight increase in the post-flight samples was due to particulates, primarily cellulose, glass fibers and then particles. When corrected for background and particulates, the post-flight PLB and Payload rinse samples would probably decrease by 25 %-50%. The majority of the particulate consisted of cellulose (cotton type) fibers and glass fiber fragments from TCS materials.

Of particular interest in this test group was the sampling of the RMS blanket surface. (Reference NASA test reports MCB 0157-94, MCB 0167-94 and MCB 0226-94). Even though this finding does not directly impact the assessment of PLB NVR, it has some significance in the overall measure of PLB contamination. Significantly higher levels of particulate were seen in the RMS rinse samples and a concern was raised about the possible degradation of RMS TCS material over time. Subsequent sampling of new RMS blanket material revealed slightly increased levels of contamination, both NVR and fibers. Reference PR RMS-301 -AOOO5.

The RMS blanket material appears to be a lower grade of material, i.e., EDS analysis showed major silicon and calcium with minor aluminum, a composition different than that used in PLB TCS blankets and liner. These results seem to suggest that the flown RMS blankets are not degrading with age or use as originally thought and further, the RMS blanket material appears to "clean-up" after each flight.

STS-66 Rinse Highlights

Again, there was a general improvement of the post-flight over the pre-flight samples. Most of the contaminants were identified as primarily hydrocarbon oil and esters. The particulates were largely natural and synthetic lint, and glass fibers. Since a possibility of optics degradation existed, (the transfer mirror on the inside of the SSBUV canister door became contaminated with a visible fog) as a result of the SSBUV's instrument door being left in the open position during the last portion of flight, the instrument was routed to Ball Aerospace for evaluation. Several tests were performed consisting of solvent rinses of the instrument exterior, the internal baffle, the diffuser plate and the transfer (collimating) mirror. NVR values ranged from 0.09 mg/0.1m^2 (electrometer cover) to 1.3 mg 0.1 m^2 (diffuser plate); the diffuser plate result was extrapolated by a factor of 12 to account for the 12 in^2 surface area. The residues were identified as consisting primarily of hydrocarbon oil and grease, (e.g., Apiezon L), some esters and a methyl silicone.

The solvent rinse of the transfer mirror did not remove the visible (fog) film, whereas a 50/50 IPA/DI water rinse did. The IPA/water rinses were performed on several surfaces with (NVR) values ranging from 0.65 mg/0.1m^2 to 1.5 mg/0.1m^2. The residue from the transfer mirror was approximately 0.8 mg/0.1m^2 and appeared to be largely a mixture of nitrates and sulfates, as were the other samples. Possible sources of these contaminants are humid environments where the water soluble residues are carried in atmospheric moisture, especially if the hardware temperature falls below the dew point.

SSBUV hardware under went a post-flight analysis vacuum bake-out at an average pressure of about 3.0 X 10^{-6} torr, +95 degrees C for more than 24 hours. The results reported by G. Harvey (LaRC) describe a total estimated mass transfer to a scavenger plate of approximately 200 mg. The NVR on the scavenger plate was identified to consist of phthalates, hydrocarbons, and MP silicones. (9) For reference, pre-flight bake-out conditions, performed at GSFC, are 1 X 10^{-5} torr at 60 degrees C for 24 hours.

Ball also performed RGA, TQCM and NVR witness plate tests of the SSBUV instrument in Feb. '95. RGA results of the vacuum test, taken at room temperature, after several days at about 40 degrees C, showed only normal amounts of water, air and small amounts of hydrocarbons. TQCM results taken at the same time showed <1 Hz/hr/cm^2 change in accumulation. The chamber witness plate NVR results showed 0.05 mg/0.1m^2 (background) before the test, with 0.10 mg/0.1m^2 after the test, again, with both before and after samples consisting of HC oil, ester(s) and some silicone. Rinse samples have revealed problems with payload contamination levels pre-flight i.e., OAST on STS 62 and CRISTA-SPAS and ERPCL on STS 66. On these payloads, targeted cleaning was performed resulting in lower NVR (<1.0 mg/0.1 m^2) levels prior to flight.

GENERAL OBSERVATIONS

There was a general trend in decreasing NVR values from pre-flight to post-flight samples. For PLB surfaces, the wiper analysis showed an overall average pre-flight NVR of 1.59 mg/0.1 m^2 and 0.35 mg/0.1 m^2 for post-flight, a 78% decrease. Reference Table 4. These values are heavily influenced by the urethane (carbamate ester) component due to wiping painted surfaces. It was interesting to learn that while urethane was the major residue collected, a significant decrease (almost 80%) occurred from pre-flight to post-flight. This pattern repeated for each vehicle on consecutive flights and suggests an on-orbit hardening effect of the paint and a subsequent softening mechanism during ground processing. Possibly the urethane is hydroscopic enough to absorb water during ground processing and thereby leaching out a greater amount of urethane during the pre-flight sampling events. The explanation for this observation is unknown. When employing the wipe method, a more accurate representation of surface NVR are the non-painted, i.e., TCS materials. These values revealed a pre-flight average of 0.19 mg/0.1 m^2 and 0.14 mg/0.1 m^2 for post-flight, a 26% decrease.

The qualitative results from the wiper and rinse samples showed hydrocarbons and some ester functions, contaminants found normally in the orbiter processing environments. The presence of a dimethyl silicone in the pre-flight wipe sampling of STS-61 was found on 5 of the 9 samples taken. In each case, the relative amounts of this contaminant to other contaminants was very low and always the least significant. It's source is unknown. The post-flight wipe samples of the previous mission (STS-57) on the same vehicle (OV-105) did not show any evidence of the silicone. Like wise, the analysis of 3 post-flight STS-61 wipe samples did not reveal any silicone. The rinse analysis found occasional traces of dimethyl silicone in STS-56 pre-flight and post-flight. There was no indication of this contaminant in the wiper analysis for this mission in which a more aggressive silicone solvent was used. As previously discussed, the higher levels of urethane could possibly mask trace amounts of silicone.

Another contaminant seen in three of the six wiper-assessed STS missions was a soap, possibly a stearate (n-octadecanoic acid). R. Manning stated that the spectra, as also seen in the rinse assessment of STS-56, resembled that of a common bathroom hand soap. Except in STS 56 results, the soap was seen very sparsely in two other missions, i.e., STS 55 (a questionable identification in 2 pre-flight samples only) and STS 58 (seen in two samples, pre-flight and post-flight different locations). Missions STS 55 and 58 were on the same orbiter, OV- 102. For STS-56, the soap constituent was found on both payloads and PLB surfaces, both pre-flight and post-flight wipe and rinse samples. It is also interesting that S. Straka of Goddard mentions an organic acid residue in the post-flight thermal vacuum test of the EMP monitor (10), as does M. Anderson of JPL in a pre-flight molecular contamination survey of the WFPC 1 on STS-6 1. (11)

The remaining contaminant found were nitrates. There was no rhyme to their discovery, i.e., post-flight, pre-flight, PL or PLB surfaces - partly due to their insolubility in the solvents used. For PLB surfaces, the wiper-assessment identified nitrate in the consecutive flights of OV- 105 (STS-57 & 61) and OV-102 (STS-55 & 58). The rinse technique found nitrate on STS-56 & STS-62 PLB surfaces. Nitrates were also found on the STS-66 SSBUV transfer mirror and diffuser plate after rinsing with IPA and water at Ball. (In conjunction with the nitrates, sulfate hydrates were also found).

To better understand their role in the STS PLB environment, KSAR (KSC Special Action Requirement) KSO 109 was initiated to evaluate orbiter PLB surfaces for water soluble inorganic salts, i.e., nitrates and sulfates. This activity is a future action involving pre and post-flight evaluations of the STS-69,73,74 and 82 payload bays. The results of this study will be presented under separate cover.

Silicon Deposition - Payload Experiences

Several experimental silicon-containing polymers in film form were exposed to LEO on the STS 46 EIOM III payload. The silicon-containing films exhibited minimum AO erosion but the silicon near the exposed surface was converted to silicate/silicon oxide which subsequently provided protection for the underlying material. (12)

The Aerospace Corporation flew 82 samples on the EIOM-III payload and performed XPS analysis on 8 of the samples, both pre flight and post flight. Surface silicon concentration increased from 4 to 11 atom % post flight, with an average of 7 atom %. They conclude that the data indicates the possibility of non-uniform contaminant deposition from localized sources on the EIOM-III experiment or from the Shuttle. (13)

Additionally, coupons of Chemglaze A276 were flown on the STS-46 EIOM-III payload. XPS results indicate changes to the surface chemical composition where a 6.5 atom % increase of surface silicon was detected on the post-flight sample. Jaggers and Meshishnek attribute this increase to on-orbit contamination and to the surface exposure of an aluminum silicate filler/extender that is used in the Chemglaze paint system.

They conclude that silicones and/or silicates tend to be oxidized by AO to form silica, SiO_2 and that contaminated surfaces containing silicones which have been oxidized to silicates or silica are resistant to further erosion. Other flight coupons, including S13GLO, Z306 and aluminum, also experienced some degree of on-orbit silicon contamination as determined by XPS analysis. (14)

In consideration of this observed effect, if significant orbiter off-gassing of silicone-type materials occurs, it would be reasonable to assume that a hardened SiOx coating might form on PLB painted A-276 surfaces. Certainly, after multiple missions, a protective layer would form and, to some degree, isolate the urethane (in the paint) from removal via solvent wiping/rinsing. The cyclic response from the pre to post mission sampling on urethane removal efficiencies does not support significant silicon-hardening activity.

Another contamination experiment was performed on EIOM-III by MSFC where magnesium fluoride over-coated aluminum mirrors were flown as optical witness samples (OWS). The results showed no significant differences in reflectance, within experimental error, of any of the OWS mirrors. In fact, the authors stated that the molecular contamination levels were representative of the small levels of "adventitious" hydrocarbons found on all samples exposed to the atmosphere of conventional laboratories. (15)

While on-orbit silicone contamination does occur, as reported by numerous investigators (16), the deposition rates, as contributed by orbiter materials, are nominal. The orbiter outgassing transport mechanism necessary to effect significant payload/PLB contamination does not occur because of the long mean free path between the contaminant (exterior orbiter surfaces) and critical surface (in PLB). With an ambient density of 2×10^{8} species/cc at an altitude of approximately 160 nm and in the RAM condition, the fraction of high molecular weight molecules that return to the PLB is 1.0×10^{-2}. If the total TPS surface would have a total outgassing rate of 1×10^{-11} g/cm^2 sec, then the return flux for a forty hour exposure would be about 1 A. Additional evidence of relatively low levels of contamination on EIOM-III surfaces are substantiated by the measured reaction efficiencies of Kapton and other polymer films and the performance of the atomic oxygen monitors (AOM). The AOM consisted of an array of thin film carbon resistors which showed increasing resistance as the carbon is removed by O-atom reaction. The AOM's showed a constant or slightly increasing rate of resistance change throughout the EIOM-III ram period which would not be observed if a coating of SiO_2 were accumulating on the carbon resistor surfaces. (15 *&* 17*)*

Koontz, Leger, Rickman, Hakes, Bui, Hunton and Cross reported that a contaminant layer of less than 20 Angstroms, containing silicon, was found on EIOM-III surfaces and recognized an internal EIOM-III contamination source. (17) This same level of contamination was also reported by S. Chung of JPL. *(18)*

Another example suggesting that silicone, with subsequent conversion to SiOx, is not a ubiquitous molecular PLB contaminant is the sporadic occurrence of loosely-held titanium particles found on PLB painted surfaces after flight. In these instances AO is able to penetrate into the polyurethane paint, an action not easily performed in the presence of a glassy SiOx coating, erode the connective organic binder matrix and expose the Ti pigments. As a result, a white "dust" has been occasionally observed on PLB surfaces. This observation was seen on several post-flight PLB evaluations, e.g., STS 39,40,43 and 28R and has not been observed since STS 48, Sept. '91. (Although, this characteristic has not been specifically assessed for several years). This characteristic of the Chemglaze A276 paint system was also seen on the EIOM III payload.

Silicone Concerns - Orbiter

Beta-Cloth

Out-gassing tests performed on both types of Beta-cloth, Form F and Form GW, reveal acceptable results for space applications. Silicone containing compounds were not detected in the CVCM condensate. (19)

Sample	TML %	VCM %	WVR %
Form F	0.02	0.00	0.00
Form GW	0.02	0.01	0.00

TPS Waterproofing

DMES is a liquid with a vapor pressure of 283 torr at room temperature, so it vaporizes very quickly after injection. Many studies have been initiated to evaluate the propensity of DMES as a contaminant source. (20-23) All of these studies have shown that waterproofing the orbiter TPS materials generates concentration profiles that are too low to create contamination effects on spacecraft materials or optical surfaces. The IR and GC/MS data show that the outgassed products are mostly water with no trace of silicone compounds. DMES is chemically bound to the silica surface and is only removed, (decomposing to a depth of about 0.1 inches during the reentry process), with heat above a temperature of 1050 degrees F. Any consequence of this oxidation will not jeopardize the payload bay environment because the PLB doors are closed. (24) Thermogravimetric analysis was performed on shuttle tiles treated with DMES to ascertain any out-gassed materials. The presence of DMES was not detected in the test results and there were no detectable differences between the treated files and the untreated tiles. (25)

Further studies performed at NASA WSTF reported no off-gassing, as determined by TGA/FTIR, from DMES - injected files under standard CTVS test conditions. In addition, RGA data indicated that hydrocarbons were evolved but ion patterns typical of silicon-containing compounds were not observed. (26)

Sealant & Adhesives -RTV 560

A study was performed at MSFC to identify the outgassing rate for a Shuttle Baseline thermal protective surface (TPS) which utilizes RTV 560 adhesive. (27) While the initial outgassing rate of the TPS structure, with no initial bake-out procedure, was as high as 6.5×10^{-8} gm/cm^2/sec, the rate diminished to an asymptotic rate of 2.73×10^{-9} gm/cm^2/sec after 70 hours. For subsequent flights a steady-state rate of 1×10^{-9} gm/cm^2/sec is approached and maintained. Outgassing tests involving RTV 560 must also be performed in the configuration in which it is used. The total system must be evaluated, not individual components separately.

SUMMARY AND CONCLUSION

This study is the most comprehensive assessment of NVR ground measurements on orbiter PLB and mated payload surfaces to date. While orbiter NVR requirements are not established, our measurements have shown that NVR rates during a typical STS mission are well within the most stringent NVR requirements stated in SN-C-0005C and MIL-STD-1246, i.e., < 1.0 ug/cm^2. The data in this report reveals PLB mission values in the range of 0.19 to 0.40 ug/cm^2 for pre-flight and 0.14 to 0.20 ug/cm^2 for post-flight. The differences between pre and post could be extrapolated to suggest LEO NVR activity of little significance with a decreasing trend.

Qualitative analysis showed background levels of hydrocarbons and esters consistent with normal ambient influences.

Although the orbiter PLB is solvent cleaned to support contamination highly-sensitive missions, sensitive analysis techniques will undoubtedly discover trace evidence of environmentally ubiquitous substances. Payload surfaces are no different.

In evaluating this information, together with many other studies as referenced in this study, significant molecular contamination found on individual payloads is most likely self induced. The evidence suggests a localized source and re-deposition behavior rather than a widespread phenomena induced by the orbiters' TCS materials to create any significant payload contamination. Further reduction of NVR contamination could possibly be achieved by payload material design considerations and advertising of critical contamination limitations to effect more favorable manifest assignments, ground processing PLB cleaning upgrades and on-orbit avoidance maneuvers.

REFERENCES

1. Williams, Donald, SSBUV Experiment/Mission Manager, STS-56 Ground Operations Working Group, KSC, Contamination Discussion, July 21, 1992.

2. Hilsenrath, E., Williams, D., Instrument Contamination Working Group Meeting, JSC, Nov. 5&6,1992

3. Manning, Roland, Ball System Engineering Report No. SBUV-RM-92-701, Aug. 17, 1992

4. Manning, Roland, Ball System Engineering Report MEMO V302092.14 1, Sept. 16, 1992

5. Results of the Interim Operational Contamination Monitor (IOCM) as Flown on the STS-44 Mission, SAIC, Oct. 1992

6. Wiltech Analysis Reports; G-3844 through G-3851, analysis performed on 8/9/93.

7. Williams, M. K., and Manning, R.R., Fourier Transform Infrared (FTIR) Microanalysis of Shuttle Bay Molecular Contamination

8. Palou, J., Beta-Cloth Liner Analysis/Evaluation Report, NASA, KSC, Mar. 26, 1993

9. Harvey, G., Vacuum Bakeout and Cleanliness Certification of SSBUV Hardware, July 1995

10. EIOM-3 Environment Monitor Package, Presentation by S.A. Straka, Goddard Space Flight Center, STS/Payload Contamination Technical Interchange Meeting, August 17-18, 1993

11. Anderson, M., Wide Field Planetary Camera-1 Contamination & CCD Window Measles Investigation, Preliminary, JPL, HST Returned Hardware Proceedings, NASA/GSFC, Dec. 15,1994

12. Connell, J., Young, P., Kalil, C., Chang, A. and Siochi, E., The Effect of Low Earth Orbit Exposure on Some Experimental Fluorine and Silicon-Containing Polymers 18th Space Simulation Conference, NASA Conference Publication 3280, Oct. 31 - Nov. 3, 1994

13. Stuckey, W.,Hemminger, C., Steckel, G., Hills, M. and Hilton, M., Spacecraft Materials Studies on the Aerospace Corporation Tray on EIOM-III, Third Post-Retrieval Symposium, Nov. 8-12,1993, Williamsburg, Virginia, NASA Publication 3275

14. Jaggers, C. and Meshishnek, M., Exposure of LDEF Materials to Atomic Oxygen: Results of EIOM III, Third Post-Retrieval Symposium, Nov. 8-12, 1993 Williamsburg, Virginia, NASA Publication 3275

15. Linton, R., Vaughn, J., Finckenor, M., Kainenetzky, R., DeHaye, R. and Whitaker, A., Orbiter Atomic Oxygen Effects on Materials: An Overview of MSFC Experiments on the STS-46 EIOM-III, Third Post-Retrieval Symposium, Nov. 8-12, 1993, Willlamsburg, Virginia, NASA Publication 3275

16. Results of the Interim Operational Contamination Monitor (IOCM) as Flown on the STS 44 Mission, SAIC, Oct. 1992

17. Koontz, S., Leger, L., Rickman, S., Hakes, C., Bui, D., Hunton, D. and Cross, J., Evaluation of Oxygen Interactions with Materials III- Mission and Induced Environments, Third Post-Retrieval Symposium, Nov. 8-12, 1993, Williamsburg, Virginia, NASA Publication 3275

18. Chung, S., Brinza, D., Minton, T. and Liang, R., BMDO Materials Testing in the EIOM-III Experiment, JPL, Third Post-Retrieval Symposium, Nov. 8-12, 1993, Williamsburg, Virginia, NASA Publication 3275

19. NASA WSTF # 92-26584 and 85, October 29, 1992

20. Fowler, M., DMES Contamination of Spacecraft Materials, JSC Internal Report, 1992

21. Kamenetzky, R., DMES Investigation, MSFC Internal report 1993

22. Fowler, M., JSC 26296, A Study of DMES Effects on Optical Surfaces, 1992

23. Bartelson, D., Contamination Measurements in the Orbiter Payload Bay During OPF Processing Using the QWS Method, Lockheed Martin Space Operations, JSC Request No. J4298, Aug. 25, 1994

24. Fowler, M., DMES Outgassing From Orbiter Tiles, JSC Report JSC 26552

25. Correspondence from A. Montoya to J. Scialdone, GSFC Report #TA0083, Thermal Analysis of Shuttle Tiles Treated With Waterproofing Agent, November 2, 1993

26. Gillis, K.A., Shelly, T. J., Beeson, H., WSTF Reports 93-27821 through 93-27825, Jan 26, 1994

27. D.W. Jex and E.L. Shriver, MSFC, Huntsville Alabama, The Outgassing Rate For A Shuttle Thermal Protective Surface Using RTV 560 Adhesive

10P
52-14
02433

GSFC SPACE SIMULATION LABORATORY CONTAMINATION PHILOSOPHY: EFFICIENT SPACE SIMULATION CHAMBER CLEANING TECHNIQUES

069347
18P.

Juan A. Roman and George F. Stitt
Space Simulation Test Engineering Section
NASA Goddard Space Flight Center

Felix R. Roman, Ph. D.
Department of Chemistry
University of Puerto Rico, Mayaguez Campus

ABSTRACT

This paper will provide a general overview of the molecular contamination philosophy of the Space Simulation Test Engineering Section and how the National Aeronautics and Space Administration (NASA) Goddard Space Flight Center (GSFC) space simulation laboratory controls and maintains the cleanliness of all its facilities, thereby, minimizing down time between tests. It will also briefly cover the proper selection and safety precautions needed when using some chemical solvents for wiping, washing, or spraying thermal shrouds when molecular contaminants increase to unacceptable background levels.

INTRODUCTION

The Space Simulation Test Engineering Section at GSFC is responsible for the design and implementation of space simulation tests in order to produce simulations of vacuum, temperature, and solar environments required for the qualification of flight hardware at the component, subsystem, system, and spacecraft levels. Examples of these tests are thermal vacuum, thermal balance, and molecular outgassing tests. The section has 10 thermal vacuum chambers ranging in size from 0.6 m x 0.6 m (2 ft x 2 ft) up to approximately 8.2 m x 12.2 m (26 ft x 40 ft). Figures 1, 2, and 3 show pictures of several GSFC thermal vacuum chambers. Table 1 provides general facility capabilities.

The section is challenged to support the testing requirements of GSFC in-house and out-of-house flight projects. These projects can vary greatly in terms of molecular outgassing test (bakeout) requirements from sounding rockets, Hitchhikers, or Get Away Special (GAS) projects that have minimum outgassing requirements up to the Hubble Space Telescope (HST) which thus far has the most stringent outgassing requirements supported by the laboratory.

In order to effectively and efficiently support this wide range of customers, the section implemented a standard molecular outgassing criteria for all the thermal vacuum chambers. The first outgassing criterion for the vacuum chambers is an accretion rate for a 10 MHz

Thermoelectric Quartz Crystal Microbalance (TQCM) of 300 Hz/hr or less for three consecutive hours with its crystal at -20°C and the chamber shroud at 100 °C or its maximum operating temperature. This represents a mass loss of 4.2×10^{-7} g/hr or 133 Å for a unit density material (ref. 1). The second criterion is a nonvolatile residue (NVR) sample of 3.0×10^{-3} grams of residue with no unusual components for the last 8 hours of every test performed. This NVR or "cold finger" sample is collected using a small electroplated stainless steel cylinder with 142 cm^2 (22 in^2) of nominal surface area. These molecular outgassing criteria were established many years ago and have been very successful at keeping all the vacuum facilities at a uniform level and provides an acceptable compromise to the wide variety of customer needs.

During fiscal year (FY) 1996, a total of 392 tests totaling 42, 848 hours were performed in the Space Simulation Laboratory. They were comprised of 76 thermal vacuum/thermal balance tests, 103 normal bakeout tests, 115 outgassing certification tests in box with cold shrouds, and 98 chamber post test recertifications. Figure 4 shows the total hours per test facility and Table 2 shows test type per facility. This workload represents one of the busiest years for the laboratory.

OUTGASSING TESTS

Normal Bakeouts

The test activities in the laboratory are divided primarily into two major groups which are thermal vacuum testing and bakeouts. The bakeout group is subdivided into two types. The first one is the "normal" bakeout where the chamber shroud heats the test item and the TQCM sensor inside the chamber measures the outgassing levels. The final outgassing rate of the test item and facility will be the same at the completion of the test. Figures 5 and 6 show the inside shroud of Facility 241 and its TQCM sensor head.

Outgassing Certification

The second type of bakeout is the "outgassing certification test" with chamber cold shrouds. The test item is heated within an isothermal outgassing measurement box shown in Figure 7. During these types of bakeouts the chamber shrouds are kept significantly colder, approximately -100 °C, than the level at which the item is being baked out in order to provide negligible contribution to the outgassing measurement being performed. The outgassing measurement box is heated by film heaters attached to the outside surface. Power is evenly distributed throughout the box and is insulated with one layer of insulation to provide a near isothermal condition inside. The box has vent holes for the outgassed molecules to escape. It also has a TQCM holder that positions the exposed crystal slightly inside the box with a view towards the test item. An outgassing measurement box inside Facility 240 can be seen in Figure 8. This is the most accurate measurement of outgassing since the conductance path is known and the TQCM outgassing measurement represents the hardware status. This type of setup has allowed the laboratory to meet the HST stringent 1 Hz/hr outgassing criteria that otherwise could have not been met under normal bakeout conditions.

COMMON PROBLEMS

A common problem faced by the laboratory during bakeouts is the presence of non vacuum compatible materials or improperly cured materials which are high outgassers within the test article. Examples of these items are electrical connector inserts, adhesives, absorber materials, tie-wraps, grommets, connector caps, and many more. These high outgassers significantly extend the duration of the bakeout and in some cases can severely contaminate the flight hardware and the vacuum chamber.

Another problem is the high level of molecular contamination on the thermal shrouds after the execution of an outgassing certification test with chamber cold shrouds. The shrouds have acted as a big scavenger plate collecting most of what was outgassed from the test item. The condition of the empty chamber after the test and after the removal of the box does not equal the outgassing rate of the hardware baked out. In order to attempt to protect the chamber; a scavenger plate is operated at near liquid nitrogen temperatures, -180 °C, to collect some of the outgassed materials throughout the test. Due to the small temperature difference between the shroud and the scavenger plate, approximately 80 °C, it does not collect all of the outgassed materials and some adhere to the shroud and the shell of the facility. This condition impacts the ability to perform any test immediately after this one, other than another box certification due to the high contamination background left on the shrouds.

Also, cryogenics pumps can be damaged by the long term exposure of high levels of molecular outgassing contamination. They operate on the principle of entrainment of molecules on a cooled surface by weak van der Waals or dispersion forces (ref. 2). Molecular contaminants can permanently condense and damage the pump condensing arrays and contaminate the pump charcoal assembly as shown in Figure 9. The cryogenic pump was removed from Facility 241 after 4,984 hours of operation.

MAINTAINING THE CLEANLINESS OF THERMAL VACUUM FACILITIES

The goal of the laboratory is to have all thermal vacuum chambers in compliance with the standard laboratory criteria established. Therefore, several measures to prevent contamination and to remove it once it is present have been instituted.

Inspection

In order to avoid the presence of unacceptable items inside the test facility during a test, the laboratory relies on the project Quality Assurance (QA) process and lead engineers responsible for the hardware to comply with the materials outgassing specification for flight hardware (ref. 3). Furthermore, the laboratory senior personnel perform a final visual inspection of the test article and related hardware after completion of the setup and before closing the chamber door

and commencing the test. In some cases this process captures these unacceptable materials which have escaped inspection, therefore, eliminating the potential contamination problem associated with them.

Post Test Recertification

After each test, if the outgassing condition for the empty chamber at maximum operating temperature is higher than the standard laboratory criteria; a post test recertification or normal bakeout with the empty chamber is performed. This post test recertification will return the chamber to its initial outgassing level. Throughout this phase TQCM data are being collected at -20 °C and when the laboratory criteria are met the chamber cold finger is flooded with liquid nitrogen for the last 8 hours of operation. After the chamber has been returned to atmospheric conditions the cold finger sample is collected and analyzed by the GSFC Materials Branch and their support contractor Unisys Corporation.

The chemical analysis of the residue is performed by Gas Chromatography-Mass Spectrometry (GC/MS) and Infrared Spectrometry. It provides quantitative and qualitative information on the contaminants present at the last phase of the test. The report indicates the amount of residue collected for a given time and lists all material in decreasing order. Also, it provides possible sources of the contaminants and background information on the chamber.

Both conditions, TQCM measurements and the chemical analysis of the cold finger, must be met in order for the facility to be considered clean and in compliance with the laboratory criteria established. From data accumulated by the laboratory the average facility post test recertification takes approximately 2.5 days.

Solvent Cleaning

As the pressure of the chamber is decreased and the temperature of the shroud is increased the vapor pressure of the compounds present in the test item increases as they are outgassed. Later they are deposited on the inside surface of the chamber as the pressure and temperature are returned to atmospheric conditions. Therefore, there is a need to establish a quick and efficient way for lowering these contaminants to acceptable background levels when they become too high.

In the case when these molecular contaminants present are not easily baked out at the chamber maximum operating temperature and/or it will require more than double the normal recertification time; another approach must be followed. This approach requires the proper selection of a solvent that can dissolve the contaminants that have been adhered to the chamber shrouds. The selection must be accomplished very carefully in order to remove the contaminants and at the same time maintain personnel safety and comply with the Engineering Services Division Safety Manual (ref. 4) and the Occupational Safety and Health Administration (OSHA) 29 CFR Part 1910.106 requirements (ref. 5).

The laboratory implemented, on examination, a solvent cleaning procedure developed to reduce the levels of molecular contaminants within acceptable levels. The solvent selection is based on a simple rule in organic chemistry "alike dissolve alike". For example, the contaminants detected in the thermal vacuum chambers are mostly hydrophobic organic compounds which are highly soluble in non polar organic solvents. This means that hydrophobic non polar, or reduced polarity, organic compounds have a high affinity (solubility) for non polar organic solvents such as pentane, hexane, decane, toluene, and xylene. However, personnel safety considerations as mentioned before, must be taken into account when evaluating these solvents. Pentane is highly volatile and flammable. Toluene and xylene are less volatile and flammable but highly toxic to humans. Therefore, hexane and decane were selected to be evaluated on the laboratory facilities.

Detailed procedures implementing the cleaning process for vacuum chambers 2.7 m x 4.3 m (9 ft x 14 ft) or smaller were developed (ref. 6 and 7) by MANTECH-NSI Technology Services Corporation -- in-house support service contractor for the space simulation laboratory.

The laboratory was not able to gather significant amount of data regarding the use of these solvents to reduce molecular contamination in vacuum chambers due to the high workload present. Facility 237 was the only one that was cleaned with hexane after not meeting the laboratory criteria after more than 70 hours in bakeout at 100 °C. Figure 10 shows the TQCM frequency change for a 10 MHz sensor at -20 °C and the chamber shroud at 100 °C before and after cleaning the facility with hexane.

The chamber shroud was wiped down three times with hexane to make sure that the maximum removal of contaminants was achieved. It was observed that the outgassing rate decreased almost 200 Hz/hr and met the laboratory criteria after approximately 50 hours of bakeout. Also, the amount of residue collected in the cold finger sample was reduced from 0.9 mg to 0.7 mg.

CONCLUSION

The Space Simulation Test Engineering Section can effectively and efficiently support a wide range of customers by maintaining all their thermal vacuum chambers at a uniform level and in a midpoint of the molecular contamination spectrum. Therefore, this enables the laboratory to be able to support stringent requirements like the ones for the HST using outgassing certification measurement boxes and at the same time support GAS payloads and sounding rockets.

To completely dedicate one or more thermal vacuum facilities for tests that possess less stringent outgassing requirements would not be cost effective. Furthermore, this would reduce the laboratory through-put and hamper its ability to support our customers by limiting the number of facilities available.

The future of molecular contamination is moving toward more stringent requirements with more sensitive optics and detectors, when needed, and less requirements for low cost and fast

track projects which are not sensitive to contamination. GSFC vacuum laboratory is taking aggressive steps to support both spectrums.

First, by performing a post test recertification after each test performed that does not meet the laboratory standard criteria, all the thermal vacuum chambers are kept clean and ready for operation with minimum effort. Secondly, by examining different solvent cleaning techniques in an attempt to minimize down time between tests and reducing molecular contaminants background present on the thermal shroud if they were severely contaminated. Therefore, reducing post test recertification time to acceptable duration with minimum impact to the workload. Unfortunately no conclusion can be achieved on this technique until further evaluations are performed and the data are assessed on a more analytical basis. Lastly, is the ability to comply with stringent molecular outgassing requirements such as by performing 1 Hz/hr outgassing certification tests with chamber cold shrouds in support of the HST project and the like.

Furthermore, the Space Simulation Test Engineering Section is moving into the future of contamination monitoring by acquiring jointly with the Contamination Engineering Section a state-of-the-art 200 MHz surface acoustic wave (SAW) sensor to research its operation on vacuum chambers. By using this high performance instrument that is approximately two orders of magnitude more sensitive than current instruments we expect to be able to precisely quantify outgassing rate in super sensitive components.

REFERENCE

1. Molecular Flux Measurement System, TQCM Model MK 10 Operating Manual. QCM Research, Laguna Beach, California.
2. A User Guide to Vacuum Technology, 2nd Edition, 1989, John F. O'Hanlon, John Wiley & Sons
3. Outgassing Data for Selecting Spacecraft Materials, NASA Reference Publication 1124 Rev. 2, November 1990.
4. Safety Manual, Engineering Services Division, September 1990, Goddard Space Flight Center
5. General Industry Standards and Interpretations, Volume 1, Occupational Safety and Health Administration, United States Department of Labor.
6. Procedure for Cleaning Facilities 225, 237, and 239 using Decane, NSI Document No. 26-01-640, MANTECH-NSI Technology Services Corporation.
7. Procedure for Cleaning 7 x 8 and Smaller Thermal Vacuum Chambers Using Hexane, NSI Document No. 26-01-611, MANTECH-NSI Technology Services Corporation.

Table 1: Thermal Vacuum Facilities at GSFC
General Capabilities

FACILITY	TEST VOLUME (meters)	OPERATING PRESSURE (Pascal)	TEMPERATURE RANGE (°C)	UNIQUE CAPABILITIES
225	2.74 D x 4.27 L	< 13.3 μPa	-190 to 150	2 Cryo-pumps, C/F, TQCM, RGA
237	2.13 D x 2.44 L	< 67 μPa	-190 to 100	Diffusion-Pump, C/F, TQCM, RGA
238	3.40 D x 4.32 H	< 67 μPa	-190 to 90	4 Cryo-pumps, C/F, TQCM, RGA
239	2.13 D x 2.44 L	< 67 μPa	-190 to 100	Cryo-pump, C/F, TQCM, RGA
240	0.91 D x 0.91 L	< 13.3 μPa	-160 to 110	Diffusion-Pump, C/F, TQCM, RGA
241	0.91 D x 0.91 L	< 13.3 μPa	-160 to 110	Cryo-pump, C/F, TQCM, RGA
243/244	0.61 D x 0.61 H	< 67 μPa	-190 to 100	Diffusion-Pump, C/F, TQCM, RGA
281	0.91 D x 1.22 L	< 213 μPa	-185 to 100	Cryo-pump, C/F, TQCM, RGA
290	8.23 D x 12.19 H	< 13.3 μPa	-180 to 75	8 Cryo-pumps, C/F, TQCM, RGA

Cold Finger (C/F)
Thermoelectric Quartz Crystal Microbalance (TQCM)
Residual Gas Analyzer (RGA)

Table 2: FY 1996 Test Type per Thermal Vacuum Facility

FACILITY	THERMAL VACUUM TEST	NORMAL BAKEOUT	OUTGASSING CERTIFICATION IN BOX	POST TEST CERTIFICATION
225	8	24	0	17
237	13	13	0	12
238	18	6	0	10
239	6	8	15	7
240	7	2	20	17
241	9	5	9	14
243	7	23	0	16
244	0	7	34	0
281	0	12	37	2
290	8	3	0	3
TOTAL	**76**	**103**	**115**	**98**

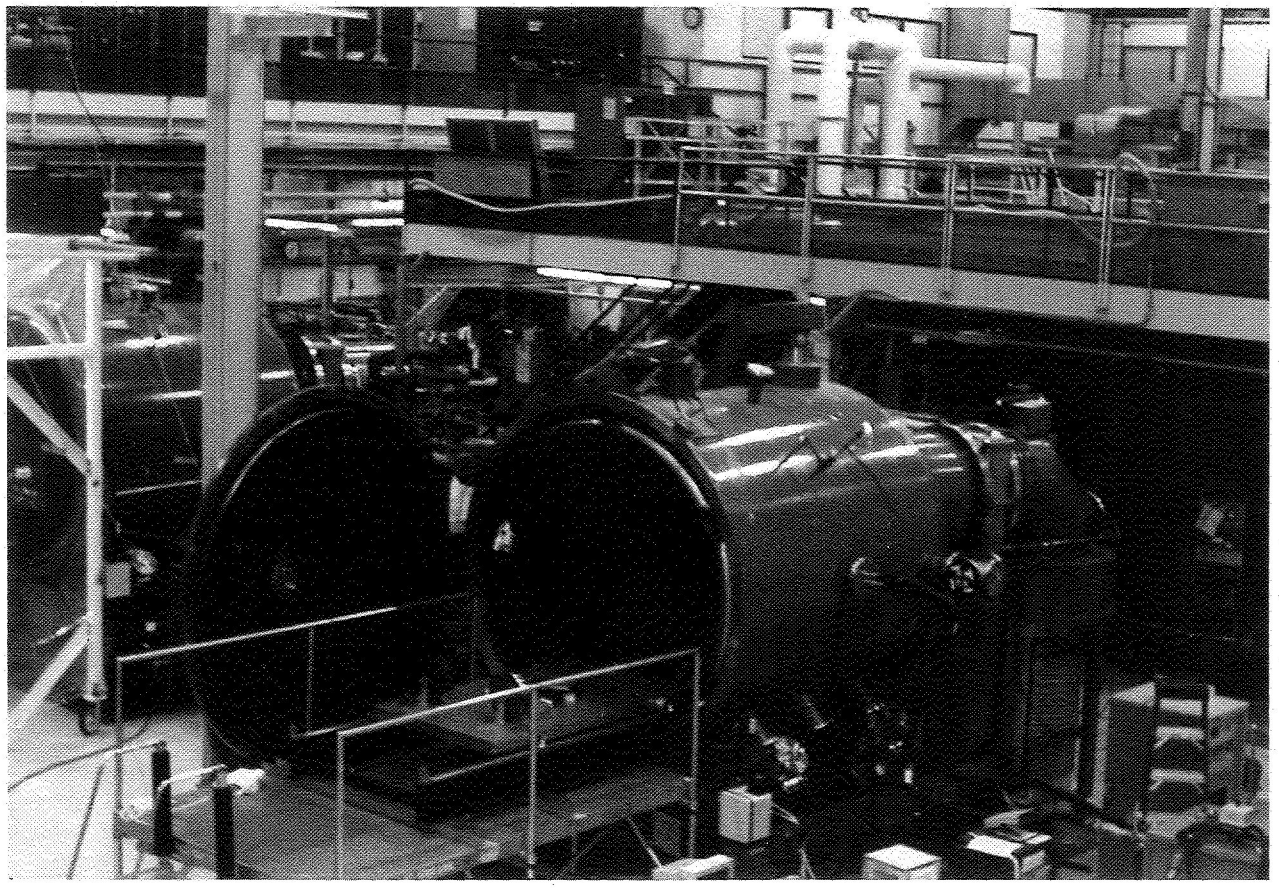


Figure 1: Facilities 237 and 239 Thermal Vacuum Chambers at GSFC

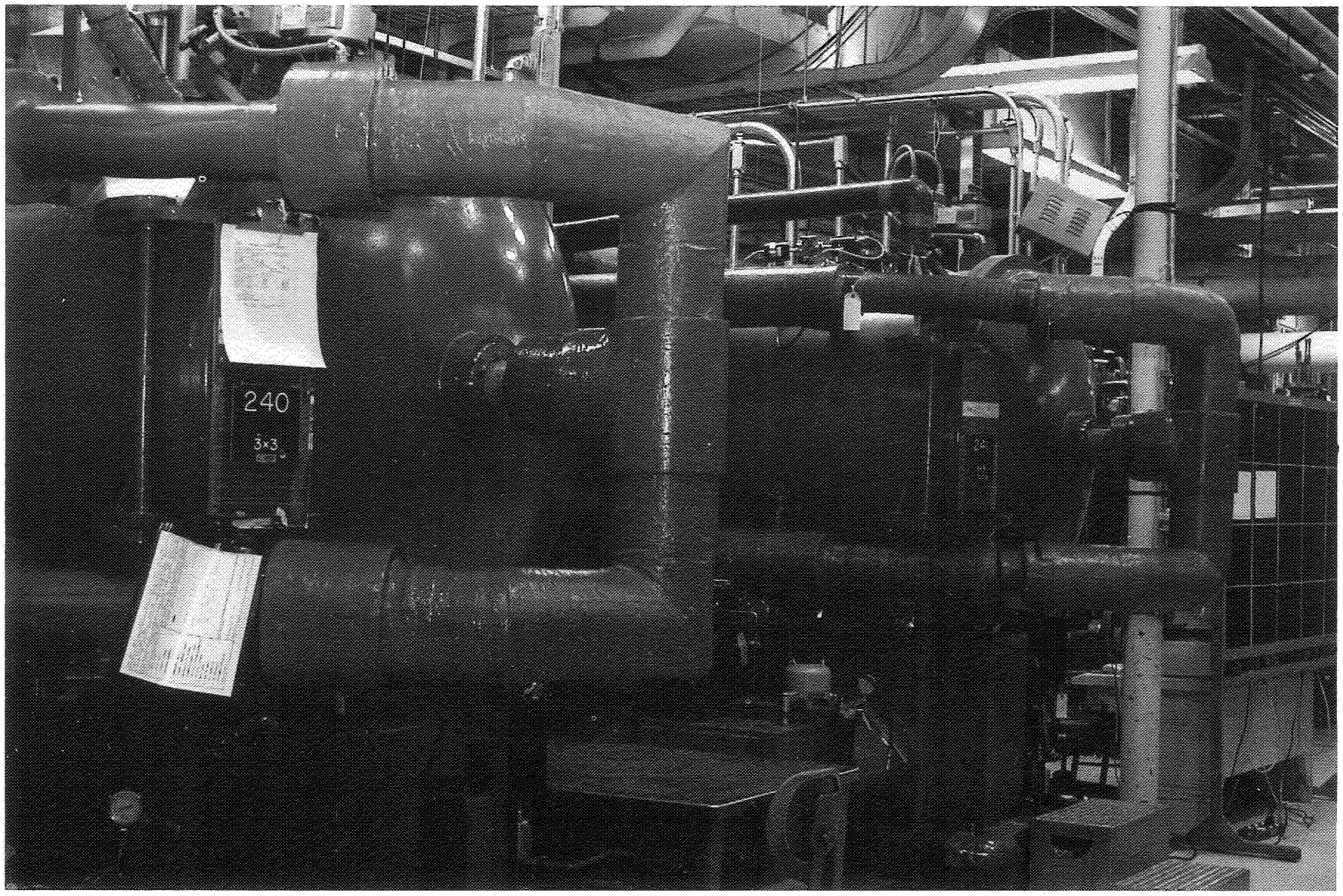


Figure 2: Facilities 240 and 241 Thermal Vacuum Chambers at GSFC

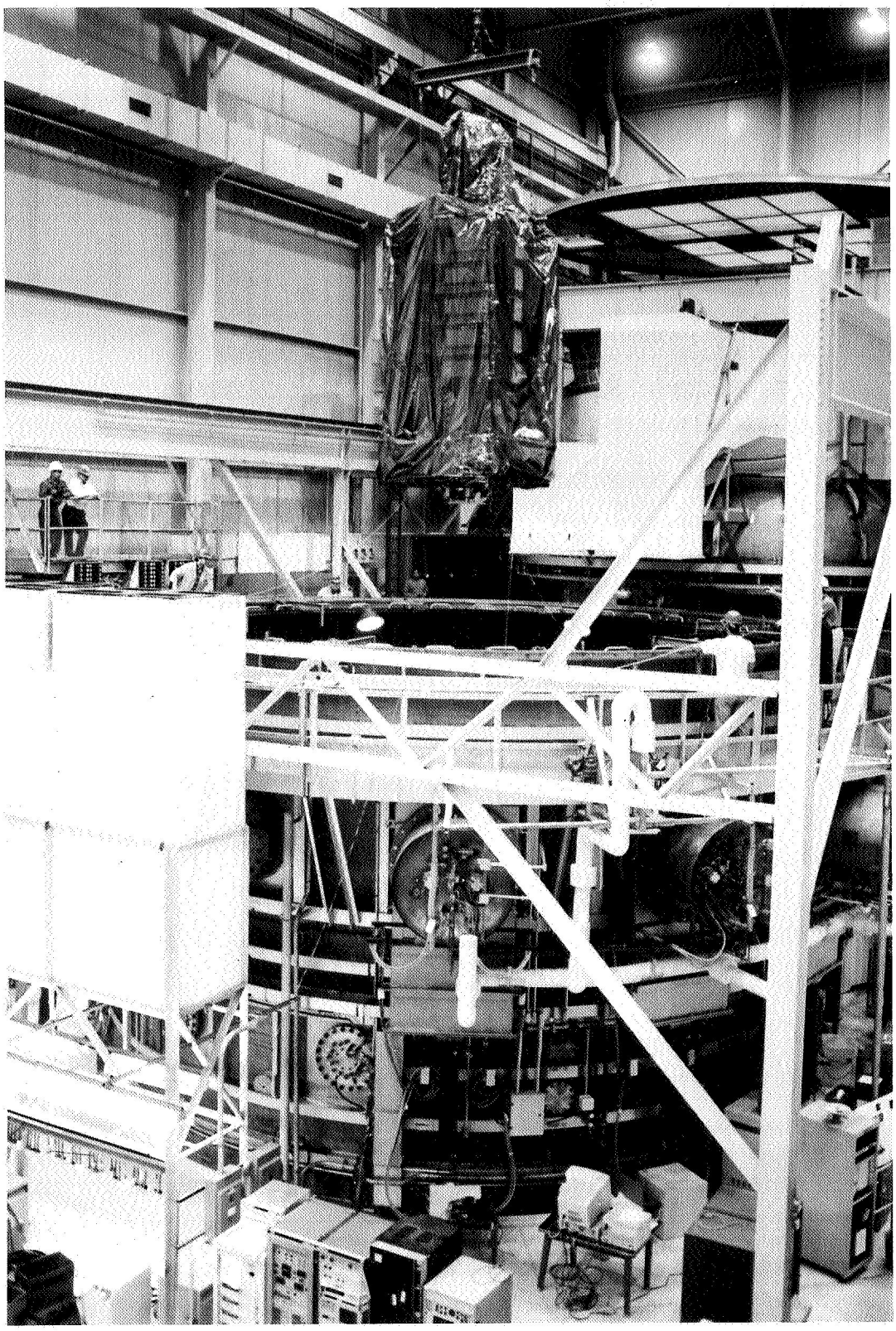


Figure 3: XTE Satellite Being Loaded Into Facility 290 at GSFC

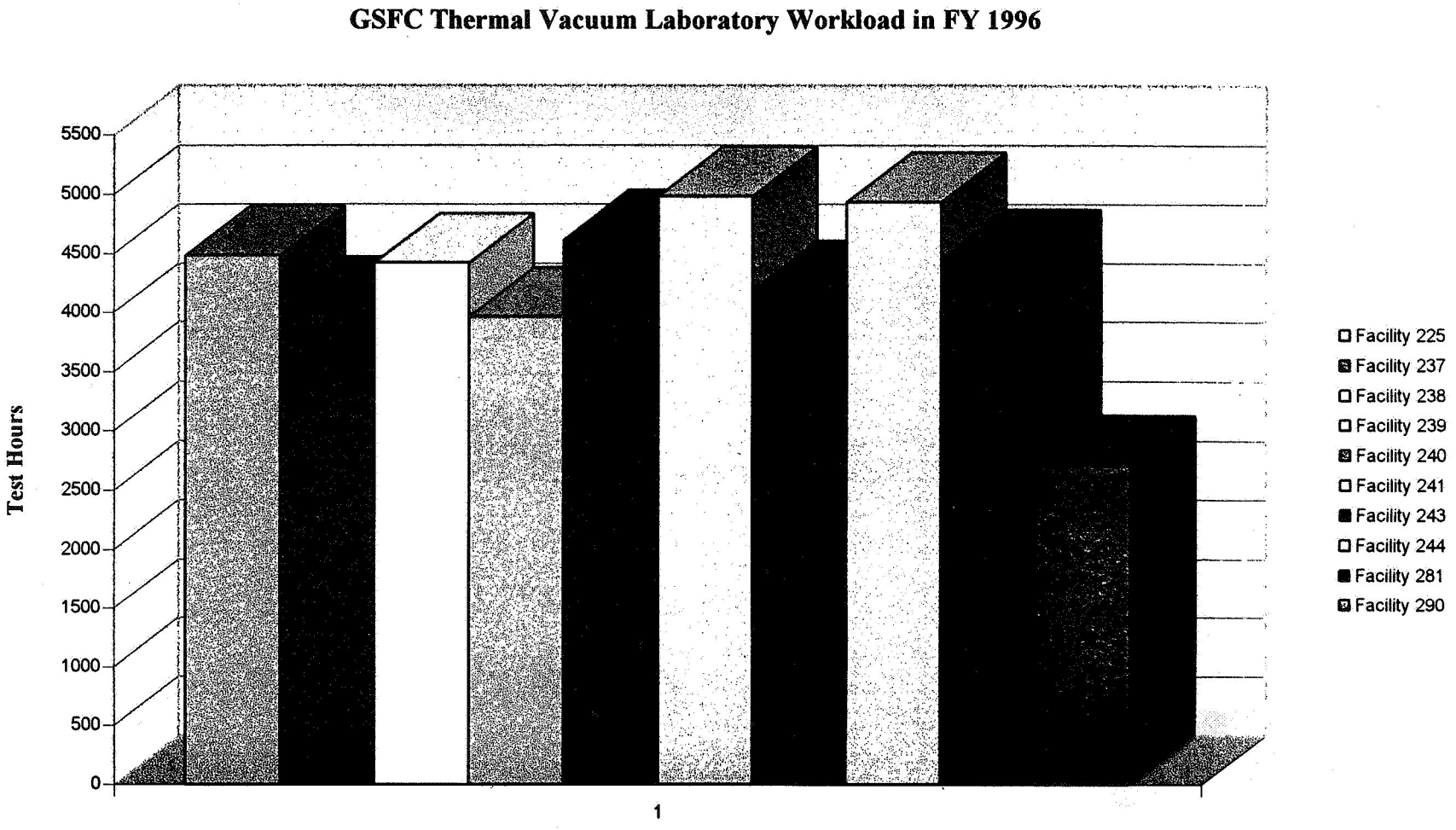


Figure 4: Total Test Hours per Facility

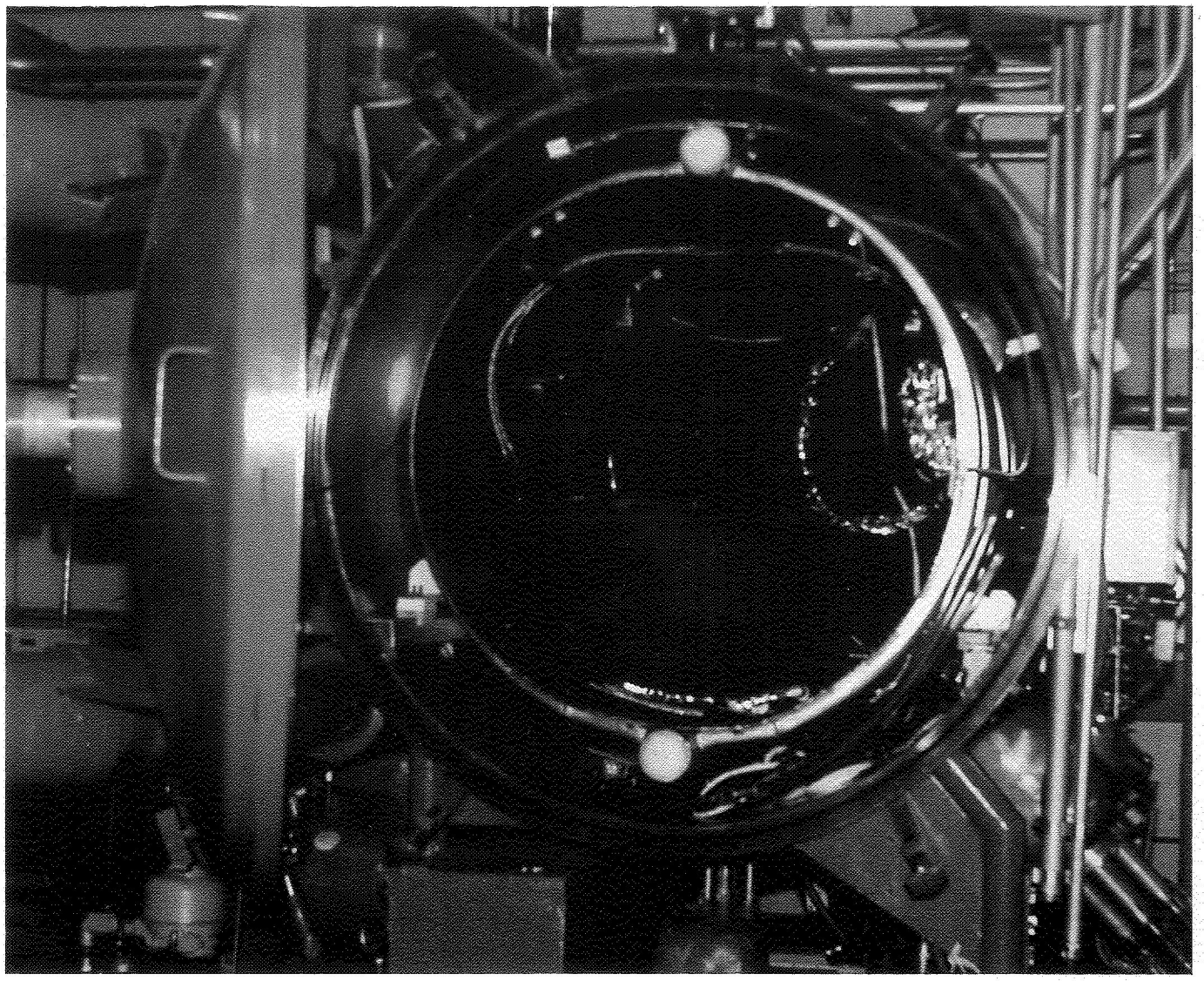


Figure 5: Facility 241 Thermal Shroud

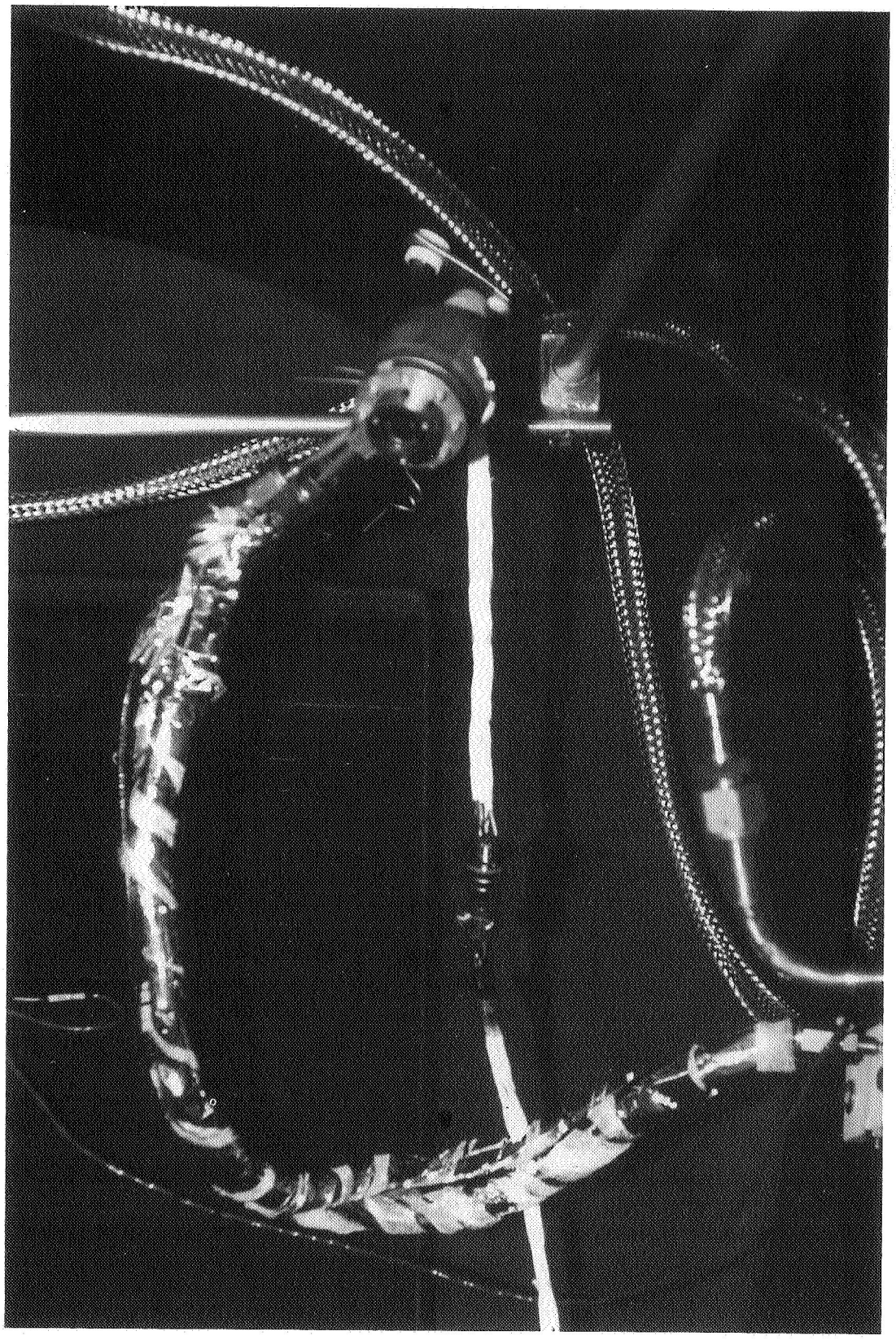


Figure 6: Facility 241 TQCM Sensor Head

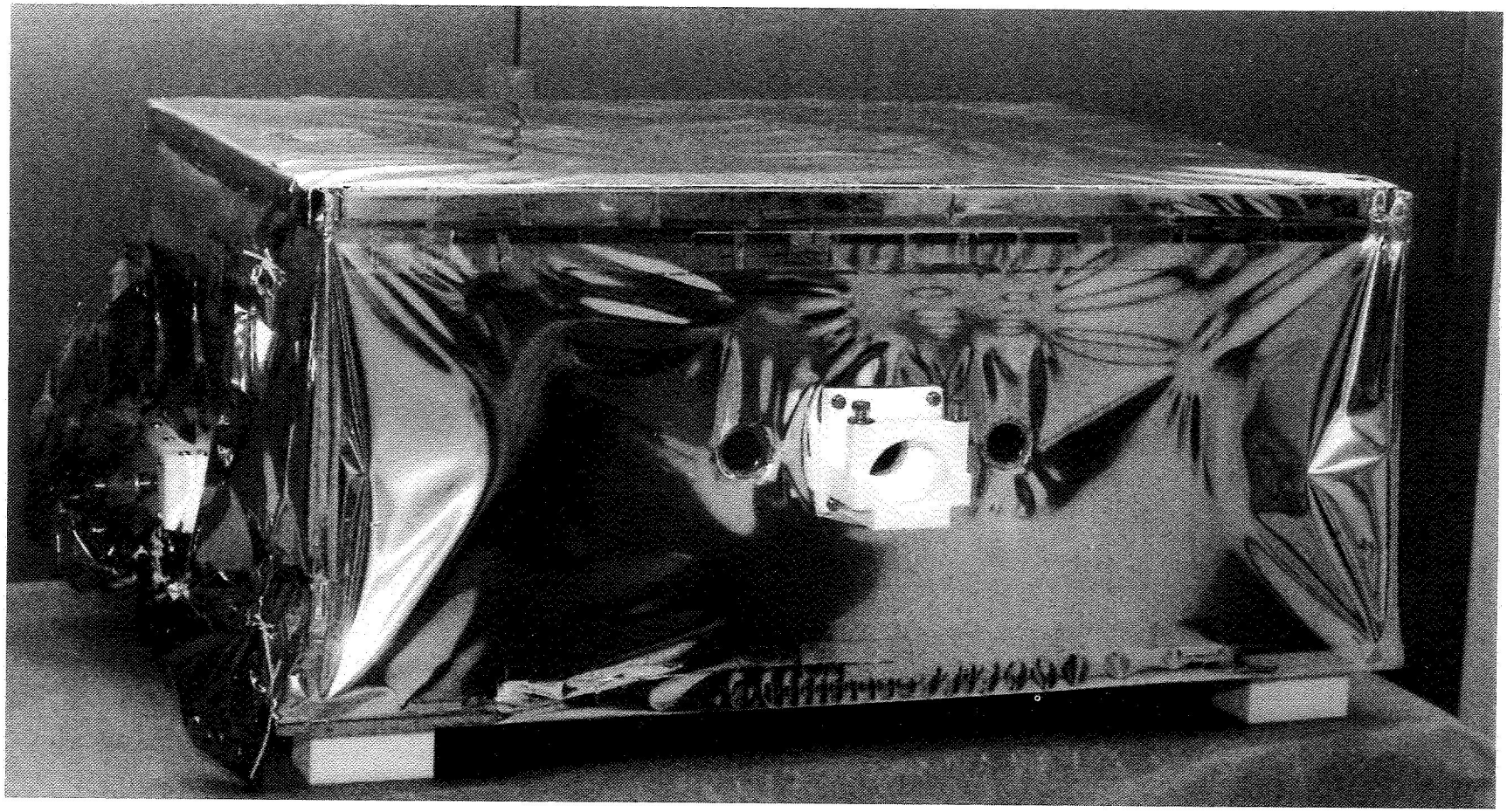


Figure 7: Isothermal Outgassing Measurement Box

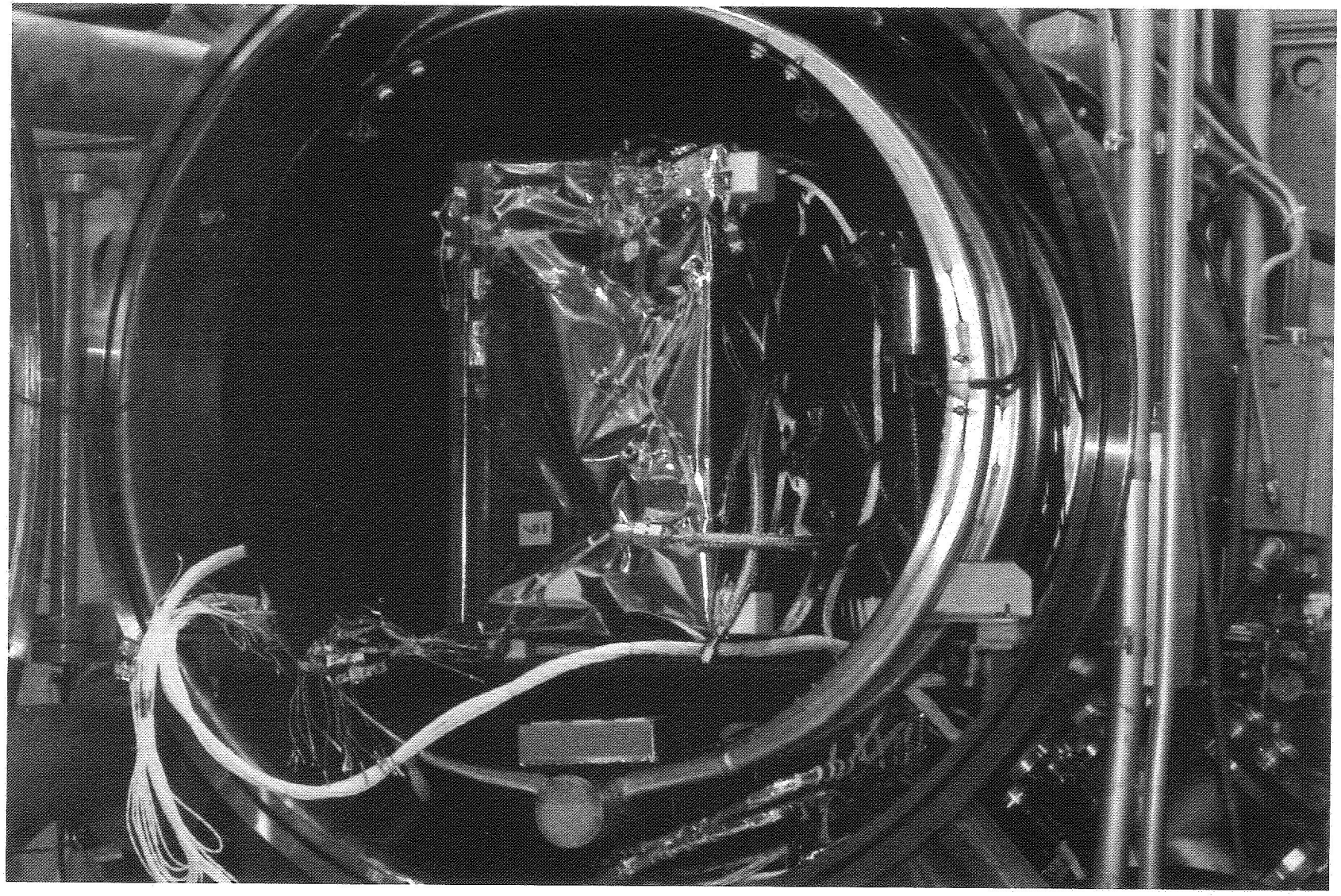


Figure 8: Outgassing Measurement Box inside Facility 240

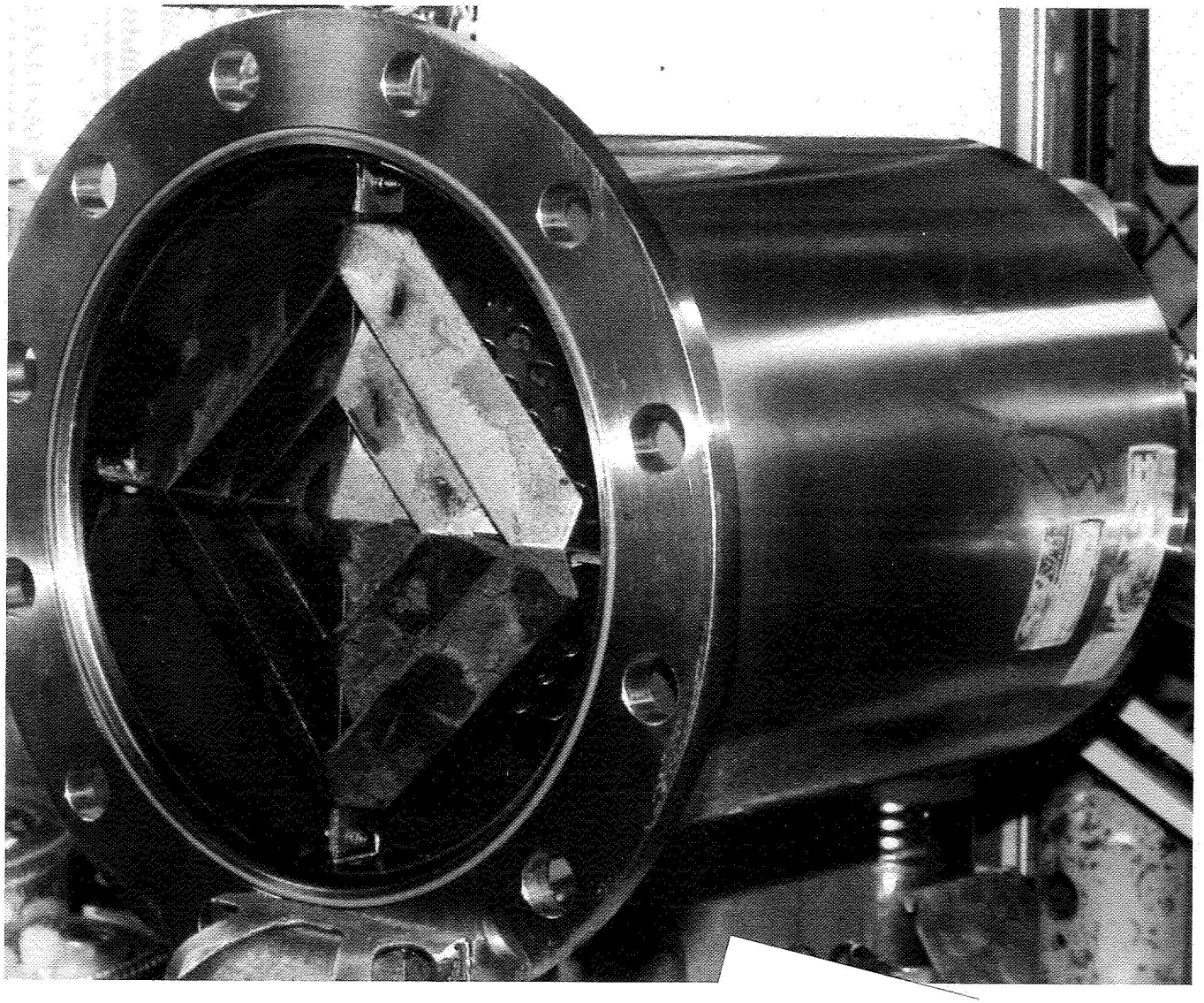


Figure 9: Facility 241 Cryogenic ! est Hours

DCR. 04.97

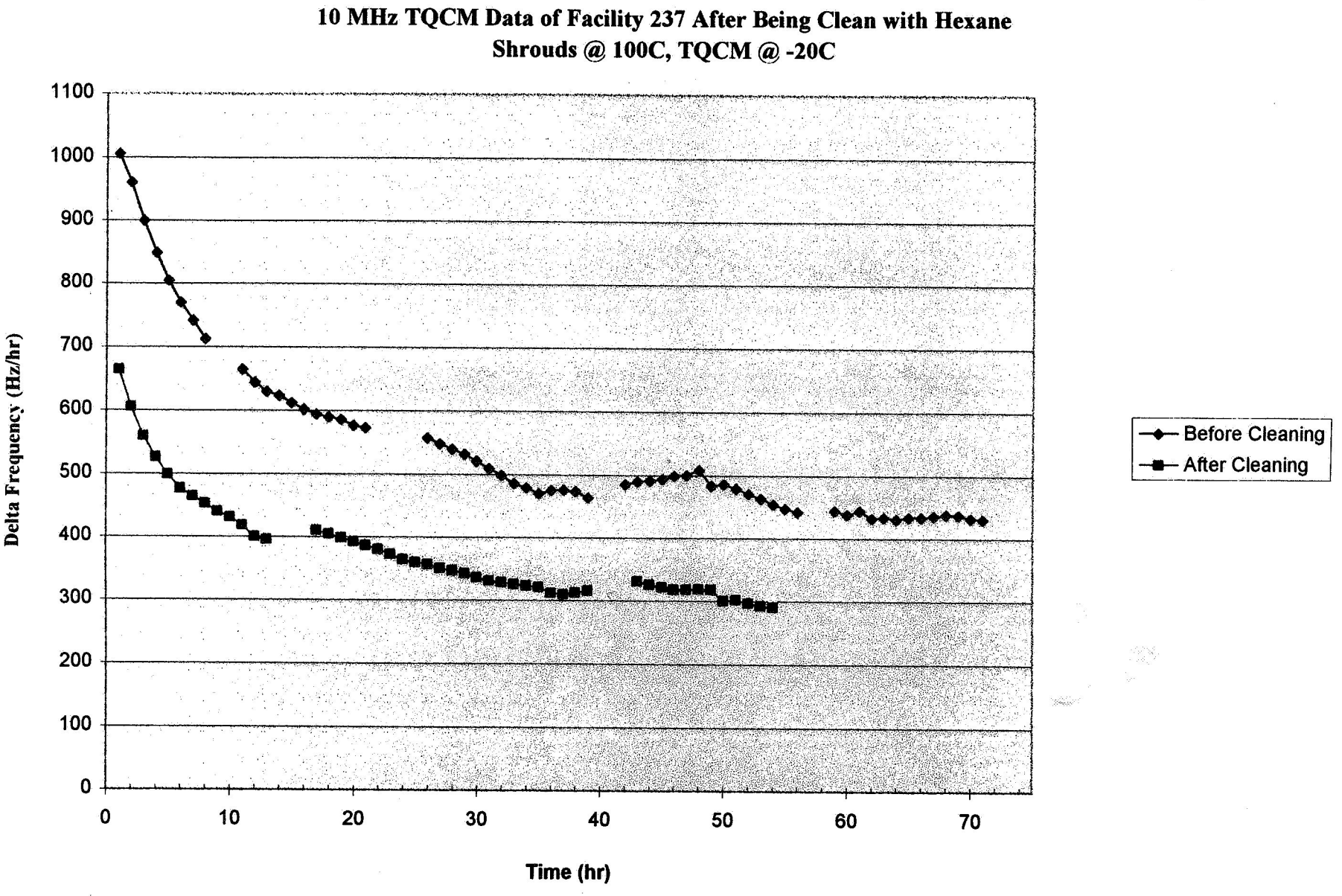


Figure 10: TQCM Data for Facility 237

53-23
069351
IOP

Verification of the baking efficiency using Micro-VCM test data

A.Zwaal-ESA/ESTEC

Abstract

Baking of spacecraft materials and/or spacecraft hardware is often done in order to reduce the risk of contamination of critical items by outgassing species. The baking parameters are often cost-effectively selected and the efficiency of the baking is unknown. Normal material selection criteria, i.e. 1.0 % TML and 0.10 % CVCM, according to the Micro-VCM test as per specification ESA-PSS-01-702 do not guarantee clean spacecraft. Initial harder requirements as a CVCM of 0.01 % were practically not feasible because of limitations in the detection limits. For contamination critical (e.g.optical) components in spacecraft and for items in the vicinity of critical elements, it is recommended to select materials, of which the contamination potential is low or can be lowered by baking. This recommendation is even more valid in case solar radiation is involved: lessons learned from the returned LDEF, STSA and EURECA are that outgassed contaminants can be "frozen" when solar radiation is involved.
Baking of materials or hardware will reduce the contamination potential and will result in a lower contamination of the spacecraft in orbit. Nowadays baking of structural parts, multilayer insulation and harness is more or less becoming standard for contamination critical spacecraft as e.g. SOHO. The efficiency of the materials baking can however be measured using the Micro-VCM outgassing tests on unbaked and on similar baked materials. Two successive Micro-VCM tests on the same sample were performed and gave information on thermal degradation effects and on the lowest achievable contamination potential.
This paper describes the effect of baking on the contamination potentials of materials and for this description, outgassing data of the Micro-VCM tests are used as a baseline.

1 Introduction

Normal material selection criteria, according to the Micro-VCM test, as per specification ESA-PSS-01-702 (ref. 1) or ASTM-E595-93 do not guarantee clean spacecraft. For contamination critical (e.g.optical) components in spacecraft and for items in the vicinity of critical elements, it is recommended to select materials, of which the contamination potential is lower than the normal requirements or can be lowered by baking. This recommendation is even more valid in case solar radiation is involved: lessons learned from the returned LDEF STSA and EURECA (ref.2a/2b/2c/2d) are that outgassed contaminants can be "frozen" when solar radiation is involved.
Baking of materials or hardware will reduce the contamination potential and will result in a lower contamination of the spacecraft in orbit. Nowadays baking of structural parts, multilayer insulation and harness is more or less becoming standard for contamination critical spacecraft as e.g. SOHO (ref. 3).

2 General effects of baking Spacecraft materials

Baking of spacecraft materials may result in a further curing of polymeric materials, also a partial or complete removal of the volatile species, which were present in the original material, can be achieved. Further curing can occur by baking, however baking should not replace the curing as in some cases baking might not reduce the contamination potential, where this is done on a fresh/not fully cured sample. So it is advised to bake the material or hardware after the cure, as recommended by the manufacturer. Atmospheric gases, e.g. water are partly or completely removed by baking, however reabsorption will take place after the bake when the hardware is again exposed to normal air.
Contaminants from manufacturing, machining and handling can also be removed and thus it is advised to bake the hardware when most of the handling has already been done.

3 Parameters which affect the removal of contaminants by baking

There are several parameters which affect the removal of contaminants from a material. These parameters are resp. temperature, activation energy of the volatile species, thickness of the material, duration of the bake, and efficiency of contaminant removal. The activation energies and thicknesses are given and cannot be changed in order to shorten the bake time.

The effect of above parameters on the outgassing is given by the following equations for each of the outgassing species:

$dW/dt = W/tau$ (eq. 1) dW/dt = mass loss rate (e.g. $g.h^{-1}$)

$W = Wo\ (e^{-t/tau})$ (eq.2) W = amount of species in the material (e.g. gram)

$dW/dt = Wo/tau\ .\ (e^{-t/tau})$ (eq. 3) tau = residence time of the specie in the material(e.g. h)

$tau = tau_o\ .\ e^{E/RT}$ (eq. 4) Wo = amount of species originally in the material

$TML = Wo - W$ (eq. 5) E = activation energy (e.g. $J.mole^{-1}$)

$TML = Wo\ (1 - e^{-t/tau})$ (eq. 6) R = gas constant (e.g. 8.31 $J.mole^{-1}.K^{-1}$)

T =Temperature (K)

t = time (e.g. hours)

TML = Total Mass Loss (e.g. gram or %)

3.1 Temperature effects

The first and most important parameter is the temperature. The maximum allowable temperature of a material depends upon the type of material. The manufacturer of the material refers to a maximum. temperature (where no noticible thermal degradation is observed) for continuous operation under atmospheric conditions. The higher the baking temperature, the higher the outgassing during that bake and consequently the higher the amount of removed volatile species. However practical temperature limitations are in general given by the maximum qualification temperature of the spacecraft hardware.

3.2 Effects of activation energies

Water desorption from materials as epoxies involves activation energies of ≈ 50 kJoule per mole (ref 4) and a factor of 10 in outgassing speed is obtained when the temperature of the material is increased by 37°C. Removal of the "heavy" condensible contaminants involves activation energies above 100 kJoule per mole (ref 4), which means that a factor of 10 in outgassing speed is already obtained when the temperature of the material is increased by 17 °C.
Polymeric materials contain in general several volatile species and the removal efficiency of these species will be different for each species because of the different activation energies concerned.

3.3 Effect of material thickness

Contaminants inside materials will diffuse through the material before they are able to outgas. The diffusion speed is according to the inverse-square of the thickness, which means that the bake of thick materials will take longer than the bake of thin materials in order to obtain the same effect. The equation for thickness correction is given as a correction for the time constant (Tau) of the species in the material:

$Tau_{real} = Tau_{test} \cdot (\text{real thickness/test thickness})^2$ (eq.4 a)

The thickness of spacecraft hardware is given by the design and cannot be changed before the bake takes place. For the Micro-VCM standard outgassing tests, the material thickness is specified to small dimensions. For VBQC-outgassing kinetics tests, the dimensions are as realistic as possible and sample masses up to 30 gram can be tested (ref. 4). The thicknesses of the material specimens for the above two outgassing tests are very important for the exact interpretation of the outgassing data w.r.t. contamination potential and baking effects.

3.4 Effect of bake duration

The parameter time, can easily be changed. A linear contamination decrease with time is not likely as most of the practical outgassing tests indicate an outgassing rate decrease as an exponential function of time. Equation 2 (para 3) gives the mass of the outgassed specie as a function of time (t). From this equation and equation 4 can be seen, that the ratio of the amount of removed species to the original amount of species (= W/Wo) varies with the type of species and the temperature (each species has basically a different activation energy E).

3.5 Effect of the environment on the baking efficiency

The last baking parameter is the efficiency of contaminant removal from the material surfaces to the surrounding environment. Under still-standing air, the removal efficiency is zero and under high vacuum conditions of space, where the mean free path of the outgassing molecules is very high, the outgassing efficiency will be maximum.
Baking conditions are often specified as "under high vacuum conditions" and for high vacuum systems it is quite normal that the outgassing molecules hit the internal surfaces of the system some 100 times before they reach the pump or trapping device. Such vacuum systems are normally pumped with a pumping system, which results in a time constant (= volume/pumping speed) of ≈ 0.1 second. A molecular speed of 500 meters per second and a mean free path of 0.5 meter, results in 100 collisions with the walls and/or hardware to be baked, before the molecules reach the pumps or trapping device.
A good transport of the outgassing species can also be achieved under atmospheric conditions, provided the gasflow over the hardware to be baked, is high enough to transport the outgassed species. Because of hardware sizes and cost aspects, baking under high vacuum conditions can be replaced by baking under atmospheric conditions. The investment costs for such an atmospheric baking system are much lower than for a high vacuum system. In latter case the contaminants have to be removed by a (warm) gas stream over the hardware. The gas leaving this atmospheric system can be used for monitoring of the contamination level using e.g. gaschromatograph, mass spectrometer or a trapping devices for further analyses.

4 Materials selection based upon outgassing potential

The outgassing requirements for European spacecraft materials are specified in ESA-PSS-01-702 issue 2 and are according to the accelerated outgassing test. The acceptance criteria for spacecraft materials are: < 1.0 % TML (Total Mass Loss) and < 0.10 % CVCM (Collected Volatile Condensable Material) for the Micro-VCM test at 125°C during 24 hours and a condensor temperature of 25°C.The acceptance criteria for materials selection are based upon contamination potentials and a go-no go selection is applied. The use of Micro-VCM data for modellisation purposes is not realistic as the actual temperatures, times and dimensions are different from those parameters of the tests. However the Micro-VCM outgassing data can, apart from the materials selection criteria, be used for contamination budget/ potential calculations and for worst case contamination predictions.

5 Micro-VCM test methods for evaluating the effects of a bake

5.1 Double Micro-VCM test on 59 material samples

Following the standard Micro-VCM test a second test is initated on exactly the same specimen. Figure 1 gives the sample mass for the two successive Micro-VCM tests as a function of time. This second test on the same specimen was named "method-B" in ESA-PSS-01-702 issue 1 (obselete). This method for material testing was initiated for contamination critical optical experiments and baking of materials and/or assemblies was foreseen on realistic hardware. This "method-B" test was introduced in order to conclude from the outgassing data of the two successive tests, whether the material was bakeable at 125 °C and secondly to see how far the contamination level of the material could be reduced after a 24 hours bake at 125°C. The bakability of a material at 125°C might be limited by the fact that decomposition of the material could occur. A decomposition could result in a subsequent measurable outgassing, which outgassing might be observed after a second Micro-VCM test on the same specimen as a mass change. The double Micro-VCM test simulates basically a bake on small material pieces. In practice the materials can be much bigger in

thickness and then the outgassing will be restricted. In the obsolete issue 1 of ESA-PSS-01-702 there were also acceptance requirements for materials as tested per method-B: i.e. 0.10 % RML and 0.01% CVCM. The reasons for the deletion of method B in issue 2 is described in the conclusion (para 6). The results of the Micro-VCM tests (A) and (B) and their ratios is given in tables 1 and 2 for the 59 materials tested.

5.2 Interpretation of "double-Micro-VCM" test data

*1-The negative value (-0.23%) for RML(Recovered Mass Loss) of Gude 718 VC (material 5 from table 1) is probably caused by a poor humidity control before test A as the WVR (Water Vapour Regain) data of this material are identical for the two tests A and B.

*2-Table 2 gives at the bottom the average outgassing values of the 59 materials tested and from these average values of both tests A and B , the following can be concluded:
- The average TML figure dropped from 0.982 to 0.524 , which results in an average reduction of the ratios from 100 % to 54 % (column K of table 2).
- The average RML figure dropped from 0.526 to 0.059 , which results in an average reduction of the ratios from 100% to 23 % (column L of table 2).
-The average WVR figure was 0.466 for test A and 0.467 for test B which means that the average water re-absorption after the two successive tests is the same within 3 percent. The water re-absorption is thus a reversible proces for the 59 materials tested.
-The average CVCM figure dropped from 0.044 to 0.007 which results in an average reduction of the ratios from 100% to 21 % (column N of table 2).
The effects of the bakes is, for water sensitive materials, hardly demonstrated by the TML figures, because the water re-absorption is reversible. In case the water content of the materials is not critical w.r.t the experiments the RML and the CVCM values can be seen as the critical contamination potentials. In that case the contamination potential, for the 59 materials tested, is reduced from 100 % to 23 % for the RML and from 100 % to 21 % for the CVCM by a 125°C vacuum bake on small material pieces during 24 hours.
-The results of the Micro-VCM test given in tables 1 and 2 indicate that of the 59 materials tested some 23 materials did not pass the < 1% TML limit. Of those 23 materials some 17 materials passed the < 1 % RML limit. Those 17 materials were mainly water sensitive materials and the high water absorption was one of the reasons to modify the acceptance limits in issue 2 of specification ESA-PSS-01-702 as water desorption is not always problematic. In order to avoid the costly system of "Request For Waivers" for unacceptable high TML , the future issue 3 of our specification ESA-PSS-01-702 will contain < 1 % RML as acceptance criterium for materials outgassing.instead of < 1 % TML.
-Of the 59 materials tested some 7 materials did not pass the 0.10% CVCM limit and 6 of those 7 materials did not pass both acceptance limits TML and CVCM .
-From the Micro-VCM masurements on 59 materials can be concluded that baking of all the materials at 125 °C is possible and that the thermal degradation cannot be distinguished from the outgassing in these tests. These conclusions are based upon the facts that there were no indications that the RML and CVCM data were the same for the tests A and B.
-The average residence times of the outgassed species can be calculated using equation 2 (para 3) and the RML data , assuming that (Wo) corresponds to the sum of the two RML data measured after the two tests. The residence times vary from ≈ 10 hours to ≈100 hours at 125 °C.
In case the activation energies are known (≥ 50 kJ.mole^{-1}), the outgassing figures at other temperatures and times can be calculated. However the activation energies are not measured here and predictions can only be made when outgassing kinetic data from e.g. the VBQC-tests (ref. 4) are known.

5.3 Double Micro-VCM test on unbaked and baked materials

Double Micro-VCM tests on 16 materials "as received" and on identical materials from the same batch after a bake, done by the supplier at 80°C, during 72 hours were performed. The test data of these 16 materials were already given earlier in tables 1 and 2. For better interpretation the data for the "as received" samples are also given in table 3. The outgassing data of the "as received + 72h/80°C bake" are given in table 4. -The average values of the TML data dropped from 0.896 to 0.699 which corresponds to an average reduction from 100 % to 78 % by the 72h/80°C bake.

-The average RML values dropped from 0.392 to 0.219 , which decrease corresponds to an average reduction from 100 % to 56 % by the 72h/80°C bake. The ratios of the 16 RML data from tables 3 and 4 indicate only an average reduction from 100 % to 70 % by the 72h/80°C bake. (ratios not given in the tables).
-The average WVR values were constant for the two tests A and B.
-The average CVCM values dropped from 0.062 to 0.018, which corresponds an average reduction from 100% to 29% by the 72h/80°C bake. This reduction is mainly due to only two materials and the individual results indicate that improvements by baking can vary emormous per material.

6 Conclusion

1-Issue 2 of ESA-PSS-01-702 includes the acceptance criteria of < 1% RML for applications where water desorption is seen as being not critical. This new acceptance criterion is based upon the fact, that of the 59 materials tested some 23 materials did not pass the < 1% TML, while 17 of those 23 materials passed the < 1% RML.
2-The Micro-VCM test data on spacecraft materials are adequate for the selection of spacecraft materials and the acceptance limits of < 1% TML and < 0.1 % CVCM are good general selection criteria, however for our future acceptance criteria in issue 3 of ESA-PSS-01-702 the < 1 % TML will be changed to < 1 % RML.
3-Issue 1 of ESA-PSS-01-702 referred to a material acceptance criterion of < 0.10 % RML and < 0.01 % CVCM for materials in the vicinity to critical hardware after a second Micro-VCM test.(i.e "method B") .
This requirement has been deleted in issue 2 because firstly the 0.01 % CVCM was around the accuracy of the test method. Secondly the tests on 59 materials indicated that baking of these materials at 125°C during 24 hours can reduce the contamination potential (= RML) from 100 % to only 23 %.
These double tests also indicated that, based upon mass loss data, no thermal degradation could be observed. Nearly all the materials, which passed the normal requirements (< 1 % TML and < 0.1 % CVCM) also passed the harder requirements (< 0.1 % RML and < 0.01 % CVCM) after a bake at 125 °C for 24 hours for materials with small dimensions.
4-The 72 hours bake at 80°C for the 16 "as received" materials resulted in an average reduction of contamination potential (=RML) from 100 % to 70%.
This result means that practical baking at ≈ 80°C of hardware will result in only a limited reduction of the contamination potential and the efficiency depends very much on the type of material.
5-For the interpretation of the above "limited reduction of contamination potential", one has to take into account that the Micro-VCM data only permit to conclude on improvements onthe contamination potentials and not on the improvements on outgassing rates. The bake improvements on outgassing kinetics can only be measured according to the VBQC-method (ref 4).
6-The bake on SOHO (ref. 3) hardware was partly done to improve the "bulk" contamination potentials and partly to reduce the surface contamination, as the enormous surfaces of the relevant hardware, collected contaminants during handling and during the long ground life.
7- A practical bake time is seen as ≥ 48 hours and especially weekends (≈ 72 hours) are quite often recommended. This practical time does however not guarantee that enough of the critical species is removed.
8-Because of very long time constants for the outgassing of several species, it is recommended to test samples at least a few weeks after the bakes in order to level out the concentration gradients of the outgassing species in the materials.

References

1-ESA-PSS-01-702 issue 2: A thermal vacuum test for the screening of space materials (test according to ASTM-E595-93, except acceptance requirements)
2a-Lessons learned from LDEF -See LDEF-Williamsburg conference-M.v Eesbeek
2b-Overall contamination on HST-SA1,M v Eesbeek, J.Guijt-ESA-ESTEC-ESA-WPP-77 page 417 (may- 1995).
2c-Post flight Material investigation of Eureca, M v Eesbeek, M. Froggatt, G.Gourmelon-ESA/ESTEC-in ESA WPP-069/p513//april 1994/ISSN 1022-6656
2d-Materials Inspection of Eureca-M. v Eesbeek,M.Froggatt,G.Gourmelon-NASA-conference publication 3275-part 1-page 71 (1993)
3-The cleanliness Aspects of the SOHO Satellite (R.Thomas-ESA-bulletin 84 November 1995-p 101)
4-VBQC-policy/test method -ESA-SP232 -v Eesbeek and Zwaal

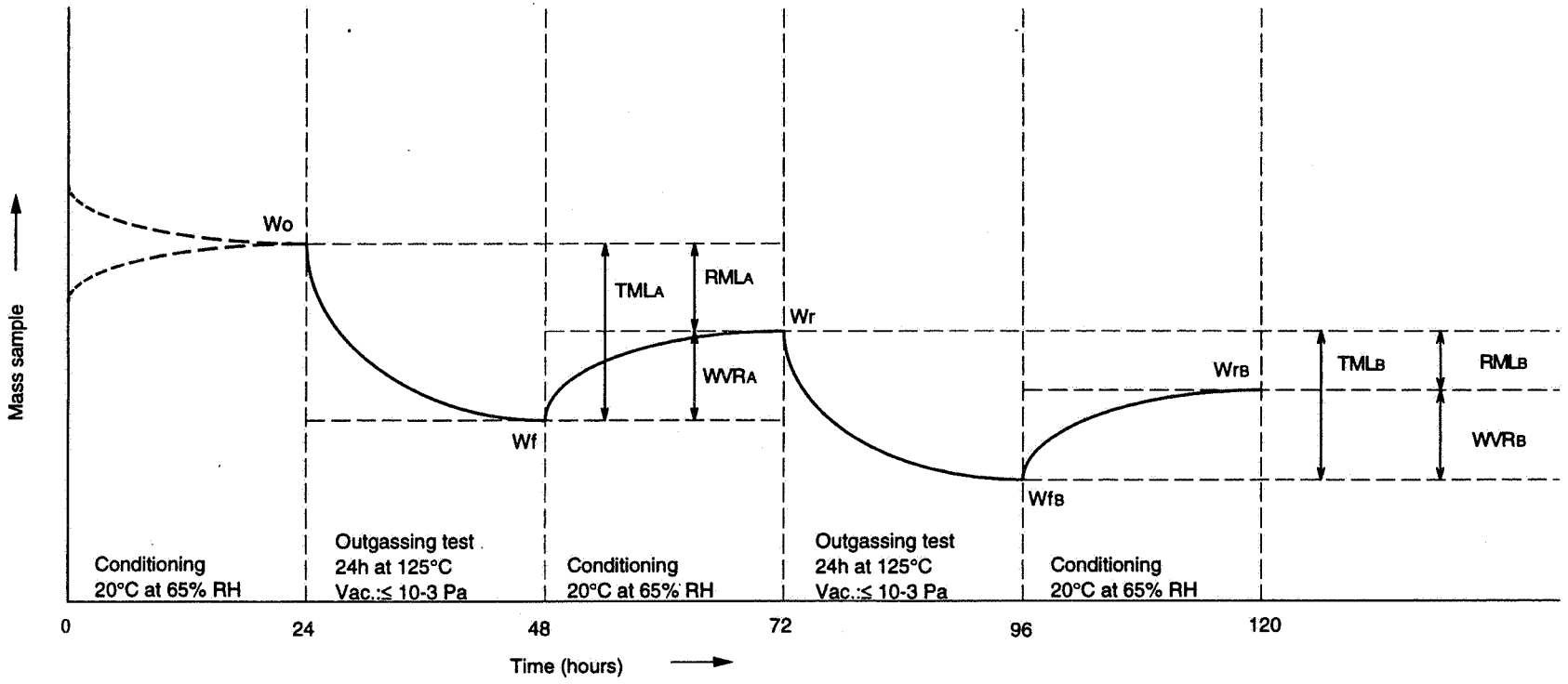


Figure 1 Sample mass evaluation during successive Micro-VCM tests

A	B	C	D	E	F	G	H	I	J	K	L	M	N	O
		Single test (A)				Double test (B)				Ratio (B/A)				
No:	Material Name and Number	%TML	%RML	%WVR	%CVCM	%TML	%RML	%WVR	%CVCM	G/C	H/D	I/E	J/F	REF.
1	FP-333 (Polyolefine shrinkable sleeve)	0.70	0.66	0.04	**0.14**	0.12	0.07	0.05	0.000	0.17	0.11	1.25	0.00	89M023
2	FP-333 "	**1.09**	**1.04**	0.05	**0.32**	0.14	0.08	0.06	0.000	0.13	0.08	1.20	0.00	89M024
3	PE-210 (polyester foil+acrylic adhesive)	0.49	0.31	0.18	0.08	0.27	0.07	0.20	**0.030**	0.55	0.23	1.11	0.38	89M025
4	PE-207 "	**1.40**	**1.15**	0.25	0.07	0.59	**0.34**	0.25	**0.020**	0.42	0.30	1.00	0.29	89M026
5	GUDE 718 VC (nomex lacing tape)	**2.97**	-0.23	3.20	0.04	3.24	0.04	3.20	0.000	1.09	*	1.00	0.00	89M027-*1
6	G 414 810 (carbon filled polyimide +Al)	0.77	0.08	0.69	0.01	0.78	0.06	0.72	0.000	1.01	0.75	1.04	*	89M028
7	Sanddal jet-black MLW (Sandoz anodizing)	0.56	0.28	0.28	0.02	0.31	0.09	0.22	0.000	0.55	0.32	0.79	0.00	89M029
8	Hysol EA 9313 (72h/60°C/100 mBar)	**1.60**	0.78	0.82	**0.12**	0.88	0.04	0.84	0.000	0.55	0.05	1.02	0.00	E413/4
9	KL 21H (epoxy adhesive 4d/RT)	**1.55**	0.96	0.59	**0.15**	0.67	0.06	0.61	**0.030**	0.43	0.06	1.03	0.20	E413/4
10	Epo Tek H20E (silver epoxy 24h/50°C)	**1.01**	0.75	0.26	0.01	0.34	0.07	0.27	0.009	0.34	0.09	1.04	*	E413/4
11	Vespel S-P1 (Polyimide - A.R.)	**1.67**	0.92	0.75	0.01	0.76	0.00	0.76	0.002	0.46	0.00	1.01	*	E413/4
12	Araldit AV100/HV100(epoxy adh.24h/RT)	**1.78**	**1.10**	0.68	0.09	0.84	**0.11**	0.73	**0.068**	0.47	0.10	1.07	0.75	E413/4
13	DC 93500 (Vac-degas-20h/40 °C)	0.15	0.13	0.02	0.02	0.01	0.01	0.00	0.005	0.07	0.08	*	0.25	E413/4
14	DC 93500 (A.R. batch GA030911)	0.13	0.10	0.03	0.00	0.05	0.01	0.04	0.000	0.38	0.10	1.33	*	E415/7
15	DC 53500 (A.R. batch GA030911)	0.12	0.09	0.03	0.01	0.05	0.03	0.02	0.005	0.42	0.33	0.67	*	E416/8
16	Sira optical cement (vac-degas /RT-cure)	**9.78**	**8.96**	0.82	**0.15**	1.36	**0.44**	0.92	**0.076**	0.14	0.05	1.12	0.51	E413/4
17	DC 61104 (A.R. batch GA030911 ??)	0.25	0.14	0.11	0.00	0.14	0.05	0.09	0.003	0.56	0.36	0.82	*	E415/7
18	DC 61104 (A.R. batch GA041430)	0.27	0.15	0.12	0.03	0.24	**0.11**	0.13	**0.016**	0.89	0.73	1.08	0.53	E416/8
19	DC 61104(A.R.batchGA012502+pr1200)	0.26	0.19	0.07	0.01	0.12	0.05	0.07	0.009	0.46	0.26	1.00	*	E415/7
20	RTV 566 (A.R. batch AB 317)	0.15	0.10	0.05	0.00	0.05	0.01	0.04	0.000	0.33	0.10	0.80	*	E415/7
21	RTV 566 +P207 (A.R batch AB317)	0.17	0.13	0.04	0.00	0.04	0.01	0.03	0.007	0.24	0.08	0.75	*	E415/7
22	CV2216 (A.R. batch 34.K.1FR)	**1.33**	0.70	0.63	0.01	0.63	0.00	0.63	0.000	0.47	0.00	1.00	*	E415/7
23	CV2216+Pr.3911/batch34.K1FR/59aop)	**1.29**	0.72	0.57	0.00	0.58	0.00	0.58	0.000	0.45	0.00	1.02	*	E415/7
24	PCBZ (4d/RT+24h/150°C)	0.08	0.03	0.05	0.01	0.03	0.03	0.00	0.004	0.38	1.00	*	*	E416/8.
25	Eccobond 55/9 (24h/RT + 2h/70°C)	0.80	0.34	0.46	0.00	0.47	0.02	0.45	0.000	0.58	0.06	0.98	*	I749A/B
26	Solithane 113 (A.R.)	0.52	0.35	0.17	0.01	0.20	0.03	0.17	0.000	0.38	0.09	1.00	*	I749A/B
27	Kapton 0.3 mil VDA perfor.-Sheldahl (AR)	**1.28**	0.10	1.18	0.00	1.26	0.08	1.18	0.000	0.98	0.80	1.00	*	I749A/B
28	Kapton 2 mil VDA perfor.- Sheldahl (AR)	**1.55**	0.05	1.50	0.00	1.46	0.02	1.44	0.000	0.94	0.40	0.96	*	I749A/B
29	Kapton 2 mil VDA nonperfor.-Sheldahl (AR)	**1.44**	0.05	1.39	0.00	1.36	0.04	1.32	0.000	0.94	0.80	0.95	*	I749A/B
30	Electrodag 501/kapton VDA-2 mil (AR)	**1.33**	0.15	1.17	0.00	1.19	0.00	1.19	0.000	0.89	0.00	1.02	*	I750A/B

Table 1 : Micro-VCM data for single (A) and double (B) tests (see also table 2)

A	B	C	D	E	F	G	H	I	J	K	L	M	N	O
		Single test (A)				Double test (B)				Ratio (B/A)				
No.	Material Name and Number	%TML	%RML	%WVR	%CVCM	%TML	%RML	%WVR	%CVCM	G/C	H/D	I/E	J/F	REF.
31	Permacel P213(glass/acrylic tape) (AR)	0.43	0.20	0.23	0.00	0.26	0.03	0.23	0.000	0.60	0.15	1.00	*	I750A/B
32	Permacel P224 (kapton/acrylic tape) (AR)	0.97	0.19	0.78	0.00	0.84	0.06	0.78	0.000	0.87	0.32	1.00	*	I750A/B
33	Scotchtape Y966 (acrylic adhes.tape) (AR)	0.55	0.44	0.11	0.00	0.19	0.07	0.12	0.000	0.35	0.16	1.09	*	I750A/B
34	Synton 70 (A.R.)	**1.39**	**1.20**	0.19	**0.58**	0.24	0.04	0.20	0.01	0.17	0.03	1.05	0.02	I752A/B
35	Gudebrod 18DPTH (A.R)	0.51	0.24	0.27	0.00	0.29	0.00	0.29	0.00	0.57	0.00	1.07	*	I751A/B
36	Kynar Fon 1.3618-4 (A.R)	0.56	0.51	0.05	0.09	0.11	0.04	0.07	0.01	0.20	0.08	1.40	0.11	I753A/B
37	Kynar Fon 1.3618-16 (A.R)	0.59	0.56	0.03	0.01	0.05	0.02	0.03	0.00	0.08	0.04	1.00	*	I754A/B
38	Raychem RT-876 (A.R)	**1.42**	**1.29**	0.13	**0.27**	0.39	**0.25**	0.14	**0.02**	0.27	0.19	1.08	0.07	I754A/B
39	Velcro#009-0599 (tape loop A.R)	0.48	0.27	0.21	0.01	0.29	0.06	0.23	0.00	0.60	0.22	1.10	*	I754A/B
40	Velcro#009-0599 (tape hook A.R.)	0.52	0.33	0.19	0.02	0.29	0.08	0.21	0.01	0.56	0.24	1.10	0.50	I754A/B
41	Araldit AV100/HV100 (A.R.)	**1.56**	0.84	0.72	0.00	0.81	0.10	0.71	0.00	0.52	0.12	0.99	*	I754A/B
42	Solithane 113 (A.R)	0.38	0.25	0.13	0.00	0.17	0.02	0.15	0.00	0.45	0.08	1.15	*	I754A/B
43	Eccobond 55/9 (A.R.)	0.92	0.35	0.57	0.00	0.58	0.01	0.57	0.00	0.63	0.03	1.00	*	I752A/B
44	Eccobond 55/9(A.R +72h/80)	0.64	0.19	0.45	0.00	0.46	0.02	0.44	0.00	0.72	0.11	0.98	*	I749A/B
45	Solithane 113 (AR + 72h/80°C)	0.52	0.35	0.17	0.01	0.20	0.03	0.17	0.00	0.38	0.09	1.00	*	I749A/B
46	Kapton VDA-0.3 mil perfor.(A.R+72h/80)	**1.26**	0.09	1.17	0.00	1.15	0.07	1.08	0.00	0.91	0.78	0.92	*	I749A/B
47	Kapton VDA-2 mil perfor.(A.R+72h/80)	**1.52**	0.05	1.47	0.00	1.44	0.04	1.40	0.00	0.95	0.80	0.95	*	I749A/B
48	Kapton VDA 2 mil nonperfor.(A.R+72h/80	**1.39**	0.05	1.34	0.00	1.33	0.04	1.29	0.00	0.96	0.80	0.96	*	I749A/B
49	Electrodag 501/kapton 2mil(A.R+72h/80)	**1.09**	0.08	1.01	0.00	1.00	0.00	1.00	0.00	0.92	0.00	0.99	*	I750A/B
50	Permacel P213 (A.R + 72h/80°C)	0.37	0.17	0.20	0.00	0.24	0.04	0.20	0.00	0.65	0.24	1.00	*	I751A/B
51	Permacel P224 (A.R + 72h/80°C)	0.90	0.17	0.73	0.00	0.78	0.06	0.72	0.00	0.87	0.35	0.99	*	I751A/B
52	Scotchtape Y966 (A.R + 72h/80°C)	0.47	0.37	0.10	0.02	0.17	0.06	0.11	0.00	0.36	0.16	1.10	*	I752A/B
53	Synton 70 (A.R. + 72H/80°C)	0.35	0.15	0.20	0.08	0.20	0.01	0.19	0.02	0.57	0.07	0.95	0.25	I752A/B
54	Gudebrod 18DPTH (A.R. + 72h/80°C)	0.39	0.13	0.26	0.00	0.27	0.00	0.27	0.00	0.69	0.00	1.04	*	I752A/B
55	Kynar Fon 1.3618-4 (A.R + 72h/80°C)	0.29	0.25	0.04	0.06	0.10	0.04	0.06	0.00	0.34	0.16	1.50	<0.16	I753A/B
56	Kynar Fon 1.3618-16 (A.R + 72h/80°C)	0.16	0.13	0.03	0.01	0.04	0.01	0.03	0.00	0.25	0.08	1.00	*	I753A/B
57	Raychem RT-876 (A.R. + 72h/80°C)	**1.04**	0.88	0.16	0.06	0.31	**0.15**	0.16	0.01	0.30	0.17	1.00	0.17	I754A/B
58	Velcro #009-0599loop (A.R+72h/80°C)	0.38	0.21	0.17	0.01	0.26	0.06	0.20	0.01	0.68	0.29	1.18	*	I754A/B
59	Velcro#009-0599hook(A.R. +72h/80°C)	0.41	0.24	0.17	0.04	0.29	0.10	0.19	0.01	0.71	0.42	1.12	0.25	I754A/B
	Average value over 59 materials	0.982	0.526	0.466	0.044	0.524	0.059	0.467	0.007	0.539	0.233	1.031	0.214	*2

Table 2 : Micro-VCM data for single (A) and double (B) tests (see also table 1)

		Single test (A)				Double test (B)				Ratio (B/A)				
A	B	C	D	E	F	G	H	I	J	K	L	M	N	O
No:	Material Name and Number	%TML	%RML	%WVR	%CVCM	%TML	%RML	%WVR	%CVCM	G/C	H/D	I/E	J/F	REF.
25	Eccobond 55/9 (24h/RT + 2h/70°C)	0.80	0.34	0.46	0.00	0.47	0.02	0.45	0.000	0.58	0.06	0.98	*	I749A/B
26	Solithane 113 (A.R.)	0.52	0.35	0.17	0.01	0.20	0.03	0.17	0.000	0.38	0.09	1.00	*	I749A/B
27	Kapton 0.3 mil VDA perfor.-Sheldahl (AR)	**1.28**	0.10	1.18	0.00	1.26	0.08	1.18	0.000	0.98	0.80	1.00	*	I749A/B
28	Kapton 2 mil VDA perfor.- Sheldahl (AR)	**1.55**	0.05	1.50	0.00	1.46	0.02	1.44	0.000	0.94	0.40	0.96	*	I749A/B
29	Kapton 2 mil VDA nonperfor.-Sheldahl (AR)	**1.44**	0.05	1.39	0.00	1.36	0.04	1.32	0.000	0.94	0.80	0.95	*	I749A/B
30	Electrodag 501/kapton VDA-2 mil (AR)	**1.33**	0.15	1.17	0.00	1.19	0.00	1.19	0.000	0.89	0.00	1.02	*	I750A/B
31	Permacel P213(glass/acrylic tape) (AR)	0.43	0.20	0.23	0.00	0.26	0.03	0.23	0.000	0.60	0.15	1.00	*	I750A/B
32	Permacel P224 (kapton/acrylic tape) (AR)	0.97	0.19	0.78	0.00	0.84	0.06	0.78	0.000	0.87	0.32	1.00	*	I750A/B
33	Scotchtape Y966 (acrylic adhes.tape) (AR)	0.55	0.44	0.11	0.00	0.19	0.07	0.12	0.000	0.35	0.16	1.09	*	I750A/B
34	Synton 70 (A.R.)	**1.39**	**1.20**	0.19	**0.58**	0.24	0.04	0.20	0.01	0.17	0.03	1.05	0.02	I752A/B
35	Gudebrod 18DPTH (A.R)	0.51	0.24	0.27	0.00	0.29	0.00	0.29	0.00	0.57	0.00	1.07	*	I751A/B
36	Kynar Fon 1.3618-4 (A.R)	0.56	0.51	0.05	0.09	0.11	0.04	0.07	0.01	0.20	0.08	1.40	0.11	I753A/B
37	Kynar Fon 1.3618-16 (A.R)	0.59	0.56	0.03	0.01	0.05	0.02	0.03	0.00	0.08	0.04	1.00	*	I754A/B
38	Raychem RT-876 (A.R)	**1.42**	**1.29**	0.13	**0.27**	0.39	**0.25**	0.14	**0.02**	0.27	0.19	1.08	0.07	I754A/B
39	Velcro#009-0599 (tape loop A.R)	0.48	0.27	0.21	0.01	0.29	0.06	0.23	0.00	0.60	0.22	1.10	*	I754A/B
40	Velcro#009-0599 (tape hook A.R.)	0.52	0.33	0.19	0.02	0.29	0.08	0.21	0.01	0.56	0.24	1.10	0.50	I754A/B
	Average value	0.896	0.392	0.504	0.062	0.556	0.053	0.503	0.003	0.561	0.224	1.050	0.031	

Table 3 : Micro-VCM data for single (A) and double (B) tests on 16 "as received" materials (see also table 4)

		Single test (A)				Double test (B)				Ratio (B/A)				
A	B	C	D	E	F	G	H	I	J	K	L	M	N	O
No:	Material Name and Number	%TML	%RML	%WVR	%CVCM	%TML	%RML	%WVR	%CVCM	G/C	H/D	I/E	J/F	REF.
44	Eccobond 55/9(A.R +72h/80)	0.64	0.19	0.45	0.00	0.46	0.02	0.44	0.00	0.72	0.11	0.98	*	I749A/B
45	Solithane 113 (AR + 72h/80°C)	0.52	0.35	0.17	0.01	0.20	0.03	0.17	0.00	0.38	0.09	1.00	*	I749A/B
46	Kapton VDA-0.3 mil perfor.(A.R+72h/80)	**1.26**	0.09	1.17	0.00	1.15	0.07	1.08	0.00	0.91	0.78	0.92	*	I749A/B
47	Kapton VDA-2 mil perfor.(A.R+72h/80)	**1.52**	0.05	1.47	0.00	1.44	0.04	1.40	0.00	0.95	0.80	0.95	*	I749A/B
48	Kapton VDA 2 mil nonperfor.(A.R+72h/80	**1.39**	0.05	1.34	0.00	1.33	0.04	1.29	0.00	0.96	0.80	0.96	*	I749A/B
49	Electrodag 501/kapton 2mil(A.R+72h/80)	**1.09**	0.08	1.01	0.00	1.00	0.00	1.00	0.00	0.92	0.00	0.99	*	I750A/B
50	Permacel P213 (A.R + 72h/80°C)	0.37	0.17	0.20	0.00	0.24	0.04	0.20	0.00	0.65	0.24	1.00	*	I751A/B
51	Permacel P224 (A.R + 72h/80°C)	0.90	0.17	0.73	0.00	0.78	0.06	0.72	0.00	0.87	0.35	0.99	*	I751A/B
52	Scotchtape Y966 (A.R + 72h/80°C)	0.47	0.37	0.10	0.02	0.17	0.06	0.11	0.00	0.36	0.16	1.10	*	I752A/B
53	Synton 70 (A.R. + 72H/80°C)	0.35	0.15	0.20	0.08	0.20	0.01	0.19	0.02	0.57	0.07	0.95	0.25	I752A/B
54	Gudebrod 18DPTH (A.R. + 72h/80°C)	0.39	0.13	0.26	0.00	0.27	0.00	0.27	0.00	0.69	0.00	1.04	*	I752A/B
55	Kynar Fon 1.3618-4 (A.R + 72h/80°C)	0.29	0.25	0.04	0.06	0.10	0.04	0.06	0.00	0.34	0.16	1.50	<0.16	I753A/B
56	Kynar Fon 1.3618-16 (A.R + 72h/80°C)	0.16	0.13	0.03	0.01	0.04	0.01	0.03	0.00	0.25	0.08	1.00	*	I753A/B
57	Raychem RT-876 (A.R. + 72h/80°C)	**1.04**	0.88	0.16	0.06	0.31	**0.15**	0.16	0.01	0.30	0.17	1.00	0.17	I754A/B
58	Velcro #009-0599loop (A.R+72h/80°C)	0.38	0.21	0.17	0.01	0.26	0.06	0.20	0.01	0.68	0.29	1.18	*	I754A/B
59	Velcro#009-0599hook(A.R. +72h/80°C)	0.41	0.24	0.17	0.04	0.29	0.10	0.19	0.01	0.71	0.42	1.12	0.25	I754A/B
	Average value	0.699	0.219	0.479	0.018	0.515	0.046	0.469	0.003	0.641	0.283	1.043	0.016	

Table 4 : Micro-VCM data for single (A) and double (B) tests on 16 "baked-72h/80°C" materials (see also table 3)

54-14
021436
269352
8P

INVESTIGATION OF NVR(NON-VOLATILE RESIDUE) PLATE RESULTS

Robert Scott Lange
NSI Technical Services Corporation

William J. Mitchell
McDonnell Douglas Space Systems Company

NASA, Goddard Space Flight Center

ABSTRACT

Experiments utilizing NVR(non-volatile residue) witness plates were conducted including a Storage Effects Test, Mixed Exposure Time Pairs Test, Filtering Test, and Doped Sample Test. The experiments were an outgrowth of previous tests in which NVR plates were evaluated after exposures ranging from one to five months and the mass per unit area collected showed no correlation to exposure time or with TQCM and SAW data. Although the additional experiments described herein did not explain the lack of correlation, they do provide some insight into the accuracy and random error sources in the use of NVR plates in the monitoring of cleanroom contamination.

INTRODUCTION

There is a need to monitor molecular contamination in clean-rooms where aerospace equipment is assembled and tested. The molecular contamination is referred to as non-volatile residue (NVR), and is caused by emitted gas, vapors, and aerosols. NVR will degrade performance of some optics and sensors when deposited on their surfaces and change the emittance of some thermal control surfaces.

NVR plates are routinely used in large aerospace cleanrooms to monitor facility molecular contaminants. Contaminants that have deposited on the plates are collected, weighed and analyzed.

In 1995, an experiment was conducted in the Goddard Space Flight Center SSDIF(Spacecraft Development and Integration Facility) cleanroom where NVR plates were evaluated after exposure periods of from one week to five months. The residue on the plates was analyzed by Fourier Transform Infrared Spectroscopy (FTIR) and Gas Chromatography/Mass Spectrometry (GC/MS). Mass accumulation with time was analyzed to determine if the accumulation rate was linear. Mass accumulation was also compared with that indicated by TQCM(temperature-controlled quartz crystal monitor) and SAW(surface acoustic wave) instruments. The results of this experiment were reported at the IES Annual Technical meeting in May, 1996 (ref. 1). The data showed a wide unexplained scatter of NVR plate mass accumulation and a lack of correlation with TQCM and SAW data. As a result, several additional tests were proposed. This paper is a report of the following additional tests which were recently completed.

Storage Effect Test. The purpose of this test was to determine if the NVR plates are subject to NVR adsorption while in storage. After NVR plates are cleaned, and prior to their deployment in the cleanroom, they are normally stored either in a storage case in the laboratory or in a transportation case in the precision cleaning area, a class 10,000 room outside of the SSDIF cleanroom. Plates were evaluated after storage in these two areas for varying periods of time.

Mixed Pairs Test. In the past, plates were handled in pairs. They received similar handling, storage, exposure, and evaluation. The results of pairs tended to be similar, but there was no trend indicating an increasing accumulation of NVR mass with exposure time as was expected. In this test, pairs of plates with different exposure times were evaluated to see if a variation in results would occur.

Filtering Test. Pairs were handled in the normal manner except that the NVR rinse from one plate was filtered and the other was not. In the previous experiment no filtering was employed. If there were a large amount of particles on the plates, they might add to the mass extracted from the rinse and be the cause of the considerably greater mass detected on the NVR plates as opposed to that indicated by the TQCM and SAW. Prior to the test, the filtering apparatus was tested with pure rinse solution and with solutions doped with known quantities of a contaminant.

Doped Sample Test. A carefully measured amount of sample contaminant was added to several cleaned and verified plates. The plates were then processed in the normal manner to determine how accurately the mass of contaminant could be detected.

Each of the above tests will be discussed and results and conclusions given. A review of the normal NVR plate methodology is first provided.

NVR PLATE METHODOLOGY

Large aluminum or stainless steel plates (one foot square) are cleaned, certified, and deployed in the cleanroom for a prescribed length of time(usually one to three months for normal cleanroom monitoring). At the completion of the exposure time, the plates are removed and transported to a laboratory where they are rinsed with high purity chloroform. The chloroform is evaporated at room temperature, and the residue is weighed to the nearest 0.1 milligram. Weights can be converted from milligrams per square foot to micrograms per square centimeter for easier comparison to TQCM and SAW results. The residue is then analyzed using a Fourier Transform Infrared Spectroscopy (FTIR) and Gas Chromatography/Mass Spectrometry (GC/MS) for molecular species.

Witness plates are cleaned by first washing with detergent and water, rinsing with water, and then rinsing alternately three times or more with isopropyl alcohol and chloroform. Each plate is certified after cleaning with the same method used for sample analysis. Acceptance criteria is 0.1 microgram per square centimeter or less.

After cleaning and certification, the plates are placed in custom aluminum storage/transport boxes. The boxes are constructed of welded aluminum sheet having a hinged door and screw type lock down. Each box holds up to three plates which can be stacked on studs and separated by clean spacers. Since there are no gaskets to the box/lid interface, an airtight seal cannot be achieved. When boxes containing plates are transported, they are sealed in cleanroom packaging film. Plates are only handled when being deployed or retrieved and are picked up by their edges by personnel wearing alcohol rinsed polyethylene gloves. In the lab, they are handled with clean white cotton gloves. Plates are deployed in the cleanroom by suspension on clean, stainless steel wires.

The witness plate methodology used at GSFC is similar to the practice described in ASTM E1235-88 and ASTM E1234-88(ref. 2, 3).

STORAGE EFFECTS TEST

During previous testing(ref. 1), two "control" plates were certified by the lab in the usual manner (less than 0.1mg) and were then transported to the building 29 SSDIF cleanroom area. Instead of deployment in the cleanroom, the transport case was placed in a heat-sealed bag constructed of low outgassing packaging film and placed in a clean cabinet dedicated to witness plate box storage. After 30 days the plates were returned to the lab for analysis and were found to have 0.2 and 0.3mg of NVR. These readings were of concern as they indicated that plates might be adsorbing NVR while in storage either in the lab, in the storage area in building 29, or in the transport process.

The purpose of the storage effects test was to gather further data on NVR plate adsorption during storage or transportation. Plate #8 had been stored in

the lab storage cabinet for almost a year. It was decided to test this plate for the effects of storage. Results were less than 0.1 mg.(see Table 1) which indicates lab storage conditions are satisfactory (based on a sample of one). Two additional pairs of plates were certified and then deployed in the SSDIF cleanroom for periods of 30 and 42 days(see Table 1). Each plate of the 30 day pair revealed 0.2mg, and each plate of the 42 day pair showed 0.6mg. The 42 day pair transport box was packaged in clean aluminum foil for the trip from the lab as no clean plastic wrap was available, a slight variation from the normal process which would not seem significant.

The results of this test show that: (1)a significant amount of NVR contaminant can be deposited when plates are stored in the transport container or (2)there is a systematic error in the processing of the sample which is related to the time at which plates are processed in the lab (pairs of plate which are processed together tend to have similar results).

Until this is resolved, plate time in the transport container will be minimized (as is usually is now). Plates will be deployed immediately after transport from the lab. Also additional effort will be expended in the cleaning of the transport containers prior to their use and consideration will be given to certification of the transport containers prior to their use.

Table 1. STORAGE EFFECTS TEST

PLATE #	START	END	TIME days	MASS mg/ft2	STORAGE LOCATION
8	6/21/95	6/5/96	349	0.1	B-30 LAB
38	6/12/96	7/11/96	30	0.2	B-29 PCR
5	6/12/96	7/11/96	30	0.2	B-29 PCR
35	7/23/96	9/03/96	42	0.6	B-29 PCR
1	7/23/96	9/03/96	42	0.6	B-29 PCR

MIXED PAIRS TEST

In the previous experiment(ref. 1) a large number of pairs of NVR plates were exposed in the cleanroom and evaluated. The reasons for this were (1)comparisons of aluminum vs. stainless steel and rough vs. smooth plates were being made and pairs would generally contain one of each, and (2)it was thought that having two samples taken under the same conditions would provide more control of the test. The resulting data showed the results of pairs to be similar but when the pairs data was compared with exposure time there was a great deal of scatter and no discernable trend with time. The TQCM and the SAW data indicated an upward trend with time with a mass per unit area of one or two orders of magnitude less than the NVR plates. Thus, there was poor correlation with TQCM and SAW data in terms of magnitude of NVR mass deposited and there was no increase in mass deposited on NVR plates with time as we had been conditioned to expect by the TQCM and SAW data.

Equilibrium Theory. One of the theories to explain the lack of increasing deposition with time is that NVR adsorbs and desorbs from the surface depending on cleanroom pressure, temperature, humidity, and/or air quality. Thus, the surface equilibrium conditions at the time the pair of plates was removed were more important than how long the plates were exposed.

Process Error Theory. Another theory is that there are errors in the analysis "process" (cleaning of the plate, handling, transporting, rinsing, evaporation, weighing, etc.), that result in variations in the results but tend

to act the same on pairs that are processed together.

The purpose of this test was to attempt to get more data on mass deposition correlation with exposure time. The lab was provided "mixed" pairs, i.e., pairs with differing exposure times but similar processing. Two plates with different exposure times were removed at the same time and processed together. If the exposure time had a significant effect, i.e., if the mass varied with exposure time, the results would tend to rule out the equilibrium theory. If each plate in a pair was similar as before, we would still not be able to distinguish between the equilibrium theory and the process error theory.

The results(see Table 2) did not show a definitive correlation with exposure time. The first pair, which was not mixed (same exposure time of 32 days) had differing results (0.2 and 0.4 mg/ft2). This result may be an indication that the accuracy of processing NVR plates may not be as good as the +,-0.1mg generally expected. Of the two mixed pairs tested, one pair had identical results of 0.4 mg/ft2 and the other had differing results with the plate having greater exposure time having the larger mass accumulation. Unfortunately, the limited results do not support a correlation with exposure time and the test was not designed to discriminate between the equilibrium theory and the process error theory. Thus, the results appear to be inconclusive when taken by themselves.

Table 2. MIXED PAIRS TEST

PLATE #	START	END	TIME days	MASS mg/ft2	MIXED PAIR?
32	6/13/96	7/15/96	32	0.4	NO
52	6/13/96	7/15/96	32	0.2	NO
H	6/13/96	8/05/96	53	0.4	YES, #1
6	7/08/96	8/05/96	28	0.4	YES, #1
82	6/13/96	9/09/96	88	0.9	YES, #2
9	7/08/96	9/09/96	63	0.4	YES, #2

FILTERING TEST

In the previous experiment(ref. 1) and in normal processing of NVR plates at GSFC filtering of the rinse solution is not employed. However, the Standard Test Method, ASTM-1235-88(ref. 2) does specify filtering. The purpose of this test was to determine if filtering is necessary to remove particles that are not part of the NVR contamination but which might be adding to the mass collected from the rinse. It was suspected that Aluminum particles generated by the plate handling and from movement in the transport containers might be significant. (Another concern with filtering is the possible loss of some of the NVR contaminant sample in the filtering process).

A test was conducted by exposing and processing several pairs of plates with identical handling except that the rinse from one plate of each pair was filtered while the other was not filtered. Prior to the filtered vs. non-filtered test, the filter apparatus was tested.

Filter Apparatus Test. A filter apparatus was assembled per the ASTM consisting of a glass microanalysis filtering assembly (Fisher P/N 09-753-E) and polytetrafluoroethylene (PTFE) filter paper (Fisher P/N F02LP02500). Several tests were conducted as a check on the set-up before the "filtering" test began. Results are shown in Table 3. A 70 ml sample of spectroscopic grade chloroform was evaporated to dryness without exposing it to the filter apparatus. The amount of NVR collected was 0.2mg. FTIR analysis indicated it consisted of

traces of aliphatic hydrocarbons. This test was disappointing in that results closer to 0.0mg were expected from a sample taken directly from the certified bottle and evaporated in a cleaned, pre-weighed dish. The lab certifies NVR plates as clean when residue is less than 0.1mg and it was generally thought that the process of rinsing, evaporation, and weighing could be kept to an error of +,-0.1mg. This test indicates the difficulty in maintaining this level of accuracy.

A 70 ml sample of chloroform was then run through the filter assembly without a filter paper installed. The amount of NVR collected was 0.1mg. FTIR showed that it contained a small amount of dioctyl phthalate(DOP). A eight inch section of Tygon tubing was used in the filter apparatus to create a vacuum at the collection container. It was suspected that the DOP was leached out of the Tygon tubing.

(A test was later made by passing 70ml of chloroform through a one foot sample of the Tygon tubing and 113 mg of DOP was collected confirming that DOP is readily leached from this tubing by chloroform).

A 70ml sample was then filtered using the same filter assembly along with a PTFE filter paper. The amount of NVR collected was less than 0.1mg. Chemical analysis indicated that it also contained a small amount of DOP.

Finally, 2.4mg of DOP was dissolved in 70 ml of chloroform and then filtered using the same assembly. The amount of DOP collected was 2.2mg.

It was concluded that the apparatus was working satisfactorily with the exception that the Tygon tubing should be replaced. Polyethylene tubing was ordered but was not immediately available. The testing was continued using the Tygon tubing.

Table 3. FILTER APPARATUS TEST

SAMPLE	AMOUNT	TYPE	MASS mg	ANALYSIS
1	70 ml	chloroform only	0.2	aliphatic hydrocarbon
2	70 ml	pass thru assy	0.1	small amt DOP
3	70 ml	thru assy+paper	<0.1	small amt DOP
4	70 ml +2.4mg	doped sample thru assy+paper	2.2	DOP
5	70 ml	thru 1 ft. Tygon	113	DOP

Filtered vs. Non-filtered Test. Three pairs of plates were deployed in the cleanroom for periods of 38, 44, and 51 days. The pairs were processed in the same manner except that one plate of each pair had its rinse solution filtered before evaporation. The results of the test are shown in Table 4. Note that for each pair, the filtered rinse yielded a greater amount of NVR. In the case of plate J, which yielded the most mass, it was noted that tap water came back through the Tygon tube used to create vacuum in the filter apparatus and contaminated the rinse solution. This sample also contained a significant amount of DOP leached from the tubing. All three filtered samples showed more DOP than the comparable non-filtered sample.

The results of the filtered vs. non-filtered test and the apparatus test indicate that filtering should not be instituted with the present methodology and apparatus. Some additional testing will be done with polyethylene tubing replacing the Tygon tubing in an attempt to gain confidence in the method.

In order to characterize the magnitude of particles on the surface of the

filters, particles were counted and sized in accordance with Mil. Std. 1246A. This process assigns a numerical cleanliness level to a surface based on the size and distribution of particles over a given area. The lower the number, the cleaner the surface. Particles were also classified by their material composition when possible. This inspection was performed in a cleanroom.

Cleanliness levels of all three filters were between level 100 and level 200, indicating that they were very clean. A total of three small metal particles (assumed Aluminum) were found, two of which were on plate 35 (see Table 4). No attempt was made to weigh the particles because of their limited number and size. The mass of the material filtered from the rinse was not significant when compared to the NVR mass collected after evaporation.

The filtering test, although imperfect because of the apparatus problem, did not indicate that a significant portion of the mass was due to particulates that could be filtered out of the solution.

Table 4. FILTERED vs. NON-FILTERED TEST

PLATE #	TIME days	FILTERED?	MASS mg/ft2	ANALYSIS (largest to smallest amount)
1	38	N	<0.1	AE, AH, DOP, BBP, PA
35	38	Y	0.3	AE, DOP, AH, PA, BBP
43	44	N	0.3	AE, AH, DOP, DP, BBP, PA
J	44	Y	1.1	DOP, AE, PA, SA, AH
7	51	N	0.3	AE, DOP, AH, DP, BBP, PA
10	51	Y	0.5	AE, DOP, AH, OA, BBP

AE = adipate esters
AH = aliphatic hydrocarbons
DOP = Di(2-ethylhexyl) phthalate
BBP = butyl benzyl phthalate
PA = palmitic acid
DP = dibutyl phthalate
SA = stearic acid
OA = organic acids

DOPED SAMPLE TEST

In the previous experiment(ref. 1), the data showed a wide scatter and no correlation was found between mass deposited and plate exposure time. In order to rule out some of the variables that may have caused the scatter, various aspects of the plate processing procedure were tested. A doped sample test was performed to determine the NVR removal efficiency and consistency of the witness plate rinsing, evaporation, and weighing technique used. This test was run with five samples using differing amounts of a readily available test contaminant, dioctyl phthalate(DOP). (In the future the test may be repeated using a silicone contaminant for comparison with the results using DOP).

In each test, a carefully measured amount of DOP was placed into a small beaker. A small amount (5ml) of spectroscopic grade chloroform was added to the sample and swirled to dissolve it. The solution was poured onto the witness plate. An additional small amount of chloroform was poured into the beaker, swirled, and poured onto the plate. The sample was allowed to stand for the chloroform to evaporate (10 minutes). The plate was then rinsed with 70ml of chloroform, collected, and processed in the normal manner.

The data obtained from the five runs (see Table 5) shows a difference of no greater than 0.2mg when the amount applied and the amount recovered are compared. As the test required two weighings (the sample applied and the recovered amount), this is within the expected accuracy. It appears that almost all of the DOP was recovered. The results of this test indicate that the rinsing

and weighing technique is not a major source of error in the process.

Table 5. DOPED SAMPLE TEST

TEST #	AMOUNT DOP APPLIED (mg)	AMOUNT NVR REMOVED (mg)	DIFFERENCE (mg)
1	0.5	0.7	+0.2
2	1.3	1.3	0.0
3	1.5	1.6	0.1
4	2.1	2.2	0.1
5	0.8	0.7	-0.1

CONCLUSIONS

The storage effects test pointed to a significant amount of contaminant being deposited on the plates while in the transport container (or to an error in the processing that gave this result). Until this is resolved, plate time in the transport container will be minimized and additional cleaning of the transport containers will take place prior to each use.

The mixed pairs test was inconclusive in that one pair showed the same amount of contaminant for varying exposure times while the other pair showed amounts that correlated with the differing exposure times. There was some indication in these tests that the accuracy of the process may not be as good as the +,- 0.1mg generally believed in the past.

The filtering test showed that particulates were not adding significantly to the NVR mass collected and that filtering does not appear to be necessary. Due to increased handling, more error may be introduced when conducting the filtering step. The test also showed that the Tygon tubing used in the filter apparatus will have to be replaced as the solvent used (chloroform) extracts DOP from the tubing.

The doped sample test showed that nearly all of the sample contaminant was recovered by the method used for rinsing, evaporation, and weighing of the NVR contaminant and that this portion of the sample processing likely does not contribute significant error.

The tests showed that there are chances for error in each step of the process that can effect the accuracy of the NVR mass collected. When collecting amounts measured in tenths of milligrams from one square foot surfaces, extreme care must be taken in each step of the process to prevent significant error from creeping into the results. A primary value of the NVR collection process lies in the FTIR and GC/MS analysis which provides a "signature" for a particular cleanroom and allows one to detect, identify, and eliminate any foreign compounds that enter the cleanroom. This paper touched only briefly on the chemical analysis of the NVR contaminant and concentrated on the mass of NVR collected. However, controlling the collection process to prevent any addition to or loss of the mass of the sample will help maintain the accuracy of the chemical analysis. In practice, for the SSDIF cleanroom at GSFC, changes of a few tenths of a milligram are not considered significant if the mass adsorbed on three month NVR plates is 1.0mg or less, the limit for Mil. Std. 1246A level A surface cleanliness (ref.4). If the mass exceeds 1.0mg, or if strange compounds are detected, investigation is required.

The question of the disagreement between the mass collected on NVR plates and that detected by TQCM and SAW instruments is still unexplained.

AREAS FOR FURTHER INVESTIGATION

As a result of the above testing, the cleaning and certification of the transport containers will be studied.

Also, more tests will be done on the filtering apparatus after replacing the Tygon tubing with polyethylene tubing.

Additional doped witness plates may be tested doping with a silicone contaminant.

Finally, the lack of correlation in the amount of mass per unit area collected by the NVR plate vs. that collected by TQCM and SAW instruments is an area for continued investigation as ideas surface.

ACKNOWLEDGEMENTS

The authors would like to thank Mary Ayres-Treusdell and Alex Montoya from the GSFC Materials Engineering Branch for their help in the planning, laboratory analysis, and consultation on the results of the testing described herein.

REFERENCES

1. Mitchell, W. J., and Lange, R. S., "A Comparison of NVR(Non-Volatile Residue) Plate and TQCM(Temperature-Controlled Quartz Crystal Microbalance) Measurements of Molecular Contamination", Proceedings of the 42nd Annual Technical Meeting of the IES, pp. 160-170, 1996.

2. ASTM E1235-88(Reapproved 1993), Standard Test Method for Gravimetric Determination of Nonvolatile Residue (NVR) in Environmentally Controlled Areas for Spacecraft, American Society for Testing and Materials.

3. ASTM E1234-88, Standard Practice for Handling, Transporting, and Installing Non-Volatile Residue (NVR) Plates Used in Environmentally Controlled Areas for Spacecraft, American Society for Testing and Materials.

4. Military Standard 1246B, 4 September 1987, Product Cleanliness levels and Contamination Control.

S5-27

REDUCTION OF CALCOFLUOR IN SOLITHANE CONFORMAL COATINGS OF PRINTED WIRING BOARDS

Michael K. Miller[1] Lt. USAF
Goddard Space Flight Center, NASA
Greenbelt, MD 20771

ABSTRACT

An investigation on the outgassing of a pigment employed as a fluorescent medium in conformal coatings has been performed. The conformal coatings in question are used to protect printed wiring boards from environmental hazards such as dust and moisture. The pigment is included in the coating at low concentration to allow visual inspection of the conformal coating for flaw detection. Calcofluor, the fluorescent pigment has been found to be a significant outgasser under vacuum conditions and a potential source of contamination to flight hardware. A minimum acceptable concentration of Calcofluor for flaw detection is desirable. Tests have been carried out using a series of Solithane™ conformal coating samples, with progressively lower Calcofluor concentrations, to determine the minimum required concentration of Calcofluor. It was found that the concentration of Calcofluor could be reduced from 0.115% to 0.0135% without significant loss in the ability to detect flaws, while at the same time significant reductions in Calcofluor outgassing and possible contamination of systems could be realized.

INTRODUCTION

Calcofluor[1] is mixed into Solithane[2] to provide detection of flaws when the Solithane-Calcofluor conformal coating is exposed to UV light. It has been found that the use of Calcofluor in Solithane conformal coatings for circuit boards may be a large source of contamination. Because of this, interest has been expressed in developing a specification for an acceptable minimum percentage Calcofluor mixed with Solithane which is still adequate to detect flaws in the conformal coatings under UV. The normal amount of Calcofluor used in a Solithane compound has been 100g of part A(Solithane 113), 74g of part B(Solithane 113-300), and 0.2g Calcofluor. These weights are referred to as a 0.2 pbw (parts by weight) Calcofluor mixture. Likewise the same mixture of Solithane components with 0.1g Calcofluor would correspond to the 0.1 pbw mixture. In order to determine the amount of Calcofluor required to detect defects in the Solithane conformal coatings, a set of 4 mil thick coatings composed of different percentages of Calcofluor were applied to aluminum test plates. The plates were visually inspected for defects and fluorescence. The set of plates included the following amounts of Calcofluor mixed with 20.0 g of Solithane 113 and 14.8 g of Solithane 113-300:

Plate Number	Calcofluor (g)	Calcofluor (pbw)*	%Calcofluor
1,2	0.0	0.0	0.0
3,4	0.04	0.2	0.115
5,6	0.02	0.1	0.0574
7,8	0.01	0.05	0.0287
9,10	0.01	0.05	0.0287
11,12	0.005	0.025	0.0144
13,14	0.0027	0.0135	0.0078

* The units pbw are a common designation used locally within GSFC, they refer to the weight in grams used per 100g of the A component of Solithane and 74g of the B component.

[1] Mr. Miller, a graduate of the Air Force Academy, carried out this research at GSFC as a participant of the Program for Research and Education in Space Technology (PREST). His advisers were Dr. J. Scialdone, Code 313 and Dr. P. Chen, Code 724. He wishes to acknowledge the help of several members of the Materials Engineering Branch.

METHOD

The study consisted of mixtures including 0.2, 0.1, 0.05, 0.025, and 0.01 pbw. The goal of the study was to determine the minimum amount of Calcofluor required for effective flaw detection in conformal coatings of circuit boards prior to exposure to vacuum conditions. The second step was to determine if this reduction in the quantity of Calcofluor would actually reduce the level of contaminant present under vacuum conditions. To determine if this was so a series of tests was carried out in a Vacuum Industries test chamber at pressures on the order of 10^{-7} and 10^{-8} torr. The 0.2, 0.1, 0.025 and 0.013 pbw test plates as well as the pure Solithane test plates were exposed to vacuum for a period of 24 hours at a temperature of 75°C. During the test, condensates were collected on a cold plate at a temperature of -25°C. After completion of the 24 hours cycle the cold plate was rinsed and condensed material was weighed to determine the collected volatile condensible mass (CVCM). Then the residue was analyzed by both Infrared and Gas Chromatograph-Quadrupole Mass Spectometry. The IR and GS/MS analysis was used to obtain the recommendation on the level of Calcofluor to be used.

A diagram of the instrumentation is shown in the appendix. The Vacuum Industries chamber includes a two stage pumping system with a mechanical backing pump and a diffusion pump which can achieve pressures down to approximately 10^{-8} torr. Backstreaming from the diffusion pump was controlled using liquid nitrogen cooled cold trap and a liquid nitrogen controller.

The chamber itself is an 18 inch diameter bell jar which contains a hot plate, cold plate and thermocouples. All of the hardware within the bell jar was chosen with the fewest number of outgassants possible, so as to hold contamination to a minimum. The hot plate rested on an adjustable scissors jack and was raised so that there was approximately 1 inch spacing between the sample and the cold plate. The hot plate itself was a simple resistance coil hot plate controlled by an external controller. The controller ran through a high limit controller which detected the hot plate temperature and would open an alarm condition switch if the temperature went above a preset value. The controller signal was sent to a 110 volt, 10 ampere solid state relay which would open and close the switch from the power source to the hot plate depending on the temperature of the hot plate. Temperatures were measured on the hot plate, the cold plate and the sample itself using a series of type T thermocouples.

The 8x6 inch cold plate consisted of a simple aluminum plate with copper tubing coiled at 1 inch intervals across the top surface. These coils carried ethylene glycol based antifreeze which was cooled by a Neslab chiller to temperatures of -25°C. This plate was covered with an aluminum foil wrap which had been cleaned using a series of isopropyl alcohol and chloroform rinses. The foil served as a surface for condensation which provided and easy method to collect and rinse the contaminant

Once the series of plates were made the first step in analysis was visual inspection of the samples for defects. Upon visual inspection of the conformal coatings under UV illumination it was apparent that as little as 0.0135 parts by weight was sufficient for detection of flaws in the conformal coating. Each coating was prepared with included flaws (nylon fibers and brush fibers) to simulate possible defects. The nylon filament was 2 mil in diameter and cut into lengths of approximately 1-2 mm. The brush hair was approximately 1 mil in diameter and was cut to lengths of less than 1 mm. In addition a certain amount of defects were created during the preparation technique. It was found that although the level of fluorescence was reduced somewhat in both the 0.025 and 0.0135 pbw Calcofluor, the fluorescence was sufficient to detect both the included flaws as well as naturally occurring defects in the coating. This demonstrated that the level Calcofluor could be reduced to as little as 0.0078% rather than the 0.115% currently used.

The following observations were made during visual inspection of the test plates under UV:

0.2 pbw Calcofluor: The entire plate demonstrated signs of fluorescence. All the included flaws (nylon fibers and brush hair) could be seen with relative ease. The plates also exhibited numerous spots which demonstrated fluorescence. These were attributed to areas of higher Calcoflouor concentrations.

0.1 pbw Calcofouor: The same observations were seen as in the 0.2 pbw Calcofluor plates. In additon a dark, pin sized hole was observed penetrating the entire thickness of the coat in plate #6. However, when the edge of a probe was used to scratch the surface of the plate, an increase in fluorescence at the scratch was observed.

0.05 pbw Calcofluor: All the included flaws could be seen with relative ease. In additon bright spots of Calcofluor were visible.

0.025 pbw Calcofluor: The bright spots due to undissolved Calcofluor were less visible, and the fluorescence was slightly less intense, but the flaws were clearly visible.

0.0135 pbw Calcofluor: The level of fluorescence was similar in intensity to the 0.025 pbw. All flaws were visible.

0.0 pbw Calcofluor: Demonstrated no signs of fluorescence from the Solithane itself. Nylon fibers could be seen because of their own fluorescence.

Once the visual inspection was completed each plate was placed in the vacuum chamber and heated to a temperature of 75°C for 24 hours at pressures ranging from 10^{-6} to 10^{-8} torr. The actual pressure was somewhat time dependent and also depended to some degree on the amount of material outgassing from the Solithane sample. Condensables were collected on the aluminum wrapped cold finger at -25°C. These deposits were rinsed from the aluminum after the test was completed with alcohol and chloroform. The collected material was weighed and then analyzed by both IR and GC/MS analysis. The results of this analysis are discussed in detail in the Results section.

RESULTS

The following data on the collected deposits and the related CVCM (mass collected/initial mass of Calco + Solithane) were obtained.

Sample Plate Initial Conditions and Results

% Calcofluor	Wt. Solithane(g)	Wt. Calcofluor(mg)	Collected Wt.(mg)	%CVCM
0.115	3.34	3.834	7.0	2.10E-03
0.057	1.18	0.678	3.7	3.14E-03
0.014	1.13	0.162	2.8	2.48E-03
0.008	2.34	0.182	4.8	2.05E-03
0.0	0.00	0.000	3.8	1.05E-03

pbw Calcofluor	% Calcofluor
0.2	0.115
0.1	0.057
0.025	0.014
0.0135	0.008

0.0 0.0

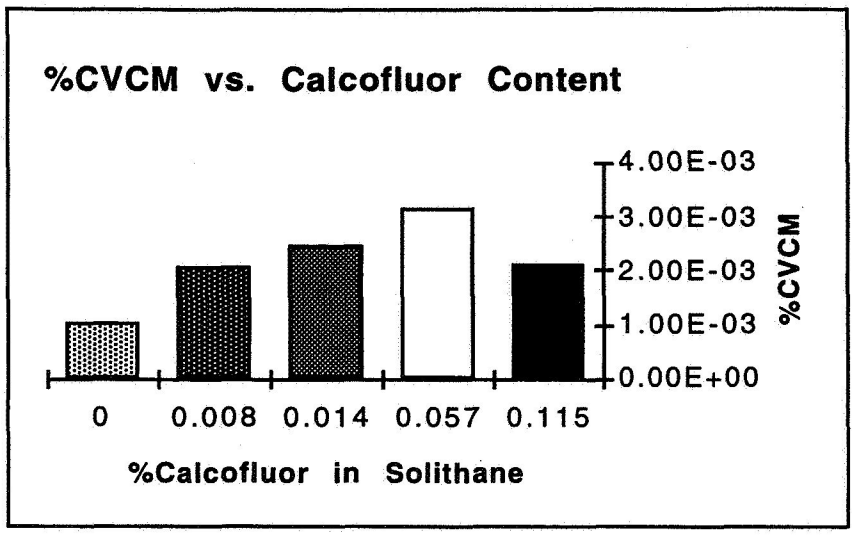


Figure 1

This results indicate that the highest concentration of Calcofluor produces by far the greatest accumulation of contamination. However there was not a linear trend towards less contamination as the concentration of Calcofluor was decreased. One possible explanation was that below a certain percentage of Calcofluor, the contamination was mainly produced by the Solithane, and that variations in the thickness of the Solithane coating itself lead to variations in the weight of the outgassants collected.

The information illustrated in Figure 1 indicates that as the Calcofluor content is increased the level of contamination also increases. However the highest Calcofluor concentration did not follow this trend. An explanation may be that the conformal coating was somewhat thicker on the sample plate for the 0.2 pbw(0.115%) sample. The thicker coating could limit the diffusion of Calcofluor out of the material leading to lower collected weights. Additional analyses were carried out to provide correlation between increased Calcofluor and CVCM.

The contaminant was analyzed by IR and GC/MS to determine the composition of the released products and quantify the amount of those materials present. Upon completion of the 24 hour test the collected deposits were rinsed into an evaporation dish and weighed once dry. The residue was then analyzed by FTIR and GC/MS. FTIR analysis primarily focused on detection of absorption peaks at 1711 and 1612 cm^{-1}. These wavelengths are indicative of the presence of Calcofluor, but 1711 cm^{-1} proved to be less useful because the several common esters cause absorption at that frequency as well. By comparing the height of the Calcofluor peaks at 1612 cm^{-1} relative to the peaks caused by silicones in the same spectra, the following charts (fig. 2) were obtained.

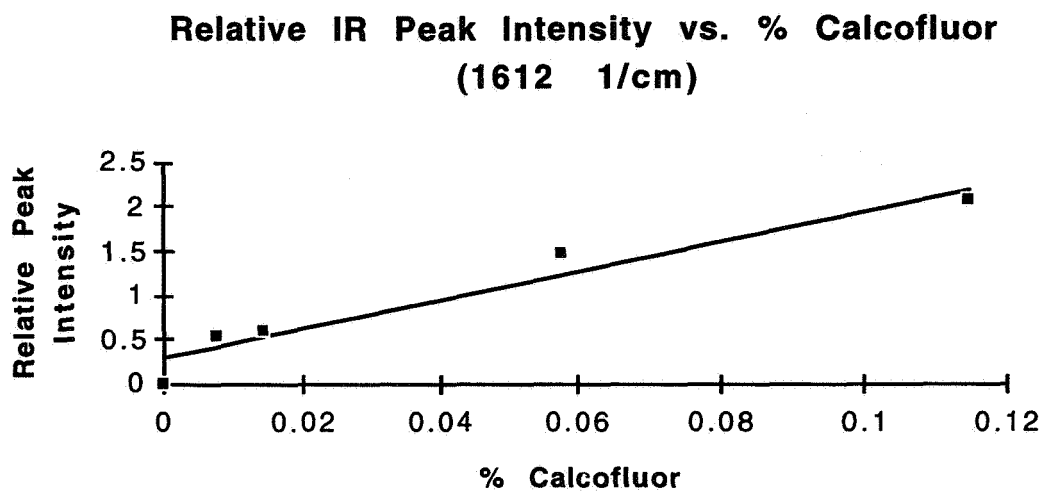


Figure 2

Figure 2 displays the Calcofluor peak at 1612 cm^{-1} relative to the peak caused by silicone pump oil at 1216 cm^{-1} as a function of the concentration of Calcofluor in the conformal coating. A second plot Figure 3 was produced by comparing the peaks due to Calcofluor relative to a peak at 1177 cm^{-1} from silicone pump oil, as a function of the Calcofluor concentration. This diagram is shown below.

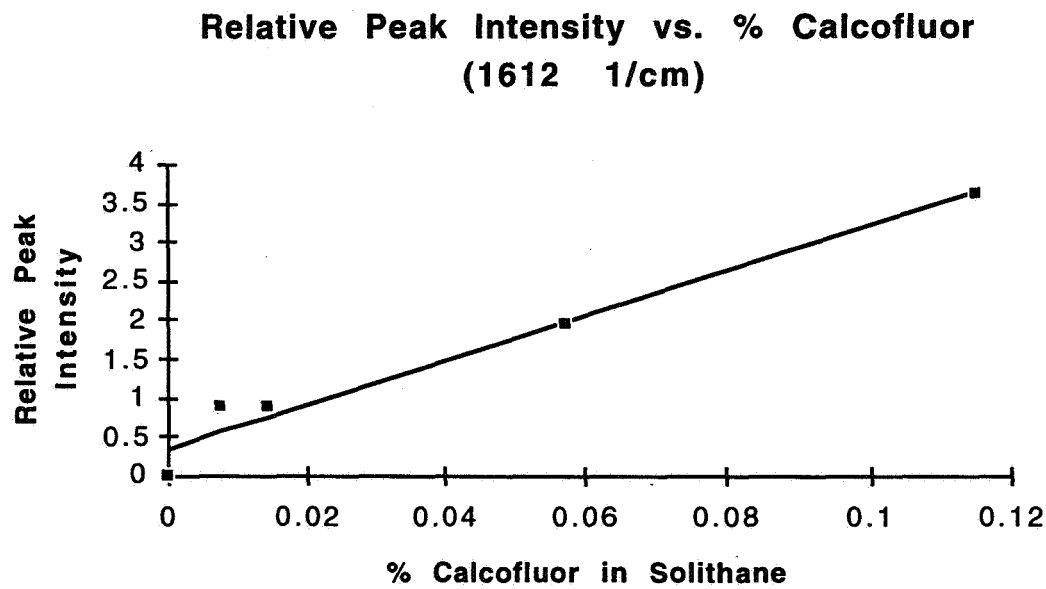


Figure 3

GC/MS analysis of the residue showed similar results. Each sample was normalized to a silicone peak caused by backstreamed diffusion pump oil present in each sample. The silicone peaks were

assumed to be relatively constant and thus could be used to compare with the peak areas for Calcofluor. This resulted in the following curves (fig. 4 and 5):

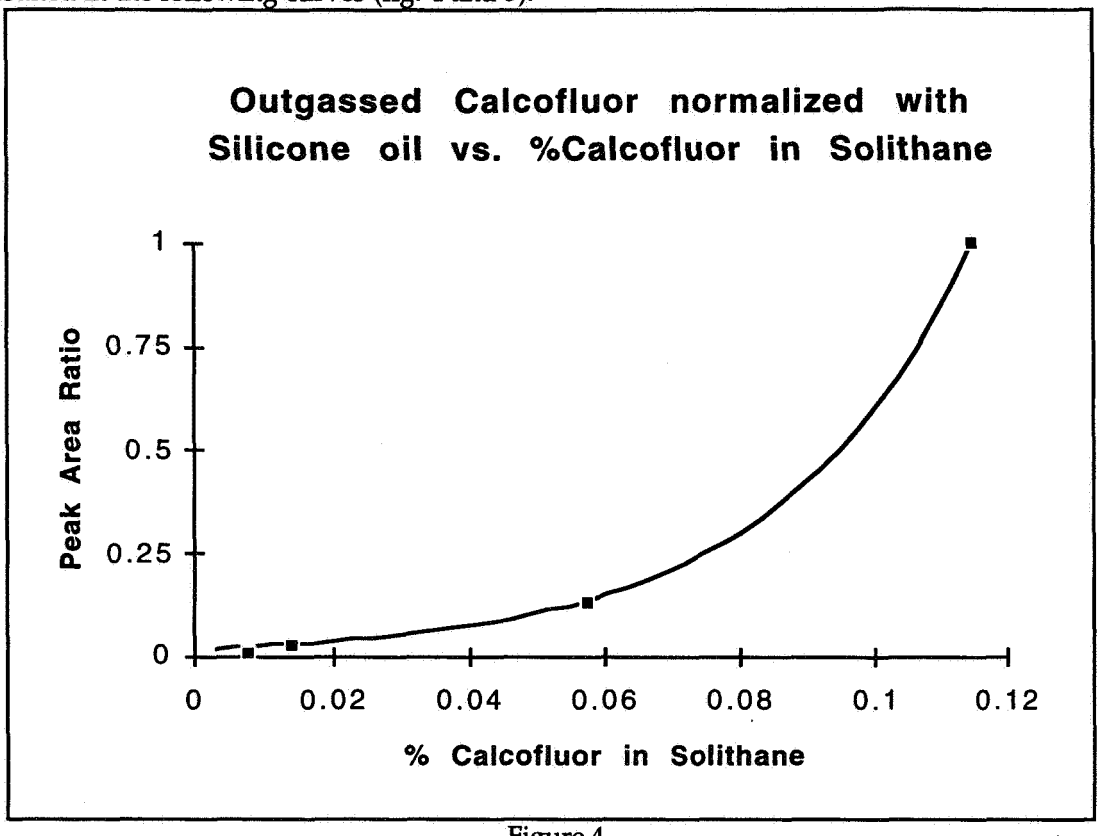


Figure 4

Calcofluor peak area normalized to diffusion pump oil

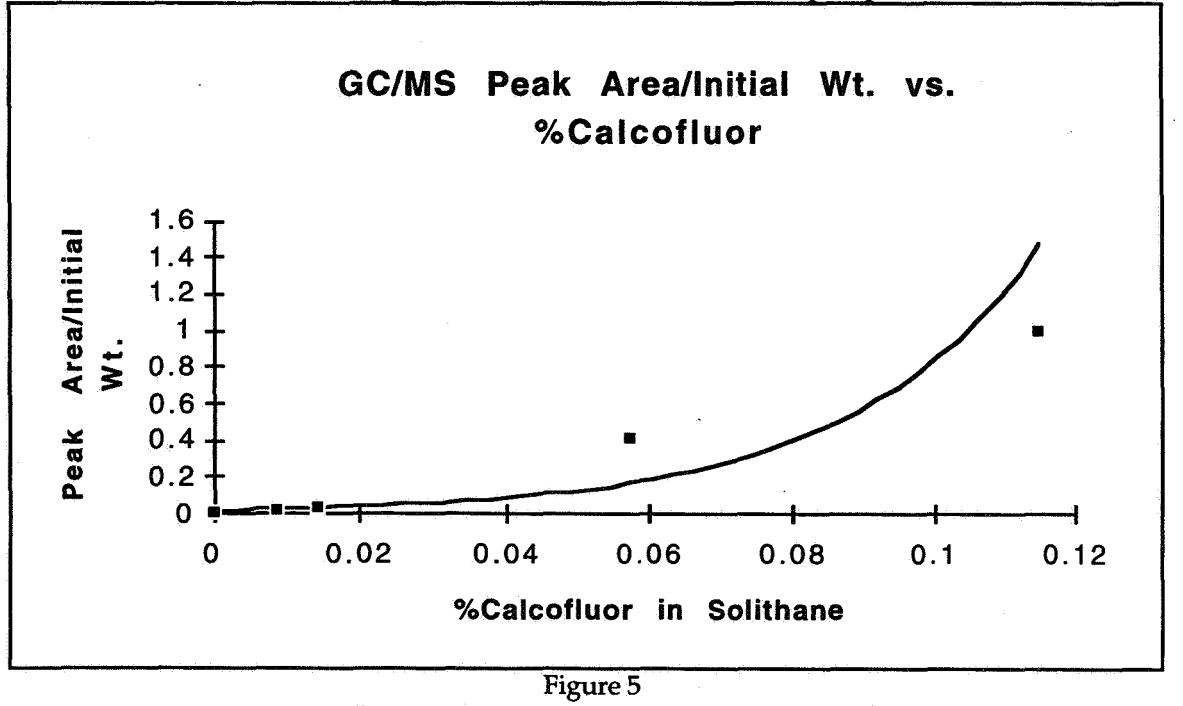


Figure 5
Calcofluor peak area normalized to initial weight

This method of analyzing the contamination is perhaps the most accurate and yet shows the most dramatic increase in the level of contamination as the concentration of Calcofluor was increased.

CONCLUSIONS

After investigating the fluorescence of different concentrations of Calcofluor in Solithane conformal coatings, as well as the contamination caused by outgassing Calcofluor in these coatings, one can recommend that the concentration of Calcofluor be reduced from 0.115% Calcofluor (0.2pbw) to 0.0078% Calcofluor (0.0135pbw). Using only 0.0135 pbw Calcofluor significantly reduced the contamination caused by the fluorescent pigment yet proved to be sufficient for flaw detection in Solithane conformal coatings.

The investigation has also indicated the methods to be followed in evaluating outgassing originating from compounds. The peak area indications of GC/MS with respect to peak areas of some reference compound can be helpful in establishing the amount of a specific contaminant over a series of initial sample concentrations.

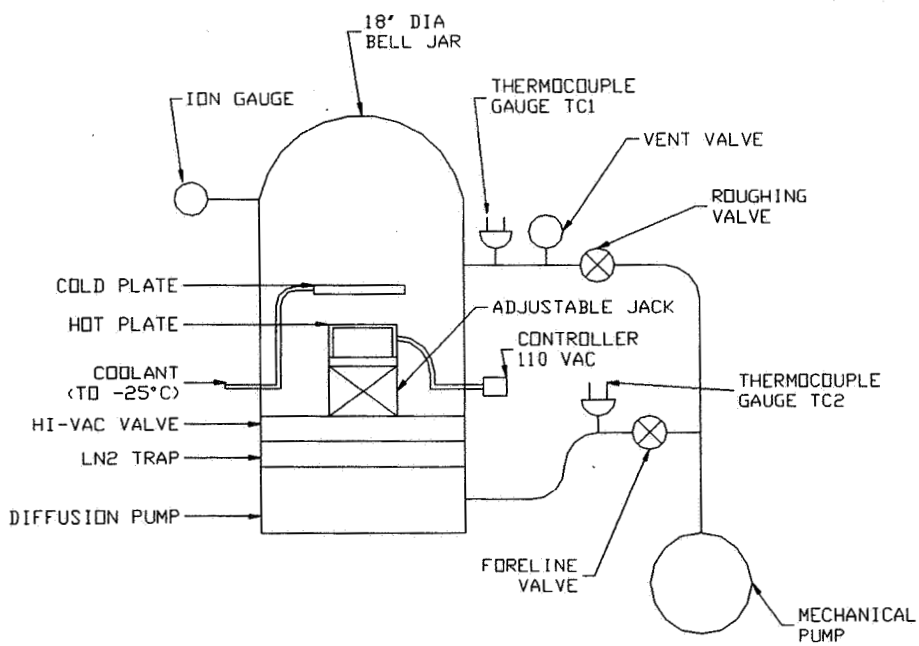
REFERENCE

[1.] Calcofluor is a trade name of American Cyanamid Co. for a fluorescent powder consisting of 4-methyl-7-diethyl amino coumarin (MDAC).

[2.] Solithane is a trade name of Thiokol Chemical Corp. for a polyurethane coating.

APPENDIX

VACUUM CHAMBER & TEST SET-UP



96-18
269360

MIDCOURSE SPACE EXPERIMENT MOLECULAR CONTAMINATION MODELING PREDICTIONS FOR EARLY ORBITAL OPERATIONS*

David M. Silver[a], R.C. Benson[a], M.T. Boies[a], J.S. Dyer[b], R.E. Erlandson[a], G.E. Galica[c], B.D. Green[c], D.F. Hall[d], J.C. Lesho[a], T.E. Phillips[a], O.M. Uy[a], B.E. Wood[e]

[a] *Applied Physics Laboratory, The Johns Hopkins University, Laurel, Maryland 20723*
[b] *Utah State University, Space Dynamics Laboratory, Logan Utah 84322*
[c] *Physical Sciences, New England Business Center, Andover, Massachusetts 02155*
[d] *Aerospace Corporation, El Segundo, California 90009*
[e] *Sverdrup Technology, Arnold Engineering Development Center, Arnold Air Force Base, Tennessee 37389*

ABSTRACT

Molecular contamination modeling results are presented for molecular outgassing and return flux, and interactions of the MSX spacecraft with the expected ambient flight environment. The modeling of outgassing source terms, which include volatile condensable material, water, argon, hydrogen and other miscellaneous molecules, are described. The modeling of return flux of contaminant molecules back to the MSX is described, leading to a return flux ratio model for collisional return. Using these source terms and return flux ratios, the predictions of mass flux return are then presented. The predicted outgassing and mass flux returns are compared with flight data from the MSX contamination experiment instruments, showing reasonable agreement. Finally, the effects of early molecular contaminants on the optical instruments is discussed. The design, fabrication and handling of the MSX spacecraft have been aimed at mitigation of contamination effects. Consequently, the predicted levels of molecular outgassing contamination are low enough to be within the tolerable limits imposed by the needs of the optical instruments.

INTRODUCTION

The Midcourse Space Experiment (MSX) spacecraft[1,2] was launched on 24 April 1996 at 08:27:40 EDT into a high inclination circular near sun synchronous orbit at approximately 900 km altitude. The potential for molecular contamination was a major concern in the period of early orbital operations immediately following insertion of MSX into its orbit, since sensitive optical instruments and other critical surfaces are potentially vulnerable to condensable molecules that outgas from some element of the spacecraft and find their way to the surface in question. As with any spacecraft, all sources of outgassing molecules are at their highest level at this point, decreasing over time. Each different optical instrument operates over a specific wavelength band, has a specific operating temperature, and a particular location on the spacecraft. The differences in these variables cause each instrument to have its own sensitivity to a specific collection of molecules and circumstances. To eliminate or reduce the potential deleterious effects of molecular contamination, considerable attention is paid to the sequencing of events, such as aperture cover openings during early operations, notwithstanding all contamination mitigation efforts in the design, fabrication, testing, integration, handling, and all pre-launch activities[3]. The purpose of contamination modeling[4] of early orbital operations is to make predictions of the spacecraft environment and its contamination interactions prior to launch[5] as an aide to early operations decisions. In this paper, some aspects of the pre-launch modeling[5] of the molecular contamination environment of MSX in early orbital operation are summarized.

PRELIMINARY CONSIDERATIONS

MSX is a multi-purpose optical platform with the additional ability to measure spacecraft contamination effects[6] and ambient environmental parameters. It carries a suite of instruments[7] as drawn in Figure 1, including a cryogenic infrared imager and spectrometer (SPIRIT III), nine ultraviolet and visible imagers and spectrographs (UVISI), a space-based visible telescope (SBV), ejectable reference objects, a neutral mass spectrometer (NMS), an ion mass spectrometer (IMS), a total pressure sensor (TPS), a cryogenically cooled quartz crystal microbalance (CQCM), four temperature controlled quartz crystal microbalances

* This work was supported in part by the Ballistic Missile Defense Organization and in part by the Department of the Navy, Space and Naval Warfare Systems Command under Contract N00039-95-C-0002.

(TQCM), a krypton flash lamp and a xenon flash lamp. The MSX is roughly a rectangular parallelepiped with its long axis designated the x axis, as depicted in Figure 1. Two rotatable rectangular solar panels are attached to opposite sides of the MSX. The MSX is divided into three main sections: the instrument section at the +x top, the truss section or Dewar bay in the middle, and the electronics section at the -x bottom. All the optical instruments, the reference objects, the NMS, the TPS, the CQCM, one TQCM and the two lamps have their fields of interest aligned along the +x axis and are physically located around the +x facial extremity of the MSX as shown schematically in Figure 1.

All of the external surfaces of MSX are insulated[8] with Multi-Layer Insulation (MLI) blankets except for the instrument apertures, antennas, beacons and receivers, one side of the Dewar bay, the radiator areas and the solar panels. The blanketing used for the instrument section consists of the following set of layers, described from the innermost spacecraft layer to the outermost space-facing layer: a 25.4 μ layer of Kapton with one side aluminized; twenty layers of 6.35 μ double-sided aluminized Mylar (DAM) with wide weave Dacron netting between layers; a layer of Dacron sailcloth; and a top layer of 127 μ Teflon coated with a 30 nm layer of silver, 5 nm layer of Inconel, and a 5 nm layer of indium-tin-oxide. The MLI blankets on the remainder of MSX consist of the layers: a 25.4 μ layer of Kapton with one side aluminized; twenty layers of 6.35 μ DAM with wide weave Dacron netting between layers; and a layer of fiberglass coated Teflon (Beta Cloth) with an embedded graphite thread forming a 10.2 cm by 15.2 cm grid. The attachment of the MLI to the spacecraft involves Dacron polyester threads and polyester Velcro tiedowns. The inner layers of the MLI blankets used on the instrument section of MSX are perforated to permit a flow of the outgassing water through the layers and facilitate an exit through the innermost layer of the blanket.

The temperature of the MLI blanketing[8] was assumed to be essentially a uniform 0 °C on day one of the MSX flight. By the second day into the flight, temperature gradients were expected through the layers of the blanketing. Exposure of different surfaces of MSX to intermittent periods of heat sources (sun, earth and Moon shine) as MSX underwent attitude maneuvers during the first days of flight were expected to affect local temperatures of the blanket surface. However, for the nominal park mode, it was expected that by the second day of flight the average temperatures for the inner and outer surfaces of the MLI blankets would stabilize. A temperature of -30 °C corresponds to the nominal beginning-of-life thermal design for the surfaces and instruments in the instrument section in park mode. This was the temperature assumed in the calculations[9] of outgassing volatile condensable molecules.

OUTGASSING SOURCE TERMS

The IMS, TPS, TQCMs and the two lamps had aperture coverings that were removed in the final pre-launch period. All the optical instruments and the NMS had covers sealing their apertures during ascent into orbit. The aperture cover for SPIRIT III was cryogenically cooled with solid argon and therefore had a steady flow of argon evolving from it. The cover opening mechanisms for the NMS and UVISI instruments involved pyrotechnical devices that were sealed in metal bellows. SPIRIT III used an o-ring sealed pyrotechnical device for its cover opening mechanism. The NMS and the nine UVISI covers rotated to an open position but stayed attached to the instruments. The SPIRIT III cover was ejected from the spacecraft when opened. The SBV cover has a motor that allows it to be opened or closed in response to uplinked ground commands. The various covers were removed, opened or exercised in the sequence: NMS, SBV, UVISI, and finally SPIRIT III. The timing of the openings depended on the expected and measured contamination environment of the +x face of MSX during early operations.

There are several sources of outgassing concern on MSX. The time course of these should follow the general pattern outlined below. Predictions of the outgassing rates for MSX in its early flight time are given in the subsections that follow.

(1) At the initial time in orbit, there should be a residual layer of about 5 nm water and 5 nm volatile condensable material (VCM). Generally these molecules are physisorbed on all surfaces, but are expected to vaporize and disappear in a timeframe of minutes and should be of no concern.

(2) The volatile condensable materials should immediately begin outgassing from all nonmetallic materials. Based on experience with isothermal tests[10] and consideration of the attention paid to thermal vacuum bakeout of MSX materials, the VCM outgassing rates of these materials are expected to reach their asymptotic values within the timespan of hours. A more conservative estimate of the time for the outgassing to reach its asymptotic limit is then a day. With a time constant of 3.5 years, the steady asymptotic outgassing rate is expected to remain on the order of years. Paint on broad surfaces may have a VCM outgassing time constant of two weeks, which may stretch out to six months due to the encapsulation within the MLI blankets. Honeycomb has a VCM outgassing time constant of 1.0 to 1.5 years, but longer if the edges are sealed or closed off. Since the optical instruments were flown with aperture covers that were not removed until after the first few days in flight, it is the asymptotic outgassing rate of the VCM that is critical to these instruments.

(3) Water outgasses mainly from the MLI thermal blankets covering most of the external surfaces of MSX. As a contaminant, water is a concern to SPIRIT III because the temperature of its mirror surface is low enough to condense water. Given the MSX space environment and the temperatures of the surfaces, water will not condense on any of the other optical instruments. Because of the temperature gradients within the MLI blankets and the expected variety of heat exposures due to early operations attitude maneuvers, the outflow of water is a fairly complex problem. Nevertheless, laboratory outgassing tests [11,12] on MLI blankets were used to set limits on the expected water environment.

(4) While the SPIRIT III cover was in place, it emitted a flow of argon. The argon itself posed no direct contamination problem with respect to condensation on any sensitive optical surface, other than SPIRIT III. Only during the cover ejection process is the argon a possible contaminant for SPIRIT III. However, prior to the cover release, the rate of outflow of argon was high enough to create a high collisional return of other molecular species. Therefore the argon needed to be considered in conjunction with other species.

(5) Hydrogen flows from the main SPIRIT III Dewar, but the outlet pipe is situated near the electronics section and the outflow is directed in a -x/+y direction that is opposite to the instrument section. Hydrogen itself will not condense on any optical surface on MSX.

(6) When an o-ring sealed pyrotechnical device is deployed for cover release, it can emit some molecules. The quantity of emitted pyro-gas was considered in conjunction with the argon environment during the SPIRIT III cover release.

Volatile Condensable Material

The volatile condensable material (VCM) consists mostly of organic or silicon based molecules that are found within the non-metallic materials used throughout the spacecraft. The VCM molecules are residual solvents, fabrication reactants, degradation products, etc. Electronic boxes are examples of venting where the non-metallic materials (integrated circuits, conformal coatings, insulators, etc.) inside the boxes release their VCM by diffusion under vacuum conditions. This VCM, by random scattering inside the box, eventually passes out through the various orifices in the box housing (vents). The encapsulation of the VCM-bearing non-metallic materials in boxes effectively reduces the diffusion rate of the VCM so that encapsulated VCM sources will usually take much longer to vent all of their interstitial VCM than if the non-metallic sources were removed from the box and their surfaces exposed directly to vacuum where molecular diffusion-limited outgassing occurs. With MSX, these venting boxes are mounted inside of a thermal control enclosure (consisting of the shroud of MLI blankets) that creates a second level of encapsulation, increasing the complexity of the vent path. The overlapping MLI blankets vent the VCM that is venting from the covered boxes and units through the Velcro strip fasteners which are used to attach the blankets to the spacecraft structures. These MLI attachment configurations only marginally reduce the effective box venting rates which depend on the unique design of each box. As the successive encapsulations decrease the net outflow rate, the total elapsed time to deplete the VCM inside of the spacecraft is proportionally longer.

The non-metallic materials containing VCM are distributed in three broad areas of the MSX spacecraft: the electronics section, the solar panels and the instrument section. By far the largest quantity of VCM is found within the electronics section, and more specifically, within the electronic boxes distributed throughout the electronics section. Using the materials inventory lists for MSX, and scaling from measured VCM box venting rates, estimates were generated [9] for the outgassing and venting of the electronic boxes on MSX. In addition to boxes, sources of VCM on MSX include the adhesives which bond together the structural components of the honeycomb mounting panels and VCM within the paint on the surfaces of the panels and boxes. For the solar panels, the outgassing materials of interest are the adhesive FM-300, which bonds the facings of the panels to their honeycomb cores, and the adhesive RTV-566, which bonds the solar cells to the facings. In addition, the lubricants found in the solar wing positioning drive and deployment mechanisms are sources of VCM.

A free molecular flow field analysis was performed for MSX by E. A. Zeiner [9] using MOLECAP. This algorithm calculates the VCM venting rates from the enclosures which contain electronic boxes, painted areas, cabling, insulation, etc. The parameters that characterize the contamination flow field are the venting VCM mass fluxes. The MSX venting analysis computes VCM vent fluxes from the three general enclosures. The first enclosure includes 123 boxes and units mounted on the six panels of the electronics section which are in turn almost completely encapsulated by MLI blankets except for occasional cutouts to expose the electronics section radiators. The second enclosure is the solar panels which vent through the gaps in the solar cells and through the honeycomb core. The third enclosure includes the instruments and units mounted on the four panels of the instrument section, which is also encapsulated with MLI blankets with cutouts to expose the instrument section instruments and radiators. The directivity of the VCM fluxes venting from the electronic section and the instrument section are obviously dominated by the design of the MLI blankets, particularly where they are closed out with Velcro around structures and where they overlap each other around corners.

The results of the MOLECAP analysis for the outgassing rates are given in Table 1. The VCM outgassing mass flux from the electronics section is somewhat greater, but close to the same order of magnitude as the outgassing from the solar panels. The instrument section has an outgassing mass flux that is two to three orders of magnitude less than that found in the electronics section. This is partly due to the lower operating temperature (-35 ^{0}C to -5 ^{0}C) of the equipment in the instrument section compared to the warmer range (-29 ^{0}C to 66 ^{0}C) in the boxes that are venting VCM in the electronics section. The outgassing mass flux from the +x face of the instrument section is greater than the mass flux emanating from the +/-z and y sides of the instrument section. The exits for the mass flux from the +x face of the instrument section are the exposed pieces of equipment located on the +x face, including the beacon panel, while on the +/-z and y faces, the mass flux follows the vent patterns designed for MSX thermal blankets. When normalized for the outgassing area, the mass flux densities from the different sides of the solar panels show a definite face to edge difference. The mass flux densities for the faces of the instrument section are closer to one another than the mass fluxes.

Water - MLI Blankets

The MLI thermal insulation blankets used on MSX consist of several different materials for both the metallized films, the interlayer netting, and the cloth reinforcement layers, as described above. However, the bulk (twenty layers) of the material is comprised of 6.35 μ thick Double Aluminized Mylar (DAM) alternating with Dacron Netting. Outgassing measurements have been performed [11] on these two materials and provide both time and temperature dependent outgassing fluxes. Less information is available for the metallized Kapton film, the Dacron sailcloth, the fiberglass coated Teflon and the various metallizations used in the MSX blankets. Therefore, the outgassing rates for these materials is necessarily more approximate.

Modeling of the outgassing of water from the MLI blankets on MSX involves both the 6.35 μ DAM and the Dacron Netting. Analytic expressions for the time and temperature dependence of the early water outgassing of DAM have been given[11] in terms of an exponential and reciprocal time factor. Fitting of the Dacron Netting outgassing data for times greater than eight hours yields a simple inverse power law that should be reasonable especially at the lower temperatures.

The water outgassing model for the MLI per layer is plotted in Figure 2, covering the range of 96 hours and -60 ^{0}C to 20 ^{0}C. A linear time scale was chosen for Figure 2 since the hour-by-hour evolution is of interest over this period. The contamination model for the MSX MLI blankets accounts for the expected initial temperature of 0 ^{0}C for the first day in orbit and then a transition to the expected flight temperatures. For MSX at day two, the distribution of temperatures amongst the layers of the complete MLI blanket is taken to be as follows: the innermost one-third of the layers assume the internal spacecraft temperature, the middle one-third of the layers continue to remain at 0 ^{0}C, and the outermost one-third take on the outside surface temperature. Outgassing of water is lowest in the truss section, which is also the coldest section. Between 10 to 40 hours, water is most rapidly coming out of the electronics section, which is the warmest section. However due to the loss of water, the outgassing rate for the electronics section falls below the rate seen for the instrument section by 40 hours. Therefore on days three and four, the instrument section is outgassing water at the highest rate, $8x10^{-12}$ gm/cm^2 sec at 48 hours and falling to $3x10^{-12}$ gm/cm^2 sec at 96 hours.

RETURN FLUX

There are four principal mechanisms by which molecular effluents from a spacecraft may impinge on spacecraft surfaces. These are illustrated in Figure 3: direct surface-to-surface return, ricochet off an intermediate surface, self-collision return and ambient collision return. In addition, there can be multiple ricochet and multiple molecular collision possibilities. The return flux ratio is the flux of outgassing molecules impinging on a surface divided by the flux of outgassing molecules.

A direct line-of-sight path from the source of outgassing to a spacecraft surface provides the strongest impingement rate. The flux of molecules at the receiving surface will be diluted by the spatial spreading that occurs, which approaches a value close to the square of the distance between the emitting and receiving surfaces. Calculation of direct molecular return fluxes is straightforward given the geometry of a spacecraft.

Depending on the interaction between the outgassing molecules and the intermediate surface, and on its temperature, material and shape, the ricochet mechanism may be the source of the next highest magnitude of molecular impingement. At one extreme, molecules may undergo a perfectly elastic collision with the intermediate surface and then proceed to the surface of interest, with only a dilution corresponding to spatial spreading. Alternatively, the molecules may spend a finite lifetime on the intermediate surface and be scattered from the surface into some kind of spatial distribution. The re-emission of molecules from

the intermediate surface and spatial spreading of the flux causes only some of the original molecules to reach the surface of interest. Another ricochet case is where the impinging molecules absorb onto the intermediate surface and only slowly re-evaporate over a much longer time scale than the scale of molecular velocities and mean free paths. Calculation of ricochet molecular return flux is straightforward given the geometry of the spacecraft and an assumption regarding the molecular interaction expected at the intermediate surface.

The molecular collision return flux is a complicated molecular dynamics problem, involving collisions between two outgassing molecules (self collision) or collisions between an outgassing molecule and an ambient atmospheric molecule. Direct Simulation Monte Carlo (DSMC) techniques have been developed to handle such problems [13]. At the MSX altitude and ambient molecular environment, collisions between outgassing molecules and ambient species predominate by an order of magnitude over outgassing-outgassing collisions. Ambient scattered return flux is proportional to the emitted flux and the ambient density (for fixed ambient velocity). Self scattering flux is proportional to the square of the emitted flux. The return flux is also proportional to the collision cross section of the molecules. For heavier outgassing molecules, the average velocity is lower, the mean free path is shorter, more collisions occur in the vicinity of the outgassing surface and therefore there are larger return fluxes. The return flux ratio is approximately directly proportional to the square root of the outgas species molecular weight for constant outgas flux rate. These generalizations permit the construction of a return flux ratio model, shown in Figure 4 for return flux onto the emitting surface. Various DSMC [14-17] and single collision calculations [18] are shown in Figure 4 for outgassing fluxes in the range 10^{-10} to 10^{-11} gm/cm^2 sec, scaled to a molecular weight corresponding to argon molecules as the outgassing species. In addition, DSMC calculations were performed [17] at considerably higher outgassing fluxes. In the outgassing flux range of about 10^{-7} gm/cm^2 sec, the outgassing changes to a multiple collision regime. At outgassing fluxes greater than 10^{-4} gm/cm^2 sec, the return flux ratio drops because there are so many collisions that it becomes more difficult to arrive back at the emitting surface. It should be noted that the self return flux is independent of the attitude of the spacecraft relative to the ram direction, whereas the ambient return flux is determined by the direction and properties of the ambient ram environment.

During the early orbital flight times of MSX, the principal interest in the mass flux return is with respect to the +x instrument section surface and the instrument apertures. Although the direct and ricochet mechanism of return shown in Figure 3 could potentially give the strongest return fluxes, none of the optical instruments have any structure in their line of sight. Therefore only collisional return is relevant for the optical instruments.

PREDICTED EFFECTS ON CONTAMINATION INSTRUMENTS

During the early orbital phase of MSX, the molecular contamination environment is dominated by copious amounts of water, with lesser amounts of VCM flux. The SPIRIT III aperture cover is supercooled before launch and therefore no argon vaporizes until the critical cryogen temperature is reached, some six hours after orbital insertion. However, once the argon begins to vaporize, then a steady diffuse argon cloud dominates the +x face of MSX. The water outgassing is at a high flux rate at the earliest times and drops as time passes. The VCM reaches its low level asymptotic outgassing rate quite early and appears to be nearly constant for short times. The water is detectable with the TPS, NMS and Krypton Lamp experiment. The argon is detectable by the TPS and NMS. The VCM is detectable with the TQCMs, and at high enough incident flux rates with the TPS and NMS. The specific quantities of contaminant species measured by the different instruments differ because of the difference in the location and environment of the respective instruments and due to differences in the mechanism of transport of contaminant species to the particular measurement zones of the instruments.

TPS [19]

Figure 5 gives flight data [19] for the TPS and a comparison with the MSX Contamination Model [5] predictions for water and for argon at the position of the TPS. During the initial six hours in orbit, while the SPIRIT III cover was in place and the argon cryogen remained supercooled, the outgassing of water was detected by the TPS. Agreement between the TPS flight data and the MSX Contamination Model is excellent during this first six hours. After the first six hours and until the SPIRIT III aperture cover was released, the pressure measured by the TPS was dominated by the incident argon. Aside from the transient pressure spikes arising from unsteady argon release, the agreement between the TPS flight data and the MSX Contamination Model is quite reasonable. The dominant mechanism responsible for the water pressure was expected to be direct facial outgassing from the MLI blankets that are in the field-of-view of the TPS. The argon pressure results from collisional return to the TPS location.

NMS [20]

The aperature cover of the NMS was deployed and the first flight data taken after 19 hours into the mission. Since the NMS can discriminate on the basis of the mass of the incoming species, the water pressure at the NMS, shown in Figure 6, was discernable even with the SPIRIT III cover in place [20]. The NMS flight data in Figure 6 is drawn with a background correction and is compared with the MSX Contamination Model [5] predictions of water at the NMS location. The agreement between the NMS flight data and the MSX Contamination Model is reasonable , although not perfect. The direct facial outgassing of the MLI blankets in the field-of-view of the NMS was expected to dominate the water signal over the entire time period.

Krypton Lamp and Radiometer [21]

The Krypton Lamp contamination experiment consists of a bank of krypton flash lamps and a Kr radiometer. The krypton lamps excite water and the subsequent radiation of the excited species is detected by the radiometer, which interrogates the krypton flash beam in a volume above the +x face of the MSX instrument section. Flight data from the Krypton Lamp experiment are shown in Figure 7 with error bounds on the measurements [21]. These are compared with the MSX Contamination Model [5] predictions for the density of water to be expected in the volume above the +x face of MSX being measured by the Kr radiometer. Agreement between the krypton flight data and the MSX Contamination Model is quite good, especially considering the high fluctuations in the flight data at the later times. Facial and vent mechanisms of water outgassing from the MLI blankets are expected to dominate in this regime.

QCM [22]

Outgassing VCM molecules can condense on the four TQCMs at their operating temperature on MSX of -50 ^{0}C. The CQCM is cold enough to condense water and everything else except helium and hydrogen. During the initial period in orbit when the bulk of the water was outgassing from the MLI blankets, the SPIRIT III aperture cover was in place and therefore the CQCM was not exposed to the earliest orbital environment. The various TQCMs are pointing in particular directions, and therefore they are subject to different levels of backscattered VCM from the respective surfaces of MSX. The arrival of outgassed VCM on TQCM1, TQCM2 and TQCM3 from the solar panels depends on the solar panel rotation angle and the view factor that the TQCMs have of these structures. With an acceptance angle of 71.5^{0}, TQCM1 has a solar panel in its field-of-view for all values of the solar panel rotation angle. TQCM2 and TQCM3 have partial views of the solar panels. As the solar panels rotate, the TQCMs are exposed either to a solar panel edge, the solar cell (sun side) face or the non-solar cell (dark side) face. In addition, TQCM1 has a portion of the electronics section in its field-of-view. The expected outgassing flux of VCM from the electronics section, the sun side, the dark side and the edges of the solar panel are specified in Table 1. The predicted response of TQCM1, TQCM2 and TQCM3 to the flux of expected VCM including the outgassing of the solar panels is given in Figure 8 [5]. Although TQCM2 has no structure other than the solar panel in its field-of-view, its frequency response to VCM is comparable to that of TQCM1 because of the closer proximity of TQCM2, by about 20 cm, than TQCM1 to the solar panel. Flight data for TQCM2 are shown in Figure 9 [22] showing the accumulation of VCM in terms of a layer thickness.

PREDICTED EFFECTS ON OPTICAL INSTRUMENTS

Considerable attention had been paid to the issue of contamination in the design, fabrication and assembly of MSX [3]. The pieces and parts of all the instruments, the electronics and components had been meticulously thermal vacuum baked to remove VCM. It would take 7.85×10^{-7} gm of VCM to form a 1 Å layer on a 10 cm diameter surface. With the outgassing rate of 2.7×10^{-9} gm/sec predicted for the +x instrument section of MSX and a return flux ratio of 1.5×10^{-6}, it would take 1.9×10^{8} sec or 6.1 years to form a 1 Å layer. The consequence is that the UVISI instruments are not expected to experience degradation from incident VCM. Water is an unavoidable molecular contaminant, since it cannot be permanently removed before flight. It would take 0.1 gm of water to form a 1 μm layer on a 40 cm diameter surface. This is the amount of water that outgasses from a segment of MLI blanket of about 40 cm x 45 cm. Fortunately, the bulk of the water outgasses from the MLI blankets in a short time, while the SPIRIT III aperture cover is still in place.

SUMMARY

Laboratory and previous in-flight measurements provide a basis for contamination modeling. The application of theoretical models and tools allows predictions of the dispositions of molecules that leave a spacecraft during orbital flight. Molecular outgassing is a temperature, pressure and species dependant diffusion, venting and evaporation process. Once

molecules have escaped from their encapsulation within the spacecraft and its materials, their molecular trajectories can be direct line-of-sight, involve ricochet off intervening surfaces, or involve collisions between outgassing, venting or ambient molecules. The interaction of an outgassed molecule at an incident surface will depend on the temperature, incident flux density, species properties, surface properties and solar insolation. The specific geometric detail of the spacecraft and the materials, placement and fastening of thermal blanketing on the outer surface of the spacecraft play an essential role in the modeling of molecular contamination. The combination of all these aspects comprises the MSX Contamination Model and procedures. Comparison of the pre-launch calculations[5] with flight data during early operations shows excellent agreement. Further comparisons between the MSX Contamination Model and on-orbit measurements at later flight times will permit continued validation and refinement of the contamination source model and procedures.

REFERENCES

1. Mill, J.D., O'Neil, R.R., Price, P., Romick, G.J., Uy, O.M., Gaposchkin, E.M., Light, G.C., Moore, W.W.Jr., Murdock, T.L. and Stair, A.T.Jr., "Midcourse Space Experiment: Introduction to the Spacecraft, Instruments, and Scientific Objectives," *J. Spacecraft Rockets*, Vol. 31, No. 5, pp.900-907, 1994.
2. Peterson, M.R., Ed., "Midcourse Space Experiment: Overview," *Johns Hopkins APL Tech. Dig.*, Vol. 17, No. 1, 1996.
3. Cranmer, J.H., Sanders, J.T.Jr., Lesho, J.C. and Uy, O.M., "Contamination Control for the MSX: An Overview," *Johns Hopkins APL Tech. Dig.*, Vol. 17, No. 1, p. 88-101, 1996.
4. Silver, D.M., "Midcourse Space Experiment Contamination Modeling," *AIAA* 96-0223, January 1996.
5. Silver, D.M., "Midcourse Space Experiment Molecular Contamination Modeling Predictions for Early Orbital Operations," *JHU/APL-RCO-96-106*, April 15, 1996.
6. Uy, O.M., Benson, R.C., Erlandson, R.E., Boies, M.T., Lesho, J.C., Galica, G.E., Green, B.D., Wood, B.E. and Hall, D.F., "Contamination Experiments in the Midcourse Space Experiment," *AIAA* 96-0219, January 1996.
7. Huebschman, R.K., "The MSX Spacecraft System Design," *Johns Hopkins APL Tech. Dig.*, Vol. 17, No. 1, p. 41-48, 1996.
8. Krein, J.A. and Mehoke, D.S., "The MSX Thermal Design," *Johns Hopkins APL Tech. Dig.*, Vol. 17, No. 1, p. 49-58, 1996.
9. Zeiner, E.A., "Molecular Contamination Modeling of the Midcourse Space Experiment Spacecraft in Orbit," MSX Contamination Experiment Principal Investigator Meeting, USAF Space Systems Division, Los Angeles, California, 16 January 1991.
10. Glassford, A.P.M. and Garrett, J.W., Characterization of contamination generation characteristics of satellite materials, WRDC-TR-89-4114, November, 1989.
11. Glassford, A.P.M., Osiecki, R.A. and Liu, C.K., "Effect of Temperature and Preconditioning on the Outgassing Rate of Double Aluminized Mylar and Dacron Net," *J. Vac. Sci. Technol.*, Vol. A2, No. 3, pp. 1370-1377, 1984.
12. Glassford, A.P.M. and Liu, C.K., Outgassing rate of multilayer insulation materials at ambient temperature, *J. Vac. Sci. Technol.*, Vol. 17, pp. 696-704, 1980.
13. Bird, G.A., "Molecular Gas Dynamics and the Direct Simulation of Gas Flows," Oxford University Press, Oxford, 1994.
14. Nelson, D.A., "Monte Carlo Modeling," MSX Contamination Experiment Principal Investigator Meeting, USAF Space Systems Division, Los Angeles, California, 16 January 1991.
15. Fong, M.C., "MSX Contamination Modeling Study Review," MSX Contamination Experiment Principal Investigator Meeting, USAF Space Systems Division, Los Angeles, California, 16 January 1991.
16. Fan, C., Gee, C. and Fong, M.C., "Monte Carlo Simulation of Molecular Flux on Spacecraft Surfaces Due to Self-Scatter of Outgassing Molecules," Lockheed Report TSS-457, 14 August 1992.
17. Monchick, L., "Molecular Scattering Experiments at High Altitudes," *Johns Hopkins APL Tech. Dig.*, Vol. 15, No. 2, pp. 164-171, 1994.
18. Ma, P.T., Zumwalt, L.C., Wang, F.C. and Yfantis, S.C., "BGK Contamination Model of the MSX Satellite and Comparison with Monte-Carlo Simulation Data," *SPIE Proceedings*, Vol. 1754, pp. 226-237, 1992.
19. Boies, M.T., Phillips, T.E., Silver, D.M., El-Dinary, A.S., Uy, O.M. and Dyer, J.S., "Total Pressure Sensor Results from the Early Operations Phase of the MSX Mission," *SPIE Proceedings*, Vol. 2864, Denver, August, 1996.
20. Benson, R.C., Phillips, T.E., Boies, M.T. and Uy, O.M., "Neutral Mass Spectrometer Results from MSX Early Operations Phase," *SPIE Proceedings*, Vol. 2864, Denver, August, 1996.
21. Galica, G.E., Atkinson, J.J., Aurilio, G., Shepherd, O., Lesho, J.C. and Uy, O.M., "Optical Measurement of the MSX Local H_2O Density," *SPIE Proceedings*, Vol. 2864, Denver, August, 1996.
22. Wood, B.E., Hall, D.F., Lesho, J.C., Dyer, J.S., Uy, O.M. and Bertrand, W.T., "Quartz Crystal Microbalance (QCM) Flight Measurements of Contamination on the MSX Satellite," *SPIE Proceedings*, Vol. 2864, Denver, August, 1996.

Table 1. Predicted VCM Mass Fluxes from MSX				
Instrument Section				
location	temperature ^{0}C	VCM mass flux gm/sec	cross sectional area cm^2	VCM mass flux density gm/cm^2 sec
+ X face	-30.0	2.70E-09	48138.2	5.61E-14
+ Z face	-30.0	4.30E-10	13304.8	3.23E-14
+ Y face	-30.0	3.50E-10	14434.8	2.42E-14
- Z face	-30.0	8.60E-10	13304.8	6.46E-14
- Y face	-30.0	0.00E+00	14434.8	0.00E+00
Solar Panels				
location	temperature ^{0}C	VCM mass flux gm/sec	cross sectional area cm^2	VCM mass flux density gm/cm^2 sec
sun side	25.0	4.28E-07	53454.8	8.01E-12
dark side	25.0	1.73E-07	53454.8	3.24E-12
+/- z edge	25.0	1.05E-07	796.6	1.32E-10
+/- x edge	25.0	5.75E-08	432.9	1.33E-10
Electronics Section				
location	temperature ^{0}C	VCM mass flux gm/sec	cross sectional area cm^2	VCM mass flux density gm/cm^2 sec
+ X face	2.8	1.84E-06	22458.0	8.19E-11
+ Z face	-13.5	4.62E-07	17583.8	2.63E-11
+ Y face	-4.6	9.79E-07	17583.8	5.57E-11
- Z face	13.1	7.37E-07	17583.8	4.19E-11
- Y face	-2.4	7.08E-07	17583.8	4.03E-11
- X face	12.3	4.79E-07	36290.3	1.32E-11

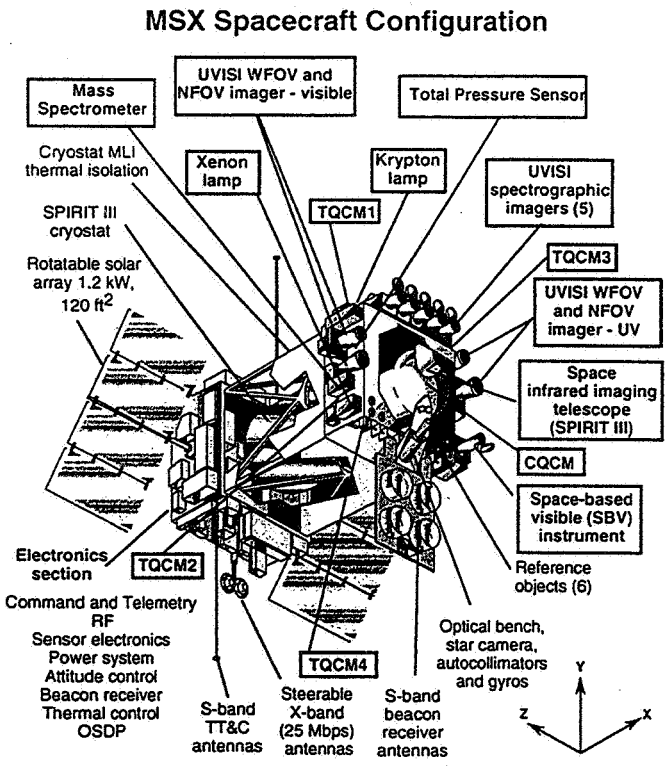


Figure 1 : MSX spacecraft configuration and local coordinate system.

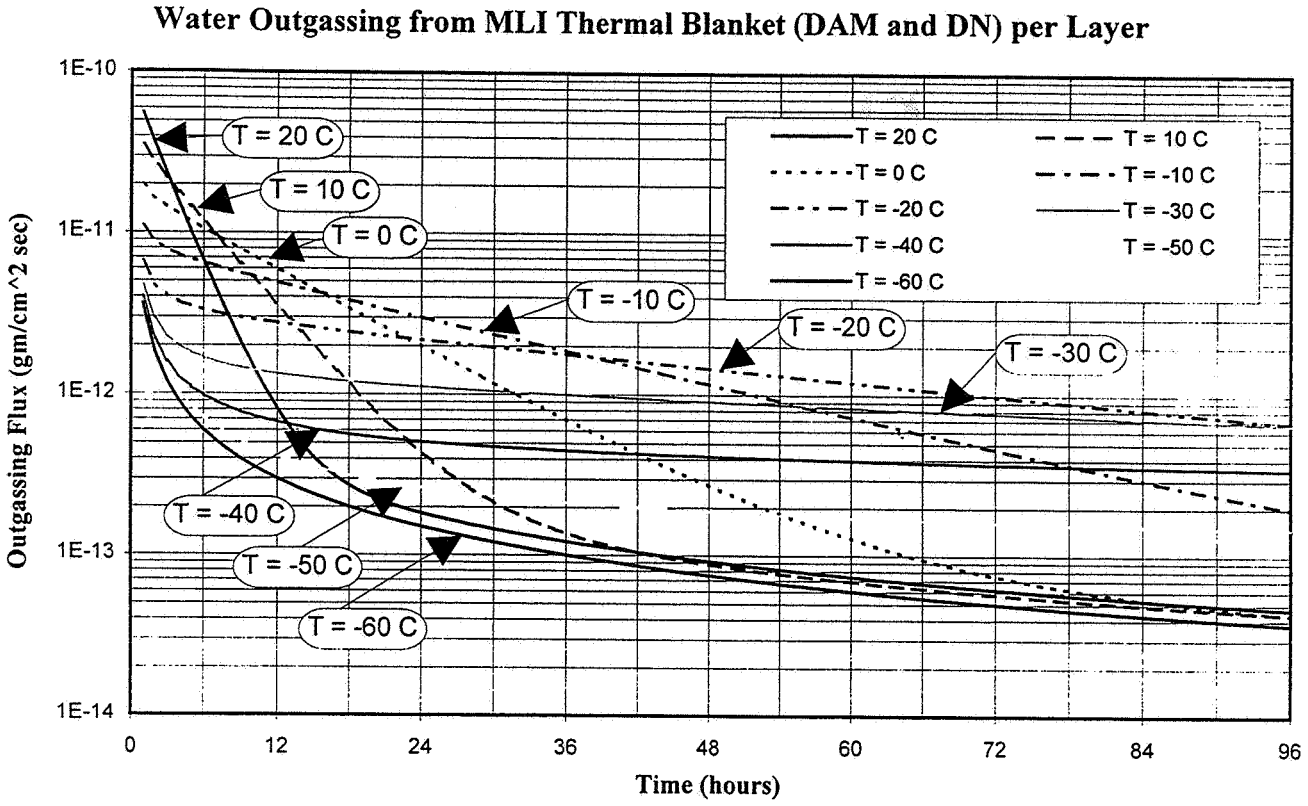


Figure 2 : Model of water outgassing from MLI thermal blanket material.

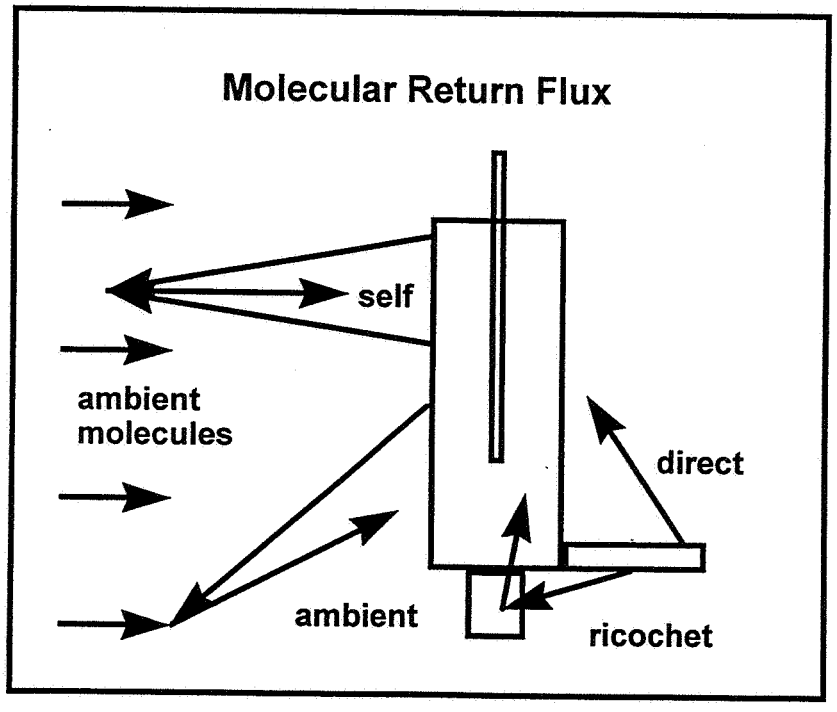


Figure 3 : Mechanisms of molecular return flux to spacecraft surfaces.

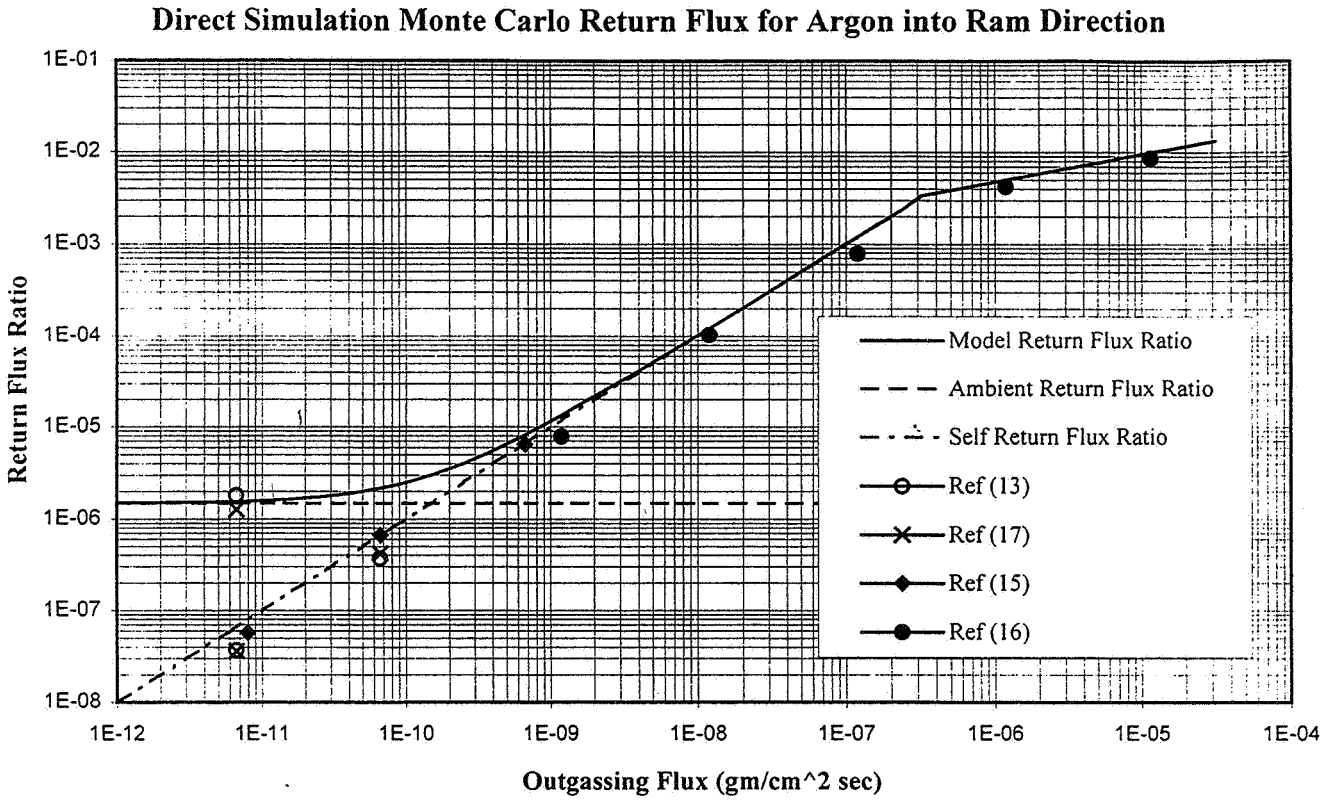


Figure 4 : Comparison of Model Return Flux Ratio with Monte Carlo calculations.

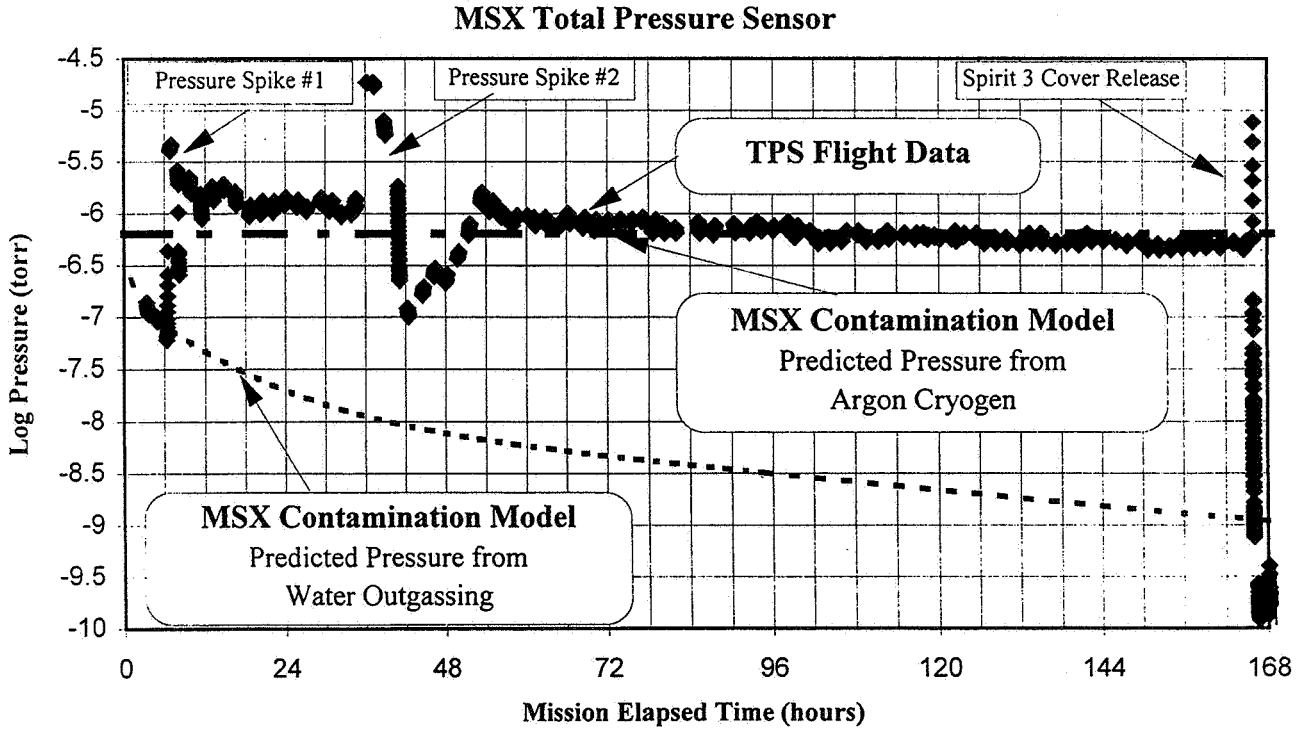


Figure 5 : Comparison of TPS flight data with MSX Contamination Model predictions.

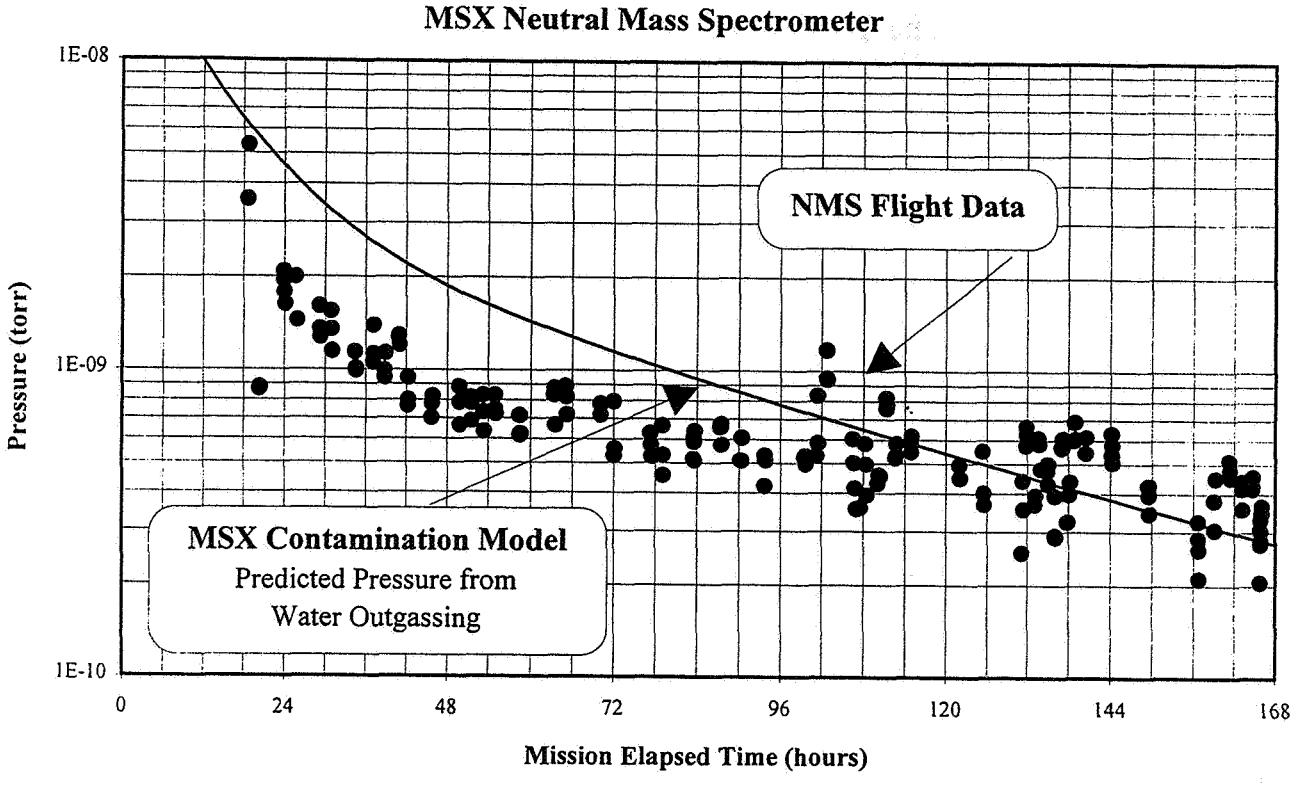


Figure 6 : Comparison of NMS flight data with MSX Contamination Model predictions.

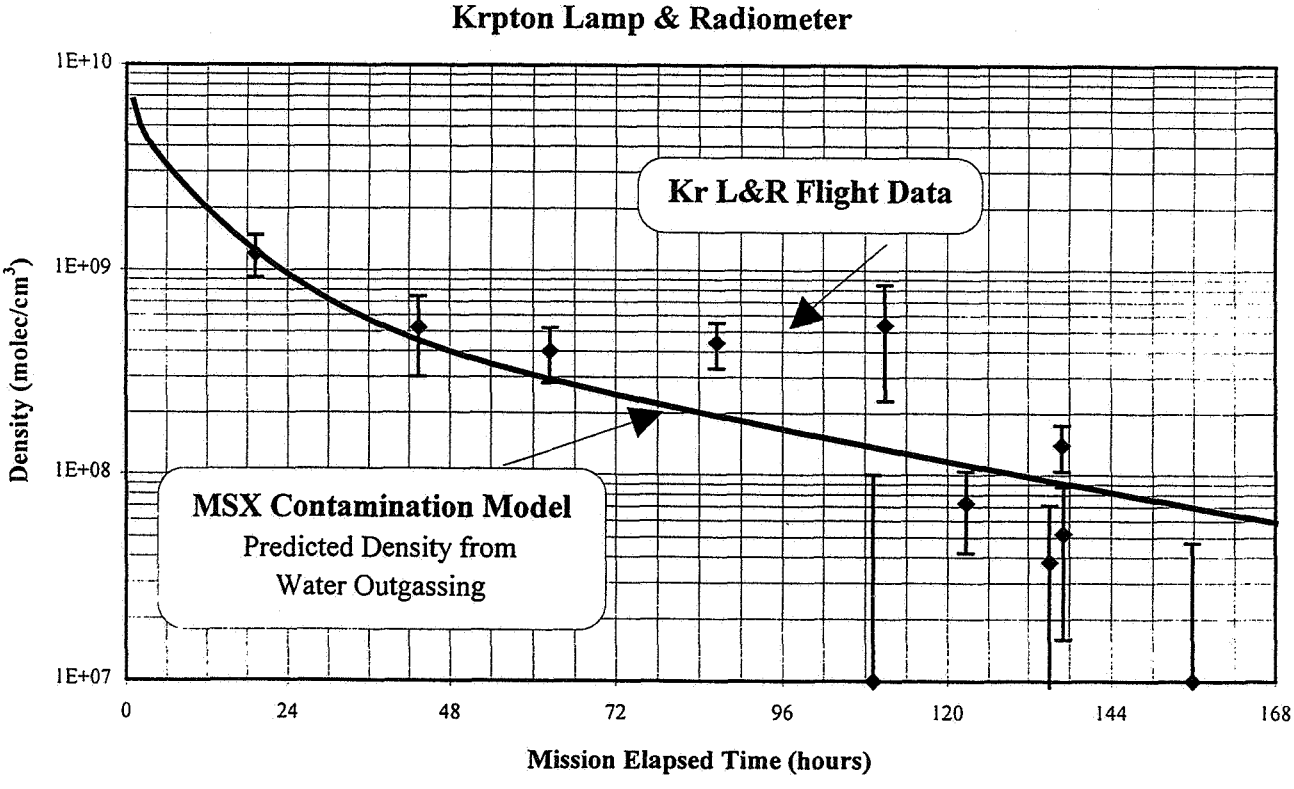


Figure 7 : Comparison of Kr Lamp & Radiometer flight data with MSX Contamination Model predictions.

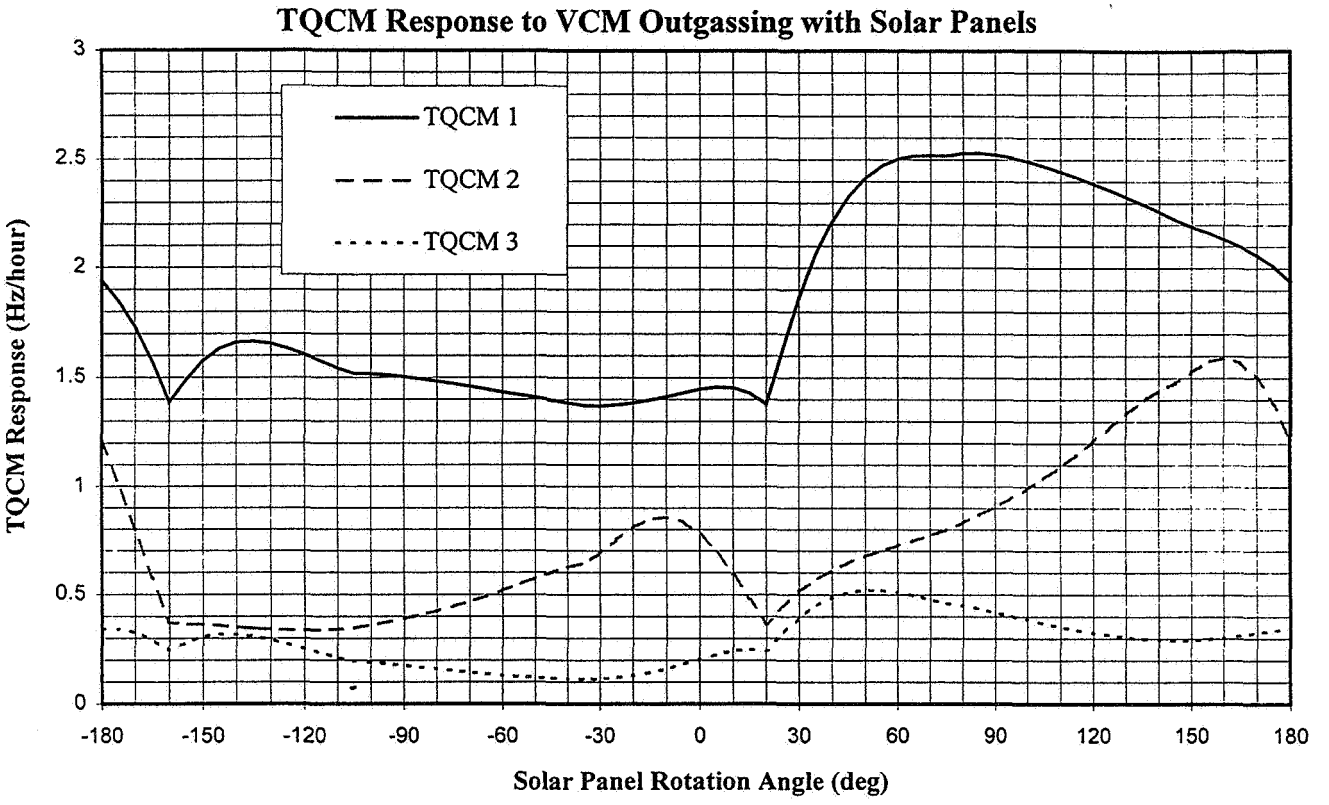


Figure 8 : The predicted response of TQCMs to outgassing from the MSX solar panels.

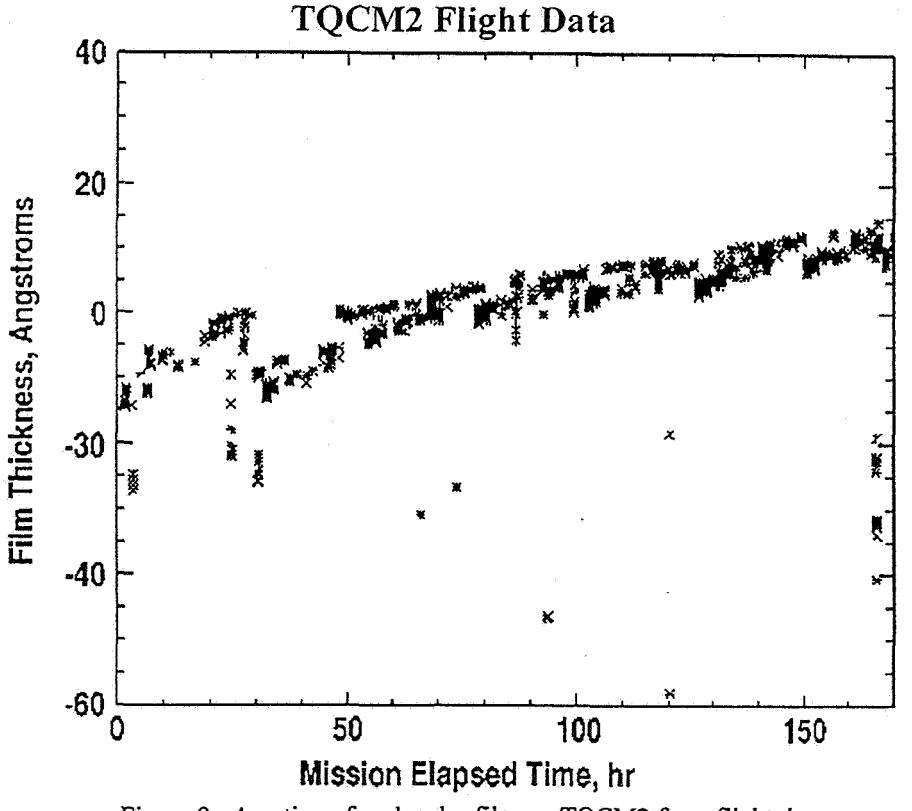


Figure 9 : Acretion of molecular film on TQCM2 from flight data.

57-18
021442
269363
20P

MARS PATHFINDER SPACECRAFT, LANDER, AND ROVER TESTING IN SIMULATED DEEP SPACE AND MARS SURFACE ENVIRONMENTS

Kenneth R. Johnson
Jet Propulsion Laboratory, California Institute of Technology

ABSTRACT

The Mars Pathfinder (MPF) Spacecraft was built and tested at the Jet Propulsion Laboratory during 1995/96. MPF is scheduled to launch in December 1996 and to land on Mars on July 4, 1997. The testing program for MPF required subjecting the mission hardware to both deep space and Mars surface conditions. A series of tests were devised and conducted from 1/95 to 7/96 to study the thermal response of the MPF spacecraft to the environmental conditions in which it will be exposed during the cruise phase (on the way to Mars) and the lander phase (landed on Mars) of the mission. Also, several tests were conducted to study the thermal characteristics of the Mars rover, Sojourner, under Mars surface environmental conditions. For these tests, several special test fixtures and methods were devised to simulate the required environmental conditions. Creating simulated Mars surface conditions was a challenging undertaking since Mars' surface is subjected to diurnal cycling between -20°C and -85°C, with windspeeds to 20 m/sec, occurring in an 8 torr CO2 atmosphere. This paper describes the MPF test program which was conducted at JPL to verify the MPF thermal design.

INTRODUCTION

The Mars Pathfinder spacecraft consists of a cruise stage (Fig. 1), a lander stage (Fig. 2) and a rover which is housed within the lander stage. A circular solar panel shades and powers the cruise stage as it travels to Mars, keeping the communications alive, the lander warm, and the batteries charged. When the spacecraft approaches Mars, the cruise stage will be jettisoned and the lander module will be propelled to enter the Mars atmosphere. The lander will descend towards the Mars surface, protected by a heat shield as it aerobrakes through the atmosphere. A 12.7 m diameter parachute (Dacron canopy with Kevlar suspension lines) will deploy at 10 km above the surface (Fig. 3). When the lander has descended to within 70 m of the surface, retro-rockets will fire to further slow the lander. Then, just before landing, a four-pod airbag made of Vectran will deploy to cushion the impact of the lander at touchdown (Fig. 4). The airbag encased lander will bounce several times before coming to rest on the Mars surface. Once settled on the surface, the airbags will be deflated and then, over a 1.7 hr period, will be retracted towards the lander using a cable-reeling winch system.

The lander in its stowed configuration is a tetrahedron which has three side "petals" surfaced with solar panels and a base petal on which the lander instruments are mounted. Once the airbag has retracted, three drive motors will slowly open the petals and, as the petals open, the lander will right itself so that the base petal will rest on the Martian surface with the side petal solar panels facing upward. The retracted Vectran airbag material will serve to cushion the petals as they open and insulate them from the cold Martian ground. Once the petals are open, the lander and the rover will be fully exposed to the Martian environment. During the first day on Mars, the solar panels will recharge the landers batteries. Also on the first day, the rover (Fig. 5) will be commanded by remote control operators on Earth to drive down a ramp from its mount on one of the petals and onto the Mars surface to begin its exploratory adventure (Fig. 6).

The Mars Pathfinder lander includes a weather station to provide metrology of the Mars surface temperature and pressure, a video camera system, and a rover. The rover will be equipped with aft and fore cameras for Mars surface surveillance, a laser-based autonomous navigation system for obstacle detection and avoidance, an Alpha-Proton X-Ray Spectrometer (APXS), and a communications system.

The testing program described in this paper was carried out at the Jet Propulsion Laboratory, California Institute of Technology, under a contract with the National Aeronautics and Space Administration.

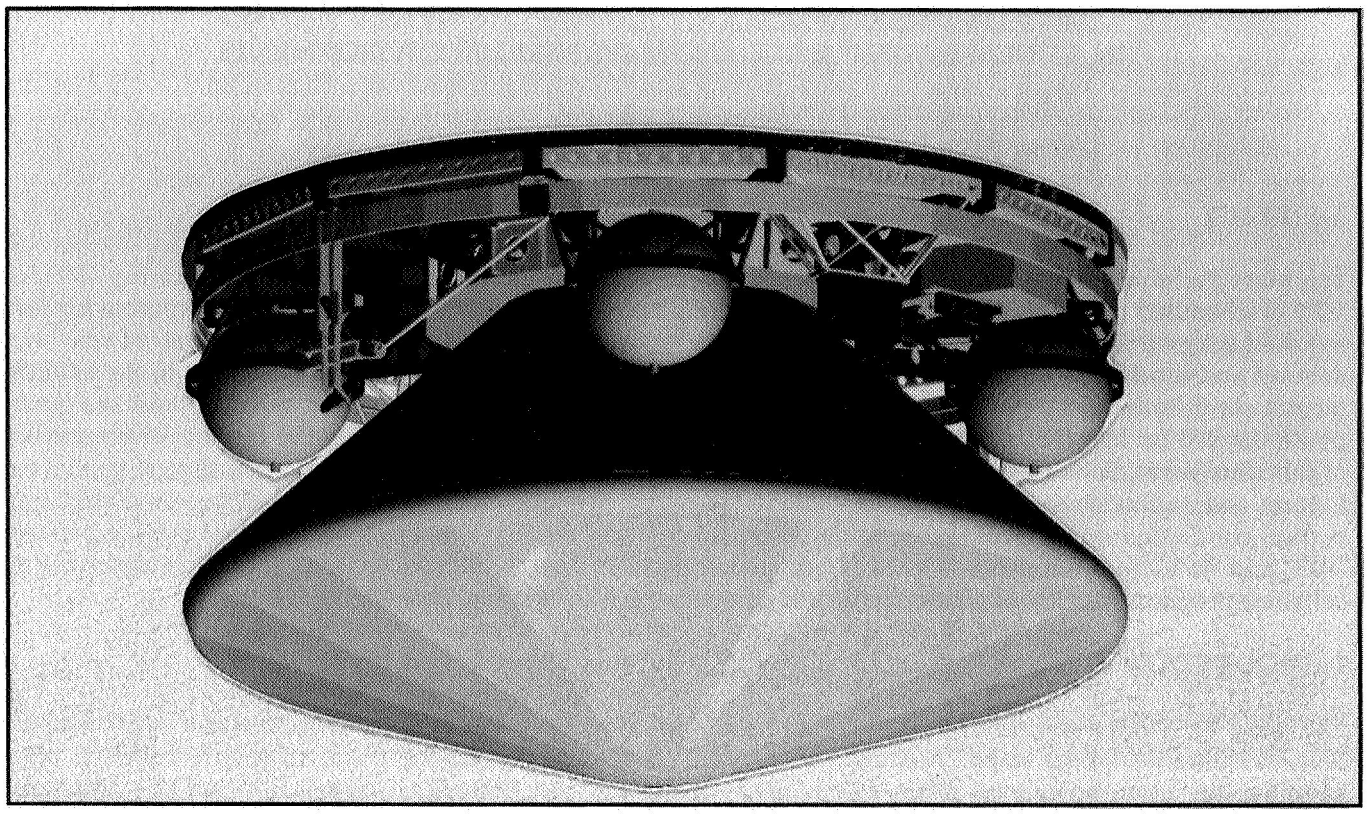


Figure 1. Mars Pathfinder Cruise Configuration

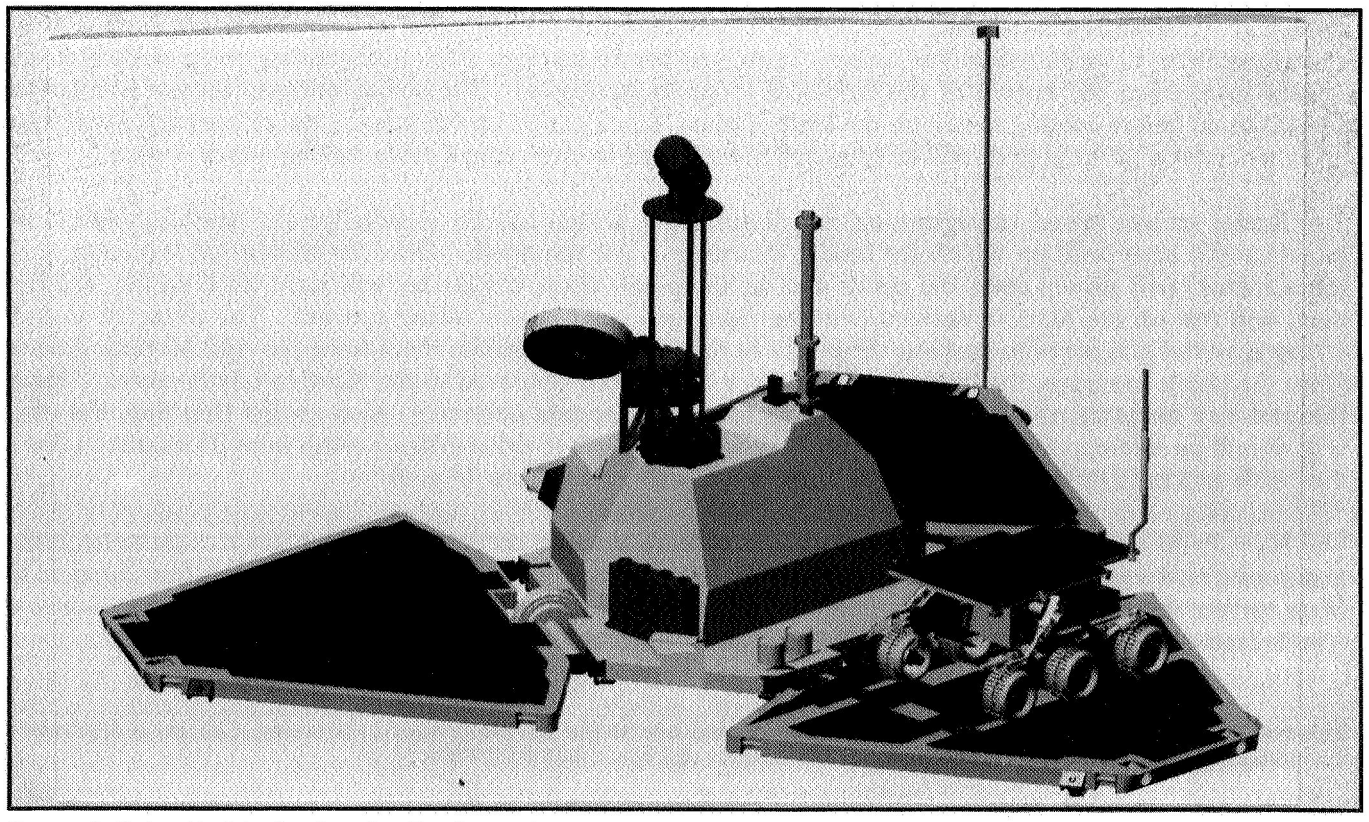


Figure 2. Mars Pathfinder Lander Configuration

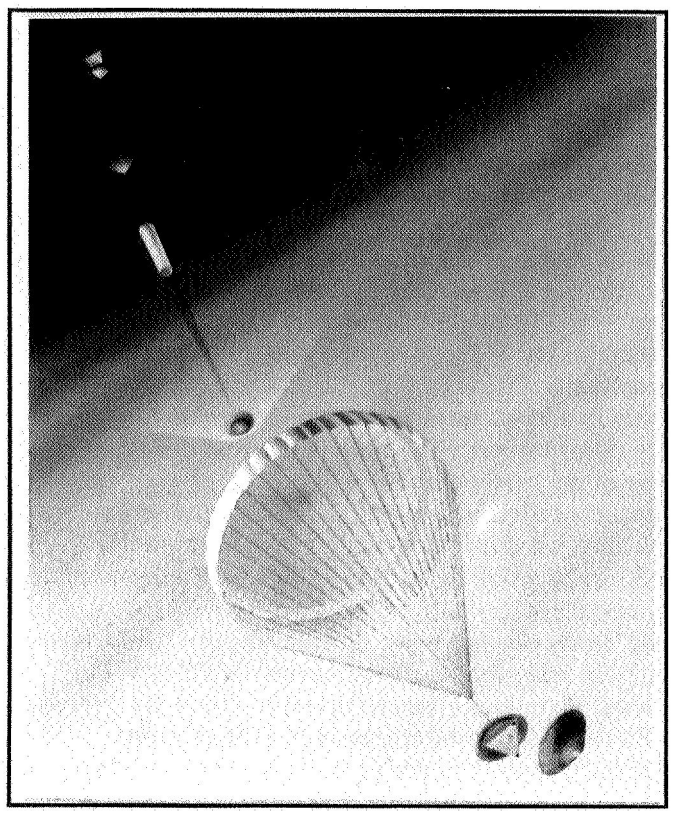


Figure 3. Descent of the Mars Pathfinder Lander

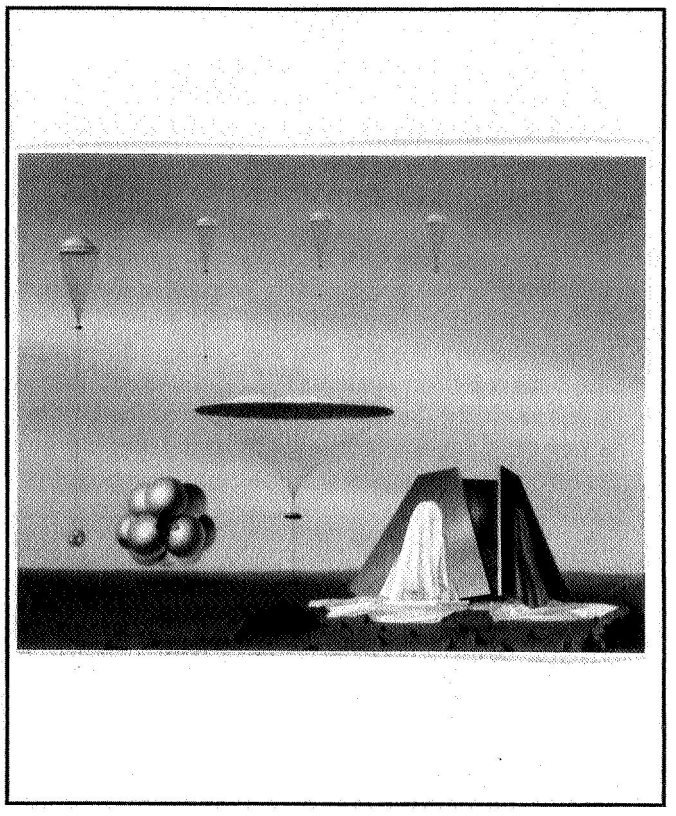


Figure 4. Mars Pathfinder Landing on Mars

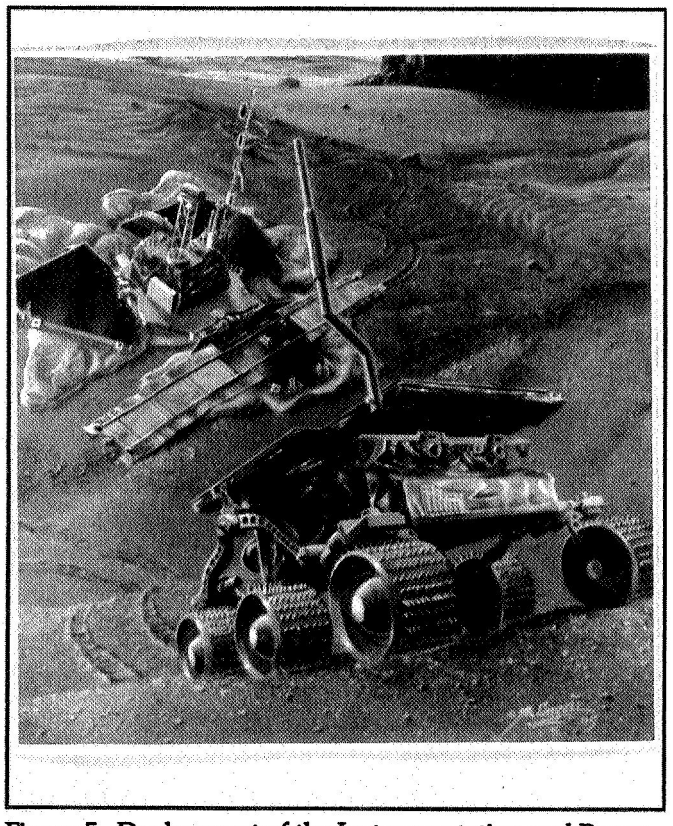


Figure 5. Deployment of the Instrumentation and Rover

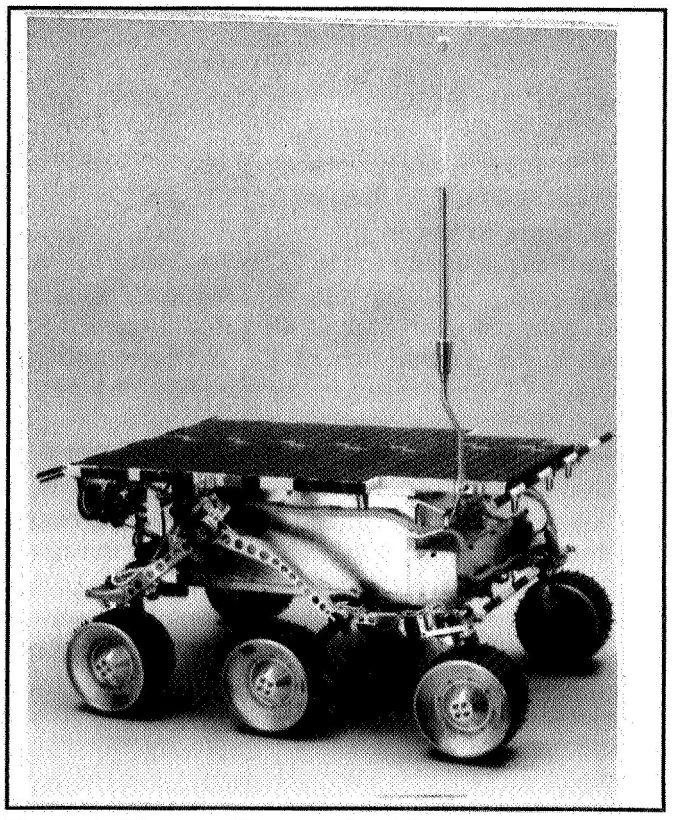


Figure 6. Close-up Photograph of the Mars Rover

The MPF test program included:

1) a test to understand the nuances of creating an 8 torr CO2 environment in a vacuum chamber for the purpose of creating as real a simulation of the Martian atmosphere as possible;
2) a test to study the thermal response of Mechanical, Thermal and Mobility (MTM) subsystems of a rover test model in cruise and landed phase conditions (this test also compared the thermal response of the rover test model in a CO2 environment against that in a GN2 environment at the same temperature and pressure conditions);
3) a test to study the thermal response of MTM subsystems of the rover test model to Mars surface conditions including wind and to verify the operation of a wind producing test assembly for use in a cold, 8 torr GN2 environment;
4) a test to study the thermal response and operational functionality of the insulated structural assembly and the heat rejection system (ISA/HRS) in the cruise environment;
5) a test to study the thermal response of the lander assembly in a Mars surface environment;
6) a test on a rover flight level System Integration Module (SIM) to verify the rover's thermal design as well as its communications software and functionality of some of the hardware ;
7) an airbag retraction test in a simulated Mars environment (cancelled because of airbag contamination);
8) a bakeout of the 25-ft space simulator (SS) to establish a baseline chamber cleanliness measurement;
9) a bakeout of a sun shade for installation in the 25-ft SS to be used to shade the infrared lamp support structure to be used for conducting the MPF-STV-1 test;
10) a proof-of-concept test of the 25-ft SS with no installed hardware to verify that the facility could safely provide the test conditions for the MPF lander full assembly solar thermal vacuum test (MPF-STV-2);
11) a test of the full MPF cruise stage assembly in a simulated deep space environment to study the thermal response of the entire spacecraft in near Earth, cruise, and near Mars conditions (MPF-STV-1); and
12) a test of the full MPF lander stage assembly, deployed in the landed, airbag-retracted configuration, in a simulated Mars environment to study the thermal response of the lander on the first and subsequent day on Mars, and to study the full functionality of the rover in a simulated Mars environment (MPF-STV-2).

In this paper, I will describe some of the more important aspects of these tests including discussions of special fixtures that were developed to create the required test conditions, and some of the results of the test program.

CREATING AN 8 TORR CO2 ENVIRONMENT IN A VACUUM CHAMBER (1)

The MPF thermal engineers started the MPF thermal test program assuming that the simulation of the Mars environment would be done using CO2 at 8 torr throughout the entire test program. This assumption was based on the desire to test in the most realistic simulation of the Mars environemtn that was possible. The first hardware subassembly test in CO2 was conducted in one of JPL's small chambers, 3-ft diameter and 5-ft long, in January 1995. For this test, the operating technicians used a standard vacuum chamber procedure which included the use of an LN2 flooded cold finger to collect outgassed contamination from the hardware. After the normal initial pumpdown of the chamber and the chilling of the cold finger with LN2, the operators introduced CO2 into the chamber to a pressure level of 8 torr.

However, operators soon noticed that the chamber pressure could not be held at 8 torr without a constant feed of CO2 into the chamber. Before anyone discovered the reason why the pressure could not be stabilized at 8 torr, a loud clunk was heard coming from inside the chamber. This prompted the operators to rapidly return the chamber to atmospheric pressure to inspect the hardware. A large block of frozen CO2 (dry ice) was found which had been formed on the cold finger inside the chamber. The block had broken off the cold finger and dropped to the floor of the chamber. A brief review of the solid-gas equilibrium data for CO2 revealed that CO2 at 8 torr solidifies at -121°C. It was clear that a standard LN2 cold finger could not be chilled below about -115°C and that maintaining an 8 torr CO2 pressure in the vacuum chambers would be difficult to achieve. Therefore, the use of GN2 was recommended as an alternative to CO2 for subsequent Mars surface environment simulations.

ROVER MTM TESTING (2)

The rover MTM testing was conducted in JPL's Chamber 10 from 4/20 to 5/5/95. This test was the first of the MPF test series to simulate the cruise stage as well as the first day on Mars conditions and several subsequent diurnal temperature cycles. A primary thermal design goal of the rover thermal engineers was to ensure that the Warm Equipment Box (WEB) was insulated with aerogel well enough that the WEB inside the rover would never get colder than -40°C even when subjected to external temperatures as low as -85°C, the projected night time low temperature of the Martian surface atmosphere. Martian surface environment simulation included the use of CO2 at 8 torr for most of the various MTM tests. A test was conducted using GN2 at 8 torr to compare the thermal effects between CO2 and GN2 environments. As part of the test set-up for the MTM tests, two aluminum reference plates with Minco film heaters were mounted inside the chamber, one surfaced with a Cat-a-lac black paint (emittance 0.87) and one surfaced with gold-coated kapton (emittance 0.06), to provide a method for calibrating the heat transfer characteristics. The black reference plate was used primarily for calibration during high vacuum operations where thermal radiation is the main mode of heat transfer. The gold reference plate, which because of its low emissivity, was used during the 8 torr operations to measure the convective heat transfer effects while minimizing the radiative heat transfer effects.

Thermal engineers L. Wen and E. Kwack planned this test. The results of this test were reported by L. Wen (ref. 1). Wen states that the free convective heat transfer coefficient on the rover surface may be 28% to 35% higher in a GN2 environment than in a CO2 environment (ref. 2). The test data indicated that rover internal components can be expected to get 3.5°C to 4°C colder in a GN2 environment than they would in a CO2 environment (ref. 3). Because of the technical difficulty and considerable expense of using CO2 in the thermal vacuum chambers to create a realistic Mars environement, it was decided that GN2 be used in place of CO2 for simulating Mars surface environmental conditions on all subsequent tests.

This test also indicated that there were significant thermal effects introduced to the rover by the free convection currents created by the temperature differentials between the chamber wall shrouds and the temperature-controlled heat exchanger panel on which the rover EM was mounted (Fig. 7). It was suggested that the next test, which would introduce wind and thus induce some forced convection, would help clarify and quantify the significance of these effects.

ROVER MTM TESTING IN THE PRESENCE OF WIND (3)

The next step was to test the rover model in a simulated Mars environment with wind blowing at various speeds to study the effect of wind on the heat transfer from the WEB and other rover components. This test was called the Rover EM Wind Test, was planned by thermal engineers L. Wen and E. Kwack, and was conducted in JPL's 10-ft SS on 6/25-30/95. A special wind-generating fixture was fabricated to blow a wind stream across the rover EM at various wind-speeds (Fig. 8). L. Wen's report on this test (ref. 4) states that the test results indicate that the forced convection heat transfer coefficient due to wind was double that of the free convection heat transfer coefficient when there is no wind. The rover interior temperature was measured to be about 4°C lower with wind than without.

In addition to simulating windspeed, an overhead skyplate heat exchanger (HX) was installed to simulate the diurnal sky temperature in both day time and night time conditions. Also, a compensator HX was mounted above the skyplate to provide trim temperature control of the circulating GN2. A mylar baffle canopy mounted directly above the compensator HX kept the circulating GN2 confined to a relatively limited volume around the test fixture and the test article. Operators had some trouble achieving a smooth diurnal temperature cycle since the temperature control of the wall and floor shrouds (which provided the background Mars surface temperature) lagged and sometimes counteracted the temperature control of the skyplate and the compensator. However, the results of this test provided the thermal engineers with enough empirical data to conclude with some confidence that the rover thermal design would be effective in keeping the rover interior components above -40°C under actual Mars surface diurnal conditions.

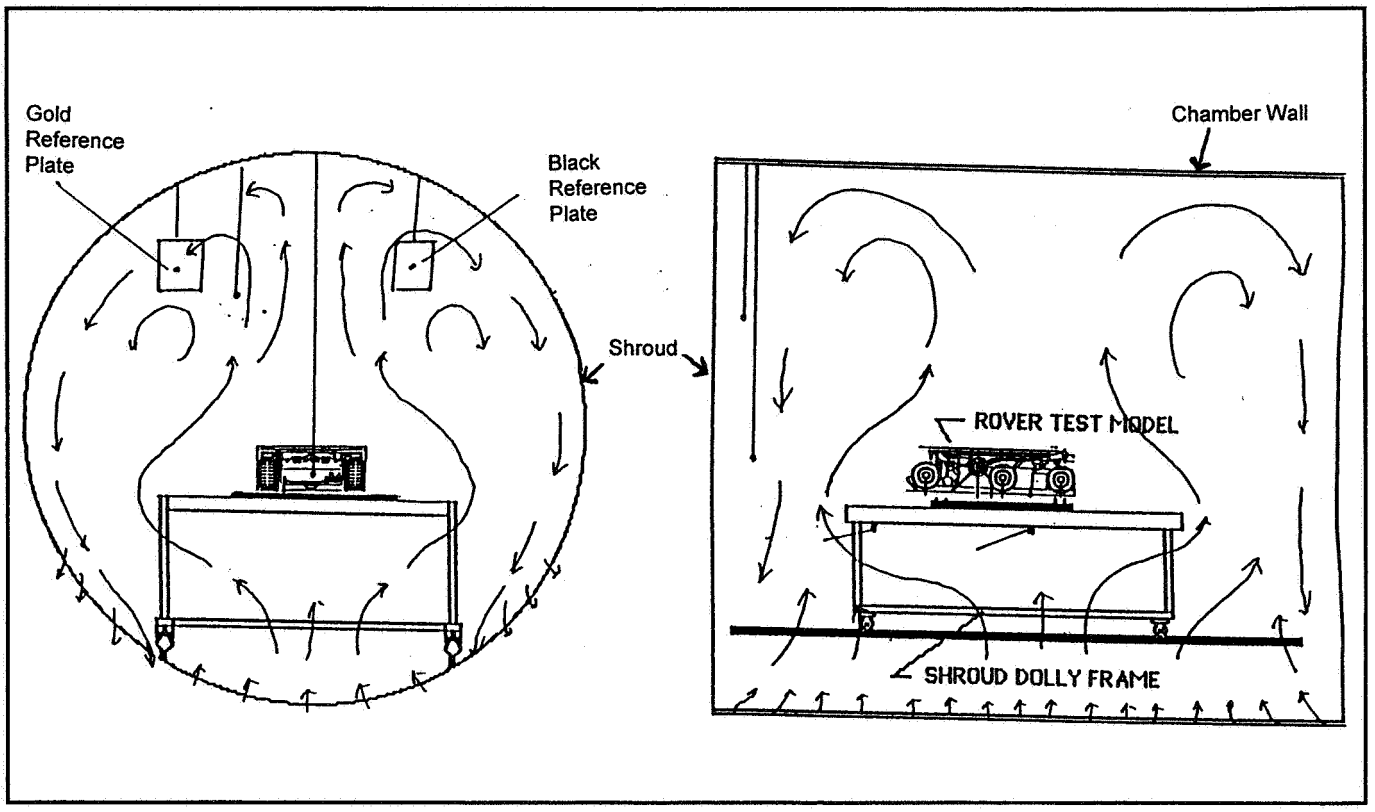


Figure 7. Free Convection Around the Mars Rover Test Model in JPL's Chamber 10

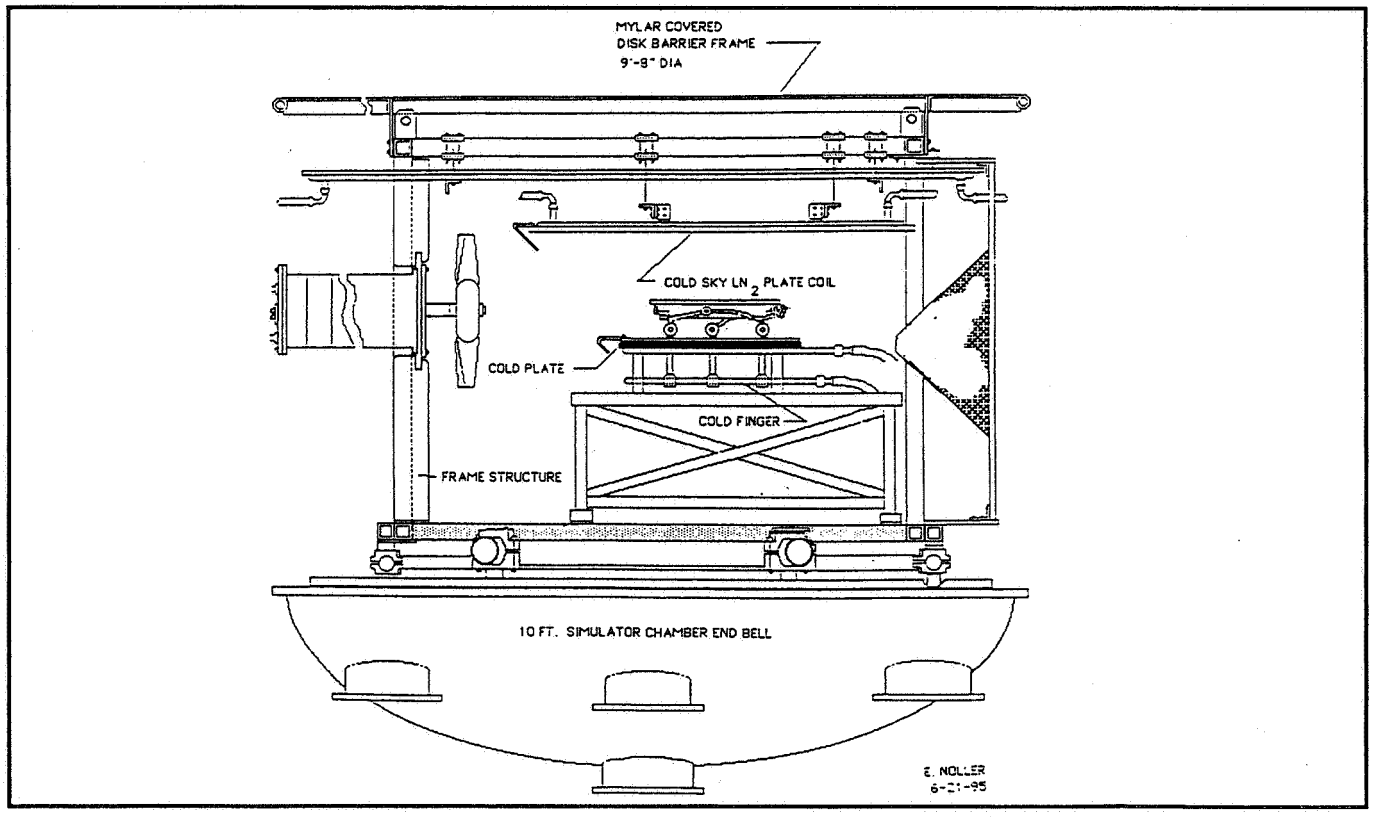


Figure 8. Test Set-up for the Mars Rover MTM and SIM QUAL Tests Including the Wind Machine Configuration

CRUISE PHASE TESTING OF THE MPF ISA/HRS (4)

The thermal control design of the MPF flight system design required most of the electronics to be used in both the cruise and Mars surface operations. To meet this requirement, the heat rejection system (HRS) was designed to dissipate the heat generated by the electronics during the cruise stage. The insulated structural assembly (ISA) was built to minimize the equipment heat loss during Mars surface operations. The HRS is a pumped closed-loop, single phase cooling system using Freon 11 as the circulating fluid (Fig. 9). Freon is warmed as it flows through the ISA electronics box. Part of the warmed freon stream is cooled as it flows through a radiator partially exposed to space while the remaining part of the warmed freon stream is by-passed around the radiator and is mixed with the cooled part to provide a temperature-controlled freon stream back to the ISA. The ISA houses the major electronics and telecommunications equipment and helps in controlling their temperatures within the general range of -40°C to +40°C during Martian surface operations. The ISA is a thermally insulated enclosure made of an Eccofoam layer and a Nomex honeycomb structural layer filled with crushed Eccofoam material. The ISA surface is coated with Cat-a-lac white paint.

The MPF ISA/HRS cruise phase thermal characterization test was planned by thermal engineers J. Lyra, K. Novak, and H. Awaya and was conducted in JPL's 10-ft SS on 8/19-26/95. The test objectives were: 1) to validate the lander/ISA/HRS integrated thermal design in the worst case cold and hot cruise conditions; 2) to determine the sensitivity of the lander/ISA/HRS to the MPF backshell temperature (since the backshell is the main boundary of the lander/ISA/HRS) in both worst case cold and hot conditions; 3) to assess the impact of an HRS failure during cruise (results used to develop a contingency plan in case of an HRS failure during flight); 4) to validate the thermal design and heater sizes of basepetal mounted equipment in a simulated Mars entry environment with emphasis on the lander petal accuator (LPA) and its electronics box, the airbag retraction actuator (ARA) and the gas generators (GG); and 5) to characterize the warmup rate of the ISA electronics after the HRS has been turned off.

The ISA/HRS cruise phase test configuration is illustrated in Figure 10. The lander in the stowed configuration was suspended above a blanket of multi-layer insulation laid on top of a heat exchanger (HX) plate which was temperature-controlled to simulate the cruise stage heatshield. The lander was hung from three cables attached to hard points on the inside chamber wall. The chamber wall shrouds were used to simulate the MPF backshell temperature. Figure 11 shows details of the HRS simulation test set-up. Figure 12 is a photograph which shows the test set-up just prior to hanging the test article in the chamber.

A method for accelerated chilling of the test article was provided to achieve cruise steady state temperature conditions as quickly as possible. A 0.25-in stainless steel tube was plumbed to feed LN2 directly into the chamber below the test article. When LN2 discharges into the chamber, it exits the tube as solid nitrogen pellets about 0.125-in in diameter. These small pellets evaporate rapidly to provide quick localized cooling. After first roughing the chamber to about 1×10^{-2} torr, backfilling once with GN2 to 400 torr to flush residual water vapor, re-roughing to about 1×10^{-2} torr, flooding the contamination plate with LN2, then chilling and LN2 flooding both the chamber wall shrouds and the heatshield HX, LN2 was fed into the chamber until the pressure reached 100 torr. When the temperature of the spacecraft side and base petals reached $\leq$ -50°C, the LN2 was drained from the shrouds and the HX, the shrouds and HX were warmed to -95°C and -145°C, resp., then the chamber was evacuated by normal procedure to $\leq 1 \times 10^{-5}$ torr to start the cruise phase test.

Results of this test were reported by J. Lyra/K. Novak/H. Awaya (ref. 5). In general, the test demonstrated that safe margins of at least 20°C will exist for all lander components in both the hot and cold conditions during the cruise phase.

LANDER PHASE TESTING OF THE MPF ISA/HRS (5)

The MPF ISA/HRS lander phase thermal characterization test was planned by thermal engineers J. Lyra, K. Novak, Y.C. Wu and H. Awaya and was conducted in JPL's 10-ft SS on 9/5-15/95. The test objectives were: 1) to characterize the thermal performance of the ISA Eccofoam/Nomex honeycomb insulation on the Mars surface; 2) to gather data to validate the thermal math models; 3) to characterize the transient behavior of the ISA equipment during at least one Mars day; and 4) to characterize the transient response of the secondary battery.

The ISA/HRS lander phase test configuration is illustrated in Figure 13. A photograph of the test set-up is shown in Figure 14. The ISA was mounted on the basepetal of the lander, the ISA/basepetal assembly was mounted on a twice-folded airbag (to simulate six layers between the basepetal and the ground), and the ISA/basepetal/airbag assembly was mounted on a "ground" HX plate used to simulate the temperature of the Martian ground surface. Solar simulation during the diurnal temperature cycling was accomplished by controlling the chamber wall shroud temperature and by powering heaters mounted on the ISA surface. A mylar canopy was installed about 4 feet above the test article to minimize convective gas circulation inside the chamber. Hardware for a propellant line thermal test (a test piggy-backed on the lander phase test) was mounted above the canopy. Accelerated chilling of the test article was accomplished in the same way as described in the cruise phase discussion. Although there was some concern about the possibility of overcooling the chamber walls and the carbon steel stiffener-ring welds on the chamber's external surface, only sweating (and no frost) on the external surface of the chamber was observed.

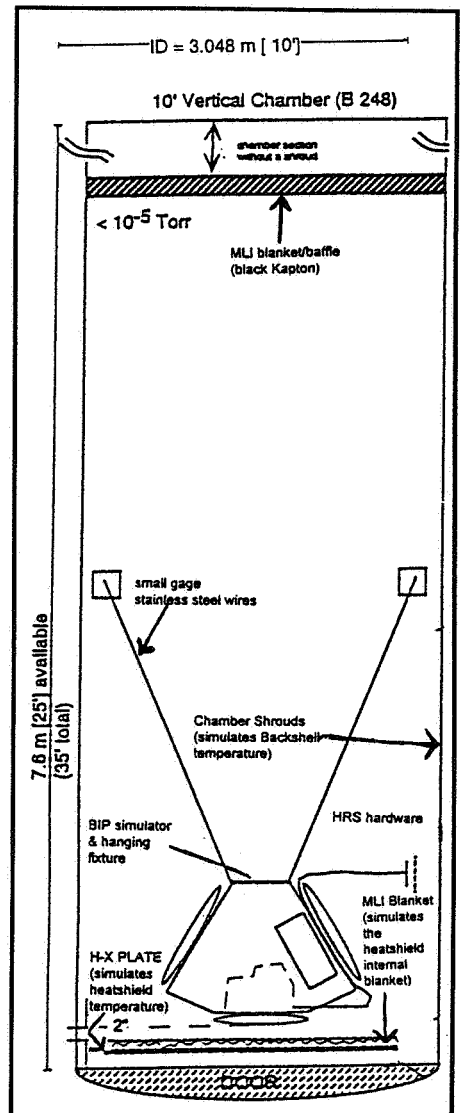
Results of this test were reported by J. Lyra/K. Novak/H. Awaya (ref. 6). Enough data was gathered to correlate the thermal math model in both radiation- and convection-dominated environments. Temperatures predicted by the math models correlated well with measured values, except for the ISA internal temperature which stayed considerably warmer than the model predicted.

MARS ROVER SYSTEM INTEGRATION MODULE (SIM) QUALIFICATION (QUAL) TEST (6)

The Mars rover SIM QUAL Test, was conducted in JPL's 10-ft SS on 10/23-28/95. This test emulated the rover MTM test in the presence of wind (3) described above. The test set-up was similar to the MTM test except that the test article now was a flight rover system integration module rather than a test model. The wind-generating machine was changed slightly to provide a forced stream of temperature-controlled GN2 directly into the motor housing to ensure that the motor would get adequate cooling. Also, a spare motor controller was brought to the test site to provide a back-up in case of a motor controller failure (which had occurred during the 6/95 test). Figure 15 shows a photograph of the test set-up. Figure 16 illustrates the details of the wind machine drive linkage.

This test was planned to occur in three phases: 1) SIM-Q1: calibration of the wind speed vs. motor rpm, followed by a steady state thermal vacuum test representing the cruise stage of the MPF spacecraft near Mars just before landing; 2) SIM-Q2a/b: with the rover stowed/unstowed, test the thermal response in nominal diurnal transient temperature conditions (at wind speeds of $\leq$ 6 m/sec); and, 3) SIM-Q3: with the rover stowed, test the thermal response in off-nominal diurnal transient temperature conditions (at wind speeds of > 6 m/sec).

The results of this test were reported by L. Wen (ref. 7), K. Johnson et al. (ref. 8), and G. S. Hickey et al. (ref. 9). During SIM-Q1, about two hours were expended performing the wind speed calibration but the measurements were unsteady and inconclusive. Because of a tight test schedule, we proceeded with the test plan without conclusive wind speed calibration data. It was decided to use the Cat-a-lac black and gold kapton coated aluminum reference plates for wind speed calibration. The reference plate wind speed calibration indicated that about 1 m/sec was achieved at a motor speed of 800 rpm. The wind-machine motor (a three-phase, 8-pole carbon brush, 5 hp dc motor) ran at about 800 rpm for four hours before it failed as a result of excessive wear of the carbon brushes as well as a disengagement of the coupling. The test was ended prematurely to find and fix the wind-machine problems. After replacing the brushes, increasing the line size of the motor-cooling GN2 line



HARDWARE

Lander
Petal Actuator (at least one)
DTM Air Bags (all)
DTM ISA
DTM equipment shelf (w/ cooling loops)
Gas Generator (1)
Air Bag Retraction Actuator (1)
Petal Actuator Electronics Box (1)
BIP simulator
cables
HRS support hardware

Thermal Development Models or Engineering Models:

IEM	PSA or PSB
DST	Lander Thermal Battery
SSPA	Wave guide
AXT	Rover
TMU (2)	
CDU	
Battery	

Figure 10. ISA/HRS Cruise Phase Test Configuration

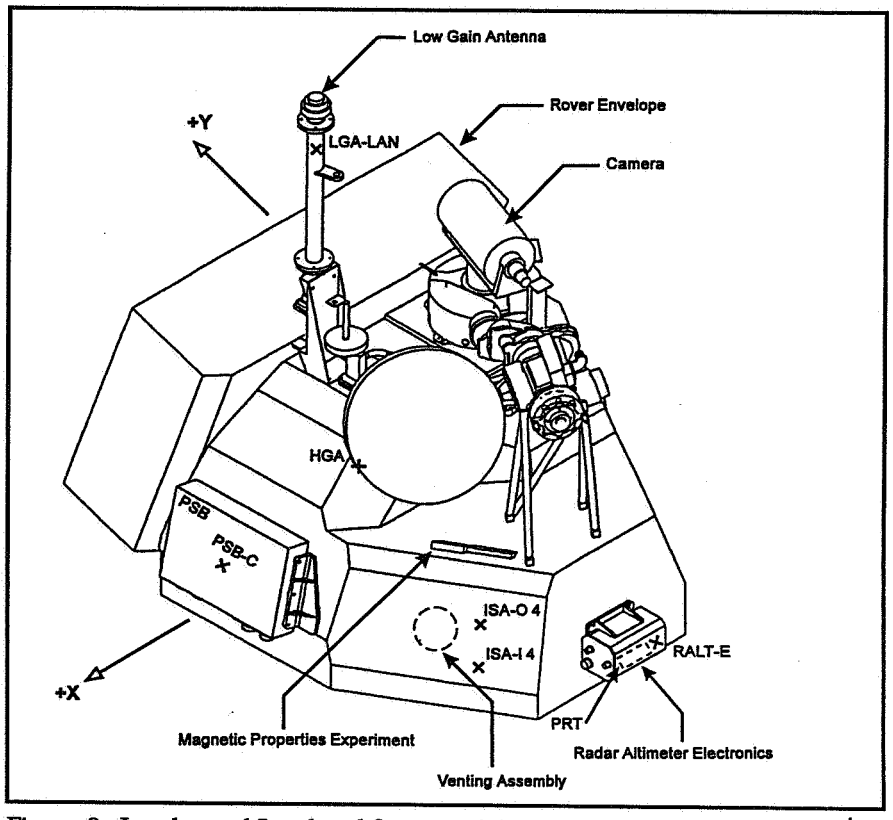


Figure 9. Lander and Insulated Structural Assembly Flight Cruise Configuration

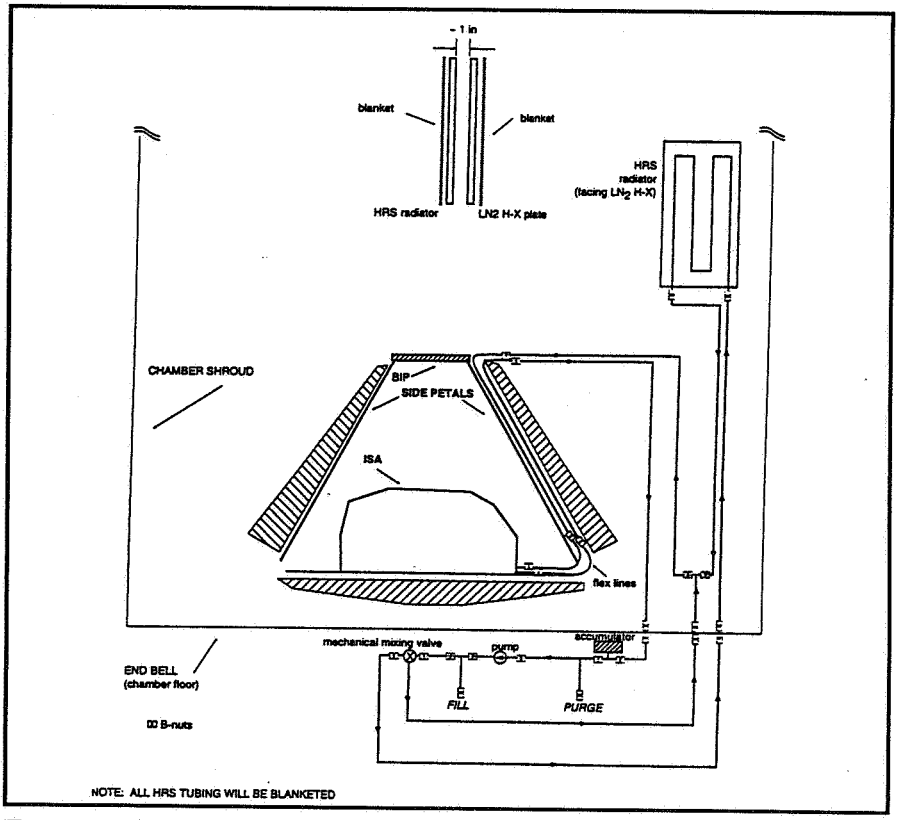


Figure 11. Details of the Test Set-up for the HRS Simulation Test

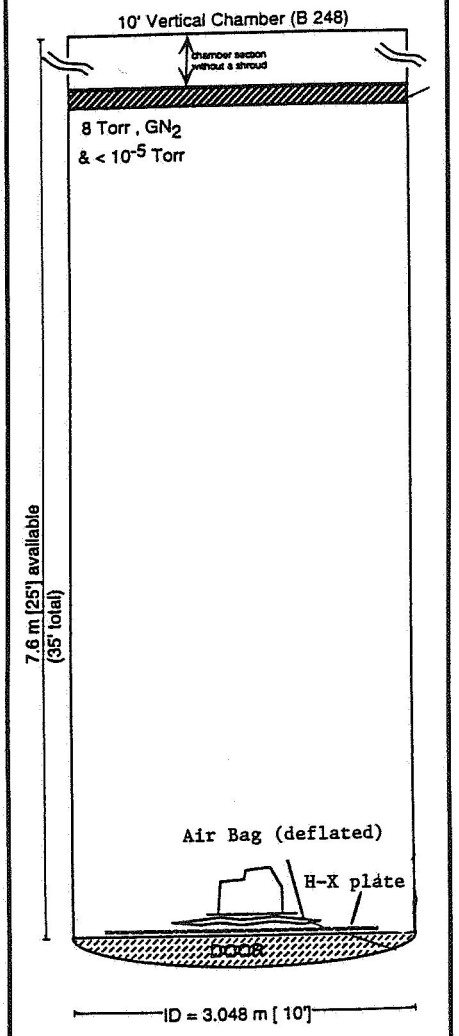


Figure 13. ISA/HRS Lander Phase Test Configuration

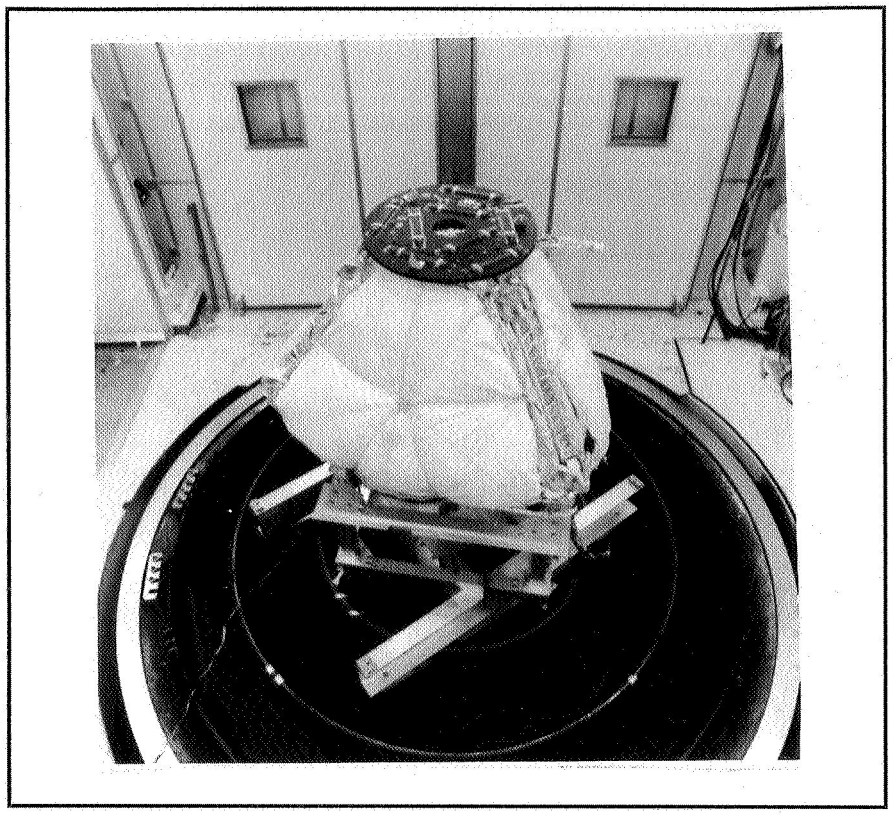


Figure 12. Photograph of the ISA/HRS Cruise Phase Test Set-up



Figure 14. Photograph of the ISA/HRS Lander Phase Test Set-up

to hopefully improve motor cooling, and re-establishing and securing the coupling linkage, the test was restarted. This time the wind machine operated at about 800 rpm for about eighteen hours before it failed again. Post-test analysis of the motor and linkage showed that the failure was again caused by excessive wear on the carbon brushes and dis-engagement of the coupling linkage. The SIM-Q2a and b test phases were concluded but SIM-Q3 was cancelled because of the wind machine failure. Figure 17a shows the prescribed Mars environmental temperature profiles for SIM-Q2a and figure 17b shows the measured Mars environmental profiles which were created for SIM-Q2a.

Wen states in his report that although the failure of the wind generation system was a disappointing setback, the overall test objective was not severely impacted. The partial wind test data that was obtained, together with the thermal math model predictions based on previous tests, provides adequate confidence that the rover thermal design meets its performance expectations when subjected to a realistic transient test environment. This test accomplished its basic thermal objectives. No further work was done to improve the wind machine .

AIRBAG RETRACTION TEST IN A SIMULATED MARS ENVIRONMENT (7)

Plans were made to test the airbag retraction mechanism in a simulated Mars environment in the 25-ft SS in early December, 1995. The purpose of this test was to study the airbag retraction mechanism and to measure the effect the cold temperature would have on increasing the stiffness of the airbag over that measured in ambient Earth onditions. This increased stiffness increases the drag friction of the airbag on both the Mars surface and on itself as the airbag retracts. The purpose of this test was to verify that the retraction system would work properly in a Mars-like environment.

About two weeks before the test was to take place, the test conductor revealed that the test airbag was not a new airbag but one which had undergone a fired deployment test at NASA Lewis and was already contaminated inside with a soot like substance which was a by-product of the airbag deployment. An analysis of this substance revealed that it was primarily ammonium chloride salt with a significant quantity of carbon soot. Because of a very major concern that this material inside the bag would outgas significantly during the chamber evacuation and thus contaminate the chamber, a small portion of the material was tested in a small chamber to study its outgassing tendency. This test revealed that about 75 wt% of the material vaporized under vacuum conditions at ambient temperature. Therefore the airbag retraction test was cancelled.

BAKEOUT OF THE 25-FT SS TO ESTABLISH A CHAMBER CLEANLINESS BASELINE (8)

After completing the test campaign in the 10-ft SS, the facility operations staff redirected their attention to readying the 25-ft SS for the upcoming MPF solar thermal vacuum tests. This was to be the first spacecraft test in the 25-ft SS since completion of a major facility refurbishment. There were still some "bugs" in the facility systems that needed to be fixed including a small pinhole GN2 leak(s) from one or more of the shrouds. Therefore, a concerted effort to find and fix these small leaks was started in 12/95. Also, blankets of multi-layered insulation (MLI) were hung in the chamber between the chamber walls and the wall shrouds. However, no blankets were installed on the chamber bottom endbell. Three leaks around 2-in Al/SS bimetal joints and one leak at an 8-in feed line Al/SS bimetal joint were discovered. These faulty bi-metal joints were replaced. Three subsequent vacuum test trials were required before all welds were finally leak-free. Finally, the 25-ft SS was ready for its chamber cleanliness baseline bakeout.

The bakeout was conducted on 3/7-8/96. The chamber shrouds were heated to a temperature of 80°C for a period of 16.5 hours. Two temperature-controlled quartz crystal microbalances (TQCM) were mounted inside the chamber to measure outgassing rates, one facing horizontally downward and one facing vertically towards the shroud wall. A first TQCM measurement was made with the crystal at 40°C to ensure the outgassing rate wasn't excessive before lowering the TQCM temperature. Five subsequent TQCM readings were done at three hour intervals with the crystal at 0°C. The latter three of these readings showed that the outgassing rate had stabilized at about 675 Hz/hr, indicating that no further baking was needed. A final TQCM measurement was

made with the crystal at -20°C yielding 30 Hz/hr for the horizontal TQCM and 70 Hz/hr for the vertical TQCM. At the end of the bakeout, the chamber pressure was 4.5×10^{-6} torr. The chamber was returned to atmospheric conditions and deemed clean and ready for MPF-STV testing.

FABRICATION AND BAKEOUT OF A SUN SHADE FOR THE MPF-STV-1 TEST IN THE 25-FT SS (9)

The MPF spacecraft will be spinning on its centerline axis as it travels to Mars to normalize the temperatures on the backshell and the radiators, thus distributing evenly the thermal effects of the solar radiation on these surfaces. In 10/95, discussions began regarding how to provide a constant solar flux to the backshell and HRS-radiators both of which would be shaded from solar beam by the MPF solar panel. After reviewing several alternate ideas, a decision was made to design and build a fixture consisting of several arrays of IR lamps to provide the needed solar flux simulation. This fixture is described below in the MPF-STV-1 discussion.

Once the fixture had been designed and was being fabricated, another problem needed to be solved. Using the existing installed optics in the 25-ft SS, the solar beam has a diameter of about 19.5-ft. By changing the integrated lens unit, a smaller beam diameter of 15-ft could be achieved. However, the spacecraft required a beam diameter of about 12-ft because a wider beam diameter would partially shine upon the fixture, heating the fixture and possibly skewing the uniformity of the simulated solar beam. To solve this problem, a sun shade with a 12-ft diameter aperture was fabricated and mounted above both the fixture and the spacecraft.

The sun shade consisted of an aluminum beam substructure with a fluoroglass material covering. However, since the fluoroglass covering would be directly impacted by the 25-ft SS solar beam during the MPF-STV-1 test, for contamination control reasons it needed to be baked to a temperature above that which it would potentially reach during MPF-STV-1.

The sun shade bakeout was conducted in JPL's 10-ft SS on 3/18-21/96. The larger fluoroglass pieces were draped in sections over two aluminum tubes (supported by cables) and the smaller pieces were laid directly on the floor shrouds. The wall and floor shrouds were heated to a temperature of 140-145°C to drive the material pieces to a temperature of 140°C. The material was baked at 140°C for 42 hours until the pressure and the water vapor content in the chamber stabilized at about 12% (determined by RGA readings) at a chamber pressure of 2×10^{-6} torr. After the bakeout, the fluoroglas was installed on the sun shade aluminum substructure in the 25-ft SS.

PROOF-OF-CONCEPT OF THE MPF-STV-2 TEST CONDITIONS IN THE 25-FT SS (10)

In January, 1996, planning for the cruise phase (MPF-STV-1) and the lander phase (MPF-STV-2) solar thermal vacuum testing of the MPF spacecraft was well underway when I was admonished by a long-time veteran of the 25-ft SS operations to study carefully the effects of creating a Mars environment in the 25-ft SS. There were a number of concerns voiced, most notably, that the chamber stainless steel shell possibly may overcool during the -135°C, 8 torr test condition causing ice to form on the chamber external surface. This ice formation, it was feared, may consequently cause overcooling of the carbon steel welds that connect the structural stiffener rings to the chamber shell and possibly cause the welds to crack and fail. If such cracks in the welds did occur, a risk of a catastrophic failure caused by collapse of the chamber wall could be the result. There were additional concerns about overcooling other primary chamber components including the door and door seals, the fused quartz solar window, electrical and instrumentation feedthrough connections, and others. To allay these concerns, a proof-of-concept test was devised to demonstrate that the chamber could safely provide the required Martian surface environmental test conditions for MPF-STV-2 without damaging any facility hardware.

The proof-of-concept test was conducted on 4/1-3/95. The test plan called for adjusting the chamber pressure to 8 torr with back-filled GN2 after roughing, then cooling the shrouds in two steps to the coldest temperature expected for the MPF-STV-2 test (first to -85°C then to -135°C). At each step, the temperature of the chamber

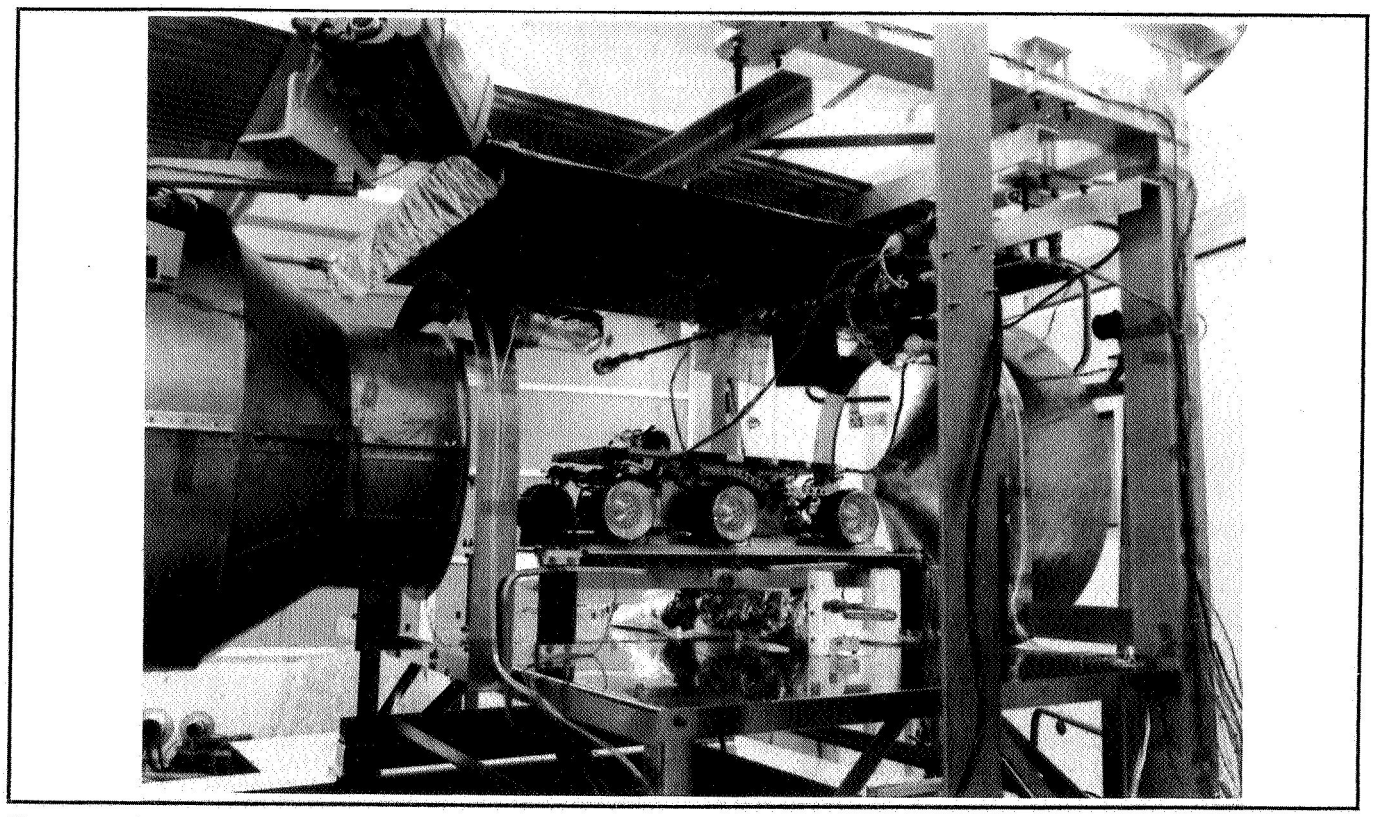


Figure 15. Photograph of the Mars Rover Engineering Model SIM QUAL Test Set-up

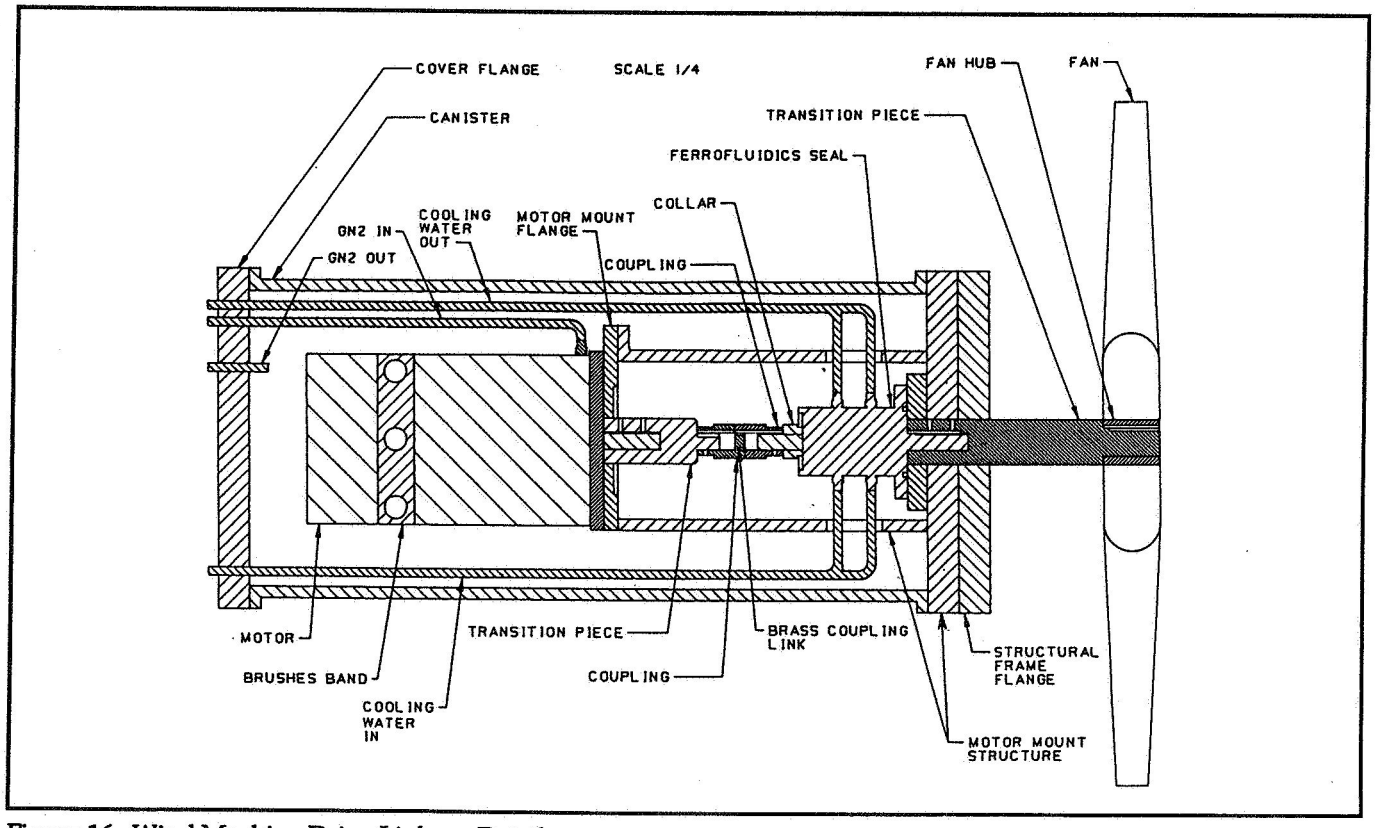


Figure 16. Wind Machine Drive Linkage Detail

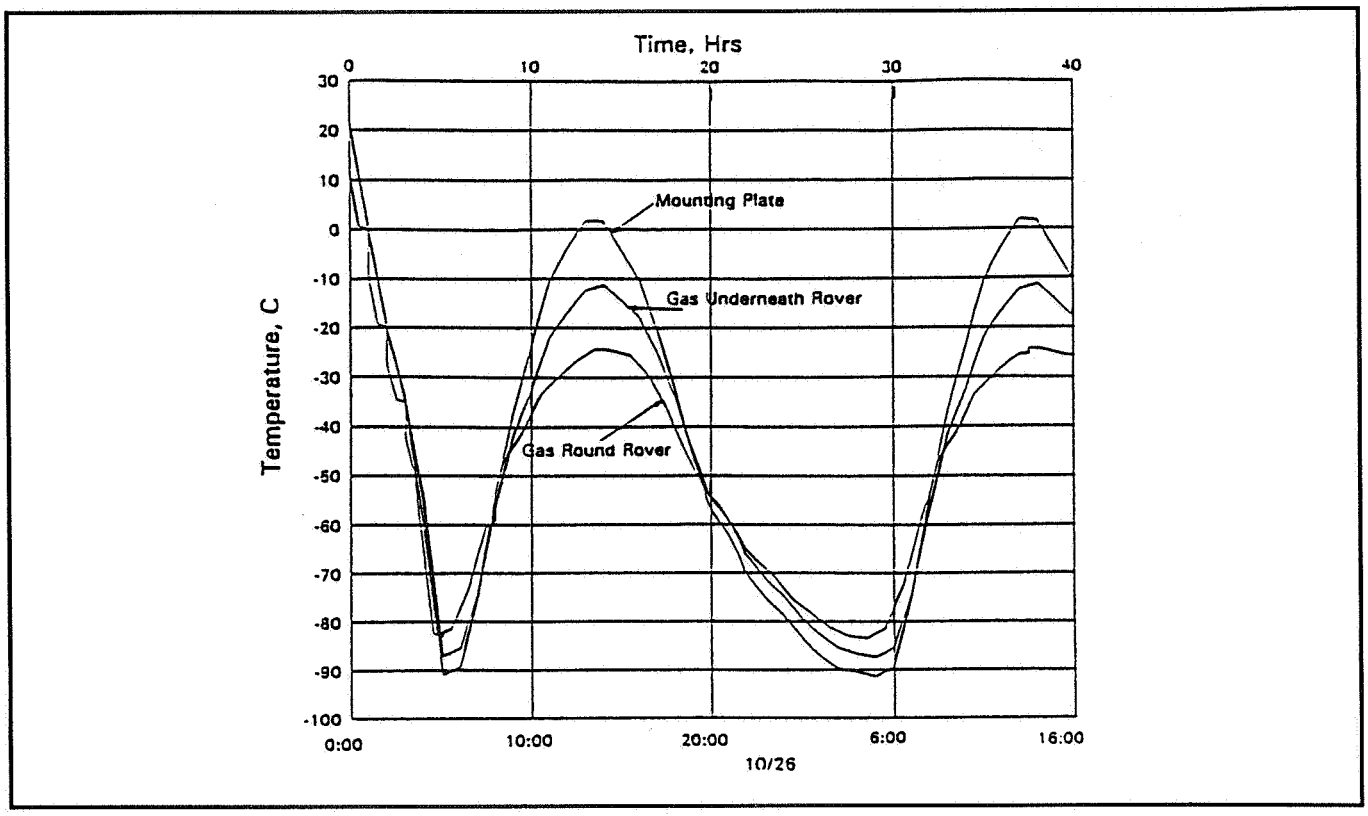


Figure 17a. Prescribed Mars Environmental Temperature Profiles for SIM-Q2a

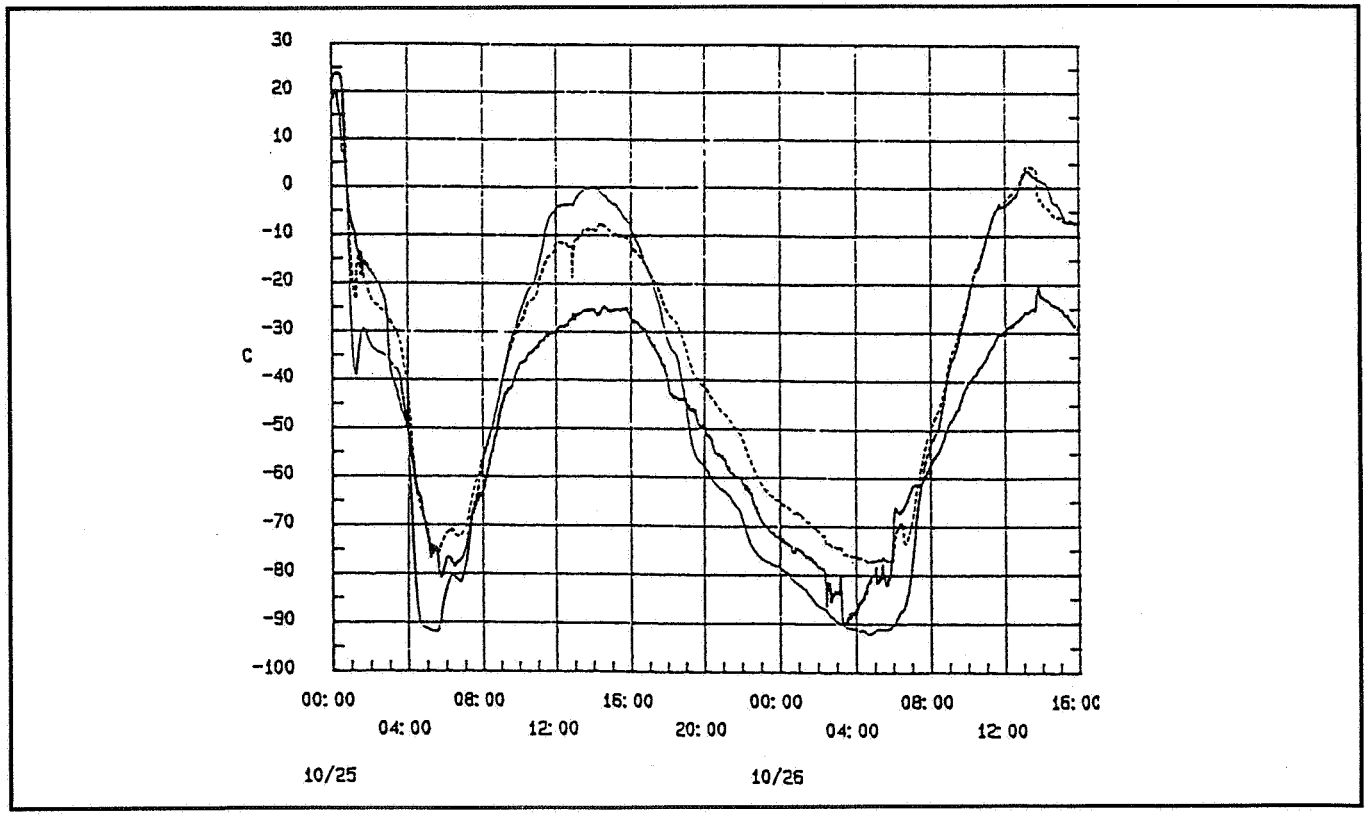


Figure 17b. Measured Mars Environmental Temperature Profiles for SIN-Q2a

shell and the carbon steel welds were carefully monitored at several locations to study the rate of cooling on the chamber external surface and to determine where frost or ice would first appear.

Results of this test indicated that no external chamber surface ever reached a temperature lower than 3°C. This lowpoint temperature was measured on the bottom endbell near a chamber feedthrough where cold gas was entering the chamber to cool the shrouds. Considerable condensation on the chamber bottom endbell was observed (since this endbell internal surface was not MLI-blanketed) but no frost or ice formed anywhere except on shroud feed lines (where it normally and typically has been observed to form). The temperature of the door and the fused quartz window frame remained well within acceptably safe limits throughout the test. Therefore, this proof-of-concept test showed that the MPF-STV-2 test conditions could be generated safely.

MPF-STV-1, THE MPF FULL ASSEMBLY CRUISE PHASE THERMAL RESPONSE TEST (11)

The MPF-STV-1 test planning began in 10/95 and by 4/15/96 all fixturing and instrumentation was ready for the test to begin. The thermal plan for this test test was prepared by J. Lyra. This test was conducted in JPL's 25-ft SS in two parts, the first part from 4/15 to 4/23/96 and the second part from 4/29 to 5/5/96. The objectives of this test were: 1) to demonstrate that the MPF spacecraft thermal design satisfies the various MPF component safe minimum/maximum temperature specifications when subjected to the most extreme environments expected over the life of the mission; 2) to obtain thermal test data to be used to correlate the analytical thermal models, to characterize the thermal behavior of various spacecraft equipment, and to determine design changes to correct any found thermal design deficiencies; 3) to verify that the spacecraft operates within the specified performance requirements and within flight allowable limits in simulated near Earth and near Mars space environments; and, 4) to verify that flight temperature sensor readings agree with comparable thermocouple readings.

Figure 18 is a photograph of the test set-up, including the sun shade, which was taken just prior to the start of MPF-STV-1. The solar fixture was made in five modular structural sections that were attached to a pentagon hub at the base. This fixture consisted of four distinct IR lamp arrays. Two of the arrays, the backshell lamp array and the HRS-radiator lamp array, were used to simulate the solar illumination on the sides of the spacecraft, since the spacecraft in flight will not always be situated such that the solar panels are directly normal to the sun (i.e., the spacecraft sides will not always be shaded by the solar panel). The backshell lamp array consisted of forty 14-in lamps. The HRS-radiator lamp array consisted of thirty 14-in lamps. In addition to these two arrays, two other safety lamp arrays were installed. The purpose of these safety lamps was: 1) to provide a way to warm the solar panel in case of a failure in either the solar simulation system or the facility power system, and 2) to provide a way to warm the heatshield in case of a facility power failure or any other unexpected overcooled condition on the heatshield. The safety lamp arrays were wired to be operated on emergency generator power. A special floor for the chamber was fabricated and installed to provide structural support for the backshell solar fixture. Both the fixture and floor were made of aluminum and were steam cleaned to remove hydrocarbon contaminants prior to being installed in the chamber. The sun shade can be seen located above the backshell solar fixture. The spacecraft was suspended about four feet above the chamber floor, hung by three cables attached to hard points on the chamber wall.

An infrared radiometer (IR) camera was mounted on the pan-tilt platform of the Satellite Test Assistant Robot (STAR, ref. 10) to provide thermal imaging of the solar panel throughout the MPF-STV-1 test.

The MPF-STV-1 test plan called for four test phases. Phase 1, the Mars Cruise-Fault Condition (1.55 AU, 0° Off-Sun orientation), a test which represented the worst case cold condition for the backshell, the lander and the cruise stage equipment, consisted of four test cases: 1-1) an accelerated cooldown of the test hardware after one pumpdown, GN2 backfill, and re-pumpdown (the accelerated cooldown for this test was done with the chamber at 8 torr GN2. No direct LN2 discharge into the chamber was used to accelerate local cooling); 1-2) a cold margin test to demonstrate the functionality of the cruise stage and lander stage electronics in the mission extreme cold environment (worst case cold condition for the backshell, the lander and the cruise stage equip-

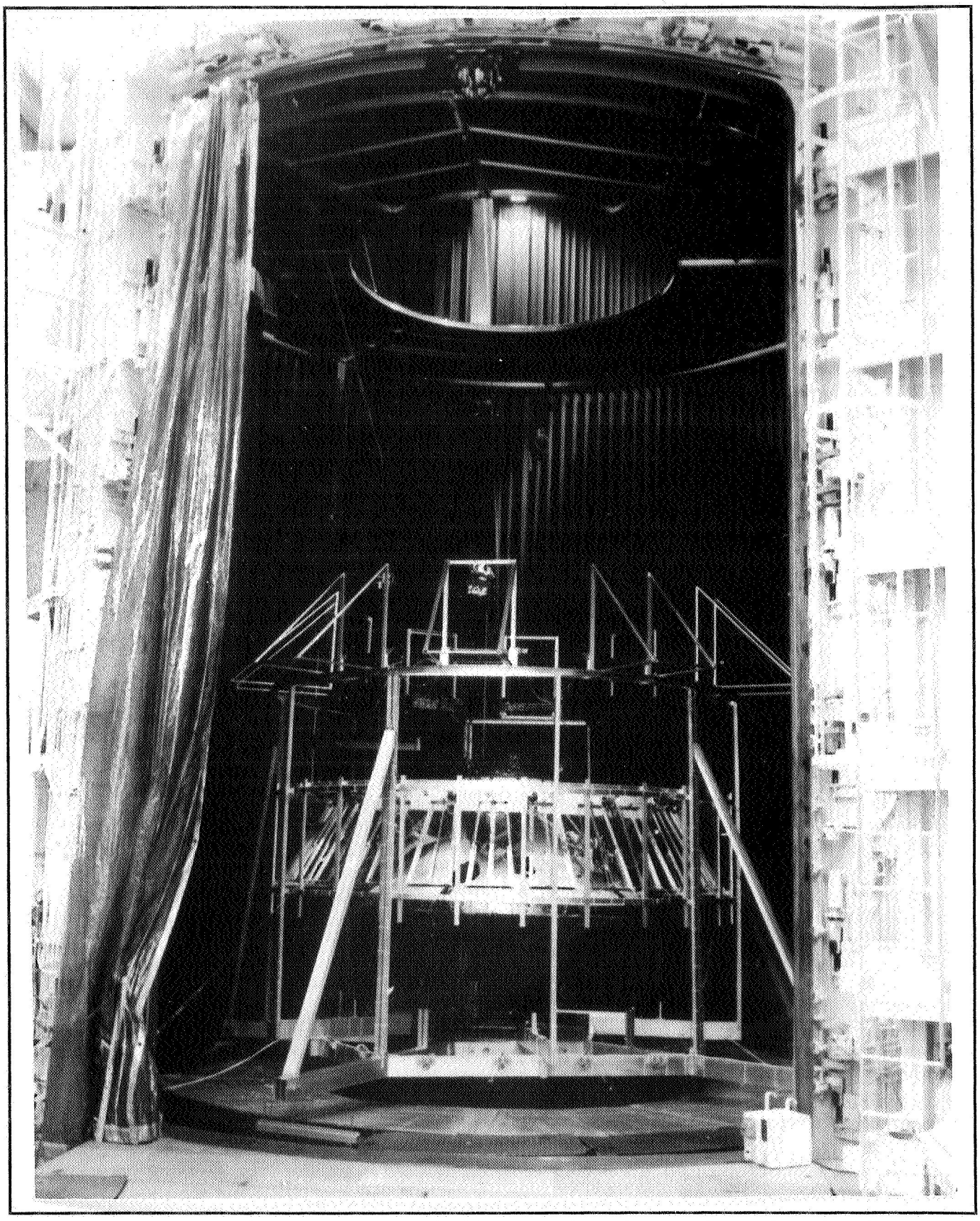


Figure 18. Photograph of the Test Set-up for the MPF-STV-1 (Cruise Phase) Test in JPL's 25-ft Space Simulator

ment); 1-3) a thermal balance period to achieve steady-state conditions and to verify thermal designs in this orientation; and 1-4) a test to verify the functionality of the thermostatically-controlled back-up heaters.

Phase 2, the Mars Cruise-Nominal Cold phase (1.55 AU, 41° Off-Sun orientation), a test which represented the worst case cold condition for the solar array, consisted of six test cases: 2-1) a thermal balance period to achieve steady state and to verify thermal designs in this orientation; 2-2) a thermal simulation of a trajectory correction maneuver (TCM) for the propulsion hardware under cold conditions to measure the valve temperatures at the end of the maneuver; 2-3) a test to demonstrate that the basepetal airbag heater is sized properly to maintain the airbag at acceptable flight temperature limits; 2-4) a simulation of the entry, decent and landing (EDL) sequence beginning 95 minutes prior to landing for the purpose of characterizing the warm-up of the ISA, specifically the solid-state power amplifier, after the HRS pump is off, and to verify the EDL heater sizes; 2-5) a test to characterize the thermal response of the ISA equipment, the rover, and the cruise shunt limiter (SLC) in case of an HRS failure and to develop a strategy for thermal recovery of this equipment after such a failure occurs; and 2-6) a hot margin test of the ISA electronics to demonstrate the functionality of these electronics in the mission extreme hot environment.

Phase 3, the Earth Cruise-Nominal Solar Array Hot phase (0.99 AU, 0°C Off-Sun orientation), a test which represented the worst case hot condition for the solar array, the shunt radiator and the deep space station heads, consisted of one test case: 3-1) a thermal balance period to achieve steady-state thermal conditions to verify that the solar panel and other cruise stage hardware stays within acceptable flight temperature limits.

Phase 4, the Earth Cruise-Nominal 60° Hot phase (0.99 AU, 60° Off-Sun orientation), a test which represented the nominal hot condition to verify flight acceptable temperature limits. consisted of five test cases: 4-1) a test to verify the proper functionality of the two HRS pumps under hot conditions; 4-2) a test to verify the performance of the battery and its charging system at design temperature; 4-3) a thermal balance period to achieve steady-state thermal conditions to verify flight acceptable temperature limits; 4-4) a test to simulate a trajectory correction maneuver for the propulsion hardware under cold conditions; and 4-5) a hot margin test to demonstrate the functionality of the cruise stage electronics in mission extreme hot conditions.

Results of the MPF-STV-1 test were still being analyzed at the time of this writing and a final test report on the thermal response results is not yet available . However, all MPF-STV-1 test objectives were met.

MPF-STV-2, THE MPF FULL ASSEMBLY LANDER PHASE THERMAL RESPONSE TEST (12)

The final test in the MPF series, MPF-STV-2, was conducted to study the thermal response and performance of the lander equipment and systems, and to test the performance of the rover hardware mechanisms and command software in a simulated Mars surface environement. The thermal plan for this test was prepared by H. Awaya.

Figure 19 is a photograph of the MPF-STV-2 test set-up. A structurally supported perforated aluminum floor was steam-cleaned then installed in the chamber above the floor shrouds to provide structural support for the lander and the rover "doghouse". The lander was configured in a fully deployed position and the basepetal was supported on three 8-in high thermal isolative standoffs to ensure that all lander components would not come in direct contact with the floor of the chamber. The three sidepetals were supported on retracted airbags, in a simulated normal landed configuration. Because of biocontamination concerns, the lander solar panels were kept covered during the test.

The rover was mounted on one of the sidepetals and the rover ramp was deployed to allow the rover to drive off the petal during the test. A special semi-circular rover floor was fabricated to provide a surface on which the rover could transverse during the rover maneuverability tests. This floor was made of fluoroglass and was painted to provide a surface with medium absorptivity and emissivity similar to the optical properties of the surface of Mars. A white tape grid was laid down on the rover floor to provide a visual reference of the rover's position during maneuvers. An obstacle was placed on the floor in the path that the rover was expected to

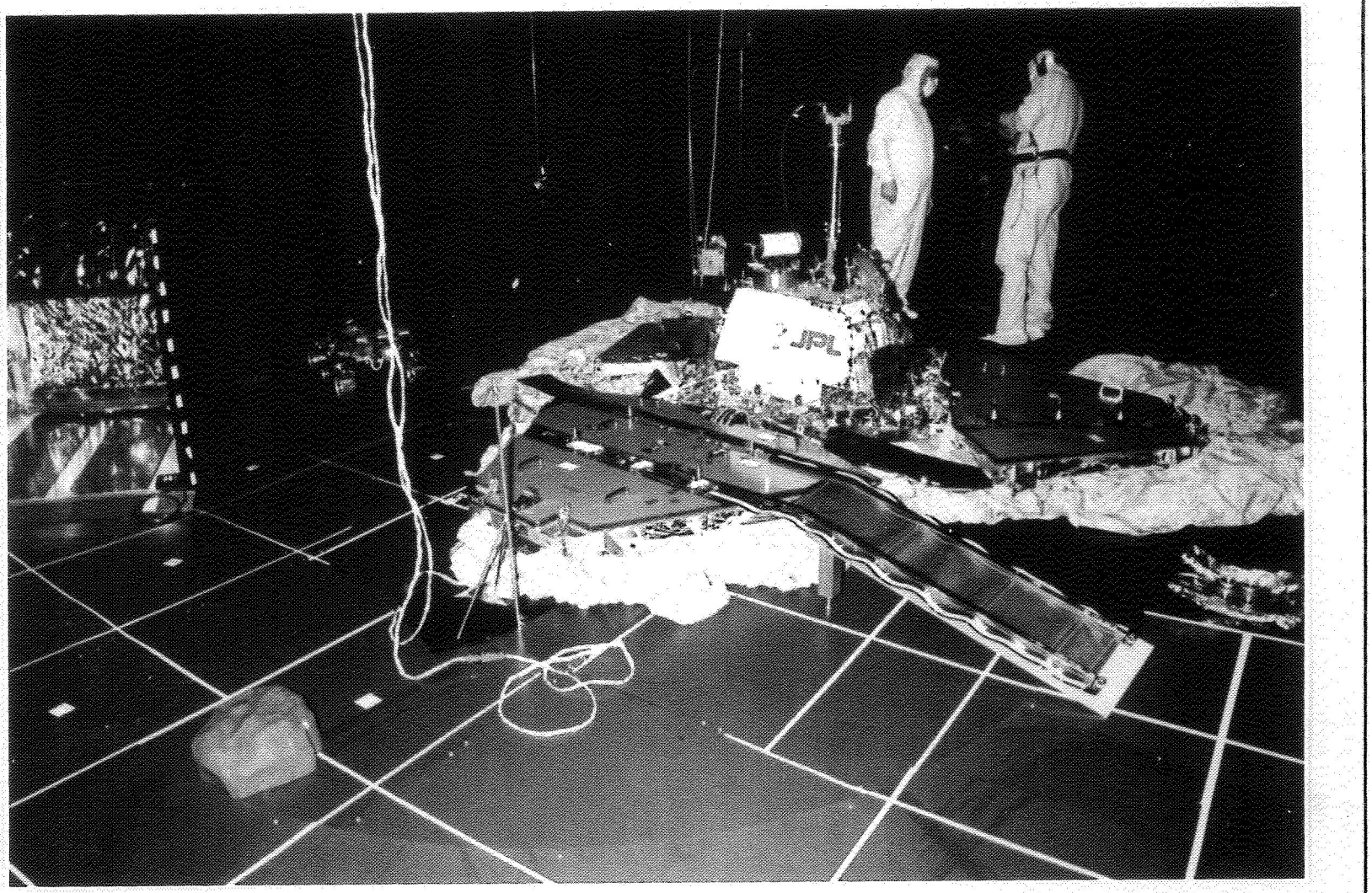


Figure 19. Photograph of the Test Set-up for the MPF-STV-2 (Lander Phase) Test in JPL's 25-ft Space Simulator

travel during the maneuverability tests. Cabling to provide communications and power to the rover was blanketed for thermal insulation and supported by a special skyhook arrangement. A rover "doghouse" was constructed with an aluminum frame, walls of reflective mylar and an infrared lamp assembly to keep the rover warm during the worst case cold test.

The test plan called for three test phases. Phase 1, the Mars Landed Diurnal Simulation phase, was a test to simulate the Mars landed environment at an atmospheric pressure of 7 torr GN2, to provide a 22 hour simulation of the diurnal solar and thermal surface conditions, and to maneuver the rover to test communication, imaging, roll-off, dead reckoning and a host of other important functional operations. Also during Phase 1, the Atmospheric Structure Instrument/Metrology (ASI/MET) Tavis pressure sensor was to be calibrated in the 1 to 9 torr range against a pre-calibrated Baritron pressure gauge attached to the chamber. Phase 2, the Mars Cold Steady State and Margin Test phase, was a test to obtain thermal characterization data for the lander in the cold case (nominally -85°C). Since the lander never obtains steady state operations during landed operations because of diurnal temperature cycling and internal power dissipation, the Phase 2 testing was done to determine the values of the thermal radiation, convection, and conduction components in a stabilized condition in order to properly characterize the thermal response of the electronics and other hardware and to verify that the response is within acceptable flight temperature conditions. Phase 3, the Mars Hot Steady State and Hot Margin Test, was performed for reasons similar to those given for Phase 2, except the test was conducted at the hot stabilized conditions (nominally -40°C).

The thermal results of the MPF-STV-2 test were still being analyzed at the time of this writing and a final test report on the thermal response results is not yet available. However, all MPF-STV-2 thermal test objectives were met. The rover maneuverability test was conducted by manually commanding the rover to travel from its mount on the petal, down the ramp, past the obstacle, and into the doghouse. The STAR system was used to provide visual feedback to the rover engineers of the rover's position during maneuvers. Further details of the rover maneuverability test will be described in a separate report. Much useful information was obtained during this test which helped both the MPF lander thermal engineers and the rover design team to improve and fine tune the various functions of the MPF lander thermal system and the rover hardware and software.

CONCLUSIONS

The MPF test program was an important part of the verification of the designed functional performance of the MPF systems during both the cruise and landed mission phases. The test program was very challenging to test designers and required the development of many new test methods and fixtures. The program proved to be very valuable in assisting the MPF thermal engineers and the rover design team to discover some design anomalies in a way which provided enough time to make any necessary design changes prior to launch. As such, the test program was very effective in helping the MPF design team to ensure the success of the overall MPF mission.

REFERENCES

1. Wen, L., and Kwack, E., "Mars Pathfinder Rover MTM Test Results," JPL-IOM 3545/TSSE:LW/035-95.TEC, 6/9/95, p. 128.
2. Ibid, p. 51.
3. Ibid, p. 76.
4. Wen, L., and Kwack, E., "Preliminary Test Results for Rover-EM Wind Test," JPL-IOM 3545/TSSE:LW/086-95.TEC, 7/12/95, p. 1.
5. Lyra, J., Novak, K., and Awaya, H., "Mars Pathfinder ISA/HRS Thermal Characterization Test Report," JPL-IOM 3535/JCL/151-95.TEC, 11/28/95, pp. 4-8.
6. Ibid, pp. 8-11.
7. Wen, L., "Mars Pathfinder Rover SIM QUAL Test Report," JPL-IOM 3535/TSSE:LW/148-95.TEC, 11/22/95.

8. Johnson, K., Wen, L., Kwack, E., and Noller, E., "Simulation of Mars Surface Conditions for Characterization of the Mars Rover Thermal Response,"Proceedings of the 16th Aerospace Testing Seminar, Manhattan Beach, CA, 3/12-14/96, pp. 195-207.
9. Hickey, G. S., Braun, D., Wen, L-C, and Eisen, H. J., "Integrated Thermal Control and Qualification of the Mars Rover," SAE 26th International Conference on Environmental Systems, 7/8-11/96, Monterey, CA.
10. Johnson, K., Siebes, G., and McAffee, D., "Utilization of the Satellite Test Assistant Robot (STAR) for Visual and Thermal Analysis of Articles in the Thermal Vacuum Test Environment," Proceedings of the 16th Aerospace Testing Seminar, Manhattan Beach, CA, 3/12-14/96, pp. 251-256.

ACKNOWLEDGEMENTS

The author wishes to acknowledge the hard work and dedication of all the engineers and technicians who were responsible for setting up and instrumenting the test article hardware, preparing test procedures and operating the JPL Environmental Test Lab and the Space Simulation Facilities throughout the MPF test program. Also acknowledged is the exemplary cooperation among the many players involved in the MPF test program, especially the project management by Brian Muirhead and Robert Manning, the test integration efforts by Cathy Cagle, Curt Cleven, Bob Galletly, Bill Layman, Mike Mangano, Linda Robeck and Tom Shain, the thermal engineering and test planning by Y.C. Wu, Jackie Lyra, Henry Awaya, L. Wen, Eug Kwack, Keith Novak and Pradeep Bhandari, the test fixture design and fabrication work by Gene Noller and Jim Willia, and the Rover engineering team, especially Jake Matijevic, Howard Eisen, David Braun, Gregory Hickey and Al Sirota. Finally, acknowledgement is deserved by all the many others not named here who contributed to this innovative, successful test program.

58-18
52144
069366
4P

SWAS SPACECRAFT T/V TEST, UNIQUE IN CHAMBER TESTS SYSTEMS ACTUATION

Jamie L. Dunn
NASA/Goddard Space Flight Center

ABSTRACT

The Sub-Millimeter Wave Astronomy Satellite (SWAS) is the third mission of the Small Explorer (SMEX) Project at Goddard Space Flight Center (GSFC). It is a path finding mission to study the chemical composition of interstellar galactic clouds to help determine the process of star formation. The spacecraft recently completed a month-long thermal vacuum/thermal balance test in the Solar Environmental Simulator, the largest thermal vacuum facility at Goddard. Rather extensive fixturing was required for the test, considering the small size of the spacecraft, and two unusual deployments were completed in order to accomplish the goals of the test. This paper discusses the space simulation testing of the fully integrated SWAS spacecraft and the unique fixturing required.

INTRODUCTION

In addition to the usual objectives of verifying the spacecraft thermal mathematical model and temperature cycling, there were two additional ones which were required for the SWAS thermal vacuum and thermal balance test. While undergoing testing at Ball Aerospace, the instrument's thermal performance did not correlate with the mathematical model that had been developed. Test temperatures differed by as much as 30°C in some instances. There was an unknown quantity of heat flow out of the instrument aperture which had to be characterized at some point during the SWAS spacecraft level test so that a valid thermal model could be created for the instrument. The other main objective during the test was to successfully deploy the solar arrays hot, cold, and while a temperature gradient existed between the inner and outer panels. All of this had to be accomplished within a short period of time due to the project's compressed schedule.

FIXTURE DESIGN

The thermal vacuum and thermal balance test was to be conducted in the Space Environment Simulator (SES), which is 8.23m in diameter and 12.19m in height. The overall length of the extended arrays, approximately 4.11m, necessitated a facility of this size. A total of nine radiator panels ranging in size from $0.065m^2$ to $0.92m^2$ were required, all of which had to be supported by the fixture while providing enough area for the deployment of the solar arrays. In order to accommodate these requirements, a versatile fixture was essential. In an effort to reduce costs and complete the project on time, the fixture was constructed using existing materials from a previous thermal vacuum test. With relatively minor modifications, the aluminum fixture was designed and built in five weeks. The SWAS spacecraft mounted in the completed fixture is shown in Figure 1.

HEATER PANELS

As mentioned above, one of the test objectives was to conduct a solar array deployment while a temperature gradient existed between the inner and outer panels. There was however, nothing in place that could simulate this condition. As a result of the order in which the flight heaters on the rear of the solar arrays were powered, a gradient of this type was impossible. Test heaters could not be applied to the solar cells or the painted rear surface, so the only possibility was to use a radiator panel. In order to avoid losing time by breaking vacuum for reconfiguration, this radiator would have to be movable, so as not to interfere with the subsequent deployment of the solar arrays. For this, two existing heater panels were hinged to the bottom of the SWAS fixture. They were tilted at approximately a 5° angle, enough for them to fall under their own weight when released. A solenoid was mounted above each panel so the pin would enter an existing hole and prevent the panel from falling. Upon activation of this solenoid, the panel would fall away from the spacecraft onto nylon chord strung tightly from supports on the floor.

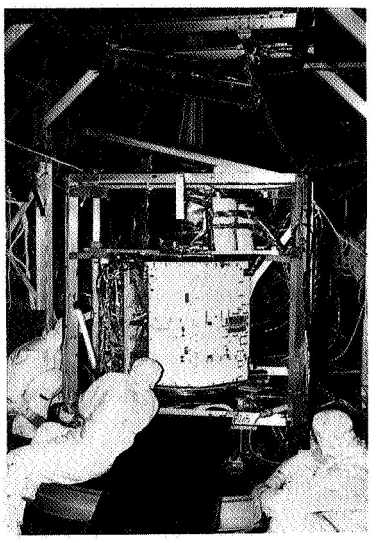


Figure 1: SWAS Spacecraft in Fixture

One heater panel required for the test had a 90° view factor to the body mounted solar array on the spacecraft. It was necessary for this panel to reach a temperature of approximately +125°C in order to simulate the hot test case. Kapton film heaters are normally chosen for test use, but in this case another method of heating had to be used, as the adhesive on the film heaters could break down at +120°C resulting in the heaters becoming detached. Stainless steel strip heaters were chosen, capable of temperatures up to +500°C, and bolted to a 78.74cm x 91.44cm x 0.318cm aluminum panel. Stainless steel braiding was placed between the heaters and the panel to increase conduction. One dozen of these heaters were used and controlled as two separate circuits. Each circuit was wired in parallel, capable of providing 500 watts. This arrangement worked well, with thermal gradients across the panel less than 1°C.

MICROWAVE ABSORBER

In order to test the instrument under vacuum, a target had to be fabricated that would absorb the emissions from the instrument and reflect as little as possible back to the instrument aperture. The end result of this criteria was a series of 1.27cm thick Plexiglas strips cut at 30° angles that ran parallel to the instrument. The temperature of this "Microwave Absorber" was controlled by a 111.76cm x 81.28cm x 0.635cm aluminum panel that rested on the flat surface of the absorber material. This absorber is shown in Figure 2. It was later conceived that this absorber could not only be used for instrument testing, but could also be used for thermal control. This required a test of the thermal performance of the absorber to determine whether its use as a radiator was feasible.

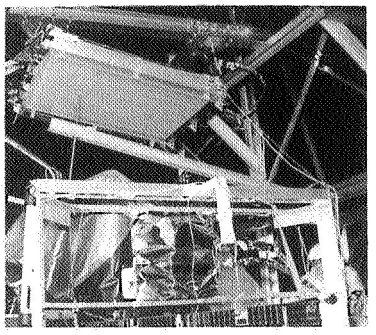


Figure 2: Microwave Absorber

The absorber panel was loaded into Facility 239, a horizontal loading chamber 2.1m in diameter by 2.4m long. The panel was hung from its support structure as it would be during the spacecraft test, and a cryopanel was placed directly beneath it, simulating the heat input from the instrument aperture. The Plexiglas would need to reach -100°C in order to be used as a target radiator. During the first test run, the aluminum control plate could only reach -115°C, well short of the -180°C temperature necessary. This was a result of poor conduction from the copper coolant lines to the panel. At this temperature, the Plexiglas itself attained a temperature of -50°C. The chamber was

returned to ambient conditions, and aluminum tape was attached to the copper lines and the aluminum plate in order to increase the conductance. This worked for the second run, as the aluminum plate reached the desired temperature of -180°C. Unfortunately, the Plexiglas only reached -75°C.

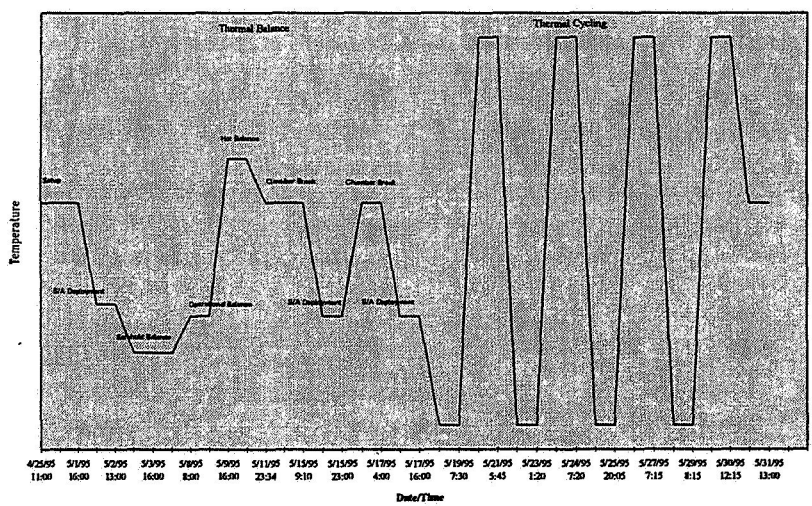
BLANKET SNATCHER

As a result of the Microwave Absorber panel being unable to achieve -100°C, another method for testing the heat loss from the instrument aperture was needed. The thermal engineer requested a blanket to be placed over the aperture, then removed in order to attain two different thermal boundary conditions. Once again, it was desirable to do this without a chamber break in order to save time. To accomplish this, one end of a nylon cord was tied to the blanket, and the other end to a five pound G-10 fiberglass block. The block rested at an angle on one of the towers that was being used to support the microwave absorber plate. A solenoid held it in place, and once activated, the block would fall, pulling the blanket away from the instrument aperture.

TEST RESULTS

The testing was an overall success. The as-run test profile is shown in Figure 3. Three solar array deployments were completed successfully, one each at -50°C and -5°C, and a third while under a temperature gradient. The temperature gradient achieved was only 9°C, though, which was less than the desired 20°C. This was acceptable, however, as it was the best result that could be achieved given the time allotted. The deployable heater panels worked well, although one of them had to be altered during a chamber break due to thermal expansion. The "blanket snatcher" operated without fault, and the instrument aperture heat loss was characterized by the thermal engineer as being 14 watts. The thermal mathematical predictions for the spacecraft were within 5°C, and a new model was developed for the instrument based on the test results.

Figure 3: SWAS Test Profile



59-18
021446
069367
16P

MSX THERMAL VACUUM TESTING

J. A. Krein
Swales and Associates, Inc.

D. S. Mehoke
The Johns Hopkins University Applied Physics Laboratory

ABSTRACT

This paper presents an overview of the Midcourse Space Experiment (MSX) satellite thermal design and the resulting spacecraft thermal vacuum test execution and results. MSX is approximately a 6,000 pound spacecraft. It flies in an 898 km nearly sun-synchronous circular orbit with a 99.2° inclination. MSX has a four year required lifetime with a five year goal. The MSX thermal design is driven by its main sensor, the cryogen-cooled Spatial Infrared Imaging Telescope III (SPIRIT III). This sensor has a minimum 11 month cryostat life.

Thermal vacuum/thermal balance testing of MSX occurred between July 25 and August 22, 1994, at the Goddard Space Flight Center (GSFC). The four week test consisted of two hot and two cold thermal balance points, a hot and cold functional test, and a hot and cold survival test. The testing simulated flight environments and ensured proper functionality of the spacecraft and all its components.

The MSX thermal vacuum test was unique in that during the test, while MSX was in the chamber, SPIRIT III argon and helium fills took place. This was the first time that cryo servicing operations have been done during thermal vacuum testing. Test heaters were necessary on the SPIRIT III lines to keep the o-rings from freezing, and ultimately leaking, during the filling operations. These temperatures and heater powers were monitored during fill operations, in addition to the usual spacecraft telemetry, and acceptable levels were maintained.

The overall results of the test were excellent. Repeated system level performance was demonstrated at the extremes of the qualification test temperatures. All spacecraft flight thermal hardware, including heat pipes, operational and survival heaters, thermostats, and temperature sensors, proved to be operating nominally. No temperature limits were exceeded, and the test temperatures correlated with the thermal analysis models to within 5°C.

INTRODUCTION

The Midcourse Space Experiment Satellite was launched from Vandenberg Air Force Base in California on April 24, 1996, aboard a Delta II rocket. MSX is approximately a 6,000 pound spacecraft. It flies in an 898 km nearly sun-synchronous circular orbit with a 99.2° inclination. MSX has a four year required lifetime with a five year goal. The SPIRIT III sensor has an 11 month cryostat life.

This paper gives an overview of the spacecraft thermal design and explains the details of the thermal testing methodology, execution and results.

SPACECRAFT THERMAL DESIGN DESCRIPTION/OVERVIEW

The MSX spacecraft has three main parts: the instrument section at the top, the truss section in the middle, and the electronics section at the bottom. These sections are thermally isolated from one another. Figure 1 shows the overall spacecraft configuration. The overall spacecraft dimensions, not including the solar arrays, are approximately 1.6 m by 1.6 m by 5.1 m tall. Additional details of the spacecraft thermal design can be found in Ref. 1.

Instrument Section

The instrument section, shown in Figure 2, is a four-sided box structure and is the platform on which most of the science instruments are mounted. This includes the Ultraviolet and Visible Imagers and Spectrographic Imagers (UVISI), Space-Based Visible imagers (SBV), and the Contamination Experiments and Mass Spectrometer (CEMS). The SPIRIT III telescope protrudes through the middle of the instrument section. The optical bench, the beacon receiver antenna, and the reference object ejectors are also mounted to the instrument section.

The Instrument Section is designed to be maintained at approximately -25°C. This is to minimize heat input to the SPIRIT III vacuum shell and be compatible with

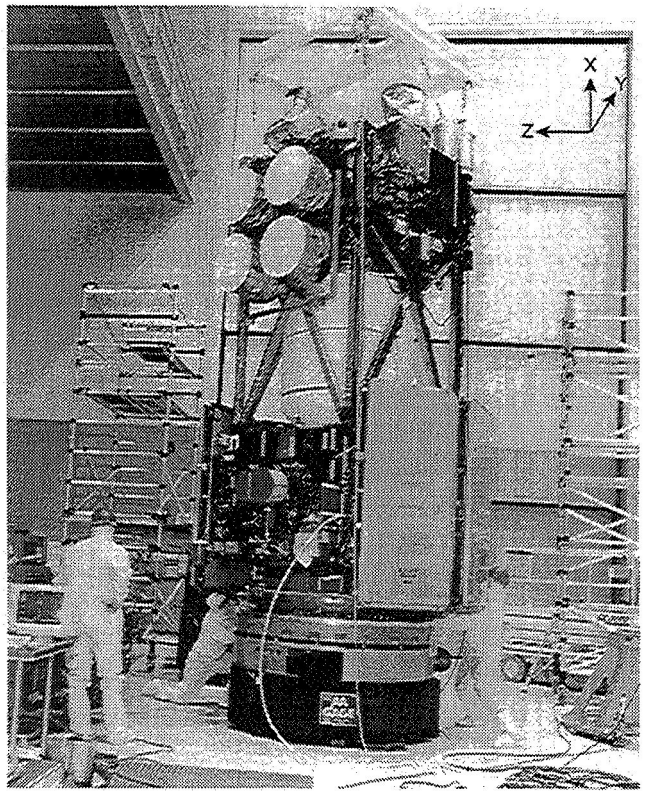


Figure 1. The overall configuration of the Midcourse Space Experiment (MSX) spacecraft with the instrument section at the top, the truss section in the middle, and the electronics section at the bottom.

the requirements of the UVISI sensors. Thermostatically controlled heaters, both survival and operational, as well as heat pipes and radiators, are used to maintain this temperature. The entire section is blanketed, except for the heat pipe radiators. The heat pipes, embedded in each of the four panels, minimize temperature gradients which control the thermal distortion of the alignment-sensitive instruments.

Optical Bench

The spacecraft optical bench, mounted to the -Y side of the top of the instrument section, provides a stable mounting platform for the primary attitude control sensors. The bench supports two gyros, one star camera, and an autocollimator. The bench structure is that of a "bent" graphite epoxy honeycomb. The bench is mounted to the instrument section panels by three kinematic joints. There are two small radiators on each of the Z sides. One radiator is used by each of the two gyros. The other two are used together by the higher powered star camera. The remainder of the area is blanketed except for two small apertures used by the autocollimator. The bench is isolated from the instrument section with G10 (fiberglass) washers and a small blanket under the mounting feet.

Because strict limits are placed on thermal distortion, the temperature control system for the optical bench is critical. As the control region is smaller than what could be obtained from a mechanical thermostat, an electrical control system was designed. An on/off electronic thermostat with a 0.5°C dead band was chosen over a proportional system because of system complexities and the electromagnetic interference problems associated with a pulse-width modulated device. The final system uses remote temperature sensing to control seven separate heater channels from one box. Two systems are used to make the system fully redundant.

Beacon Receiver

A beacon receiver antenna is mounted to the -Y instrument section panel below the optical bench. It comprises four parabolic dish antennas and the flat deck to which they are mounted and can be seen in its stowed position in Figure 1. Thermal distortion in the antenna deck is minimized through the use of a highly stable graphite epoxy honeycomb structure. The beacon bench is completely blanketed except for the top of the four antennas. The beacon bench has a heater circuit to maintain minimum temperatures.

Truss

An open truss structure, manufactured from graphite epoxy, connects the instrument section to the electronics section. The graphite epoxy as well as titanium fittings was selected to keep the electronics section isolated from the instrument section while maintaining the spacecraft thermal distortion/pointing requirements. The truss section also provides a stable mounting structure for SPIRIT III. The truss is blanketed on three sides, but

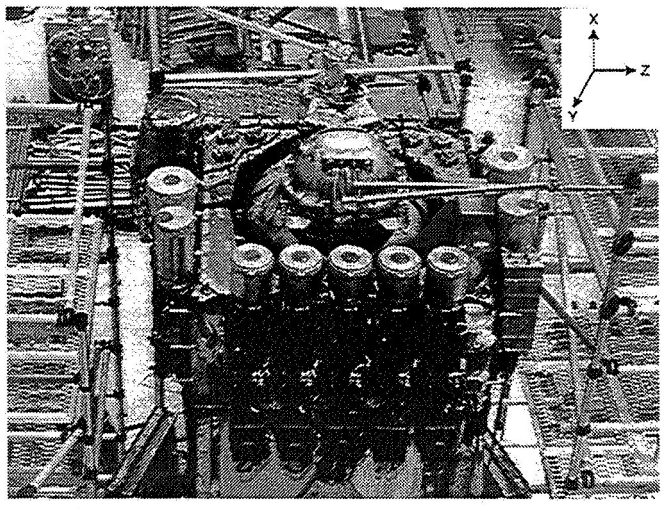


Figure 2. The MSX instrument section with SPIRIT III in the center.

remains open on the anti-sun side (+Y) to allow the SPIRIT III vacuum shell to radiate to deep-space.

Electronics Section

The electronics section houses all the spacecraft housekeeping equipment, (tape recorders, reaction wheels, batteries, etc.), instrument support electronics, and provides the mounting location for the solar array panels. The electronics section is designed to run between -19°C and +56°C, except for the battery and tape recorders which have tighter temperature limits. Most of the components on the electronics section are mounted to the outside of the section panels. The boxes are thermally tied to the structure with Cho-seal thermal gaskets. The outside faces of individual boxes are used as spacecraft radiators. The boxes are internally designed to conduct heat to the external face. The remaining electronics section area (non radiator) is blanketed. Heaters, both operational and survival, are mounted to the inner panel surface. The battery assembly is thermally isolated and is mounted to the spacecraft's -X panel within the launch vehicle adapter ring. The external face of the battery assembly is a radiator surface. Its thermostatically controlled heaters maintain minimum temperatures.

SCIENCE INSTRUMENT DESCRIPTIONS

SPIRIT III

The primary instrument on MSX is the SPIRIT III, a solid hydrogen cooled telescope. The top protrudes through the center of the instrument section. A gold coated aperture shade shields the telescope from the Sun and Earth. This shade is blanketed on the sun side and has a highly reflective gold surface on the side that faces the telescope aperture. The bottom portion of the instrument is a cryogenic dewar, which extends down through the truss section to the top of the electronics section. The integration of SPIRIT III with the spacecraft is shown in Figure 3. The SPIRIT III vacuum shell temperature must be maintained below 250°K. This is accomplished by using the open and anti-sun side of the truss (+Y) as a radiator. The dewar shell is painted with a high-emissivity, low-absorptivity white paint to maximize heat rejection to space.

The SPIRIT III support electronics boxes, the Radiometer Analog Signal Processor (RASP), Rockwell Interferometer Pre-amp (RIPR), Laser Reference Unit (LRU) and Mirror Monitor Box (MMB), are mounted in the area of the instrument section and are isolated. Each box has its own radiator area as well as flight heaters, thermostats, and temperature sensors.

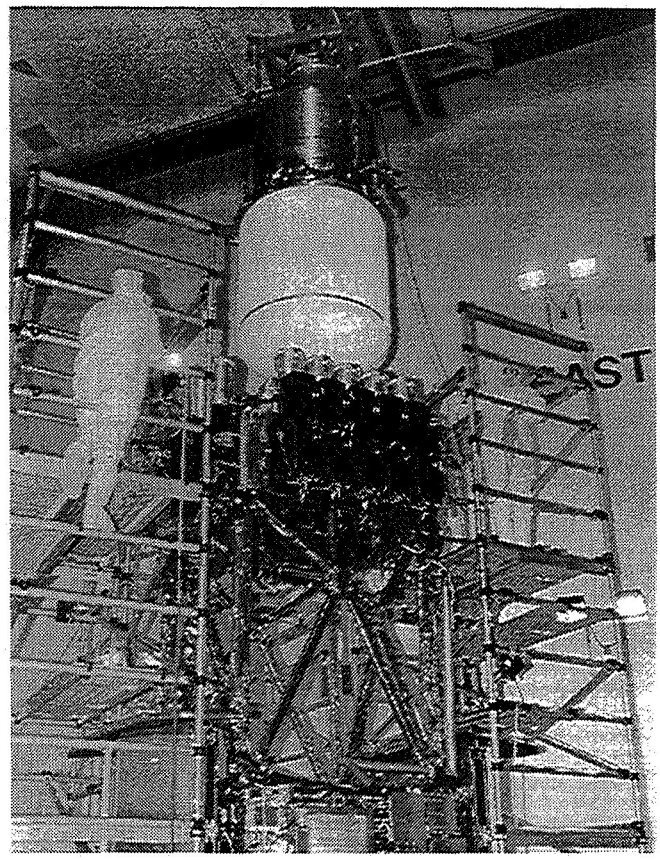


Figure 3. The SPIRIT III instrument being integrated with the MSX spacecraft.

SBV

The SBV instrument is divided into two sections: the telescope units mounted to the instrument section and the electronics units mounted to the electronics section. Both units are thermally isolated from their respective mounting panels and incorporate dedicated Optical Solar Reflector radiators (OSRs) and heater control systems. The telescope units are mounted to the -Z instrument section panel. The local radiator faces along the -Z axis. The telescope sunshade design incorporates a recloseable door, which has an opening mechanism located on the -Y side of the SBV instrument and is thermally controlled using the Sun's input to that surface. The electronics support assembly is mounted to a honeycomb panel suspended by a truss support structure off the +Y electronics section panel.

UVISI

The UVISI comprises three electronics boxes mounted to the electronics section and nine imaging telescopes mounted to the instrument section. The latter includes two ultraviolet imagers mounted to the +Z instrument

section panel, two visible imagers mounted to the -Z panel, and five spectrographic imagers mounted to the +Y panel.

The heat pipes (see discussion of instrument section) remove local heat inputs from the various UVISI sensors and minimize thermal gradients in the instrument section structure. The heat pipes are bonded internally to the external face of the honeycomb panels. The pipes in the panels are level to allow ground testing but are arranged to pass near as many of the instrument's mounting feet as possible. Where feasible, the mounting foot insert and heat pipe cradle were machined in the same piece.

Covers controlled by a one-shot opening mechanism protect each UVISI sunshade. The covers were opened after orbit was achieved. A special set of protective heaters was used to maintain the opening mechanism within its operating temperature range.

Contamination Experiment

To measure contamination, a number of sensors are used to monitor particle type and density on orbit. The sensors are mounted to the instrument section and include a pressure sensor, a mass spectrometer, four temperature controlled quartz crystal microbalances, and two lasers. Since these sensors are low powered their operation does not have a great impact on the thermal system.

THERMAL TEST SETUP AND CONFIGURATION

The MSX Spacecraft Thermal Vacuum Test occurred between July 25 and August 22, 1994, at Goddard Space Flight Center (GSFC). The four week test consisted of two hot and two cold thermal balance points, a hot and cold functional test, and a hot and cold survival test.

The test took place in the large thermal vacuum chamber (#290) at GSFC. The spacecraft was placed on a mounting fixture and was in a flight configuration (100% flight hardware) with all instruments installed. The Beacon Receiver was in a deployed position. The solar array panels were the only flight component not included in this test.

Spacecraft Mounting in Chamber

Controlling the heat leak from the spacecraft through its mounting interface is an important requirement in any thermal balance test setup. The conflicting requirements of thermal isolation and structural support both have to be addressed. Due to the weight and size of the MSX spacecraft, simple G-10 isolation blocks were not adequate.

The mounting configuration for the spacecraft is shown in Figure 4.[1] The actual satellite mounting surface is a ring called the payload adapter that is 1.6 m in diameter with a 2.2 cm wide contact surface. The satellite's payload adapter mounts to the rocket's Payload Attach Flange (PAF). It is required that the joint be a metal-to-metal interface to ensure proper seating of the clamp strap. It is across this joint that we needed to eliminate heat flow.

Providing an adiabatic surface between two thermally conductive surfaces requires good definition of the temperatures on each side of the joint, and the capability to control the temperatures on the test side of the interface. Thermocouples were mounted at four points around the payload adapter and the PAF on each side of the mating interface. Heaters were installed at the thermocouple locations on the payload adapter and PAF. By using the heaters, the local PAF temperature could be set to follow the corresponding temperature on the flight side of the interface. The PAF heaters can be seen in Figure 5. As the difference in temperature across the interface is reduced, the corresponding heat flow is minimized. The result is a nearly adiabatic condition in a highly conductive mounting interface.

Between the PAF and the chamber test bed a double isolation scheme was incorporated, also shown in Figure 4. The main thermal isolation was provided by 4" high G-10 blocks placed under the eight mounting feet of the Brown stand. Large heaters were installed on the legs of the Brown stand. These heaters were used to keep the Brown stand temperature slightly below that of the PAF. This allowed for the tight temperature control which is required on the PAF, but is not necessary on

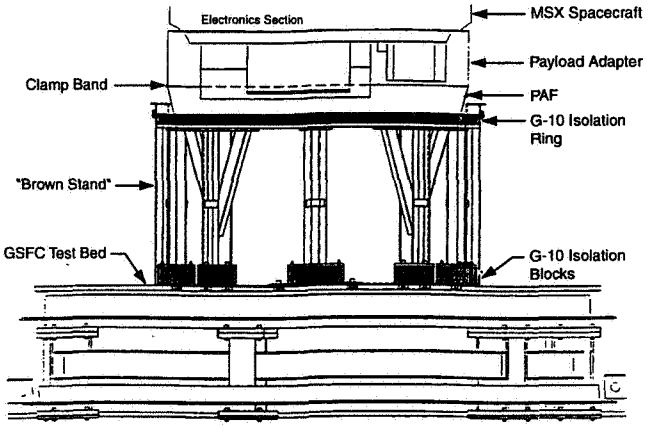


Figure 4. The MSX thermal test mounting configuration.

[1] Fox, H., *MSX Program GSFC/APL Test Interfaces and Requirements Document (TIRDOC)*, 7334-9040, May 17, 1994.



Figure 5. Test heaters, mounted to the payload attach Flange (PAF), help to maintain an adiabatic interface.

the Brown stand. The Brown stand heaters were used mainly to isolate the adapter heaters from variations in the chamber environment or test conditions. Between the Brown stand and the PAF there was a 2" high G-10 ring. Because of its large surface area and short height, the ring provided a rather poor isolation value, but it was effective in providing enough isolation to allow vernier control of the PAF heaters.

One of the more difficult aspects of controlling the interface heaters was the large time constant of the Brown stand and PAF. Changes in Brown stand or PAF heater settings were followed by very slow reactions in the surrounding temperatures. This problem became even more difficult as the size of the desired temperature change became smaller. One of the main goals of the balance portion of the test was to provide an overall power balance on the spacecraft. With an expected value of about 600 W, it would be easy for the overall balance to be off by 10% or more due to an improperly adjusted interface heater.

To reduce uncertainty it was decided that a heat leak in a known direction, coupled with the four balance cases, would give enough of a statistical variation to provide confirmation of the design. During the cold cases the payload adapter temperatures were kept just below the PAF temperatures, and for the hot cases the payload adapter temperatures were kept just above the PAF temperatures. Sample temperature distributions are shown in Figure 6 for all four cases.

Spacecraft Environmental Control

Temperature control of the spacecraft during the thermal vacuum test was maintained with a set of heater shrouds. The shrouds formed an irregular octagon that completely surrounded the spacecraft. Figure 7 shows the heater shroud. The shroud temperatures were set to simulate the range of orbital environments to which the spacecraft will be exposed. The heater shroud was used to provide equivalent sinks and the chamber cold wall was set to LN_2 temperatures.[2] Heater shrouds were used in those locations where the desired sink temperature was above -70°C. Where colder temperatures were required, cryopanels were used as shown in Figure 7b. The shroud was designed and built for MSX. The shroud is modular in design to make it reusable. Portions of the shroud were used for the Near Earth Asteroid Rendezvous (NEAR) spacecraft thermal vacuum test, and the same structure is planned for use during the Advanced Composition Explorer (ACE) spacecraft thermal vacuum test.

This thermal vacuum test attempted to simulate flight environments for the MSX spacecraft; however, with respect to the SPIRIT III sensor, this was not possible. In flight the SPIRIT III shell temperatures will be below -25°C. There are internal o-rings in the sensor that have to be kept above -25°C for ground testing to keep the o-rings from freezing and to maintain the integrity of the seal. In order to protect these o-rings, the minimum shell temperature during the test was approximately -10°C. Since the SPIRIT III instrument is isolated from the spacecraft's instrument and electronics sections, this did not impact the validity of the test results for those areas. The only areas affected by the higher-than-flight shell temperature were the LRU and the truss.

The LRU mounts to the SPIRIT III telescope shell. The LRU is isolated from the shell with low conductivity mounting feet. In flight, the gradient between the LRU and the shell may be as high as 50°C, but for the reasons mentioned above this was not the case during the test. A test heater was installed on the LRU to drive the gradient between the LRU and the dewar and measure the mounting resistance. Based on those resistance measurements it was determined that the isolation and available heater power are adequate for flight.

The temperatures that the truss sees in flight were not simulated in the test. The truss is colder in flight than it was during the test. The truss was designed to run at these colder temperatures, and so even though the flight conditions were not simulated exactly, there is no cause for concern.

The UVISI sunshade covers were not deployed during the spacecraft thermal vacuum testing. They were kept closed to avoid contamination and test stimulators (lamps) were used for functional testing. The proper

[2] Mehoke, D., *MSX Spacecraft Thermal Vacuum Test Plan*, 7334-9044, June 25, 1994.

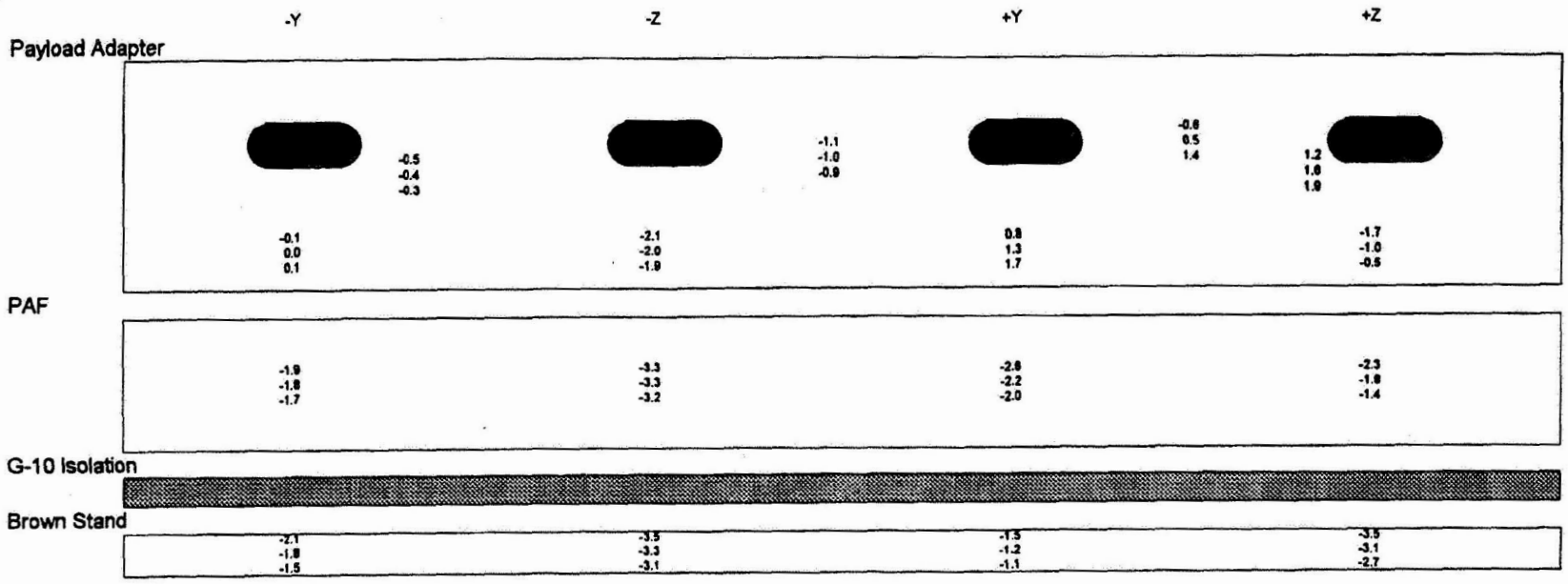


Figure 6a.

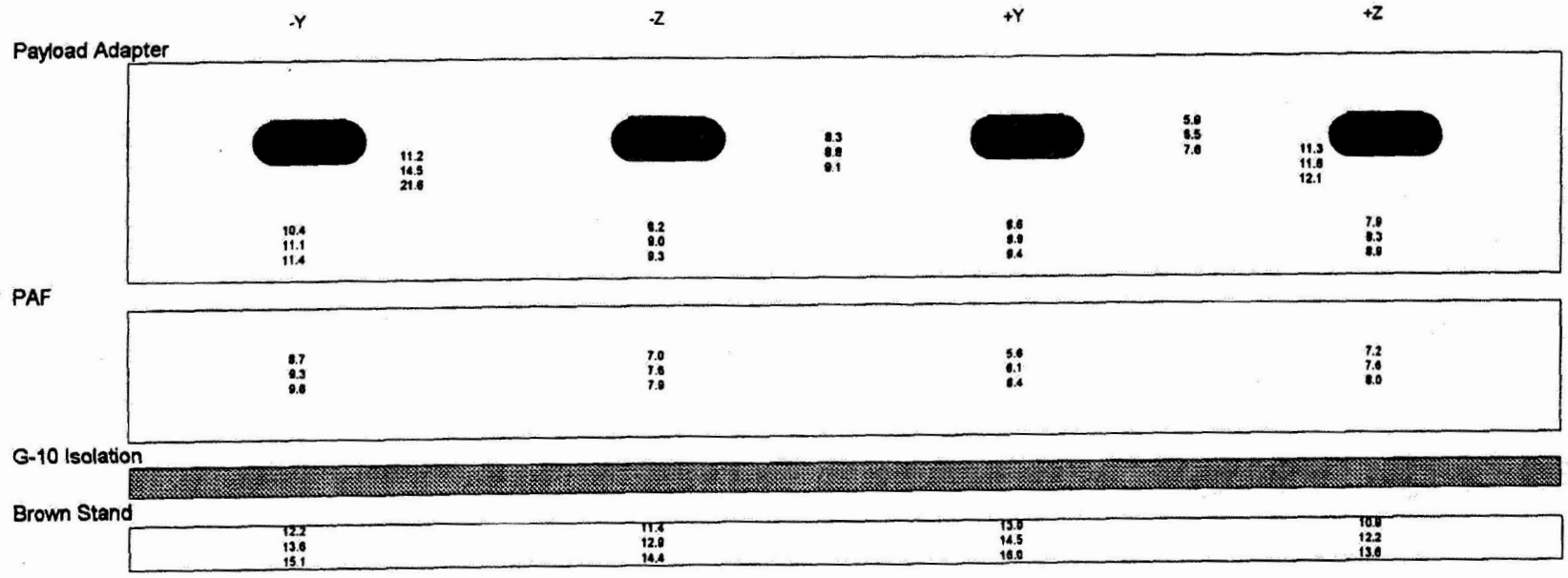


Figure 6b.

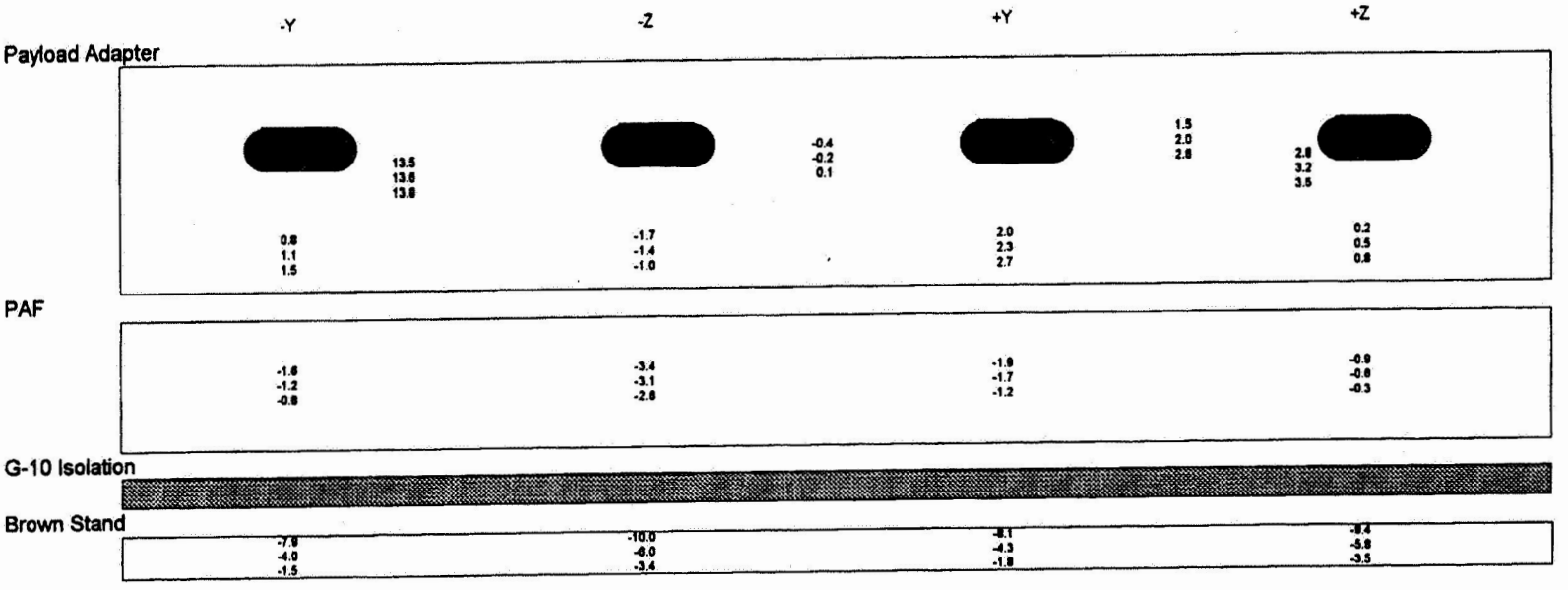


Figure 6c.

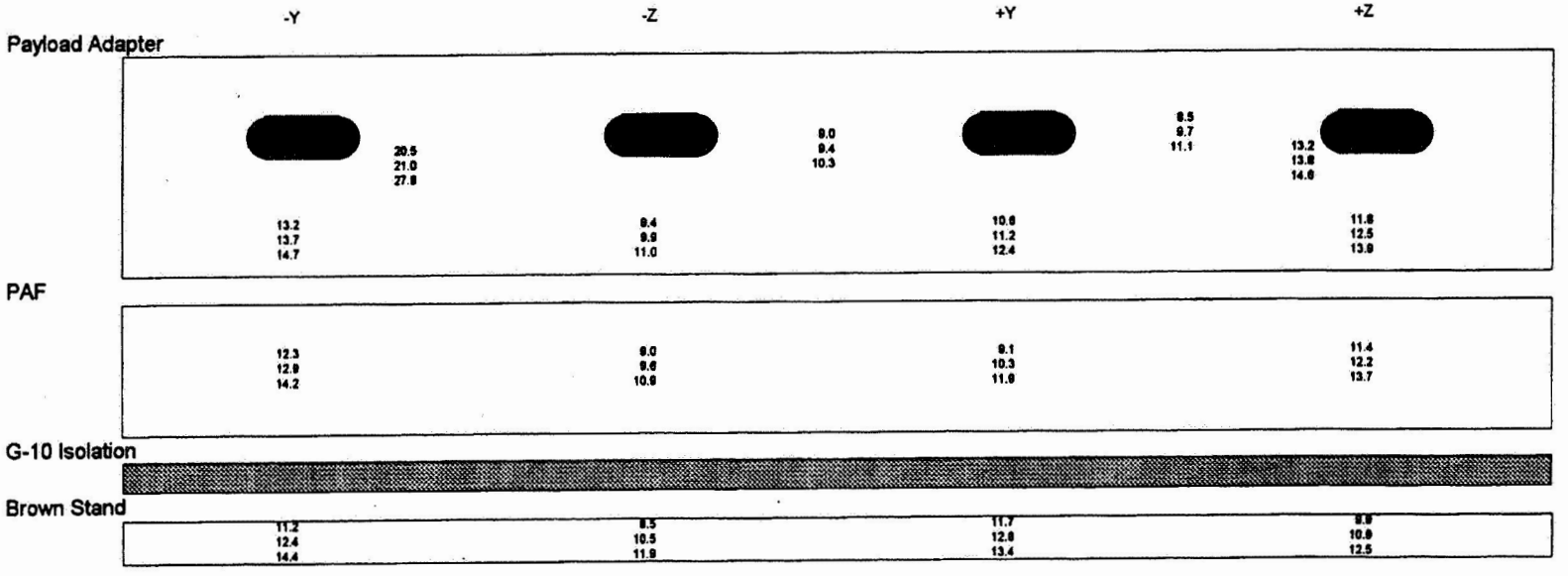


Figure 6d.

Figures 6a through 6d. Sample temperature distribution around the mounting interface for the four thermal balance cases.

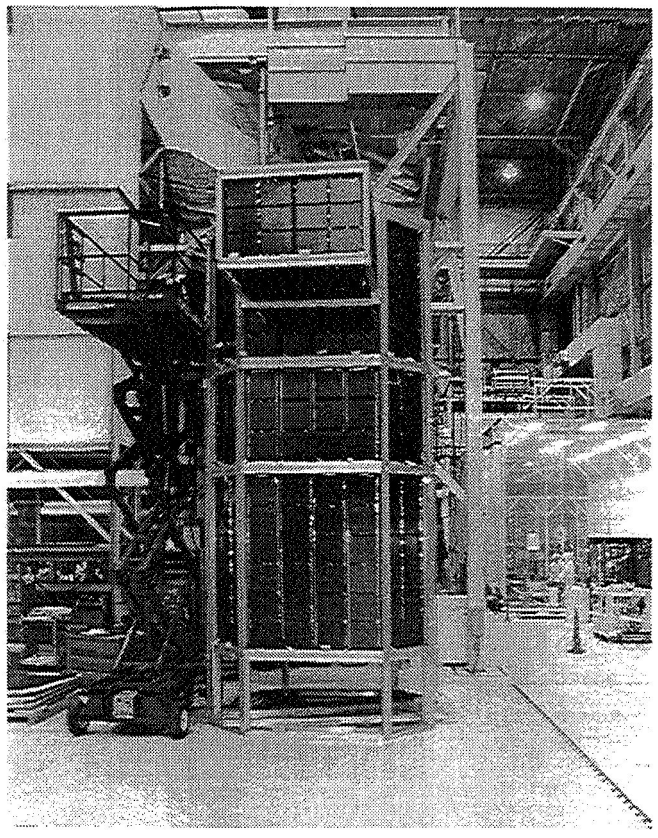


Figure 7a. The heater shroud, shown here outside the chamber, surrounds the MSX spacecraft for thermal testing. It is located between the spacecraft and the chamber wall and provides temperatures to simulate orbital environments.

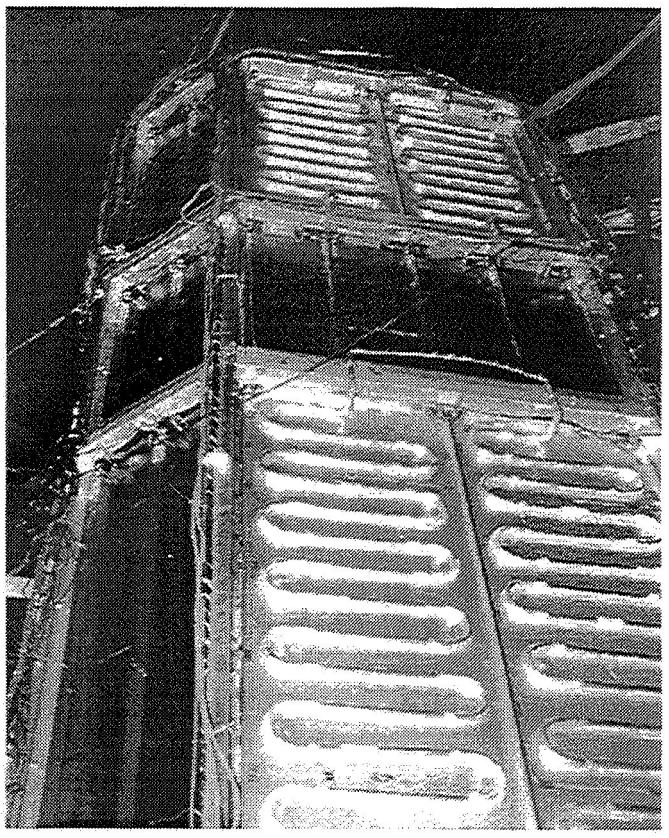


Figure 7b. The other side of the heater shroud, in the chamber, showing the cryo panels.

operation of these covers was verified by a separate thermal vacuum test of the sunshades. In flight, with the sunshades open, there will be an additional heat input to the sensors and heat rejection to space that was not simulated in the test. These additional factors are accounted for in the thermal models and are reflected in the on-orbit temperature predictions.

The SBV instrument has a motor located on the -Y axis of the telescope sunshade that is heated in flight by the Sun. During the test this solar heating was simulated with the use of a quartz lamp. The lamp was installed to point directly at the exposed motor and maintain the minimum operating temperature of 20°C.

SPIRIT III Cryogen Setup

Early in the test planning, constraints were placed on the temperature range of the SPIRIT III cryostat. Even though the chamber and the cryostat were both under vacuum, the two vacuum spaces needed to be kept separate. It was feared that the sensitive optical surfaces of the SPIRIT III instrument would be degraded by the small, but continuous, outgassing occurring in the test chamber, or that during a sudden re-pressurization of the chamber, the instrument would not keep its vacuum space intact. Since the vacuum connections were all controlled through the use of o-ring joints, these joints had to maintain tight seals. In the thermal vacuum test this requirement meant that the o-rings be kept above their freezing points. Previous testing by Lockheed Missile and Space Company, the supplier of the cryostat, indicated the o-rings would freeze around -25°C. Therefore, it was necessary that the dewar surface temperature be kept above -25°C.

The SPIRIT III instrument contains two cryogen systems: a main dewar using solid hydrogen for the flight cryogen and a smaller argon dewar mounted in the aperture door of the instrument. During testing liquid helium replaced the hydrogen to minimize safety concerns. During normal ground operations, the helium dewar had a hold time of about a week, and the argon dewar on the aperture door had a hold time of three days. The vacuum part of the thermal test was designed to last about 20 days. The dewar shell temperatures are colder during thermal vacuum testing than during normal ground operations, but even with these reduced

shell temperatures, it was not probable that the two cryogen systems could last for the full test. Therefore, the spacecraft was installed in the vacuum chamber with a complete set of cryogen support lines.

While the o-ring requirements on the cryostat itself were understood beforehand, the impact that the temperature limits would have on the cryo lines was not so clear. Seven cryo lines penetrated the chamber walls at two points, and ran from the chamber ports to four areas on the spacecraft. Photos of the cryo line installation in the chamber are shown in Figure 8a and 8b. It was recognized that the o-rings in the cryogen connections would be under the same requirements as those on the dewar. However, these connections are not only coupled to the cold of vacuum chamber LN_2 shroud, they are also subject to parasitic cooling from the cryogen flowing through the lines. It was estimated that a heater sized at 20 watts would be required at each connection. The heaters were placed on both sides of each connection, as near as practical to the o-ring location. Thermocouples were attached near the heaters for control purposes. After the heaters and thermocouples were attached, the connection area was wrapped with Multi-Layer Insulation (MLI) blankets. It was originally thought that thermal protection would only be required at the dewar end of the cryo lines, with the connections at the chamber wall side being kept warm by their connection to the room temperature vacuum wall. As the test progressed, we found that the chamber wall connection required the same active control as the dewar spacecraft connections.

The chamber environment was monitored by a Residual Gas Analyzer (RGA). An RGA is a typical way of monitoring the outgassing products in a vacuum chamber. However, during the MSX test it also served to monitor the integrity of the cryogen systems. In the case of a degradation in the vacuum seals, either helium or argon would make its way through the o-ring seals and into the chamber. During the initial chamber pump down, as the cold wall was flooded with LN_2 and the wall temperature fell below -25°C, the helium level on the RGA readout spiked. The most probable cause was that the cryo line connections at the chamber were leaking.

It was thought that helium was leaking at the connection to the chamber wall, either from a frozen o-ring, or from a joint stressed by movement of the cold wall. The chamber was opened, and heaters and thermocouples were installed on the cryo line connections at the chamber wall. After installation, the hoses were wrapped with MLI. Photos of one of the chamber connections, before and after heater and MLI installation, are shown in Figure 9a and 9b. While the

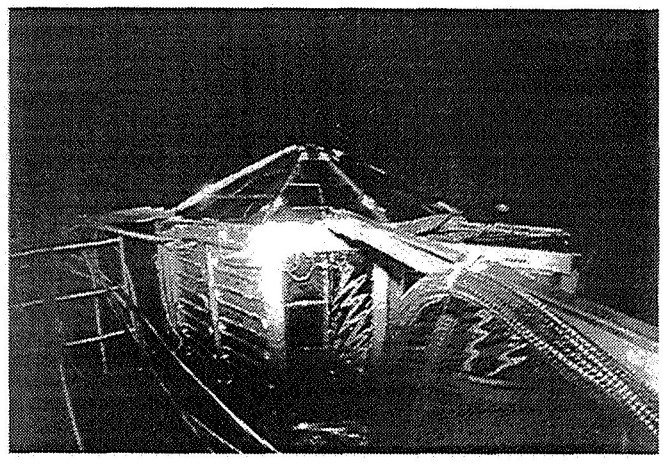


Figure 8a.

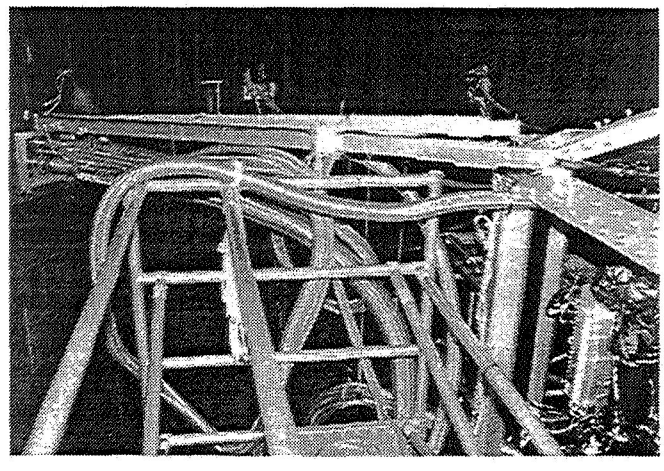


Figure 8b.

Figures 8a and 8b. The SPIRIT III cryogen support lines in the thermal vacuum chamber.

heater installation was underway, scratches were noticed on the cryo line hoses near the point where they penetrated through the cold wall. Clearly, the cold wall had moved with respect to the lines and the chamber wall. Since the lines were supported off the cold wall, movement could impart a bending moment at the wall joint and cause a catastrophic leak. The GSFC test personnel said that the cold wall "floats" inside the chamber and could move as much as 1" vertically and 0.5" radially. Considering this input, the cryo line connections at the cold wall were changed from a hard mount to a more flexible support. Also, the openings in the cold wall through which the cryo lines passed were enlarged. Subsequent pump down and cold wall flooding with LN_2 proceeded uneventfully.

Thermal Test Profile

The thermal vacuum test consisted of four thermal cycles, including both thermal balance and thermal

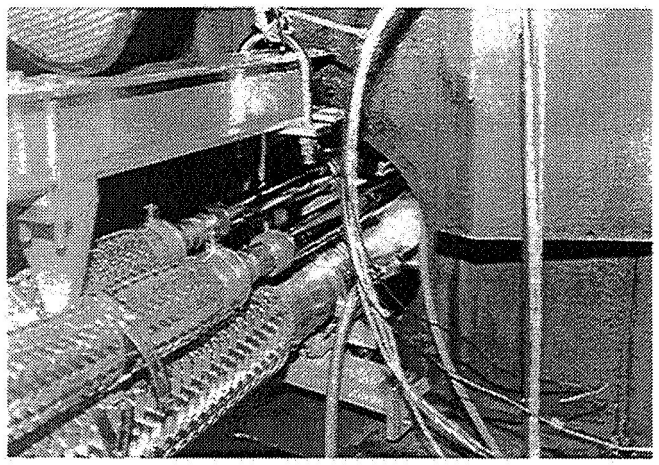


Figure 9a.

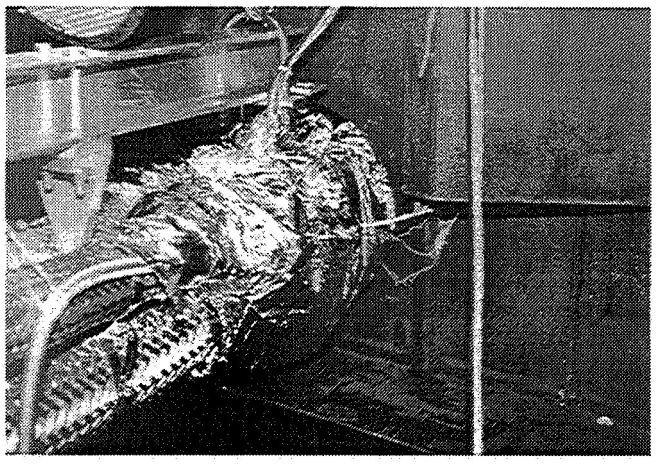


Figure 9b.

Figures 9a and 9b. One of two SPIRIT III cryo line connections at the chamber wall (a) before and (b) after heater, thermocouple, and MLI installation.

cycling cases. The test profile is shown in Figure 10.[3] The test had two goals: to provide verification of the thermal design and modeling effort, and to allow functional testing of the spacecraft at the extremes of its thermal environment.

There were four thermal balance cases: two hot and two cold. The balance points were chosen to span the expected extremes of the mission. The first two cases simulated eclipse operation, and the second two simulated full Sun operation. The cold case of each cycle included beginning-of-life optical properties, minimum environmental inputs, and the low power operating condition (Parked Mode). The hot case includes end-of-life optical properties, maximum environmental inputs, and the high power condition (20% duty cycle Background Mode).

[3] Huebschman, R., *MSX Thermal Vacuum Electrical Test Plan*, 7334-9132, July, 1994.

A goal of the balance testing was to provide information on the operation of the spacecraft thermal design. The thermal design is based on the power dissipated in the satellite and the way that power flows through the structure. To verify the predicted power usage, operational balance cases were designed to simulate actual flight events. The cases included transient simulation of the electricity generated by the solar panels, functioning of the shunt system that dissipated some of the excess power, typical ground contacts, and operation of the attitude control reaction wheels. The flow of power through the spacecraft was verified by comparing the observed temperatures with the analytical predictions. Thermocouple data was monitored for temperature data, and spacecraft telemetry was checked for both temperatures and currents.

The balance cases showed that both the instrument section and the electronics section were operating very close to their analytical predictions. Because of the temperature limitations placed on the dewar, the balance tests provided little information on the proper functioning of that portion of the spacecraft. Thermal control of the thermally isolated SPIRIT III electronics boxes (other than the LRU, which was discussed above), battery, optical bench, beacon antenna, and horizon sensors was demonstrated.

After the balance cases, the remaining two cycles were used for spacecraft functional testing in hot and cold conditions. The test shrouds, coupled with the internally dissipated power, were used to keep the various parts of the spacecraft near their thermal limits. The electronics section upper and lower temperatures were limited by the requirements of the tape recorders (0°C to 35°C head temperature). The instrument section was cycled between -25°C and -5°C. All instruments and spacecraft components demonstrated proper operation at both thermal extremes.

THERMAL HARDWARE PERFORMANCE

Heat Pipes

The instrument section contains a heat pipe network embedded in the honeycomb panels, as discussed above. These heat pipes reject heat through two external radiators (one on each of the Z sides). The use of heat pipes was required to minimize gradients across and between the instrument section panels and maintain the instrument pointing requirements.

The test results show that the heat pipes performed flawlessly and there was an even better spreading of heat

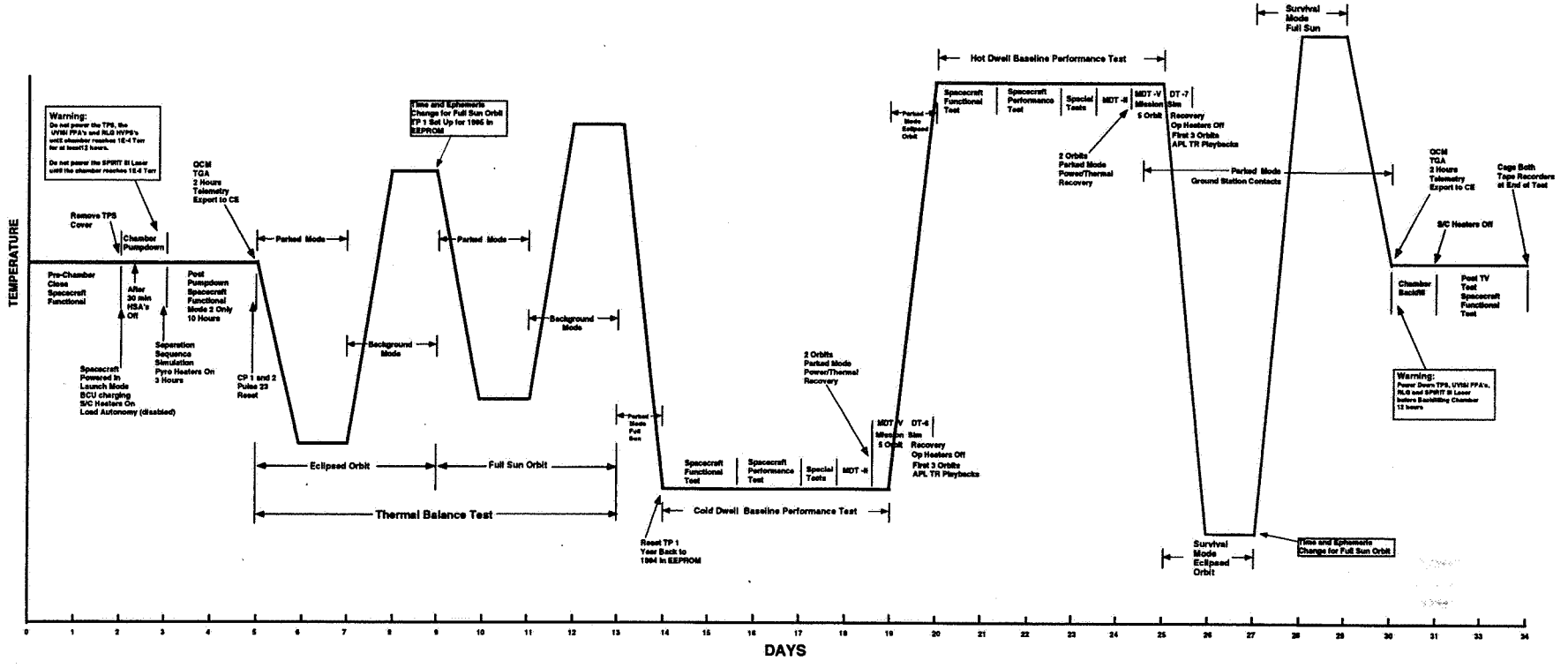


Figure 10. MSX thermal test profile.

through the panels than was predicted in the thermal models. Figures 11a through 11d show the temperature distribution around the instrument section for the thermal balance cases. It can be seen that the requirement of less than a 10°C gradient between panels was easily met. In the fourth thermal balance test case an attempt was made to simulate an orbit where the +Z side of the spacecraft was tilted towards the Sun. For this case a gradient was forced from one radiator to the other. Even in this skewed case, where the radiators were operating at different temperatures, the heat pipes were able to spread the heat and maintain the 10°C maximum gradient.

Temperature Sensors

There are 134 flight temperature telemetry points on the MSX spacecraft. There are two types of temperature sensors used. The first type, an AD590, is used in the majority of locations. The second type, a PT103, is used in regions where the temperature goes outside the normal region of operation of the AD590 (e.g., the solar array panels). The flight temperatures are used to monitor proper operation of the heater system, provide warning to limit operation of critical items outside their proper temperature range, and to provide information about the ability of the spacecraft to perform extended operational events. All flight telemetry is monitored and recorded through the MSX Ground Support Equipment (GSE) system.

In addition to the spacecraft telemetry, 420 test thermocouples were installed before the thermal test to monitor the spacecraft and test hardware temperatures. The thermocouple data was used to control the test environments and to verify spacecraft temperature telemetry points. Thermocouple data was monitored and recorded through the GSFC test data system.

The thermocouple data was compared to the spacecraft telemetry temperatures and was in agreement. There was one telemetry point where a discrepancy existed and it was found to be a problem in the software. The problem was corrected and the proper operation verified.

Heaters and Thermostats

Thermal control of the spacecraft is maintained through the operation of 209 heaters and 119 thermostats. Standard Kapton foil heaters and mechanical thermostats are arranged around the spacecraft into 119 circuits. The heater system is partially, but not fully, redundant. A design approach was taken that allows continued spacecraft operation with some heater failures, but protects critical components. The heater design is broken into two general categories: fully redundant systems, and partially redundant systems. Those items that are thermally isolated from the main body of the spacecraft are protected by fully redundant heater systems. These items include the optical bench and the isolated SPIRIT III electronics boxes. The heaters controlling the spacecraft instrument and electronics sections are partially redundant. They have operational and survival circuits. All of the circuits in these zones are run off a single relay.

Thermostat set points and heater operation were verified for both the operational and survival heaters. All circuits operated as expected. Figure 12 shows a typical temperature profile, confirming the operation of heaters between thermostat set points.

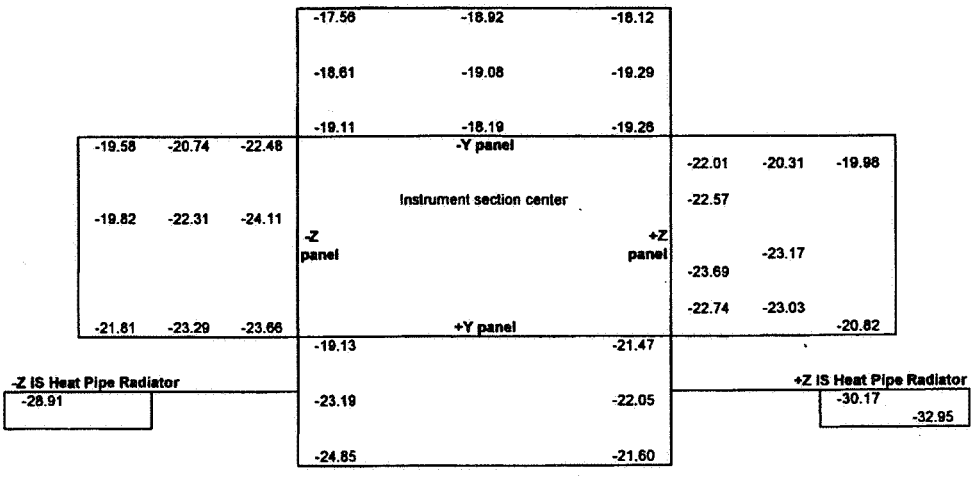


Figure 11a. Thermal Balance 1.

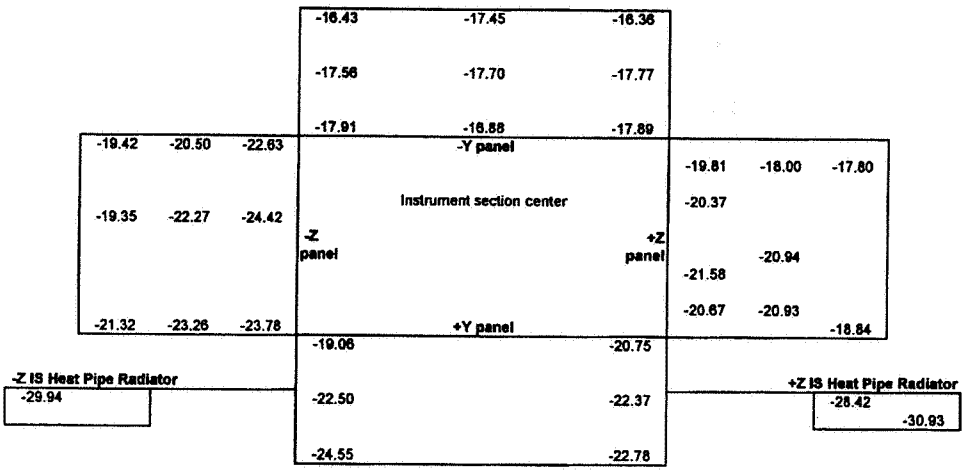


Figure 11b. Thermal Balance 2.

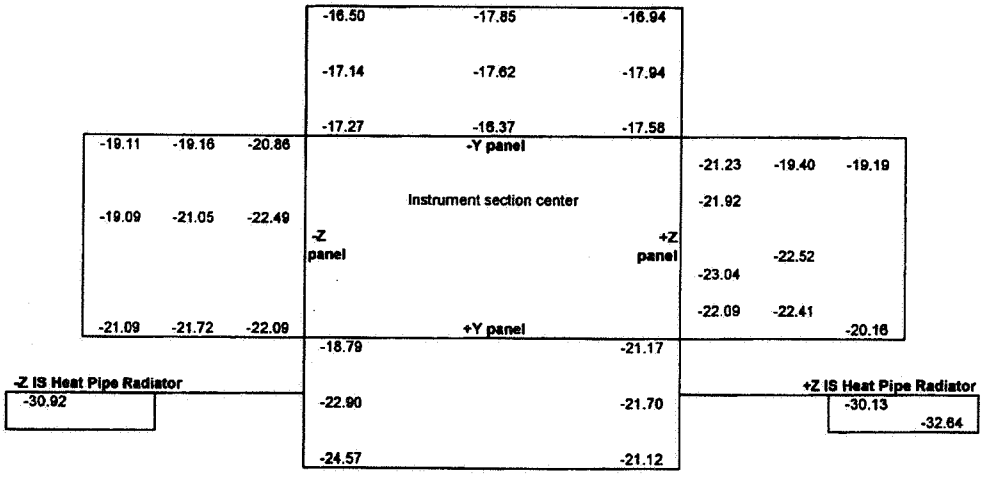


Figure 11c. Thermal Balance 3.

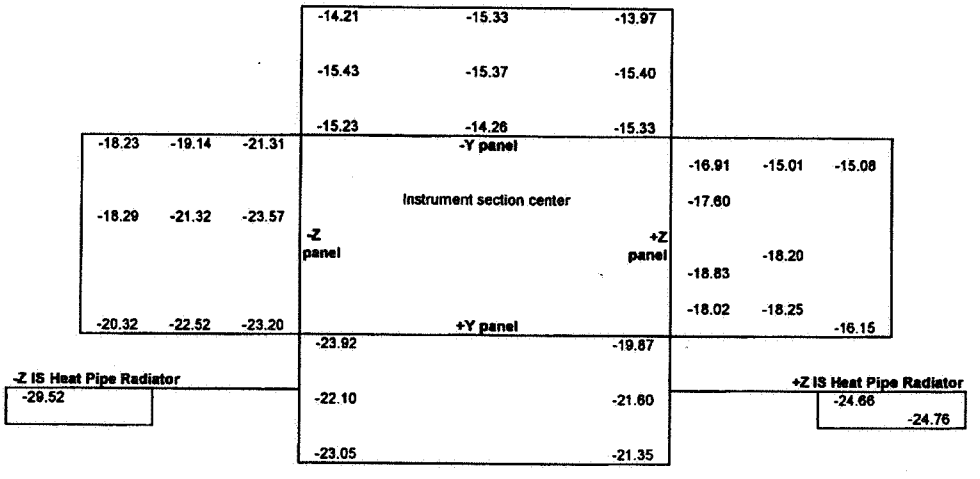


Figure 11d. Thermal Balance 4.

Figures 11a through 11d. The temperature distribution (in °C) across the instrument section showing successful operation of the heat pipes for the four thermal balance cases.

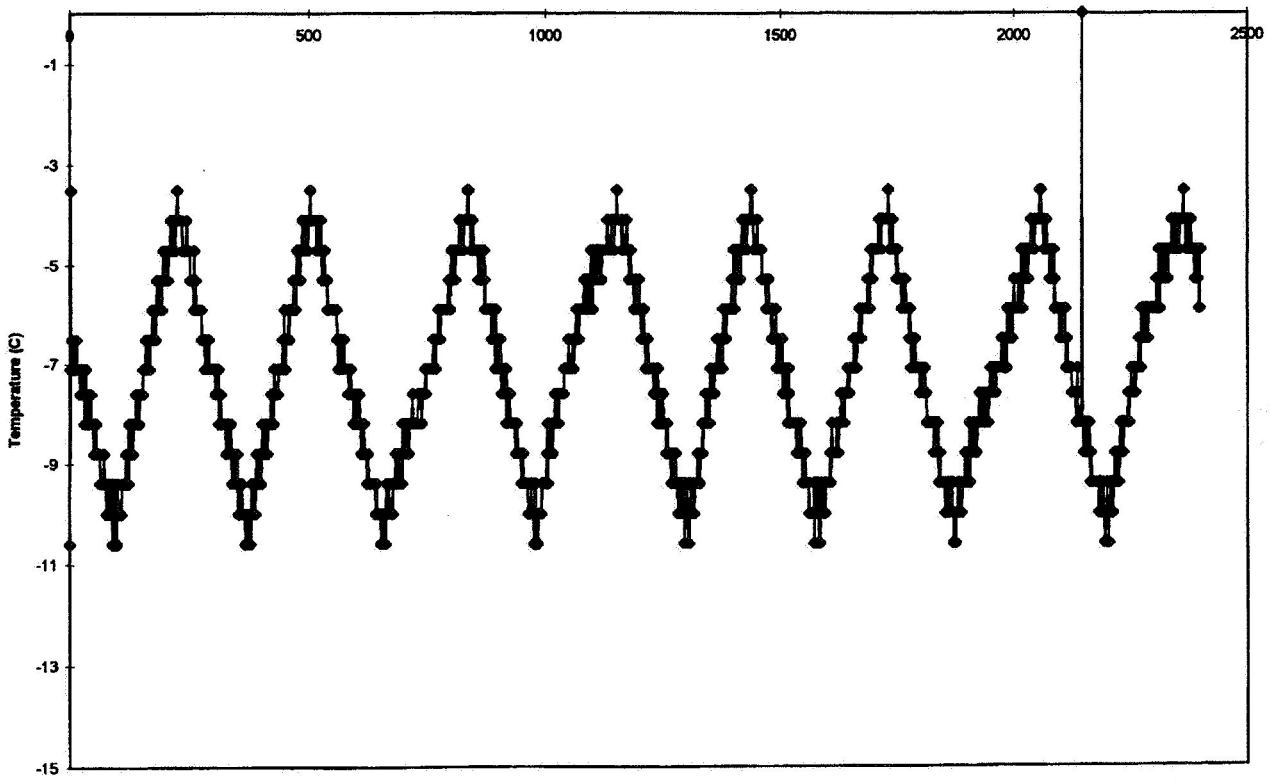


Figure 12. A typical test temperature profile showing proper heater operation between thermostat setpoints.

Thermal Blankets

Most of the external surfaces (except radiator area) of the spacecraft are covered with thermal blankets. Approximately 95 blankets are used that weigh a total of 130 pounds. The blankets serve two purposes: they provide thermal insulation against the space environment, and they serve to route spacecraft outgassing away from the science sensors. The same basic blanket construction is used throughout the spacecraft; however, two different external surfaces are used. For the electronics and truss sections Beta-glass is used as the external surface. For the instrument section Indium Tin Oxide (ITO) coated Aluminized Teflon (AL FEP) is used as the external layer. Figure 13 shows the spacecraft after all blankets were installed, just before transfer to the launch pad.

The radiator surfaces on MSX are ITO coated Silver Teflon (AG FEP) except for SBV which uses OSRs.

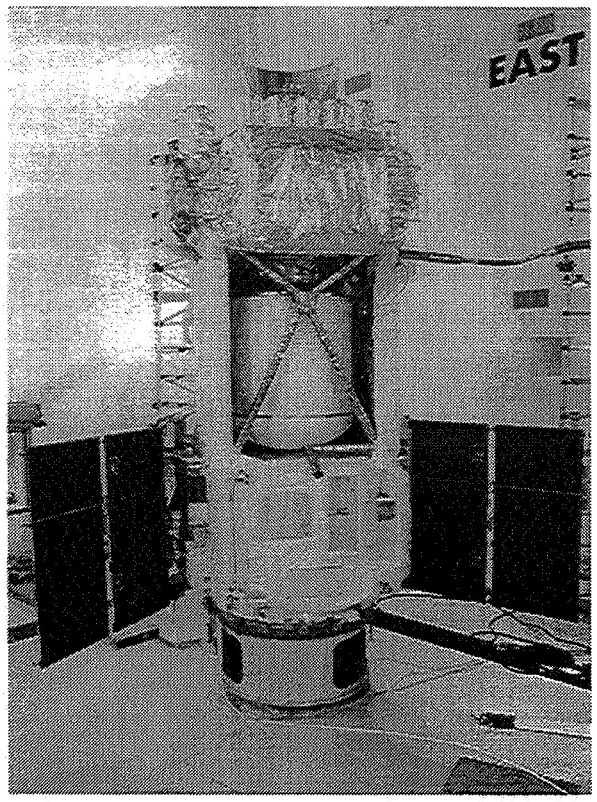


Figure 13. The MSX spacecraft with all thermal blankets installed.

THERMAL MODELING AND CORRELATION

The thermal analysis models used for on-orbit predictions were modified to represent MSX in its testing configuration. These updated models were used to give temperature and heater power predictions for the different test cases. After the test these predictions were

compared to the spacecraft temperature telemetry and the test thermocouple data. Figure 14 gives the correlated temperatures for the balance cases. The instrument section temperatures correlated within 5°C and the electronics section temperatures correlated within 6.5°C. The resulting total power usage of the spacecraft, shown in Figure 15[4], was quite consistent between the cold and hot cases.

CHANGES AS A RESULT OF THE TEST

After completion of the testing and review of the data it was determined that the total spacecraft power was more than anticipated. To help alleviate this problem some of the spacecraft radiator area was optimized and heater power reduced. Each of the instrument section heat pipe radiators (+Z and -Z) was reduced by one square foot (one third of the original area). The electronics section radiator area was also reduced. Individual box radiators on the +Y and -Z sides of the electronics section were reduced by a total of approximately two square feet. This reduction of radiator area lowered the total heater power requirements for the cold case by about 50 W while still maintaining the temperatures within limits for the hot case.

CONCLUSIONS

Despite the complexity of the MSX spacecraft, a thermal test was developed and executed that verified the operation of a majority of its components. Nominal operation of flight hardware was observed and no temperature limits were exceeded. A good correlation of the analysis models was obtained, giving confidence in the thermal design and on-orbit predictions. The thermal vacuum/thermal balance test successfully flight-qualified the MSX spacecraft for normal flight operation.

REFERENCE

1. Krein, J. A. and Mehoke, D. S., *The MSX Thermal Design*, Johns Hopkins APL Technical Digest, Volume 17, Number 1, 1996, pp. 49-58.

[4] *Midcourse Space Experiment Spacecraft Pre-Ship Review*, JHU/APL Internal Document, September 13-14, 1994.

		Predict - TC (degrees C)	Predict - Telem. (degrees C)
Thermal Balance 1			
Electronics Section	+Z	2.8	0.3
	+Y	4.7	6.2
	-Z	2.5	0.2
	-Y	3.4	0.9
Instrument Section		3.9	4.1
Thermal Balance 2			
Electronics Section	+Z	4.2	1.8
	+Y	0.2	0.9
	-Z	1.7	1.0
	-Y	0.6	1.2
Instrument Section		4.3	3.6
Thermal Balance 3			
Electronics Section	+Z	4.6	2.2
	+Y	3.1	4.6
	-Z	3.7	0.8
	-Y	5.1	2.6
Instrument Section		4.3	3.8
Thermal Section 4			
Electronics Section	+Z	4.2	1.8
	+Y	0.2	0.9
	-Z	1.7	1.0
	-Y	0.6	1.2
Instrument Section		4.6	5.0

Figure 14. Results of the MSX model correlation.

	Load	Shunt	Heater	Total
Thermal Balance 1 (Cold 1)	362	50	312	724
Thermal Balance 2 (Hot 1)	545	26	80	651
Thermal Balance 3 (Cold 2)	371	76	307	754
Thermal Balance 4 (Hot 2)	515	59	52	626

Figure 15. Total power usage of the spacecraft for the thermal balance cases.

5/0-18
02145
269392
10P

SOLAR THERMAL VACUUM TESTING OF THE MARS GLOBAL SURVEYOR SPACECRAFT

William N. Breeden III, G. Dean Chambers
Lockheed Martin Astronautics
Denver, Colorado

ABSTRACT

Reflecting NASA's new policy of streamlining the development and deployment of new planetary missions, the Mars Global Surveyor (MGS) Program was on a 28 month timeline from contract award to launch. The challenges faced by the MGS Program and the Space Simulation Laboratory Test Team in coping with compressed lead times to develop testing philosophies, concepts, plans, procedures, procurement and fabrication of tooling and fixtures are discussed in this report. Emphasis was placed on utilization of existing test fixtures and resources to achieve test goals, thereby avoiding costly and lengthy acquisition of special test equipment. Test objectives, concepts, configuration, and conduct will be reviewed. The spacecraft was tested in the 8.8m x 19.8m (29' x 65') solar thermal vacuum chamber at Lockheed Martin's Denver Facility.

The Mars Global Surveyor (MGS) is the first in a new series of spacecraft to explore the Martian environment. The spacecraft will be launched in November 1996, spend ten months in transit, arriving at Mars around September 1997. Four months of aerobraking and thruster operations will place the spacecraft in a nearly circular, two hour polar orbit. Mapping operations will begin in January 1998. The spacecraft will provide high-resolution global maps of the Martian surface, profile the planet's atmosphere, and study the nature of the magnetic field.

INTRODUCTION

"Faster, cheaper, better" satellites require "faster, cheaper, better" space simulation testing techniques. This was the philosophy adopted by the test planning and readiness team that was formed to meet the challenge of testing a satellite that was still in the design stages.

A team comprised of laboratory and MGS program personnel was formed, tasked with developing a test concept which satisfied the stated technical objectives and requirements while adhering to strict cost and schedule constraints. The goal of the team was to perform a high fidelity, "test it like you fly it" space simulation test on a satellite that was to be built and launched in a 28 month span. Historically, a satellite of this complexity has required from 3-5 years to build and test. The team began meeting regularly in January of 1996 allowing only five months to firm up test requirements, develop concepts, develop test designs, procure materials, fabricate fixtures, prepare the facility and setup the test. Three groundrules were essential to successfully accomplish this task:

1. Rely on laboratory experience gained through the recent testing of the Transfer Orbit Stage (TOS), Magellan, and Tethered Satellite.
2. Utilize existing laboratory capabilities
3. Minimize custom built test fixturing

Historically, the laboratory has designed and built custom test fixturing to support the unique requirements of each spacecraft tested. In this case, the design and fabrication time coupled with an average procurement cycle of two months meant that each apparent requirement for fixturing should be carefully scrutinized. Instead, the test was designed around existing capabilities to the extent possible. When custom built fixturing was warranted, the designs were uncomplicated and utilized proven laboratory methods.

Lockheed Martin's Space Simulation Laboratory is well equipped to test interplanetary satellites. The following paragraphs highlight the laboratory's standard capabilities that were available to the team.

Large Thermal Vacuum Chamber: The 8.8m dia x 19.8m high (29'x65') top loading chamber is cylindrical in shape. It is a high vacuum, chamber capable of being evacuated to a pressure of 1x10-5 torr or less. It has a work space of 7.9m x 12.2m (26'x46') The chamber is equipped with a thermal shroud which can be flooded with LN2 or controlled with GN2 between-155°C and 38°C (-250°F and 100°F).

4.8m dia(16') Solar Simulator: The 16 foot Solar Simulator system is part of the 8.8m dia x 19.8m high (29'x65') thermal vacuum chamber. The system is capable of producing a cylindrical test volume 4.8m (16') diameter and 4.8m (16') high with high fidelity and variable intensity. It is an off-axis, collimated beam system capable of .35 to 1.4 solar constants, with beam uniformity of +/- 5%. The beam is spectrally filtered for close air mass zero solar spectral match.

Two Axis Gimbal: The Gimbal is a stainless steel support structure that is 3.8m (12' 6") high and has a support beam 6.4m (21') long. The position of a test article mounted to the gimbal turntable can be controlled in two axes. The beam can tilt ± 90° off vertical at varying speeds from .018 RPM to 3 RPM. The turntable can rotate 360° at varying speeds from .018 RPM to 3 RPM both forward and reverse. The structure is capable of supporting a dynamic load of 2268 kg (5000 lbs) and has a maximum moment capability of 2268 kg (5000 lbs) at 1.2m (4') = 2716 nm (20,000 ft-lb). The gimbal system is computer driven to provide programmable control to both axes.

94 Channel Power Control System: This system provides power for auxiliary test heaters used to drive the hardware to temperature, or protect hardware which cannot tolerate the temperature extremes of the chamber. The system provides thirty channels rated for 20kW, 16 channels rated for 4.5kW, and 48 channels rated for 1kW. Two computers are utilized in the system. One, serves as a host computer for the seven temperature controllers, the other controls the overtemperature kill system.

TEST OBJECTIVES

The objectives of the Mars Global Surveyor Thermal Vacuum/Thermal Balance (MGS TV/TB) test were as follow:

1. Provide data for the validation of the thermal math models
2. Verify thermal subsystem performance
3. Demonstrate integrated spacecraft performance at cold and hot temperature levels
4. Provide for instrument systems calibration at vacuum conditions to the extent possible

In addition, the vacuum environment provided an opportunity to perform a vacuum dryout of the propulsion system that had been loaded with isopropyl alcohol for dynamics testing. Evacuating the propulsion system at atmospheric pressure is not possible without collapsing the tanks; therefore, the laboratory was tasked to develop a method for evacuating the tanks while the spacecraft was under vacuum.

Protecting the spacecraft from contamination drove additional requirements. All test cabling, tooling, MLI blankets, etc. were vacuum baked prior to being used in the system level test. Also, a GN2 purge to the instruments was required throughout the roughing stage of pumpdown.

The following aspects of the mission environment were to be simulated in order to produce "flight like" conditions:

1. High vacuum, 1x10-5 torr or less; 1x10-6 torr desired for instrument operation
2. Solar simulation from 0.35 solar constants to 1.0 solar constants
3. Proper spacecraft attitude with respect to the solar beam
4. Planetary albedo and planetary IR emission
5. Deep space cold sink
6. Test heaters to simulate heat loads not present in the test configuration and to nullify heat leaks

TEST CONCEPTS

In the process of developing a final test concept, a number of ideas were considered for each individual aspect of the test. The technical value of each of these concepts was weighed against cost and schedule. As a result, numerous changes were made to the overall test concept during the first several weeks. The remaining paragraphs will summarize the iterative process that lead to the final test concept.

In order to meet both the thermal and instrument objectives, it was initially thought that a two phased test approach with a chamber break between phase 1 and phase 2 was necessary. The concept was to operate the instruments in phase 1 and to perform the thermal balance of the spacecraft in phase 2. This was thought to be necessary because the original configuration of instrument targets required the spacecraft to be oriented vertically with targets overhead, while the thermal balance configuration required the spacecraft to be oriented horizontally, with no obstructions above the instruments. Since the solar simulator was not required for the instrument checkout, phase 1 was to be performed with the chamber in its "short stack" configuration, that is, without the spool piece installed. This configuration would have the potential for a higher level of vacuum that was desired for instrument operation . This concept was rejected due to schedule and cost constraints. In order to operate horizontally, some instrument targets were redesigned; others were eliminated. In one case, the chamber shroud and planet simulator became the target for an instrument.

To achieve the proper spacecraft orientation, both the laboratory's two axis gimbal and a custom built support stand were considered. The requirements of the support stand were as follows:

1. Full solar beam coverage of the spacecraft
2. Minimize the thermal effects of the stand
3. Adequate personnel access to the spacecraft
4. Variable orientation was desired

Initially, the two axis gimbal did not appear to be the best solution. The standard support base for the gimbal did not provide full solar beam coverage of the spacecraft, the thermal effects of its massive structure were significant, and access to the spacecraft once it was installed was extremely difficult. It did, however, provide the variable orientation capability that was desired. A custom built stand could be designed to allow for easier access and provide minimal thermal effects and full solar coverage; although, providing variable orientation capability was not feasible. Nevertheless, the two axis gimbal provided one overwhelming advantage, it was available. Once again, cost and schedule were the deciding factors. Rather than take on the large task of designing and building a support stand, the team opted to design and build fixturing to enable use of the two axis gimbal. In order to achieve full solar beam coverage of the spacecraft in a horizontal orientation, it was necessary to shift the gimbal to one side of the chamber. After some research, it was discovered that the gimbal offset used for the Magellan thermal vacuum test was available and would solve this problem. Minimizing the thermal effects of the two axis gimbal required fabricating three LN2 cooled plates. Two plates, the gimbal cryo shields, would be placed on either side of the turntable. A third plate, the aft cooling plate, would be placed inside the gimbal interface fixture which attached the spacecraft to the gimbal. Together, these plates would have the effect of simulating deep space on the aft end of the spacecraft, which is a nominal flight condition. The remainder of the gimbal structure was covered with multi-layer insulation.

Once installed on the gimbal, the base of the spacecraft would be over 4m off the floor making personnel access difficult. In place of custom built access platforms, the team determined that off-the-shelf scaffolding could be purchased and adapted to the setup. Since the gimbal provided the desired variable spacecraft orientation capability, the problem of cable management during rotation had to be considered. In an attempt to simplify this potentially complex task, the test cases were selected and ordered to fall within a single 180° rotation. The cable management concept was reduced to strategically placed guides that would allow the cabling to be routed prior to pumpdown and then allowed to unwrap as the gimbal was rotated under test. It is worth noting that the gimbal to spacecraft interface tool further demonstrated the laboratory's efficient use of fixturing. The tool was designed to be dual purpose, used not only to adapt the spacecraft to the gimbal but also to the spin balance table used for mass properties testing.

Two approaches to simulating the Mars planetary albedo and planetary IR emission were considered. The initial concept was to duplicate the configuration used for the Magellan thermal vacuum test. That simulator was fabricated using panels from another existing laboratory test tool, the Thermal Environment Simulator (TES). Eighteen of the 1.8m x1.8m panels were mounted in a custom built frame for the Magellan test. Each panel is comprised of eight heated louvers which can be opened to allow the spacecraft to view the LN2 cooled chamber shroud. The Magellan fixture, however, was not available, and the cost of duplicating it was substantial. In addition, modeling the TES louvers was complicated. As a result, it was decided that the best solution was to utilize the laboratory's extensive experience in the design and build of thermal plates and build a 3.1mx3.1m heated panel capable of being cooled to LN2 temperature.

Spacecraft undertemperature protection was given a great deal of consideration due to the test concept. The chamber walls were to be flooded with LN2 throughout the test, and the primary source of heat was the solar simulator. Although the laboratory is equipped with an emergency generator, supplying the solar simulator via the generator is not feasible. Therefore, auxiliary heat sources would be required to safe the spacecraft in the event of a power failure. An IR cage was considered but was rejected due to cost and schedule. The final concept utilized Kapton film heaters applied directly to the spacecraft side of the MLI blankets. The heaters were sized for a radiation only environment to ensure they would not fail.

Additional test heaters were identified for a number of purposes including the nullifying of heat losses through cabling, maintaining test hardware above minimum limits, and simulating heat loads that were not present in the test configuration of the spacecraft.

The first concept of the vacuum dryout of the propulsion system utilized the large chamber's roughing system. It was determined that this system could not achieve the desired level of vacuum. A pumping system used for rough pumping two of the laboratory's 1.2m x 2.4m (4'x8') chambers was available. This system, consisting of a roughing pump, blower, and cold trap, was utilized in place of the large chamber system. A fail-safe pressurization system was designed utilizing existing gages and equipment wherever possible. This fail-safe system monitored chamber pressure with redundant gages, and in the event of a loss of vacuum, would automatically repressurize the propulsion system.

TEST CONFIGURATION

The gimbal offset used for Magellan was installed into the chamber. The two axis gimbal was placed on the offset. The gimbal cryo shields were installed on either side of the gimbal turntable. The gimbal interface was installed on the two axis gimbal's turntable. The aft cooling plate was installed inside the gimbal interface. The scaffolding was erected. The planet simulator was positioned in front of the gimbal. The test configuration prior to spacecraft installation is depicted in figure 1.

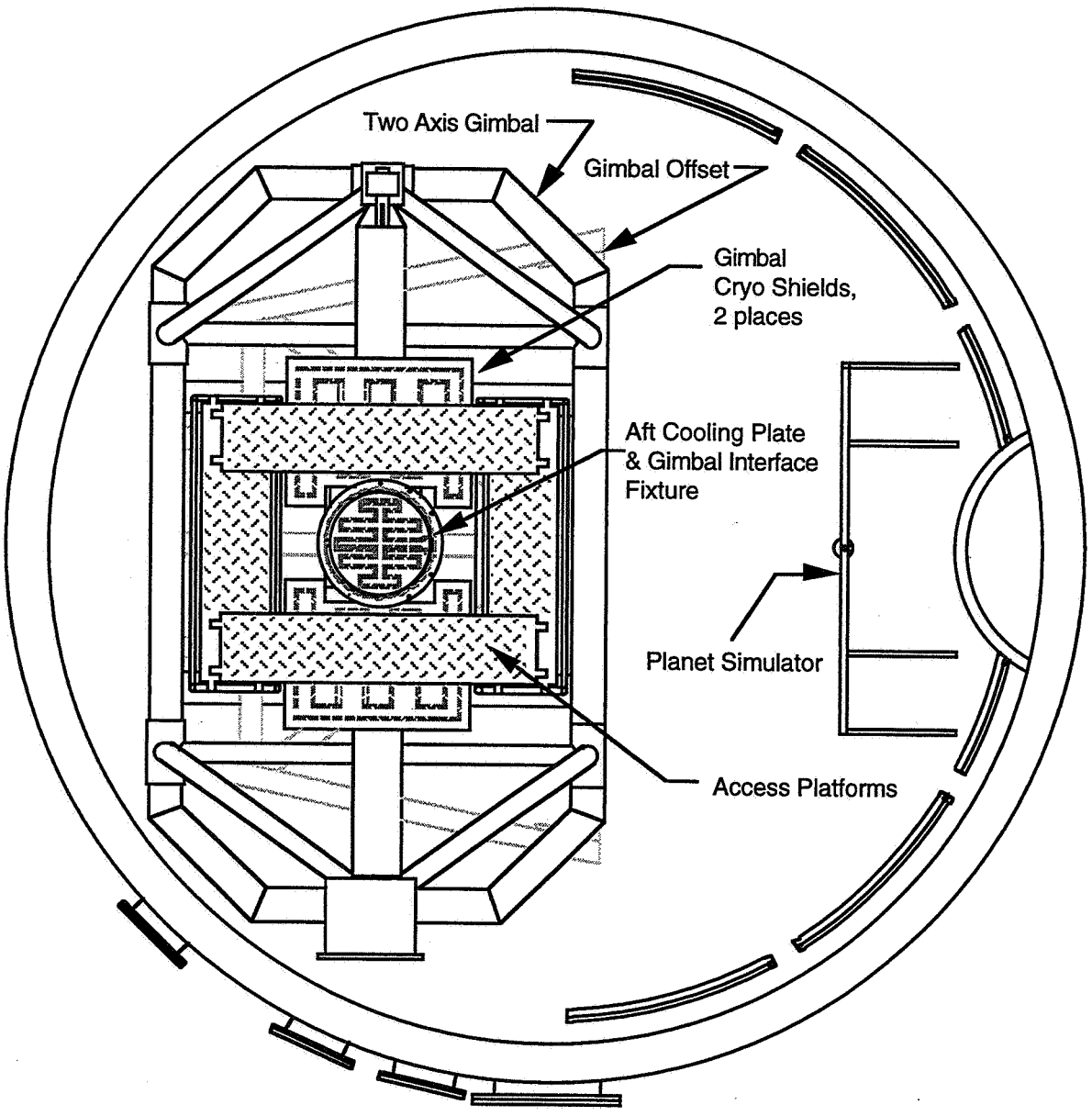


Figure 1 - Top View Prior to Spacecraft Installation

Once the spacecraft was installed, the unit was rotated to a horizontal position, see figures 2 and 3. With the spacecraft horizontal, the aft cooling plate, gimbal cryo shields, and planet simulator were connected to separate LN2 supplies. The vacuum dryout system was connected to the propulsion system. Test and instrumentation cabling was mated and routed through the guides of the cable management system. A Temperature-controlled Quartz Crystal Microbalance (TQCM) was installed as well as Non-Volatile Residue (NVR) plates. The chamber is equipped with a Residual Gas Analyzer (RGA).

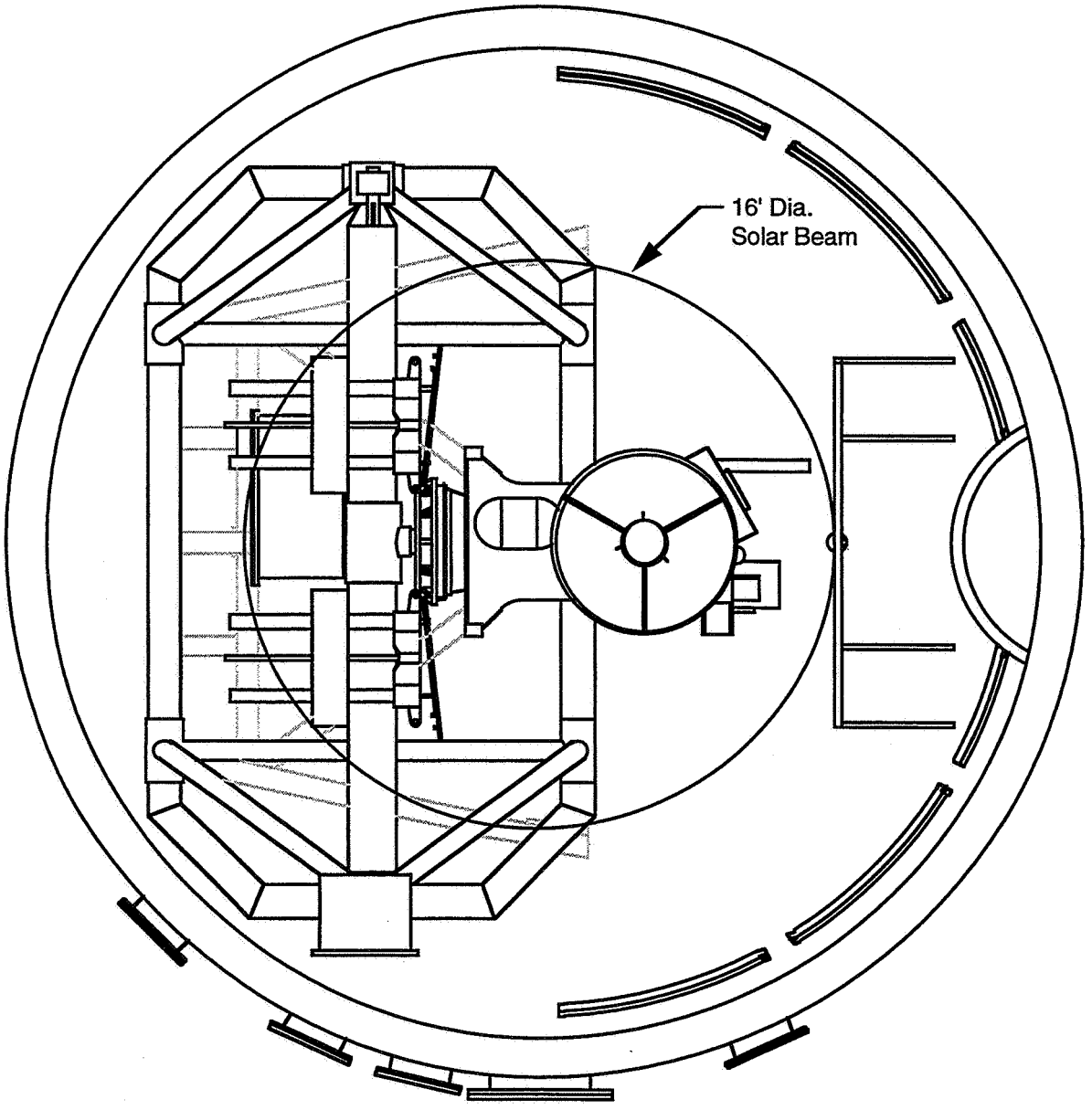


Figure 2 - Top View, Spacecraft Installed, Gimbal Rotated 90°, Turntable at 0°

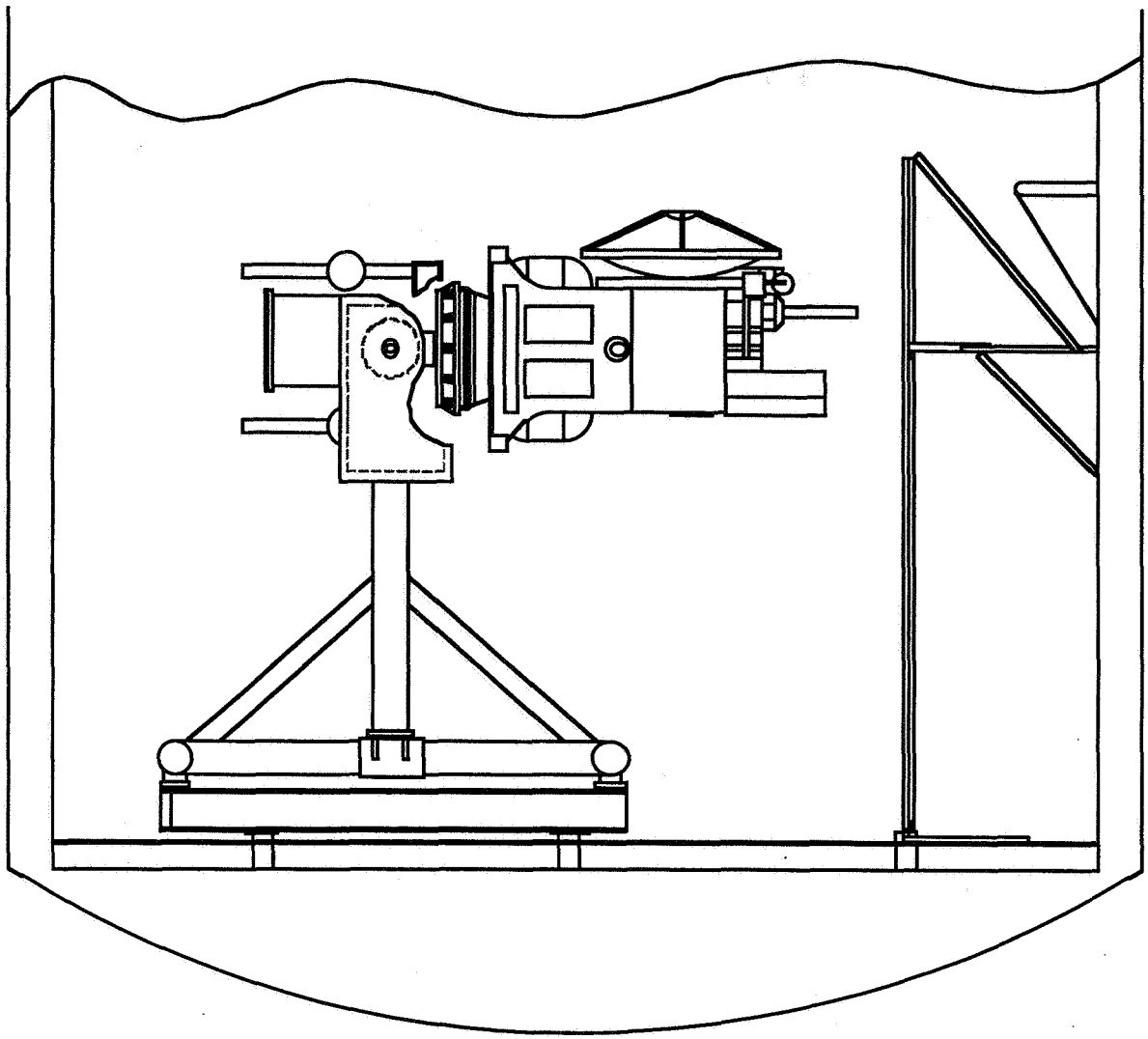


Figure 3 - Side View, Spacecraft Installed, Gimbal Rotated 90°, Turntable at 0°

The test heaters utilized 57 of the 94 independently controlled heater channels available on the laboratory's system. The table below summarizes the categories of test heaters and explains their function.

Test Heater Category	Function
Thermocouple Cable Guard Heaters	Prevent heat leaks via thermocouple cabling.
RF Cable Heaters	Maintain RF cable at constant temperature.
Electrical Cable Guard Heaters	Prevent heat leaks via electrical test cabling.
Tank Purge Line Heaters	Prevent alcohol vapor from freezing and maintain purge line flexibility during spacecraft rotation.
MLI Blanket Heaters	Serve as radiant heat sources in emergency.
Quad Coupler	Simulate heat load.
Remote Power Switch Box	Maintain RPS box above minimum allowable temperature.
V-Band Heaters	Maintain V-Band temperature above minimum allowable.
Gimbal Interface Heaters	Limit heat loss to the gimbal.
Planet Simulator Heaters	Simulate Mars hot and Mars cold conditions.
Battery Heaters	Serve as heat sources in emergency.
Antenna Strut Heaters	Serve as heat sources in emergency.

The spacecraft was instrumented with approximately 450 thermocouples. These thermocouples performed monitor, feedback control and overtemperture kill functions. All thermocouple data was available nearly real-time to the program's thermal engineering staff.

TEST CONDUCT

The test consisted of a single pumpdown to $\leq$ 1x10-5 torr. To ensure instrument cleanliness during pumpdown, a GN2 purge was maintained to the instruments until the chamber pressure reached 10 torr. Once the chamber was in high vacuum, the propulsion system was evacuated using the vacuum dryout system. The solar simulator, shroud temperature control system (STC) and 94 channel power control system were then brought on-line. The chamber shroud was ramped to -150°C using the STC and then flooded with LN2. The shroud remained at LN2 temperature throughout the remainder of the test.

A total of six test cases were performed. Each case varied with respect to solar intensity, spacecraft orientation, spacecraft power mode and planet simulator temperature. Orbits were simulated by simply opening and closing the solar simulator's douser. The following table summarizes the six cases.

			Solar Intensity (solar constants)				
Case	Intent	S/C Position	Steady State	Transient Day (Open Douser)	Transient Night (Close Douser)	Planet Sim. Temp	S/C Power Mode
1	Illuminate/Verify -X EM & +Y Battery Radiators - Verify Heaters	-110°	0.50	—	—	-59°C Mars Hot	Map Aver
2	Simulate Perihelion Mapping @ worst case Hot - Verify Batt ΔT Control	-65°	0.60	0.90	0.00	-59°C Mars Hot	Map Aver
3	Simulate Aphelion Map @ worst Case Cold (with / without ΔT heaters) - Verify Batt ΔT cntrl, Verify Heaters	-65°	0.00 / 0.35	0.50	0.00	-73°C Mars Cold	Map Aver
4	Simulate worst case Cruise Cold, verify heaters, prop ΔT control - Illuminate PSA radiators	0°	0.35	—	—	LN2 Deep Space	Cruise
5	Gather thermal balance data (sun change only) - illuminate/verify PSA radiators	0°	1.00	—	—	LN2 Deep Space	Cruise
6	Illuminate/Verify TWTA, -Y battery & IMU radiators	70°	0.50	—	—	LN2 Deep Space	Cruise

Chamber pumpdown was initiated on June 22, 1996, at 2150. Case 1 began at 0300 on June 24. Case 6 was completed on July 5 at 1840. Figure 4 graphically represents the actual test timeline.

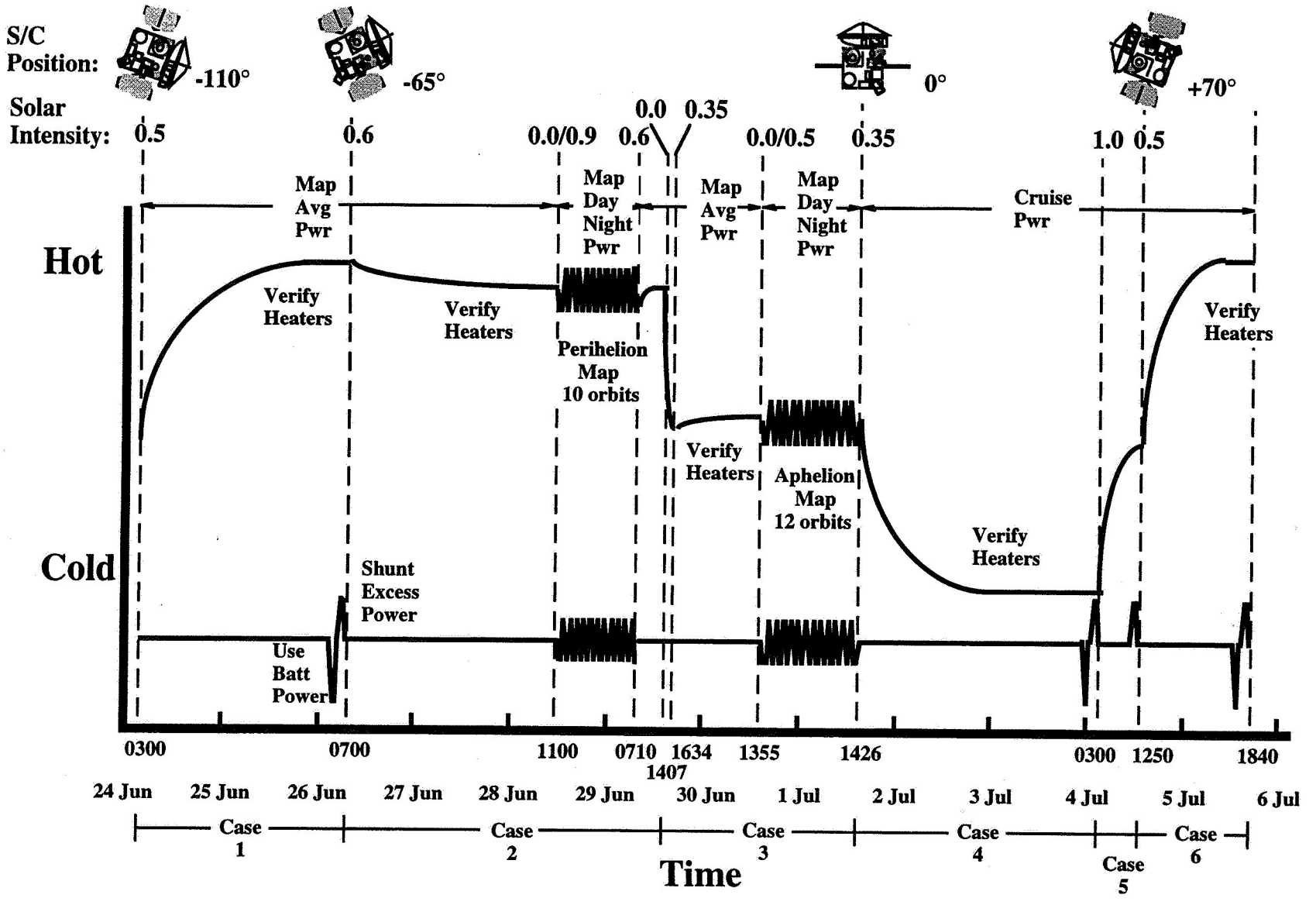


Figure 4 - Actual Test Timeline

CONCLUSIONS

The Mars Global Surveyor Thermal Vacuum/Thermal Balance test was completed on schedule and within budget. By relying on the experience of program and laboratory personnel, utilizing existing laboratory capabilities, and minimizing custom built test fixturing, the team proved that a high fidelity, flight-like, solar thermal vacuum test is possible in a "faster, cheaper, better" environment.

In order to meet the demands of future testing in this type of environment, three things are imperative. Test facilities must have a wide range of standard capabilities. Where these capabilities are lacking, facilities must begin systematically acquiring them in concert with strategic planning goals. Additionally, test facilities must have ready access to supplies of raw materials and consumables in order to reduce procurement lead times. Finally, experienced facility and program personnel are essential to the success of these efforts. There must be continuity from program to program. Critical skilled personnel should move from one program to the next, bringing the experience and heritage required to enhance the process and ensure Mission Success.

REFERENCES

1. Neuman, James C.: Solar Thermal Vacuum Tests of the Magellan Spacecraft, Proceedings of the 16th Space Simulation Conference, NASA Conference Publication 3096, 1990, pp.1-15

511-18
051443
269376
128

NEAR SPACECRAFT THERMAL VACUUM TESTING

Carl J. Ercol
The Johns Hopkins University Applied Physics Laboratory

Stephen J. Krein
Orbital Sciences Corporation

ABSTRACT

The Near Earth Asteroid Rendezvous (NEAR) mission was the first launch in the Discovery program, a NASA initiative for small-scale, low cost, and quick turnaround planetary missions. The NEAR mission successfully commenced with the February 17, 1996, launch from Cape Canaveral, Florida. Following ejection from the 7925 Delta II launch vehicle, the NEAR spacecraft entered a deep space transit trajectory for nearly three years of semi-dormant cruise mode that will culminate with the scheduled February 1999 rendezvous with the near-Earth asteroid 433 Eros. After an initial close pass at 433 Eros, the NEAR spacecraft orbital operations will allow the first systematic scientific exploration of an asteroid. In order to accomplish this task, the spacecraft contains a suite of sensors that operate in a complementary fashion to measure the bulk, surface, and internal properties of 433 Eros. The structure supporting these sensors is part of a 3-axis stabilized, solar-oriented spacecraft that employs fixed co-planar solar arrays to provide a constant voltage, regulated power bus. The NEAR propulsion system incorporates the unique thermal design of a single 450 N bipropellant thruster embedded in the spacecraft, accompanied by four external 22.5 N and seven external 4.5 N monopropellant thrusters.

In order to provide a comprehensive verification of the NEAR spacecraft thermal design and system operational functionality while meeting the stringent project constraints, a creative and cost-effective testing approach was taken. NEAR spacecraft thermal vacuum testing took place at the NASA Goddard Space Flight Center between October 31, 1995, and November 20, 1995. The actual test profile consisted of three hot and three cold balance cases with four hot and cold full system functional tests. Simulation of the space environment was accomplished in a vacuum chamber using a combination of IR heater shrouds, body-mounted test flux heaters, and the liquid nitrogen flooded chamber cold wall. Electronics and instruments were operated at power levels expected during the different mission scenarios for both functional and balance testing.

The overall test results were excellent indicating that all spacecraft flight hardware performed nominally with all thermal requirements met. Pre-test thermal model predictions compared favorably with thermal balance simulation temperature data, therefore post-test thermal model correlation efforts were minimal. The test results showed a cold biased design which allowed for selected radiator areas to be reduced.

This paper describes the test thermal objectives, configuration, results, TMM correlation, and also the relevant conclusions and corresponding lessons learned that were derived from both the thermal balance and functional testing.

INTRODUCTION

The NEAR spacecraft (see Figure 1), designed and built by The Johns Hopkins University Applied Physics Laboratory for NASA, was launched on February 17, 1996, aboard a 7925 Delta II vehicle. As the first mission in the Discovery Program, NEAR will serve as an early indicator of the success or failure of the Discovery Program approach to scientific missions. The Discovery Programs are small planetary missions that have very specific programmatic guidelines which limit both development costs and time while constraining the spacecraft size and weight to ensure compatibility with a launch vehicle of capability no greater than Delta II. In addition to these imposed constraints, the Discovery Program dictates a specific set of technical goals for each spacecraft which define the purpose of the mission. The purpose of the NEAR mission is to conduct the first detailed, systematic exploration of an asteroid.

The thermal design challenge posed by the NEAR spacecraft stemmed from its externally mounted sensors and widely varying mission environments. The mission thermal environment varies as a function of both spacecraft attitude and solar distance. During the extended cruise mode, the solar distance varies considerably which induces sizable fluctuations in the solar heating inputs to the spacecraft. In addition, the spacecraft attitude will deviate from the default solar-normal orientation provided that the attitude is maintained

within the boundaries required to enable communication with the earth-based ground station. Further compounding the design complexity is the wide variation in internal spacecraft power dissipations that are expected throughout the mission. The internal power dissipation is directly linked to the overall system objectives at any given mission phase, thus the thermal load can vary from minimal housekeeping power during the semi-dormant cruise mode to maximum power during science data acquisition at the asteroid.

SPACECRAFT OVERVIEW

Simplicity and low cost were the main drivers in developing the NEAR spacecraft design. Simplicity was achieved by requiring that the three major components, the instruments, solar panels, and high-gain antenna, would be fixed and body mounted. Although this requirement will increase the complexity of the spacecraft operations to some extent, it was an important factor in overall cost containment. The spacecraft in the deployed flight configuration is shown in Figure 1. The primary structure is composed of two aluminum honeycomb decks connected by eight aluminum honeycomb side panels. The instrument payload consists of a Magnetometer, IR Spectrograph, Multispectral Imager/Spectrometer, X-Ray/Gamma-Ray Spectrometer and Laser Rangefinder which are mounted to the outsides of the aft and forward decks. The magnetometer is co-located with the high gain antenna feed on the forward side of the spacecraft. The aft deck mounted instruments point in a common direction, diagonally opposite the 450 N thruster.

Also mounted on the forward and aft decks are the spacecraft and instrument electronics. With the exception of pre-existing electronic boxes, all electronics were packaged using magnesium alloy chassis to minimize weight. The propulsion module which consists of three fuel, two oxidizer, and one pressurant tank as well as all propellant and pressure regulation hardware is located inside the spacecraft and occupies most of the internal volume. The fixed antenna and solar array configuration dictated that the 450 N thruster be buried inside the spacecraft adding to the thermal design challenge. There are also eleven mono-propellant thrusters grouped into six different pods externally mounted to the spacecraft.

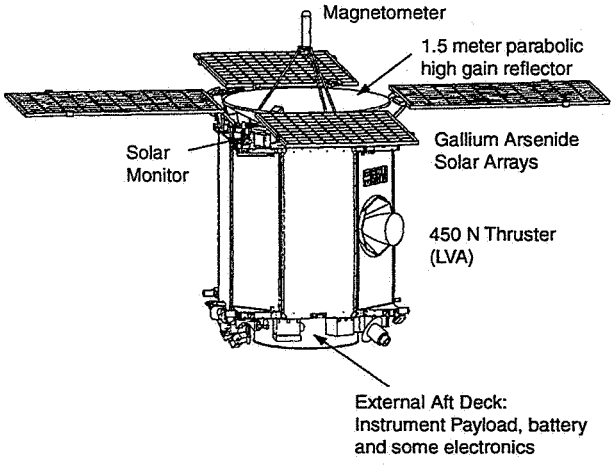


Figure 1. NEAR Spacecraft.

MISSION ENVIRONMENTS

The two primary factors affecting the thermal design are spacecraft attitude and solar distance. The spacecraft attitude is dictated by the mission communication and navigation requirements which define the mission trajectory and optimal geometry. An important attribute of the selected mission geometry is that the Sun-spacecraft-Earth angle is always less than 40 degrees, except for the first two months after the launch and the first two months after Earth flyby. The constrained sun angle pointing limits solar illumination of the aft deck instruments and thus reduces the variations in their thermal environment which simplifies the instrument design process. Because the instruments are fixed, instrument pointing must be achieved by rotating the spacecraft around the axis of the high gain antenna while the spacecraft orbits the asteroid in a plane that is normal to the asteroid-earth line. The solar loading on the spacecraft can therefore be defined in terms of a cone angle (theta) defined from the sun line to the spacecraft +Z axis (see Figure 2), and a clock angle (phi) which defines the side panel illumination area as the sun walks around the spacecraft +Z axis. As shown in Figure 2, theta can vary from 0-45° during cruise mode, and from 0-30° at the asteroid. Phi can vary from 0-360° provided that theta is greater than 0°. The intensity of the solar loading varies as a function of the spacecraft distance from the Sun as depicted in Figure 3.

The mission trajectory brings the spacecraft within close proximity to the Earth during two separate periods. The first is immediately following the launch during the ascent and transfer phase. The primary heat inputs to the spacecraft during this phase are from free molecular heating following fairing jettison, and from heat soakback from the booster third stage engine dome. The relatively brief exposure to environmental inputs from the Earth ensures that the resulting heat inputs are negligible. The second period of Earth exposure occurs during the Earth swingby nearly 2 years after launch. During the Earth swingby, the NEAR spacecraft will experience transient heating effects from the Earth's albedo and emitted infrared radiation.

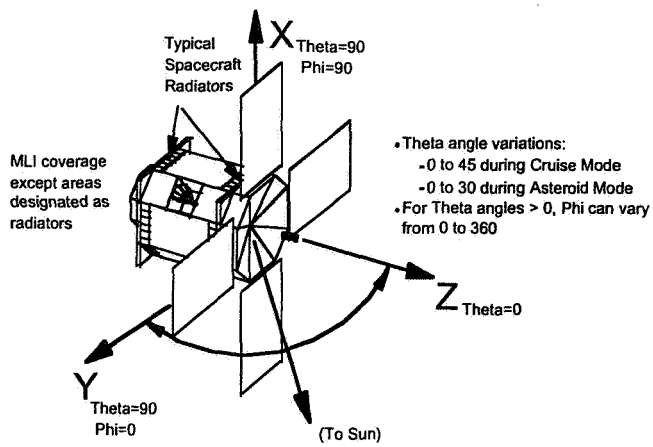


Figure 2. Spacecraft Coordinate Configuration.

THERMAL DESIGN SUMMARY

The spacecraft and instruments thermal design was simple and robust using a passive philosophy of selectively placed radiators, MLI, and optical coatings. Thermostatically controlled heater power was allocated with great discretion due to very limited power at mission aphelion (2.2 AU). Temperature critical components such as the propulsion subsystem, battery, and instruments were thermally isolated from the spacecraft structure to minimize total heater power and allow temperature control within a tighter range. All antennas were also conductively isolated to reduce heater power demand.

The main spacecraft radiators are located on the side panels below the plane of the solar panels. During nominal spacecraft operation the radiators are shadowed from direct solar flux but receive IR backloading from the solar panels. The inside of the spacecraft as well as all electronics are coated with high emittance black paint and are radiatively coupled to the side panel radiator surfaces. The side panel face sheets are so thin (0.127 mm per face) that radiative heat flow dominates while heat flow via conduction is a second order effect.

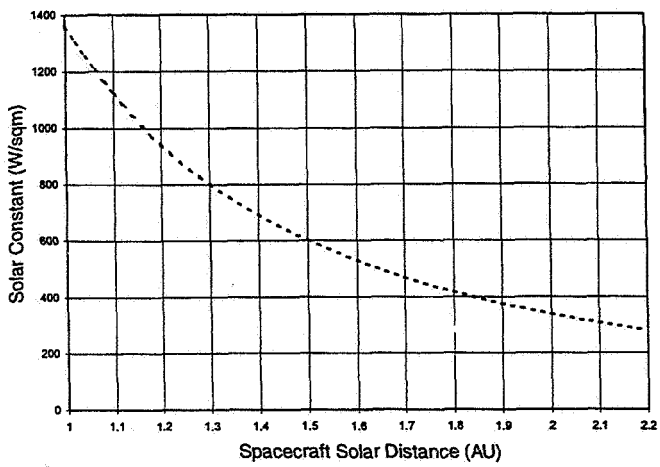


Figure 3. Solar Constant Variation.

THERMAL VACUUM TESTING

The NEAR thermal vacuum test was performed at Goddard Space Flight Center between October 31, 1995, and November 20, 1995, in the Space Environmental Simulation (SES) chamber 290. Figure 4[1] depicts the as-run spacecraft thermal balance and functional testing profile. The test flow interspersed thermal balance conditions and thermal performance testing in order to minimize time delays due to temperature transition times and also to accommodate the availability of the JPL DSN trailer, which is GSE that simulates the DSN communications. The planned profile was modified to accommodate two extra balance tests and some extended functional test time. The testing simulated flight environments with all electronics and instruments powered at the levels expected during selected worst-case mission scenarios.

The testing sequence was carefully planned in order to include the requisite number of thermal balance cases for design verification while still allowing sufficient time for extensive spacecraft system functional testing. The pre-test planning focused on determining the most efficient means of satisfying all of the test objectives while remaining within the dictated program cost and schedule constraints. The thermal test objectives included:

(1) Verify the adequacy of the NEAR thermal design;

(2) Verify the NEAR analytical Thermal Math Model (TMM);

(3) Verify the proper operation of all flight heater/thermostat circuits;

(4) Verify spacecraft system functionality at the hot and cold temperature plateaus;

(5) Verify the accuracy of flight telemetry.

TEST PHILOSOPHY AND CONDITIONS

Simulation of expected space environments was accomplished in a vacuum chamber using test heaters, IR heater shrouds, the LN_2 flooded chamber cold wall,

[1] Ercol, C. J. and Krein, S. J., "NEAR Spacecraft Thermal Vacuum Test Plan, Rev A," October 20, 1995, APL Specification Number 7352-9042.

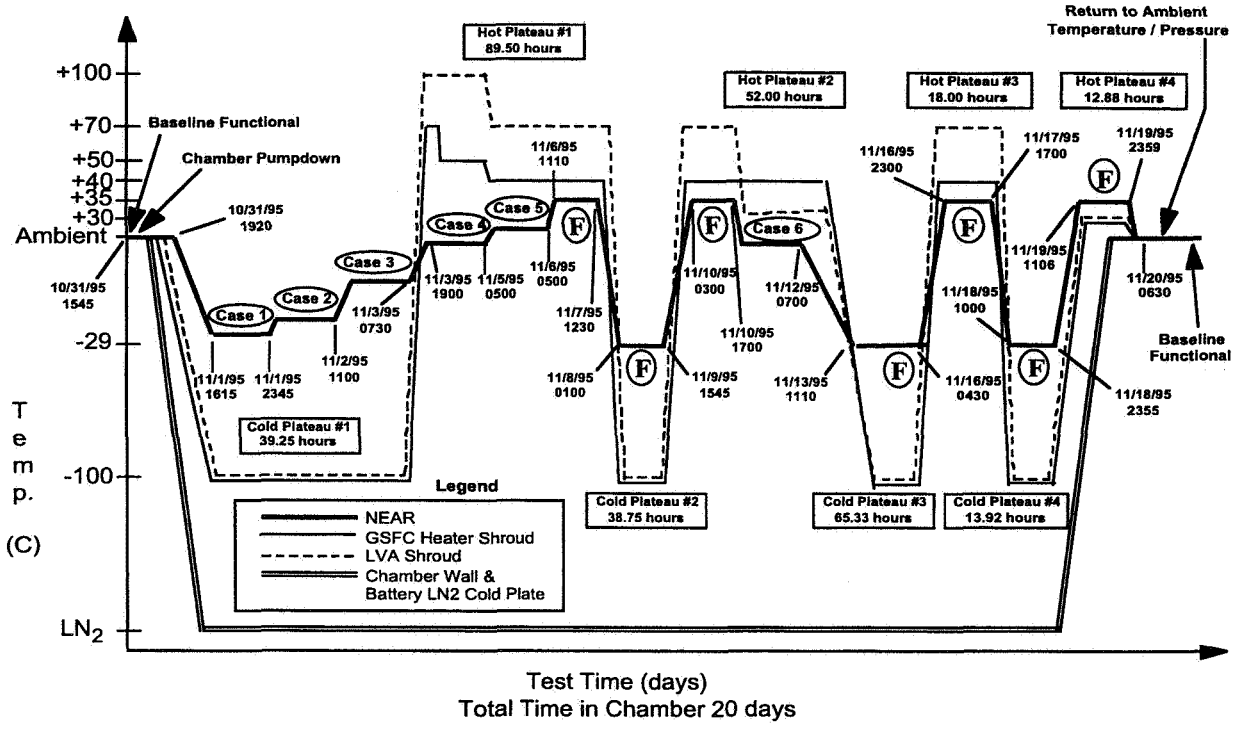


Figure 4. NEAR Thermal Balance/Thermal Vacuum Test Profile (as run).

and an LN_2 cooling plate equipped with heaters. Because the mission thermal environments are significantly different between the solar-illuminated spacecraft forward deck and the remainder of the spacecraft which receives only minimal off-angle solar exposure, the spacecraft was divided into two distinct temperature simulation zones (see Figure 5):

(1) The forward section which contained all hardware at and above the plane of the solar panels (the solar panels were not present during TV testing).

(2) The lower section which included the remainder of the spacecraft and aft deck instruments.

The forward spacecraft section was encased inside an IR heater shroud which was designed to simulate expected solar-induced thermal environments between 0.98 and 2.2 AU. Multi-layer insulation between the spacecraft at the solar array plane and the heater shroud prevented thermal interactions between the two zones. The spacecraft main radiators, which were located in the lower section, had a direct view to the LN_2 cold wall. This was critical because the heat leak from the radiators needed to be accurately measured during the simulated worst case cold mission conditions (aphelion) due to the minimal solar heating inputs and available spacecraft power expected for flight. During hot case simulations, the heat inputs (calculated values) from direct solar flux and IR backloading from the solar arrays were impressed on the radiators using test heaters placed over the entire radiator surface. The main spacecraft flight radiator surface finish was silver Teflon for flight; however, this finish was not present during TV testing. The IR emittance of the test heaters closely matched the actual emittance of the flight silver teflon radiator surface.

TEST CONFIGURATION

The NEAR spacecraft was fully integrated for the thermal vacuum test with all the science instruments, flight connectors, and flight harnesses included. The spacecraft contained the full complement of flight hardware and flight components with the exception of the solar arrays, the propellant, and the final balance mass. As all equipment that comprised the NEAR spacecraft assembly had been thermally cycled during stand-alone component thermal qualification and acceptance tests, the focus of the spacecraft thermal vacuum test was on system-level performance testing and verification. This approach saved schedule time and corresponding testing expense by eliminating the need for special tests to qualify individual components.

The spacecraft was mounted to a test stand which was thermally isolated from the floor of the vacuum chamber. The spacecraft-to-stand thermal interface was

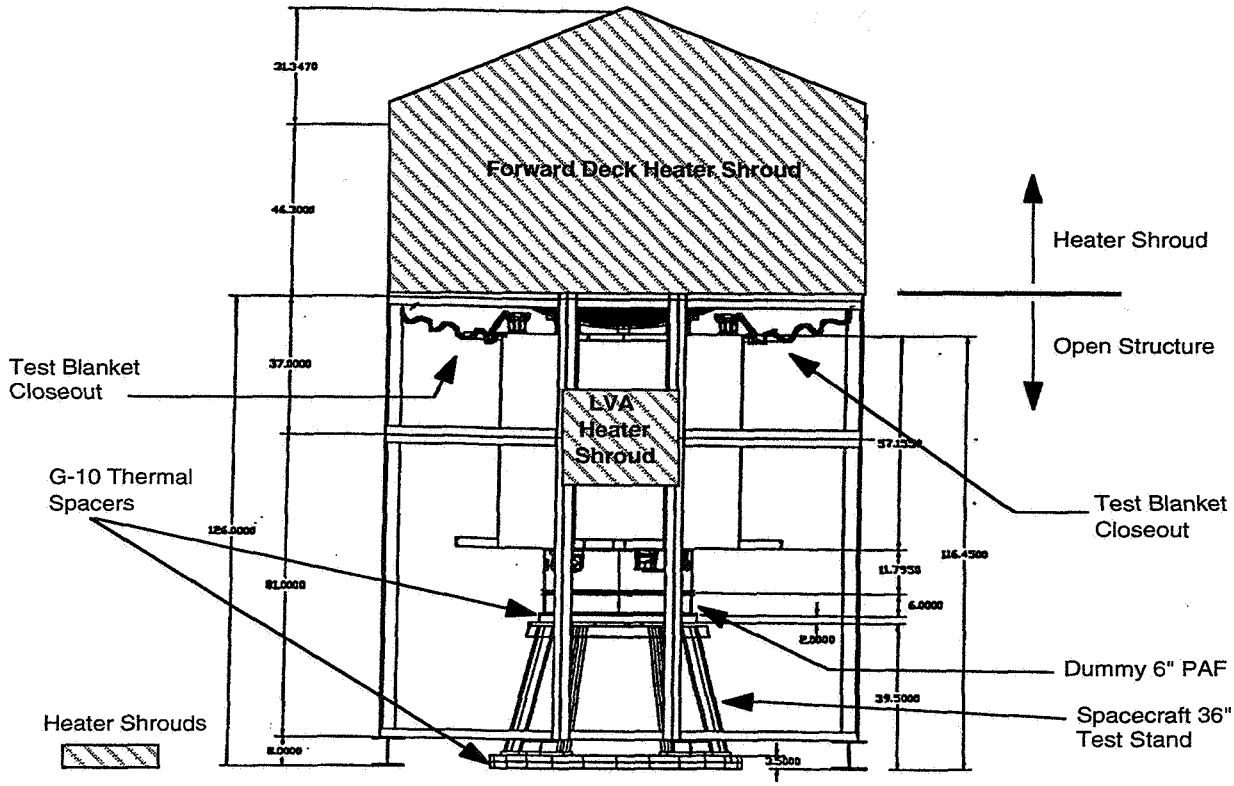


Figure 5. NEAR Spacecraft test Heater Shroud Configuration.

designed to be "zero-Q" (nearly adiabatic) in order to eliminate heat leaks unique to the test configuration that would be difficult to quantify and account for in the subsequent thermal model correlation effort. This was accomplished by using a 50.8 mm G-10 isolation ring between the spacecraft adapter and the test stand. Heaters placed on the test stand were powered to match a reference temperature on the spacecraft side of the interface, thus heat flow across the mounting interface was virtually eliminated. All external GSE cables were also "zero-Q" to prevent heat leaks and anomalous test results. The "zero-Q" technique used for the cables was essentially the same as the spacecraft-to-test stand method. The solar arrays were not present during testing, but the effects of IR backloading from the arrays to the spacecraft radiators was accounted for.

In order to minimize costs, the thermal vacuum test was designed to use existing heater shrouds and support structure originally designed and built for the MSX spacecraft test. The shroud configuration consisted of the skeleton support structure (see Figure 5) with only the two upper shroud panel levels, the uppermost vertical section and the dome section, in place. When controlled concurrently, these shroud sections behaved as a large effective heater shroud that allowed accurate simulation of the expected mission environments for the spacecraft forward deck and components. Close-out MLI was used to thermally isolate the zones above and below the shroud. The open support structure, which allowed spacecraft radiators to directly view the LN_2 flooded liner, enabled an accurate simulation of the cold extreme environmental conditions expected during mission aphelion. The support structure was oriented so that the radiators would have the least obstructed view of the chamber cold wall. Environmental heating due to absorbed solar flux and solar array IR backloading was simulated using test heaters. The test heater power levels for each thermal balance condition were determined using detailed thermal modeling of the mission environmental condition to be simulated.

The test configuration was geared toward simplicity both in the test hardware setup and the corresponding control processing needed to ensure the proper thermal environments during testing. However, there were several local areas on the spacecraft that required customized provisions in order to ensure optimized thermal control during testing. In the original test configuration, the battery radiator viewed the chamber floor. Due to concerns regarding the uncertainty in the chamber floor temperature, a cold plate with LN_2 cooling capacity was placed over the battery radiator. This local cold plate ensured that the battery radiator would view

a known mission-equivalent thermal environment that was independent of the chamber floor temperature. The cold plate also allowed precise temperature control of the battery cells during chamber transitions at the beginning and end of test. In addition, a local shroud was placed over the LVA rocket engine exhaust port to simulate off angle solar entrapment inside the gold-plated heat shield.

The test instrumentation consisted of 324 thermocouples which were located on the spacecraft and thermal shrouds. Of the 324 total thermocouples, 126 were located on the shrouds, support structure, GSE, and spacecraft temperature control zones. The remainder were placed throughout the spacecraft and on all instruments. The philosophy used to determine thermocouple placement was as follows:

(1) At least one T/C for each electronics box interface;
(2) One T/C for each instrument thermostat/heater zone;
(3) One T/C for each thruster valve;
(4) One T/C for each propellant line thermostat;
(5) At least one T/C for each radiator zone;
(6) One T/C at each bracket-to-deck/edge member interface;
(7) At least one T/C on previously temperature-qualified hardware that was thermally isolated from the spacecraft (such as antennas).

The propulsion subsystem had undergone thermal vacuum acceptance testing prior to spacecraft integration and therefore was not heavily instrumented. Flight temperature sensors located on the propellant tanks were used to monitor tank temperatures during testing. Select thermocouples (thruster valves and lines) used during the previous pre-integration testing were left in place and re-used during the full spacecraft test.

THERMAL BALANCE TESTING

Methodology

Thermal balance was achieved by maintaining constant power levels on all spacecraft and instrument components until all temperature monitors met the following stability criteria:

(1) A 1.0°C/hour or less change was measured on all temperature monitors for three (3) consecutive hours with temperatures showing neither an increasing or decreasing trend.
(2) All heater duty cycle extreme temperatures met the above criteria and cycle periods were consistent.

The thermal balance test consisted of six cases which simulated expected hot and cold spacecraft mission conditions. Three cold simulations were performed at mission aphelion environmental conditions using three different spacecraft electrical load scenarios. Two hot balance cases simulated near earth cruise mode (0.98 AU) and one hot simulation represented asteroid mode at its closest solar approach (1.13 AU). During the cold case simulations the operational integrity of all heater and thermostat circuits was verified.

The use of heater shrouds as radiative temperature sinks was limited to spacecraft surfaces not utilized as radiators. Although the use of heater shrouds accurately simulates hot environmental conditions, the heater shrouds at or near the radiator surfaces would preclude attaining the cold temperature sinks needed during cold balance cases in order to accurately simulate the cold mission extreme environments. During hot thermal balance conditions, test flux heaters were used to simulate expected incident solar fluxes and solar array IR backloading onto the radiators. During cold thermal balance conditions, no impressed heat was applied. Using heaters instead of shrouds (or simulated sinks) allowed the spacecraft radiators to view the coldest possible environment which was representative of the spacecraft aphelion mission condition when a typical radiator sink temperature is approximately -140°C. Table 1 lists the temperature settings used for the environmental sinks during hot and cold testing.

Cold Balance Testing

Figure 4 illustrates the thermal balance and functional temperature plateaus desired for the spacecraft

Table 1. Thermal Shroud and Cold Plate Temperatures.

Thermal Control Zone	Cold	Hot			Cycle Testing
	Cases 1-3 (°C)	Case 4 (°C)	Case 5 (°C)	Case 6 (°C)	Cold/Hot Plateaus (°C)
Chamber 290 Liner	LN_2	LN_2	LN_2	LN_2	LN_2
Forward Heater Shroud	-100.00	+50.00	+40.00	+50.00	-100/+20
LVA Shroud	-100.00	+100.00	+70.00	+100.00	-100/+20
Battery Cold Plate	LN_2	LN_2	LN_2	LN_2	LN_2

during testing. Chamber evacuation began on October 31, 1995, at 15:45. During pump down all electronics boxes specified to be operating during launch were enabled so that the spacecraft was powered in the launch configuration. The transition to the first cold balance case officially started at 16:15 on November 1, 1995, when chamber pressure and cold wall temperature were established. The spacecraft electronics were configured to the power levels listed in Table 2 and spacecraft operational and survival heater relays were configured per Table 3. The bus voltage was maintained at 33.28 VDC throughout all balance cases because the NEAR

Table 2. Spacecraft Measured Power.

		Cold			Hot		
Spacecraft Electronics	Pumpdown	Case 1 (W)	Case 2 (W)	Case 3 (W)	Case 4 (W)	Case 5 (W)	Case 6 (W)
Receiver #1	7.72	7.69	7.69	10.15	7.62	10.15	7.63
Receiver #2	7.71	7.69	7.74	10.22	10.12	7.62	10.13
Magnetometer Electronics	0.00	0.00	0.00	0.00	0.00	1.95	0.00
PSE	2.44	3.99	4.33	3.99	20.63	11.98	20.65
C&T Processor #1	0.00	6.06	6.05	6.22	5.82	6.02	5.83
C&T Processor #2	0.00	6.06	6.10	5.92	5.79	5.92	5.80
TCU #1	3.62	3.74	3.78	3.53	3.43	3.46	3.43
TCU #2	0.00	0.00	0.00	0.00	0.00	0.00	0.00
CDU #1	5.92	1.40	1.40	1.40	1.40	1.40	1.40
CDU #2	5.93	1.40	1.40	1.40	1.40	1.40	1.40
Solid State Recorder #1	0.00	0.00	0.00	0.00	0.00	5.19	0.00
Solid State Recorder #2	3.96	4.03	4.08	4.08	4.03	4.03	4.03
Power Switching	0.83	0.83	0.83	0.83	0.83	0.83	0.83
SSPA #1	0.00	0.00	0.00	29.94	28.45	29.61	28.48
SSPA #2	0.00	0.00	0.00	0.00	0.00	0.00	0.00
NIS Electronics	0.00	0.00	0.00	0.00	0.00	5.77	0.00
Reaction Wheel 1 / Elec	0.00	1.40	2.33	1.23	2.50	1.86	2.50
Reaction Wheel 2 / Elec	0.00	1.86	1.66	1.56	1.56	1.56	1.57
Reaction Wheel 3 / Elec	0.00	1.86	1.56	2.03	1.56	1.73	1.57
Reaction Wheel 4 / Elec	0.00	1.70	3.00	2.66	1.86	1.56	1.87
Stack 1 HVPS	0.00	0.00	0.00	0.00	0.00	1.00	0.00
Stack 2 HVPS	0.00	0.00	0.00	0.00	0.00	0.93	0.00
Stack 3 HVPS	0.00	0.00	0.00	0.00	0.00	0.83	0.00
IMU	0.00	23.63	23.40	23.40	25.53	25.79	25.55
DSAD electronics	0.00	2.50	2.46	2.46	2.50	2.38	2.50
AIU #1	10.94	0.00	0.00	11.11	0.00	0.00	0.00
AIU #2	0.00	10.43	10.43	0.00	10.42	10.35	10.43
Flight computer #1	0.00	0.00	0.00	4.88	0.00	0.00	0.00
Flight computer #2	0.00	4.97	5.10	0.00	5.01	4.75	5.02
NLR electronics	0.00	0.00	0.00	0.00	0.00	7.00	0.00
NLR converter	0.00	0.00	0.00	0.00	0.00	4.00	0.00
XGRS electronics	0.00	0.00	0.00	0.00	0.00	11.75	0.00
XGRS DPU	0.00	0.00	0.00	0.00	0.00	7.83	0.00
NIS/MAG DPU	0.00	0.00	0.00	0.00	0.00	2.23	0.00
MSI DPU	0.00	0.00	0.00	0.00	0.00	6.29	0.00
Pressure Transducers	0.00	1.33	1.59	1.33	1.33	1.56	1.33
Battery	0.00	4.47	4.25	4.89	4.03	4.89	4.03
Star Tracker	0.00	6.72	6.80	6.88	6.79	6.63	6.80
Internal Shunts:							
Forward Deck Shunts	0.00	0.00	0.00	22.20	22.30	0.00	0.00
Aft Deck Shunts	0.00	0.00	22.30	22.20	22.30	0.00	22.32
*Total Internal Heat Dissipated:	49.07	92.57	117.24	172.76	186.38	188.74	164.25

*Battery and Star Tracker Not Included

power system is regulated and designed not to use the battery. (The only expected battery discharge occurred for approximately one hour after launch.) The environmental simulation heaters were powered to levels listed in Table 4 and the heater shroud temperatures were set to the levels specified in Table 1. During the different cold balance cases the operational integrity of each spacecraft operational and instrument survival heater circuit was individually isolated and checked. The spacecraft achieved equilibrium at the final cold thermal balance condition, cold case 3, on November 3, 1995, at 07:30. Results of the testing showed:

(1) All primary and secondary instrument survival heater/thermostat circuits operated properly.

(2) All primary and secondary spacecraft operational heater/thermostat circuits operated properly.

(3) All primary and secondary propulsion system operational heater/thermostat circuits operated properly.

(4) Internal spacecraft bus electronics power was about 20 W less than expected. This was due to lower

Table 3. Spacecraft Heater Relay Configuration.

Control Relays	Relay No.	Pumpdown (On/Off)	Cold Case 1 (On/Off)	Cold Case 2 (On/Off)	Cold Case 3 (On/Off)	All Hot Cases (On/Off)	Cycles (On/Off)
Internal Shunts							
Aft Deck	53	Off	Off	On	On	On/Off	Off
Forward Deck	18	Off	Off	Off	On	On/Off	Off
Primary Survival Heaters							
Spacecraft	17	Off	On	Off	On	On	On/Off
NLR Pri/Sec	48	On	On	On	On	On	On
Instruments	55	Off	On	Off	On	On	On/Off
PS Tank	32	Off	On	Off	On	On	On/Off
PS Valve & line	34	Off	On	Off	On	On	On/Off
LVA Flange	33	Off	On	Off	On	On	On/Off
Side A Cat-Bed	35	Off	Off	Off	Off	Off	Off
Side B Pri/Sec Cat-Bed	38	Off	Off	Off	Off	Off	Off
RF Panel Pri/Sec	59	Off	On	On	On	On	On/Off
Secondary Survival Heaters							
Spacecraft	52	Off	Off	On	On	On	On/Off
Instruments	16	Off	Off	On	On	On	On/Off
PS Tank, Valve & line	00	Off	Off	On	On	On	On/Off
LVA Flange	31	Off	Off	On	Off	On	On/Off
Side A Cat-Bed	54	Off	Off	Off	Off	Off	Off

Table 4. Measured Test Heater Power Configurations.

	Cold		Hot		
*Flux Simulation Zone	Cases 1-2 (W)	Case 3 (W)	Case 4 (W)	Case 5 (W)	Case 6 (W)
Zone 1 Radiator	6.50	0.00	6.40	6.92	5.89
Zone 2 Radiator	0.00	0.00	7.62	7.95	32.90
Zone 3 Radiator	0.00	0.00	16.10	6.79	13.10
Zone 4 Radiator	0.00	0.00	0.00	0.00	0.00
Zone 5 Radiator	0.00	0.00	30.28	18.81	26.80
Zone 6 Radiator	0.00	0.00	1.54	1.86	6.80
Zone 7 Radiator	0.00	0.00	1.02	2.00	10.10
Zone 8 Radiator	0.00	0.00	4.63	2.97	12.90
Star Tracker Sunshade	0.00	0.00	8.35	1.95	8.63
**Total Power:	6.50	0.00	67.59	47.30	108.49

* Impressed power equals predicted plus 25%
** Star Tracker excluded

than expected power in the reaction wheels (1.65 W/wheel compared to 5 W/wheel) and several electronics packages.

(5) Because the spacecraft power was lower than expected, certain spacecraft radiators were oversized. Spacecraft electronics boxes that were running close to -30°C, namely the CDU and TCU in zone 1 and the reaction wheels in zone 7, were maintained above their respective minimum operational temperature limits by applying heater power (from the test flux heaters) into the appropriate radiator zone. The measured values for this additional impressed heater power as well as all the measured electronics box powers were incorporated into the thermal model on a real-time basis. The temperature predictions from the updated thermal model matched well with measured thermocouple and spacecraft telemetry temperatures for each of the three cold balance conditions.

(6) During the worst case cold test conditions, the Star Tracker required survival heater power (25% duty cycle) when operational. Pre-test analysis had predicted that no survival heater power would be required when the Star Tracker was operating. The spacecraft power budget was subsequently modified to account for the average Star Tracer survival heater power draw of 2 W during operational modes.

Hot Balance Testing

As shown in Figure 4, the first segment of hot balance testing started on November 3, 1995, at 19:00 and ended on November 6, 1996, at 11:10. The first hot balance test simulated the spacecraft power level and mission thermal environment expected at 0.98 AU. It was apparent late in this test sequence that the test operators had not properly configured the spacecraft per the Thermal Vacuum Test Specification. This discrepancy was discovered when thermal model predictions which were based upon measured powers for the radiator zone test heaters and spacecraft electronics did not match measured temperatures as expected. The spacecraft status and relay configurations were checked, and the source of the problem was traced to the forward internal shunt heaters which were mistakenly enabled. The thermal model had simulated the correct spacecraft configuration with the forward shunt heaters disabled, therefore model temperature predictions were lower than measured thermocouple temperatures. In order to maintain the proper timeline required to meet the JPL DSN trailer availability window, the spacecraft was reconfigured for the second hot balance test case, and the test proceeded. However, it was agreed that if there was no adverse schedule impact, then hot balance case one would be repeated later in the test profile following a hot functional test. The second hot balance test simulated the asteroid mapping mode at 1.13 AU with all instruments and associated electronics powered on.

The third hot balance test, which was essentially a repeat of the aborted hot balance case one, began after the second spacecraft hot functional test and was completed on November 12, 1995, at 07:00. For the retest, the spacecraft was correctly configured (see Table 2) with the forward shunt heaters disabled. Table 1 and Table 4 list the shroud and test heater configurations for hot balance case three while Table 2 and Table 3 list the spacecraft power and relay configurations. As can be seen from Table 4, the test flux heater powers were increased for hot case three from the values initially used in hot case one. This step was taken in order to add another data point for thermal model correlation. It was apparent from the pseudo-balance temperatures witnessed during hot case one that the spacecraft had plenty of hot thermal design margin. The increase in the test flux heater power impressed on the spacecraft radiators was the equivalent of two internal shunt heater circuits at the maximum expected flight voltage of 33.5 VDC.

The results from the hot balance testing showed:

(1) The spacecraft thermal design includes ample hot temperature margin. With the exception of the Power Systems Electronics (PSE), all electronics interface temperatures ranged from 22°C to 38°C. During hot balance case 1, the maximum PSE interface temperature was 49°C. This hot temperature condition occurred solely because the forward internal shunt heater circuit was mistakenly enabled. The PSE interface temperature dropped to 41°C when the spacecraft was properly configured during hot case 3.

(2) All instrument primary and secondary operational heaters performed as expected. The operational heater/thermostat circuits were verified during the first cold functional test conducted from November 8 through November 9, 1995. During hot balance testing cases that simulated asteroid mapping mode, sensor temperatures were maintained within the required temperature levels for science data acquisition while the instrument operational heaters exhibited low duty cycle heater demand. This performance verified that positive heater control and the resulting fine-tuned sensor temperature response was possible at the maximum instrument interface temperatures.

(3) The thermal model predictions matched very closely with measured thermocouple and spacecraft telemetry temperature data when measured electronics

and test flux heater powers were used as inputs for the model test condition simulation runs.

(4) Internal spacecraft electronics power was about 50 W less than expected. This was due to lower than expected power in all instrument electronics (~30 W) in addition to the 20 W spacecraft bus electronics deficit described earlier.

SPACECRAFT FUNCTIONAL TESTING

During spacecraft functional testing, the spacecraft was held at the hot and cold temperature plateaus shown in Figure 4 while all spacecraft electronics and instruments were exercised to verify proper operation at the extreme hot and cold temperature levels. The purpose was to demonstrate repeated hardware and software functionality at temperature extremes while exposing any workmanship related problems. A minimum of three thermal cycles and 108 hours of accumulated time at each plateau was deemed necessary in order to accelerate incipient failures in marginal designs and stress spacecraft components and connectors. The radiator zone test heaters were used to establish and maintain proper temperature plateaus during the hot and cold functional portions of the thermal vacuum test. A total of 157 hours was spent at cold soak temperature levels and 172 hours was spent at hot soak temperature levels during four complete thermal test cycles.

TESTING RESULTS SUMMARY

In general, the test thermal model predictions matched very well with the measured test thermocouple and spacecraft telemetry temperature data. The majority of critical temperature predictions (i.e., mission-critical flight hardware) were within 2°C of actual measurements. The maximum deviation between predictions and measurements occurred for the Star Tracker during the hot case one thermal balance condition. The Star Tracker temperature prediction (13°C) was about 5°C colder than the measured temperature (18°C); however, the measured temperature was still 12°C within the desired upper operating limit. The Star Tracker temperature prediction was about 3°C warmer than the measured value during worst cold case testing conditions.

Real-time thermal model predictions were very useful in helping to assess and understand test results. As mentioned earlier, the spacecraft electrical configuration was improperly selected for the first hot balance case. Real-time thermal analysis facilitated quick identification, understanding, and correction of this anomaly. The thermal model predictions matched measured component temperatures closely during the hot and cold balance tests which established a high degree of confidence in the accuracy of the thermal model and its temperature prediction capability. Test results and real-time analytical predictions indicated that the spacecraft thermal design was cold-biased, therefore it was decided to close-out radiator zones 1 and 5 with MLI and reduce the size of radiator zone 2 after thermal vacuum testing was completed. This decision was driven by a complete re-analysis of critical mission scenarios using the flight thermal model which had been modified to include electrical powers measured during testing as well as appropriate changes derived from the test TMM.

During the last three days of functional testing an RF anomaly was discovered. Temperature cycling of the forward test shroud exacerbated a loose connection in the RF hardware. Originally thought to be a GSE induced anomaly, subsequent independent RF testing supported by thermal cycling of the forward shroud indicated that it was indeed a flight hardware connector problem. At the completion of the thermal vacuum testing, the lead RF engineer inspected all RF connectors and determined that the critical connection to the RF feed was loose as a result of not being staked. Following completion of the test, this interface was staked and taped to prohibit any similar reoccurrence during flight.

LESSONS LEARNED

Several lessons learned during the process of planning, implementing, and executing the NEAR environmental test include:

(1) Having real-time thermal analysis capability during the test permitted quick assessment of anomalies and special unplanned tests.

(2) The use of test flux heaters mounted to the spacecraft structure was beneficial in aiding temperature transitions, and it was also an invaluable tool for fine-tuning the spacecraft heat balance to ensure equilibrium for the thermal balance conditions. This precise heat balance determination facilitated post-test radiator size tailoring for the NEAR spacecraft which provided additional on-orbit temperature margin.

(3) When using test heaters mounted directly to spacecraft flight panels with thin face sheets, it is essential to properly instrument the panels local to the heater footprints (T/Cs at the heater edges and center). This allows accurate monitoring of the panel maximum temperature and helps prevent overdriving the heater power levels (and the resultant local face sheet/adhesive high temperatures) during cold to hot transitions.

CONCLUSIONS

Test results show that the NEAR thermal design successfully maintained all spacecraft components within allowable flight temperature limits during worst case simulated cold and hot mission environmental conditions. The operational integrity of all spacecraft thermostat/heater circuits has been verified. In addition, insight gained from the test results prompted post-test tailoring of selected radiator zones and removal of others in order to provide additional temperature margin during worst case mission cold conditions. These radiator modifications have negligible effects on the maximum temperatures experienced during the worst case mission hot condition due to locations that are relatively isolated from spacecraft hot spots.

The spacecraft test thermal model was correlated to predicted temperatures to within 5°C of the actual test temperatures. The flight thermal model was modified to account for the test thermal model correlation updates and then used to redesign the zones 1, 2 and 5 radiator sizes. The flight model is now being used to predict on-orbit temperatures for mission operational scenarios.

NOMENCLATURE

AIU	Attitude Interface Unit
APL	Applied Physics Laboratory
AU	Astronomical Unit
C	Celsius
Cat-Bed	Catalyst Bed
CDU	Command Detection Unit
C & T	Command and Telemetry
DPU	Data Processing Unit
DSAD	Digital Solar Attitude Detector
DSN	Deep Space Network
Fe^{55}	Iron 55 Source
GSFC	Goddard Space Flight Center
GSE	Ground Support Equipment
HVPS	High Voltage Power Supply
IMU	Inertial Measurement Unit (Gyro)
IR	Infra-Red Radiation
JHU	The Johns Hopkins University
JPL	Jet Propulsion Laboratory
LN_2	Liquid Nitrogen
LVA	Large Velocity Adjustment (450 N thruster)
MAG	Magnetometer
MLI	Multi-Layer Insulation
MSI	Multispectral Imager (Visible Imager)
MSX	Midcourse Space Experiment
N	Newton
NASA	National Aeronautics and Space Administration
NEAR	Near Earth Asteroid Rendezvous
NIS	NEAR-Infrared Spectrograph
NLR	NEAR Laser Rangefinder
OSC	Orbital Sciences Corporation
PAF	Payload Adapter Fitting
PS	Propulsion System
PSE	Power Systems Electronics
RF	Radio Frequency
SES	Space Environment Simulation
SINDA	Systems Improved Numerical Differencing Analyzer
sq. m	Square Meter
SSPA	Solid State Power Amplifier
T/C	Thermocouple
TCU	Telemetry Conditioning Unit
TMM	Thermal Math Model
TRASYS	Thermal Radiation Analyzer System
TV	Thermal Vacuum
VDC	Voltage Direct Current
W	Watt
XGRS	X-Ray/Gamma-Ray Spectrometers
Zero-Q	No Heat Flow (Adiabatic Interface)

REFERENCES

1. Ercol, C. J. and Krein, S. J., "Thermal Design of the Near Earth Asteroid Rendezvous Spacecraft," 26th International Conference on Environmental Systems, SAE Paper No. 961573, Monterey CA, July 8-11, 1996.
2. Santo, A. G., Lee, S. C., and Gold, R. E., "NEAR Spacecraft and Instrumentation," The Journal of Astronautical Sciences, Volume 43, No. 4, October-December 1995, pp. 373-397.
3. Farquhar, R. W., Dunham, D. W., and McAdams, J. V., "NEAR Mission Overview and Trajectory Design," The Journal of Astronautical Sciences, Volume 43, No. 4, October-December 1995, pp. 353-371.
4. Thermal Radiation Analysis System II User's Manual, prepared for the National Aeronautics and Space Administration (NASA), Lyndon B. Johnson Spacecraft Center under contract NAS9-15832, October 1986.
5. SINDA/FLUINT User's Manual, Version 2.4, National Aeronautics and Space Administration (NASA), Lyndon B. Johnson Space Center (JSC), 1991.
6. SINDA/G (Formerly SINDA/1987/ANSI) Version 1.44 User's Manual, Network Analysis Associates, 1993.

5/2-18

02/445

269378

MECHANICAL TESTING OF THE NEAR SPACECRAFT

209

David F. Persons
Johns Hopkins University Applied Physics Laboratory
Laurel, Maryland

ABSTRACT

The Near Earth Asteroid Rendezvous mission was the first launch in the Discovery Program, a NASA initiative for small planetary missions with a maximum 3-year development cycle and a cost capped at $150 million for construction, launch and 30 days operation. The NEAR mission is managed for NASA by the Johns Hopkins University Applied Physics Laboratory. The primary mission objective for the NEAR spacecraft is to rendezvous with and orbit the asteroid 433 Eros in February, 1999.

This paper describes the system-level mechanical test program undertaken to qualify the NEAR spacecraft and mechanisms for flight. Thermal vacuum testing is not discussed in this article. The overall protoflight testing philosophy of this cost-and-schedule driven program is presented, along with a description of the test flow, instrumentation configuration and results of the tests performed. Correlation between analytical and test results is presented. The tests performed on the NEAR spacecraft at JHU/APL included sine vibration and pyrotechnic shock. Tests completed at Goddard Spaceflight Center were spin balance, mass properties, and acoustic vibration. A final spin balance was successfully performed at Kennedy Spaceflight Center prior to launch.

INTRODUCTION

The NEAR spacecraft was launched from Cape Canaveral Air Station on February 17, 1996 using a Delta 7925-8 launch vehicle. The spacecraft was designed and integrated by JHU/APL in only 26 months from full-funded start to launch. The following constraints were the most influential in determining the philosophy and final makeup of the spacecraft mechanical test program:

- Procurement of a pre-qualified propulsion subsystem, with a completely independent structure internal to the spacecraft. Schedule and logistic constraints dictated parallel development for the propulsion structure and spacecraft structure.
- Based on the start date for spacecraft integration, only a total of 4 weeks could be allocated for system-level mechanical testing.

The NEAR program most closely matches category B of DOD-HDBK-343, with a 5 year life, medium to high complexity, soft failure modes with redundancy, limited flight spares, short schedule with a critical launch date. Integration of the spacecraft could not begin until the main propulsion subsystem, built by GenCorp Aerojet, was delivered to JHU/APL in the first week of May, 1995. It was recognized early in the program that this hard date compressed the integration and test schedule severely. In addition, the cost and schedule impact of mass simulators and the extensive use of long-lead aluminum honeycomb for the spacecraft structure resulted in the decision not to build an engineering model qualification structure. As a result, a protoflight approach was adopted for the spacecraft test program. JHU/APL has extensive experience conducting a protoflight test regimen on spacecraft programs. This decision allowed mechanical qualification of the spacecraft primary and secondary structure, solar arrays, hinges and despin system to occur simultaneously. Spacecraft mechanical testing began the last week of September and continued through the third week of October, 1995.

SPACECRAFT DESIGN DESCRIPTION

The spacecraft all-aluminum primary structure consists of honeycomb forward and aft decks, separated by 8 honeycomb side panels, and a monocoque cylindrical launch vehicle adapter attached to the bottom of the aft deck. 4 of the side panels are removable for ease of access to the spacecraft interior. 4 solar panels, hinged at the forward deck, are folded down along the spacecraft sides for launch and restrained by 2 despin cables wrapped twice around the spacecraft at the aft deck level. The interior of the spacecraft contains the propulsion module which is attached to the forward side of the spacecraft aft deck. Most of the electronics boxes are mounted to the decks. A 1.5 m graphite/epoxy antenna is mounted on the forward side of the forward deck. Figure 1 shows the PS mounted to the spacecraft structure with 4 spacecraft side panels removed for clarity.

MECHANICAL DESIGN ENVIRONMENTS

A relatively standard set of Delta II mechanical design environments were developed for the NEAR program by McDonnell Douglas Aerospace with appropriate modifications based on the spacecraft/vehicle coupled loads analysis. Summarized below is the sequence of relevant launch events and the flight acceptance level requirement generated by each:

Liftoff, Transonic, MECO

At liftoff, the spacecraft is subjected to the quasistatic accelerations given below as well as acoustic noise reflected off the launch pad. Besides the liftoff load case, the MDA coupled loads analysis also generates load cases for the maximum dynamic pressure on the vehicle, and as the vehicle reaches transonic speed.

Spacecraft CG Limit Load Factors

Axis	Liftoff/Transonic (G's)	MECO (G's)
Lateral	±3.0	±0.1
Thrust	-2.5/+0.2	-6.1+0.6

Spacecraft Flight Acceptance Acoustic Vibration

138 dB Peak at 500 Hz
144.6 dB Overall for 5 seconds
dB Ref.: 2.0×10^{-5} N/m^2

Third Stage Burn

The Delta II third stage is spin stabilized. The 3rd stage and payload are mounted on the second stage spin table, with rotary motion generated by firing 4 small tangentially mounted rockets. The resulting flight acceptance angular and centrifugal accelerations generated are significant.

Axis	Spin-Up Angular Accel (rad/sec^2)	Spin Centrifugal Accel (G's)	3rd Stage Max (G's)
Lateral/Radial	9.4	0 - 6	±0.1
Thrust	--	--	-8.5

3rd Stage Despin and Spacecraft Separation

Spacecraft separation from the third stage introduces pyrotechnic shock into the spacecraft due to the ignition of the separation clampband release ordnance. After separation, the spacecraft is despun and the solar arrays are released by the activation of a yo-yo despin mechanism. This mechanism imparts a 4.1 rad/sec^2 angular deceleration to the spacecraft through a 110 lb. maximum tension in each despin cable.

PROTOFLIGHT MECHANICAL TEST PROGRAM ISSUES

For protoflight testing, MDA recommends a spacecraft mechanical test program consisting of static load or centrifuge testing, acoustic testing, clampband-induced shock testing, and spin balance testing (for a vehicle with a 3rd stage). Use of swept sine testing to generate protoflight-level structural loads is permitted in place of static or centrifuge testing. Resonant responses can be limited to produce load levels in the structure equal to those uncovered in the coupled loads analysis. Swept sine testing was chosen for the NEAR program in light of the extensive heritage this technique has at JHU/APL.

Although a protoflight level test program increases risk to flight hardware, this approach has been followed successfully on many JHU/APL built spacecraft. The final form of the spacecraft mechanical test program was highly dependent on decisions made early in the program regarding the propulsion subsystem. The most significant issues associated with the PS were:

- The size of the propulsion subsystem, 54% of the spacecraft total weight.
- The requirement to follow an independent and accelerated schedule.
- The inaccessibility when integrated, especially if a problem or failure occurred.
- The difficulties associated with having 2 organizations, 2500 miles apart, co-developing a single structure to support the PS subsystem and the spacecraft subsystems.

These issues led JHU/APL to the following decisions:

- The PS-to-spacecraft interface should be as simple as possible. Figure 2 shows the PS mounted on it's shipping 'cage'. The interface consists of a single 32 bolt structural interface with the spacecraft aft deck, and 6 thruster modules attached to the forward and aft spacecraft decks.
- The PS would be shipped completely qualified to protoflight vibration levels.
- The PS and spacecraft should be designed to have sufficient separation between their fundamental natural frequencies in the lateral and thrust directions as to not couple during system-level swept sine vibration testing.
- Due to this separation, not enough participating mass would be available at any one frequency to generate protoflight levels loads in the spacecraft adapter structure. This required the adapter to be qualified by performing a static load test.

Another benefit of the decision to follow a protoflight spacecraft test program involved the solar array and it's release mechanism. As in previous JHU/APL protoflight programs, it was decided that the solar panels would not be vibrated as components, but qualified at the system level along with the spacecraft structure. This allowed the array to be vibrated using the actual boundary conditions as for flight while simultaneously qualifying the array deployment hinges, ball and socket supports, and despin cable combs. The actual delivery schedule for the NEAR solar panels proved to be tight enough that performing a component-level vibration before integration would have been difficult.

PROPULSION SUBSYSTEM MECHANICAL TEST PROGRAM DEVELOPMENT

The propulsion subsystem was treated more as a separate spacecraft than as a subsystem. The following list of design requirements and tests were developed for GenCorp-Aerojet by JHU/APL:

Quasi-Static Design Loads

Over the course of the program, the initial design loads set by JHU/APL were reduced after the MDA coupled loads analysis was completed. The final quasi-static loads for the PS were:

Liftoff:

Thrust Axis: -2.5/+0.25 G's
Lateral Axes: ±3.0 G's
Applied simultaneously to the PS CG.

3rd Stage SS:

Thrust Axis: -7.5 G's
Radial Axis: Centrifugal acceleration due to a 70 rpm (3-sigma maximum) 3rd stage spin
Applied simultaneously to the PS CG.

Stiffness

PS modes with significant mass participation were designed to be greater than 55 Hz in thrust, 30 Hz in lateral. This provided a comfortable frequency offset which minimized any coupling between the spacecraft outer structure and the PS.

Sine Vibration Testing

The structural loads test for the PS was accomplished at GenCorp-Aerojet using swept sine vibration to apply 1.25 times the quasi-static limit loads given above, with the sweep continued to 100 Hz to apply a protoflight level test representation of Delta II vehicle transients to the structure. Unlike the spacecraft-level swept sine test, which used the response at the spacecraft outer structure's fundamental frequency to generate loads, analysis done by GenCorp-Aerojet revealed that not enough participating mass was available in the PS fundamental modes below 100 Hz to allow use of the recommended MDA swept sine test. Therefore a higher level test shown below was developed for PS structural qualification:

NEAR Propulsion Subsystem Sine Vibration Levels:

Thrust Axis

Frequency (Hz)	Acceleration
5 to 22.0	0.38 in. (double amplitude)
22.0 to 23.0	9.4 G's (zero to peak)
23.0 to 100	1.4 G's (zero to peak)

Sweep rate = 4 octaves/min.

Lateral Axes

Frequency (Hz)	Acceleration
5 to 11.0	0.62 in. (double amplitude)
11.0 to 12.0	3.8 G's (zero to peak)
12.0 to 100	1.0 G's (zero to peak)

Sweep rate = 4 octaves/min.

Random Vibration Testing

Prior to spacecraft integration, the PS was exposed to base excited protoflight random vibration. The levels were based on structure-borne random vibration levels recorded by MDA during past Delta II flights. With the integrated PS surrounded by spacecraft structure, analysis predicted that the spacecraft-level acoustic test would fail to excite the PS to these minimum levels.

Propulsion Subsystem Random Vibration Levels:

Frequency (Hz)	PSD Level
100	0.001 g^2/Hz
100-300	+9.3 dB/Oct.
300-700	0.03 g^2/Hz
700-2000	-3.2 dB/Oct.
2000	0.010 g^2/Hz

Overall Amplitude = 6.0 Grms
Duration = 60 seconds
3 Orthogonal Axes

INTEGRATED SPACECRAFT TEST PROGRAM DEVELOPMENT

The following protoflight tests were developed for qualification of the integrated NEAR spacecraft:

NEAR Spacecraft Sine Vibration Test

A design strength qualification test is recommended by MDA where a set of loads equal to 1.25 times the limit loads is applied the spacecraft structure. MDA recommends both a structural loads test (static or acceleration) to verify structural strength, and a swept sinusoidal vibration test to represent transient conditions that occur during flight. The spacecraft-level swept-sine vibration test outlined below covers both the structural strength test and the simulated flight environment. For spacecraft static load, centrifuge or swept sine strength testing, MDA requires protoflight levels to be 1.4 (+3 dB) times flight acceptance levels. Protoflight swept sine testing consists of one sweep through the specified frequency range at a logarithmic sweep rate of 4 octaves/minute. The protoflight levels as recommended by MDA are:

Thrust Axis

Frequency (Hz)	Acceleration
5 to 7.4	0.5 in. (double amplitude)
7.4 to 100	1.4 g's (zero to peak)

Lateral Axis

Frequency (Hz)	Acceleration
5 to 6.2	0.5 in. (double amplitude)
6.2 to 100	1.0 g's (zero to peak)

Sweep rate = 4 octaves/min.

To support the structural qualification effort, a MSC-NASTRAN test FEM was created using an updated version of the coupled loads FEM. The test levels shown above were input in a forced response analysis to predict the response limiter levels required during swept sine testing. Responses at ~50 locations in the model were recovered and plotted for each axis. These locations corresponded exactly to the locations used in the coupled loads analysis performed by MDA. A spreadsheet was created which listed the maximum response and it's corresponding frequency at each location for both the coupled loads and test response analyses. For each axis, at the spacecraft fundamental frequency, a notch was generated based on the coupled loads analysis which would generate the proper loads in the structure. The spreadsheet automatically factors the responses at all locations that exhibited their maximum response at the notched spacecraft fundamental frequency. This spreadsheet proved very useful for predicting locations for concern during testing and provided a quick reference to allow for real-time comparison of analysis verses test results.

With the accelerated test schedule planned for sine, shock and acoustic testing, it was anticipated that a major bottleneck in data acquisition and post-processing existed at JHU/APL. With only a 16 channel Gen-Rad 2515 Digital Acquisition system available, the other 30-40 channels per axis would have to be recorded on tape and replayed 16 channels at a time. Time estimates for data replay per run ranged from 2 to 4 hours, making mandatory the use of other means of data acquisition if schedule was to be maintained. The solution offered by GSFC proved to be very satisfactory. The GSFC Digital Data Acquisition System consists of a VAXSTATION 4000 Model 90 workstation providing setup, control and archiving functions, and a rack of front end equipment consisting of 4 independent signal processing systems which provide signal conditioning, filtering, A/D conversion, data storage and network access. The DDAS routinely provided a complete set of 45+ frequency response plots within 20 minutes of the end of a sine test run. With 64 channels available from a single rack, the capability of this system allowed the JHU/APL 16 channel GenRad 2550 system to provide all control and limiter channels, with the GSFC DDAS system providing all response channels. This division of labor and responsibility would prove to save additional time.

NEAR Spacecraft Shock Test

The primary source of shock for the NEAR spacecraft is the clamp band ordnance used to separate the payload attach fitting from the spacecraft. The spacecraft separation shock test uses a test PAF and clampband supplied by MDA, which must be assembled to the spacecraft adapter and separated using live ordnance. To account for the scatter associated with the actuation of the same device, this test is required to be performed twice. The maximum expected shock levels for a MDA 3712 PAF configuration peak at 4100 G between 1500-3000 Hz.

The pyrotechnic devices used to release booms, solar arrays, protective covers, etc. produce a local source of shock. To expose the rest of the NEAR spacecraft to these local shock sources, shock testing was conducted at the spacecraft level by firing the ordnance and allowing the release of the solar array, instrument covers, etc. These tests must also be performed twice.

NEAR Spacecraft Acoustic Test

To verify the ability to survive the lift-off acoustic environment and provide a workmanship acoustic test, MDA recommends a payload level acoustic test in a reverberant sound pressure field. The maximum expected flight levels for an 8 foot fairing were provided by MDA. For spacecraft acoustic testing, MDA requires increasing flight acceptance levels by +3 dB for protoflight level tests. The protoflight duration is 60 seconds, identical to the flight acceptance duration, with a protoflight overall sound pressure level of 147.6 dB relative to 2.0×10^{-5} N/m^2, with a 141 dB peak at 500 Hz.

NEAR Spacecraft Mass Properties Test

The objectives of this test are to determine the mass properties of the NEAR spacecraft with the integrated propulsion subsystem and to perform a spin balance of the system. To maintain third stage orbit insertion accuracy, MDA requires the NEAR spacecraft to meet the following requirements:

- Principal Z axis (spin axis) within 0.05 inches of the geometric Z axis.
- Principal Z axis misalignment of less than 0.25° with respect to the geometric Z axis.

To control spacecraft torques during burns involving the 100 lb. side-mounted thruster, the axis of the large thruster must intersect the spacecraft CG in the orbital configuration within 0.25 inch. In addition, Izz must be precisely known to accurately size the yo-yo despin weights.

To properly distribute the mass of the propulsion subsystem, the mass properties of the system must be measured with the pressurized propulsion subsystem fuel and oxidizer tanks filled with deionized water. Analysis indicated that the items that needed to be measured were CGx, CGy, CGz, Ix', Izz, Ixz, and Iyz, with the remaining items determined by analysis using the mass properties spreadsheet.

The spin rate during spin balance operations was predicted to vary from 25 - 69 RPM. For the NEAR spacecraft, the 3 sigma maximum spin rate of the 3rd stage was predicted to be 69 rpm. As a qualification strength test, during spin balance testing, the spacecraft would be exposed to this spin rate for 10 minutes.

NEAR Spacecraft Modal Test

GEVS-SE and MIL-STD-1540B both recommend a payload level modal survey to verify the dynamic characteristics of the payload. A well instrumented sine survey (at 0.1 g from 5-100 Hz, 4 octaves/min.), followed by the swept sine test at Delta II protoflight levels outlined above was chosen to satisfy the requirement for dynamic characteristic verification with the least impact on cost and schedule.

NEAR SPACECRAFT AND MECHANISM TESTING RESULTS AT JHU/APL

Spacecraft Adapter Strength Testing

Test Date: 4/24/95

Two load cases, liftoff and third stage maximum acceleration, were applied to the spacecraft adapter upper flange. The loads were reacted through a MDA-supplied and installed non-flight clampband and test PAF. The following forces were developed at the spacecraft separation plane:

Load Case 1: Third Stage Max Acceleration
16650 lb. Axial Compression

Load Case 2: Liftoff
6220 lb. Axial Compression
6910 lb. Lateral

The loads levels were set at 1.25 x the maximum expected loads derived from the MDA coupled loads analysis. Displacements. load and strain were measured. Load case 2 was applied twice, with the lateral component 90° rotated. Each load was maintained for 5 minutes with no changes noted in the adapter. Hydraulic cylinders were used to apply the load into the adapter through a welded steel assembly which duplicated the aft deck interface with the adapter. The clampband tension was set at the flight level, 3000 lb.

Pre-Vibration Mechanism Tests:

Solar Array Hinge Thermal Vacuum Deployment:

Test Date: 9/9/95

Before integration with the spacecraft, a pair of solar array hinges was chosen for a low temperature deployment test in the JHU/APL vacuum chamber. The purpose of the test was to demonstrate that the design displayed adequate thermal clearances and to size the torsion damper so that the panel would halt before impacting the overtravel stop. An array mass simulator was designed to mimic the solar panel bending stiffness and inertia. This was G-negated using an aluminum support frame designed for another program. The simulator was successfully deployed and the flight torsional damper size established.

Instrument Door Pre-vibration Deployments:

Test Date: 9/26/95

Before beginning spacecraft-level environmental testing, spacecraft commands were used to fire the ordnance for each instrument door to demonstrate proper door operation and verify the operation of the electrical harness. A limit switch on the MIS door failed to function and was readjusted.

NLR and NIS Doors:	Successfully deployed
MIS Door:	Successfully deployed

Despin System Deployment Test:

Test Date: 9/26/95

Demonstration of the proper deployment of the yo-yo despin system was necessary before spacecraft environmental testing began. The despin cables were tensioned to 40 lb. which was the maximum predicted tension at the instant of deployment. After successful release of the despin weights, the cables were walked around the spacecraft and allowed to release from their hooks to verify the cable routing chosen for NEAR.

Spacecraft Protoflight Sine Vibration Testing:

Test Dates: 9/30/95 through 10/4/95

The test objective was to develop 1.25 x max expected structural loads in the spacecraft honeycomb outer structure. The propulsion system and adapter were previously qualified.

The spacecraft was in full flight configuration with the exception of the use of non-flight despin helper cables (loosely mounted), certain aft deck, aft side thermal blanket simulators in place of flight blankets, and a non-flight safeing plug. The spacecraft was attached to the vibration table through a Delta II test PAF and test clampband. The PS tanks were filled with deionized water to represent a fully loaded system at launch. The propellant tanks and the helium tank were pressurized to 140 and 1700 psig respectively, with nitrogen, duplicating the flight mass while giving at least a 4:1 safety factor relative to burst pressure to allow for personnel access during testing.

Testing proceeded smoothly, with the X axis completed in one day, Saturday, 9/30/95, with post-axis electrical checkout consuming the next day. Testing resumed on Monday, 10/2/95, with the Y axis completed that same day. Post-axis electrical checkout was finished the morning of Tuesday, 10/3/95. Thrust axis testing was started that afternoon and completed the morning of the next day. Figure 3 shows the test configuration during thrust axis testing.

X and Y Axes (Lateral) Swept Sine Tests

The results for both lateral axis tests are presented together due to the similarity in setup and results for this essentially symmetric spacecraft. Two stud mounted control accelerometers (1 in-line channel each) and 4 bonded limit accelerometers (2 lateral channels each) were input into the JHU/APL GenRad 2550 Vibration Control system. One limiter was located on the center of the forward deck, 2 on a stiff corner of a side panel at the spacecraft CG, and one on a corner of the aft deck. In addition, to monitor shaker control, a separate stud-mounted in-line accelerometer was connected to the JHU/APL Unholtz-Dickie AM123 Monitor system. 46 response channels, attached with Kapton tape/acrylic adhesive, were acquired through the GSFC DDAS.

The NEAR finite element test model gave good agreement with the fundamental frequencies uncovered during test:

FE Model Summary:

Item	X Axis FE Model Prediction, (Hz)	X Axis Actual Frequency, (Hz)	Y Axis FE Model Prediction, (Hz)	Y Axis Actual Frequency, (Hz)
Spacecraft Outer Structure	17.1	16.7	17.1	16.5
Propulsion System	29.3	32.4	29.3	32.3
Solar Array Cg	42	55	42	55
Solar Array Cg	90	80	90	92

The spacecraft outer structure and PS predictions correlated well with the test results. The FEM did not account for the non-linearity associated with the solar panel hinges and the boundary condition imposed on the solar panels from the 2, 2-wrap despin cables which strap down each panel under tension. Structural damping (NASTRAN Param G = 2(C/Cc)) was set at 5% for the test FEM analysis; for the X axis 16.7 Hz mode it was measured at just under 10% during the pre- and post-test 0.1 G sine surveys; for the Y axis 16.5 Hz mode it was measured at 8.5% during the pre- and post-test 0.1 G sine surveys.

X and Y Axis Loads Summary:

Listed below are the protoflight accelerations (1.25 x max expected) as given by the NEAR coupled loads analysis to be achieved during X axis structural testing. The protoflight sinusoidal test levels given above were successfully applied to the integrated spacecraft. At the fundamental spacecraft lateral resonance of 16.6 Hz., the following accelerations were generated:

Location	X Axis Level to Achieve, (G's)	X Axis Level Generated During Testing, (G's)	Y Axis Level to Achieve, (G's)	Y Axis Level Generated During Testing, (G's)
Forward Deck	4.6	5.0	5.3	5.3
Spacecraft CG	2.0	3.0	2.0	3.1
Aft Deck	1.2	1.2	1.2	1.2
Propulsion System CG	2.7	2.5	2.7	2.7

As shown above, the acceleration levels needed to generate protoflight structural loads in the spacecraft outer structure were achieved. As recommended by GSFC, a 1/2 level swept sine test was performed before and after the full level test to check for any changes in structural response. No change in any part of the spacecraft was noted after comparison of the data obtained from both tests.

Z Axis (Thrust) Swept Sine Test:

Two stud mounted control accelerometers (1 in-line channel each) and 4 bonded limit accelerometers (1 thrust channel each) were input into the JHU/APL GenRad 2550 Vibration Control system. One limiter was located on the center of the forward deck, 2 on a stiff corner of a side panel at the spacecraft CG, and one on a corner of the aft deck. In addition, to monitor shaker control, a separate stud-mounted in-line accelerometer was connected to the JHU/APL AM123 Monitor system. 56 response channels, attached with Kapton tape / acrylic adhesive were acquired through the GSFC DDAS.

The NEAR finite element test model again gave good agreement with the fundamental frequencies uncovered during test:

FE Model Summary:

Item	Z Axis FE Model Prediction, (Hz)	Z Axis Actual Frequency, (Hz)
Spacecraft Outer Structure	31.5	32.6
Propulsion System	72.4	70.4
Solar Panel Cg	19	24.5

The spacecraft outer structure and PS predictions once again correlated well with the test results. Although the panels proved to be slightly stiffer than predicted, the FEM correctly predicted the large *lateral* response of the solar panels to thrust axis vibration, caused by the rotation of the rather long, offset hinge arm about the hinge axis. Structural damping (NASTRAN Param G = 2(C/Cc)) was set at 5% for the test FEM analysis; for the 32.6 Hz mode it was measured at 7.4% during the pre- and post-test 0.1 G sine surveys.

Z Axis Loads Summary:

Listed below are the protoflight accelerations (1.25 x max expected) to be achieved during Z axis structural testing as provided by MDAC for the NEAR thrust axis 3rd stage cutoff event. The propulsion system had previously been qualified to 10.6 G's in thrust. A JHU/APL memo recommended 1.25 x 2.48 = 3.1 G's (max expected from coupled loads analysis) as a reasonable workmanship level for the propulsion subsystem to achieve during spacecraft

thrust axis testing. The Z axis protoflight sinusoidal test levels given above were successfully applied to the integrated spacecraft. At the fundamental spacecraft resonance of 32.6 Hz., the following accelerations were generated:

Location	Z Axis Level to Achieve, (G's) (-1 G added by gravity)	Z Axis Level Generated During Testing, (G's)
Forward Deck	+8.4/-9.4	12.4
Spacecraft CG	+8.4/-9.4	8.7
Aft Deck	+8.4/-9.4	6.4
Propulsion System CG	3.1	2.8

The thrust axis mode shape of the spacecraft outer structure at 32.6 Hz resulted in an uneven acceleration distribution through the structure. Limiters were set based on the mass distribution within the structure to generate the proper structural loads at the top of the spacecraft adapter. When factored by mass, the outer structure saw an equivalent quasi-static acceleration of +8.9/-9.9 G's, comfortably above the +8.4/-9.4 G's needed.

As shown above, the acceleration levels needed to generate protoflight structural loads in the spacecraft outer structure were achieved. As recommended by GSFC, a 1/2 level swept sine test was performed before and after the full level test to check for any changes in structural response. No change in any part of the spacecraft was noted after comparison of the data obtained from both tests.

Post-Vibration Mechanism Tests:

Clampband Separation Tests:

Test Date: 10/5/95

The clampband was successfully separated from the spacecraft adapter and dropped approximately 18 inches onto foam. The ordnance was fired using MDA- supplied hardware. The test was performed twice.

Instrument Door Post-Vibration Deployments:

Test Date: 10/6/95

NLR and NIS Doors: Successfully deployed
MIS Door: Successfully deployed

Spacecraft commands were used to fire the ordnance for each instrument door to demonstrate proper door and electrical harness operation after vibration.

Despin System Deployment Test:

Test Date: 10/6/95

The configuration consisted of the flight despin weight assembly and cabling, with flight plunger lubrication, mounted on the spacecraft. The despin cable tension was set to the flight tension (20-25 lb.). Both pyros were fired using spacecraft commands, successfully deploying both weights with no problems noted.

NEAR SPACECRAFT TESTING RESULTS AT GSFC

Protoflight Acoustic Testing

Test Date: 10/19/95

The test was conducted in the GSFC Reverberate Acoustical Test Facility. The spacecraft was in full flight configuration with the exception of the use of non-flight despin helper cables (loosely mounted), certain aft deck, aft side thermal blanket simulators in place of flight blankets, and a non-flight safeing plug. The spacecraft was attached to the handling dolly through a Delta II test PAF and test clampband. The PS tanks were filled with deionized water to represent a fully loaded system at launch. The propellant tanks and the helium tank were pressurized to 140 and 1700 psig respectively, with nitrogen, duplicating the flight mass while giving at least a 4:1 safety factor relative to burst pressure to allow for personnel access during testing.

The test objective was to apply protoflight (+3 dB above max expected) acoustic noise to the spacecraft. 147.2 dB spl overall was achieved, fulfilling the requirement of 147.6 $\pm$ 1 dB. Test duration was 60 seconds.

Fifty-six channels of data were recorded using the GSFC DDAS. No change or degradation of any part of the spacecraft was noted.

Spacecraft Mass Properties Testing

Test Dates: 10/17, 10/18/95; 10/20, 10/23/95

The test article consisted of the NEAR spacecraft with the integrated propulsion subsystem. The spacecraft used the dummy attach fitting and dummy clampband for attachment to the mass properties mechanical GSE. The propulsion subsystem tanks were filled with deionized water as described above.

Originally scheduled to be performed before vibration testing at JHU/APL, a failure in the JHU/APL mass properties machine (the day before testing was to have begun) caused the test to be rescheduled to be performed at GSFC. To streamline the test schedule at GSFC, mass properties testing of the tare items were performed before acoustic testing, with mass properties of the spacecraft measured after acoustics. The objectives of the test were to generate a partial set of mass properties by measurement, with the spacecraft spin balance and CGz measurements being the most important. Based on the measurements, the spacecraft mass properties spreadsheet was updated to duplicate the results; the spreadsheet in turn was used to generate the required items which were not measured. A proof test of the spacecraft's ability to withstand a 3 sigma high (69 rpm) spin rate could not be accomplished due to the lack of horsepower available from the GSFC spin machine. This test was accomplished during KSC spin operations. The loads generated by the proof spin test were not design loads and are enveloped by the sine vibration testing done previously.

Spin balance testing was accomplished in 3 spin runs with a total of 16 lb. of weights required, while only 11.25 lb. were predicted before testing was begun. After a careful review of the location of the CG of the electrical harness (the least known of the items in the sheet), the mass properties spreadsheet was used to shift slightly the locations of the various components of the harness, with the end result being the proper prediction of the magnitude and location of the actual balance weights. Figure 4 illustrates the test setup for the horizontal mass properties measurements, CGz and Ix', using the turnover yoke.

After thermal vacuum testing, the spacecraft was weighed again for the official pre-ship weight.

Of interest is the measured Izz value of 182.5 slug-ft^2, an increase of approximately 11% over the spin inertia value of 165 slug-ft^2 as predicted by analysis. The updated inertia was used to modify the final yo-yo despin release weights. Investigation into the discrepancy revealed three main causes for the increase:

- An increase of approximately 5 lb. in the required vs. predicted balance weights.
- A poor representation of the despin weight assemblies as a point mass located at the spacecraft spin axis vs. distribution of the despin system at the aft deck corners.
- An inaccurate distribution of the spacecraft harness. The spacecraft harness was redistributed to better reflect the four vertical columns of harness which run inside the side panels.

After these changes were made to the mass properties spreadsheet, the predicted value of Izz was within 2% of the measured value. Confirmation of the accuracy of the value for Izz was obtained after launch when the NEAR yo-yo mechanism successfully deployed and despun the spacecraft to less than 0.8 rpm.

NEAR SPACECRAFT TESTING RESULTS AT KSC

Test Date: 1/30/96

Final spin balance operations were held in the NASA SAEF II Payload Processing facility with the fully flight configured NEAR spacecraft including the spin weights added during GSFC spin testing. Due to the excellent job KSC personnel did centering the test GSE on the spin table, a total of 2.26 lb. of balance weights were *removed* from the spacecraft for balancing. Final tilt angle for the spacecraft was calculated to be 0.10° (vs. 0.25° maximum allowable). The final static offset of the spacecraft CG was calculated to be 0.004 inches (vs. 0.050 inches maximum allowable). A total of five runs were required.

SUMMARY

The protoflight test program designed for NEAR successfully met schedule yet provided an adequate set of conservative mechanical tests which qualified the spacecraft for flight. Use of a relatively simple interface between the propulsion subsystem and the spacecraft essentially allowed each major piece of the spacecraft to be qualified separately, compressing the overall program schedule. Good correlation between analysis, test and flight performance was achieved.

DEFINITIONS AND ACRONYMS

CCAS	The Cape Canaveral Air Station
DDAS	NASA/GSFC Digital Data Acquisition System
FEM	Finite Element Model
Flight Acceptance	The maximum expected level and duration for a load or environment
GEVS-SE	GSFC General Environmental Verification Specification
GSE	Ground Support Equipment
GSFC	The Goddard Spaceflight Center
JHU/APL	The Johns Hopkins University Applied Physics Laboratory

MECO	Main Engine Cutoff
MDA	McDonnell Douglas Aerospace
MIS	Multispectral Imager
MSC	MacNeal-Schwendler Corporation
NASA	The National Aeronautics and Space Administration
NASTRAN	NASA Structural Analysis - a general purpose finite-element structural analysis code.
NEAR	Near Earth Asteroid Rendezvous
NIS	Near-Infrared Spectrograph
NLR	Near Laser Rangefinder
PAF	Payload Attach Fitting
Primary Structure	Load bearing structure carrying the main structural loads
PS	Propulsion subsystem
Protoflight	Qualification environmental level applied for a flight acceptance duration
Qualification	The maximum expected level and duration for a load or environment, multiplied by a program-specific factor to add design margin.
Secondary Structure	Structure such as brackets, clips, etc. not in the main load path of the spacecraft.
TIRDOC	Test Interfaces and Requirements Document

Acknowledgments

The test team for NEAR involved scores of people, all of whom provided timely and much appreciated help. I wish to especially thank the following people: the JHU/APL Vibration Test Lab personnel, Harold Fox, Leon Garvin, Craig Hughes, and Robert Tomkiewicz, who are to be commended for their thorough pre-test preparation and excellent support during testing. Ed Schaefer and Bill Skullney of JHU/APL, and Monty Kennedy representing GenCorp-Aerojet supplied valuable insight during data review between vibration axes. Ted Hartka, the NEAR Mechanical Engineer, whose far-ranging responsibilities included supplying all mechanical test GSE, as well as the NEAR spacecraft itself. At both JHU/APL and GSFC, the GSFC DDAS team of Don Baker, Dan Keith, and Beth Montgomery provided seamless and very professional support during the NEAR vibration tests. Development of the TIRDOC, which greatly aided overall coordination between JHU/APL and GSFC was accomplished by Bill Wilkinson for JHU/APL and Joe Stecher for GSFC. For the mass properties and spin testing at GSFC, Don Hirshfeld and K. C. Shah were instrumental in organizing and conducting a successful test on very short notice after the failure of the JHU/APL mass properties machine. Finally, at KSC, Randy Hick's knowledge and help proved invaluable to the successful and timely completion of spin balance testing.

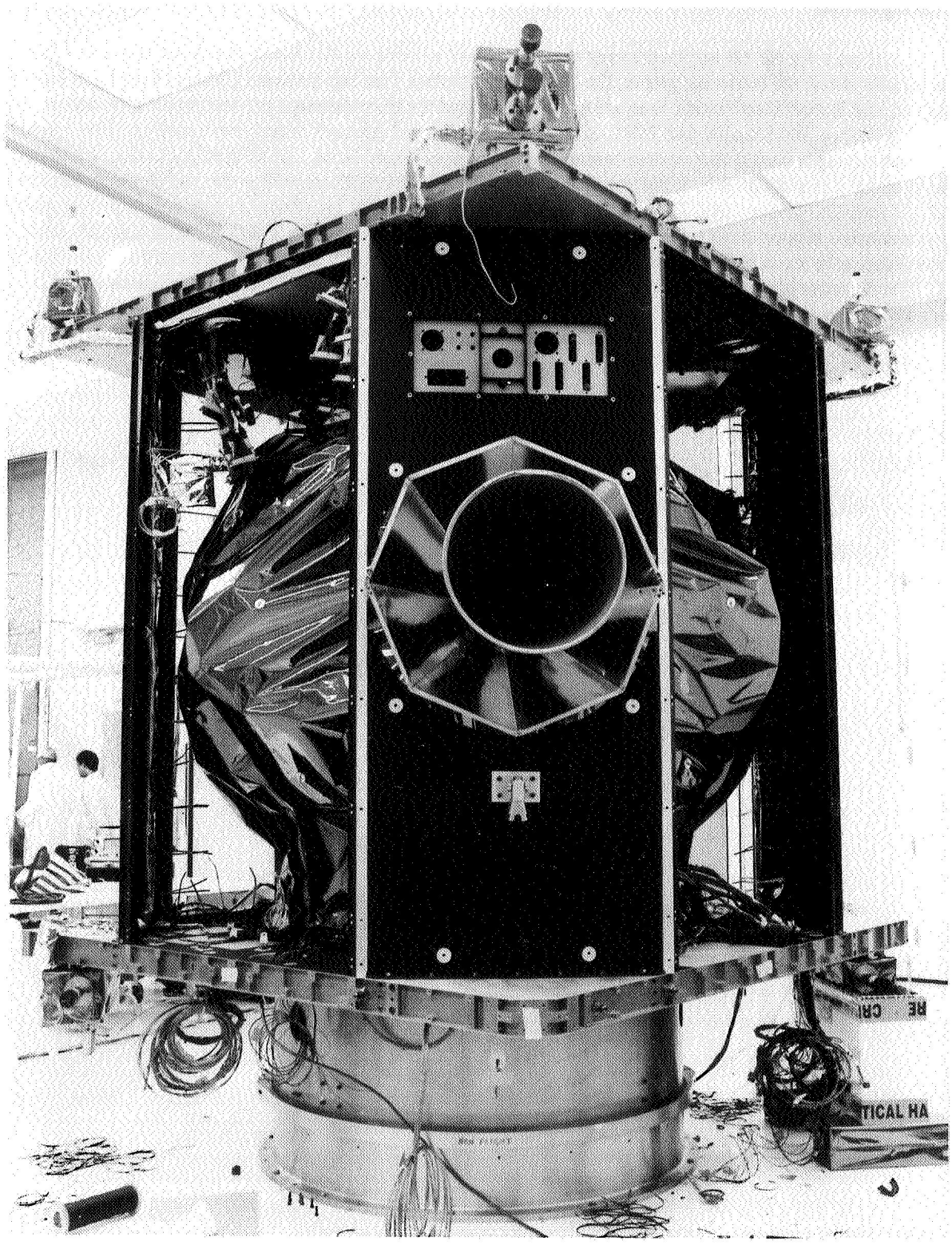


Figure 1. **The NEAR spacecraft aluminum honeycomb structure with the blanketed propulsion subsystem visible during integration.**

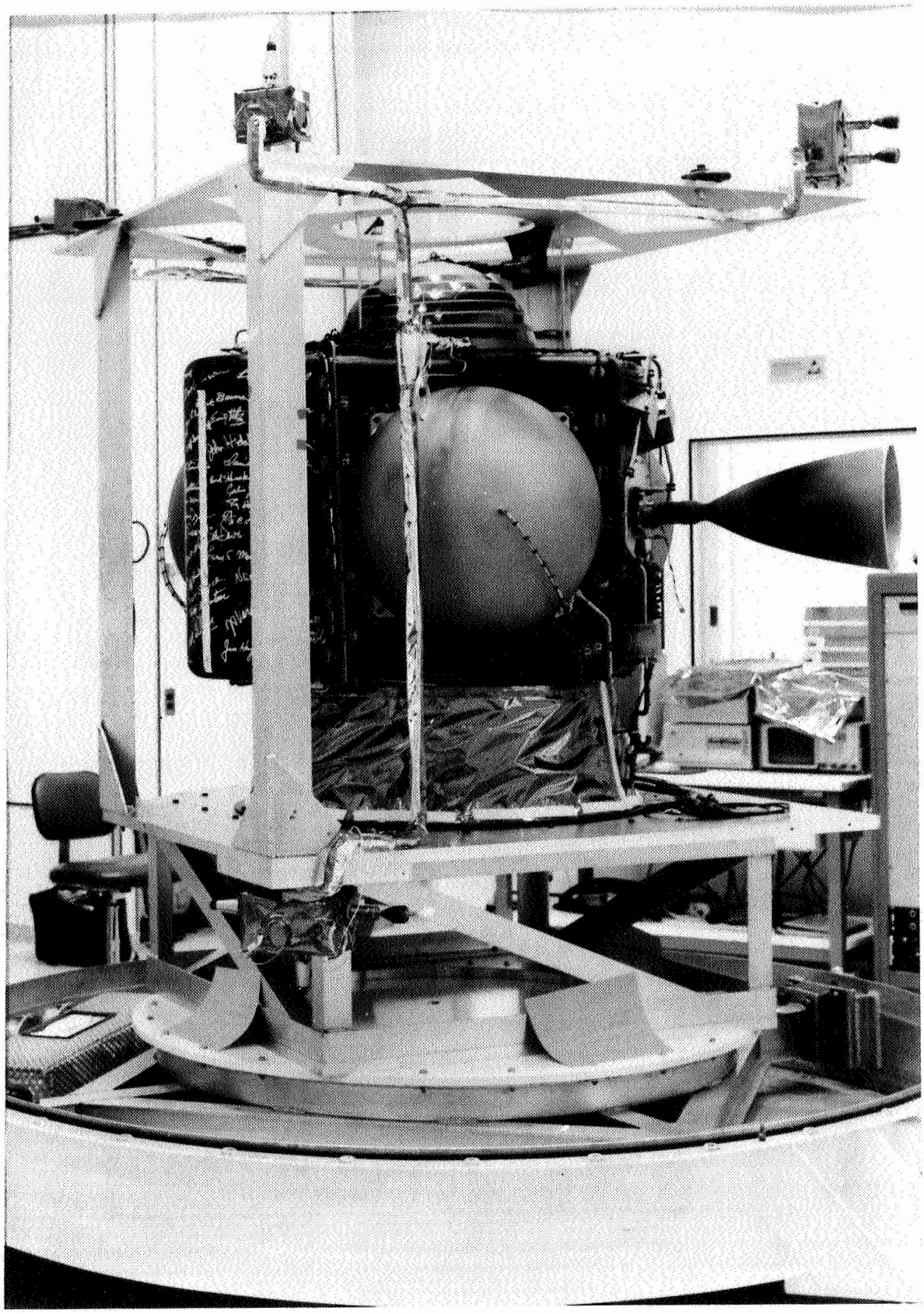


Figure 2. **The propulsion subsystem shown before integration in its shipping frame. Note the titanium tanks and the large 100 lb. side-mounted main thruster.**

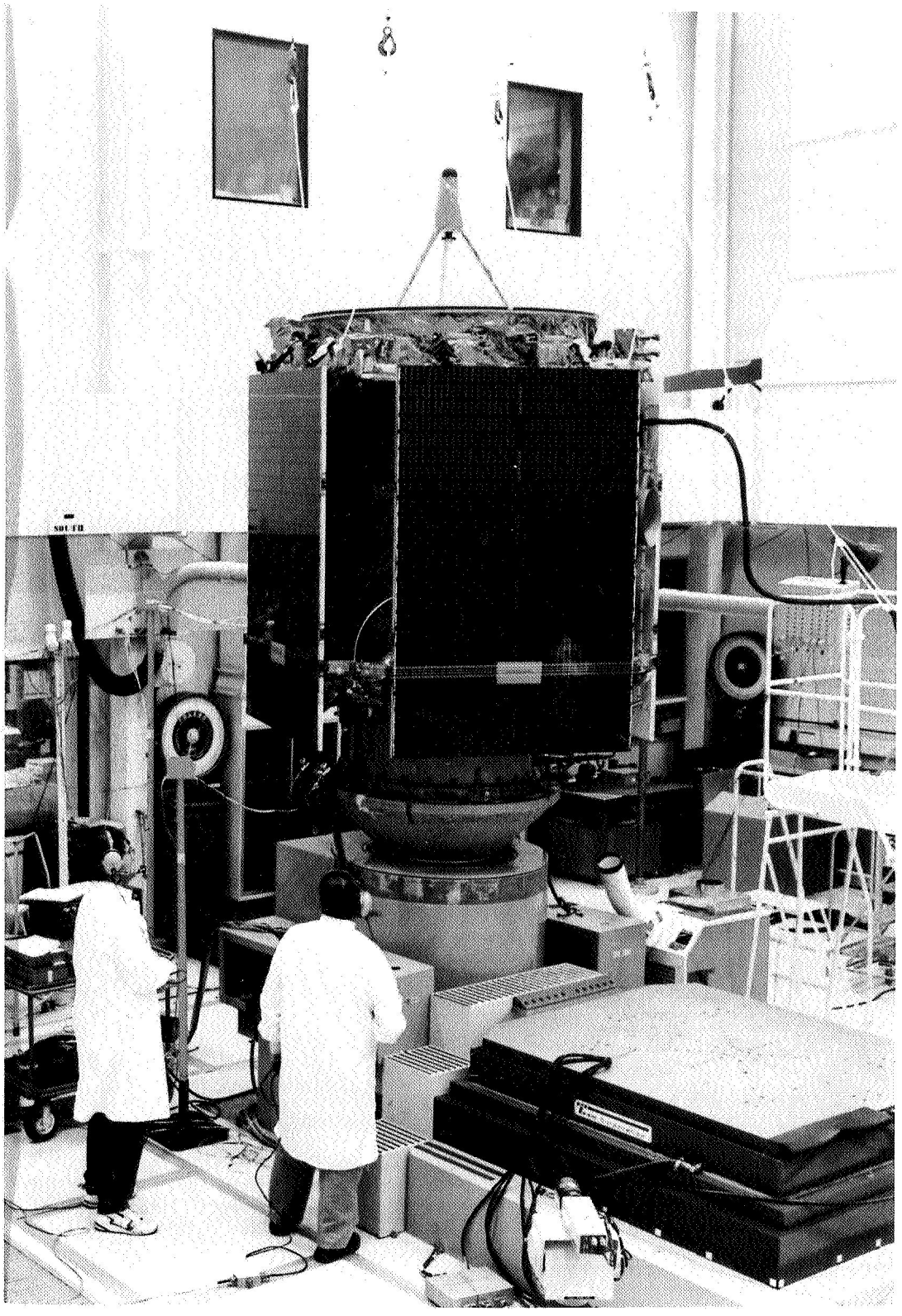


Figure 3. **The NEAR spacecraft during thrust axis vibration testing at JHU/APL. Note the despin cable wrapped around the solar arrays.**

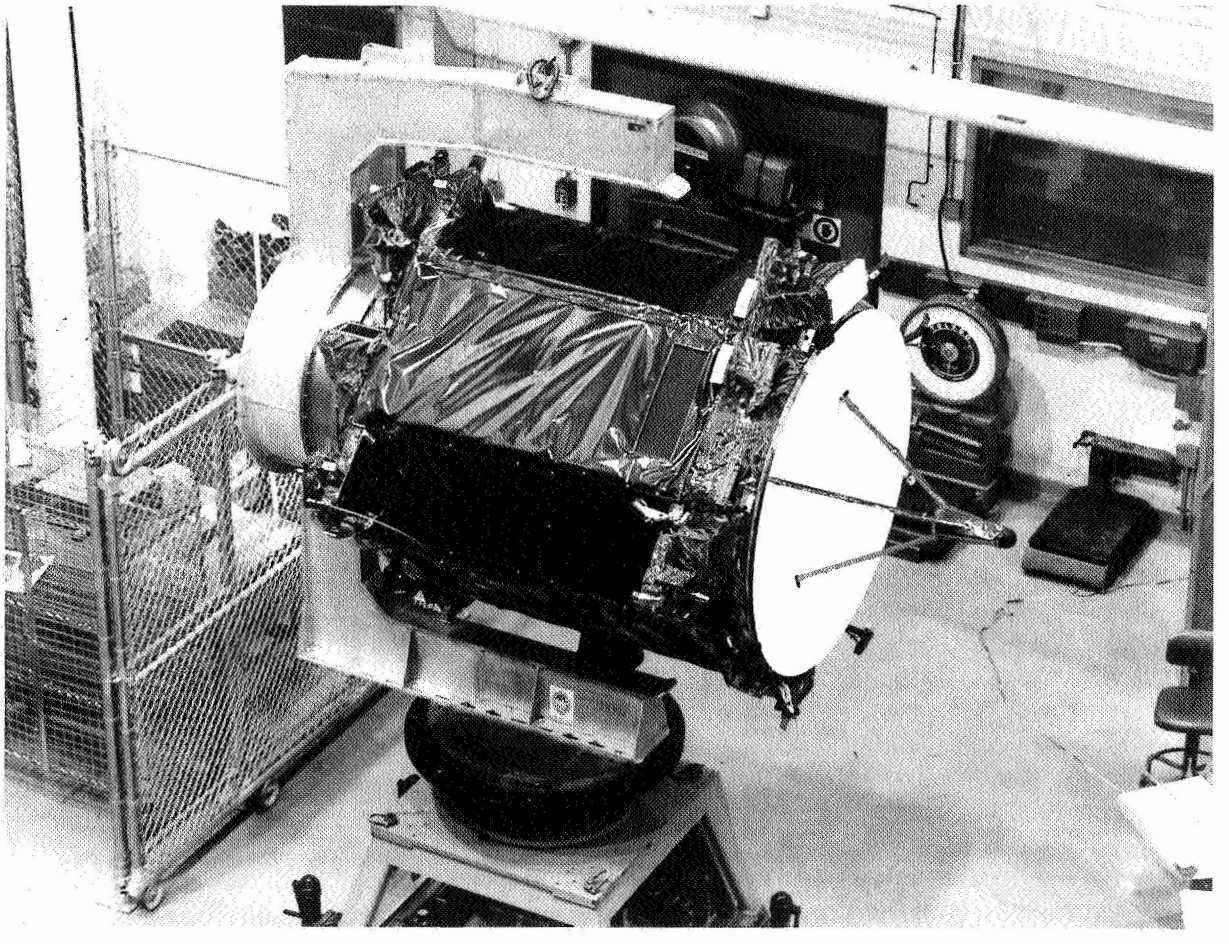


Figure 4. **The spacecraft with the solar arrays removed during horizontal mass properties testing at GSFC. Note the 1.5 m. diameter high gain antenna assembly.**

021452 S13-18 ABS. ONLY

Launch Vibroacoustics Simulation and Validation of Transmitting Antennas of Telecommunications Satellites

M. Fornesi, L. Trittoni, P.C. Marucchi-Chierro, and M. Milano

1P 069382

Spacecraft structures during launch phase are submitted to heavy acoustic excitation mainly generated by the engines and the aerodynamic forces over the vehicle.
Since satellite dimensions are getting larger, as well as structures are getting lighter, sensitivity to acoustic enviornment increases and the vibration levels become critical, especially for large panels with small thickness.
A tipology of substructures which can be included in this category are transmitting antennas of telecommunications satellites.
The activity reported in the present work concerns the vibroacoustic analysis performed on the HOTBIRD 3 antenna, considering launch noise excitation and covering the complete frequency range related to the acoustic spectrum.
In the low frequency field, a deterministic approach, based on FEM method, has been followed.
The high number of d.o.f. of the model and the wide extension in frequency of the acoustic load require the choice of a limited number of load cases that could be used to reproduce the excitation.
In the high frequency field, a statistical approach, based on Statistical Energy Analysis (SEA), has been employed; this method considers the effect of many, closely spaced modes, simultaneously active, and is therefore particularly suited to treat high modal density problems.
Due to the difficulty to accurately evaluate both damping coefficient and joint acceptance, it is opportune that a turning of the mathematical model is performed on the basis of test experiences conducted an analogous structures.
In this study, this activity of correlation has been conducted on HOTBIRD 3 antenna.
From the comparision between acceleration levels analytically evaluated and experimentally measured, the effectiveness of the analytical approach chosen to perform the vibroacoustic analysis of the antenna in the whole requested frequency range (typically for octave bands with center frequency 31.5Hz up to 8Khz) is pointed out.
In particular, the agreement between the results obtained with deterministic and statistical methods has to be highlighted.

314-39
021456
10P
45V
269384

ACCELERATION TESTING-A BETTER, FASTER, CHEAPER ALTERNATIVE FOR STRENGTH QUALIFICATION TESTING

Carmine F. Mattiello
Environmental Test and Integration Branch
Goddard Space Flight Center
Greenbelt, Maryland

ABSTRACT

This paper addresses the advantages of utilizing a centrifuge test over the conventional static load test methods to structurally qualify aerospace structures. Three recent test cases are reviewed and used as examples to highlight these benefits. In addition, the overall capability of Goddard's High Capacity Centrifuge (HCC) is outlined along with some unique features that were designed specifically to reduce costs, test turn around time, and increase test item safety.

INTRODUCTION

A strength qualification test as referenced by this paper is defined as the method used to demonstrate that the test item remains structurally sound under simulated conditions more severe than expected from ground operations, launch, orbital operations and landing (ref. 1). There are basically three methods for strength qualification testing: acceleration testing, static load testing , and vibration testing. There are many issues to consider in deciding which method fits test item requirements the best. This paper will assume that vibration testing is not an option or will be used as a supplemental test. Therefore only static load and acceleration testing are considered.

Static Load Testing:

For static load testing the loads are applied at selected points in an effort to simulate some uniform load distributed over the entire structure. If desired, specific points may be selectively loaded while leaving others unloaded. At Goddard Space Flight Center (GSFC), static load testing requirements are implemented using hydraulic actuators that are attached to designated load application points on the test item, and controlled manually with a mechanical hand pump. The load is controlled by monitoring load cells and hydraulic pressure. Occasionally, load application points will be tied together and controlled by a single load line (one hydraulic actuator, one load cell). This method of testing works well in applying the required loads, but it can be very labor intensive in terms of test design, fabrication, and set up. For static load testing the test item remains fixed and the load source is moved to get the desired effect.

Acceleration Testing:

During acceleration testing the load is essentially uniformly distributed throughout the structure. This is accomplished by fixturing the test item on an acceptable centrifuge and allowing the centrifugal force to load the structure. An acceptable centrifuge has a large enough payload radius to minimize the centrifugal force gradient over the entire test item. Passive restraints are used to minimize damage in the event of a structural failure since the test item cannot be unloaded quickly at high speed (however, passive restraints have never been needed). Therefore, for acceleration testing the test item is fixtured and the resulting centrifugal force applies the proper load vector. In addition, at GSFC all facility fixturing for static load and acceleration testing is designed to a safety factor of three on the material yield strength, and proof tested to a factor of 1.5 on the maximum loading condition.

ADVANTAGES -Acceleration Testing:

- The structural load distribution is much more representative of the actual flight loading condition than a static load test.
- Problems with load application point identification and location go away since there is no load line attachment to the test item.
- Load application control and coordination is no longer an issue.
- Use of the innovative fixturing minimizes test reconfiguration time.
- The total cost of the test can be reduced since that an HCC test can be far less labor intensive than a static load test.
- Changes in the load vector can be easily accommodated.

ADVANTAGES -Static Load Testing:

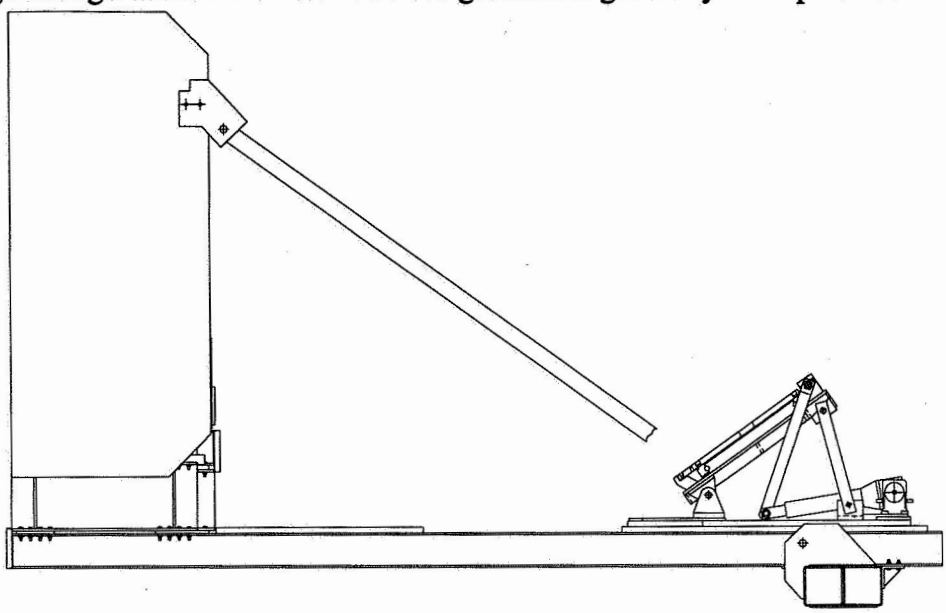
- If a problem arises the test item can be unloaded quickly.
- Particulate contamination is not a concern (a stirring of the air during acceleration testing has raised questions about particulate contamination, but it has never been a problem).
- The ability to apply a load to selected points while leaving other points essentially unloaded.

GENERAL INFORMATION:

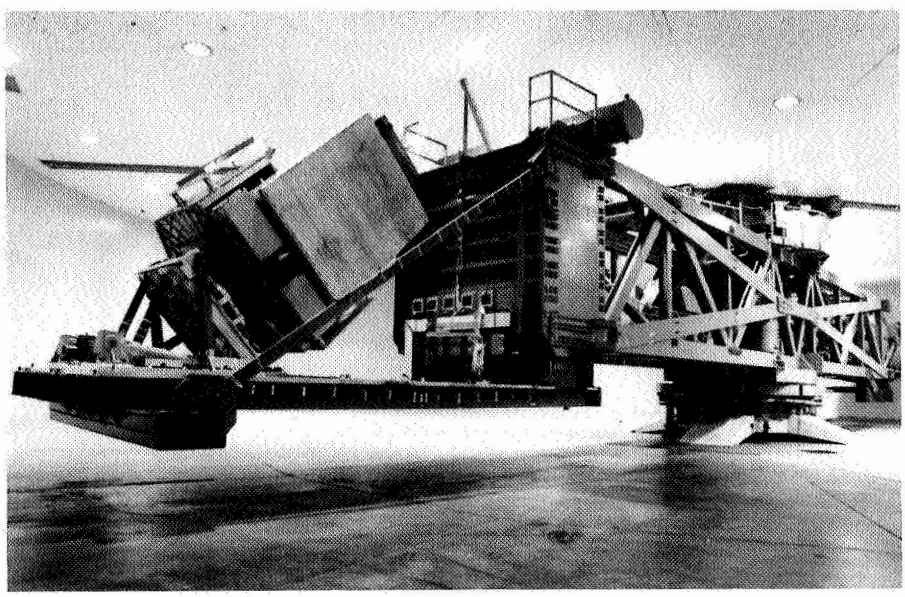
The High Capacity Centrifuge (HCC) is a Goddard Space Flight Center (GSFC) facility used to qualify aerospace structures for flight by subjecting them to a centrifugal force field.

- 38m (125 ft) diameter
- 18m (60 ft) nominal payload radius

- Powered by two 1250 HP DC motors
- Top speed of 38 rpm- 30 g's at the payload interface
- Designed to handle a moment of 846,000Nm (7,500,000 lb.in) or a shear load of 668kN (150,000 lb) at the platform interface.
- Instrumentation capability of 192 channels
- Large enough that the acceleration field gradient is generally not a problem.



The Goddard Space Flight Center High Capacity Centrifuge (HCC)
Test Platform

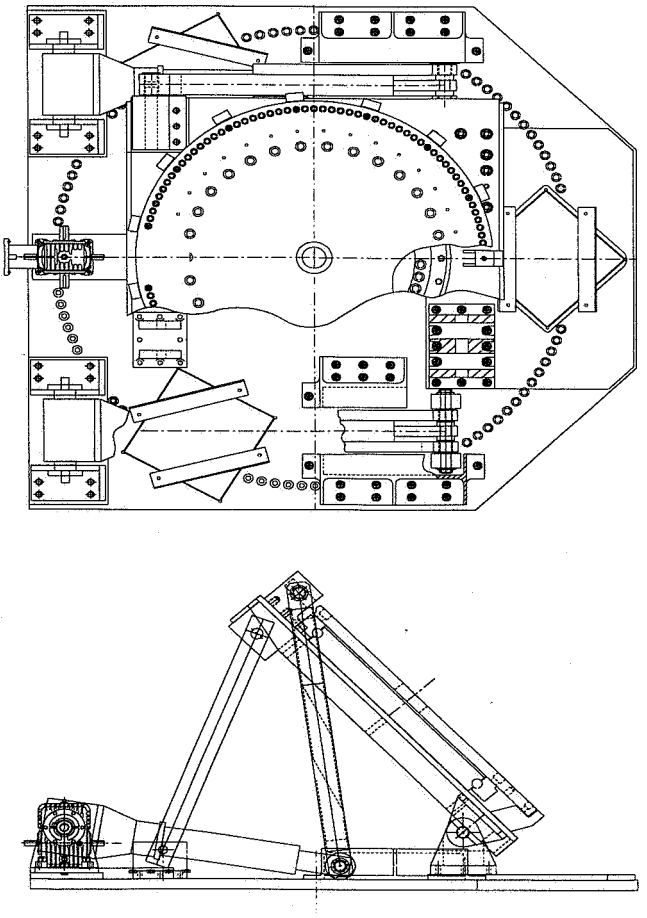


High Capacity Centrifuge-Overall View

FIXTURING

The Low Profile Tilt Fixture (LPTF) allows aerospace structures to be lifted and mounted vertically, secured and rotated into position. Subsequent reconfiguration to other load cases without unbolting and moving the spacecraft minimizes the handling risk and greatly reduces the reconfiguration time.

The LPTF allows three degrees of freedom. The first degree comes from rotating the entire payload tilt fixture assembly about the vertical axis via air bearings. This allows an inboard or outboard tilting attitude. The second degree of freedom is achieved by rotating the test item on the bearing mounted top plate, and the third degree is attained by tilting the top plate to the desired angle. Low profile comes from the fact that this fixture is less than 50cm (20 in) thick. The tilt fixture top plate is moved by two ball screw actuators coupled together and driven by an electric motor through a 60:1 gear reduction interface mechanism. Once the test configuration is achieved, custom stanchions are put into place to take the driving mechanism out of the load path during the test.



Low Profile Tilt Fixture

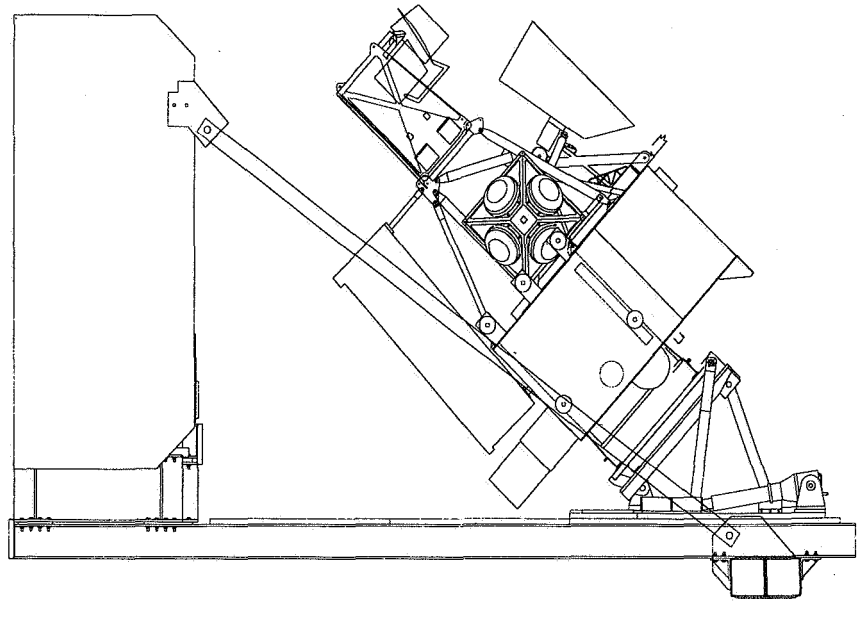
TEST CASES

Tropical Rainfall Measuring Mission (TRMM)

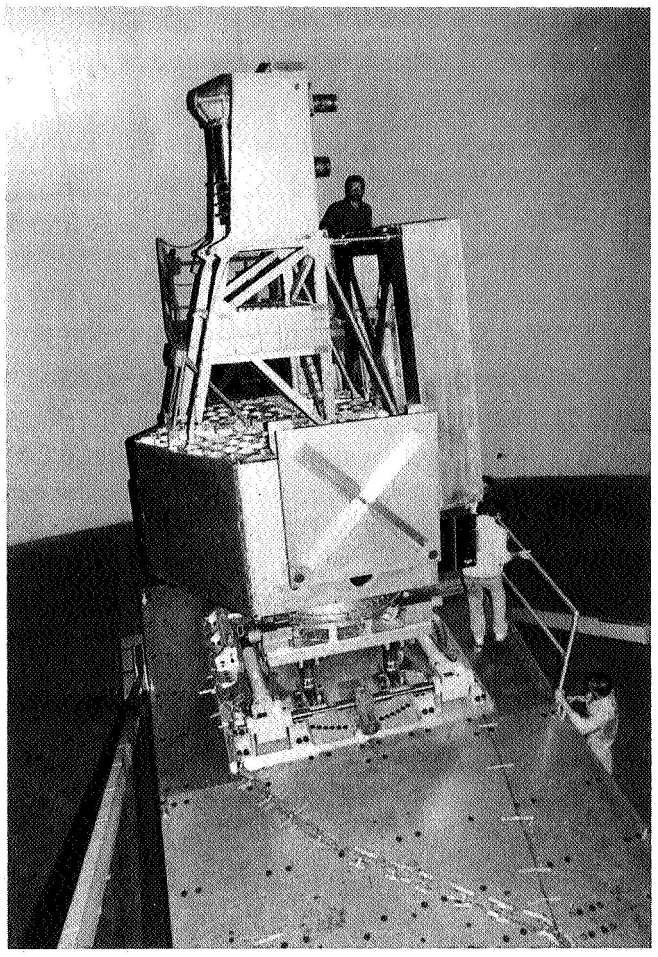
The TRMM spacecraft will be launched on a Japanese H-2 rocket in 1997.

TRMM is a large spacecraft structure at 3627kg (7980 lb) and a height of about 5m (17 ft) including a simulated internal fuel load of 909 kg (2000 lb). A feasibility study determined that an acceleration test was the most cost effective method of achieving the desired test loading. There were a number of difficult to access load application points on the spacecraft and dimensional restrictions on our Static Load Test facility that contributed to the acceleration testing decision. One of the most difficult loads to simulate was the internal spacecraft fuel load.

The load cases were performed in a sequence that allowed for the quickest turn around time between tests. Figures 1 and 2 show the TRMM Spacecraft on the HCC configured for testing. The inboard oriented load cases 1 and 3 were run at 19.60 rpm corresponding to a 7.28 g centrifugal force on the test item. Load case 2, oriented outboard was run at 13.94 rpm with a resultant 4.13 g loading.



TRMM Load Case #3
Fig. 1



TRMM Load Case #2
Fig. 2

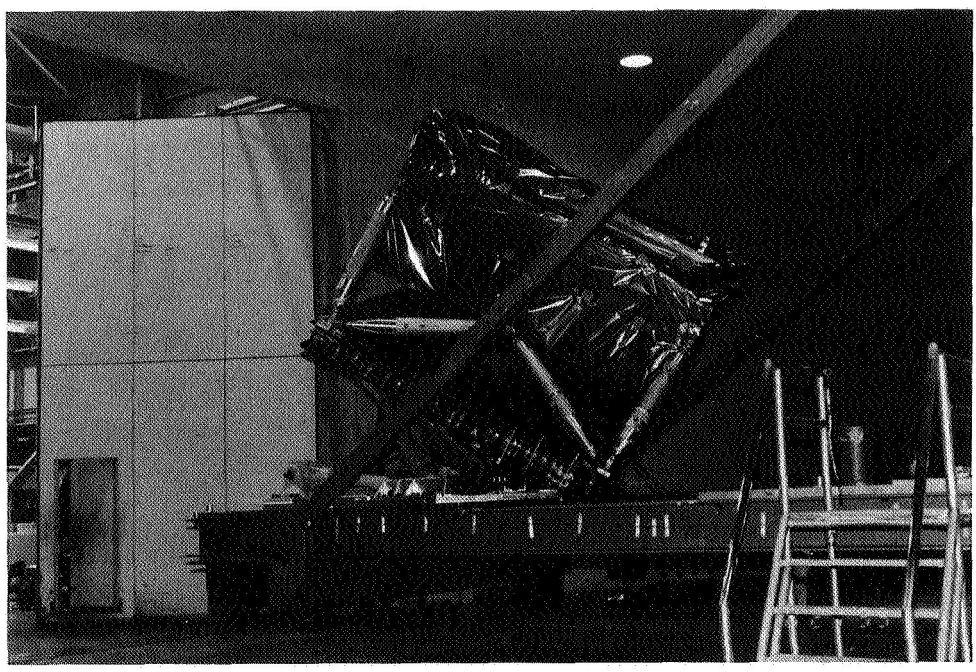
The TRMM spacecraft was instrumented with 93 strain gages, 4 string potentiometers, and 1 Linear Variable Differential Transformer (LVDT). Also, 3 accelerometers were mounted on the HCC platform at the TRMM Center of Gravity (C.G). location to obtain a direct measurement of acceleration vector components. In addition, 32 strain gages, 4 string potentiometers and 1 LVDT was mounted on the HCC structure itself. The allowable test tolerances were -5% to +1% on g load.

Initial test runs up to 40% of maximum load were done for the first two load cases to review the data and to remove any hysteresis. Data was acquired to disk and printed out at each load increment. Also, 20 channels were monitored and 6 others graphed in real time. The entire test was successfully completed in less than 4 days.

Hubble Space Telescope (HST) Axial Scientific Instrument Protective Enclosure (ASIPE)

The ASIPE will be used as a protective enclosure for an upgraded instrument on the upcoming second HST servicing mission.

This test required an unusual fixturing to simulate the load distribution of eight "load isolators" intended to act as shock absorbers during the launch environment. The ASIPE was tested on the HCC primarily because the instrument mass simulator was located inside the ASIPE and was inaccessible for the direct application of external forces. Acceleration testing afforded the ability to load the ASIPE internal instrument attachment points. In addition, the quick reconfiguration time resulted in a short overall test and completely eliminated the need for potentially hazardous load application hardware adjustments in close proximity to flight hardware. Figure 3 shows the HST ASIPE in one test configuration.



HST ASIPE
Fig. 3

The two ASIPE test configurations both oriented inboard, were run at 18.96 and 19.40 rpm. The resulting centrifugal force was measured at 7.09 and 7.37 g's respectively. The ASIPE was instrumented with 88 strain gages; 32 evenly divided among the 8 struts, 16 on the clevises and 40 on the ASIPE. An LVDT was used to monitor movement and an accelerometer was mounted for a direct measurement of acceleration components. The

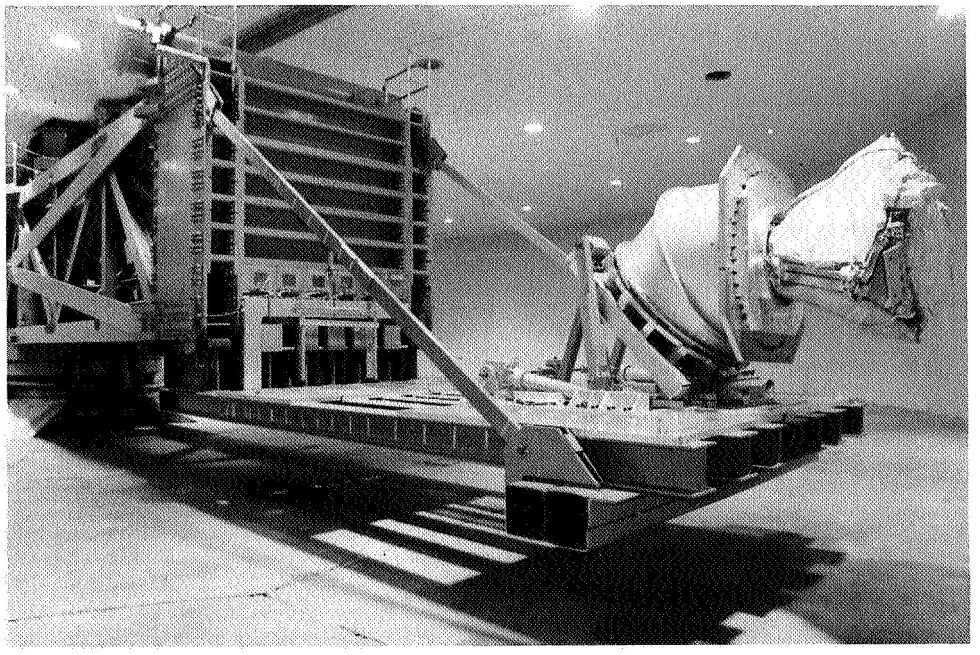
weight of the ASIPE and struts was 887 kg (1930 lb) and the weight of the fixturing was 1803 kg (3968 lb) for a total test weight of 2690 kg (5898 lb).

Mars Pathfinder

The Mars Pathfinder will be launched in late 1996 and arrive on Mars in July 1997.

The complete test program from initial contact with the project until completion was accomplished in a total of 9 days. It would have been extremely difficult to design a static load test to meet the requirements in such a short time. The acceleration loads achieved during this test were the highest in recent experience (26g's). The Mars Pathfinder project was very interested in the acceleration effects on the stowed gas bags and restraint system. This information was unobtainable with conventional static load testing. Once all the test and interface requirements were known, the Pathfinder/facility interface hardware needed to be proof tested to 1.5 times the maximum test load. The LPTF allowed facility fixturing to the Mars Pathfinder quickly and between test reconfiguration without delay. The addition of a conventional tilt fixture to the LPTF gave the capability to attach the Pathfinder to the HCC in the vertical and configure for a 90 outboard run.

The test item weighed 227 kg (500 lb) and the fixturing an additional 993 kg (2185 lb) for a total test eight of 1220 kg (2685 lb). Figure 4 shows the Mars Pathfinder in the outboard test configuration. The inboard load case was run at 24.82 rpm resulting in an 11.6 g loading. The outboard case was run at 33.64 rpm and resulted in a 26 g loading.



Mars Pathfinder
Fig. 4

SUMMARY

The HCC is capable of simulating loading conditions which cannot be duplicated by conventional static load testing. Experience has shown that this method of strength qualification testing can be superior in terms of cost, test fidelity, and overall test completion time. Not all aerospace structures are candidates for centrifuge testing because of size, fixturing constraints, or other unique requirements. However, acceleration testing should not be dismissed without serious consideration.

References:

1. Milne, J. S., 1990, "General Environmental Verification Specification for STS Payloads, Subsystems, and Components," NASA Goddard Spaceflight Center p.1-5

S15-39
021457

A METHOD FOR IMPLEMENTING FORCE-LIMITED VIBRATION CONTROL

369398 14P

Daniel B. Worth
NASA Goddard Space Flight Center
(301) 286-5140
daniel.worth@gsfc.nasa.gov

ABSTRACT

NASA/GSFC has implemented force-limited vibration control on a controller which can only accept one profile. The method uses a personal computer based digital signal processing board to convert force and/or moment signals into what appears to be an acceleration signal to the controller. This technique allows test centers with older controllers to use the latest force-limited control techniques for random vibration testing. The paper describes the method, hardware, and test procedures used. An example from a test performed at NASA/GSFC is used as a guide.

INTRODUCTION

Overview of Force Limiting

During a conventional random vibration test, a slip table or a shaker head is driven to a specified acceleration power spectrum. The specification is usually derived from an envelope of flight tests with similar payloads. This conservative approach insures that an undertest will not occur. In some frequency bands, this approach produces a significant overtest — especially at the fixed-base natural frequencies of the test item. When the test item (space craft or instrument) is mounted on the launch vehicle or spacecraft, the item will act as a frequency absorber near the region of fixed base natural frequency. In other words, peak accelerations and possibly damage will occur during testing at certain frequencies which in flight will be sharply reduced and will show up as dips in the spectrum.

Force limiting is an attempt to reduce the effectively infinite impedance of the slip table or shaker head by limiting the interface forces. At the frequencies where the test item will resonate and act like an absorber, the interface force will limit the vibration level and produce a dip in the acceleration spectrum. One could also limit based on moments or any other measured phenomenon. Methods for determining the force limiting spectrum are described in various papers [1,2,3].

System Description

Figure 1 is a sketch of a typical force-limiting control system. The outer loop, consisting of accelerometers, charge amplifiers, controller, drive amplifier, and shaker, is the conventional capability of any vibration control system. Force-limiting adds a force gage conditioning system, shown in the shaded boxes of figure 1. The force gages are added at the interface of the test item and the shaker head or table. The signals are conditioned by charge amplifiers and the force gage signal processing system. The signals are then sent to the controller.

The signal from the force gages is compared to a limit spectrum. Some controllers cannot handle more then one spectrum. The system discussed in this paper is designed to allow test facilities with such controllers to test using force limiting. The system described in this paper shapes the force gage signal into an acceleration signal that can be compared to the same specification used for the accelerometers. This system is described in detail in the following sections.

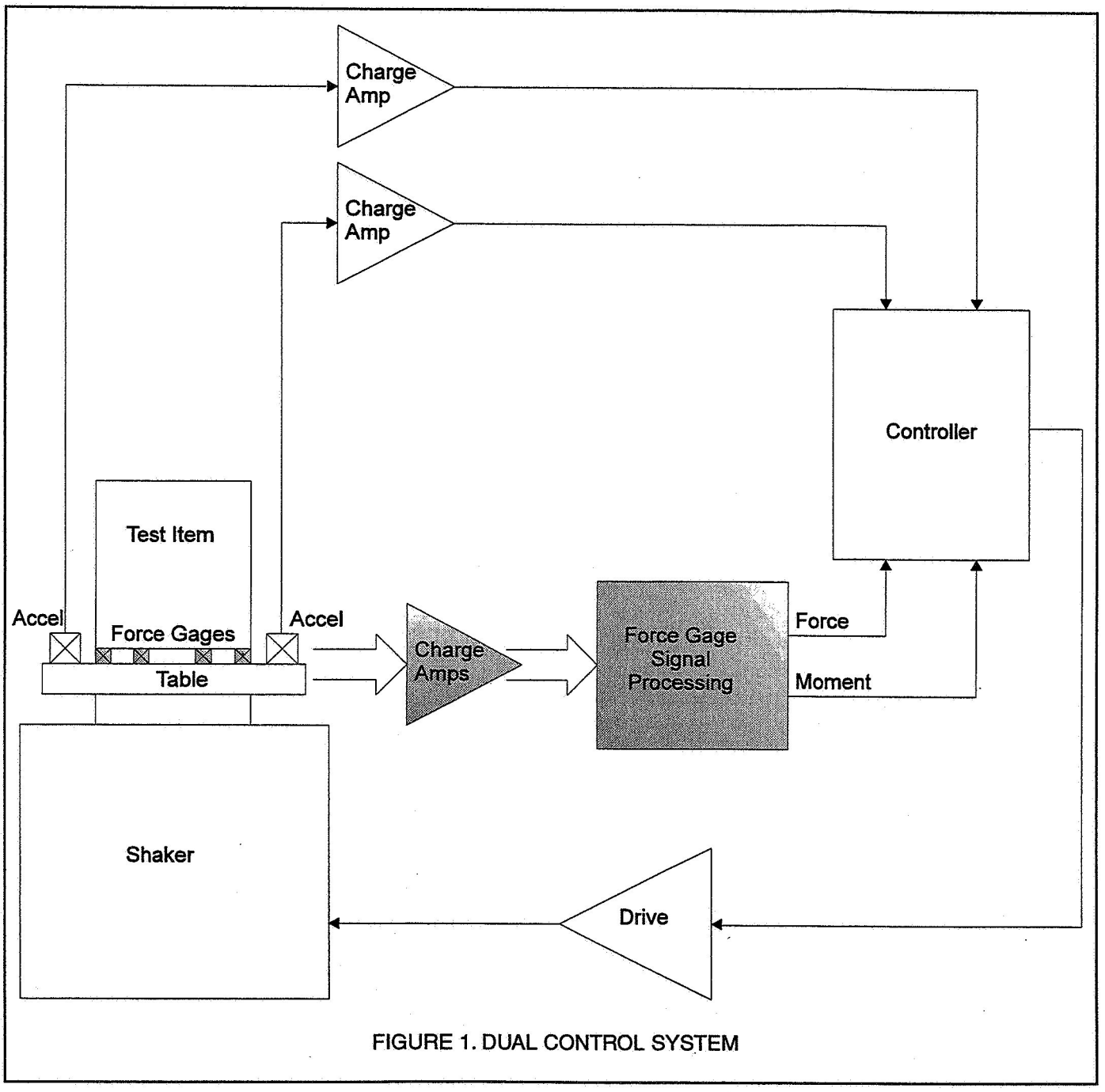


FIGURE 1. DUAL CONTROL SYSTEM

FORCE GAGE SIGNAL PROCESSING SYSTEM

A drawing of the force gage signal processing system is shown in figure 2. This system is designed to handle up to eight triaxial force gages, but can be expanded to a larger number by the addition of more Sum and Difference amplifiers. The number of force gages and the wiring between the Sum and Difference Amplifiers and the Digital Signal Processing (DSP) boards can be changed depending on the test configuration. Figure 2 is wired for a case where six triaxial force gages are used to measure six degrees of freedom — three translational forces and three moments.

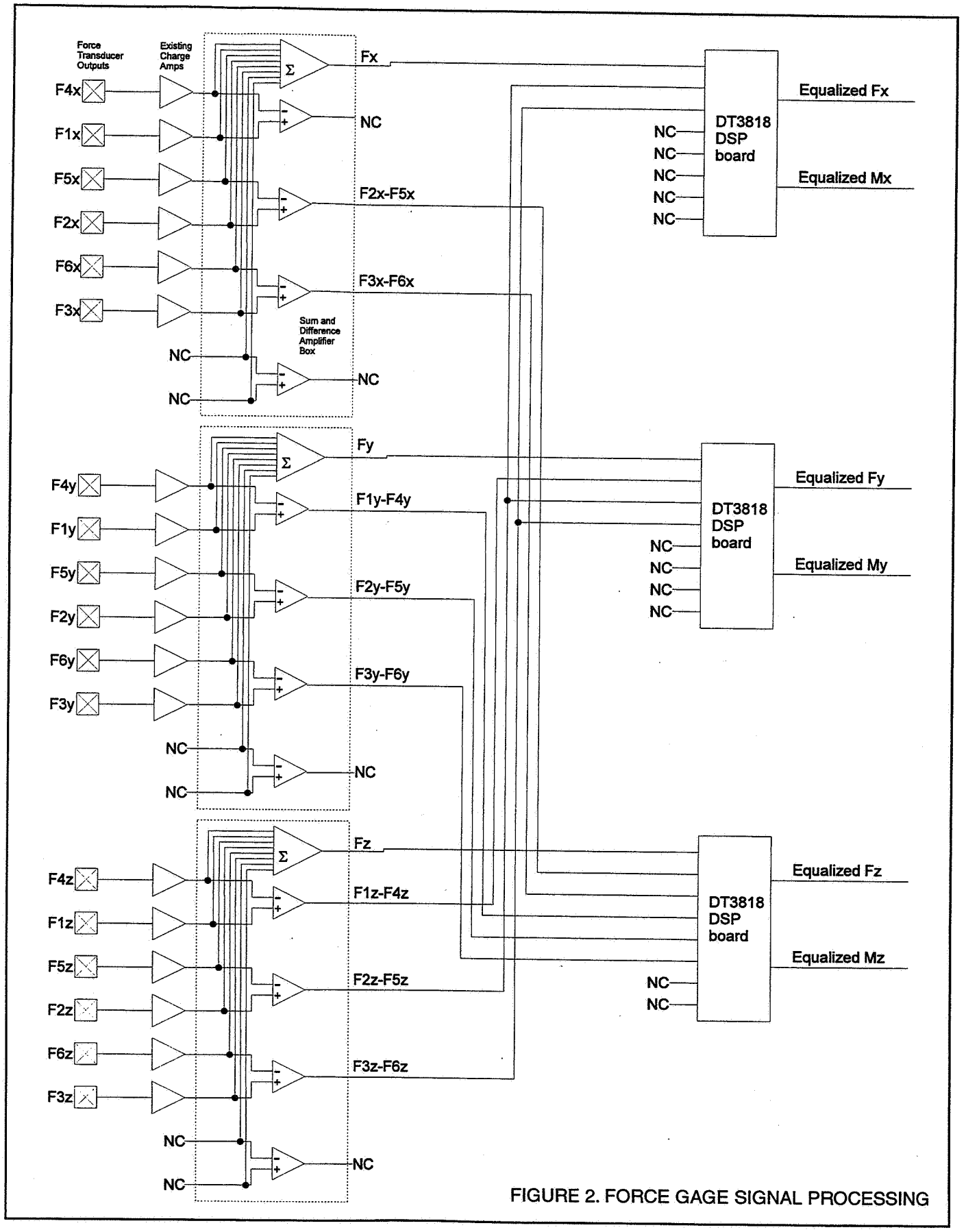


FIGURE 2. FORCE GAGE SIGNAL PROCESSING

Each force gage output is conditioned using charge amplifiers. Charge attenuators are sometimes used between the force transducers and the charge amplifier to prevent saturation of the amplifier input signal or clipping of the amplifier output signal.

The signals from each charge amplifier are fed into Sum and Difference Amplifier boxes. These boxes, as the name implies, sum all of the signals fed into the box and also compute differences between symmetrical pairs of conditioned force gage outputs. These computed difference signals are used to calculate moments. If no moments are to be calculated, or no individual monitoring of each force gage is desired, then a simple charge summing device can be used instead of the Sum and Difference Amplifier.

TABLE 1. SPECIFICATIONS OF DSP BOARD

Data Translation DT3818 DSP board (Fulcrum)
Texas Instruments TMS320C40 DSP @ 50 MHz
Eight Analog Inputs
A 16 bit Analog/Digital (A/D) converter for each channel
1 to 52 kilosamples per second maximum sampling rate per channel
Anti-Aliasing Filters for each channel
Two Analog Outputs
A 16 bit Digital/Analog (D/A) converters for each channel
Reconstruction Filter for each output channel
Data Translation DSP-EZ software runs on the board
 Basic language programming of TMS320C40
 Mathematical manipulation of buffers
 Highpass, Lowpass, and Bandpass Filtering available
 User defined filter
 Fast Fourier Transform (FFT) and Inverse FFT (IFFT)
Visual Basic VBX control runs on the Personal Computer
Properties of VBX control operate the A/D converter, D/A converter, and
 execute the DSP-EZ program.

The outputs of each Sum and Difference Amplifier Box are then routed to the DSP boards for scaling and equalization. The specifications of the DSP board are shown in table 1. The DSP board front-end amplifier and mixer provides scaling of each symmetrical pair of force gage signals to compute a given moment, or sum multiple gage outputs to produce a force sum. The front-end of the processing is shown in figure 3. The board accepts up to eight inputs (label F1 through F8 in figure 3) and computes two outputs (labeled F and M).

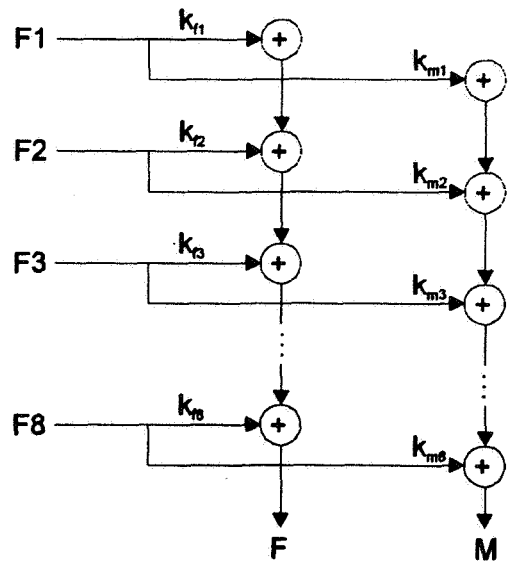


FIGURE 3. SUM, DIFFERENCE AND SCALING STAGE OF DSP BOARD

The output from the DSP board front-end is then equalized using the board's digital signal processor. A finite-impulse response (FIR) digital filter is used to perform the equalization. The FIR algorithm is shown in figure 4. Time-delayed samples from the front-end amplifier and mixer, x(n) through x(n-N), are scaled by constant coefficients a_1 through a_N and summed to produce one output sample y(n). This process is repeated continuously to produce a filtered, or equalized, signal. The advantages of a FIR filter include linear phase response (with proper choice of coefficients), and stability (since there is no feedback signal).

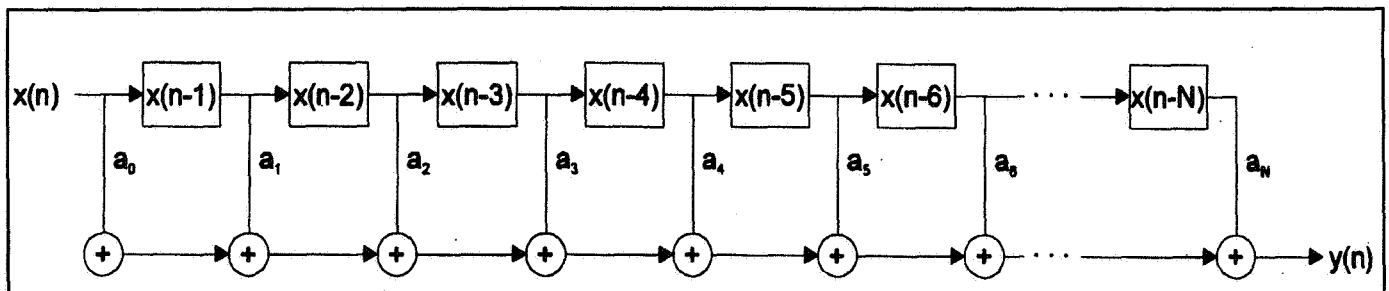


FIGURE 4. FINITE IMPULSE RESPONSE DIGITAL FILTER ALGORITHM

The equalized signal from the DSP board is then sent to the vibration control signal and is compared to the same profile used for the accelerometer signal. The only thing left to discuss is how to determine the coefficients used in the FIR equalizer.

DESIGN OF THE FIR FILTER

The steps used to design the FIR filter are summarized in table 2. These steps are discussed below using the Cryogenic Infra-Red Sensor (CIRS) instrument force-limited vibration test as an example.

TABLE 2. DESIGN OF FIR FILTER

Determine transfer function
Convert breakpoints to a real frequency spectrum
Perform IFFT
Rotate result
Truncate to a reasonable number of coefficients
Evaluate design using FFT
Test the filter

The CIRS instrument engineering test unit was tested in January and February of 1996. A photograph of the test setup is shown in figure 5. The locations of two of the six force gages are also shown in figure 5.

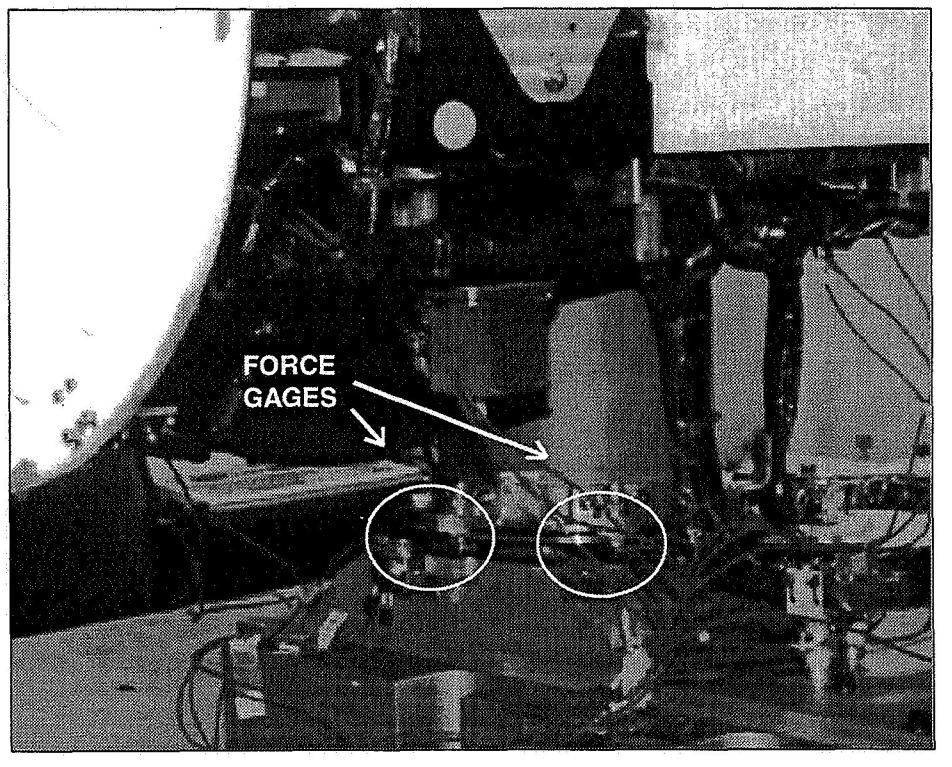
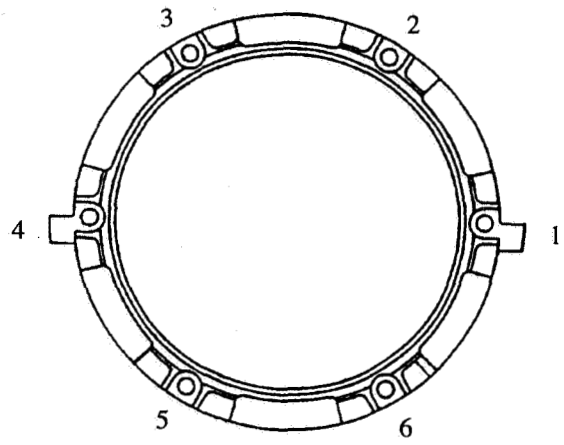


FIGURE 5. CIRS VIBRATION TEST

The CIRS instrument interfaces to the rest of the CASSINI spacecraft through a collar attached with six bolts. The bolt arrangement and the equations that determine the total forces and moments are shown in figure 6.



r = radius
a = 0.866r
b = 0.5 r

$$F_x = F_{1x} + F_{2x} + F_{3x} + F_{4x} + F_{5x} + F_{6x}$$
$$F_y = F_{1y} + F_{2y} + F_{3y} + F_{4y} + F_{5y} + F_{6y}$$
$$F_z = F_{1z} + F_{2z} + F_{3z} + F_{4z} + F_{5z} + F_{6z}$$
$$M_x = aF_{2z} - aF_{5z} + aF_{3z} - aF_{6z}$$
$$M_y = -rF_{1z} + rF_{4z} - bF_{2z} + bF_{5z} + bF_{3z} - bF_{6z}$$
$$M_z = rF_{1y} - rF_{4y} - aF_{2x} + aF_{5x} + bF_{2y} - bF_{5y} - aF_{3x} + aF_{6x} - bF_{3y} + bF_{6y}$$

FIGURE 6. CIRS COLLAR

Determine Transfer Function

How to determine the test acceleration specification and force specifications are not the subject of this paper. Given the CIRS z-direction acceleration and force specification power spectral densities (PSD), shown in figure 7 and figure 8 respectively, the transfer function breakpoints of the filter are determined by dividing the acceleration PSD by the force PSD and taking the square root. The result is shown in figure 9. A phase of zero for the transfer function is assumed with this approach.

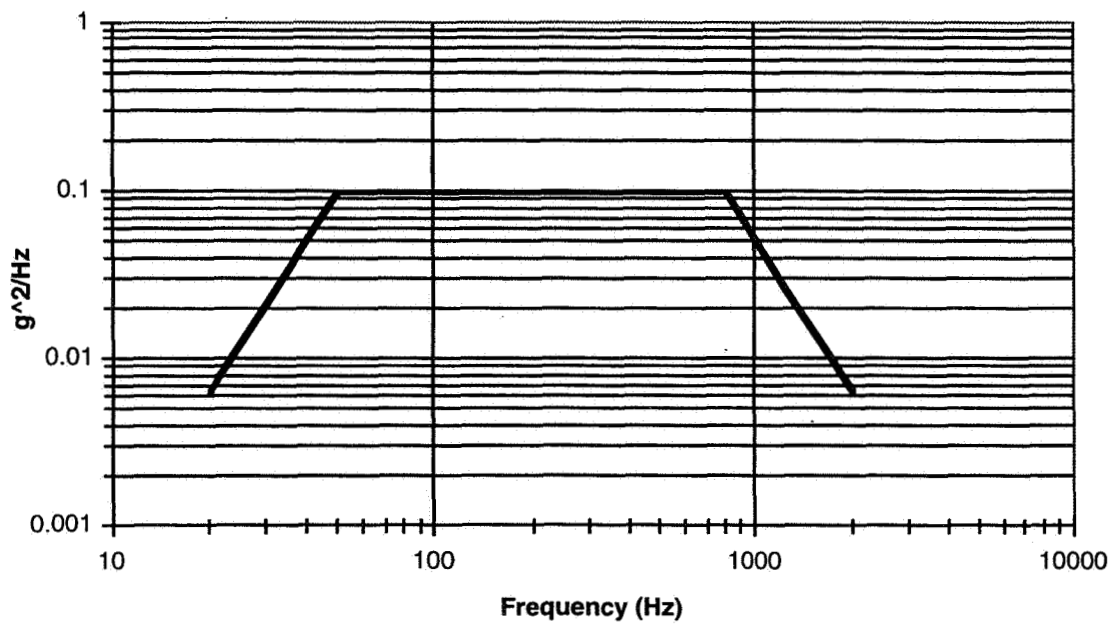


FIGURE 7. CIRS Z-DIRECTION ACCELERATION PSD SPECIFICATION

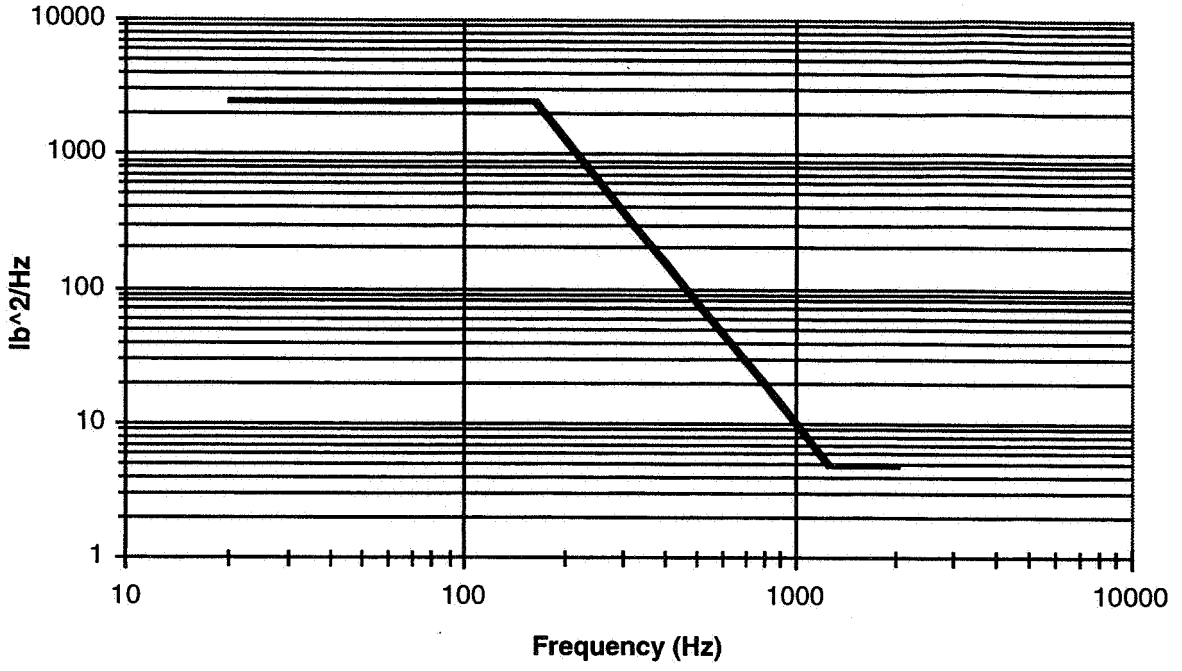


FIGURE 8. CIRS Z-DIRECTION FORCE PSD SPECIFICATION (FORCE LIMIT)

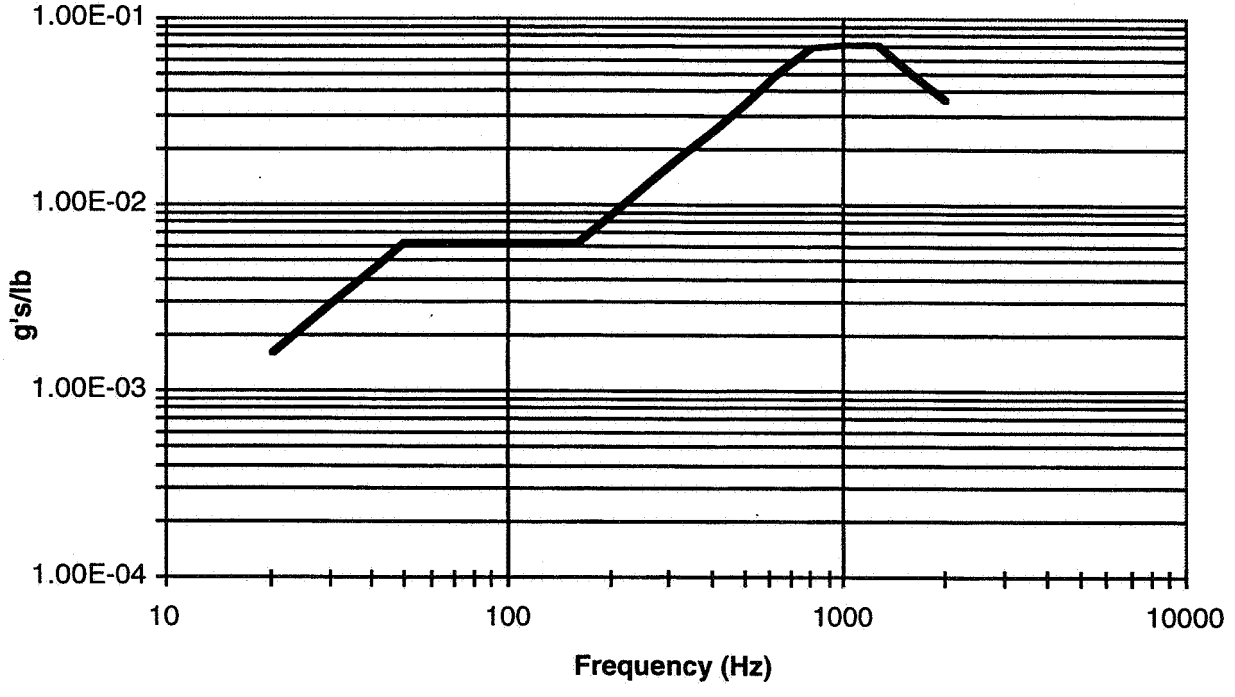


FIGURE 9. CIRS Z-DIRECTION FIR FILTER TRANSFER FUNCTION

Convert breakpoints to a real frequency spectrum

Real (as opposed to complex) filter impulse responses produce an FFT in which the mirror image values of one half are complex conjugates of each other[4]. The right half spectrum can also be considered the negative frequency spectrum. It is also desirable to create a filter which has zero or linear phase characteristic. This is done by taking the transfer function breakpoints from the previous step, interpolating linearly spaced values, and reflecting those values into the right half of the spectrum. The resulting spectrum is shown in figure 10.

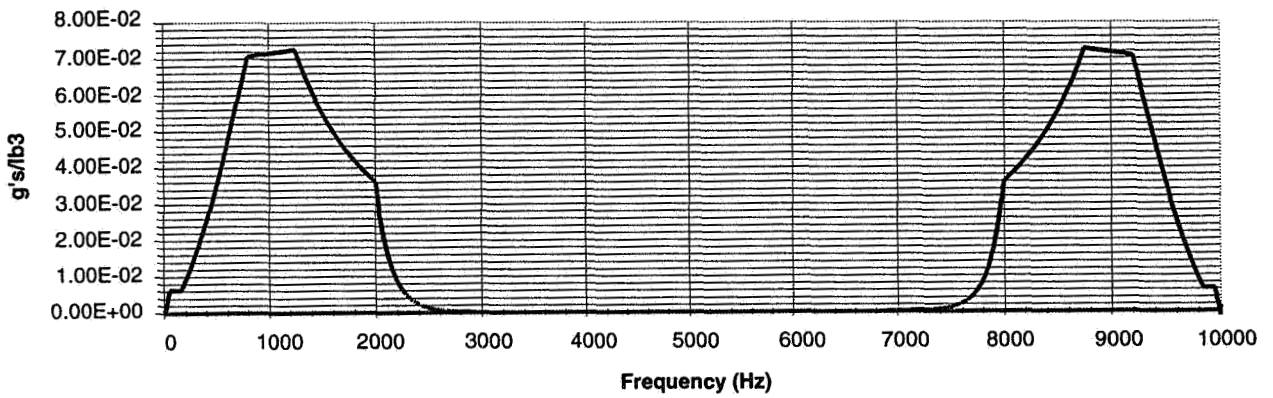


FIGURE 10. CIRS Z-DIRECTION FIR FILTER TRANSFER FUNCTION WITH NEGATIVE FREQUENCIES

This plot can be either be considered as a real spectrum with zero imaginary spectrum or a magnitude spectrum with zero phase. A zero phase spectrum is much easier to compute then a linear phase spectrum.

Perform IFFT

The impulse response of the desired filter is determined by performing an IFFT on the modified transfer function. This is shown in figure 11. One can think of the right-half of this plot as being the negative time response. This implies that the filter must have predictive behavior — that is, the response must begin before the input arrives. Because of the predictive behavior, the filter is non-realizable. Also note that most of the response occurs around zero time (or 0.04 seconds)..

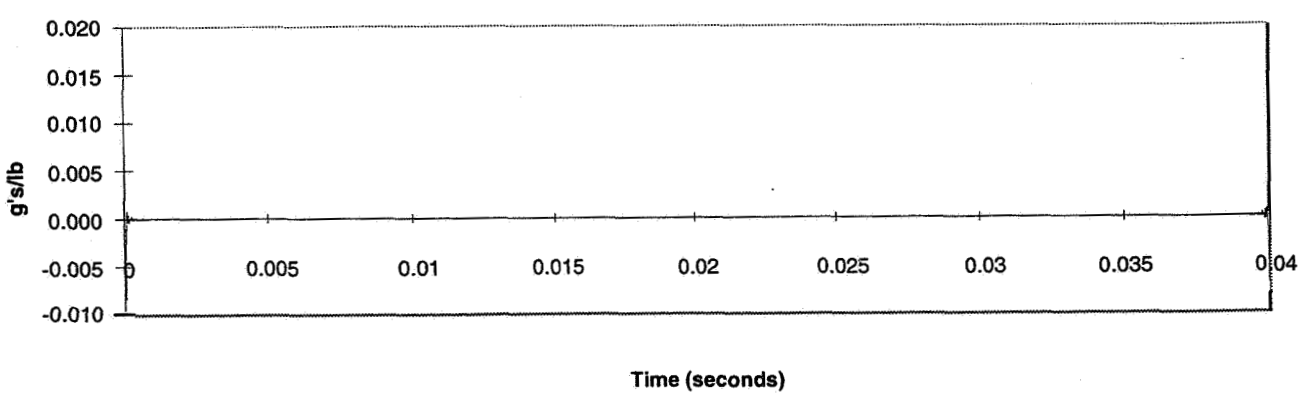


FIGURE 11. CIRS Z-DIRECTION FIR FILTER IMPULSE RESPONSE

Rotate result

To make the filter realizable, the response is delayed (or rotated) by 20 milliseconds. The resulting filter is shown in figure 12. This filter requires 4096 multiplications to be performed for each output sample. This would require a DSP that can perform 40 million multiplications and additions per second, which currently do not exist. The filter would also have a delay of 20 milliseconds, which is probably too much lag for a control loop.

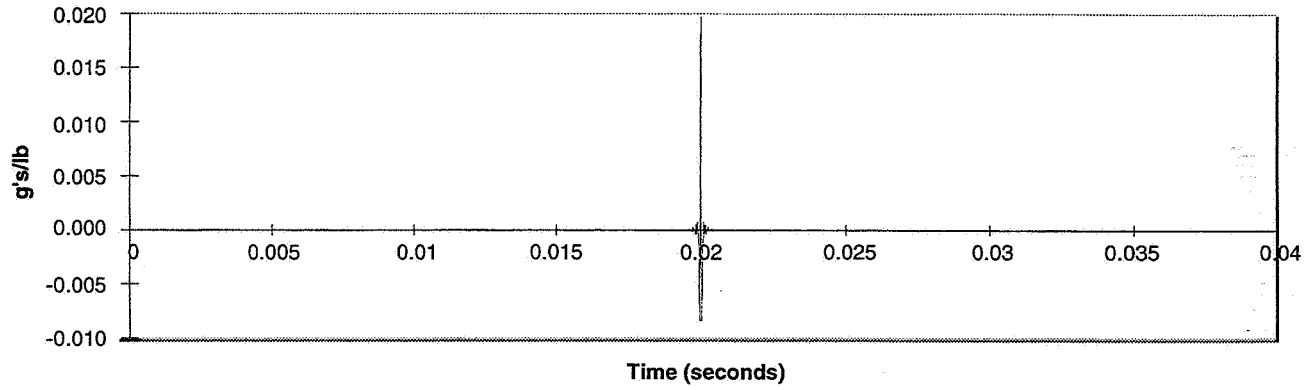


FIGURE 12. CIRS Z-DIRECTION FIR FILTER ROTATED IMPULSE RESPONSE

Truncate to a reasonable number of coefficients

Fortunately, not all of the coefficients are needed. Most of them are small compared to the ones clustered about the zero point. In this step the coefficients are truncated to a reasonable number and tested. A filter with 201 coefficients is shown on figure 13. Since the filter has bandpass characteristics, an odd number of coefficients should be chosen [5].

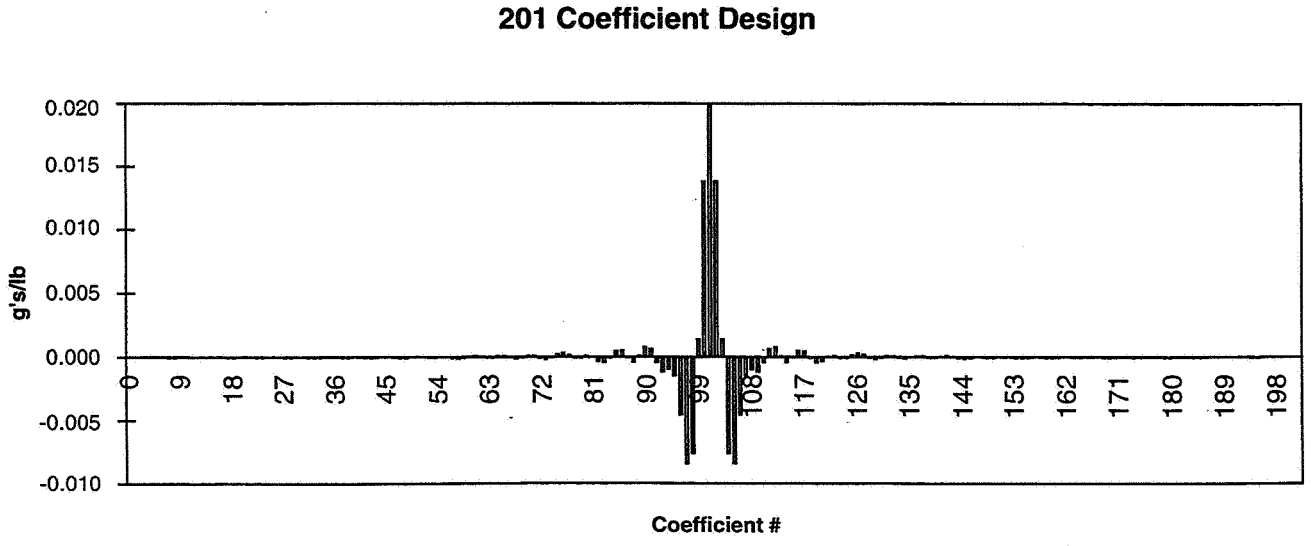


FIGURE 13. CIRS Z-DIRECTION FIR FILTER ROTATED AND TRUNCATED IMPULSE RESPONSE

Evaluate design using FFT

Various numbers of coefficients are tried and compared to the original specification. Figure 14 shows a comparison of 201 and 511 coefficient filters. Most of the deviation is at the 50 Hz region of the specification curve. The 201 coefficient filter would be acceptable for this application. Since the DSP currently in use by GSFC can handle 511 coefficients before overflow, we usually use 511 coefficients.

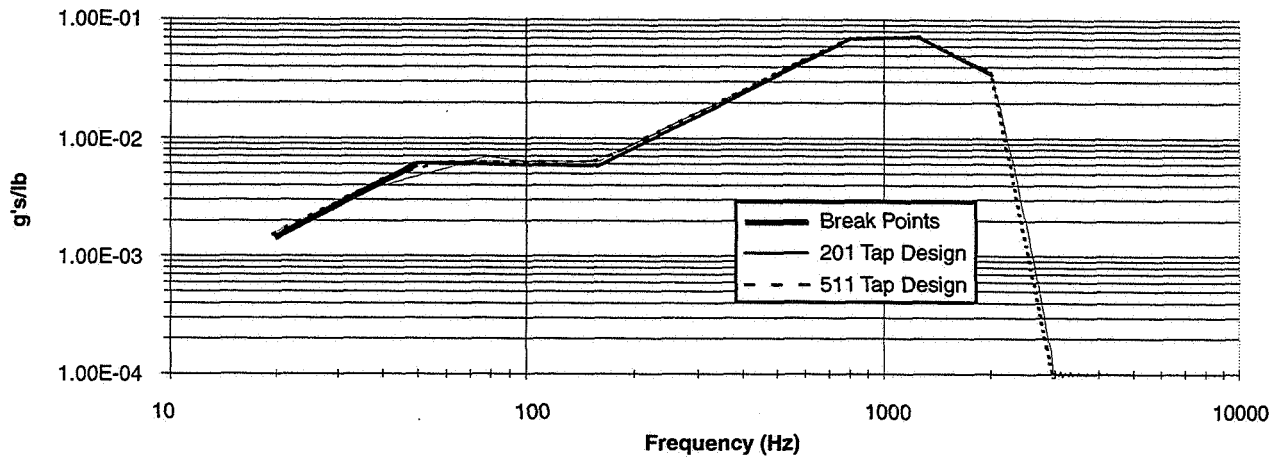


FIGURE 14. CIRS Z-DIRECTION FILTER — COMPARISON OF VARIOUS NUMBERS OF COEFFICIENTS

Test the filter

The filter characteristics are confirmed off-line by testing using a sine sweep test of the filter. At GSFC we use a Hewlett Packard 3566A FFT Dynamic Signal Analyzer to do this. A slow sweep must be used because of the significant filter delay.

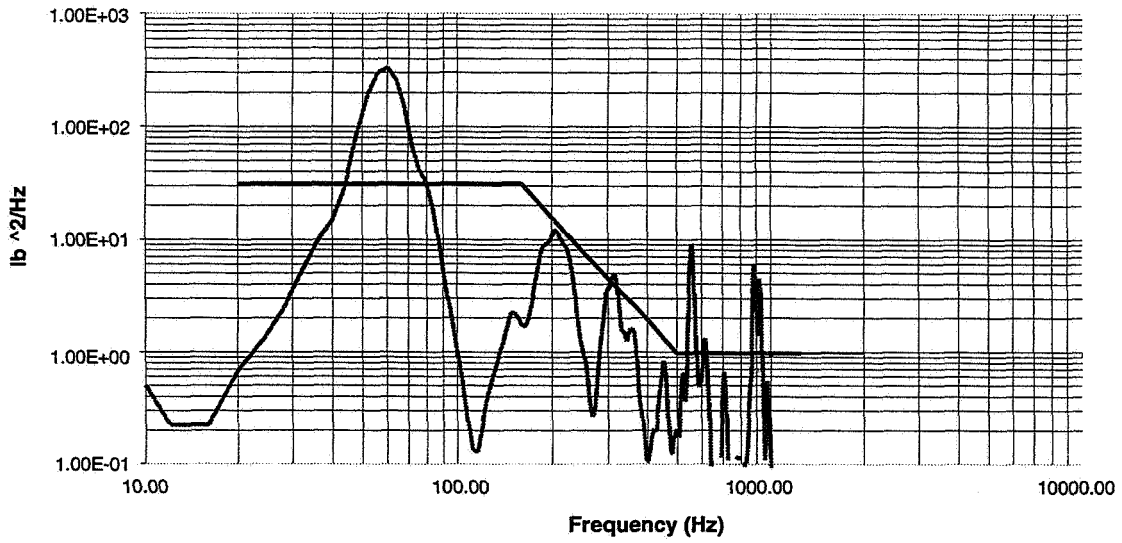


FIGURE 15. UNEQUALIZED FORCE COMPARED TO FORCE LIMITS

Recently GSFC has begun testing the filter during the actual random vibration test of the article. A test at low level (-12 or -18 dB) is performed without force control. The unequalized forces or moments are compared to the appropriate force or moment limits as shown in figure 15. The equalized forces or moments are compared to the acceleration specification as shown in figure 16. Places where the force or moments limits exceed the force or moment limits are noted and compared to the exceedances on the acceleration specification. They should match exactly. In the examples shown in figure 15 and figure 16, these exceedances occur at approximately 50 Hz, 530 Hz, and 900 Hz.

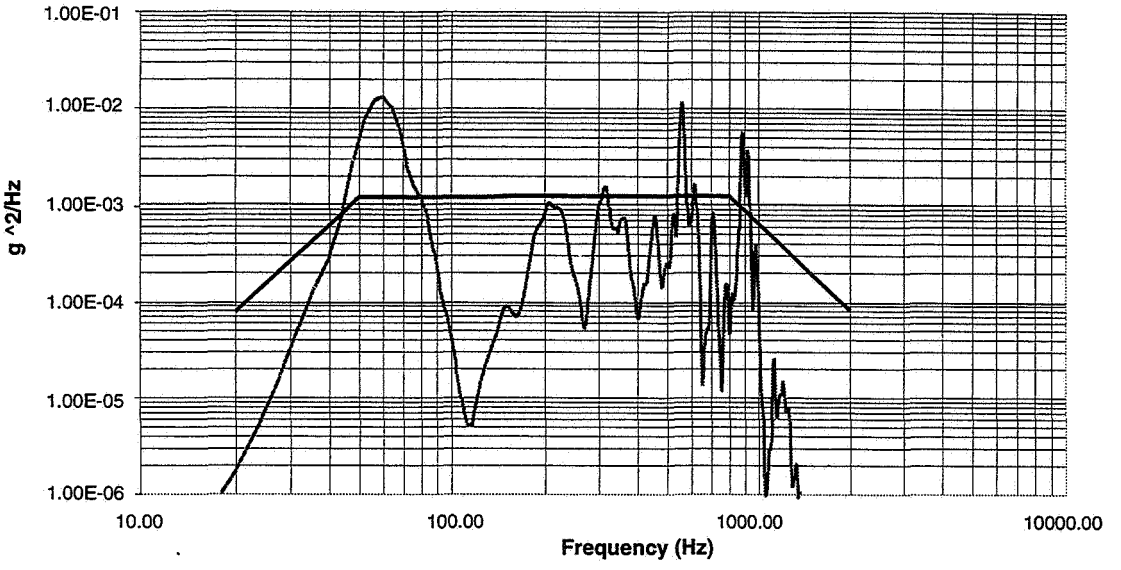


FIGURE 16. EQUALIZED FORCE COMPARED TO ACCELERATION LIMITS

Summary

A MS-DOS program was written in the C language to perform all of the steps required to design the FIR filter required to equalize the waveform. The software takes a text file containing the transfer function breakpoints as input and, with information about sampling rate and number of taps, produces another text file containing either the filter coefficients or the FFT of the coefficients for comparison purposes.

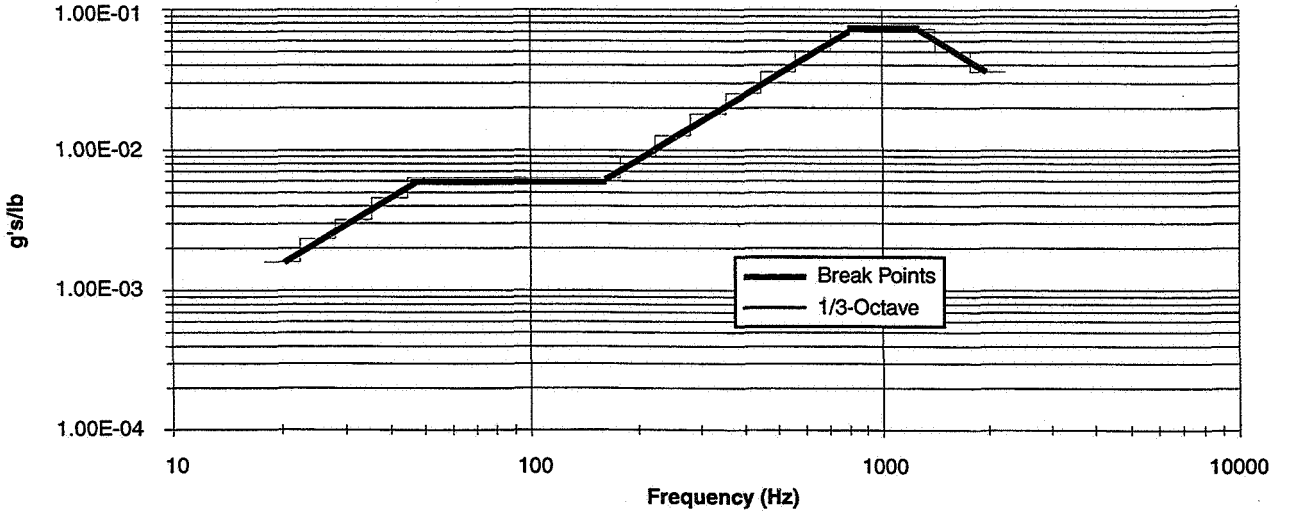


FIGURE 17. CIRS Z-DIRECTION FILTER — COMPARISON WITH 1/3-OCTAVE FILTER

CONCLUSIONS

Comparison With 1/3-Octave Filter

Another popular means of implementing an equalizer is to use a 1/3-octave filter. The resolution of such a filter is much more coarse then a DSP implementation as shown in figure 17. The figure assumes that the amplitude at each band could be set accurately which is not always the case. The minimum amplitude resolution is usually limited to 1 dB steps. Also, the deviation from the desired transfer function would be much worse if the slope of the curve is greater.

Other Advantages

A DSP implementation does not introduce any phase distortion. Also, the DSP board can be used for other applications such as: stepped/swept sine/cosine generator, shaped noise sources, constant force modal excitation systems, and signal analyzers. Some DSP boards have also been programmed for vibration control.

Disadvantages

The time delay of FIR filters cause problems with control strategies used for swept sine vibration which limits the equalizer filter's use to random vibration. There is also a tracking problem at low frequencies especially at higher transfer function slopes.

Projects

So far, the described system has been successfully used on the following projects:

Cassini/Cryogenic InfraRed Sensor
Mars Geophysical Surveyor/Mars Overhead Laser Altimeter II
Clark/Goddard Experimental Module
Advanced Composition Explorer

GSFC expects to be using the system described in this paper until the current controllers are replaced in the near future.

REFERENCES

1. Scharton, Terry D., "Force Limits For Vibration Tests," Spacecraft Structures and Mechanical Testing Conference Sponsored by CNES 21 June 1994.

2. Smallwood, David O., "Development of Force Envelope for An Acceleration/Force External Controlled Vibration Test," *61st Shock and Vibration Bulletin*, Los Angeles, CA, October 1990.

3. Scharton, Terry D., "Vibration in Test Force Limits Derived from Frequency Shift Method," *AIAA Journal of Spacecraft and Rockets*, March-April, 1995.

4. Oppenhiem, Alan V. and Schafer, Ronald W., *Discrete-Time Signal Processing*. Prentice Hall, Inc, NJ, 1989, pp 525.

5. Loy, Nicholas J., *An Engineer's Guide to FIR Digital Filters*. Prentice Hall, Inc, NJ, 1988, pp 80.

516-39
00 0458
269401
6P

STRUCTURAL EVALUATION OF TOPAZ II—THE RUSSIAN SPACE-BASED NUCLEAR REACTOR

Edward D. Schaefer
Space Department
The Johns Hopkins University
Applied Physics Laboratory
Laurel, MD 20723-6099
(410) 792-6000

Jeffrey M. Lacy
Idaho National Engineering Laboratory
Idaho Falls, ID 83415-3760
(208) 526-2937

ABSTRACT

This paper presents an evaluation of the Russian built space-based Topaz II nuclear reactor. Our purpose was to verify its overall structural integrity and margins of safety for possible launch on a U.S. vehicle. This evaluation involved developing finite element models and performing a modal survey and a series of vibration tests in order to prequalify the reactor. The results from the U.S. team were significantly different from what was expected and from the data provided by our Russian counterparts.

INTRODUCTION

The potential of nuclear power to improve both our access to and our utilization of deep space has long been recognized. In 1992, the Strategic Defense Initiative Organization (now the Ballistic Missile Defense Organization) funded the Nuclear Electric Propulsion Space Test Program (NEPSTP) to develop a spacecraft test bed. The purpose was to evaluate electric propulsion technologies using the existing Russian-built Topaz II reactor as the power source.

The design of the reactor, which began in 1969, evolved into a flight-qualified system in 1989. Twenty-six Topaz II systems were manufactured, most of which were expended on test programs. Topaz II was never launched by the former Soviet Union. Five systems in their final configuration are now available. Two reactor units minus their fuel were delivered to the New Mexico Engineering Research Institute in early 1992 for evaluation. Concurrently with this effort The Johns Hopkins University Applied Physics Laboratory was developing a preliminary design for a spacecraft that would use the reactor as the power source.

SYSTEM DESCRIPTION

The Topaz II reactor is based on thermionic power conversion generating 135 kW thermal, which produces 5 to 6 kW electric. The system (Figure 1) consists of fissionable material, a moderator, a reflector to conserve escaping neutrons, provisions for heat removal, and a system to control the reaction. It

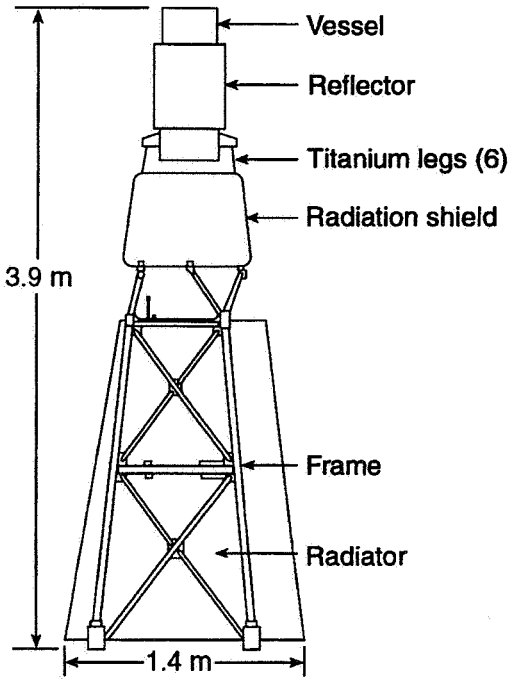


Figure 1: Topaz II reactor

contains 37 single-cell thermionic elements fueled with uranium dioxide pellets that are 96% enriched ^{235}U in a zirconium hydride moderator. The cylindrical reactor casing, which serves as the reflector, is made of beryllium. Twelve cylindrical control drums are located around the perimeter of the reactor to control the reaction. A radiation shield is attached to the aft end of the reactor. The shield is composed of a stainless steel vessel containing lithium hydroxide, which provides both gamma ray and neutron shielding. The reactant coolant system uses liquid sodium/potassium eutectic to transfer heat from the reactor core to the radiator. The truncated cone-shaped radiator is attached to a tripod frame which supports the entire system. (A more detailed description of the reactor system is given in Ref. 1).

The Topaz II tripod support structure (Figure 2) consists of a welded tubular stainless steel frame. This tripod frame is fabricated using Russian-designated 12X18H10T stainless steel, which has similar chemistry to our AISI 321. The base of the frame lies on a 1.2-m radius and is 2.1 in height. The top of the tripod has a 0.7-m radius and supports the radiation shield. The six titanium posts are located atop the radiation shield and are used for attaching the reactor. The thermal radiator is attached to the tripod structure using a series of pinned and slotted connections to allow for thermal expansion. The tripod structure also supports the thermal shroud during launch. In this configuration the system is expected to weigh 1043 kg, with a center of gravity 2.3 m above the base.

STIFFNESS EVALUATION

The objective of this evaluation was to determine if the Topaz II system had adequate margins of safety in terms of its stiffness and strength to qualify for a U.S. launch. The Russian design philosophy during the period in which these reactors were being fabricated relied heavily on prototype development and to a lesser extent on analytical evaluations. Therefore, the Russian mechanical test data became the primary means for evaluating the design.

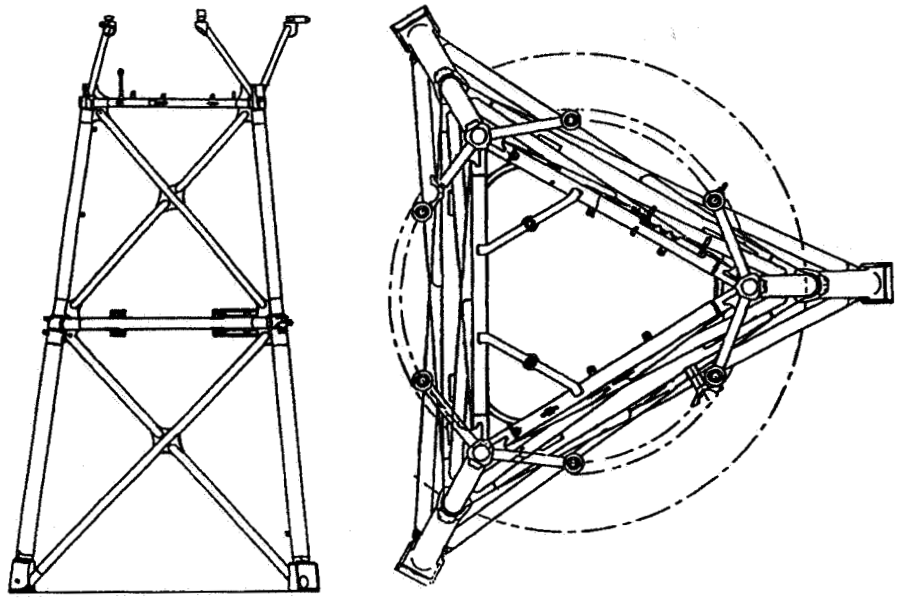


Figure 2: Topaz II tripod structure

The results of the documented Russian mechanical tests (Ref. 2) stated that the reactor structure had its first lateral bending mode at 5.5 Hz. This low natural frequency concerned the U.S. team because of possible interference with the control system used on our launch vehicles. In addition, the launch configuration (Figure 3) had the Topaz II unit located atop the spacecraft bus, thus making any efforts to increase this low frequency impractical.

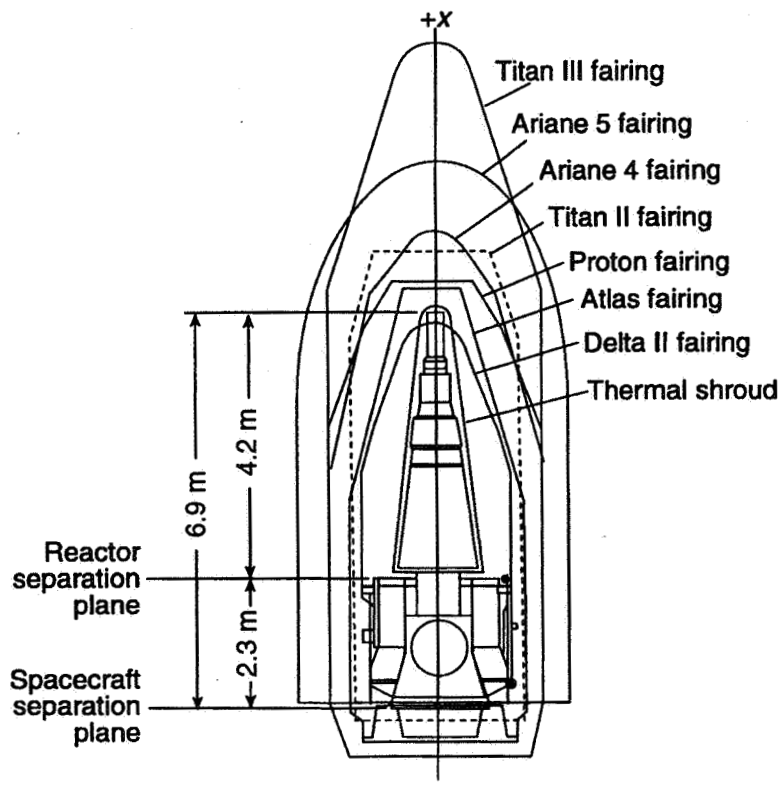


Figure 3: Launch configuration

The Russian test setup was described as having the base of the reactor attached to a flanged cylinder, which in turn was mounted to a thick, reinforced concrete floor. The top of the reactor was pulled in the horizontal direction by a wire such that the reactor unit was displaced 5 mm. The force to produce this horizontal displacement was not recorded, nor was the base of the reactor unit instrumented to detect any relative movement. At this point the wire was cut, allowing the reactor unit to oscillate freely. This test was repeated several times and resulted in the stated frequency of 5.5 Hz. Interestingly, with respect to later discussions of nonlinearities in the system, the response accelerometer traces from this test series were very smooth and sinusoidal, and showed no shift in frequency as magnitude decreased.

To better understand the Russian design, a finite-element model (FEM) was developed. The results of this initial analysis showed the first lateral bending mode occurring at 10.5 Hz. Subsequently, a more refined model was developed, which modeled the gusseted connections and the foot design and verified the diameters and wall thickness of the tripod frame. The results of this analysis showed the first lateral bending mode occurring at 10.8 Hz; no evidence of the 5.5-Hz mode described in the Russian document was found.

A modal survey of one of the reactor units, minus the fuel and ballast, was performed at Sandia National Laboratory in mid-1993 to assess the discrepancies between the Russian and U.S. findings. The purpose of this test was to provide data from which the modal parameters could be extracted for use in connection with the FEMs and the Russian test data. The reactor structure was excited using random burst; the magnitude of this force was less than 4.5 kg. Table 1 lists the modal parameters obtained.

During data collection both the coherence and frequency response functions were obtained. The multiple coherence functions were close to 1 at all the significant resonant frequencies, indicating that the measured outputs were, in fact, due to the measured inputs. No nonlinearities were discovered during this test sequence. The global modes of interest included the first and second bending modes (in orthogonal pairs) as well as the first torsional and first axial modes. These modal parameters included not only the reactor but also a 9,500-kg seismic mass, supported on air bladders, to which the reactor was attached for the test sequence. The structural modes of the Topaz II reactor were obtained by correlating these test results with the FEM and the known test boundary conditions.

Once these data were obtained, the fixed-base condition was recalculated. The results of this work are summarized in Table 2. Our primary interest was the first bending mode, which showed a 2.4% error between the modal test and the FEM. The calibrated FEM showed a first bending mode of 10.8 Hz. Adjusting the FEM for the flight configuration, which was approximately 146 kg heavier than the test unit, gives the first bending mode at 10.5 Hz, which compares with the original mode of 10.8 Hz. Again, the U.S. results did not correlate with the Russian findings.

Table 1. Modal parameters

Mode number	Description	Frequency (Hz)	Damping (%)
1	First bending (y)	20.3	0.5
2	First bending (x)	20.9	0.9
3	First torsional	31.7	0.8
4	Second bending (y)	35.7	1.2
5	Second bending (x)	36.7	1.1
6	First axial	55.5	0.5

Table 2. FEM correlation with modal test

Mode number	Modal survey results (Hz)	FEM with modal boundary conditions (Hz)	Correlation error (%)	FEM fixed-base test unit (Hz)
1	20.3	19.8	−2.4	10.8
2	20.9	20.7	−0.9	10.8
3	31.7	29.0	−8.5	28.8
4	35.7	43.8	22.7	42.9
5	36.7	44.2	20.4	43.1
6	55.5	59.7	7.5	57.2

A series of meetings was held with the Russians to discuss these results. The Russian position was that many nonlinearities were present in the system and that the modal survey did not yield the proper results because the forces were too small to properly excite the mass of the reactor. No consensus was ever reached.

In mid-1994, a series of vibration tests was undertaken to prequalify the reactor. Results showed that the first lateral bending frequency of the combined vibration test setup (including the shaker with its slip plate, test fixturing, and the reactor unit) occurred at approximately 9.0 Hz. This was less than either the results from the modal survey or the FEMs. We believe that the flexibility of the test setup produced this lower level. Again, no indication of a 5.5-Hz resonant mode was found. The consensus on the U.S. team was that the low frequency recorded in the Russian report was primarily an artifact of the test setup and fixturing and not the primary first lateral bending mode of the reactor structure.

STRENGTH EVALUATION

The strength of the reactor unit and its ability to meet launch safety requirements were also of concern to the U.S. team. The Russian document stated that the reactor unit was designed using quasi-static design loads of 7.0 *G* thrust and 2.0 *G* lateral, with a test factor of 1.3. This sets the test levels at 9.1 and 2.7 *G*, respectively. These levels were, however, based on the Topaz II oriented in an inverted launch configuration, that is, with the reactor unit closest to the launch vehicle interface. These loads compare relatively well with the maximum enveloped U.S. launch vehicle requirements of 6.0 and 3.0 *G*, respectively, except that the launch configuration (Figure 3) has the reactor up.

The loads used in the Russian static load test for the configuration shown in Figure 3 were applied to the U.S. FEM for comparison. These test levels were based on limit load factors of 5.0 *G* thrust and 3.0 *G* lateral, with a test factor of 1.35. This represented a test level of 6.75 and 4.0 *G*, respectively. The results of the Russian test and the U.S. modeling efforts in terms of their lateral displacements are illustrated in Figure 4, which clearly indicates that the more rigid, unmodified model best represents the Russian test data.

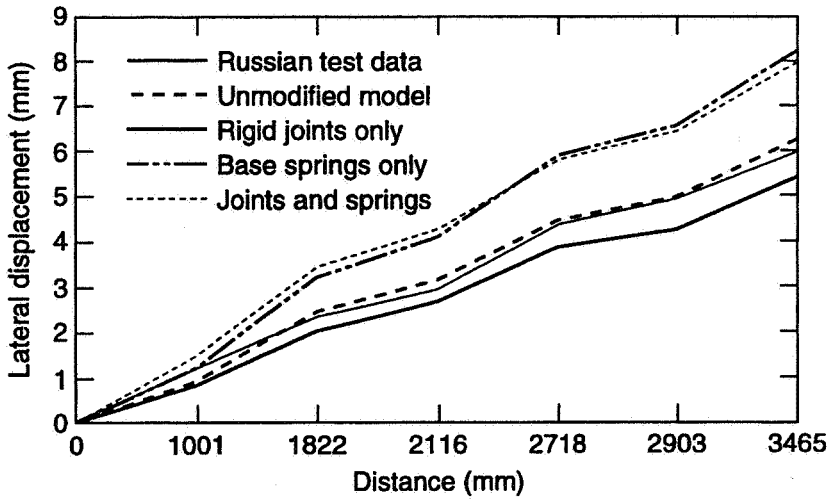


Figure 4: Lateral displacement comparison—test vs. finite element models

CONCLUSIONS

U.S. analytical models of the reactor unit predict the fixed-base natural frequency at 10.8 Hz for the current launch configuration. No evidence was found that could support the 5.5-Hz mode described in the Russian documentation. The U.S. team believes that the Russian test was flawed by the test fixturing.

Although our FEMs agree with the modal test results, they do not agree well with either the Russian stiffness or strength tests. In addition, our finite-element analysis indicates that the quasi-static limit loads produce margins of safety below current practice.

REFERENCES

1. Polansky, G. F., et al., "A Plan to Flight Qualify a Russian Space Nuclear Reactor for Launch by the US," AIAA paper No. 93-1788, AIAA/SAE/ASME/ASEE 29th Joint Propulsion Conference, June 1993.

2. Inertek, J. V., *Topaz II NPP Reactor Unit Mechanical Tests* , Volumes 1–7, St. Petersburg, Russia, 1993 (translated by the New Mexico Engineering Research Institute).

269404 S/7-18
ABS ONLY

Modal Testing of the Midcourse Space Experiment (MSX) Spacecraft

021459
1P

Teresa M. Betenbaugh & Robert L. Tomkiewicz
Johns Hopkins University Applied Physics Laboratory
Laurel, Maryland

Abstract

The Midcourse Space Experiment (MSX) Observatory is a Ballistic Missile Defense Organization (BMDO) project with the primary mission of identifying and tracking ballistic missiles during their midcourse phase flight. The Johns Hopkins University Applied Physics Laboratory (JHU/APL) is under contract to BMDO to develop, integrate, test, launch and operate the MSX Spacecraft. JHU/APL was responsible for all spacecraft mechanical testing, which included static load, modal, acoustic, and shock testing. This paper describes the modal testing of the MSX Spacecraft, correlating analytical and test results.

18-39
021460

EVALUATING THE VIBROACOUSTIC RESPONSE OF HONEYCOMB PANELS

269406 10P

Edward D. Schaefer, Space Department
The Johns Hopkins University Applied Physics Laboratory
Laurel, Md. 20723-6099

ABSTRACT

This paper evaluates some of the available techniques for predicting the response of honeycomb panels to an acoustic excitation. These techniques include numerical methods such as the finite element method, the statistical energy method of analysis, and semi-empirical methods. These results, in turn, are compared with acoustic test data obtained from spacecraft designed by The Johns Hopkins University Applied Physics Laboratory, as well as with NASA's environmental specification. The results are summarized and compared graphically.

INTRODUCTION

A spacecraft is exposed to a fluctuating pressure field, typically referred to as the vibroacoustic environment, throughout the boost phase of its flight. The maximum acoustic environment occurs during liftoff, when the exhaust plume from the booster is reflected from the launch pad, engulfing the launch vehicle, and again during transonic flight, when the vehicle goes through a region of maximum dynamic pressure. These pressure waves propagate along the vehicle at the speed of sound. They are also transmitted through the payload fairing, acoustically exciting the spacecraft inside. Structure-borne noise is also transmitted from the launch vehicle to the spacecraft via its structural attachment. The predominant source of the vibroacoustic loads imparted to the spacecraft is the acoustics generated inside the payload fairing. Both of these effects are launch-vehicle dependent and manifest themselves as random vibrations to the spacecraft structure and its subsystems.

A common spacecraft structural configuaration uses flat honeycomb panels for their primary structure. These panels provide large surface areas for mounting equipment packages, instruments and subsystems. These instruments and subsystems often involve sensitive optics and electronics. An example of this type of packaging is illustrated in Figure 1. These panels typically have large area-to-weight ratios that respond strongly to a diffuse acoustic field. Solar panels, which also consist of relatively large flat surfaces, fall into this category. The vibroacoustic environment and the quasistatic load factors specified by the launch vehicle contractor define the structural design criteria for the spacecraft, instruments, and subsystems. The emphasis of this paper is not on sound transmission through structure; it is rather on the response of the structure to the fluctuating pressure and on being able to predict the dynamic response early in the design cycle.

HISTORICAL DEVELOPMENT

Over the years many different techniques have been used to predict these panel responses, from grandfathering, similarity, and experience to various analysis techniques. Some of the early analytical

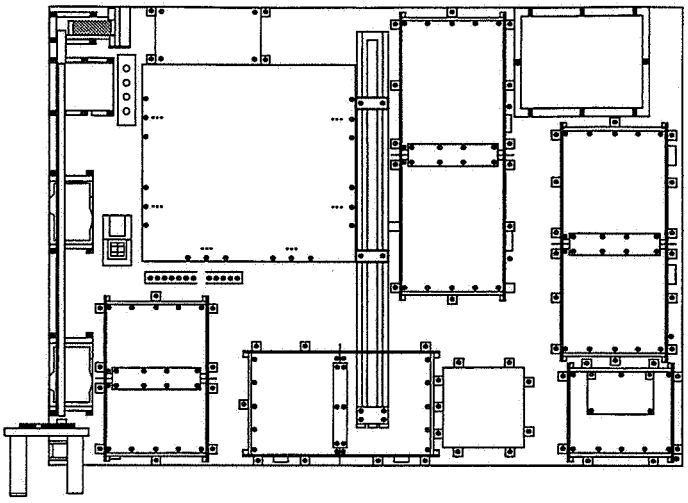


Figure 1: Typical Panel Configuration

work predicted the response of cylindrical launch vehicles to a diffuse acoustic field. Franken (Ref. 1) noted that the ratio of the rms acceleration to the rms pressure reached a maximum at the ring (resonant) frequency of the vehicle and fell off rapidly above this frequency. In addition, he noted that the response of the structure followed the mass law except in the area of structural resonance. The structural response exceeded the mass law behavior, indicating the structural properties of the cylinder, namely, its stiffness and damping characteristics, dominated the response in this region.

Eldred et al. (Ref. 2) noted that this behavior was similar to the response of a single resonator where the mean square acceleration response is defined as

$$[a^2] = [(\pi \times \beta^2 \times S_p(f) \times f) / (2 \times \eta \times w^2)] \quad (1)$$

where β is an empirical factor that measures how well the pressure field is able to excite the modes of the structure. $S_p(f)$ represents the pressure spectral density, f is the frequency, η is the loss factor, and w represents the surface density of the structure.

AVAILABLE TECHNIQUES

On this basis, Spann and Patt (Ref. 3) developed a semi-empirical method for estimating the response of honeycomb panels to an acoustic environment. This method calculates the acceleration spectral densities and is defined as

$$S_a(f) = S_p(f) \times (\beta \times Q \times A / W)^2 \quad (2)$$

where the loss factor η has been replaced by the quality factor Q. The panel has an area A and a total weight including all of the components mounted on it W. Based on experimental test data a β factor of 2.5 and a quality factor of 4.5 is recommended. Integrating this equation over the frequency range yields the same mean square response as defined by equation (1). This method was correlated and compared with a large variety of honeycomb panels, and it has been used by Boeing since the mid 1980s. Recently it was slightly modified to include additional test data obtained over the past 10 years. Spann (Ref. 4) recommends increasing the quality factor to 5.0 to ensure that the 95% probability level is maintained.

From this point on our efforts focus on being able analytically to predict β, or how well this fluctuating pressure field is able to excite the modes of the structure. Several automated methods are available for handling problems that involve the interaction of the coupled motion of the elastic structure in a fluid. The numerical methods approach encompasses both the finite element method (FEM) and the boundary element method (BEM), examples being the NASTRAN and COMET methods. The second approach is the statistical energy analysis (SEA), examples being SEAM and AutoSea.

The finite element method is used to solve acoustic problems such as those involving noise generated in the interior of an enclosure. This method is limited to the lower-frequency range, i.e., less than 2000 Hz. The limit results from to the practical limitations on the number of the elements required to spatially map a sinusoidal wave and thus accurately represent the high-frequency modes. The boundary element method is applicable to unbounded problems where the region of interest extends to infinity, such as the noise radiated from a vibrating structure. The indirect boundary element method is capable of solving problems which involve an acoustic medium on both sides of a structure. Brebbia and Dominguez (Ref. 5) and Vallence (Ref. 6) describe this method and its application in greater detail. This technique was not evaluated because the code was unavailable.

Statistical energy analysis was developed by Lyon (Ref. 7) and is an outgrowth of the work in high-frequency acoustics. It is based upon the solution of the power balance equations and assumes that the majority of the energy flow between subsystems is due to resonant structural or acoustic modes. In addition, it assumes closely spaced modes of vibration in a frequency band. For example, the classical two-coupled oscillator is illustrated in Figure 2. The steady-state power balance equation for the two-coupled oscillator is as follows:

$$\Pi_1 = \omega E_1 \eta_1 + \omega E_1 \eta_{12} - \omega E_2 \eta_{21} \tag{3}$$

$$0 = \omega E_2 \eta_2 + \omega E_2 \eta_{21} - \omega E_1 \eta_{12} \tag{4}$$

where Π_1 is the power input; η_1 and η_2 represent the internal damping of the two subsystems; E_1 and E_2 are the vibration energies associated with each subsystem; η_{12} and η_{21} are the coupling loss factors or the

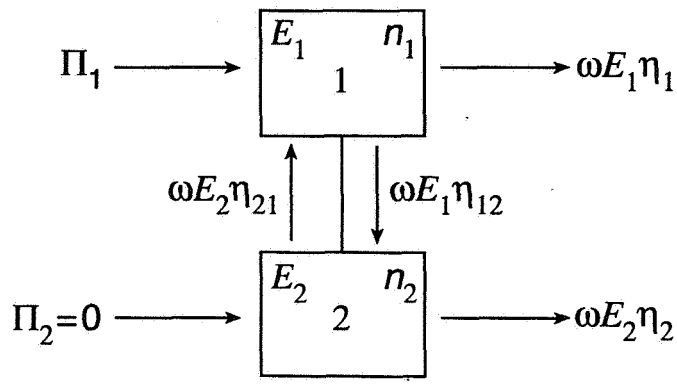


Figure 2: Two-Coupled Oscillator

power transmitted between the two subsystems; and ω is the circular frequency. This set of simultaneous equations is solved for the energy in each of the frequency bands of interest. Once the energy is known, the velocity on the surface of the plate and the corresponding acceleration spectral density are obtained. The statistical energy analysis is typically not valid below about 40 Hz. For a more detailed description of this analysis technique, see Norden (Ref. 8).

The following techniques can be considered deterministic. Miles' work on sonic fatigue (Ref. 9) assumed a broadband noise in which only the fundamental mode of vibration contributed to the response of the structure. Blevins (Ref. 10) extended this approach to include the higher modes and narrowband noise. Blevins uses the mass-weighted mode shape for the shape of the pressure field on the surface of the structure. A finite element modal analysis is performed over the frequency range of interest in which the mode shapes, their nodal displacements δ and stresses σ are obtained. From these data the characteristic modal pressure P is obtained, where ρ_h is the mass per unit area of the plate at a reference point:

$$P = \rho_h \times (2\pi f)^2 \times (\delta) \tag{5}$$

For narrowband applied pressures where the excitation bandwidth is smaller than the response bandwidth at frequency f, the ratio of the rms deformation and rms stress to the corresponding modal deformation and stress is given by:

$$(\delta_{\text{rms}} / \delta) = (\sigma_{\text{rms}} / \sigma) = \{[\pi f\, S_p(f)]/(4\zeta P^2)\}^{0.5} \tag{6}$$

where ζ is the damping factor.

MacCoun (Ref. 11) calculates a mass normalized modal parameter ϕ, similar to the Blevins method. In addition he calculates two generalized forces Γ, one for the low-frequency region and a second for the higher frequencies. The transfer function that relates pressure spectral density to acceleration spectral density is defined as

$$[H(f)] = \sum \{\phi\Gamma \times [f^2/(f_n^2 - f^2 + 2j\zeta f_n f)]\} \tag{7}$$

The acceleration spectral density is then defined as

$$S_a(f) = [H(f)]^2 \times S_p(f) \tag{8}$$

RESULTS

Acoustic test data from several APL-built spacecraft were used as the basis for evaluating the above analytical techniques. The characteristics of these panels are listed in Table 1. They were selected to cover a broad range of area-to-weight ratios, ranging from 4.58 to 136.3. The weight of the equipment packages was assumed to be spread uniformly over the surface of the panel. The fundamental resonant mode of these panels ranged from 37.5 Hz. to 70.1 Hz. For this investigation a constant damping factor ζ of 0.017 was used as representative for honeycomb panels (Ballentine, Ref. 12). The results are presented in Figures 3 through 12 and represent the maximum expected response at the center of the panel.

From these Figures, it can be seen that the in-plane responses are generally less than the responses normal to the panels below 1000 Hz. In addition, they indicate that all the methods had some difficulty at

Table 1. Characteristics of the Selected Aluminum Honeycomb Panels

Panel Size (L × W × T)(in.)	Total Weight of Panels & Components (lb)	Area-to-Weight Ratio	Fundamental Frequency (Hz)
58 × 42 × 2.0	245.0	9.98	58.6
58 × 42 × 2.0	362.0	6.76	48.0
58 × 42 × 2.0	412.5	5.93	45.0
58 × 42 × 2.0	534.0	4.58	39.7
58 × 28 × 1.25	122.2	13.35	70.1
58 × 28 × 1.25	158.0	10.32	61.5
58 × 28 × 1.25	203.0	8.04	54.2
58 × 28 × 1.25	223.7	7.30	51.6
72 × 48 × 1.0	25.3	136.30	37.5
72 × 48 × 1.0	25.3	136.30	37.5

frequencies greater than 1000 Hz. However, these results are consistent with the assumption that the equipment package weight is spread uniformly over the surface of the panel. The high-frequency responses are probably a result of equipment packages vibrating relative to the panel or the structure to which the panels were attached.

The semi-empirical and Blevins methods both conservatively enveloped the data and were in good agreement with each other. These two methods were typically within a 1.5 dB of each other over the frequency range. The statistical energy method, for the most part, more closely enveloped the data but with a lower margin and showed the same trends as the two previous methods. The MacCoun method tended to overestimate the low-frequency response even when the narrowband peaks were undercut by 3.0 dB, and often it underestimated the high-frequency responses.

The *General Environmental Verification Specification for STS and ELV Payloads, Subsystems, and Components* (GEVS) (Ref. 13) is a generalized vibration test specification which recommends test levels

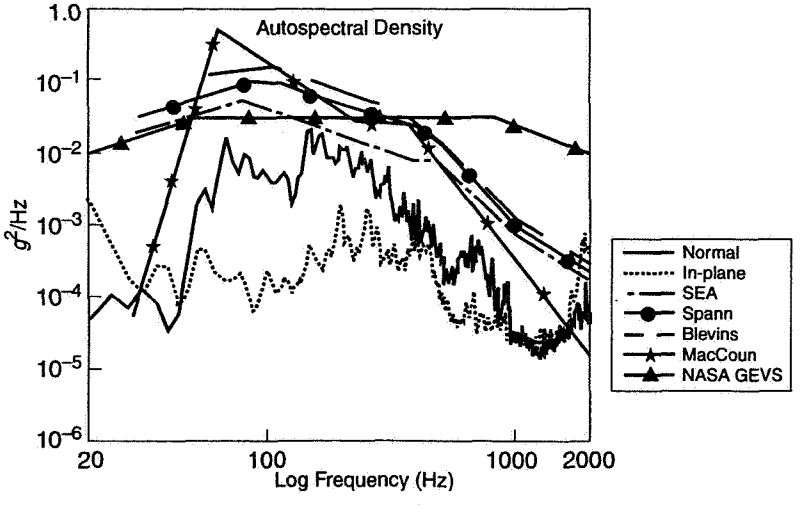


Figure 3: Panel Area-to-Weight Ratio 9.98

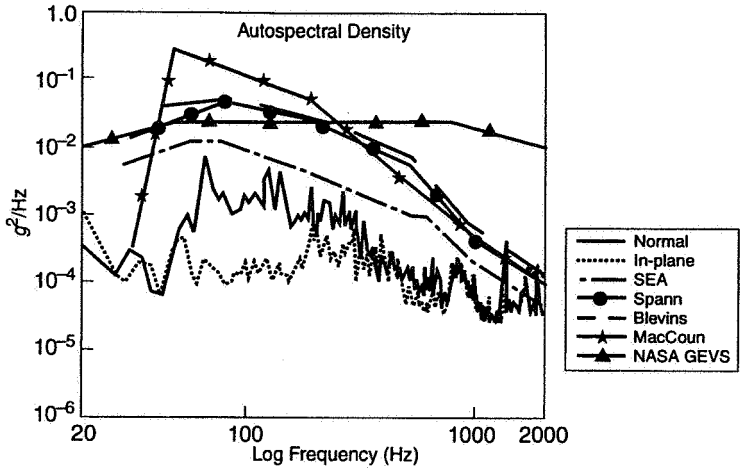


Figure 4: Panel Area-to-Weight Ratio 6.76

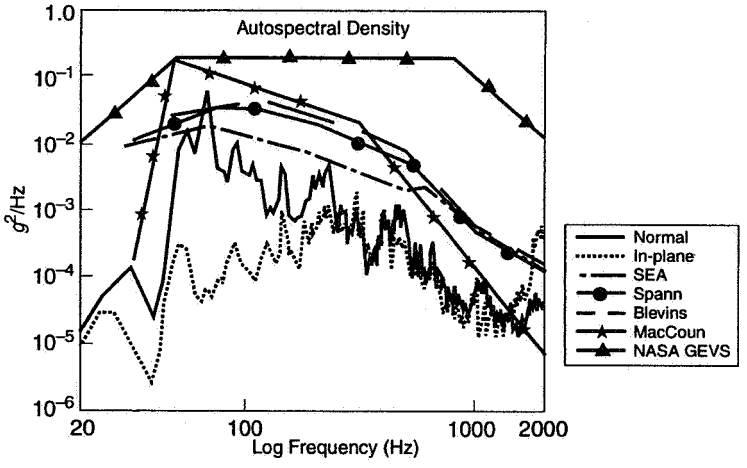


Figure 5: Panel Area-to-Weight Ratio 5.93

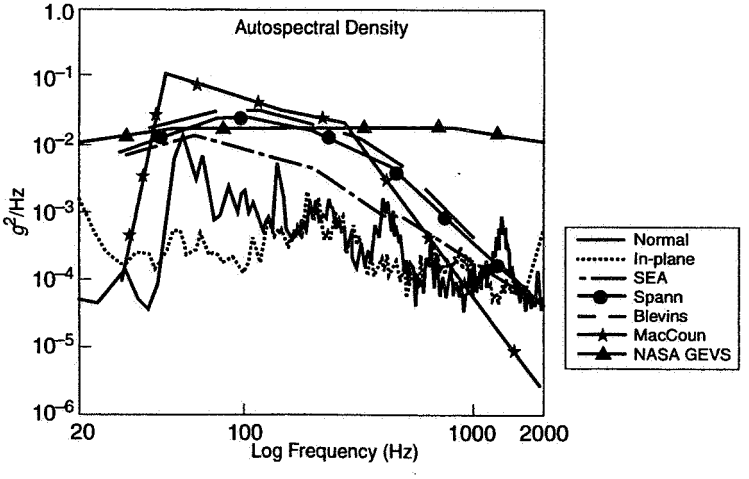


Figure 6: Panel Area-to-Weight Ratio 4.58

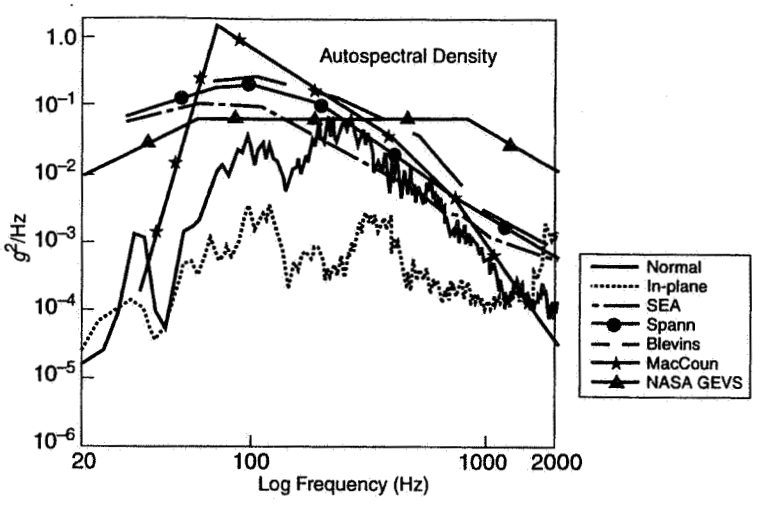


Figure 7: Panel Area-to-Weight Ratio 13.35

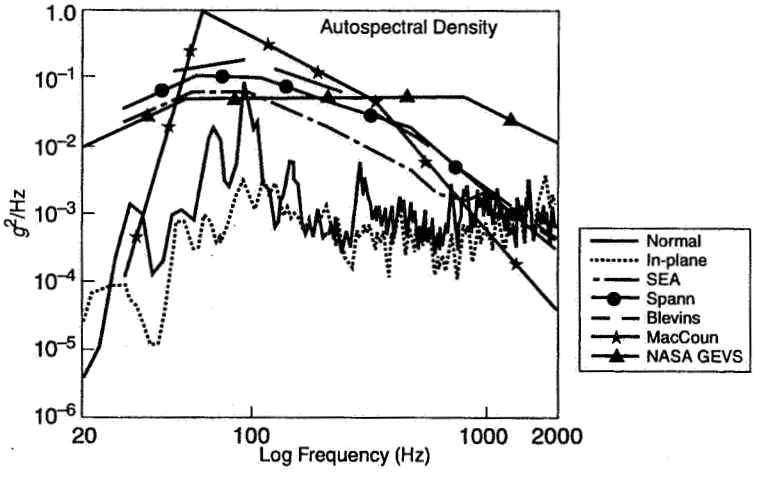


Figure 8: Panel Area-to-Weight Ratio 10.32

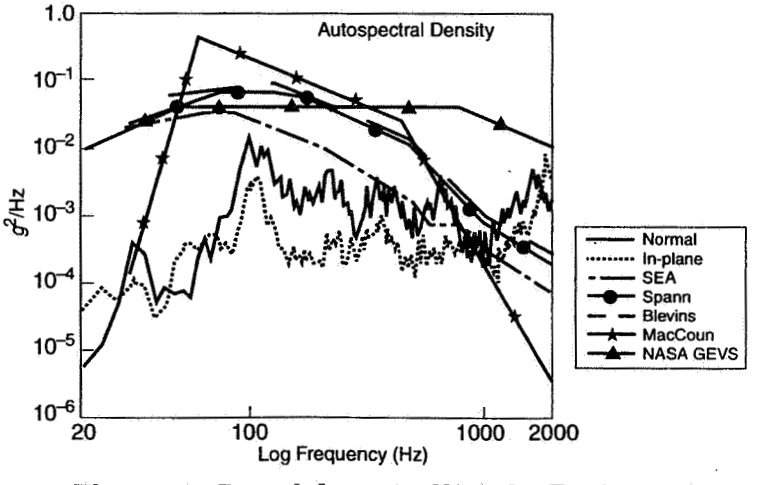


Figure 9: Panel Area-to-Weight Ratio 8.04

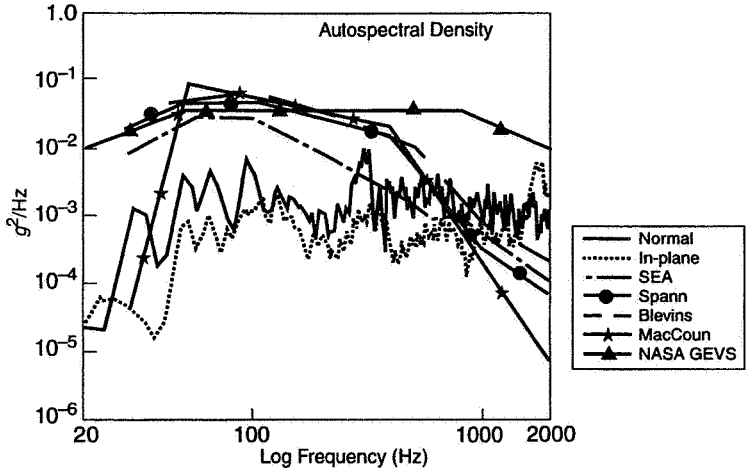


Figure 10: Panel Area-to-Weight Ratio 7.03

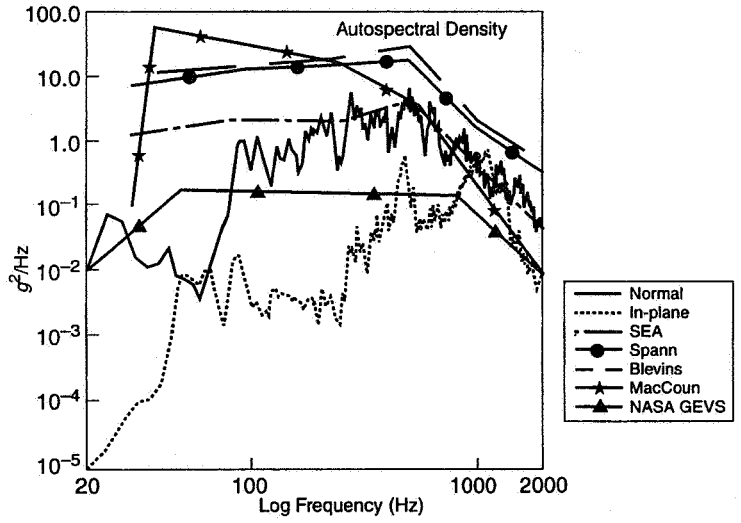


Figure 11: Panel Area-to-Weight Ratio 136.3 (+*y* Side of Spacecraft)

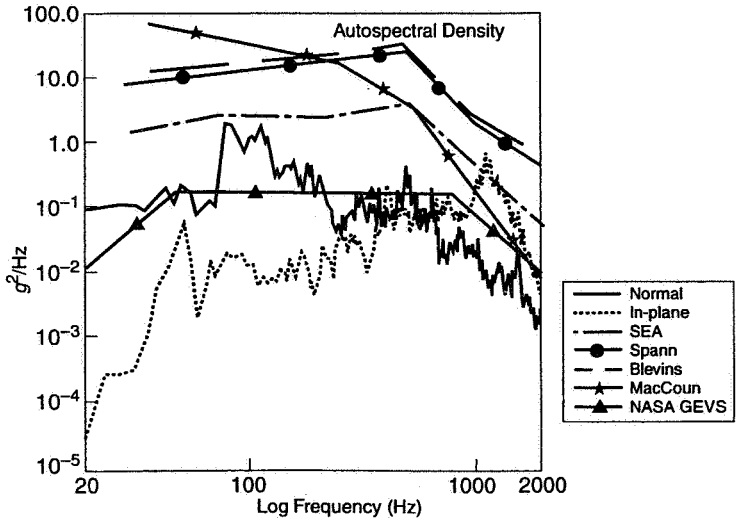


Figure 12: Panel Area-to-Weight Ratio 136.3 (+*x* Side of Spacecraft)

for equipment packages when there is no other source of data. It is based on the weight of the package and gives a maximum acceleration spectral density level of 0.16 g^2/Hz. This level is modified based on the weight ratio of the component or equipment package. Referring to Figures 3 through 12, it can be seen that this technique is adequate except for the very lightly loaded panels, for which the test specification is not adequate. These results indicate that the response of the equipment package is primarily dependent upon the overall weight of the panel with its components and not on the weight of an individual package.

CONCLUSIONS

To avoid the problem of underestimating the high-frequency response due to either equipment package response or the response of the primary structure, the straight line technique recommended in Ref. 4 or the 6-dB roll-off above 800 Hz in Ref. 13 can be used.

The in-plane responses can be reduced by approximately 3.0 dB below 500 Hz. This is consistent with the recommendations in Ref. 4.

The semi-empirical method enveloped the test data with some margin. Its empirical nature, however, makes it somewhat limited because β has been determined only for aluminum honeycomb panels. None of the other techniques has this limitation.

The statistical energy method typically did a good job in enveloping the test data. However, this technique requires adjusting the damping to give sufficient margin.

Blevin's method also showed good correlation with the test data. This technique has the advantage of using the output from a modal analysis, which is typically available.

MacCoun's method was found to be the least accurate.

Without developing a complete acoustic model, it appears that the best way to account for the sound transmitted up through the launch vehicle–spacecraft interface is to simply add a constant acceleration spectral density over the frequency range. For a medium-weight launch vehicle it appears that this would be in the range of 0.02 to 0.05 g^2/Hz.

Perhaps the recommended test level given in Ref. 13 should be based on the weight of the panel with its components mounted on it rather than on the weight of an individual component.

REFERENCES

1. Franken, P. A., "Sound Induced Vibrations in Cylindrical Vehicles," *Journal of Acoustical Society of America*, Vol. 34, pp. 453–454, 1962.

2. Eldred, K., R. W. White, and D. J. Bozick, "Empirical Correlation of Excitation Environment and Structural Parameters with Flight Vehicles Vibration Response," AFFDL-TR64-160, December 1964.

3. Spann, F., and P. Patt, "Component Vibration Predictor," *Journal of Environmental Sciences*, September/October 1984.

4. Spann, F., "Evaluation of a Semi-Empirical Component Vibration Predictor," 15th Spacecraft and Launch Vehicle Dynamic Environments, June 6–8, 1995.

5. Brebbia, C. A., and J. Dominguez, *Boundary Elements, an Introductory Course,* McGraw Hill, New York, 1989.

6. Vallance, C., "Structural Noise Induced Vibration Prediction for a Component of a Launch Vehicle," 15th Spacecraft and Launch Vehicle Dynamic Environments, June 6–8, 1995.

7. Lyon, R. H, *Statistical Energy Analysis of Dynamical Systems*, MIT Press, Cambridge, Mass, 1975.

8. Norden, M. P, *Fundamentals of Noise and Vibration Analysis for Engineers*, Cambridge University Press, 1989.

9. Miles, J. W, "On Structural Fatigue Under Random Loading," *Journal of Aeronautical Sciences*, Vol. 21, pp. 753–762, 1954.

10. Blevins, R. D, *Flow-Induced Vibrations*, Van-Nostrand Reinhold, New York, 1990.

11. MacCoun, J. L., "Vibroacoustic Response Analysis," in *Spacecraft Structures & Mechanisms from Concept to Launch*, Sarafin T. P. (ed.), Section 7.7, Microcosm Inc. & Kuwer Academic Publishers, 1995.

12. Ballentine, J. R., and F. F. Rudder, "Refinement of Sonic Fatigue Structural Design Criteria," AFFDL-TR67-156, 1968.

13. *General Environmental Verification Specification for STS and ELV Payloads, Subsystems, and Components*, NASA, GEVS-SE, 1990.

519-35
ABS ONLY
021461
269709 1P

A Near Perfect Spin Balance

(Measurement In Chaos)

R.A. Luntz

The title of this paper, "A Near Perfect Spin Balance, Measurement in Chaos" describes that chaotic state that the output of test equipment approaches as a near perfect balance condition is reached. The body of this paper will describe the progression of events leading up to the final selection of a spin balance process. The device under test is a direct driven 155 pound cylindrical unit which rotates about its longitudinal axis. This paper is intended to give the reader an insight into the final approach used for spin balancing and describe the extraordinary efforts necessary to understand; the test, the equipment, and methods selected to achieve balance.
In the body of this paper the device under test (DUT) will be described as the Sensor or the SSMIS (See Figure 1). SSMIS stands for Special Sensor Microwave Imager Sounder, which is space born multichannel radiometer.

Background:

The stringent spin balance requirements arise from the predecessor of SSMIS, the SSMI. The SSMI sensor spinning portion weighed only 85 pounds and contained 7 channels of radiometeric data. The Aerospace Corporation recommended to pass on the same requirements from the smaller SSMI to our larger SSMIS (with slight change for increased weight). The SSMIS spinning portion will weigh about 155 pounds and contain 24 channels of radiometeric data.

The SSMIS, on orbit, spins a CCW direction at 31.6 RPM its own drive motor. The packaging of this SSMIS is unique, as it combines three sensor into one unit. This combination allows for concurrently reading data in one beam. The unit will have a polar orbit about 500 miles above the earths surface. One of the primary influences for our receipt of the follow-on contract for the next generation sensor, was the ability to package 24 channels of radiometeric data into about the some volume as its predecessor. The data from SSMIS will be used to measure the following: 1) Ocean surface wind speed, 2) Rain over land an ocean, 3) Cloud water over Ocean, 4) Soil moisture, 5) Ice Concentration, 6) Ice age, 7) Ice Edge and snow edge, 8) Water vapor over Ocean, 9) Surface type, 10) Snow water content, 11) Land surface Temperature, 12) Cloud amount over ocean.

S20-44
021462
269711
12P

Holddown Interface Load Cells , A Validation Tool

Gerrit Slagter and Berend Winter
Henk J. Cruijssen

Leiden, The Netherlands

ABSTRACT

This paper deals with the definition and application of a test tool used during dynamic testing at Fokker Space. It shows the reason for introducing such a tool. Also, a short description is given of the development testing which was done at Fokker Space. Finally, it shows that with the help of this test tool, mechanical overloading of solar arrays can be avoided and that the customer can be convinced that required interface loads to be seen during testing have been achieved.

INTRODUCTION

At Fokker Space various types of solar arrays are built and tested for commercial spacecraft and for research satellites. In order to demonstrate to the customer that the solar arrays fulfil the requirements, the hardware is subjected to a range of environmental testing. These tests encompass thermal, electrical and mechanical tests. To meet the mechanical requirements the solar array wings are subjected to deployment tests, deployed stiffness and alignment checks, acoustic noise testing and sine vibration testing. Hereafter the problems arising during sine vibration testing and the application of a tool able to measure interface forces is discussed. Figure 1 shows such a typical FEM model of a solar array wing.

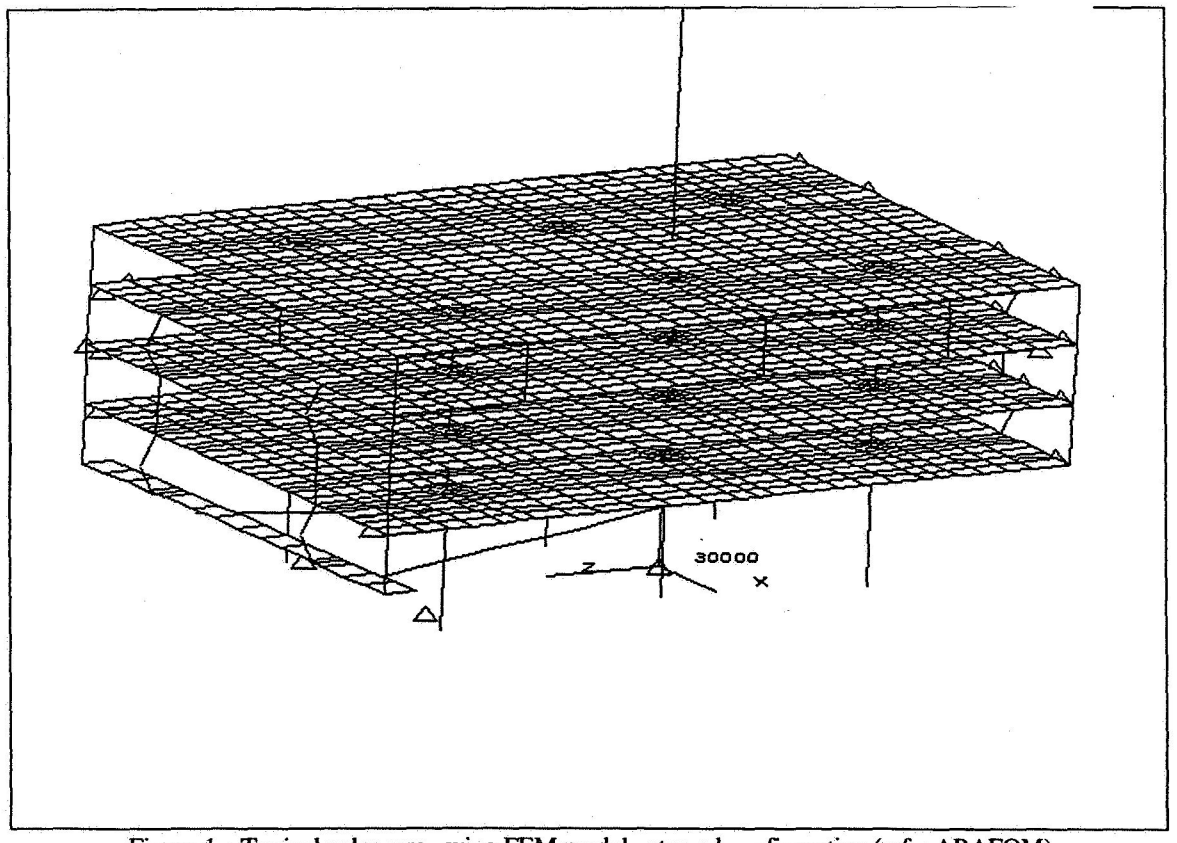


Figure 1 : Typical solar array wing FEM model , stowed configuration (ref. : ARAFOM)
Out of plane scale blown up factor 20

Two of the main problem areas during sine vibration testing of a solar array wing are the interface with the spacecraft and the required input. The solar array as a subsystem of the spacecraft is designed and tested on a rigid interface. With respect to these problems the following remarks apply:

1. Vibration testing is done on subsystem level to qualify the solar array. This means that the solar array wing is clamped to a rigid test fixture representing the interface with the actual spacecraft. In no way does this ground support equipment represent the real flexibility of the spacecraft sidewall. Actually, the vibration fixture is stiff, attracting different loads during the subsystem test than during the actual test on spacecraft (system) level.

2. In reality when the complete spacecraft including both solar array wings is subjected to spacecraft vibration testing, the loads at each holddown point vary from each other both in magnitude and in phase angle. This is caused by the spacecraft flexibility. The interface loads are derived from the coupled analysis. For subsystem vibration testing, an envelope load case is defined with one magnitude and phase angle valid for all holldown points simultaneously. For the ARAFOM wing testing, discussed in section 6, this led to the requirement that notching of the input acceleration was allowed to protect the wing from being overloaded as long as equivalent quasi-static interface loads were reached. Thus the input of the sine vibration test envelopes the interface load spectra derived from the coupled analysis.

3. The finite element model represents the mechanical behaviour of the wing as close as possible. However, this may deviate from the actual hardware. The predictions are based on an extensive finite element analyses in which the worst case loads and stresses in the skins of the panel substrate are predicted for the critical locations. Also the loads at the interface points are predicted. These predictions rely on the accuracy of the mathematical model. The finite element model sensitivity towards changes in load paths is of importance as well as the damping values belonging to each major structural mode. The analysis results are an estimate of the loads expected during the test The actual loads encountered during the test should (ideally) be measured.

In the past, to prevent the solar array wing from being overloaded, each wing was equipped with either strain gauges or accelerometers at critical locations. Also, a prediction was given of the worst case holddown loads which may occur. In general, the wing will reach its maximum allowable stresses and strains before the holddown points will be subjected at their critical load condition. As a result, the solar array wing is protected very well because the input loads are "notched" in such a way that the maximum stresses and accelerations never exceed a pre-set value. *However, the final proof that the required interface loads were also achieved during the actual test could not be given.* Only by elaborate correlation analyses it was demonstrated that the loads at the holddown interfaces were enveloping the spacecraft interface loads. To overcome this short coming, it was proposed to implement a "notching" philosophy based on the worst case of the following points:

1. Worst case stresses in the panel substrate skins
2. Worst case accelerations , resulting in chatter or impact loads from 2 adjacent panels
3. Worst case interface loads based on the overall spacecraft quasi static load environment

To implement point number 3, an interface load cell is required allowing actual measurements during the dynamic testing both of bending moment and of axial out-of-plane forces, equal to the worst case loads acting on a spacecraft structure. As a first step, a load cell was selected and used during development tests at Fokker Space. The second step was to apply the selected load cells as a pilot, during the qualification tests of the ARAFOM solar array wing.

ABBRIVIATIONS and DEFINITIONS

ARAFOM	Advanced Rigid Array For an Olympus type of Mission
ARTEMIS	European experimental communication satellite
Notch	Decrease in required sine vibration input

IMPROVED TEST METHOD

The conventional method to protect the solar array during a fixed base excitation vibration test is to use the information from accelerometers and/or straingauges representative for those areas considered critical for the solar array or other test structure. Finite Element Model predictions, for instance the results of a 1g response analysis, are used to compare with the experimental test results. More about this can be found in (ref. 1)

Based on this comparison, a typical "notch" curve is defined in order to prevent that the critical areas are exceeding the allowable stress limits (See: figure 2). This however does not necessarily correspond with the (predicted) interface loads which are experienced by the solar array wing structure during launch. Whether or not the loads introduced during the vibration testing (e.g. sine and/or quasi-static) cover the launcher or spacecraft loads is not clear, since they are derived from the accelerations and stresses measured during testing. An interface load cell would allow *actual* measurements during the dynamic testing both of bending moment and axial out-of-plane forces.

With the load cells implemented at each holddown point, the loads at all the interfaces (e.g. the individual holddown forces and moments) are measured directly. Once the requirements on this subject are achieved, this can also be implemented in "notching" curves, and as a result, unnecessary and undesirable stressing of the structure under test can be avoided.

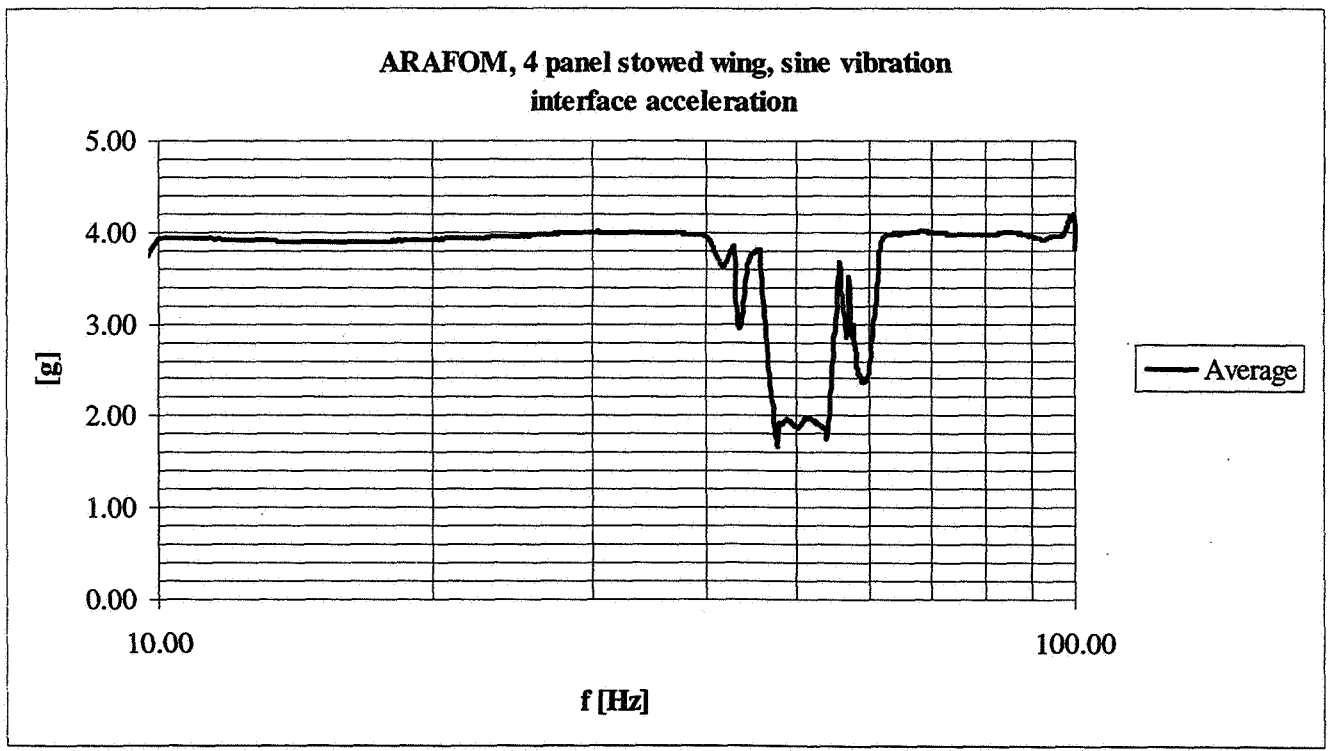


Figure 2: Dynamic input curve showing a typical "notch" for a solar array wing during dynamic testing (ARAFOM)

Figure 2, shows a typical notch curve. The required input was 4 g over the whole frequency range (5-100 Hz) The input was notched at 41, 43.5, 48-54 and at 59 Hz in order to protect the stowed wing from overloading. Note that the notch between 48 and 54 Hz was programmed. The other notches were generated automatically by the control computer of the shaker facility based on the measured strains during the test. The notches were generated to prevent the wing from overloading with respect to skin stresses in the sandwich panels. No notches were generated due to measured interface forces.

IMPLEMENTATION METHODOLOGY

A development program was started during which three basic steps were introduced:

1. Selection of type of load cell
2. Bread board engineering testing with small samples and load cells
3. Testing at full scale wing level (ARAFOM)

Selection of required hardware

The basic criteria for the selection of a holddown interface force measurement device (:load cell) at the start of the process were the following:

1. standard available commercial device
2. versatile device, useful in many (dynamic) applications
3. multi-components e.g. compression, shear (forces), bending (moments), torsion
4. reliable, safe to use, easy to use and implement in common test laboratories.
5. minimal bias on the mechanical behaviour of the test object

The multi-component load cell should preferably allow the measurement of the three orthogonal components of the dynamic forces and moments acting upon the interfaces between the spacecraft structure. As already said before, when these dynamic tests take place at Fokker Space the spacecraft structure itself is represented by a rigid sidewall simulator or a vibration fixture in general. During the test, the solar array structure under test (typically : the hold down points) and the ground support equipment (typically: the simulated spacecraft sidewall annex fixture), shall contain *at least* a three-component load cell, allowing measurement of all the forces in x-, y- and z-direction as these are the governing loads. The load cell itself should be relatively stiff (i.e. high natural frequency, above 2 kHz.) in order to prevent any coupling effects or dynamic amplification effects which may occur as during the vibration tests the load cell forms part of the load carrying structure.

BREADBOARD / ENGINEERING TESTING

Early 1993 a single unit four component load cell (i.e. compression-, two shear forces and the torsion moment), was used for the first trial testing on the 90 kN electro-dynamic shaker system available at Fokker Space. For this test program, a lumped mass as well as a simple one degree-of-freedom (i.e. 1 d.o.f.) mass-spring system was used as a test structure. This test program was successfully completed, providing reliable test data for the out-of-plane mode shapes.
With the knowledge that all the bending moments and shear forces could however not be detected with this simple four component device, the fixed base vibration testing on a T-shaped test structure was extended in 1993 using *now* a six component load cell (with signal conditioning) . The basic characteristics of this device were tested including the "notch" philosophy.

Late 1994 and early 1995 comparative testing at Fokker Space was performed on a test structure which was representative for a 4 panel stacked solar array supported by two holddowns (see figure 5), one with and one *without* the implementation of the 6 component load cell (See: figure 6). This allowed the test engineer and the stress engineer to evaluate the differences in dynamic behaviour as the mechanical structure of the load cells forms an integral part of the load path.

Having successfully completed vibration testing on this test structure and using the finite element modelling techniques for test-analysis correlation, it was decided early 1995 to purchase five samples of the "six component" load cell, together with the multi-channel signal conditioning.
Together, standard available multi-channel signal conditioning equipment (i.e. charge amplifiers) and analogue summation unit will record not only the three orthogonal components of the forces, but also the three orthogonal moments. For this reason the load cell is equipped with four assemblies of three component force sensors, fitted under a high preload between

a baseplate and a coverplate. Each force sensor assembly consists of three pairs of quartz plates, one sensitive to pressure, the other two responding to shear in two orthogonal directions (See: Cross section in figure 4). The voltage outputs, which are proportional to the forces acting on the built-in sensors are connected to allow not only for multi-component measurement of forces, but also moments. The characteristics of the selected load cell are listed hereafter.

main physical characteristics:

dimensions	:	140 mm. x 170 mm. x 60 mm. (length x width x height)
mass	:	8.4 kg
stainless steel		
hermetically sealed		
electrically insulated from ground		

main technical characteristics:

force range	:	compression	+10,000 N / - 5,000 N.
	:	shear	+ 5,000 N / - 5,000 N.
output voltage	:	+20Vac/-20Vac	
unloaded eigen frequency.	:	compression	3,500 Hz.
		shear	2,300 Hz.
stiffness	:	compression	> 2,000 N/mm.
	:	shear	> 1,000 N/mm
accuracy	:	< 3%	

The allowable loads listed above are valid in an area of 20 mm above the top plate of the load cell. For an extension of the allowable load volume, the manufacturer gave the following envelope. The maximum envelope for the following load case is given in figure 3 :

simultaneously force in shear	:	+2,500 N. / -2,500 N.
forces in compression	:	+3,250 N. / -3,250 N.
moments (all directions)	:	+175 Nm. / -175 Nm

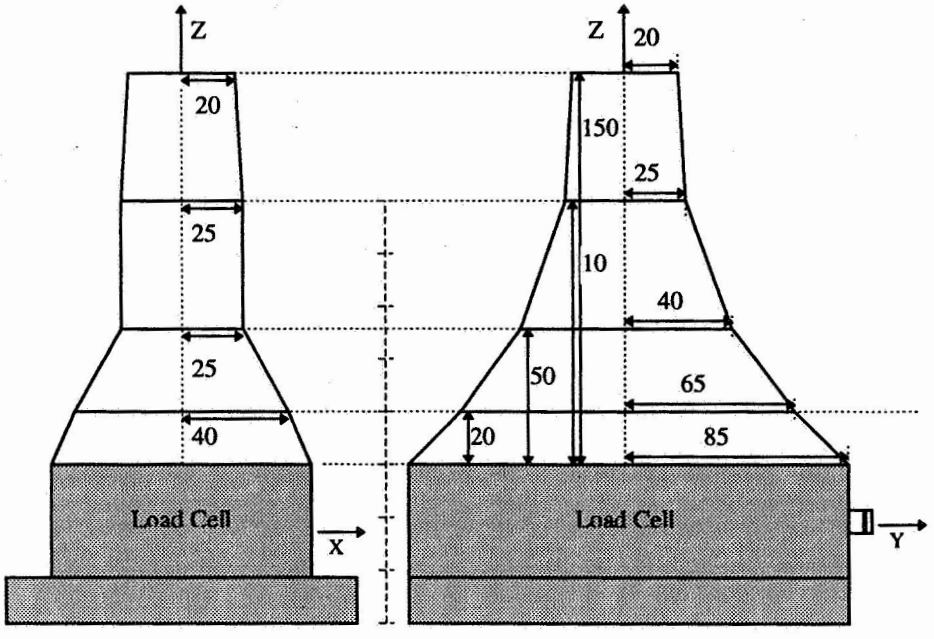


Figure 3: Combined load envelope six component load cell [mm]

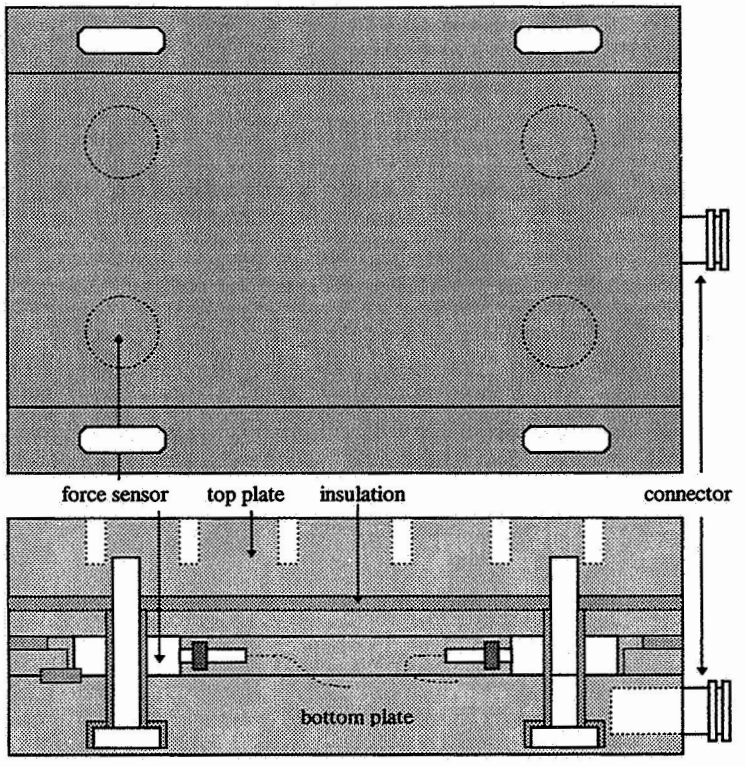


Figure 4: cross section of six component load cell

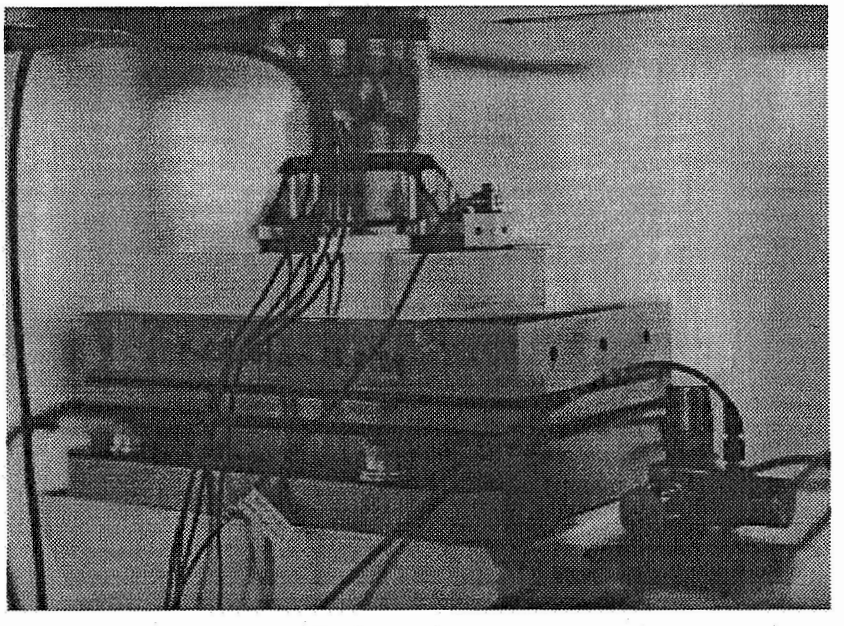


Figure 5: Close-up 6 component load cell selected for future Space (solar array) test programs.

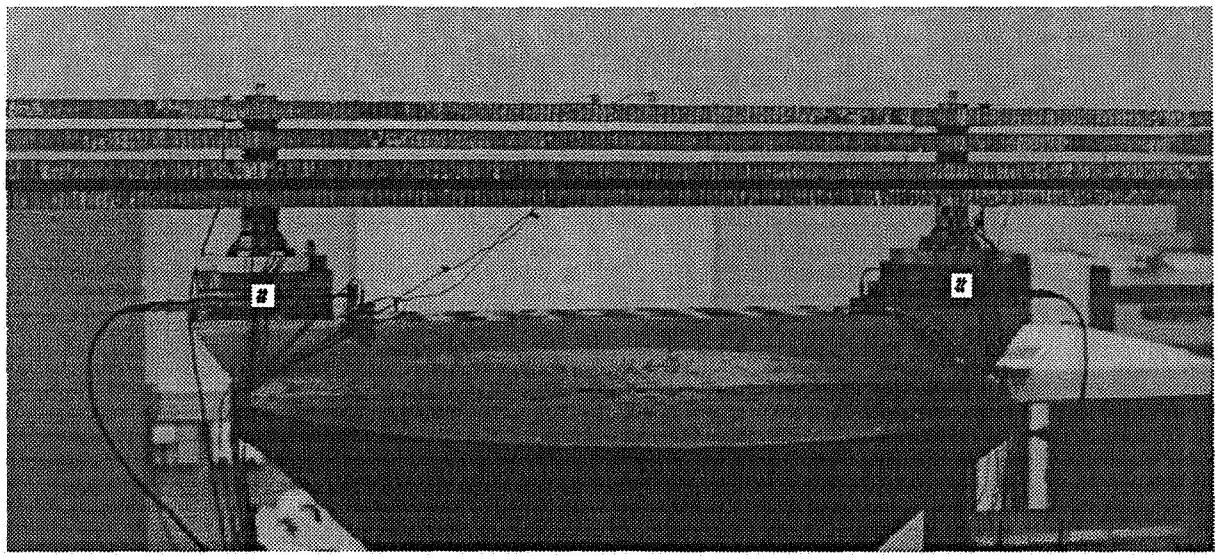


Figure 6: Engineering testing at Fokker Space on solar array representative test structure
The load cells are marked with #

During the testing it was found that care should be taken on the following points

1. No physical overload protection is installed on the load cells. If maximum force levels are exceeded, load cell physical limitations need to be pre-set, e.g. implemented in the "notching" strategy.
2. Although the influence on the mechanical behaviour of the tested objects is proven to be small, a coupled finite element model analysis is necessary to asses before testing whether the load cells can be installed
3. The scaling of both shear forces must be identical, this could lead to measurements having bad signal to noise ratio's.
4. The mass of the top half of the load cell participates in the force measurement, the inertia forces due to the acceleration of this mass affect the measured forces and moments. This 'noise' has to be subtracted from the measurements. It is therefore necessary to measure the accelerations of the top half in all directions if one wants to measure all forces and all moments

The following step was that this test equipment would be used in the newly developed ARAFOM solar array wing (ref. 2) which was now ready to be subjected to a full qualification wing test program. Following success, the test method would also be used for future solar array (proto)qualification test, such as the ARTEMIS solar array wing.

ARAFOM WING QUALIFICATION PROGRAM

The ARAFOM wing test program consisted of a further improvement of the already existing and qualified ARA-MARK II wing. For instance, new materials were used for the panel structure allowing more structural margin against the stringent requirements. Figure 1 shows the solar array wing. The test program consisted of a range of qualification testing (i.e. certification) of this new type solar array. The qualification wing was subjected to a full dynamic vibration test program. In this section the measurement of the ARAFOM 4 panel wing interface forces due to sine vibration is discussed

The objective of the ARAFOM program, executed at Fokker Space, is to design and qualify a new generation of solar array's. The ARAFOM program is the successor of the successful ARA mk II range. ARAFOM is designed to generate more power and withstand higher launch loads than ARA mk II. ARAFOM will be flown on the new generation of HOTBIRD satellites, NILSAT, ST1 (communication) and XMM (ESA, scientific).

The range of ARAFOM is typically between 3 and 10 kW with wings consisting of 3 to 5 panels. The qualification program qualifies the configurations for Hotbird consisting of 4 to 5 panels per wing. The 4 panel wing has been qualified and will be flown on Hotbird 2, to be launched at the end of 1996. During the qualification of the 4 panel wing a sine vibration test

has been executed. During this test the interface forces between the (rigid) interface and the wing were measured. See for a sketch of the 4 panel stowed wing configuration figure 7.

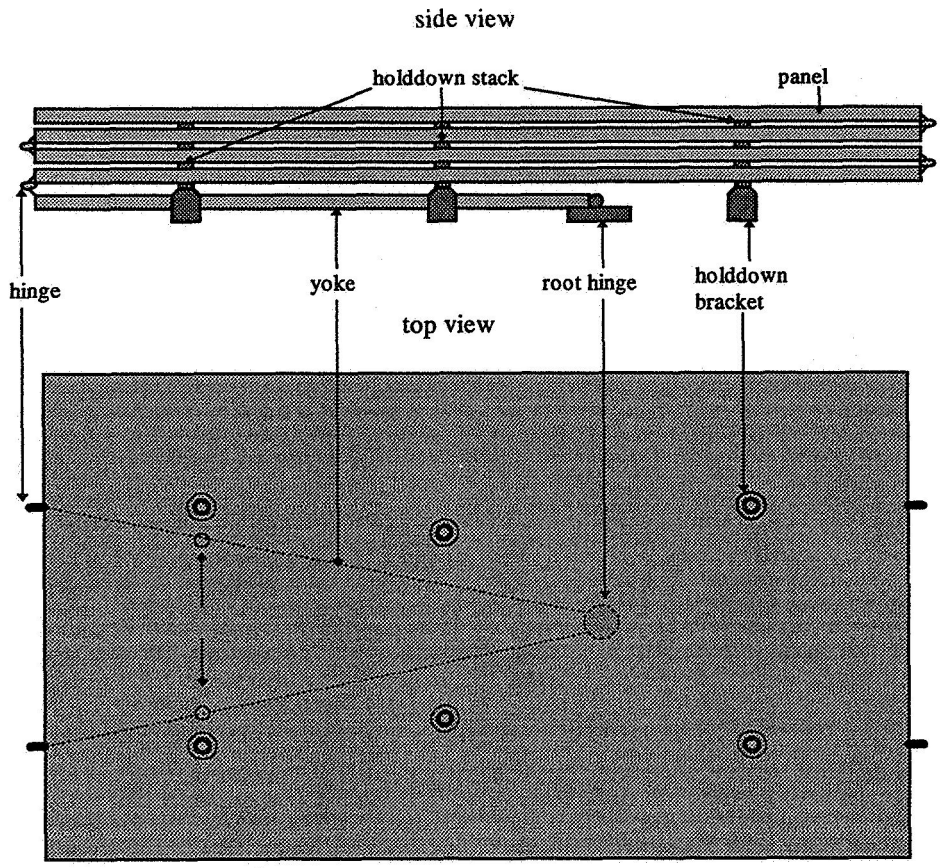


Figure 7: Schematic view of stowed solar array wing

The solar array consists of rigid sandwich panels. The sandwich has an aluminium honeycomb core with a CFRP skin. The panels are covered on one side by solar cells. The panels are linked by spring loaded hinges, actuating the deployment of the wing. The deployment is synchronised using synchro cables. The deployment speed is damped using an eddycurrent damper at the root hinge (interface with sidewall). The dimensions of the panels are 2.736 x 2.250 x 0.022 m^3. The panels are separated from the satellite sidewall by a yoke (1.673 m). The panels have 6 internal holddown points. The panels are clamped together at the holddown points with an aramide cable with a preload of 7 kN. Underneath the holddown points the wing is supported by holddown brackets, interfacing with the satellite. Wing release is activated by cutting the holddown cables with thermal knifes. The thermal knifes are mounted in the holddown brackets. Apart from the six holddown bracket interface points there are three extra interface points. Namely the root hinge (connection yoke-root hinge) and two yoke snubbers (supporting the yoke during launch).

ARAFOM STOWED WING VIBRATION TEST

During the qualification sine vibration tests, the wing had to withstand inputs of 6 g between 5 and 60 Hz for the in plane directions and 4 g input between 60 and 100 Hz. For the out of plane direction the required input was 4 g between 5 and 100 Hz. In order to show the principle, only the out of plane excitation and resulting out of plane interface force is discussed.

The requirements with respect to notching issued by the main contractor for Hotbird (Matra Marconi Space) were the following:

1. Minimum input 2 g
2. Equivalent quasi static acceleration should be covered (10 g out of plane)
3. Notching due to skin stresses allowed (not conflicting 1 and 2)

The primary purpose of the test for Fokker Space was to show the maximum allowable input, demonstrating the capability of this configuration. The weakest component in the stowed wing load path were the sandwich panels. Therefore the input was limited by the stresses in the CFRP skins of the sandwich panels (figure 2).

During the sine vibration test, the interface forces were measured using interface force load cells located between the holddown brackets , root hinge and the rigid interface. The interface loads between the yoke snubbers and the rigid interface were not measured, due to the limited number of interface force load cells available. The influence of the yoke snubbers on the summed interface forces is however limited. The primary load path is through the holddown brackets and secondary through the root hinge (in stowed configuration).

The following checks were performed, in order to confirm a correct measurement of the summed interface forces.

1. The measured interface forces were summed in the quasi-static frequency range and compared to the mass of the wing multiplied by the input acceleration. Both quantities should be equal.
2. The individual interface forces were compared with the analysed interface forces.
3. The mass operator was compared with the measured and summed interface forces.

The interface forces were summed algebraically taking into account the phase. The above listed checks are mathematically described by:

$$\sum_{mi=1}^{7} F_{mi} = m_{wing} a \tag{1}$$

$$F_{mi} = F_{ai} \tag{2}$$

$$\sum_{mi=1}^{7} F_{mi} = \sum_{j=1}^{n} \sum_{i=1}^{n} m_{ij} a_j \tag{3}$$

Where

F_{mi}	Measured interface force at interface point i
m_{wing}	Measured wing mass
a	Input g level
m_{ij}	element of condensed mass matrix (taken from condensed mathematical model)
a_i	measured acceleration at point I
n	number of accelerometers

All above listed forces and accelerations are summed taking the phase into account, the magnitudes of the resulting responses are compared.

According to the notch criterion (2) the equivalent quasi-static acceleration should be equal to or exceed 10 g. This yields the following criterion to be met:

$$\frac{\sum_{mi=1}^{7} F_{mi}}{m_{wing}} \geq 10g \tag{4}$$

Hereafter results of the sine vibration test are given, as well as the results of the checks.

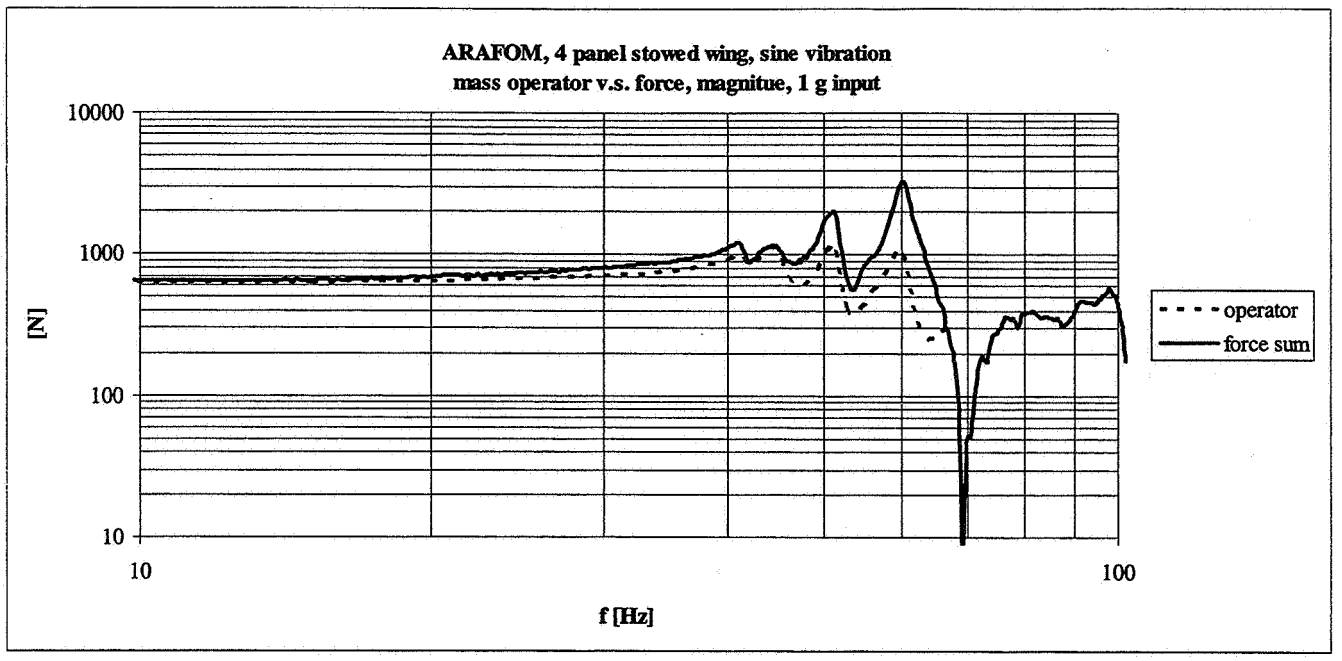


Figure 8: Mass operator versus tested interface forces summed

Figure 8 shows the comparison between the mass operator and the measured interface force. In the quasi-static frequency range (<20 Hz) it shows that the mass operator and the measured summed interface forces are equal. The mass of the wing is 66 kg and the input is 1g, resulting in an interface force of 650 N. All but one response peaks are underestimated by the mass operator. This can be explained. At the locations where the highest response peaks were expected, accelerometers were mounted. However these locations did not include the concentrated masses on the panels edge (hinges), since predictions showed that these were not having the highest response at the eigenfrequencies. Although these concentrated masses do participate in the wing response, their mass is not included in the mass operator since it is lumped mainly to the holddown points. Therefore their contribution to the (summed) interface load is lost and the mass operator underestimates the interface force.

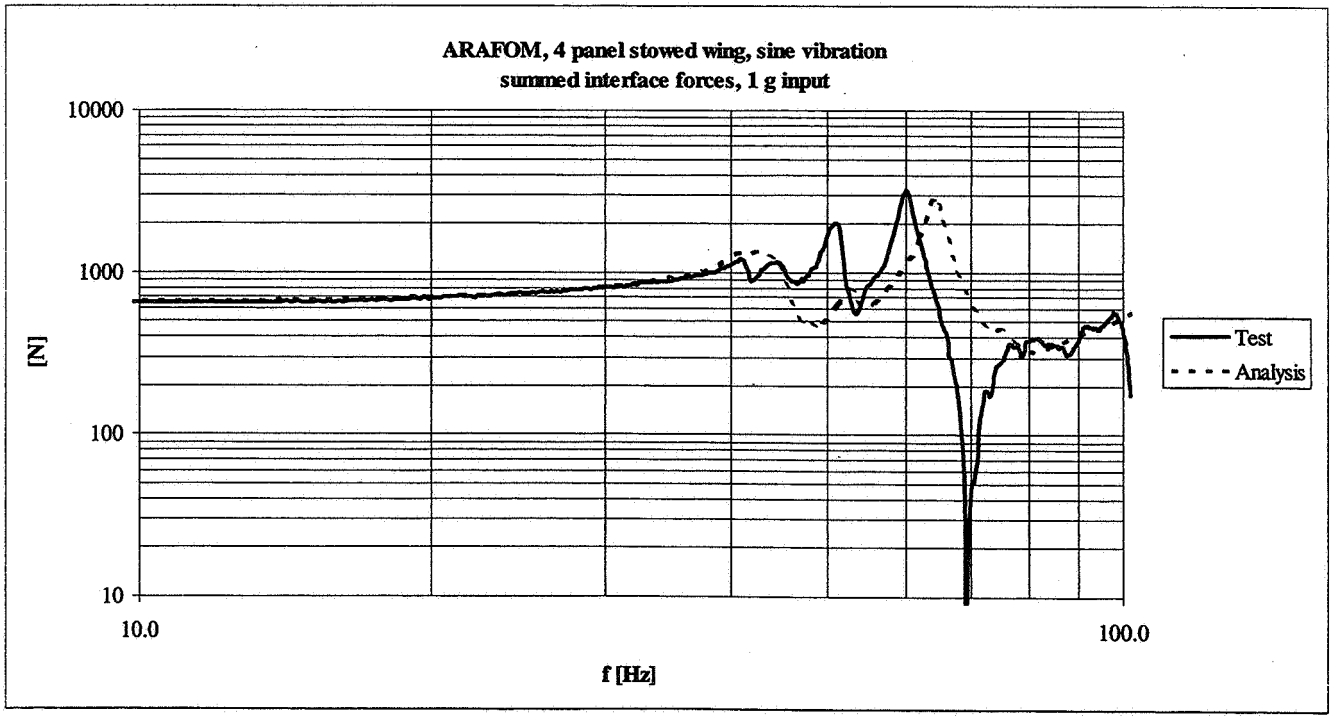


Figure 9: Tested versus analysed interface forces summed

Figure 9 shows the analysed interface force and the tested interface force. The structural damping applied in the analysis is derived from the test results. The mathematical model underestimates 3 out of 4 modes with respect to their eigenfrequency. The magnitude of the interface forces are however predicted accurately by the model (within 20%) except for the mode at 51 Hz (test).

According to the notch criterion, notches are allowed, but not below 2 g. At the notch, the interface force should not drop below the equivalent interface force at 10 g (quasi-static). Therefore at the notch, the summed interface forces should be equal or higher than 6500 N. Figure 2 shows the notch curve for the qualification run. Table 1 shows the input levels at the notches and the measured interface forces. Also the equivalent quasi-static acceleration is given.

Table 1: measured interface forces at qualification level and equivalent quasi-static acceleration

Hz	g_{input}	F [N]	$g_{equivalent}$
41.0	3.6	3960	6.1
43.5	3.0	3300	5.1
51	2.0	4000	6.2
59	2.4	7680	11.8

As can be seen, the equivalent quasi-static interface force is not reached for the first three modes. For the 59.0 Hz mode the notch could have been deeper, down to 2 g (as minimal required). The summed interface forces did not meet the quasi-static criterion. However, the customer accepted the notch because the interface loads (as analysed during the coupled analysis between spacecraft and wing) were covered by the individual *measured* interface forces.

CONCLUSIONS

Benefits:

1. the mass operator can underestimate the interface force considerably
2. the measurement of the interface forces has proven to be a powerful tool to convince the customer that the required input levels have been reached, based on the measurements of the individual interface forces, even if a global input requirement has not been fulfilled
3. It has been proven at this stage that the load cells can be used in many solar array applications. This is possible without any special precautions. Other applications are likely to follow.
4. Installation of the load cells can attribute to limit the stressing the solar array in critical frequency ranges, if launcher specified interface force levels are reached.

Drawbacks:

1. The architecture of load cell excludes (as yet) direct measurement of moments for complete wing testing. The measured interface forces have to be corrected for the inertia forces of the top half of the load cell.
2. As was chosen for a commercial device, the patterns used for fixation of the test structure and the load cell are fixed and are considered a compromise.
3. Verification that the interface forces and moments are measured correctly during the test is not straight forward. The forces and moments have to be summed in each direction taking into account phase shifts. Also the forces and moments have to be corrected for the inertia effects of the top half of the load cell. This is a rather complex operation if a relatively large number of interface load cells are involved

FUTURE DEVELOPMENT

The load cells will be installed during the testing of the ARTEMIS solar array stowed wing. The load cells will also be installed during the 5 panel stowed wing vibration test of ARAFOM. During this test the interface forces will be analysed using post processing software in order to facilitate the checks that have to be made. This was not done during the 4 panel wing test. The measurements appeared to be not always correct, due to (electronic) interface noise between the load cell conditioner and the data acquisition system. Since the measurement data was only available on paper plots, the processing of the summed interface forces was done after the test campaign.

(1) *Solar array qualification through analyses*, P. Zijdemans, J.J Wijker, H.J. Cruijssen ; AGARD-R-772: AGARD Symposium, Sorrento (Italy, 1990)

(2) *ARAFOM Baseline Concept Description*, R van Hassel, AFO-SE-047-FOK, issue 5, 23-09-1993

S21-29
021463
269713
12p

SIMULATION OF THE ZERO-GRAVITY ENVIRONMENT FOR DYNAMIC TESTING OF STRUCTURES[1]

David A. Kienholz
CSA Engineering, Inc.
2850 W. Bayshore Road
Palo Alto, CA 94303

ABSTRACT

Simulation of unconstrained (free-free) boundary conditions is a longstanding problem in ground vibration testing of spacecraft. The test article weight must be supported without introducing constraining forces due to stiffness, inertia, or friction from the suspension system. High-fidelity simulation of the space environment requires that such constraint forces be kept small compared to forces inherent in the experiment. A multipoint, six degree of freedom suspension system for dynamic testing is described. Intended primarily for highly flexible space structures, it uses a combination of passive pneumatic and active electromagnetic subsystems. The suspension offers a wide payload range, near-zero stiffness, zero static deflection, small added mass, and zero friction. The electromagnetic system can also provide active cancellation of added mass, accurate ride-height control, and integrated disturbance input. Several versions of the system are described, aimed at test articles ranging from very flexible solar arrays to a 7000-lb simulated optical truss. The concept and hardware are described, test results are given, and applications experience from several industry, government, and university installations is discussed.

INTRODUCTION

A primary characteristic of the space environment is the lack of gravity. This leads to a fundamental problem in space simulation for dynamic testing of structures. The weight of the test article must be supported in such a way that no significant constraining forces are imposed at the support points. Such constraints would change the normal modes of the test article and thereby produce unrealistic dynamics. Mathematically, the requirement is accurate simulation of so-called "free-free" boundary conditions.

Free-free conditions can be accurately simulated if the forces of constraint from the suspension system are small compared to internal forces due to stiffness and inertia. A common rule-of-thumb is that the vertical plunge frequency on the suspension should be at least an order of magnitude below the first flexural natural frequency of the test article. For natural frequencies above about 20 Hz, this requirement can often be met by hanging the test article from simple linear springs. For large or very flexible test articles with first frequencies below about 10 Hz, this simple approach becomes impractical due to static sag and surge modes of the springs themselves. As test article frequencies approach 1 Hz or less, the suspension problem becomes quite challenging. The most difficult cases occur when rigid-body dynamics (zero-frequency modes) are of interest.

Dynamic testing of low-frequency structures under simulated zero gravity requires a specialized suspension system. This paper describes such a system in several variants. Begun in 1988 as a research topic under the NASA/LaRC Dynamic Scale Model Technology Program [1] [2], the development has produced systems now in daily use on a number of aerospace programs as well as several specialized spin-off products. Called the pneu-mag system because of its combination of passive pneumatics and active electromagnetics, it provides a unique combination of wide payload range, very low stiffness, low added mass, and zero friction. These allow high-fidelity space simulation in a wide variety of applications.

The following section describes in general terms the requirements and figures of merit for a suspension system for zero-gravity simulation. The operating principle, analytical model, and current hardware implementation of the CSA Engineering pneu-mag system are described. Performance test results are given for comparison to the figures of merit. Finally, some recent developments for specialized applications are reviewed.

[1]Portions of the work reported here were supported by the Air Force Phillips Laboratory, Kirtland AFB, NM through the Small Business Innovation Research program.

SUSPENSION SYSTEM REQUIREMENTS

The essence of the suspension problem is to support the weight of the test article without imposing constraints or dynamic forces at the support points that would change its normal modes. Constraint forces can be produced by stiffness, mass, friction, or resonances of the suspension devices. The figures of merit described below are primarily measures of the degree to which these undesired forces are minimized.

Historically, efforts to develop hardware for zero-G simulation have often concentrated simply on achieving very low stiffness with adequate payload capacity. However, experience in the development reported here has shown that the low-stiffness requirement is only one of several and is not necessarily the most difficult or even the most important. A particular example of neglecting other effects in order to minimize stiffness has been the use of helium-filled balloons to suspend a test article. While vertical stiffness is small (zero were it not for density gradients in the surrounding air), it can easily be shown that the mass added by the balloons can never be less than about 16% of payload mass. This added mass will corrupt even the lowest modes of the test article and will fundamentally change the higher modes due to inertia constraint forces. Further, the added mass cannot be accurately included in the analytical model because both it and its coupling to the article are anything but rigid. A systematic, balanced approach is necessary that considers all sources of undesired constraint forces.

Suspension systems for dynamic testing have usually taken the form of support-from-above cable arrangements with a soft spring in series with each cable. Pendulum action gave a simple, effective soft restraint in the horizontal direction, given adequate cable length. Two versions of the pneu-mag device described here uses this overhead arrangement. Two others support their payloads from below, thus removing the headroom requirement and pendulum effects.

The remainder of this section describes specific requirements and how they have affected the development of the pneu-mag system.

Payload Applications to date have required from 15 to 600 lb per support point (i.e., per suspension device) for overhead suspension and as much as 3000 lb per device for support-from-below devices. While there is obviously no limit to what might be required, most applications seem to fall between 30 and 400 lb per support point. Since the suspension system is always soft relative to the payload, there is no limit to the number of devices that can be ganged to support a single payload: static indeterminacy is not a disadvantage. Of practical interest is the range of payloads that can be supported by a given system. The pneu-mag devices described here can typically accommodate a weight range of over 6/1 by immediate on-the-spot adjustments (no changing of parts) and about 20/1 with simple changes.

Static Deflection Linear springs, regardless of their implementation, are usually ruled out for low frequency applications by the contradictory requirements for low stiffness and small static deflection. A primary feature of pneumatic springs, shown later, is that they decouple the local tangent stiffness from static deflection. Pneu-mag devices use this feature to operate at zero static deflection.

Stiffness Allowable stiffness is usually specified in terms of the vertical rigid-body plunge frequency on the suspension. For a first flexural frequency of 1.0 Hz and plunge frequency of 0.1 Hz, this translates to approximately 0.1 lbf/inch of stiffness per 100 pounds of payload. Linear springs are obviously excluded; the static deflection would be 1000 inches. Figure 1 shows a more payload-specific method of determining suspension stiffness effects. It shows the gradual loss of cross-orthogonality between true free-free modes and modes including suspension stiffness as the suspension stiffness is increased. The example structure is a dynamic scale model of an early configuration of the space station. Physically, it is a number of rigid masses held together by light trusswork. Modes 7 and 8 are the first global flexing modes at slightly over 1 Hz. The example shows that the 10/1 frequency separation criterion is, in this case, probably conservative. It also shows that the effect of suspension stiffness varies greatly from mode to mode. The pneu-mag devices have been designed from the outset to have a variable suspension frequency with a range extending down to 0.1 Hz for most payloads.

Moving Mass Any suspension device adds some amount of mass to the payload, and can thus change its properties regardless of suspension stiffness. For very light, flexible payloads, it often occurs in low frequency testing that inertia constraint forces due to moving suspension mass exceed stiffness constraint forces for frequencies over a few Hz. Allowable added mass for the example structure described above was determined by finite element analysis to be about 5%. The pneu-mag device easily meets this for payloads towards the upper end of its range. For very light payloads, an active mass canceling feature has been developed. Described in a later section, it has

demonstrated the ability to cancel about 85% of the 3.4-lbm moving element of a pneu-mag device with good stability margin. This allows testing a 20-lb payload with less than 3% added mass.

Stroke Modal testing of even large spacecraft typically requires only a modest amount of vertical suspension stroke, on the order of one inch. The real requirement is set by measurement of local modes of very flexible appendages such as solar arrays, or by other dynamic tests involving rigid-body rotations of the payload. To meet these requirements, the current generation of pneu-mag devices has a vertical stroke of 6.0 inches. A large system concerned with rigid body modes has a stroke of over 10 inches.

Friction This is perhaps the most difficult requirement and has been an important driver in developing the pneu-mag concept. Unlike forces due to suspension stiffness or moving mass, friction is inherently nonlinear, often not repeatable, and always expensive to model in structural dynamics. A high priority was therefore given to reducing friction to the point where it had no measurable effect. This leads to a requirement that can be formulated in two ways. Either the friction force in the device must be small compared to its stiffness force, or friction force must be too small to produce a measurable change in payload acceleration based on typical accelerometer noise floor levels. Either leads to an allowable friction force on the order of 0.01% of payload weight. The nominal specification for the pneu-mag devices was set at 0.005%.

Controllability The projected large, flexible spacecraft applications that motivated the pneu-mag suspension system would have required 10-20 support points to avoid excessive weight-induced stresses. Even then, weight distribution between devices would have to be carefully controlled by tuning the ride height of each device. Testing efficiency required that this be done remotely, probably by a computer. While no such grand-scale application has actually materialized, the need for remote control was basic to the pneu-mag concept. The feature has proven to be valuable in day-to-day testing of smaller test articles. It has become a de facto requirement that a single operator be able to adjust from one location all devices of a multipoint suspension system in order to obtain a desired weight distribution.

Local Modes Accurate modal testing demands that the suspension devices contribute no local modes of their own within the test frequency band. Failing this, the suspension becomes part of the test article, a serious complication that the test engineer would much rather avoid. The pneu-mag devices are designed such that their only moving part is relatively light and stiff, with its first free-free mode well over 100 Hz.

PNEUMATIC-MAGNETIC PRINCIPLE

Figure 2 shows the basic operating principle of the pneu-mag device. Two parallel subsystems, one pneumatic and one electromagnetic, give the device its name. Figure 3 shows a somewhat simplified version of the analytical model for the device. In the figure, the constant forces F_p and F_m represent actions of the pneumatic air spring and magnetic fine-trim control respectively. The stiffness K_m is produced by the active system and K_p by the pneumatic system. The dashpot C_p is produced by the action of the pressure regulator.

The entire payload weight is borne by a special frictionless air piston operating vertically in a closely fitted cylinder. By porting the cylinder to an external volume through a large diameter line, the stiffness of the air spring thus formed can be made very small while retaining a large payload capacity. A precision pressure regulator maintains the mean cylinder pressure and supplies makeup air. For small volume changes, the regulated air spring behaves like a linear spring in series with a dashpot (Figure 3). The spring stiffness can be determined from elementary thermodynamics by assuming isentropic pressure changes. The result, expressed in terms of vertical suspension frequency, is as follows.

$$f_s = \frac{1}{2\pi}\sqrt{\frac{\gamma g A}{V}}\sqrt{1+\frac{p_{amb}}{p_g}} \tag{1}$$

where
f_s = suspension frequency, Hz
γ = specific heat ratio for air (1.40)
A = piston area, in^2
V = tank volume, in^3
p_{amb} = ambient pressure, psia
p_g = gage pressure in air spring, psig

Eq. (1) and Figure 3 illustrate two well-known advantages of air springs. For p_g of several atmospheres or more,

f_s is nearly independent of payload weight. That is, the suspension stiffness automatically changes in proportion to payload. Secondly, by adjusting the cylinder pressure to equilibrium with the the payload weight, there is no static deflection of the spring.

The series dashpot is the result of the action of the regulator. It vents air in or out of the external tank, attempting to keep the pressure constant in spite of piston movement. The spring-dashpot combination has a frequency-dependent stiffness with a first-order, high-pass break frequency determined by the size of the external tank and the characteristics of the regulator. The regulated pneumatic spring has no static stiffness at all: it can be in equilibrium with the payload weight at any vertical position of the piston within the cylinder. This property can be a disadvantage since the payload can float to the end of the stroke and strike the limit bumper. Thus arises the need for the parallel magnetic system.

The active part of the system includes a custom long-stroke, voice-coil magnetic actuator, a displacement sensor, controller, power amplifier, and (optionally) an acceleration sensor. A negative-feedback, low-gain displacement loop is implemented to serve as a noncontact "spring" with a very small, variable stiffness. It keeps the moving element of the device near the center of the working stroke, thus preventing it from striking the limit bumpers when excitation is applied to the payload. A secondary use of the displacement loop is to provide fine-trim control of ride height. This is required if the payload contains optics that must be kept in registration with some off-payload datum. A small, variable DC offset voltage can be injected into the displacement loop. It serves the same purpose as adjusting the pressure regulator set point but does so with much faster response and much greater resolution.

The active system also provides other useful features. A positive-feedback acceleration loop can be added to cancel most of the moving mass of the suspension device. This can drastically improve the fidelity of the zero-G simulation for small payloads, on the order of 20 pounds, where the added mass can have a significant effect [3]. An external dynamic signal can be summed into the loop to provide a controlled vertical excitation to the payload. This is useful in situations where the payload is very flexible and would be affected by the rotational constraint of a shaker pushrod. A modest multipoint-excitation modal test can be performed using only the actuators and sensors built into the pneu-mag devices. The DOF's are, of course, limited to the vertical direction at the hang points.

Special versions have been built with a lowpass filter in the displacement loop such that DC stiffness could be increased for improved centering without imposing constraining stiffness at higher frequencies. Negative velocity feedback was necessary to stabilize the loop in the presence of the phase lag of the filter. The arrangement was not entirely satisfactory because the velocity feedback slightly increased the apparent damping of the lowest modes of the test article [4]. The eventual solution was a basic redesign with much longer stroke (described below) which eliminated the need for enhanced DC stiffness. Frequency-dependent stiffness is one of many features that have been investigated in a research context during the pneu-mag systems development.

HARDWARE IMPLEMENTATION

Passive/Active System

Figure 4 shows two views of a current pneu-mag version along with nomenclature. Figure 5 shows the pneumatic and electronic control panels for a system at NASA Langley Research Center. Figure 6 shows several views of a system in use at NASA/Jet Propulsion Laboratory with the Microprecision Interferometer test bed. The active capabilities are particularly useful in this latter application because of the need to maintain accurate ride height. Optics on the suspended payload must receive the image of a synthetic star from an optical bench supported off the laboratory floor.

Referring to Figure 4, the pneu-mag device is composed of a carriage that moves vertically in a rectangular box frame on four air journal bearings. The moving carriage is composed of a single main rail down the center with a horizontal crossmember fixed to it about one-third of the way from its upper end. Two identical frictionless piston/cylinder sets are used, one on either side of the main rail, with each piston lifting against one end of the crossmember via a connecting rod. Both cylinders are ported through the bottom of the box frame to hoses connected to a common accumulator tank. The single-main-rail, twin-piston geometry is used to avoid bending stress in the rail and allow a high payload capacity (large piston area) with minimum carriage mass. The design replaced an earlier single-piston configuration with shorter stroke [4][5].

The payload is connected to the carriage by a cable that attaches to the lower end of the main rail. An optional

load cell may be interposed between the cable and carriage to sense cable tension.

The magnetic voice-coil actuator is a custom, long-stroke design that uses a coil connected to the carriage crossmember and a magnet body mounted to the frame. High-energy NdFeB magnets are used for maximum force capacity. The magnet structure is designed to produce a high flux density in the air gap with minimal variation in the stroke direction.

The carriage displacement sensor is a non-contacting LVDT mounted behind the carriage main rail. A piezoresistive (DC-coupled) accelerometer is mounted to the carriage for the mass-canceling loop. A pressure sensor transduces the cylinder pressure to obtain a continuous analog reading of piston force. Each suspension device connects to the control panel by a single electrical cable and two compressed air lines.

The key to the performance of the device is the fact that the load is supported completely on air. The combination of air bearings, noncontacting actuator and displacement sensor, and floating pistons eliminates any source of friction. The only connections between the moving and fixed parts of the device are the small wires carrying current to the actuator coil and (optionally) the small signal cable from the accelerometer.

Nominal specifications for the device as shown are: maximum payload (at 80 psig): 500 lb; active stiffness: variable over 0.05-2.0 lbf/inch; vertical suspension frequency: 0.1-0.2 Hz; breakaway friction: under 1 gram; stroke: 6.0 inches; carriage mass: 6.0 lbm.

All-Passive Device

Figure 7 shows a version of the device which substitutes a simple mechanical extension spring for the electromagnetic active system. This all-passive device came about in response to applications which would use the active system only for centering control and which did not require precision ride-height maintenance or other active features. The passive device has the advantages of being substantially simpler, cheaper, and lighter. It retains the high payload, low stiffness, long stroke, and zero friction attributes of its predecessor. Devices of both types can be mixed in a single system to utilize the advantages of both.

PERFORMANCE TEST RESULTS

This section presents some typical test results for pneu-mag suspension devices. A rigid test payload was used in all cases.

Figure 8 shows the measured vertical displacement/force FRF with two different payloads. The displacement loop was closed with a loop gain of about 0.2 lbf/inch. The internal actuator and displacement sensor were used to allow FRF measurements at the very low frequencies involved. The series-dashpot effect of the pressure regulator becomes progressively more evident as the payload is increased. At 350 lb, the suspension resonance has disappeared due to regulator action. This is exactly what is needed in a suspension device; the load is virtually floating with negligible vertical constraint.

Figure 9 shows a typical breakaway friction test result. The pneu-mag device was loaded to 150 lb (68 kg), active loop stiffness was set to 1.5 lbf/inch, and a 1.1 gram weight was carefully lifted from the carriage while monitoring the position sensor output. Transient motion of the carriage, small but clearly visible against the quiet background, shows that even this tiny load step was more than sufficient to cause motion. Friction is too small to measure.

SPECIAL VERSIONS

The pneu-mag devices shown above are third and fourth generation designs. They were designed primarily around the requirements of modal (i.e., small displacement) testing of low frequency structures in a typical laboratory setting. Several more specialized variants have also been developed [6].

Large-Scale Pointing and Tracking Experiments

A variant of the pneu-mag suspension is in use at the Air Force Phillips Laboratory, Kirtland AFB, NM. Designed and built by CSA Engineering, it supports a large precision truss structure (Figure 10). The facility, simulating a large, orbiting optical system, has been developed for ground-based pointing and tracking experiments.

The zero-G suspension consists of three identical devices, each supporting a hard point of the truss. Each device uses a frictionless air spring and air bearing carriage similar to those described earlier. However the devices are much larger; each is capable of floating about 3000 lbs. Also, the system supports the payload from below. Horizontal motion at each support is accommodated by a flat air bearing sliding on a ceramic platen that forms

the upper crossmember of the vertically moving carriage. This eliminates the horizontal stiffness and other limitations of support-from-above pendulum systems. Each support point can accommodate a vertical stroke of 10.5 inches and horizontal motion of 8.7 by 10.7 inches. Vertical plunge frequency is nominally 0.1 Hz and is heavily damped by the action of the air pressure regulator. As in the smaller versions, the system is completely frictionless over its full range of motion.

High-Performance Airborne Vibration Isolators

The very soft, frictionless character of the pneu-mag suspension suggests its application to vibration isolation. It is potentially capable of 1-2 orders of magnitude improvement in isolation relative to conventional passive systems. Also, it can provide a long stroke, easily 3 orders of magnitude longer than active piezoelectric-based systems. These properties make it well suited for airborne optics where precision beam pointing must be performed in the presence of significant broadband base vibration.

A variant of the support-from-below pneu-mag system has been developed for such applications. A single suspension device is shown in Figure 11 and a full-scale demonstration testbed system is shown in Figure 12 with a simulated 1500-lb optical bench payload. Like the system described in the last section, this testbed has been designed and built by CSA Engineering for the Air Force Phillips Laboratory.

A unique feature of the airborne problem is low-frequency inertial forces on the isolated payload due to aircraft maneuvering. As the aircraft turns and banks, it will impose significant g loading on the payload. This would produce unacceptable static sag on a suspension designed for a very low break frequency. This situation is countered by the active system. The isolation mounts incorporate voice coil actuators and DC-coupled acceleration sensors. The actuators use rare earth magnets and air-jet coil cooling to produce a force rating of about 230 lbf from a 96-lb actuator with a 1.25-inch stroke. Similar actuators also act on the payload in the horizontal direction to provide inertia force compensation and damping of suspension modes. Various software-based control schemes are being investigated to optimize the performance of the active system for airborne isolation.

CONCLUSIONS

A suspension system has been described for producing near-unconstrained boundary conditions in dynamic testing of flexible structures. Called the pneu-mag system, it provides a unique combination of high payload, low stiffness, low added mass, and zero friction. It has reached the status of a commercial product and is in daily use on several current aerospace programs. Work is continuing to develop new versions for specialized applications.

REFERENCES

[1] Letchworth,R., McGowan,P.E., and Gronet, M.J., "Space Station: A Focus for the Development of Structural Dynamics Scale Model Technology for Large Flexible Space Structures," 29th Structures, Structural Dynamics, and Materials Conference, Williamsburg, VA, April, 1988.

[2] Gronet, M.J., Crawley, E.F., and Allen, B.R. "Design, Analysis and Testing of a Hybrid Scale Structural Model of a Space Station," 30th Structures, Structural Dynamics, and Materials Conference, Mobile, AL, April, 1989.

[3] Miller, D., Sepe, R., Saarmaa, E., Crawley, E., "The Middeck Active Control Experiment (MACE)," Fifth NASA/DoD Control-Structure Interaction Technical Conference, Lake Tahoe, NV, March, 1992.

[4] Cooley, V.M. and Giunta, A.A., "Laboratory Evaluation of Two Advanced Suspension Devices for Ground Vibration Testing of Large Space Structures," 33rd Structures, Structural Dynamics, and Materials Conf., Dallas TX, April, 1992.

[5] Kienholz, D. "A Pneumatic/Electric Suspension System for Simulating On-Orbit Conditions," Proc. ASME Winter Annual meeting, Dallas, TX, Nov. 1990.

[6] Kienholz, D. "Defying Gravity with Active Test Article Suspension Systems," *Sound and Vibration*, April 1994, pp. 14-21.

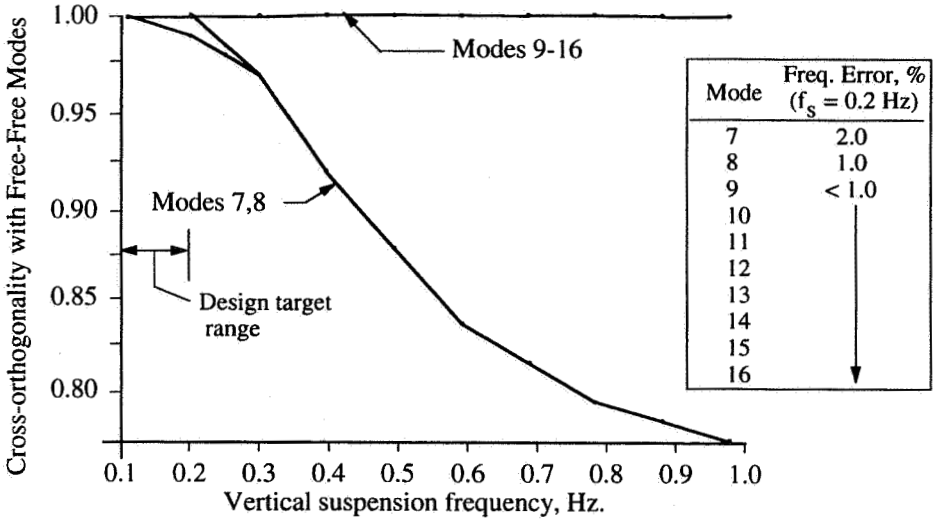


Figure 1 Effect of suspension stiffness on cross-orthogonality between unconstrained and suspended modes of a mass-loaded truss

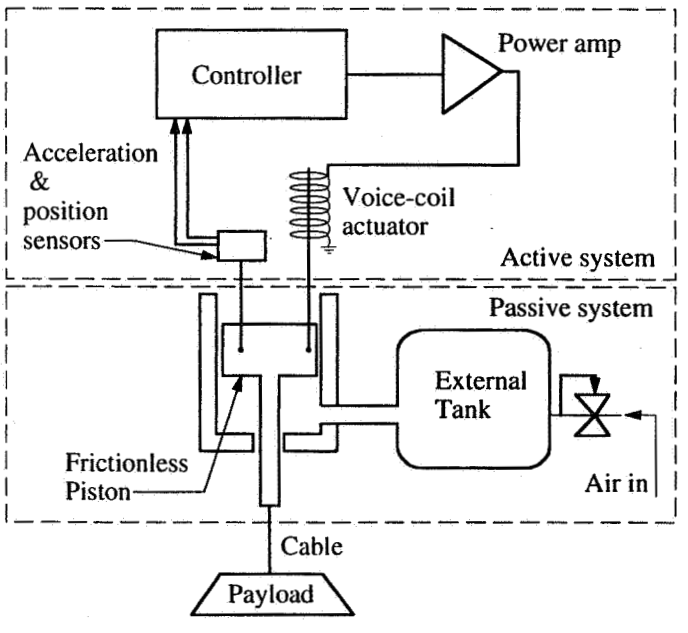


Figure 2 Principle of pneumatic-magnetic suspension device

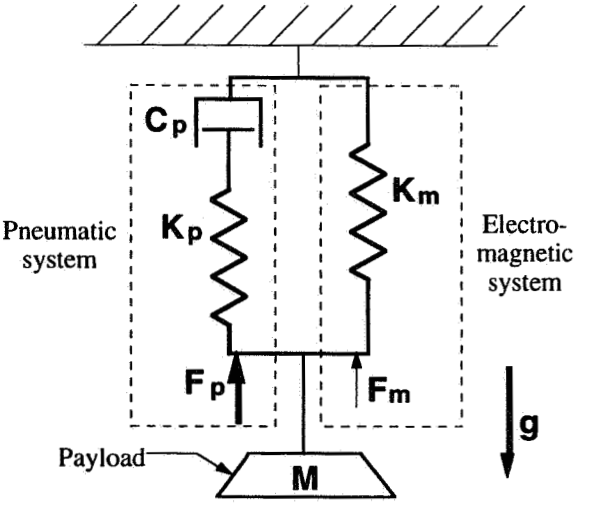


Figure 3 Simplified analytical model of pneu-mag suspension device.

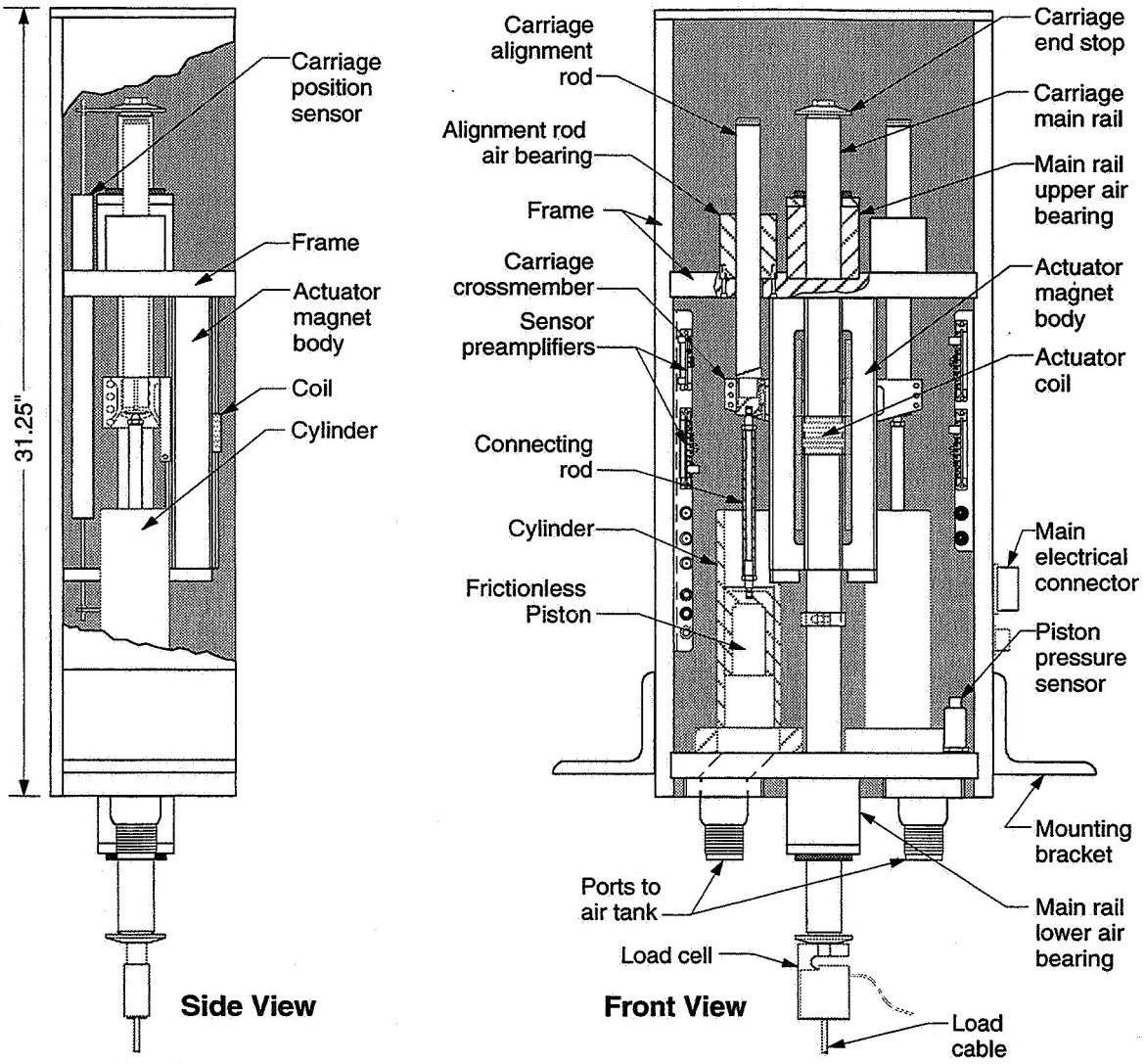


Figure 4 Passive-active suspension device currently in use at NASA/Jet Propulsion Laboratory (Microprecision Interferometer test bed) and NASA Langley Research Center (Large Structures Lab).

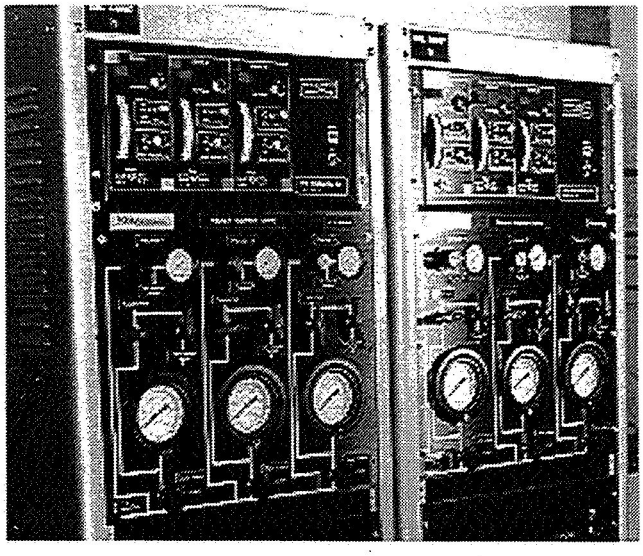


Figure 5 Pneumatic and electronic control rack for 6-device suspension system

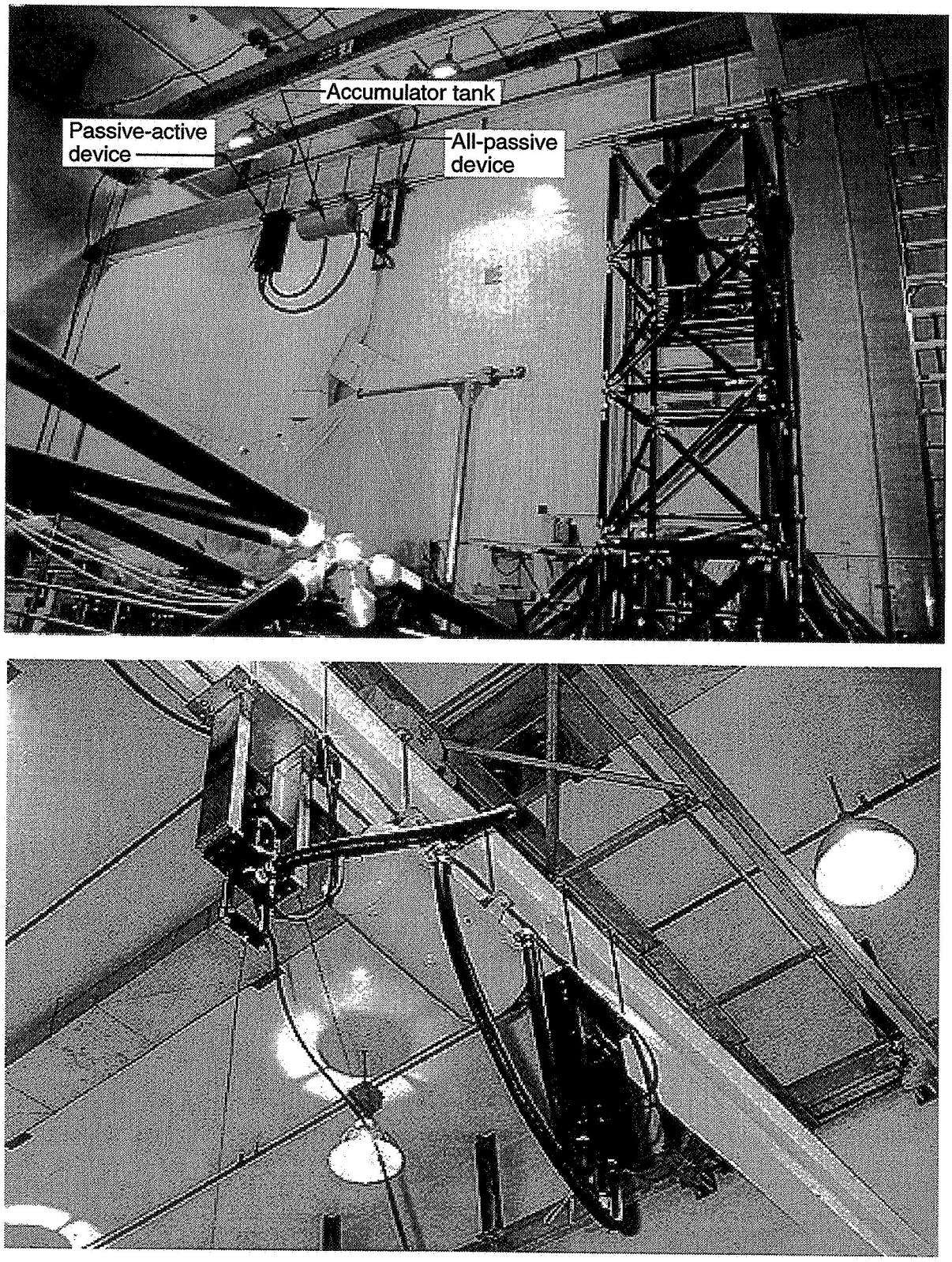


Figure 6 Zero-G suspension system being installed at NASA/Jet Propulsion Laboratory for the Microprecision Interferometer test bed. Top photo shows one passive-active and one all-passive device ganged to support the MPI optics boom. The two devices are connected to a common accumulator tank. Bottom photo is a close-up of the devices. The full system uses three passive-active devices and one all-passive.

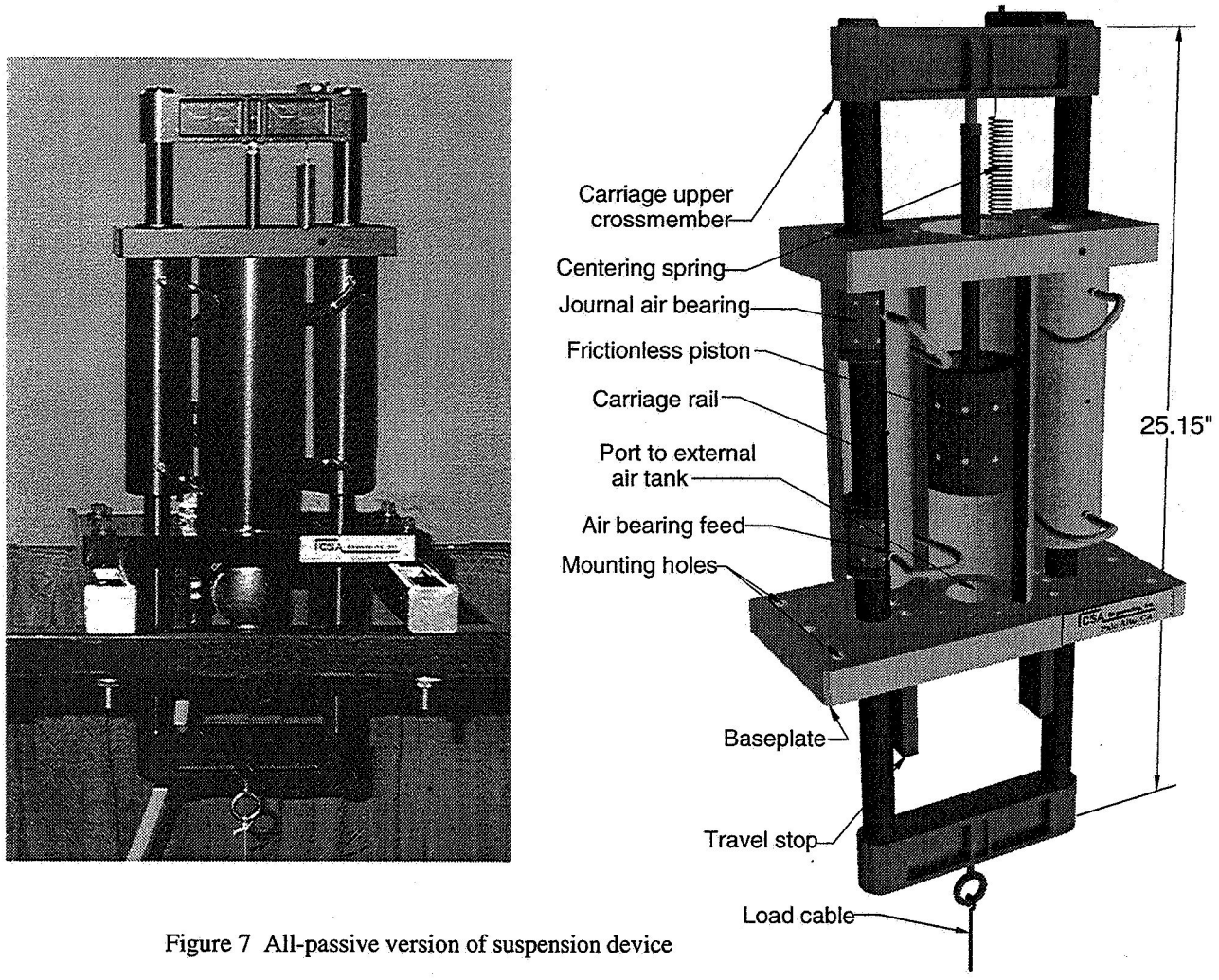


Figure 7 All-passive version of suspension device

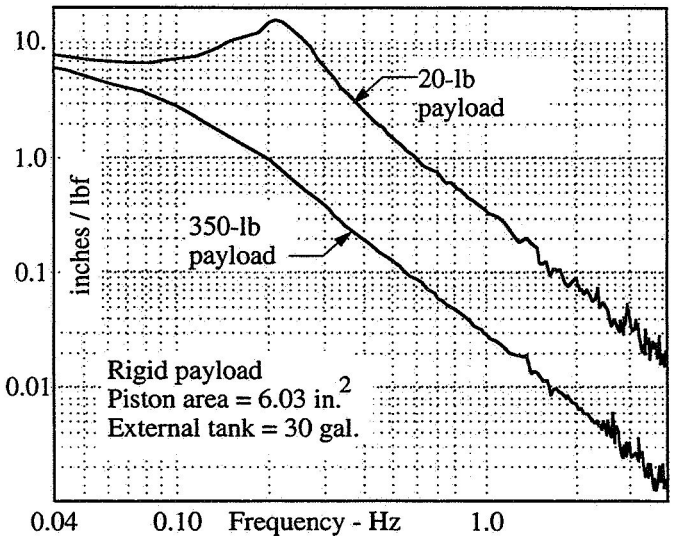


Figure 8 Vertical displacement/force frequency response function measured for passive-active device with rigid payload.

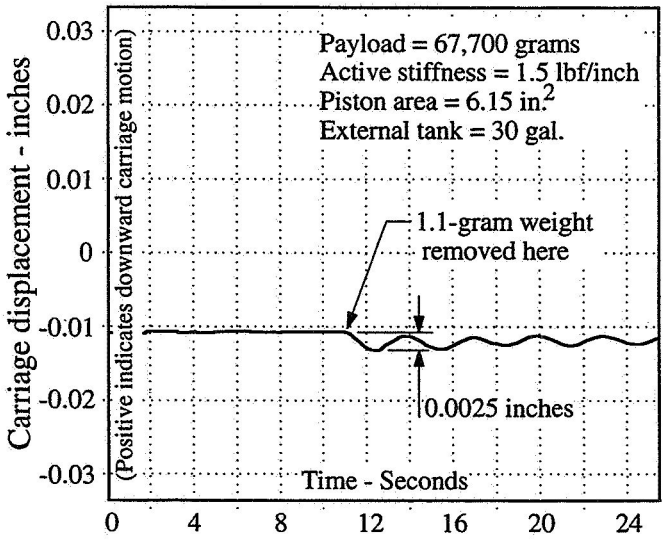
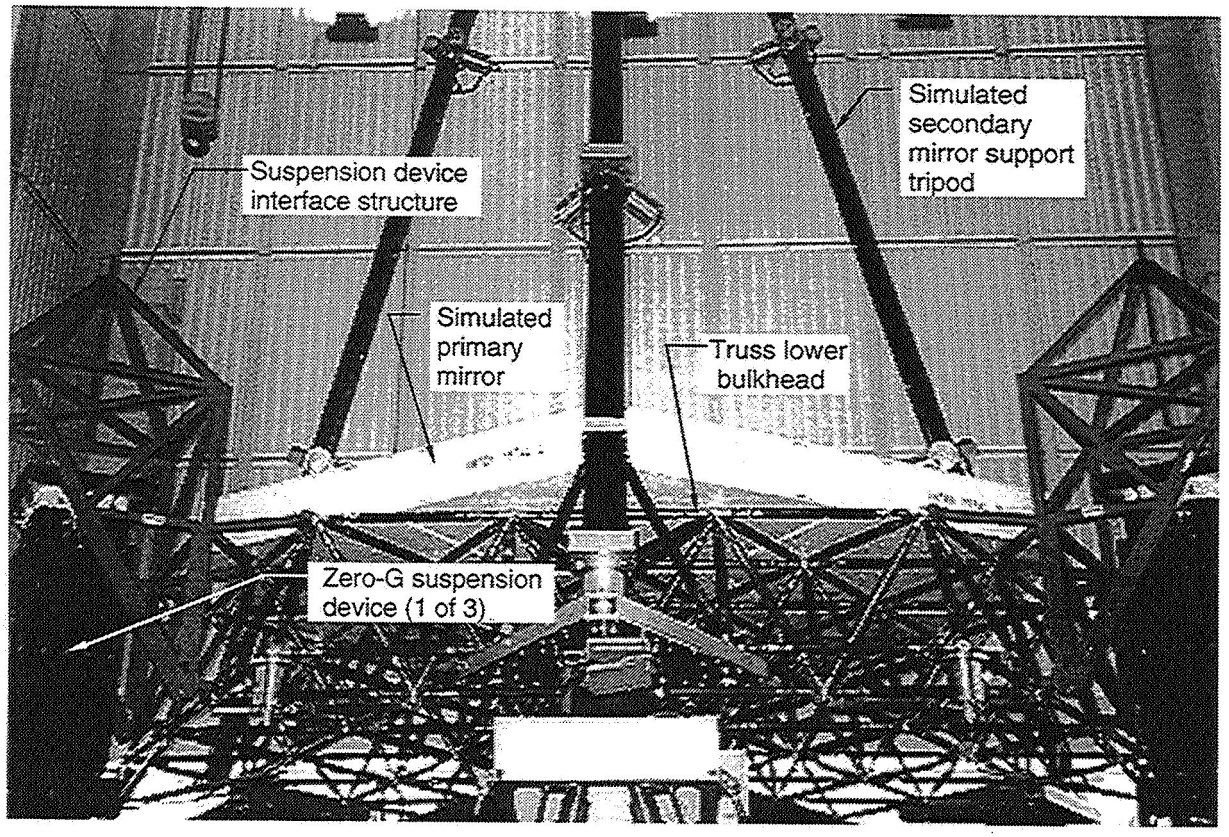


Figure 9 Typical breakaway friction test result for passive-active suspension device



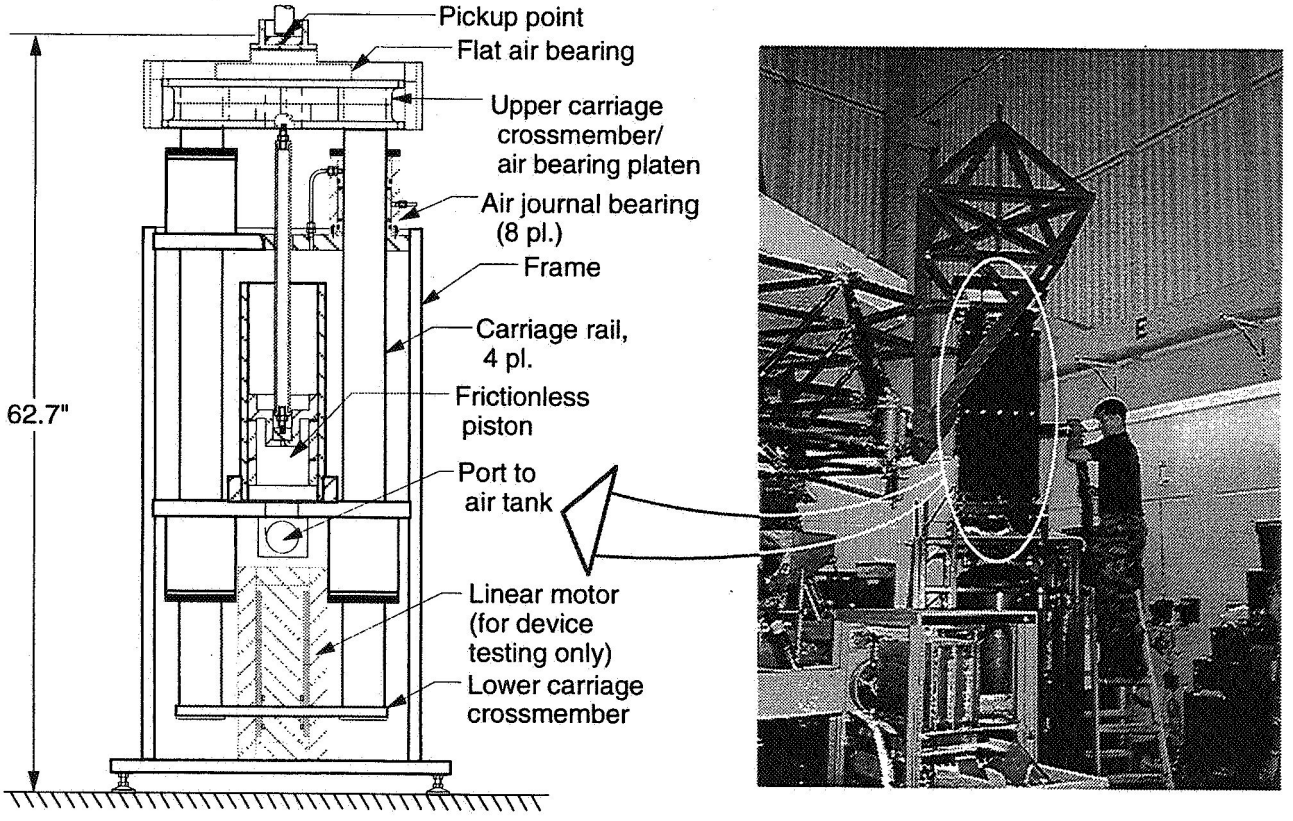


Figure 10 7000-lb truss testbed structure floated on three floor-standing zero-G suspension devices. Horizontal motion at each support point is allowed by a flat air bearing running on the ceramic upper crossmember platen of the device.

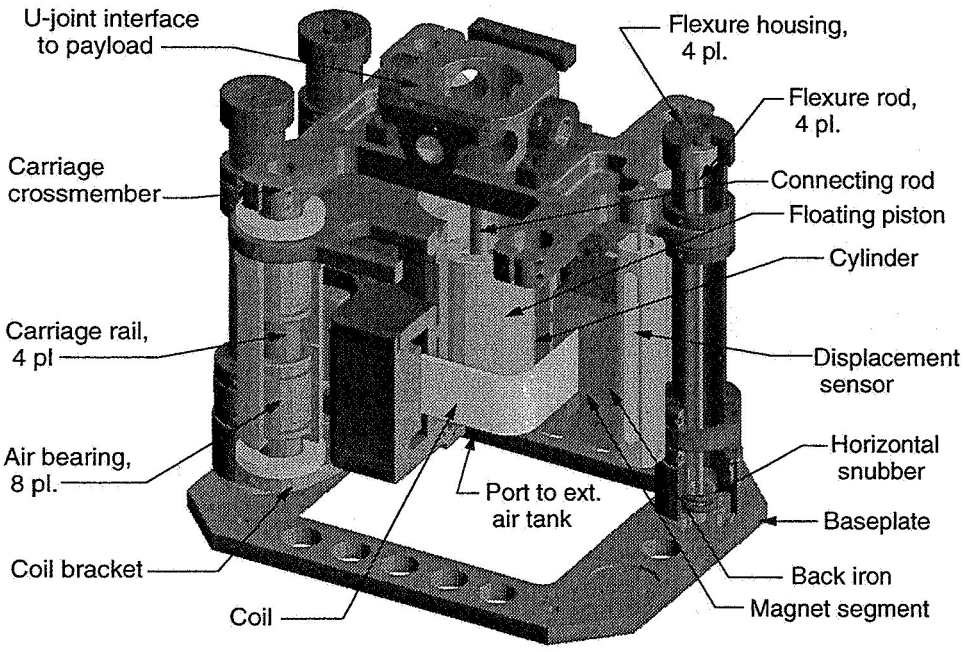


Figure 11 6-degree of freedom pneumatic mount with integral voice-coil actuator. The device is derived from zero-G suspension technology and is sized for payloads up to 1200 lb per device.

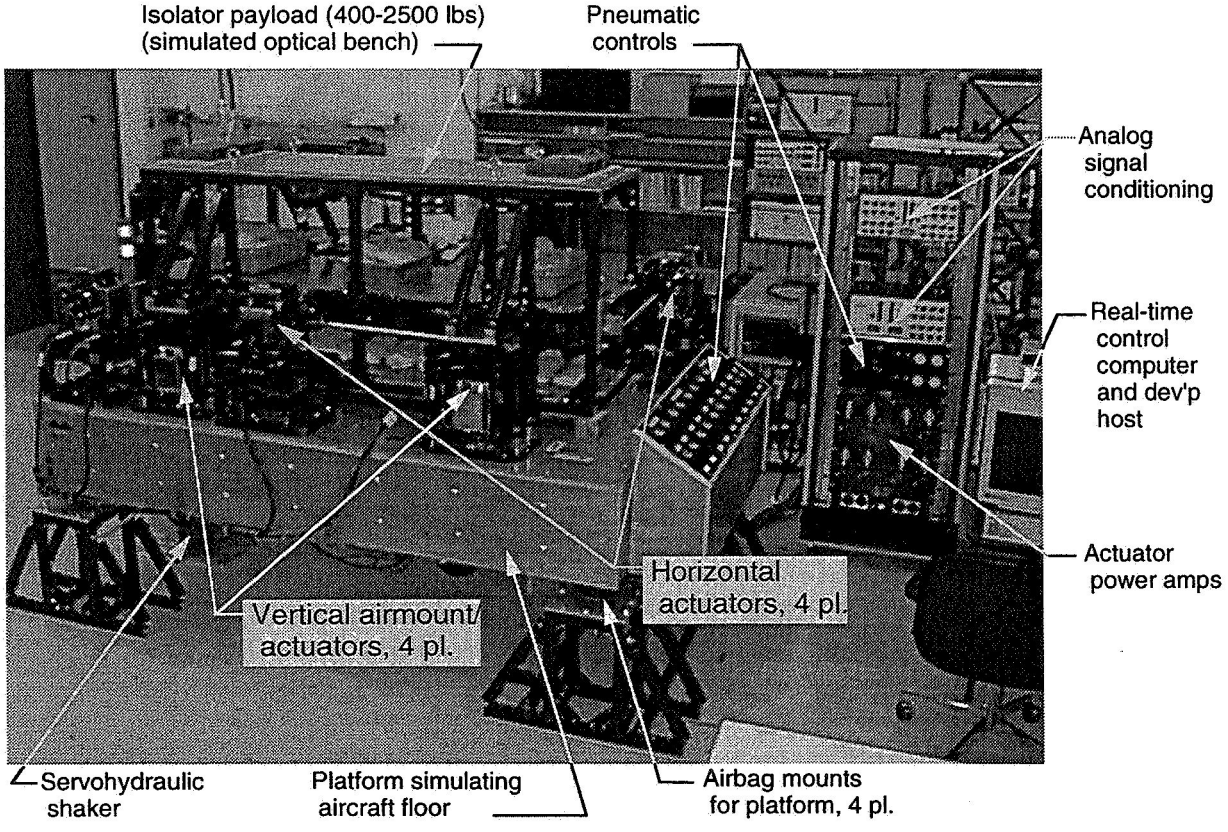


Figure 12 Demonstration testbed for passive-active isolators. The payload is a 1500-lb simulated optical bench. Enhanced active features are provided by a VMEbus real-time control computer.

S22-74
021464
20P
269414

End-to-end System Test and Optical Performance Evaluation for the Solar and Heliospheric Observatory (SOHO) Ultraviolet Coronagraph Spectrometer (UVCS) [1]

Paolo A. Carosso
Swales and Associates, Inc.
Beltsville MD 20705

Larry D. Gardner
Harvard Smithsonian Center for Astrophysics
Cambridge MD 02138

Murzy Jhabvala
NASA Goddard Space Flight Center
Greenbelt, MD 20771

P. Nicolosi
Universita' di Padova
I-35131 Padova, Italy

1. ABSTRACT

The UVCS is one of the instruments carried by the Solar and Heliospheric Observatory (SOHO), a joint NASA/ESA Spacecraft launched in November 1995. It is designed to perform ultraviolet spectroscopy and visible light polarimetry of the extended solar corona. The primary scientific objectives of the UVCS investigation are to study the physical processes occurring in the extended solar corona, such as:

- the mechanism of acceleration of the solar wind,
- the mechanism of coronal plasma heating,
- the identification of solar wind sources, and
- the investigation of the plasma properties of the solar wind.

The UVCS End-to-End test activities included a comprehensive set of system level functional and optical tests. Although performed under severe schedule constraints, the End-to-End System Test was very successful and served to fully validate the UVCS optical design. All test results showed that the primary scientific objectives of the UVCS Mission were achievable.

[1] This work was performed under contract NAS5-31250

Following an introductory description of the UVCS Instrument, this paper describes the preliminary UVCS AIV activities, and the rationale for performing the end-to-end system test. The process for the selection of the most appropriate facility for the test is then summarized. The SAO laboratory is then described, as well as the preliminary work that was necessary to be performed to enhance the laboratory test environment. This includes the design, fabrication and installation of a special cryogenically cooled shroud for the vacuum chamber, and upgraded cleanroom facilities.

The test philosophy, performance goals, and a summary of the test results are also given.

2. INTRODUCTION

The Ultraviolet Coronagraph Spectrometer[1] (UVCS) is one of the instruments carried by the Solar and Heliospheric Observatory (SOHO)[2], a joint NASA/ESA Spacecraft, currently in orbit and fully functioning. The SOHO spacecraft and its complement of payloads, including the UVCS, is shown in Figure 1.

The UVCS is an instrument designed to perform ultraviolet spectroscopy and visible light polarimetry of the extended solar corona. The primary scientific objectives of the UVCS investigation are to study the physical processes occurring in the extended solar corona, such as:

- the mechanism of acceleration of the solar wind,
- the mechanism of coronal plasma heating,
- the identification of solar wind sources, and
- the investigation of the plasma properties of the solar wind.

3. INSTRUMENT DESCRIPTION

The UVCS consists of a Telescope / Spectrometer Unit (TSU), and a Remote Electronics Unit (REU). The TSU is a telescope in which each of the three channels is optimized for observations respectively at the Lyman-α, O VI, and Visible Light wavelengths. The telescope has external and internal occultation, and includes a high resolution Spectrometer Assembly (SPA).

The Lyman-α section of the SPA is a toric grating spectrograph with an entrance slit mechanism, a neutral density filter inserter, a grating mechanism, and a windowed XDL detector[6]. The spectral range 1100 to 1361 Å is achieved by the detector size and by grating motions, and includes the primary H I line at 1216Å.

The O VI section is a toric grating spectrograph with an entrance slit mechanism, a neutral density filter inserter, a grating mechanism, and an open XDL detector. This detector is optimized for measurements of the O VI lines at 1032 and 1037 Å, plus additional lines in the 937 to 1126 Å (first order), and 469 to 563 Å (second order) range.The OVI section includes a mirror to focus the first order diffracted H I Lyman- α line on the O VI detector, thereby providing a redundant capability to detect that spectral line.

The White Light Channel (WLC) is designed to perform measurements of the polarized radiance of the corona. It consists of an entrance aperture, a polarimeter assembly, and a photomultiplier tube. The polarimeter assembly includes a rotatable half-wave plate, a fixed linear polarizer, a bandpass filter and a lens.

A schematic diagram of the UVCS is reported in Figure 2, and its optical path is shown in Figure 3. The internal occultation and telescope mirror motion is provided by the Mirror Occulter Mechanism (MOM) Assembly, illustrated in Figure 4.

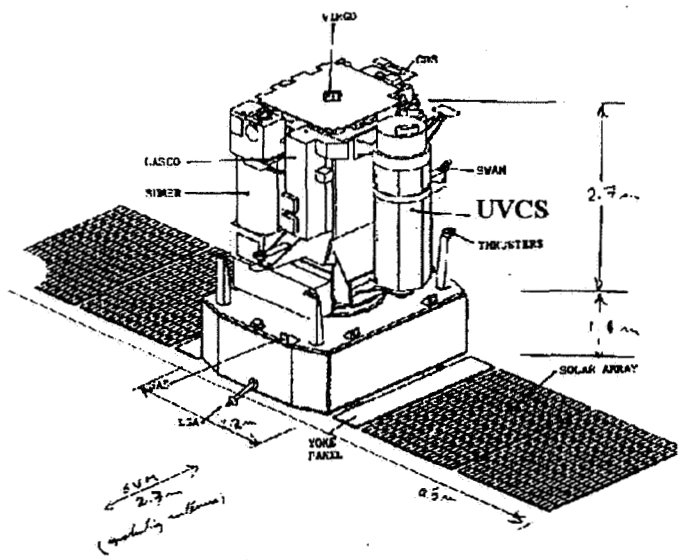
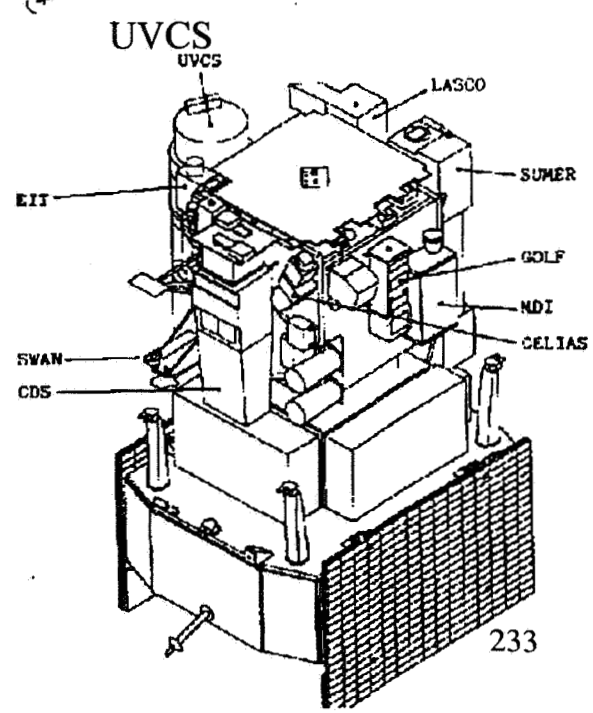
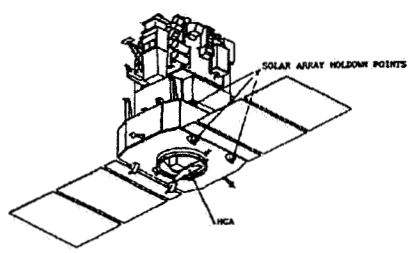


Figure 1 - The SOHO Spacecraft





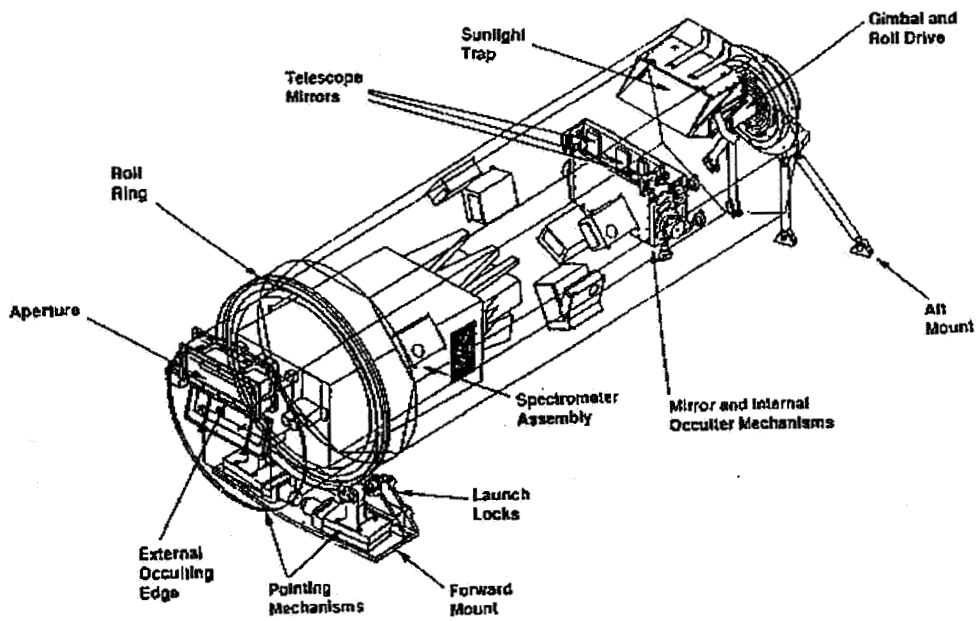


Figure 2 - The UVCS Instrument

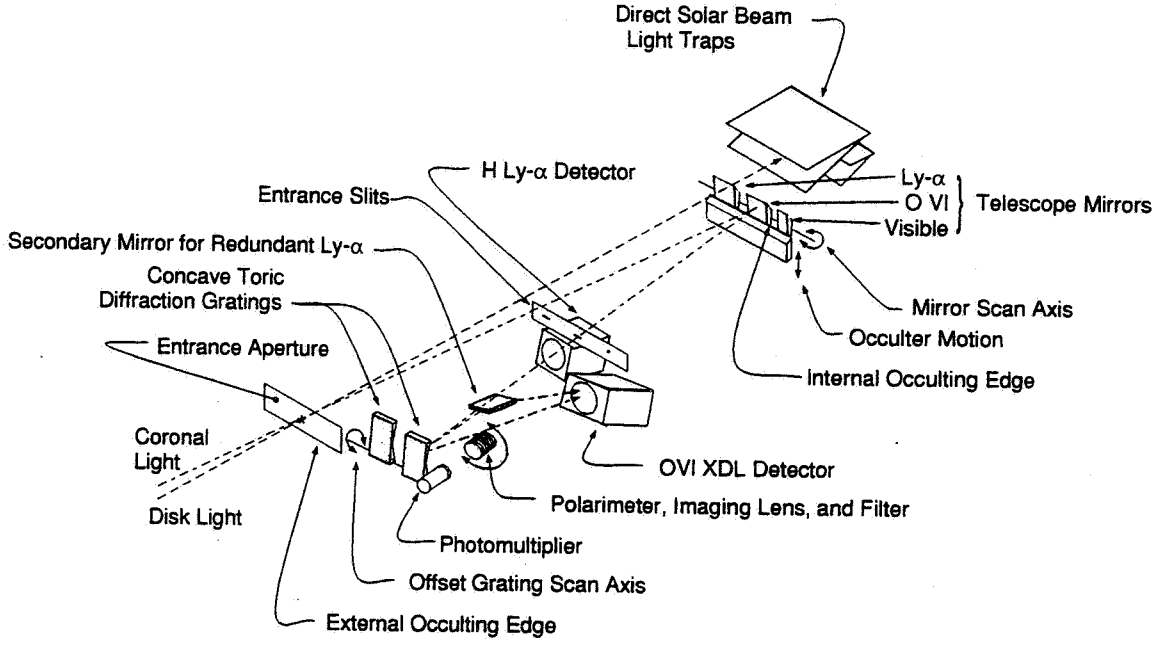


Figure 3 - The UVCS Optical Path

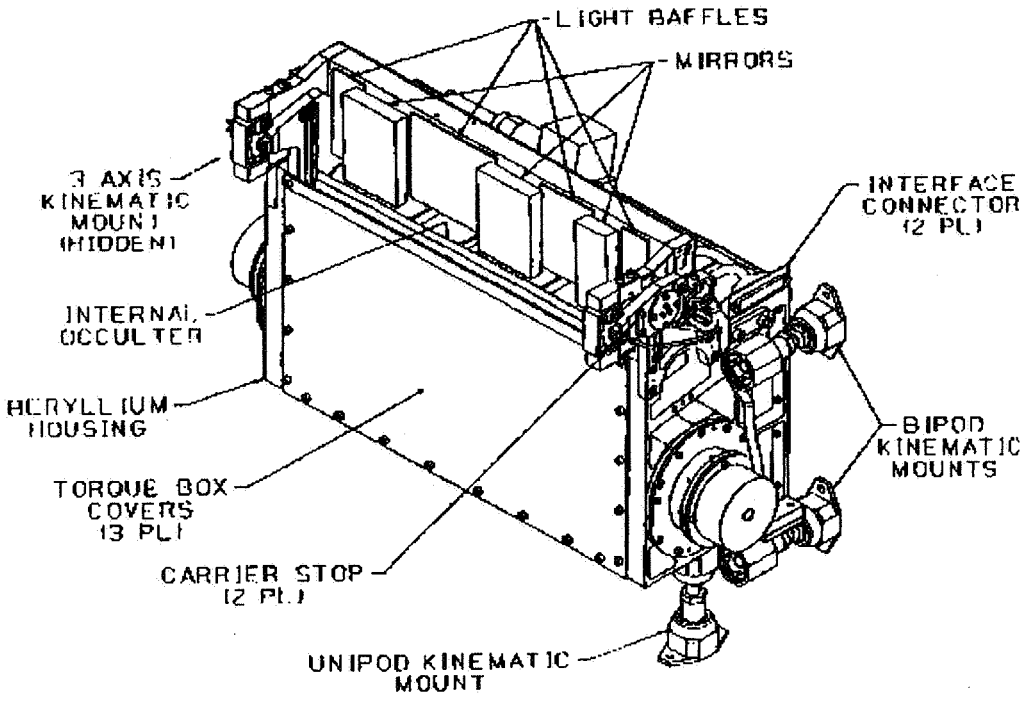


Figure 4 - The Mirror Occulter Mechanism (MOM) Assembly

4. UVCS END-TO-END TEST BACKGROUND

The International Solar Terrestrial Project (ISTP) planned for and performed an End-to-end System Test on the Ultraviolet Coronagraph Spectrometer[1] (UVCS) in the June-July 1995 time frame.

The major goals of the test were:

- to verify the UVCS Instrument functionality at system level, and
- to measure key optical performance parameters of the Instrument in its flight configuration.

All the UVCS subsystems had previously undergone qualification testing at various facilities, per the UVCS Product Assurance Plan[3], and the integrated Instrument had undergone a verification program, including vibration test, functional, EMC, etc.

The performance of some flight-like models of the major UVCS optical components had been measured by SAO.

Some of the optical performance properties had been measured on the Spectrometer Assembly (SPA), in vacuum, in November 1994, at Alenia Spazio, Torino, Italy. That test program utilized non-flight optical components to simulate the telescope, and provided an initial evaluation of the Spectrometer spectral and spatial resolution[5].

Although this preliminary testing and characterization work provided valuable information, a system level test was required to verify the functionality of the Instrument in its full flight configuration, its end-to-end optical performance, and to validate the optical design. The decision to actually perform such a test was not straightforward, however, due to severe schedule constraints. The SOHO AIV and launch processing schedule did not allow for extended periods of time to be dedicated to Instrument activities.

The UVCS test schedule had therefore to be optimized such that it would ensure achievement of the desired results in the limited time available, and under safe conditions.

The ISTP Project negotiated with the SOHO Project the release of the UVCS from the Spacecraft to allow for transportation of the UVCS to the U.S.A. from France. A period of approximately 49 days was allocated to this test.

5. TEST FACILITY SELECTION

Several options were considered in the process of selecting the facility for the execution of the UVCS End-to-end test:

- the Goddard Space Flight Center (GSFC) in Greenbelt, MD,
- the Smithsonian Astrophysical Observatory in Cambridge, MA, and
- the Intespace Facility in Toulouse, France.

The factors that had to be traded against each other included:

- Risks during transportation
- Logistics support
- Suitability
- Optical environment
- Management complexity

Transportation risks are always a significant factor, especially when moving from an overseas location is required.

Logistics support, such as mechanical and electrical support facilities capable of fast turn around are required for any unplanned rework or fix.

Suitability of the facility, in terms of facility layout, space available, support equipment (e.g. lifting equipment), and cleanliness control, were an extremely important consideration in the decision process. Familiarity with and knowledge of the facility was also important. Factors such as facility certification and utilization history were considered in the trade study.

The optical properties of the vacuum facility were obviously an important factor, due to the need to minimize any adverse optical background during the optical measurements in vacuum.

Management complexity factors were also considered, e.g., for instance, the establishment and implementation of contractual arrangements with foreign organizations.

The Intespace facility was very attractive because it minimized transportation risks, as it is located very close to the Matra facilities in Toulouse. It also offered good supporting facilities. The vacuum facility, however was not sufficiently large to guarantee the desired optical environment, and certification data were unavailable.

Having decided that the move from France was necessary, the final selection was made by giving the highest priority to the fact that the primary goal of the test was to measure the

Instrument optical functionality, thus requiring the best optical environment. The SAO Ultraviolet Coronagraph Laboratory includes a unique vacuum facility that is optimized for stray light testing, and was therefore selected for the test.

A thorough evaluation of the SAO facilities was conducted and a number of facility improvement measures were identified. These upgrades were implemented prior to the test, to ensure that all environmental control and safety requirements were in place. The cleanrooms were upgraded. A low temperature shroud was designed, fabricated and installed in the existing vacuum chamber. Comprehensive contamination monitoring equipment was also installed. Strict contamination control procedures were enforced in the laboratories.

5.1. *THE SAO TEST FACILITY*

The test facility located in the Ultraviolet Coronagraph Laboratory of the SAO consists of a vacuum chamber fitted with a light source, a removable monochromator, an articulated collimating mirror, and an Instrument Support Fixture (ISF), plus various articulated stages for the insertion and removal of filters and light diodes in the incident beam.

Light sources are easily interchangeable, to accommodate the various wavelengths needed throughout the test. Colored and neutral density filters, and diffusers, can be inserted into the beam as needed.

The incident beam is reflected towards the instrument by an articulated collimating mirror (See Figure 5). To minimize the chamber background stray light, a light trap is located just behind the collimating mirror, the beam travels a distance of approximately 12 m prior to entering the instrument's entrance slit, and a baffling system is placed in the elongated section of the chamber.

When fitted with the appropriate light sources, the optical system provides the beam divergence required for proper solar simulation.

To measure the incident beam intensity, NIST calibrated diodes can be inserted and removed from the incident beam by means of motorized stages controlled from the exterior of the chamber. For the optical measurements in vacuum, the UVCS was placed on the ISF, located in the ~1.8 m diameter section of the chamber. The ISF itself was in effect a motorized optical table with capability for translation in two dimensions and pivot about one.

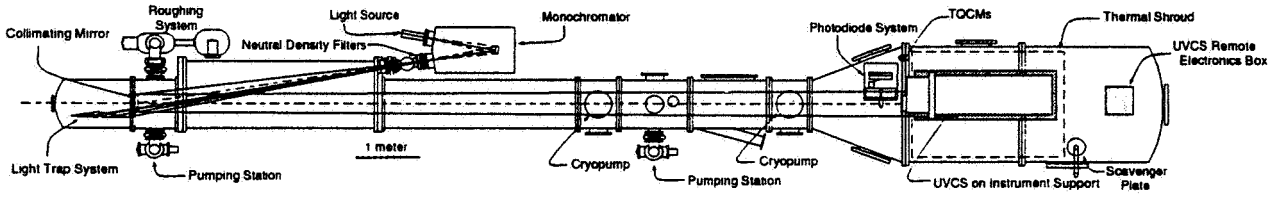


Figure 5 - The SAO Vacuum Chamber

6. TEST SCHEDULE

The International Solar Terrestrial Physics (ISTP) Project negotiated the release of the UVCS from the Matra facility for the 27th of May, 1995. The Instrument was to be returned to KSC on July 27th.

The work to upgrade the facilities at SAO began at the end of March, and a facility walkthrough was held on May 10th to verify the facility readiness. The UVCS arrived at the GSFC early on May 30th, to allow for switching to a smaller shipping container, and arrived at SAO late on the same day.

The UVCS End-to-end System Test was initiated immediately thereafter. The Instrument Diagnostics and Characterization phase was performed first. This was followed by a Rework / Retest phase, during the last two weeks of the test period.

7. TEST PHILOSOPHY

As previously mentioned, the 49 days allowed for the test were allocated to two test phases. During the initial Diagnostics phase, originally intended to last approximately two weeks, a series of functional and performance tests were planned, aimed at evaluating a broad spectrum of key instrument parameters. Should any malfunction or problem be identified at the end of this phase, of such a magnitude that work on the Instrument would be required, the test would be suspended to allow for such repairs.

A two week Rework phase was also included in the initial plan, to perform the repair work pertaining to a number of open items leftover from the Pre-ship Review.

Any additional time remaining after the Diagnostics and Rework phases was planned to be used for additional Instrument characterization.

No major malfunctions were identified during the Diagnostics phase that would require repair work. It was therefore decided to continue testing in vacuum, and to immediately proceed to an extended Instrument characterization testing phase. This decision allowed the maintaining of vacuum and the loss of the instrument alignment within the test setup, and resulted in a significantly more effective use of the limited time available.

The planned rework phase, entailing a well determined amount of time, was performed at the end of the test period.

An overall test procedure was generated by the Science Team and reviewed prior to the test inception, addressing the above mentioned test phases. Based upon this overall procedure,

detailed procedures were generated for the execution of all the planned tests (i.e. Visible Light Channel Stray Light, Lyman-α Channel Efficiency, etc.).

8. UVCS PERFORMANCE GOALS

The performance goals for the UVCS Instrument are reported in Table I.

These values were determined based on the UVCS optical design, the preliminary component level tests, and the expected orbital conditions. Although they were not formal program requirements, these goals constituted a reference for the End-to-End test values.

Table I - UVCS Performance Goals

	λ [Å]	Efficiency	Stray Light	Spectral Resolution	Off Band Stray Light Suppression
Visible Light Channel	4500-6000	0.01	3.2×10^{-9}		
Lyman-α Channel	1216	0.01	1×10^{-8}	0.141	
Redundant Lyman-α Path	1216	0.0038	1×10^{-8}	0.1	
O VI Channel	1048	0.0084	1×10^{-8}	0.09	
Lyman-α & O VI	2537				4×10^{-10}

9. PRELIMINARY TEST FACILITY EVALUATION

The ISTP Project required that comprehensive certification of the vacuum facility be performed prior to test inception. Such certification had to include:

- Cleanliness

 Non-Volatile Residue (NVR) samples were taken from both the chamber internal surfaces and the shroud. The chamber was operated prior to test inception, including all the test mechanical and electrical GSE. The molecular environment was monitored by Residual Gas Analyzer (RGA) and Thermal Quartz Crystal Microbalances (TQCMs). Witness plates were also placed in the chamber and sampled for NVR after the test.

 This test indicated that the environment in the chamber was very clean. Only water vapour and traces of hydrocarbons were detected at the beginning of the test. Their partial pressure decreased significantly throughout the test.

- Verification of low temperature shroud functionality

 A preliminary chamber test allowed to verify operation of the shroud at the required temperature (-70 ° C). This temperature was achieved by chilling ethilic alcohol using two low temperature chillers and pumping it through the shroud.

- Instrument Support Fixture load test

 A static pre-load test of the Instrument Support Fixture (ISF) was successfully performed.

- Vacuum chamber background stray light

 This test is described in the following paragraph.

9.1. UVCS MOCKUP TEST

Due to the very stringent UVCS stray light requirements, preliminary testing was necessary to measure the vacuum chamber intrinsic stray light background, and to verify that this level was below the required instrument stray light level.

This test was performed in May 1995, prior to the arrival of the UVCS at SAO, utilizing the UVCS Mockup, an engineering unit available at SAO which very closely reproduces the UVCS optical design and configuration. The Mockup components are mostly flight-like, with the exception of the light trap, the PMT unit, and the internal occulter which were expected to be

functionally representative. A spare flight telescope mirror was used for this test.

The UVCS Mockup test was performed in air utilizing visible light. The measured light level was approximately $4x10^{-8}$ of the simulated disk intensity, which indicated acceptably low stray light levels in the vacuum chamber.

10. UVCS END-TO-END SYSTEM TEST RESULTS

10.1. *OPTICAL ALIGNMENT*

After successful completion of the facility certification tests discussed previously, the UVCS was installed on the support fixture and aligned to the test facility, so that the Instrument optical axis would be in the direction of the light source. For the stray light measurements, the incident beam diameter was large enough to cover the entire entrance aperture. A sketch of the test set-up is reported in Figure 5.

Optical alignment was achieved by maximizing the signal from the WLC detector, while progressively reducing the dimensions of the simulated sun by means of a diaphragm. Motion of the UVCS optical axis was achieved by small movements of the support fixture and the UVCS pointing system itself.

10.2. *WHITE LIGHT CHANNEL STRAY LIGHT EVALUATION*

The WLC Stray light test was performed first, due to its inherently more lenient experimental conditions. The initial test is in fact performed in air, thus allowing for time efficient optimization of the set-up and of the Instrument alignment. Should the chamber stray light have proven to be unacceptably high, it would have still been relatively simple to modify the chamber set-up (i.e. baffling system, light source, etc.), avoiding the time losses due to recovery from vacuum and subsequent pump-down cycles.

A high pressure mercury arc lamp (1kW) was utilized in the WLC Stray light test. A filter was utilized to eliminate the infrared portion of the light emitted by the source. Several neutral density filters were used as needed, to reduce the incident beam intensity, as well as a green filter to isolate the 546 nm Hg line.

The values for the stray light levels were obtained as the ratio of the apparent "coronal" intensity to the simulated "solar disc" intensity, obtained respectively by pointing the UVCS into the 2.7 R_o direction and into the simulated sun center direction. Note that in the experimental set-

up, the simulated sun is corona-less. Values of approximately $2x10^{-8}$ were measured for the WLC stray light.

10.3. *VISIBLE LIGHT CHANNEL EFFICIENCY*

A value of 4.0×10^{-3} was measured at 5460A (Hg) for the efficiency of the UVCS visible light channel.

As in all the efficiency measurements performed during this test campaign, the end-to-end radiometric efficiency was obtained as the ratio of the intensity measured at the UVCS detector to the intensity of the incident beam, as measured by an NIST calibrated diode.

10.4. *DETECTOR OPERATIONS*

Cross Delay Line (XDL) Detectors[6] are utilized in both the Lyman-α and the O VI Channels of the UVCS. The test procedures included provisions for safe operation of the detectors, in terms of:

- vacuum chamber pressure, and
- incident beam intensity.

The XDL's are operated safely at a pressure equal or less than $3x10^{-5}$ Torr. A vac-ion gauge was installed in the vacuum chamber to monitor the pressure in the volume immediately surrounding the detectors.

On the initial chamber pump-down, although the ambient vacuum chamber pressure was well below the XDL operational limit, it was noted that the pressure internal to the Spectrometer Assembly (SPA) was not sufficient to allow XDL operation. To achieve the required vacuum level in a practical amount of time, it was decided to partly remove one of the SPA side panels, to allow for enhanced vacuum conductance into the SPA. This issue resulted in the modification of one of the SPA flight panels, which was required to assure proper and safe operation in flight.

The intensity of the incident light beam was closely monitored throughout all test phases to avoid damage to the detectors. Neutral density filters of various transmission factors were used as necessary to maintain the light at safe levels at all times when high voltage was applied to the detectors. High voltage was always applied in small increments, up to the operating voltage.

10.5. *LYMAN-α CHANNEL EFFICIENCY AND STRAY LIGHT EVALUATION*

The efficiency of the Lyman-α channel was measured at 1165 Å (Kr I), 1216 Å (H_2 Lyman-α), and 1236 Å (Kr I).

Various light sources were utilized for the UVCS calibration in the UV, to allow for the measurement of the desired parameters.

For the efficiency measurements, a Samson glow discharge lamp was used, in conjunction with the appropriate gas (Ar, Kr, etc.).

The efficiency values measured[1] for the Lyman-α Channel are reported in Table II.

Table II - Lyman-α Channel Efficiencies

1165 Å (Kr I)	2.5×10^{-3}
1216 Å (H I Lyman-α)	2.0×10^{-3}
1236 Å (Kr I)	1.9×10^{-3}

The stray light level[1], defined as the ratio of the stray light count rate to the simulated solar disc count rate is $<1 \times 10^{-8}$. This value is an upper limit, since it may be dominated by stray light in the vacuum facility.

10.6. *REDUNDANT LYMAN-α PATH EFFICIENCY AND STRAY LIGHT EVALUATION*

The efficiency of the Redundant Lyman-α channel was measured at 1236 Å (Kr I).

The efficiency value measured for the Lyman-α Channel is reported in Table III[1]. The reported value includes the reflectance of the telescope mirror, the efficiency of the grating, the reflectance of the redundant mirror, and the counting efficiency of the XDL detector. The instrument stray light level, defined as the ratio of the equivalent stray light count rate to the simulated solar disk count rate was $<5 \times 10^{-8}$. Based on the more extensive stray light

measurement of the Lyman- α channel, this value is probably limited by the test arrangement.

Table III - Redundant Lyman-α Channel Efficiencies	
λ	Efficiency
1236 Å (Kr I)	1.0×10^{-3}

10.7. *O VI CHANNEL EFFICIENCY*

The efficiency of the O VI Channel was measured at 1025 Å (H_2 Lyman-β), 1048 Å (Ar I), and 1066 Å (Ar I)

For the efficiency measurements, a Samson glow discharge lamp was used, in conjunction with the appropriate gas.

The efficiency values measured for the O VI Channel are reported in Table IV[1].

Table IV - O VI Channel Efficiencies	
1025 Å (H2 Lyman-β)	3.0×10^{-3}
1048 Å (Ar I)	4×10^{-3}
1066 Å (Ar I)	3.4×10^{-3}

The stray light level for the O VI channel was measured as part of the reduntant Lyman-α path test. (See Section 10.6).

10.8. *SPECTRAL RESOLUTION*

A platinum / neon light source was utilized for the spectral resolution and wavelength scale measurements of the Lyman-α Channel, due to its high number of very narrow peaks.

The Berlin PTB hollow cathode lamp (with Xe and Ar gas) was used for the spectral resolution test of the O VI Channel.

The spectral resolution is expressed as the Full Width at Half Maximum of the measured profile (in pixels), as obtained by a gaussian fit of the experimental data. The measured results are summarized in Table V[1].

Table V - UVCS Spectral Resolution

	FWHM [pixels]
Lyman-α Channel	1.7
Redundant Lyman-α Channel	~3.5
O VI Channel	< 2.5

The value for the O VI channel is considered to be an upper limit, since the intrinsic line width of the light source (as operated) was not known.

10.9. *OFF-BAND STRAY LIGHT SUPPRESSION*

The off-band stray light suppression was measured with a pen ray Hg lamp at 2537 and 1800 Å.

The measured off-band sensitivity was 3×10^{-11}, which is significantly better than the performance goal value of 4×10^{-10}.

10.10. *FLAT FIELD CALIBRATION*

A microwave (Kr) source was used for the flat field calibration of the Lyman-α channel.

The Samson lamp (Ar) with monochromator was used for the O VI Channel flat field calibration.

10.*11. MECHANISM CALIBRATION*

In addition to the optical characterization discussed so far, various UVCS mechanisms were calibrated, leading to the update (or initial definition) of many of the UVCS flight software tables. This effort included:

- Entrance slits
- Occulter plate
- Telescope mirrors
- Gratings
- Telescope roll mechanism

10.*12.SOFTWARE TESTING*

Extensive flight software testing was also accomplished during the UVCS End-to-End System Test campaign. A new flight software version was installed and tested, as well as a new version of the UVCS Telemetry and Command software.

11. SUMMARY OF RESULTS

In the period from June 1 until July 24, 1995, a comprehensive set of system level functional and optical tests were perfomed on the SOHO UVCS Instrument.

Although performed under severe schedule constraints, this End-to-End System Test was very successful and served to validate fully the UVCS optical design. All test results showed that the primary scientific objectives of the UVCS Mission are achievable.

12. REFERENCES

1. J.L. Kohl, et al., Solar Physics **162**, 313 (1995)
2. V. Domingo, B. Fleck, and A. Poland, Solar Physics **162**, 1 (1995)
3. UVCS Product Assurance Plan, IN0043-125, Rev. C
4. "UVCS for the SOHO: Optical Testing", S. Fineschi, M. Romoli, L. Gardner, J. Kohl , G. Noci, SPIE Vol.2283, 1994.
5. "Spectral resolution improvement technique for a spectrograph mounting a discrete array detector", C. Pernechele, L.Poletto, P. Nicolosi, G. Naletto, SPIE Vol 2517, July 1995.
6. Siegmund et al., SPIE Vol. 2280, 1994

523-14
031465
26974
12P

MAGNETIC TEST PERFORMANCE CAPABILITIES AT THE GODDARD SPACE FLIGHT CENTER AS APPLIED TO THE GLOBAL GEOSPACE SCIENCE INITIATIVE

Darryl R. Mitchell
Environmental Test Engineering and Integration Branch
Engineering Services Division
Goddard Space Flight Center
Greenbelt, Maryland

ABSTRACT

Goddard Space Flight Center's (GSFC) Spacecraft Magnetic Test Facility (SMTF) is a historic test facility that has set the standard for all subsequent magnetic test facilities. The SMTF was constructed in the early 1960's for the purpose of simulating geomagnetic and interplanetary magnetic fields. Additionally, the facility provides the capability for measuring spacecraft generated magnetic fields as well as calibrating magnetic attitude control systems and science magnetometers. The SMTF was designed for large, spacecraft level tests and is currently the second largest spherical coil system in the world.

The SMTF is a three-axis Braunbek system composed of four coils on each of three orthogonal axes. The largest coils are 12.7 meters (41.6 feet) in diameter. The three-axis Braunbek configuration provides a highly uniform cancellation of the geomagnetic field over the central 1.8 meter (6 foot) diameter primary test volume. Cancellation of the local geomagnetic field is to within ±0.2 nanoTesla with a uniformity of up to 0.001% within the 1.8 meter (6 foot) diameter primary test volume. Artificial magnetic field vectors from 0-60,000 nanoTesla can be generated along any axis with a 0.1 nanoTesla resolution. Oscillating or rotating field vectors can also be produced about any axis with a frequency of up to 100 radians/second.

Since becoming fully operational in July of 1967, the SMTF has been the site of numerous spacecraft magnetics tests. Spacecraft tested at the SMTF include : the Solar Maximum Mission (SMM), Magsat, LANDSAT-D, the Fast Auroral Snapshot (FAST) Explorer and the Sub-millimeter-Wave-Astronomy Satellite (SWAS) among others. This paper describes the methodology and sequencing used for the Global Geospace Science (GGS) initiative magnetic testing program in the Goddard Space Flight Center's SMTF. The GGS initiative provides an exemplary model of a strict and comprehensive magnetic control program.

INTRODUCTION

The GGS Initiative is part of the International Solar Terrestrial Physics (ISTP) science initiative. The GGS Initiative consists of the two NASA managed spacecraft, WIND and POLAR, and the Japanese Institute of Space and Astronautical Science's (ISAS) Geotail satellite. The purpose of the GGS mission is to study the physical mechanisms and various regions controlling the transport of mass, energy and momentum between the Sun and Earth in geospace.

Due to the extreme sensitivity of many of the science instruments onboard WIND and POLAR to magnetic disturbances, the GGS project imposed highly stringent magnetic test

limits on both spacecraft at the instrument level. Table 1 shows the GGS instrument level magnetic test limits. This approach relies on the minimization of contributions from individual sources at the component and instrument levels, coupled with the net vectorial cancellation of residual fields at the fully integrated spacecraft level, to produce a magnetically ultra-clean spacecraft.

The severity of the GGS magnetic test limits was evidenced when only three of the boxes tested for WIND and POLAR were able to meet the GGS test specifications. None of the fully assembled instruments on WIND or POLAR tested at GSFC were able to meet the magnetic test limits set forth in table 1 in its entirety. On the other hand, the majority of instruments flown on the POLAR spacecraft were able to meet their generally more lenient POLAR magnetic allocations.

Magnetic control specifications on the POLAR spacecraft were handled in a different manner than those for the WIND spacecraft. A set of magnetic allocations was setup for each instrument on POLAR. Each instrument was still to attempt to meet the GGS test limits, but levels within the given allocation were deemed acceptable. Where the GGS magnetic test limits were generated from limits formerly established on the International Sun-Earth Explorer (ISEE) spacecraft, the POLAR magnetic allocations were generated by taking into account the position of each instrument on the spacecraft with respect to the position of the science magnetometer probe. Using an inverse cubed fall-off rate, maximum field levels at 1.0 meter and 0.5 meters from each instrument were calculated that would result in levels below the science magnetometer's sensitivity at the magnetometer probe . Magnetic allocations for instruments flying on the POLAR spacecraft are given in table 2.

MAGNETIC TESTING

Purpose

Magnetic testing furnishes a means for advance mitigation of unwanted orbital torques produced by the interaction of a spacecraft's magnetic moment with ambient magnetic fields. Also, as in the GGS case, magnetic testing provides a mechanism for the characterization and minimization of magnetic fields generated by a spacecraft when flying instrumentation sensitive to magnetic disturbances, such as magnetometers and particle detectors.

The effect of a spacecraft magnetic disturbance torque was first observed on the Vanguard I satellite which was launched in late 1958. Interaction of the geomagnetic field with eddy currents generated in the spacecraft's rotating outer shell caused Vanguard I to be continuously despun. As a result the satellite's spin rate was reduced from an initial value of 2.7 revolutions/second at launch, to less than 0.2 revolutions/second two years later. Reference 1 gives a detailed analysis of this effect.

Magnetic disturbance torques can be generated by one of three mechanisms. The spacecraft's permanent magnetic dipole component can create perturbations as it attempts to align itself with the ambient magnetic field. Materials with large permeability values can generate torques due to hysteresis effects. Finally, as in the case of Vanguard I, eddy currents induced in conductive materials by changing flux levels on orbit can create eddy current damping torques.

The general equation governing magnetic disturbance torques is very straightforward :

$$\vec{T}_{S/C} = \vec{M}_{S/C} \times \vec{B} \qquad (1)$$

where

$\vec{T}_{S/C}$ = spacecraft magnetic disturbance torque vector in dyne-cm

$\vec{M}_{S/C}$ = spacecraft magnetic dipole moment vector in gauss-cm^3

$\vec{B}$ = ambient magnetic induction vector in gauss

A detailed explanation of the application of this equation to the cases of hysteresis and eddy current damping torques can be found in reference 2.

The detriment posed by spacecraft magnetic torques is the additional load imposed on the attitude control system. Averaged over numerous orbits the energy loss due to correction of magnetic torques can become very significant. With power consumption always a major concern onboard spacecraft, the need for minimizing unnecessary magnetic torques is obvious.

Present day state-of-the-art magnetometers exhibit sensitivities of 0.1 nanoTeslas or better. Controlling the magnetic properties of large spacecraft such as WIND and POLAR in order to minimize biases at the magnetometer probe can therefor become a major concern. This problem is distinct from magnetic disturbance torque considerations in that it focuses on the field at a particular location on the spacecraft rather than emphasizing the equivalent dipole moment of the entire spacecraft. However, enacting procedures for maintaining magnetic cleanliness in a spacecraft also generally result in a minimization of the spacecraft's dipole moment.

Data Acquisition and Analysis

Data acquisition at the SMTF is achieved utilizing an array of four triaxial fluxgate magnetometers interfaced to a personal computer. During the tests of the GGS instruments at the SMTF a Hewlett Packard model HP86 computer and model 9427A data acquisition/control unit were used for data acquisition. The magnetometers used were developed and built by Doctor Mario Acuña of GSFC code 695. The test hardware has recently been updated with a Macintosh Quadra 800 computer and National Instruments SCXI signal conditioning box. The newer data acquisition system provides many enhanced capabilities not available in the older setup including : improved resolution; continuos sampling; higher data processing speed and increased options for data representation.

Since the early 1970's field mapping techniques have been used at the SMTF for determination of magnetic dipole moments. Figure 1 shows a typical test configuration. Data is obtained while rotating the test item past an array of triaxial magnetometer probes. All probes are located in a plane at radial distances D_n from the centroid of the test item. Data is taken in the near-field region in order to maintain a high signal-to-noise ratio. The algorithm used to analyze the data is based on the assumption that the test item's magnetic field can be modeled by the summation of its constituent multipole fields. The test data is inputted into a set of fourier equations to calculate an equivalent dipole moment. Detailed derivations of the equations used for the analysis are given in references 3 and 4. The general equations used to analyze the test data are :

$$\frac{1}{18}\sum_{\theta=0^\circ}^{360^\circ} B_{xn}(D_n,\theta)\cos\theta = \left(\frac{2A_{11}}{D_n^3} - \frac{6A_{31}}{D_n^5} + \frac{45A_{51}}{4D_n^7} - \frac{35A_{71}}{2D_n^9}\right) \quad (2)$$

$$\frac{1}{18}\sum_{\theta=0^\circ}^{360^\circ} B_{xn}(D_n,\theta)\sin\theta = \left(\frac{2B_{11}}{D_n^3} - \frac{6B_{31}}{D_n^5} + \frac{45B_{51}}{4D_n^7} - \frac{35B_{71}}{2D_n^9}\right) \quad (3)$$

$$\frac{1}{18}\sum_{\theta=0^\circ}^{360^\circ} B_{yn}(D_n,\theta)\cos\theta = -\left(\frac{B_{11}}{D_n^3} - \frac{3B_{31}}{2D_n^5} + \frac{15B_{51}}{8D_n^7} - \frac{35B_{71}}{16D_n^9}\right) \quad (4)$$

$$\frac{1}{18}\sum_{\theta=0^\circ}^{360^\circ} B_{yn}(D_n,\theta)\sin\theta = \left(\frac{A_{11}}{D_n^3} - \frac{3A_{31}}{2D_n^5} + \frac{15A_{51}}{8D_n^7} - \frac{35A_{71}}{16D_n^9}\right) \quad (5)$$

$$\frac{1}{36}\sum_{\theta=0^\circ}^{360^\circ} B_{zn}(D_n,\theta) = -\left(\frac{A_{10}}{D_n^3} - \frac{3A_{30}}{2D_n^5} + \frac{15A_{50}}{8D_n^7} - \frac{35A_{70}}{16D_n^9}\right) \quad (6)$$

where :

n			=	magnetometer number (1 to 4)
A_{11}			=	X axis dipole moment coefficient
B_{11}			=	Y axis dipole moment coefficient
A_{10}			=	Z axis dipole moment coefficient
A_{31}	A_{51}	A_{71}		
B_{31}	B_{51}	B_{71}	=	multipole moment coefficients
A_{30}	A_{50}	A_{70}		
B_{xn}, B_{yn}, B_{zn}			=	X,Y and Z components of magnetic field at probe n
D_n			=	magnetometer distance
θ			=	rotation angle

Test Sequence

A complete magnetic test sequence as implemented on WIND and POLAR consists of permanent magnetism, induced magnetism and stray field measurements as outlined below. Figure 2 shows a typical test data printout. Results from some of the tests run for instruments flying on the WIND spacecraft are summarized in figure 3.

Permanent Magnetism

The permanent magnetism test sequence is comprised of three distinct measurement conditions. Data for all three test conditions is acquired in an identical manner. The test item is rotated about it's vertical axis in the center of the facility coils while an array of magnetometers collects the magnetic field data. See figure 1 for details. The distinction between measurements comes from the magnetic state of the test item during each test.

Initial perm measurements characterize the test item "as received", i.e., before exposing the test item to any influences that might alter the magnetic state of the item. The "as received" magnetic state of the test item indicates:

(a) A possible level of perm that the newly assembled item might be expected to maintain.

(b) A relevant magnitude of field that can be used to determine the effectiveness of the deperm treatment.

(c) The stability of the items perm field by initiating a record of its magnetic history.

Post exposure (perm) measurements determine the magnetic state of the test item after exposure to a 15 Gauss steady state field along one of the horizontal axes. Post exposure measurements give an indication of the extent of soft magnetic materials present on the test item, as well as a possible level of perming the test item may attain during the environmental test sequence.

Post deperm measurements determine the magnetic state of the test item after exposure to a slowly diminishing 30 Gauss AC field. The deperm treatment is conducted inside the zero-field environment. The deperm must be conducted in zero-field in order to reach the lowest remanence level possible. Deperm treatments performed in the geomagnetic field can result in a net increase in the test item's magnetic field. When performed properly, post deperm measurements represent the lowest level of remanence field for the test item.

If following the deperm treatment the test item still exceeds it's test specification, then magnetic compensation can be applied as a corrective measure. Magnetic compensation involves affixing a small bar magnet to the test item to reduce its dipole moment. The compensation magnet is oriented on the test item such that its dipole moment is in opposition to the test item's dipole moment. This results in a net cancellation between the fields produced by the two moments in the far-field region.

Induced Magnetism

Induced field measurements attempt to measure the presence of any soft ferromagnetic materials present within the test item. Induced moments can be generated by the interaction of soft ferromagnetic materials onboard a spacecraft with ambient magnetic fields. If present, induced moments can create hysteresis damping torques on the spacecraft as discussed previously.

For the induced field test, a field vector is generated inside the SMTF coils to simulate the magnetic field environment the test item will experience while on orbit. A 0.3 gauss field is typically used to simulate low earth orbit. The test item is placed inside the magnetic field and data is acquired in a similar manner to that of the permanent magnetism test. The magnetometers used in the SMTF have the capability to internally bias out fields of up to 1.0 gauss. This capability enables the magnetometers to maintain the sensitivity needed to discern the induced fields in the much larger artificial field. Test results are then compared to the post deperm results with any differences attributable to induced moments.

Induced magnetic moments are not as easily corrected as are those due to permanent magnetism. The only means for correcting induced magnetic moments is replacement of the offending material. Neither deperming or compensation magnets are effective cures for

this problem. Since moments generated by soft materials are variable with ambient field strength and direction, a fixed permanent magnet can not effectively compensate for an induced moment which varies continuously with orbital position.

Stray Field Magnetism

Stray field measurements are taken in order to characterize magnetic fields generated by circulating currents within the test item. Current loops of large cross sectional area and electric motors are the most common causes of stray magnetic fields. Measurements are made of both static and dynamic magnetic fields. Dynamic measurements are conducted over a frequency range of 1 to 30 hertz.

Baseline measurements are made with the test item powered off. Successive measurements are taken as the test item is powered on and then switched to various operational modes. This process is performed separately for static and dynamic field measurements.

Static field measurements can be acquired by up to 4 triaxial magnetometers in any configuration desired. For dynamic fields only one single axis probe is used. Output from the test magnetometer is sent to either a Hewlett Packard model 3562A signal analyzer or strip chart recorder depending on the spectral resolution desired. Due to the long acquisition time required by the signal analyzer for frequencies below 1 hertz, measurements below 1 hertz are typically made using a strip chart recorder and a series of low and high pass filters.

Magnetometer Calibration

The SMTF provides a controllable, high precision magnetic field environment perfectly suited for calibrations of magnetic attitude control systems and science magnetometers. In addition to calibration data, sensor orthogonality and magnetometer frequency response can be measured. A laser or theodolite is used for mechanical alignment to facility coils. Facility calibration is achieved using a proton magnetometer.

Artificial magnetic fields can be generated with magnitudes of 0 to 60,000 nanoTesla along any facility axis. Maximum field resolution is 0.1 nanoTesla. Static field vectors are stable to ± 1.0 nanoTesla over a 48 hour period. Rotating fields are produced with magnitude uniform to within 2% or 0.5 nanoTesla, whichever is larger, over a 48 hour period. Rotation rates are variable from 0 to 100 radians/sec with an accuracy of 0.03 radians/sec or 3% of the value, whichever is larger. Resolution is 0.01 radians/sec or 1%, whichever is larger.

RESULTS

Measurements conducted on the WIND and POLAR spacecraft at the Martin Marietta facility in East Windsor, New Jersey indicate that the magnetic control programs implemented on both spacecraft were highly successful. Measurements of WIND at the spacecraft level indicated an estimated dipole moment of 2200 pole-cm. A moment of 2200 pole-cm magnitude generates a resultant field at the outer Magnetic Fields Investigation (MFI) sensor of 0.1 nanoTesla. This is within the project goal of 0.5 nanoTesla.

A similar test of the POLAR spacecraft measured a field strength at the outboard Magnetic Fields Experiment (MFE) probe of 0.3 nanoTesla. This is also within the project goal of 0.5 nanoTesla. Detailed reports of both tests are given in references 5 and 6.

Due to the enforcement of extremely rigorous instrument level test requirements, both spacecraft were able to meet their test specifications. The success of the magnetic control program on these two spacecraft illustrates the effectiveness of a stringent and comprehensive magnetic control program monitored in a properly equipped test facility.

REFERENCES

1. Wilson, R. H., Jr., "Magnetic Damping of Rotation of the Vanguard I Satellite," Sci., February 13, 1960, pp. 355-357

2. Fischell, Robert E., " Magnetic Damping of the Angular Motions of Earth Satellites," ARS Journal, September, 1961

3. W.L. Eichhorn, "Magnetic Dipole Moment Determination by Near-Field Analysis," NASA Technical Note TN D-6685, July, 1972

4. W.L. Eichhorn, "A New Method for Determining the Magnetic Dipole Moment of a Spacecraft from Near-Field Data," NASA Document X-325-69-350, August, 1969

5. *GGS WIND Static Magnetics Test Report.* GGS-54-163, Martin Marietta Astro Space, September 1994.

6. *Performance Verification Report POLAR Static Magnetics Test.* GGS-95-134, Martin Marietta Astro Space, October 1995.

Table 1 GGS Magnetic Limits

Magnetization	Background Tesla (Gauss x 10E+04)	Maximum Magnetic Field in Nanotesla (gamma) 50 cm	Maximum Magnetic Field in Nanotesla (gamma) 100 cm	GEVS Ref. ¶
Initial Perm	0	6.40	0.8	2.5.4.1
Permanent				
Post 15E-04 Tesla Exposure (15 gauss)	0	24.00	3.00	2.5.4.2
Post 50E-04 Tesla Deperm (50 gauss)	0	1.60	0.2	2.5.4.3
Induced	3.00E-05	1.60	0.2	2.5.4.4
Stray Field				
DC	0	1.60	0.2	2.5.4.5
0.0001-0.1 Hz AC	0	0.40	0.05	2.5.4.5
0.1-1.0 Hz AC	0	0.40	0.05	2.5.4.5
1-3 Hz AC	0	0.30	0.04	2.5.4.5
3-10 Hz AC	0	0.22	0.03	2.5.4.5
10-30 Hz AC	0	0.07	0.01	2.5.4.5

Table 2. GGS POLAR Magnetic Allocations

ITEM	STATIC nT @ 1m	STATIC nT @ 50 cm	VARIABLE nT @ 1m peak-to-peak	VARIABLE nT @ 50 cm peak-to-peak
HYDRA				
DPU	1.0	8.0	0.2	1.6
Sensor A	1.6	12.8	0.2	1.6
Sensor B	1.6	12.8	0.2	1.6
MFE				
Electronics	1.4	11.2	0.2	1.6
Lanyard Boom	1.4	11.2	0.2	1.6
TIMAS	20.0	160.0	2.0	16.0
EFI				
Main Electronics	5.4	43.2	0.6	4.8
Motors	1.6	12.8	0.24	1.9
PSI				
Electronics	4.8	38.4	31.6	252.8
PWI				
Electronics	32.4	259.2	3.2	25.6
Search Coil	0.4	3.2	0.2	1.6
Loop Antenna	0.4	3.2	0.2	1.6
Lanyard Boom	1.4	11.2	0.2	1.6
CEPPAD				
DPU	5.6	44.8	0.6	4.8
IES DPU	2.4	19.2	0.2	1.6
VIS	TBD	TBD	24.6	196.8
PIXIE				
Camera	TBD	TBD	6.0	48.0
Electronics	TBD	TBD	5.6	44.8
UVI				
Sensor	TBD	TBD	10.0	80.0
Electronics	TBD	TBD	6.6	52.8
SEPS	TBD	TBD	7.4	59.2
CAMMICE				
HIT	1.6	12.8	0.2	1.6
MICS	1.6	12.8	0.2	1.6
TIDE	8.0	64.0	0.8	6.4

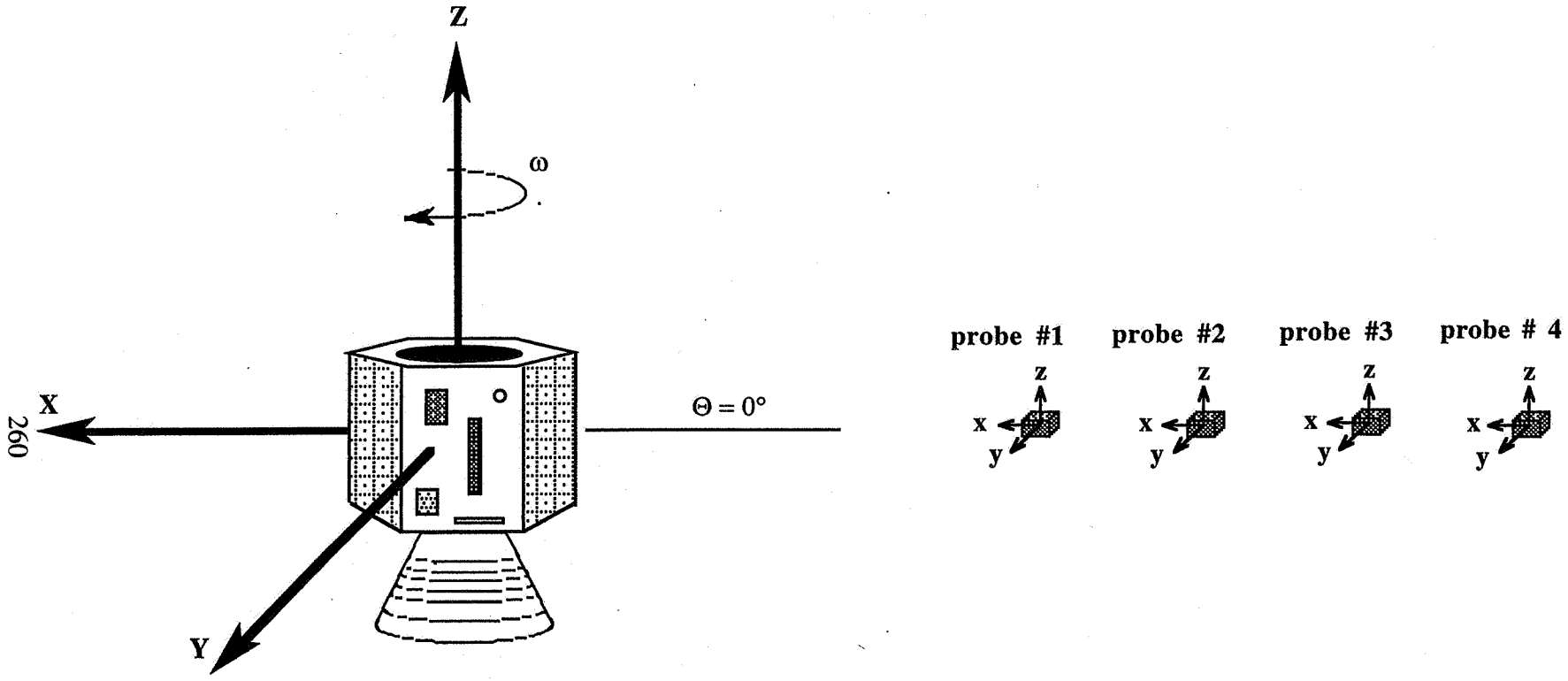


Figure 1. Spacecraft Orientation for Magnetic Testing

06/08/92

ISTP/WIND MFI 02

MAGNETIZATION DISTANCE (M)

POST DEPERM 0.5 : 0.75 : 1.0

FIELD MAGNITUDE IN NANOTESLA

ANGLE	X1	Y1	Z1	X2	Y2	Z2	X3	Y3	Z3
DATA SCANS									
0	-0.4	0.6	0.4	0.1	0.8	0.0	-0.1	0.1	0.3
10	-0.5	0.5	0.4	0.0	0.8	0.1	-0.1	0.1	0.2
20	-0.4	0.6	0.4	0.1	0.8	0.0	-0.1	0.1	0.1
30	-0.4	0.5	0.2	0.1	0.7	0.0	-0.1	0.1	-0.1
40	-0.4	0.5	0.2	0.1	0.7	0.0	-0.1	0.1	-0.1
50	-0.3	0.5	0.2	0.1	0.7	0.0	-0.1	0.1	-0.2
60	-0.4	0.3	0.2	0.1	0.7	0.0	0.0	0.1	0.0
70	-0.4	0.3	0.2	0.1	0.7	0.0	0.0	0.1	0.0
80	-0.5	0.3	0.2	0.0	0.6	0.0	-0.1	0.1	0.1
90	-0.4	0.3	0.2	0.1	0.6	0.0	-0.1	0.1	0.1
100	-0.4	0.2	0.3	0.0	0.5	0.0	-0.1	0.1	0.1
110	-0.4	0.1	0.2	0.0	0.4	0.0	-0.1	0.1	0.1
120	-0.3	0.0	0.3	0.0	0.3	0.0	-0.1	0.1	0.0
130	-0.1	-0.1	0.3	-0.1	0.2	0.0	0.0	0.0	-0.1
140	0.0	-0.2	0.2	0.1	0.1	0.0	0.0	0.0	-0.1
150	0.2	-0.3	0.3	0.0	0.0	0.0	0.1	0.0	-0.1
160	0.5	-0.3	0.2	0.1	-0.1	0.0	0.1	0.0	0.0
170	0.6	-0.4	0.3	0.2	0.0	0.0	0.2	0.0	0.1
180	0.8	-0.2	0.4	0.1	0.1	0.0	0.2	0.0	0.2
190	0.9	-0.3	0.4	0.2	0.0	0.0	0.2	0.0	0.2
200	1.1	-0.2	0.4	0.1	-0.1	0.0	0.3	0.0	0.1
210	1.2	-0.1	0.4	0.1	0.0	0.0	0.2	0.0	0.1
220	1.1	0.0	0.8	0.1	-0.1	0.1	0.2	0.0	0.0
230	1.1	0.1	0.9	0.0	-0.1	0.1	0.0	0.0	0.0
240	1.0	0.1	1.0	0.1	0.0	0.1	0.1	0.0	0.1
250	0.9	0.1	1.0	0.1	0.0	0.1	0.1	0.0	0.1
260	0.9	0.0	1.1	0.2	0.0	0.2	0.3	0.0	0.2
270	0.9	0.2	1.1	0.1	0.0	0.2	0.3	0.0	0.3
280	0.7	0.0	1.2	0.2	-0.1	0.3	0.3	-0.1	0.2
290	0.6	0.0	1.2	-0.1	-0.3	0.2	0.3	-0.1	0.2
300	0.4	-0.1	1.2	-0.1	-0.2	0.2	0.2	-0.1	0.1
310	0.4	-0.3	1.1	0.0	-0.5	0.2	0.2	-0.1	0.0
320	0.3	-0.2	1.1	0.0	-0.4	0.2	0.2	-0.1	0.0
330	0.2	-0.3	0.9	0.0	-0.4	0.2	0.1	-0.2	0.0
340	0.2	-0.4	1.0	0.1	-0.5	0.2	0.2	-0.2	0.2
350	0.0	-0.5	0.9	0.1	-0.7	0.2	0.2	-0.2	0.3

DIPOLE MOMENTS IN POLE-CM

X	Y	Z	T
-0.2	-0.4	-0.7	0.8

Figure 2. Typical Magnetic Test Data Printout

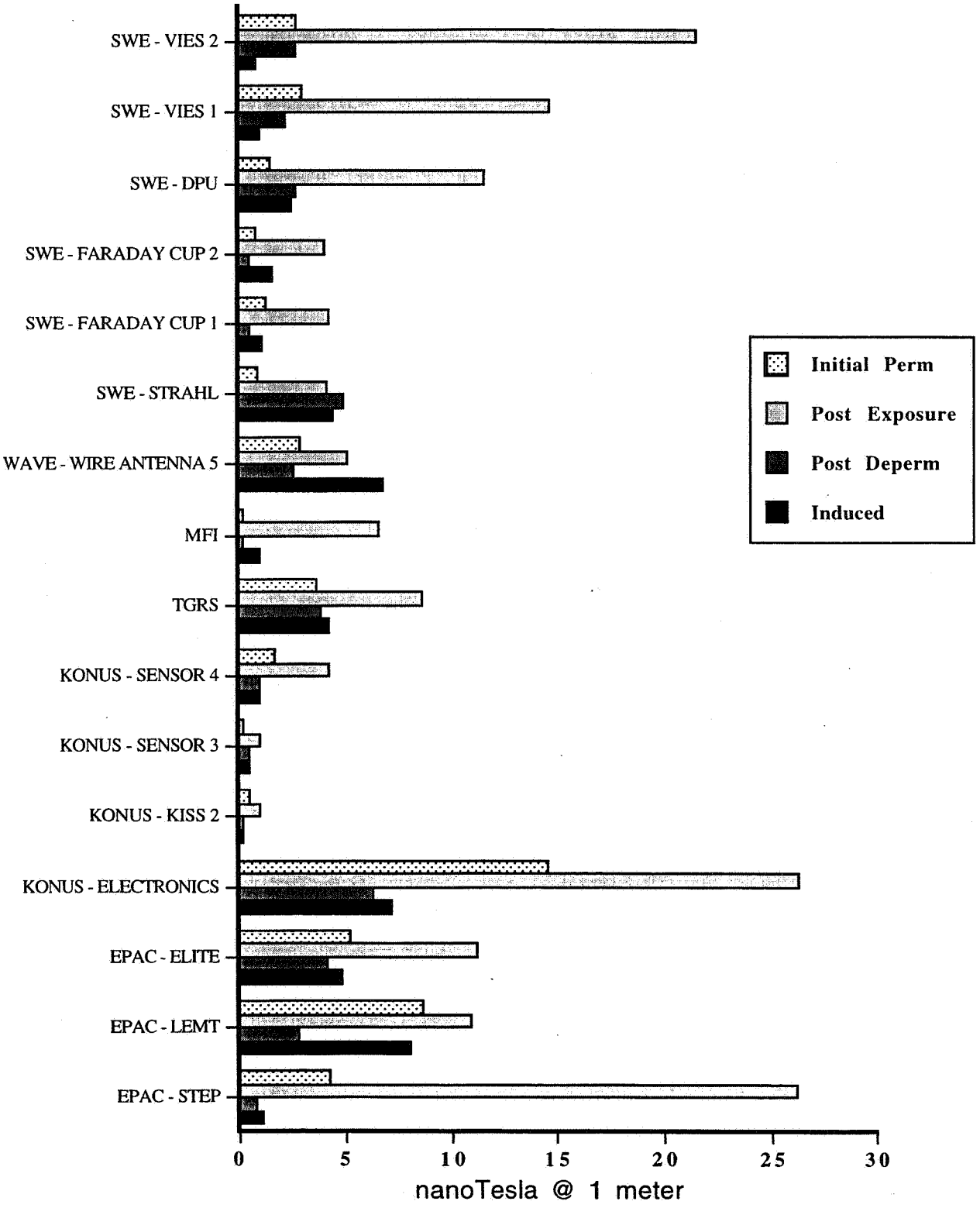


Figure 3. WIND Instruments Static Field Test Results

524-14
021466
269420 14P

19TH SPACE SIMULATION CONFERENCE
INTESPACE FROM 1970 TO THE PRESENT DAY

J.L. MARCÉ - J.C. PASQUET
INTESPACE

ABSTRACT

The decision to create the SOPEMEA Test Center and then INTESPACE, taken by the CNES (French Space Agency) 25 years ago, made it possible to set up and gradually build a Center capable of receiving and testing satellites weighing several hundred kilograms in the 70s up to satellites weighing as much as 3.5 tonnes at the present time.

In oder to meet the ever-changing requirements of the space industry over the last 25 years, the Center has never ceased to increase its test capacities and modernize its installations, in particular with the creation of an integrated complex including:

- A high-power (300 kN) vibration installation.
- A large (1100 m^3) acoustic chamber.
- Two large (600 m^3) space simulators.
- A large, compact antenna range (30 m x 20 m x 16 m).
- An electromagnetic compatibility chamber (16 m x 10 m x 11 m).
- A technical data management system based on the DynaWorks® software package.

The technical solutions devised when designing the Center, in order to meet the new requirements, facilitate testing logistics and improve quality, will be presented.

Besides the constant technical efforts made over the last few years, INTESPACE has managed to meet the changing demands by adapting its technical and human resources to make it competitive on the international marketplace.

INTRODUCTION

The INTESPACE test center is located in TOULOUSE (FRANCE) and had been created for testing space experiments and spacecrafts launched by ARIANE or others USA and Russian Rockets.

In a position to act throughout products' lifecycle - from design to removal from service, the compagny has been structured to en compass three complementary areas of activity :

1) Testing.
2) Design, Research, Consulting and Engineering.
3) Data processing.

At the moment, the test center capable to lead a complete test campaign on experiences from some kilogrammes up to satellites of 3,5 tons.

The development of center has been carried out following three fondamental criterions :

- To offer to our customers modern facilities, services of quality, a maximal security for the goods and persons and all of this with competitive prices, and with condimous effort in order to shorten testing duration.

- To offer a completly integrated center which enables to do the whole test under the same roof without the rupture of cleanliness class.

- To provide to every customer an independent center.

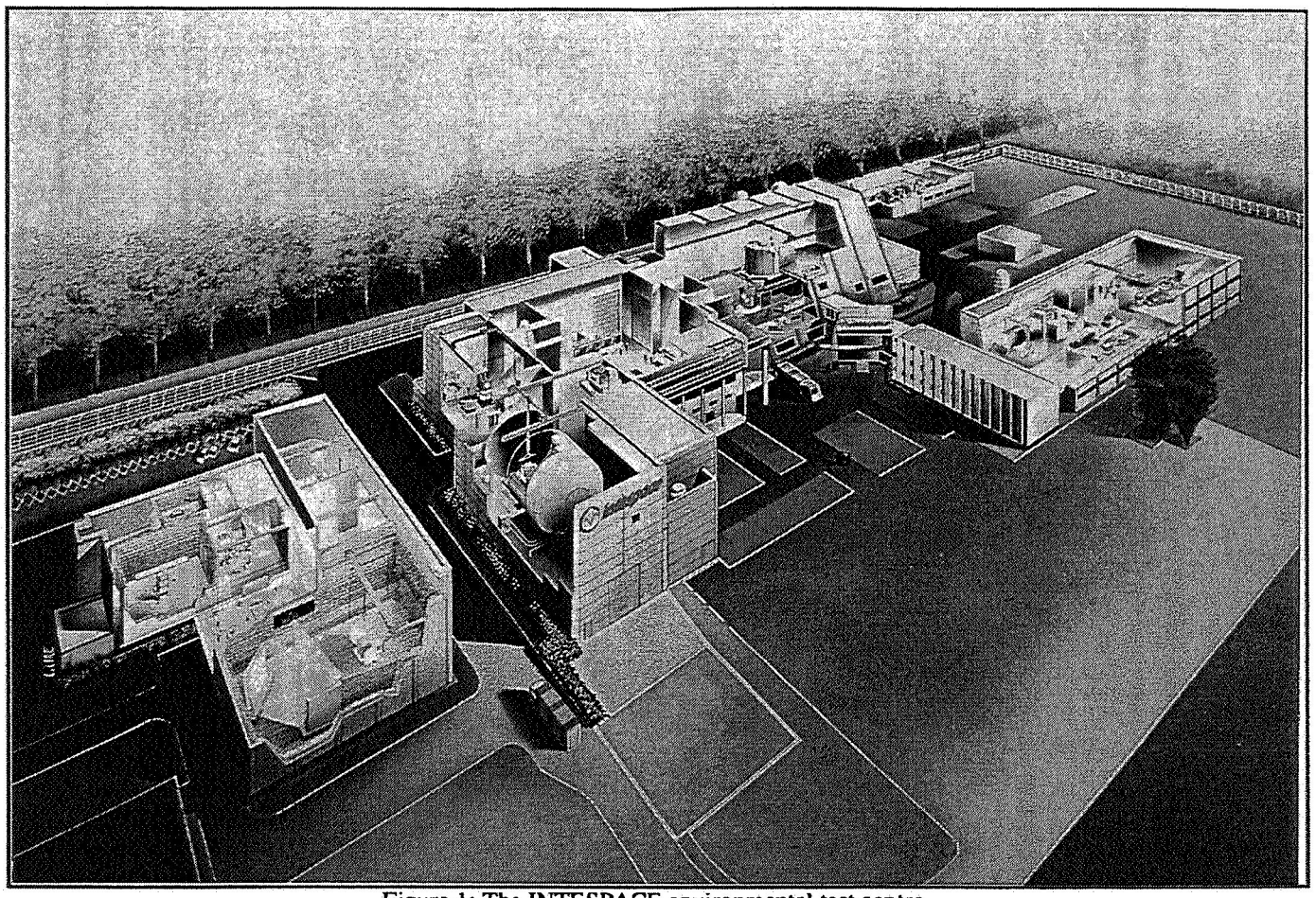


Figure 1: The INTESPACE environmental test centre

INTESPACE offers a wide range of test facilities and technical support services, specifically designed to test spacecraft and launcher subsystems.

These test facilities include :

- a 1100m^3 reverberant acoustic chamber,
- a 300 kN multi-vibration system,
- a 6 m diameter solar thermal vacuum chamber (SIMLES),
- a 10 m diameter thermal vacuum chamber (SIMMER),
- a 1760 m^3 electromagnetic compatibility facility,
- mass properties facilities.
- a compact antenna range which is currently under development and will be operational at the end of 1996.

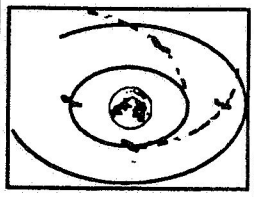
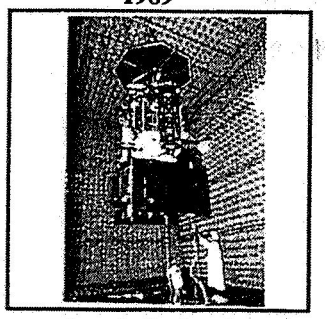
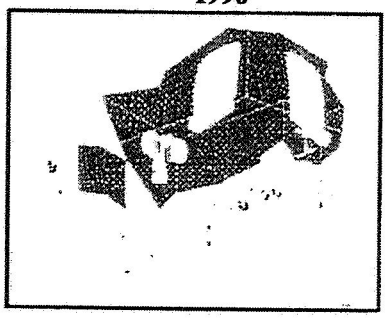
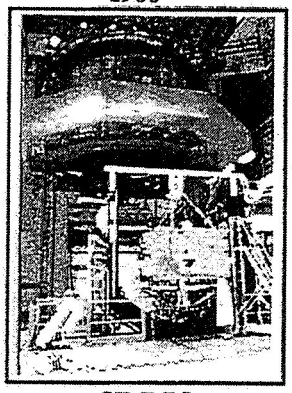
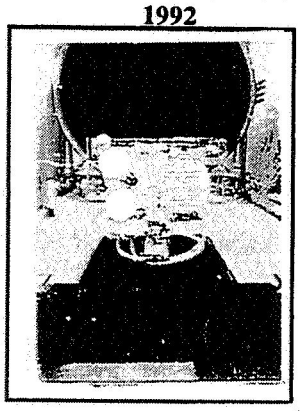
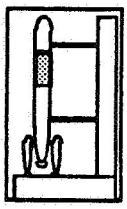
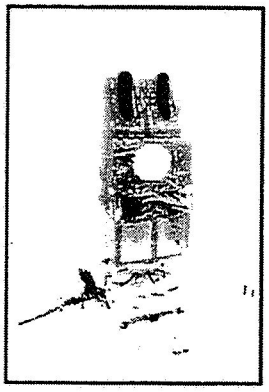
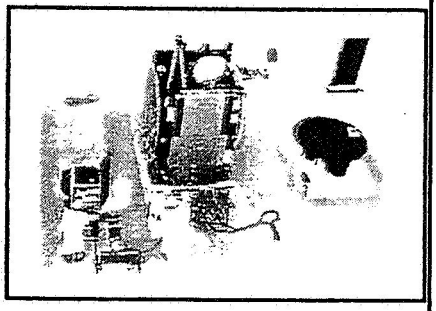
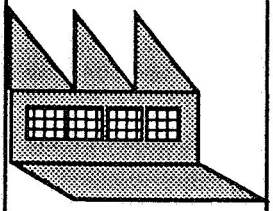
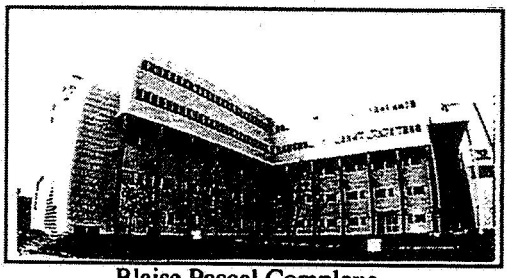
To which are added calibration and metrology test facilities a design office and a mechnical workshop.
All the above facilities, together with the preparation high bays, are located in a single building permitting thereby to reduce the time spent on moving a spacecraft from one facility to another and, consequently, the overall cost of the tests. Cleanliness conditions correspond to Federal Standard 209, 100 000 class and can be improved in some areas if so required.

The large anechoïc chamber for electromagnetic compatibility testing and compact antenna test range located next to the test building. Here, spacecraft can be submitted to EMC measurements and antenna measurements in the widest frequency range used for space communications.

The test facilities include integrated computerised control & command and data acquisition systems, both to ensure the protection of the test specimen and to provide information on, and analyses of, its behaviour during and after the tests.

A number of complementary technical support services include calibration equipment for both French and European standards, large-scale computers, consultancy services, plus a design office and a workshop. A team of over 150 highly-qualified staff is available on site.The INTESPACE Environmental Test Centre provides test services, technical expertise, test software development to governmental and European space agencies, and to international aerospace industries throughout the world.

An overview of the evolution of the center over the last 10 years is given herunder

SITUATION	ENVIRONMENTAL TESTS AND CHECKS	FACILITIES
 Orbital life	**Functional test** - EMC - Autocompatibility - Performances Antennas - RF budget	**1989**  Anechoïc chamber (extension) **1996**  **MISTRAL**
	Natural Environmental - Vacuum - Temperature - Radiation	**1986**  **SIMLES** Space simulation improvement **1992**  **SIMMER** Thermal vacuum chamber
 Launch	**Induced environmental conditions** - Vibrations - Pyro. - Acoustic noise - Accceleration	**1984**  Acoustic chamber **1987**  **MVS** Multi Vibrations System
	- Final integration - Test configuration - Mass properties measurements	**1984 à 1992**  Blaise Pascal Complexe 2 integration high bays

Space simulation testing at INTESPACE

INTESPACE's thermal facilities comprise two chambers in which the space environmental conditions --high vacuum, low temperatures, solar radiation-- can be simulated for the purposes of qualifying the thermal design of a spacecraft and performing the acceptance tests. These facilities can also be used for the mechanical tests in vacuum.

The SIMLES solar thermal vacuum facility consists of two chambers: a vertical main chamber (6 m dia. and 7 m high) and a horizontal auxiliary chamber (5.1 m dia. and 8.75 m long) placed side-by-side. The chamber's bottom loading system, at the base of the cylinder, facilitates the installation of spacecraft of up to 3000 kg on the gimbal system.

The attitude simulator has two main functions :

- first, to simulate the satellite's movements in relation to the Sun (two-axis motion : tilt motion + to -90° and spin motion; one rotation/24 hours to 10 rpm);
- second, to provide an electrical interface and TC measurements (600 TC) between the satellite and its ESGE for the measurements to be made on the satellite itself and for temperature measurements as well (using the 220 channel-rotating collector).

The solar simulator, based on a Cassegrain system, features 36 optical blocks equipped with xenon arc lamps, a field lense, and a folding mirror as prime power sources, all of which being outside the chamber at normal atmospheric pressure. The collimation mirror, in the auxiliary chamber, is under vacuum conditions. The collimated horizontal solar beam, up to 4 m in diameter, delivers 400W/m^2 to 1600 W/m^2 per user test requirements.

The chamber is equipped with stainless steel shrouds heated and cooled by circulating gaseous nitrogen for temperatures controlled in a range from 100 to 360 K. The pumping system produces high-vacuum conditions of 10^{-5} mbar.

This facility has its own preparation bay -- 580 m^2 and 22 m high-- used to integrate the specimen prior to its testing.

The SIMMER thermal vacuum chamber consists of a large horizontal chamber (10 m dia. and 13.6 m long) equipped with a horizontal loading system. An adaptable trolley is used to install the spacecraft in either a vertical or horizontal position inside the chamber's test volume (9 m in dia. and 8.8 m long; possible extension up to 15 m).

The chamber is equipped with stainless steel shrouds that are temperature-controlled, using either gaseous or liquid nitrogen in a range from 100 to 360 K. High-vacuum conditions of 10^{-5} mbar can be achieved with the pumping system.

SIMMER also has its own preparation high bay (560 m^2 and 13 m high) used for final integration prior to testing.

The SIMLES and SIMMER chambers are both connected to dedicated data handling systems, each with 500 channels for data acquisition and reduction to yield real-time test results.

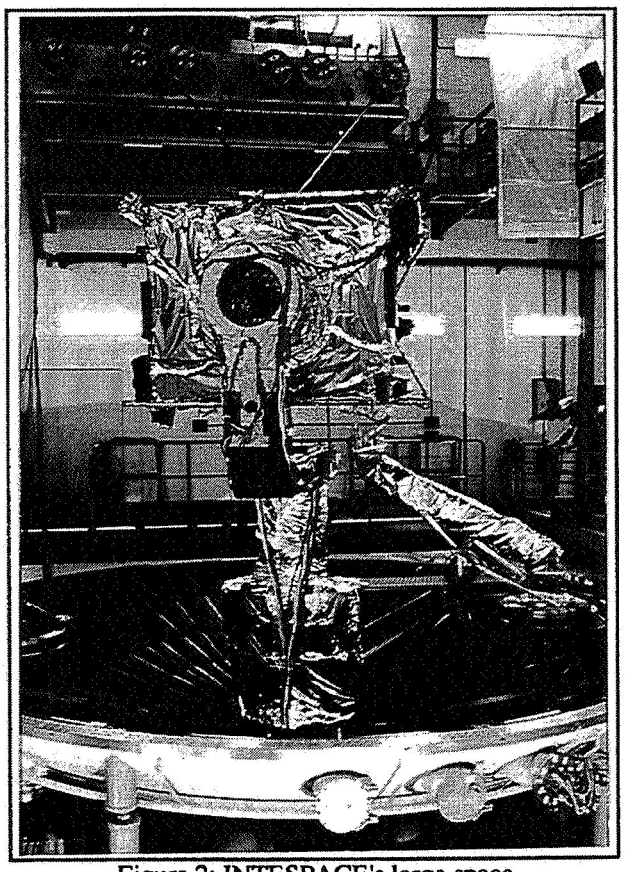


Figure 2: INTESPACE's large space simulation chamber (SIMLES)

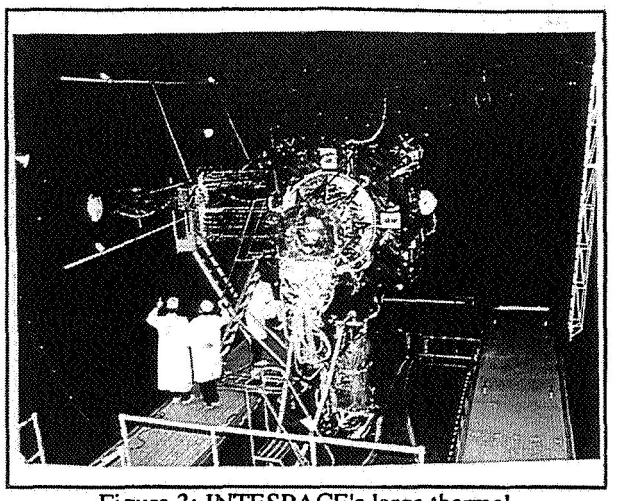


Figure 3: INTESPACE's large thermal vacuum chamber (SIMMER)

Dynamic testing at INTESPACE

INTESPACE's mechanical test facilities include a vibration test facility, an acoustic noise test facility, (reverberant acoustic chamber) and the mass properties machines to verify the integrity of the structural design of spacecraft and of their subsystems.

The controller ensures the safe operation of all subsystem and protects the specimen against excessive vibration levels via sensors placed over 15 points and at the shaker/specimen interface over eight points (as a maximum).

The acoustic noise facility simulates the noise generated by launch vehicles' engines and the vibration test facility reproduce the vibrations space vehicles are submitted to at launch. Qualification tests are performed on structural or protoflight models and acceptance tests on flight models.

The multi-vibration system consists of two shakers. Two 150 kN shakers are coupled to a hydrostatic head expander (2.1 m in dia.) for tests in the vertical axis, and to a large slip table (2.1 m x 2.1 m) for tests in the horizontal axis.

Vibration levels are programmed and the specimen monitored and safeguarded from a multi-channel controller, and its safety ensured.

A specific preparation high bay (200 m^2 and 13 m high) facilitates final integration prior to testing.

Finally, the vibration test facility satisfies the constraints due to the use of isopropyl alcohol in spacecraft pressurised tanks.
The reverberant acoustic chamber simulates the spectral noise levels encountered by the spacecraft and portions of the launch vehicle during launch. An overall noise level of 156 dB can be reached in the 1100 m^3 reverberant acoustic chamber.

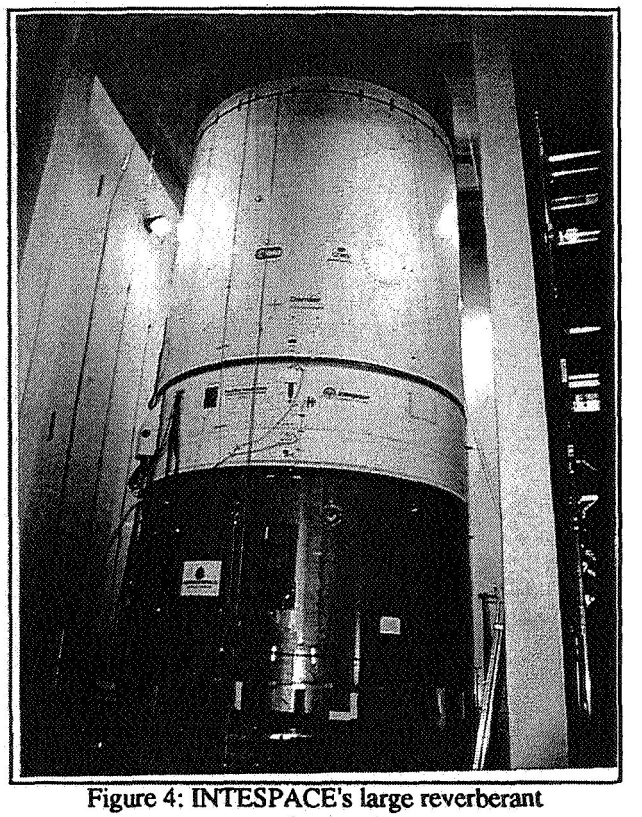


Figure 4: INTESPACE's large reverberant acoustic chamber

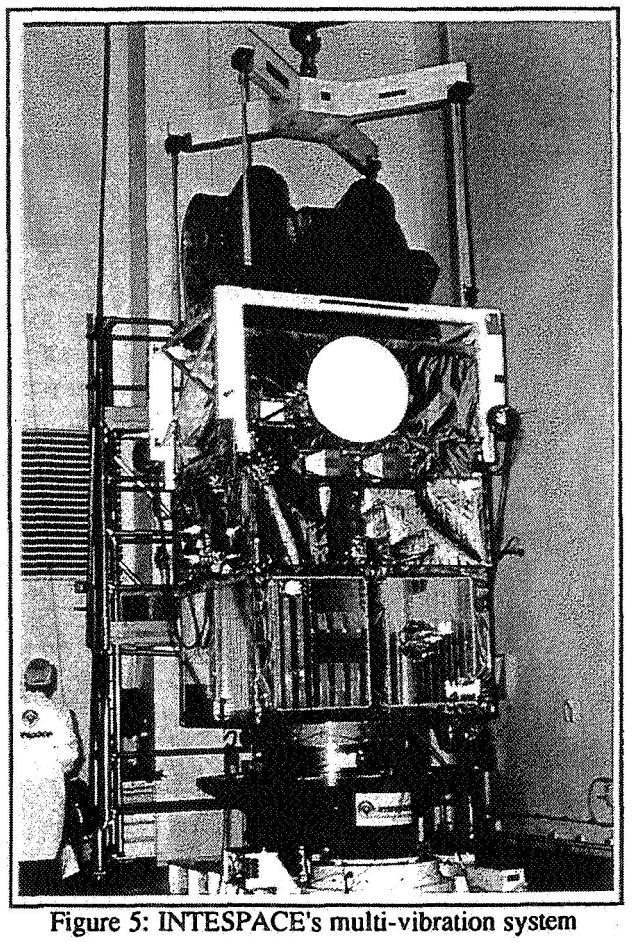


Figure 5: INTESPACE's multi-vibration system

Noise generation is ensured by pressurised gaseous nitrogen passing through three horns.

A flexible data acquisition subsystem provides for the acquisition and storage of the necessary vibroacoustic data from both the multi-vibration and the acoustic test facilities (accelerometers, strain gauges, microphones, etc).

This subsystem consists of a 256 channel-data acquisition system and a data processing system being equipped, in addition to standard sinusoidal, random and acoustic data handling functionalities, with the DynaWorks® software package. DynaWorks® provides rapid sequences of operations for quicker visualisation, statistical comparison and analysis, permitting thereby to significantly reduce preparation times and test durations.

INTESPACE's mass properties machines are used to determine the mechanical characteristics of spacecraft (balancing, cog, moments of inertia). Specimens can be placed in either a horizontal or vertical position by means of a specific L-shaped associated with a turn-over device.

These facilities were specifically designed for the purpose of reducing test sequence durations.

The particularities of dynamic testing are :
- No changement of shakers configuration during vibration test, due to this configurationthe acceptance test duration for Telecom spacegraft is 5 days.
- No sensors disconnection between vibration and acoustic tests.
- Utilisation of the same data acquisition for vibration and acoustic tests and consequently no changement of configuration.

Electromagnetic testing at INTESPACE

INTESPACE's electromagnetic test facility is available for electromagnetic and electrostatic tests on either fully-integrated spacecraft or individual subsystems for the purpose of ensuring that mission performances will meet spacecraft specifications.

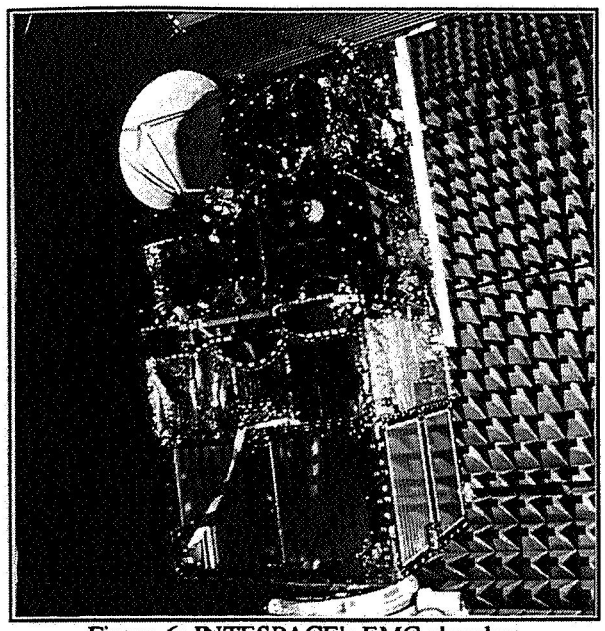


Figure 6: INTESPACE's EMC chamber

The test range consists of a large Faraday chamber with a useful test area 14 m long, 8 m wide and 10 m high. The walls and floor of the chamber are lined up with anechoïc materials. This shielded chamber is large enough to test large spacecraft with an antenna fully deployed for electromagnetic compatibility and auto-compatibility. A second Faraday cage is used for accommodation of the checkout equipment and a 200 m^2 area adjacent to the anechoïc chamber is used for spacecraft test preparation activities and accommodation of the EGSE.
Development and qualification tests are conducted according to space test specifications. Conducted and radiated emission tests and susceptibility tests are performed in the 30 Hz to 40 GHz frequency range. Electrostatic discharge and high-field susceptibility measurements for large devices can also be performed.

INTESPACE's testing capabilities were improved to meet more stringent requirements, as defined in MIL-STD-461.

Electrical field levels are now 200V/m over 90% of the 10 kHz to 18 GHz frequency range. In the 18 to 40 GHz range, they are limited to 80 V/m. Test operations are fully automated via a real-time and closed-loop software.

High-field testing can be carried out on smaller subsystems in a third anechoïc test chamber.

INTESPACE's EMC anechoic chamber is designed to ensure that all system tests on integrated spacecraft --i.e. RF health tests, auto compatibility tests, "pimp tests"...-- are performed in the most effective way.

INTESPACE also provides EMC consultant services to the experimenters in the elaboration of the specifications and specific test procedures, and for test analysis.

Auxiliary test equipment --including antennas and antenna masts-- and microwave measuring equipment is made available to the customers. Finally, EMC test equipment is redundant on a stand-by mode to ensure test continuity and reduce test durations.

A new compact test range --MISTRAL-- will enter operational in 1997.

Situated in the INTESPACE's Coulomb building, the MISTRAL compact antenna test range is a new test facility specifically designed for radiofrequency tests of spacecraft in their flight configuration.

The RF test range operates in the fully-controlled and isolated environment of the shielded anechoic chamber (30 x 20 x 15.5 m).

In a restricted space area, the Compact Test Range provides for the creation of a flat radiofrequency wave showing the same characteristics as those generated in a far-field range.

A series a RF sources covering the 1.47 to 40 GHz frequency band (provision is being made for 200 GHz) is placed in the focal plane of a hyperboloid subreflector which reflects RF radiations to a main paraboloid reflector. Its Cassegrain-type design provides for a test volume (5.5 x 5 x 6 m) within a short distance of the main reflector.

The spacecraft to be tested is placed on top of a 3-axis positioner.

The following measurements could be performed : antenna patterns measurements, end to end tests, transponder tests, Pimp, RF saturated flux density.

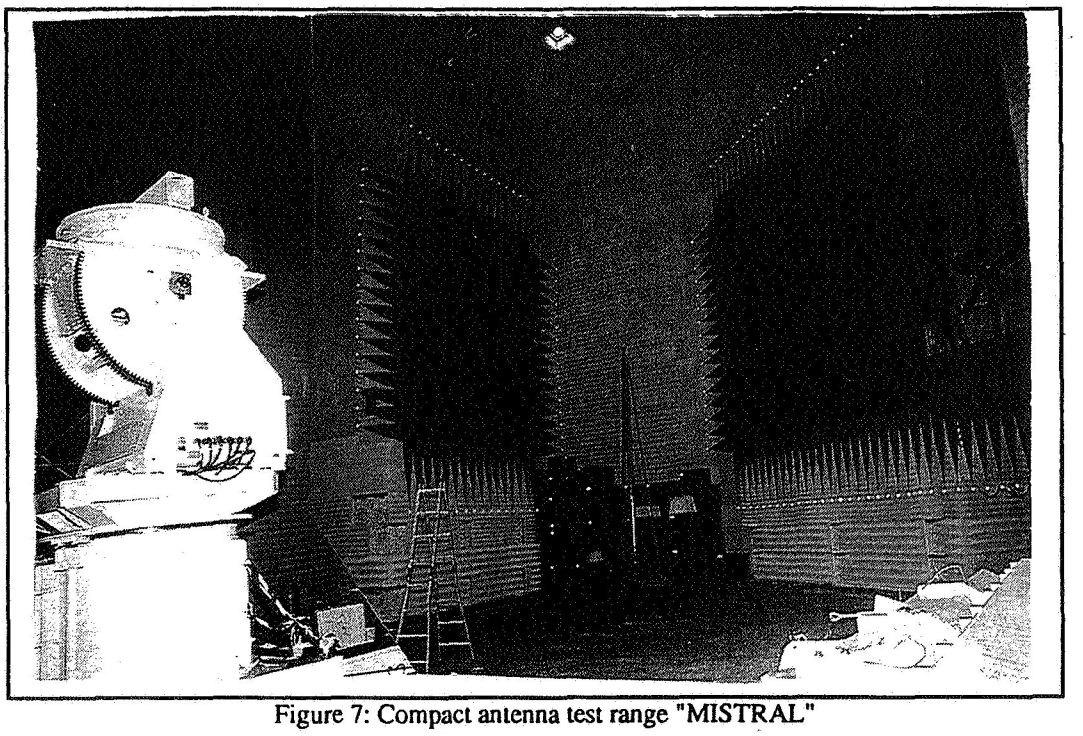


Figure 7: Compact antenna test range "MISTRAL"

INTESPACE : A UNIQUE TEST CENTRE IN EUROPE

The INTESPACE Space Test Centre features unique characteristics for satellite projects, which positions it as one of the leading test centres in Europe. The major distinctive characteristics of INTESPACE are as follows:

INTESPACE: a specialist in satellite testing

INTESPACE is a company specifically dedicated to the control of environmental conditions, with satellite and subsystem tests representing approximately two-third of the total activities of the company. The management of INTESPACE's personnel and technical facilities is entirely oriented towards space projects and turnkey test services and associated logistics support services.

INTESPACE carried out more than 70 test campaigns on satellites and large systems to the benefit of the international space community over the last ten years (1984-1994).

All the test facilities under one roof

- The major test facilities at INTESPACE are grouped under one roof, with all the test high bays beingcontrolled as per class 100 000 cleanliness conditions (Fed. Std 209).

 The integrated spacecraft to be tested can thus move smoothly and quickly from one facility to another without having to be reconfigured between the tests, thus reducing the risk of not fulfilling all cleanliness conditions. A centralised control system helps the experimenters in monitoring and verifying the cleanliness parameters, via terminals distributed in all the test areas.

- INTESPACE offers a full range of test facilities specifically adapted to the testing of spacecraft, including acoustic, vibration, thermal balance, thermal vacuum, electromagnetic compatibility, physical properties facilities.

 The last test facility to be added to the already-existing ones is a Compact Test Range for antenna measurements, of which the construction is under way. This Compact Test Range --MISTRAL-- will enter operation early '97 and will supplement a number of test facilities for complete satellite qualification or acceptance programmes.

Optimised mechanical test facilities for a better productivity

- Vibration tests are performed on two dedicated vibration test facilities:
 - a shaker for tests in the longitudinal axis of the satellite (coupled to a vertical head expander 2.1 m in diameter);
 - a shaker for test in the lateral axis of the satellite (coupled to a horizontal slip table 2.1 x 2.1 m).

 This configuration is used to avoid loosing time when tilting the shaker in the case of a single shaker configuration.

- In addition, the interconnection panels of the accelerometers are mobile and maintained connected to the satellite throughout the vibration and acoustic tests. This specific characteristic offers two advantage : (1) ensuring that the test is being performed ina most riskfree manner in terms of error, connection, cable damage, and (2) contributing to reduce preparation durations and increase the overall quality of the tests.

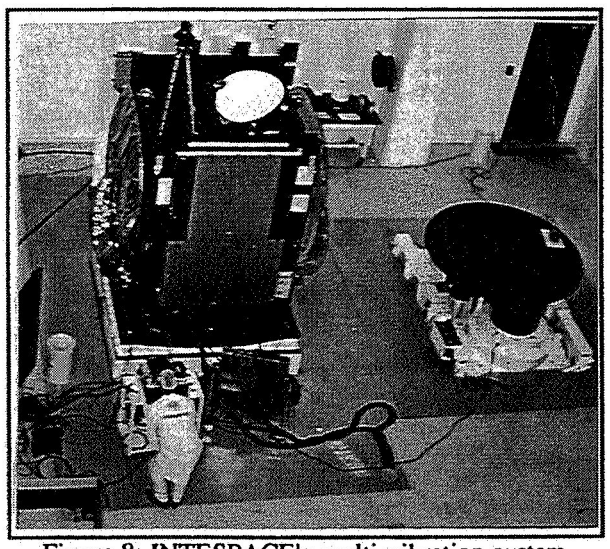


Figure 8: INTESPACE's multi-vibration system

Effectiveness increased through test predictions

The vibration tests are performed with increased effectiveness due to the use, by INTESPACE, of a test prediction tool allowing to determine the satellite/test facility interaction in advance, and thus, to adjust the test facility's control parameters.

Test predictions for tests on an electrodynamic shaker per given specifications can be obtained by coupling a model of the shaker --derived from analysis or modal survey-- with either a physical, matrix or modal-type model of the specimen and of its adapter. Control predictions can also be obtained from the simulation of the control loop and the use of previous test results or data. All of these predictions will yield analyses that

will respond to any situation, i.e. from feasibility studies for such aspects as the shaker's performance capabilities, parasitic motions, and specimen behaviours to the determination of the shaker's optimum control prior to or between the test runs.

The shaker, adapter, and specimen models together with the control parameters, feasibility test results, adapter performance, specimen behaviours, and control performance capabilities can be obtained from given test specifications to prepare the test campaign and/or ajust the test parameters prior to or between the test runs.

This methodology is likely to be applied to the INTESPACE's multi-vibration test facilities, with an updated finite element model of the moving part of the shaker. This will be achieved in two steps for taking basic requirements first into account and then for providing a general tool.

Improving test productivity : the DynaWorks® response

INTESPACE develops solutions for today's applications to ensure the successful integration of the tests in the industrial development of the product.

The DynaWorks®, software is the result of INTESPACE's eminent experience in testing.

DynaWorks®, is the response to the necessity for improved productivity and when environmental factors are extensively involved in sectors of industry such as the aeroanautics, space, defence, automation and transport, energy, shipbuilding, etc. sectors. It is a valuable tool intended to design and structure analysis departments, environmental testing laboratories, in-site environment measuring instruments, environmental engineering specialists and management teams.

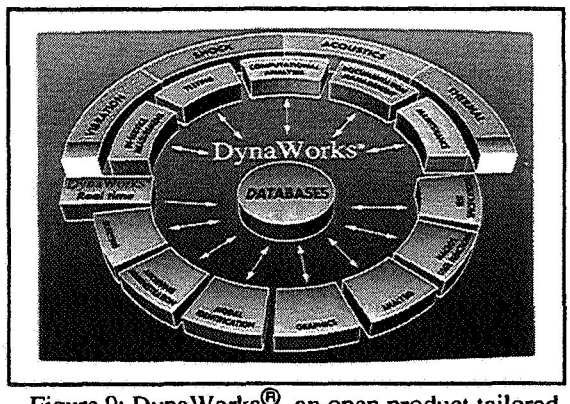


Figure 9: DynaWorks®, an open product tailored to your individual needs

DynaWorks®, is a powerful relational test data management and analysis system that allows product designers and test engineers to capture, analyse, and organise the test results generated throughout the product's life cycle. The test results obtained from heterogeneous systems during the vibration, shock, acoustic, thermal balance, ... tests can now be standardised and organised effectively with DynaWorks.

The powerful query functions of DynaWorks® provide for quick and comprehensive analysis of complex correlations such as the correlation of predicted results against experimentally obtained results, reducing thereby the development cycles of the products. With an excellent 2D and 3D graphics, a user-friendly X-WindowsTM interface, and context-sensitive on-line helps, the users will enjoy immediate increases in productivity.

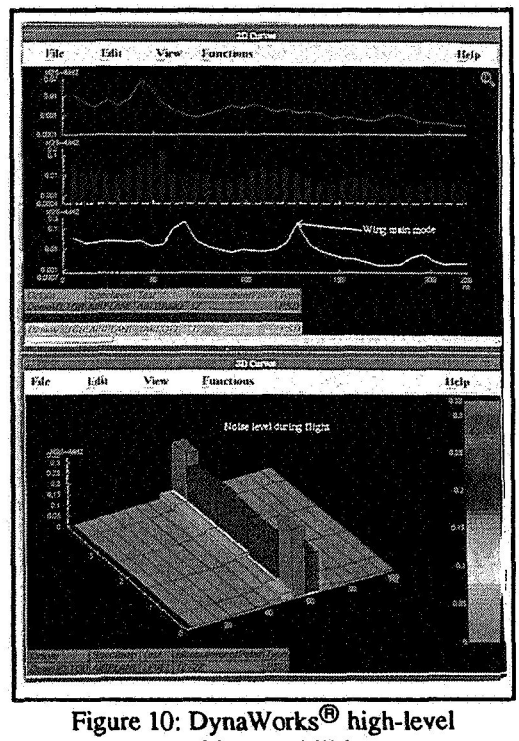


Figure 10: DynaWorks® high-level graphics capabilities

Combining physical measurement facilities for high-performance measurements

INTESPACE performs all the measurements related to the physical properties of a satellite (i.e. inertia, cog, balancing) on a combined test facility coupled with a tilt device to safely position the satellite on its three-axes.

This unique combined test facility configuration facilitates the handling of the satellite and significantly reduces the duration of the measurement campaign.

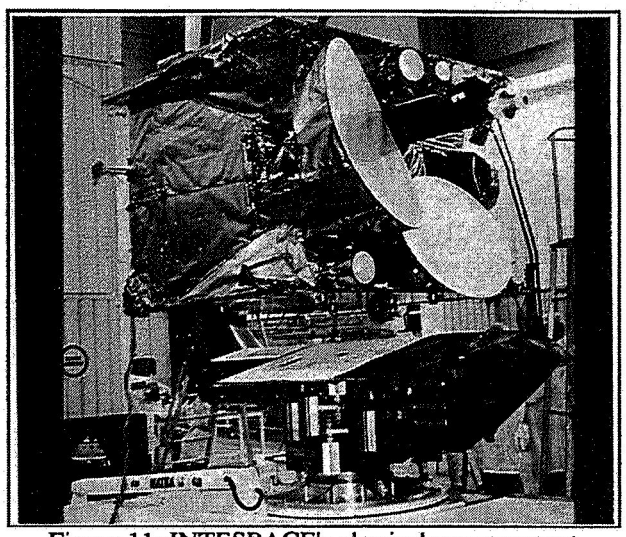


Figure 11: INTESPACE's physical measurement combined facility

Redundant and flexible thermal test facilities

INTESPACE has two large thermal-vacuum chambers, mutually compatible, dedicated to satellite acceptance tests :

- the SIMLES test chamber --a vertical chamber with a useful volume of 200m^3,
- the SIMMER test chamber --a horizontal chamber with a useful volume of 560m^3.

Both test facilities are perfectly compatible with one another in terms of mechanical and electrical interfaces with the satellite. Likewise, the measuring systems and test data processing systems are identical for both test chambers.

A high availability rate for the thermal test facilities is ensured to customers --even in the case of a failure during the test-- through the provision of redundant facilities.

Improving predictions and analysis tests results

INTESPACE offers design, research and consulting services in environmental techniques for the design of sophisticated mechanical systems and prediction of their behaviour. These activities cover the following :

- In the acoustic and vibrations tests area :
 - solving vibration and noise problems,
 - environment diagnosis,
 - verifying and readjusting previsional models in view of testing,
 - development platform of an analysis for structural dynamics,
 - vibroacoustic transmission analysis,
 - system or equipment qualification,
 - creation of environment databases.

- In the advanced dynamic tests area :
 - accurate measurement of the transfer function,
 - experimental modal analysis (multipoint excitation or shaker-induced excitation),
 - microdynamic tests (equipment or transmission characterization),
 - transient vibrations.

Calibration

Sensors and measuring equipment in the following areas :
- Acceleration.
- Temperature.
- Mass.
- Electrical quantities for which INTESPACE has COFRAC* calibration accreditation.
- Particule counters.
- Flowmeters.
- Pressure sensors.
- Acoustics, an area in which INTESPACE has earned industrywide recognition.

* COFRAC : French certification organization.

- In the development area of new thermal testing methods:
 - infrared tests,
 - tests with temperature-regulated plates.

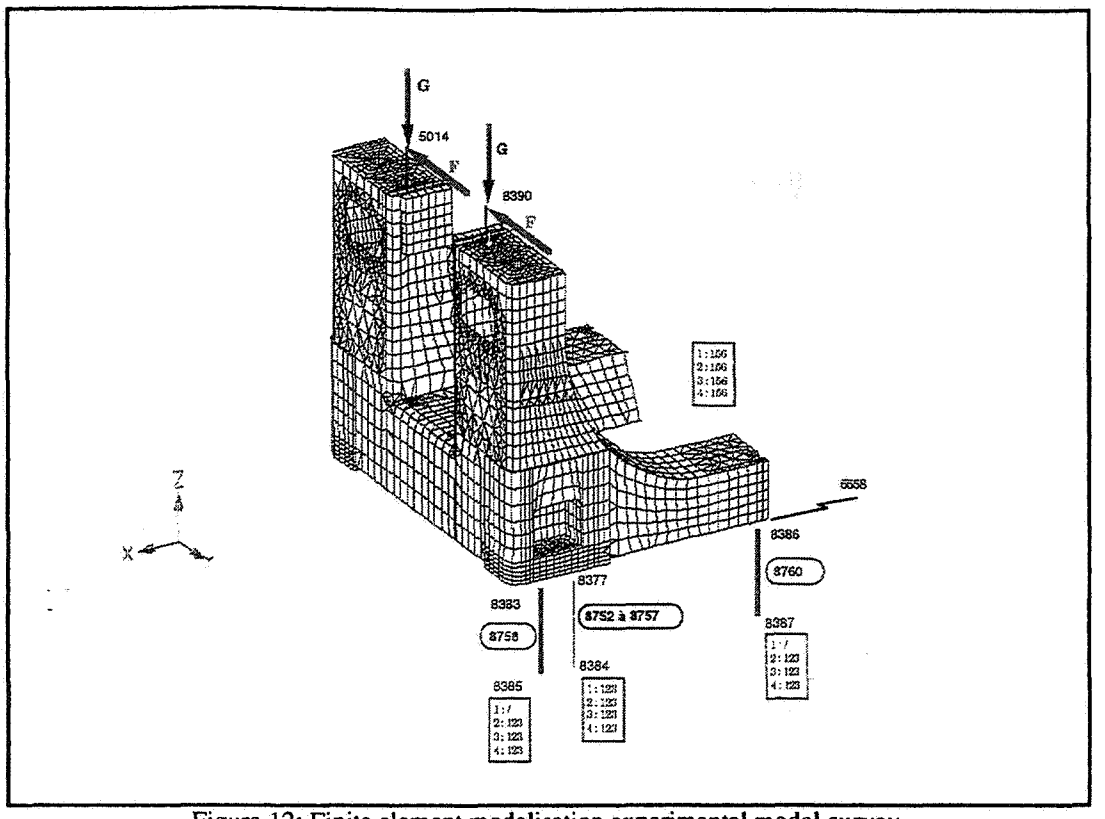


Figure 12: Finite element modelisation experimental modal survey

Improving the quality of the test

INTESPACE offers a high-quality service encomparsing calibration, verification and adjustment of out - of - tolerance measuring equipment.

Metrology

Simulating the space environment calls for highly sophisticated vacuum, cryogenic, optical and thermal technologies that must be closely monitored by skilled personnel applying a strict methodology. INTESPACE qualifies materials, paints, test facilities and other items for the space industry.

Engineering

INTESPACE also offers a variety of services relative to test centre and test facility engineering, including consulting, technical assistance, 'turnkey' missions and personnel training.

INTESPACE's competence in terms of test centre engineering is the result of :

- INTESPACE test laboratories' consolidated experience with more than 300 tests each year;
- INTESPACE's effort to establish cooperations with industrial partners, whether Prime Contractors, reasearch laboratories, universities and institutes;
- INTESPACE's participation in launch campaigns via permanent representatives in the European Space Launch site in Kourou (French Guiana);
- the direct payoffs from the previous installation of test centres in Europe, Brazil, Israël, South Korea and Republic of China.

INTESPACE involves the best European experts in the whole spectrum of the activities required by the polyvalence of the techniques to be implemented within an integration and test centre.

INTESPACE : INDEPENDENT CENTER

INTESPACE was created in 1983 in pursuance of SOPEMEA - Toulouse space activities in the form of a CNES-SOPEMEA joint-venture. In addition to CNES and SOPEMEA (35 % each), INTESPACE shareholders are major French space industrials: MATRA MARCONISPACE (9 %), AÉROSPATIALE (9 %), ALCATEL ESPACE (3 %) - plus the Employees' Mutual Funds (9 %).

INTESPACE is one of the 4 European coordinated test centres and formally approved by the European Space Agency, to conduct a number of services on behalf of the main international space industrials involved in European programmes. INTESPACE is RNE/COFRAC- and BNM/COFRAC- accredited at national level.

INTESPACE is an independent center and is a garanter for our customers and the customers of our customers.

MAIN PARAMETERS OF THE INTESPACE FACILITIES
Thermal testing facilities

THE SIMLES SOLAR SIMULATOR

Configuration (main chamber)

Orientation	vertical
Test volume	6 m dia. x 7 m high
Access	bottom loader

Pumping system

Working pressure	$< 10^{-5}$ mbar
Roughing	mechanical : 12 000 m^3/h
Booster	turbomolecular : 6500 l/s
High vacuum (cryopumps)	20 K. 130 000 l/s

Thermal shrouds (main chamber)

Temperature range	100 - 360 K
Temperature uniformity	± 10 K at 100 K
Emissivity	≥ 0.85
Absorptivity	≥ 0.95

Solar simulation

Solar beam (horizontal)	up to 4 m dia.
Intensity	400 - 16000 W/m^2
Intensity uniformity	± 4 %
Collimation angle	± 1.9
Stability	< ± 1%
Spectrum	xenon

Gimbal system

Two-axis	S/C mass : 2500 kg
Spin axis in vertical position	S/C mass : 3000 kg
Spin motion (variable)	1 rotation/24hr to 10 rpm
Attitude motion :	
• alternating	± 90°
• speed	7.5°/min

THERMAL DATA ACQUISITION AND PROCESSING SYSTEM

- Acquisition and storage of 396 Cu-Con thermocouple signals
- Acquisition and storage of 96 voltages and 96 currents
- Real-time analysis of test results using dedicated software packages
- Transfer of test results via a dedicated Transpac link (X.25 packet switching network)

THE SIMMER THERMAL VACUUM CHAMBER

Configuration

Orientation	horizontal
Overall dimensions	10 m dia. x 13.6 m long
Test volume	9 m dia. x 8.8 m long
Access	horizontal loader
SIMMER bay	560 m^2 x 13 m high

Pumping system

Working pressure	$< 10^{-5}$ mbar
Roughing	mechanical : 12 000 m^3/h
Booster	turbomolecular : 6500 L/s
High vacuum	130 000 L/s

Thermal shrouds

Temperature range	standard 100 - 360 K option 80 K
Temperature uniformity	± 10 K
Emissivity	≥ 0.85
Absorptivity	≥ 0.95

Platform (load capacity)

Vertical axis	4000 kg
Horizontal axis	2500 kg
Interface plane: horizontally	accuracy 0.5 mm/m
adjustable during test	range : ± 30 mm/m

THE ELECTROMAGNETIC COMPATIBILITY TEST FACILITY

Configuration

Chamber	
. overall dimensions	16 x 10 x 11 m high
. test volume	14 x 8 x 10 m high
Door access	5 x 6 m high
Preparation bay	16 x 14.5 x 13 m high
Crane	100 kN
Cleanliness	class 100 000

EMC test capability

RF performance of the shield anechoïc chamber

• reflectivity	UHF > 30 dB
	L band > 40 dB
	C band > 50 dB
	K band > 50 dB

EMI isolation

• electric fields	14 kHz - 200 MHz
	atten. > 12 dB
• plane waves	200 MHz - 1 GHz
	atten. > 100 dB
	1 - 10 GHz, atten. > 80 dB
• magnetic fields	14 kHz, atten. > 70 dB
	250 kHz, atten. > 100 dB

Measurement system

• emission measurement	emission receivers
• spectrum analysis	30 MHz - 1 GHz
	range 100 Hz - 22 GHz
	extension to 40 GHz with mixers

Susceptibility system

• generators	10 Hz - 10 GHz
• amplifiers (range)	10 Hz - 18 GHz
	power 10 - 2000 W
	18 - 40 GHz, 3 W power

THE COMPACT ANTENNA TEST RANGE

Shielded anechoic chamber

Dimensions	30 x 20 x 15.5 m
Environmental parameters :	
• temperature	21°C ± 2°C
• humidity	50% + 10%
• cleanliness	100 000 class (Fed. Std 209)
Seismic ground isolation	
Faraday cage	

Reflectors

Dimensions	7.5 x 6 m (66 tons)
Subreflector dimensions	5.6 x 5.3 m (44 tons)
Serration length	150 cm
Surface accuracy	25 µm RMS
Equivalent focal length	130 m

Quiet zone performance

Dimensions :	
• height	5 m
• depth	6 m
• width : . focused :	5.5 m
. defocused :	up to 5.5 m left
	up to 3.3 m right
Frequency range	1.47 - 40 GHz (provision to 200 GHz)
Polarisation	linear, circular
Ripple amplitude	± 0.5 dB
Ripple phase	± 6°
Typical cross polarisation	< -40 dB
Cross polarisation accuracy at -30 dB	± .75 dB
Measurement accuracies :	
• Side lobes at -30dB	±.75 dB
• Gain	± .25 dB

Ground support equipment

Positioner	5 axes
Load capacity	6 000 kg
Travelling overhead crane capacity	10 tons
Anechoic chamber access door	6 x 11 m
Experimenters room	128 m2
Automatic access controlled area	
Fire detection and fighting systems	

THE 1100 m^3 ACOUSTIC TEST FACILITY

Configuration (chamber)

Volume	1100 m^3
Dimensions	10.3 x 8.2 x 12 m high
Door access	6 x 11.5 m high
Crane load (max.)	100 kN
Cleanliness	class 100 000

Acoustic capability

Overall sound pressure level	156 dB
Chamber suspension resonant frequency	16 Hz
Lowest frequency cut-off	13 Hz
Excited frequency	22.4 Hz - 11.2 kHz
Max. contr. frequ. bandw. random :	125 - 1000 Hz
Modal density	5 modes/1/3 oct. at 31.5 Hz
	> 100 modes per 1/3 octave at 100 Hz
Mean reverberation time	10 s

Control capability

Control	8 microph. in chamber
Processing	multiplexing, real-time analyser

THE 300 kN MULTI-VIBRATION SYSTEM

Vibration capability

Force ratings	
• longitudinal axis	300 kN sine mode
• lateral axis	
- standard	150 kN sine, random
- push pull	300 kN sine
Frequency bandwidth	
• sinusoïdal low level	2 - 2000 Hz
• sinusoïdal high level	2 - 500 Hz
• random	10 - 2000 Hz
Maximum payload	3500 kg
Maximum velocity	1.6 m/s
Displacement	50.8 mm in random and shocks
	38 mm peak to peak in sine mode
Maximum acceleration (unloaded)	14 g
Vertical head expander	2.1 m
Horizontal slip table	2.1 x 2.1 m

Control capability

Digital console	
• control channels	8 max. sine
	16 max. random
• monitoring channels	15 for notching
	and/or S/C safety

MECHANICAL DATA ACQUISITION & PROCESSING SYSTEM

Vibro-acoustic data handling system

• Accelerometer channels	176
• Strain gauge channels	64
• Microphone channels	16
Acquisition capabilities	256

Reduction capabilities

- Sine : global and/or filtered amplitude transfer function, distortion
- Random : PSD (narrow band, 1/3 octave, octave), RMS value, transfer function, coherence function
- Acoustic
 - accelerometers and others as random process
 - microphones : ASPL (narrow band, 1/3 octave, octave), OASPL

10P

525-18

021467

26940Y

LABORATORY SIMULATION OF HYPERVELOCITY DEBRIS

R. Roybal, J. Shively, C. Stein, P. Tolmak
Air Force Phillips Laboratory
Kirtland Air Force Base
Albuquerque, New Mexico

ABSTRACT

Efforts to simulate the space environment over the past years have consisted of looking at individual effects of the space environment such as atomic oxygen, ultra violet radiation, electron bombardment, and debris impact on space craft materials. The effects of hypervelocity impacts on the properties of materials have been the subject of numerous studies (ref. 1). As the interest in long duration space missions increased the interest in the synergistic effects of the entire space environment has also increased. In order to simulate the space environment in a more complete fashion it has been necessary to build simulation chambers capable of simulating many space effects. With this in mind it was easily seen that the design criteria for a space source such as a debris simulator consisted of two factors. First, the simulation technique must be able to reproduce the space environment parameters of interest, secondly and just as important the simulation technique must be compatible with the space effects chamber including all other sources and diagnostic instrumentation used. This work looked at a relatively new method to simulate space debris, the laser driven flyer accelerator, and its usefulness in a space environment effects chamber.

INTRODUCTION

The space debris parameters of interest were plate like debris particles, such as paint flakes, small in size with high impact fluxes. The damage to a space-craft surface over a long time period from multiple debris impacts in conjunction with other space effects working in a synergistic manner was of primary interest. The scope of this effort did extend into larger particles capable of catastrophic structural penetration from a single impact. The following were the parameters of interest.

Size : .5-3 mm diameter
Particle geometry : flat plate
Density : 2.7 gm/cm^3
Velocity : 7-10 km/s
Flux : 1-100 hits/m^2/yr

These parameters were determined by data recovered from previous low earth orbit space experiments and from input from the space effects community. (ref. 2)

A few of the space effects chamber compatibility criteria parameters were as follows.

Vacuum : The debris simulator must not degrade the chamber vacuum below operational thresholds for devices such as a time of flight mass spectrometer (TOFMS). (10^{-9} torr) The vapor pressure generated by impact was not considered as a design criteria, but was addressed in individual experimental setups.
Residual Chemistry : It was desirable to characterize the chemistry produced from impact. This was done using a TOFMS. The debris simulator must not introduce any residual organic chemistry as a result of propellant release. Chemistry in the form of metal vapor or metal plasma was acceptable because it was distinguishable from organic chemistry generated by impact.
Size : The agglomeration of such a diversity of instrumentation produced a vast number of incompatibilities problems, one of which that was often overlooked during initial design phases was the size constraint. The debris simulator must be able to work in the limited space available in the effects chamber. There was often a limitation to the amount of space surrounding the chamber.

Electromagnetic Field (EMF) effects : The debris simulator must not produce any EMF that can not be shielded from the sensitive instrumentation involved with the space environment effects chamber.

Several methods used to accelerate particles were investigated. Gas guns, exploding foils, Van de Graff accelerators, and explosives were looked at. Each method had its positive and negative attributes but over all none of the methods fit the design criteria set before us. While investigating a proposed idea to use explosives to accelerate particles we learned that the explosives were detonated by laser ablation of a foil attached to the explosives as shown in (Fig. 1). While the use of explosives did not fit our design criteria the application of a laser to accelerate a metal foil was intriguing.

EXPERIMENTAL

In order to produce the desired space debris parameters and achieve the compatibility criteria a relatively new technique was used, the laser driven flyer method. A laser launched flyer-plate method was used to simulate impact from space debris. This technique had two configurations. In the first configuration a thin metal foil was accelerated by focusing a laser on the interface of a metal foil bonded to a glass substrate as in (Fig. 2). The bonding method used will be addressed later. The laser produced a confined plasma at the interface which further absorbed laser energy and generated high pressure which accelerated the flyer toward the target. A similar method has been used to accelerate flyers for the shock detonation of explosives. (ref. 3) A second flyer configuration, also shown in (Fig. 2), was attempted. In this method the laser was focused on a polymer disc in contact with a metal disc placed in a barrel. The polymer was vaporized and the expanding gas drove the metal disc toward the target. This configuration was attempted in hopes of increasing the transfer of the laser energy into kinetic energy of the flyer. However the use of a polymer as a propellant would contaminate any chemistry produced by impact.

The bonding method used to adhere the metal foil to the glass substrate was a field assisted diffusion bond. (Fig. 3) shows the basic setup for this technique. A metal foil was placed in contact with the glass substrate. The foil and glass were heated to 370 C. At this temperature the glass was electrically conductive. A voltage was applied across the laminate. Between 700 and 1500 volts were used. When the voltage was present the mobile positive ions in the glass began to diffuse out of the glass, this produced an eletro-static space charge in the glass that draws the metal to intimate contact with the glass. At this time mobile ions in the metal diffuse into the glass and produced the bond. (Fig. 4) shows a current versus time plot for a typical bond process. As time increases the current dropped off. This was a good indication that the population of mobile anions were depleting from the glass.

The experimental setup used to accelerate the flyers is shown in (Fig. 5). The characteristics of the flyer as well as the characteristics of the target impact features were of interest. Flyer velocity, shape in flight and residual chemistry were looked at. The target impact crater and impact produced vapor were also characterized.

A high power pulsed laser was used, capable of up to 20 joules in 20 nanoseconds. Simple optics were used to direct the laser beam onto the flyer. The flyer velocity was measured with a VISAR (ref. 4). An argon laser was focused onto the front surface of the flyer via a fiber optic probe introduced into the vacuum chamber. The reflected light was sampled by the probe and sent to the VISAR unit. A TOFMS was used to characterize the chemistry produced by flyer impact with a target.

RESULTS AND DISCUSSION

(Fig. 6) is a calibration curve for laser energy versus flyer velocity. A maximum velocity of 10 km/s was measured for this flyer configuration.. A streak camera image made at Los Alamos Labs is shown in (Fig. 7). This was a typical streak image of an aluminum flyer 5 micron thick, 1 mm in diameter, and shows that the flyer comes off very flat.

The size of flyers used to impact a sample target was based on the space debris parameters of interest. Smaller flyer plates less than 1 mm in diameter were used when looking at the chemistry generated from impact. Larger 3 mm diameter plates were used when characterizing shock damage to targets. While we generally used an aluminum flyer, materials other than aluminum have been launched, however aluminum was preferred since it closely represented an average density of space debris. The target materials were various carbon composites. (Figs. 8-11) show impact craters on a graphite/ polysulfone (g/ps) composite target From (Fig. 8) it was easily seen that the technique lends itself to multiple shots on the same target. Different damage features are shown in the remaining figures. Evidence of melt, and fiber breakage are clearly shown.

Damage from a 3 mm diameter flyer traveling at approximately 4.5 km/s is shown in (Fig. 12) and (Fig. 13). The target material was a carbon/carbon composite coated with a silicon carbide coating. Upon initial viewing of the target after impact the damage seemed minimal with only removal of one layer of coating from the front surface. When viewing the back surface, the damage due to spall was striking. Damage extended into the first two layers of the composite. Much of what happened inside the material after a hypervelocity collision apparently occurred after the initial compressive shock wave had passed through the material and had reflected back as a rarefaction wave. Reflective rarefaction waves occur when the density suddenly changes as at the back surface or at internal discontinuities such as precipitates or fibers.

(Fig. 14) shows the configuration used to study the chemical species by hypervelocity micro-flyer impacts of space structural materials. The chemistry of the vapor produced by the simulation technique was analyzed with a TOFMS. The arrangement used provided a favorable orientation for the vapor ejecta to escape and to enter the mouth of the TOFMS.(ref 5) This study used an ultra high vacuum chamber instrument with a TOFMS capable of producing time-resolved spectra of vapor species being generated by the impact simulation method. (Fig. 15) is a typical TOFMS spectra generated by impact. Characterization of the vapor chemistry produced by impact was of importance to understanding secondary contamination of space-craft optics and other surfaces. The chemistry of impact process may also lend insight to shock physics analysis of debris impact with polymer matrix composites.

From the spectra produced, it was evident that the resin vaporized and the polysulfone polymer fragmented. Sulfur, which was one species easily removed from the polysulfone mer, showed up at 32 amu on the spectrum. The sulfur species could have been overshadowed by the oxygen molecule which also had the same mass, 32 amu. However, the amount of oxygen that was present was already combined with aluminum. Therefore, the peak at mass 32 amu, was attributed to sulfur and was a verification that the polysulfone resin had been fragmented. Other species present also came from the fragmentation of the polysulfone resin. (ref. 6) These included the aromatic species C_6H_x, and the monomers of carbon-hydrogen species, such as C_2H_2. The aluminum-oxygen species detected may be attributed to the ionized layer Al_2O_3 that drove the flyer plate toward the target. It was believed that plasma from this layer accelerated around the flyer and entered the TOFMS. This did not seem to be a problem since this species was easily distinguished from that of the vapor species.

CONCLUSIONS

The laser driven flyer technique proved to be a feasible way to simulate hyper-velocity space debris in a manner suitable for a synergistic space effects chamber. Both design criteria were met, space debris simulation was achieved while maintaining the compatibility criteria.

The flyer-plate technique used in this experiment had several advantages over conventional methods of producing hypervelocity particles. The method was compact and fit conveniently into the space effects chamber. Very little chemical contamination was produced in accelerating a flyer-plate with this method compared to that generated by Van de Graff accelerators or explosives.

A continued effort will be made to increase the efficiency of coupling the laser energy into flyer kinetic energy. This will be looked at for both flyer configurations. As higher velocities are desired the material limits of this technique will be investigated. Acceleration of different flyer materials of interest will also be attempted. Materials such as ice and glass are to be included in future testing.

REFERENCES

1. Daveson, L. and Graham, R. A.. "Shock Compression in Solids", Physics Reports Phys Rev Ltr. 55, 4, p.255-379, (1979).

2. Johnson, N.L., and McKnight, D.S., Artificial Space Debris, p.25ff, Orbit Enterprises Inc., Glen Ellyn, IL., 1991

3. Paisley, D. L., Warnes, R. H., Kopp, R. A., " Laser-Driven Flat Plate Impacts to 100 GPA With Sub-Nanosecond Pulse Duration and Resolution for Material Property Studies", in Shock Wave in Condensed Matter, 1991, p. 825, S. C. Schmidt, R. D. Dick, J. W. Forbes, D. G. Tasker, Eds., Elsevier Science BV, 1992.

4. Barker, L. M. and Hollenbach, R.E., "Laser Interferometer for measuring High Velocities of Any Reflecting Surface", J. Appl. Phys., Vol. 43, p.4669-4675, 1974

5. Roybal, R.E., Shively J. H., " Chemical and Structural Effects Caused By Hypervelocity Impacts To Polysulfone Graphite Reinforced Composite And Its Resin", PL-TR-92-1076, Phillips Laboratory, Kirtland AFB NM, April 199

6. Pallix, J. B., et al, "Characterization of Polymer Decomposition Products by Laser Desorption Mass Spectrometry", NASA Conference Publication LDEF Second Symposium, 1993

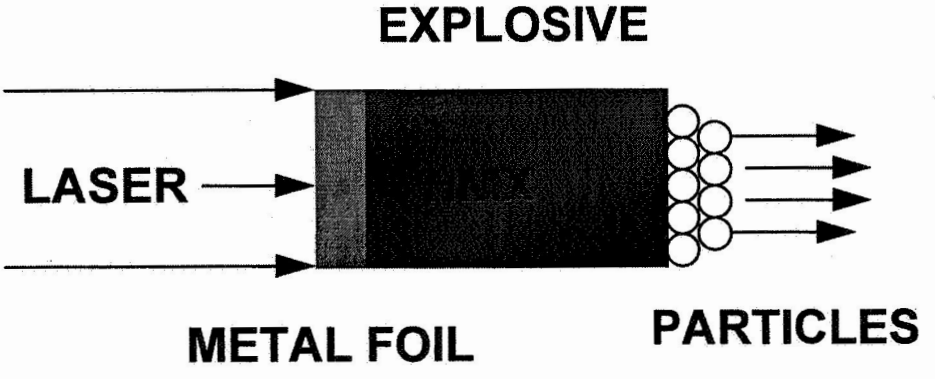


FIGURE 1. EXPLOSIVE METHOD USED TO ACCELERATE PARTICLES

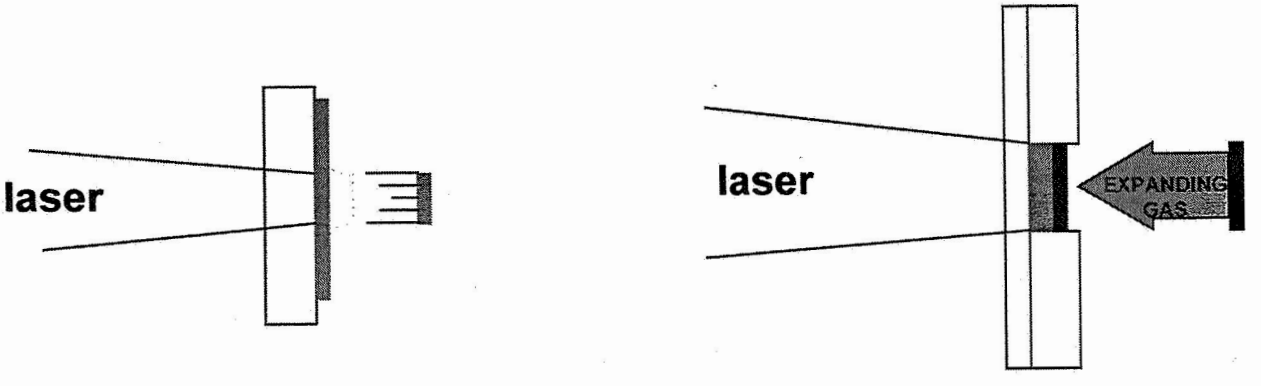


FIGURE 2. LASER DRIVEN FLYER TECHNIQUE SHOWING BOTH CONFIGURATIONS.

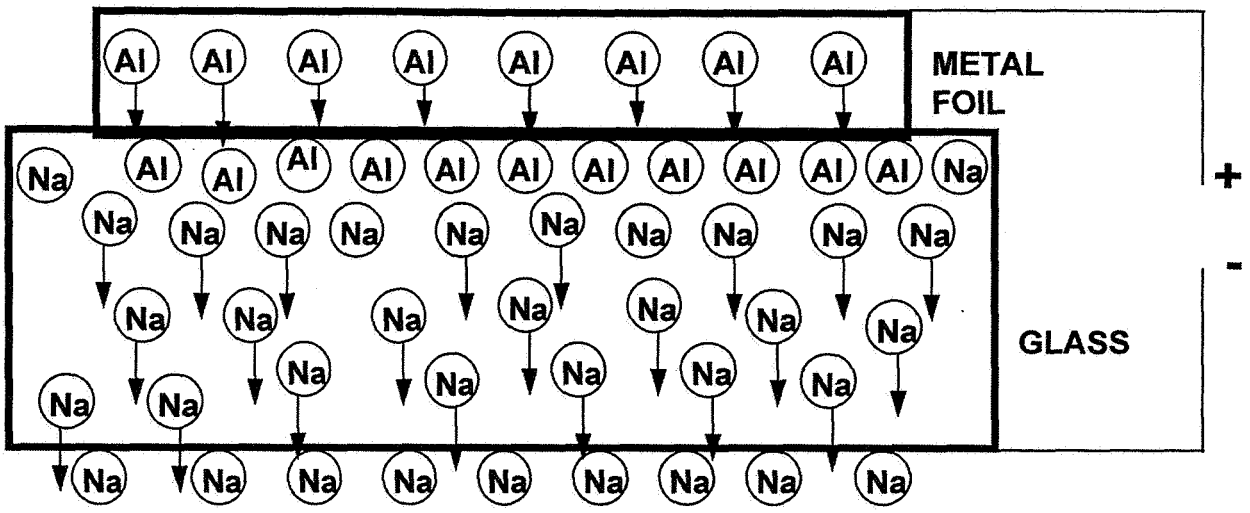


FIGURE 3. FIELD ASSISTED DIFFUSION BOND METHOD USED TO ADHERE METAL TO GLASS

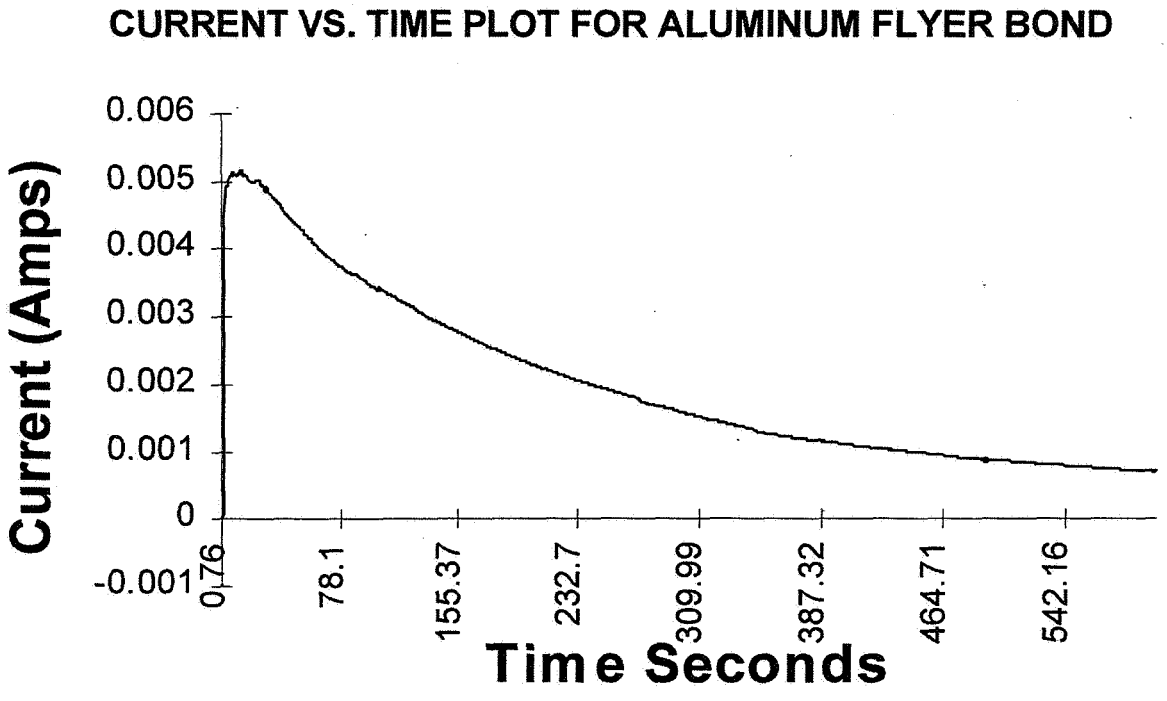


FIGURE 4. CURRENT VS TIME PLOT FOR DIFFUSION BOND METHOD

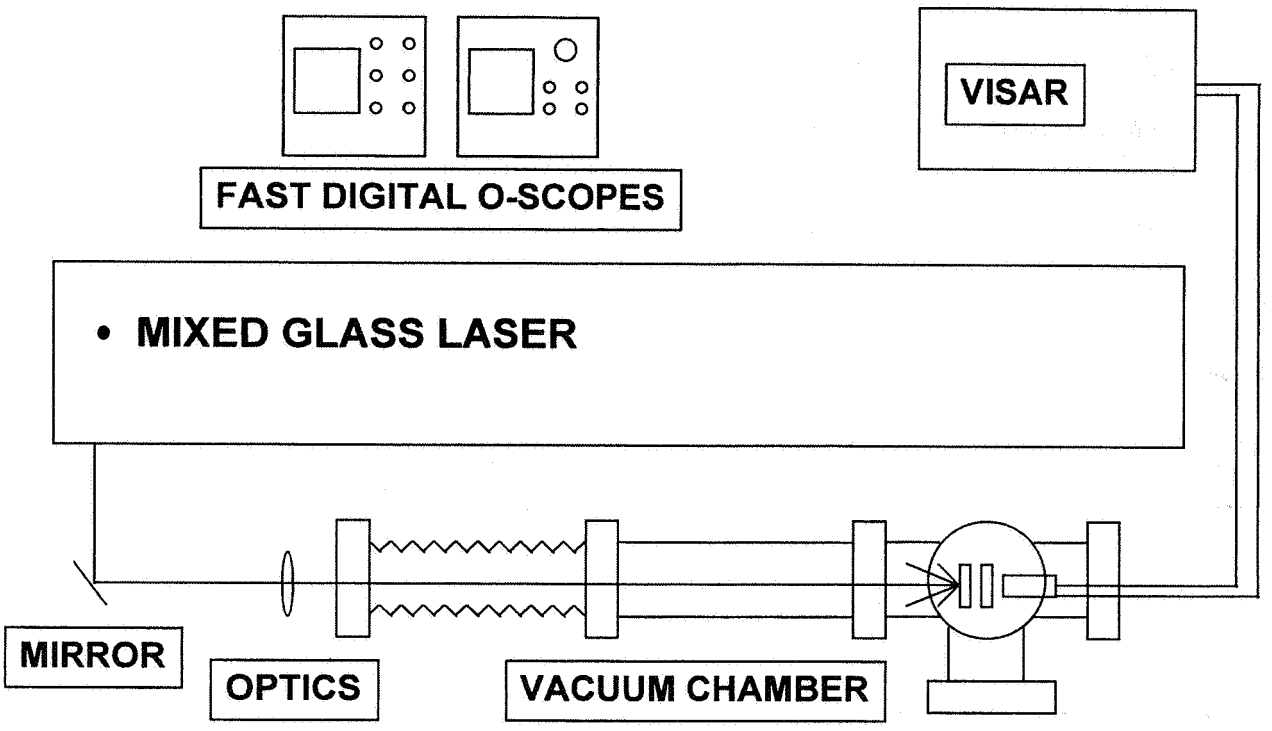


FIGURE 5. EXPERIMENTAL SET UP FOR LASER DRIVEN FLYER INCLUDING VISAR

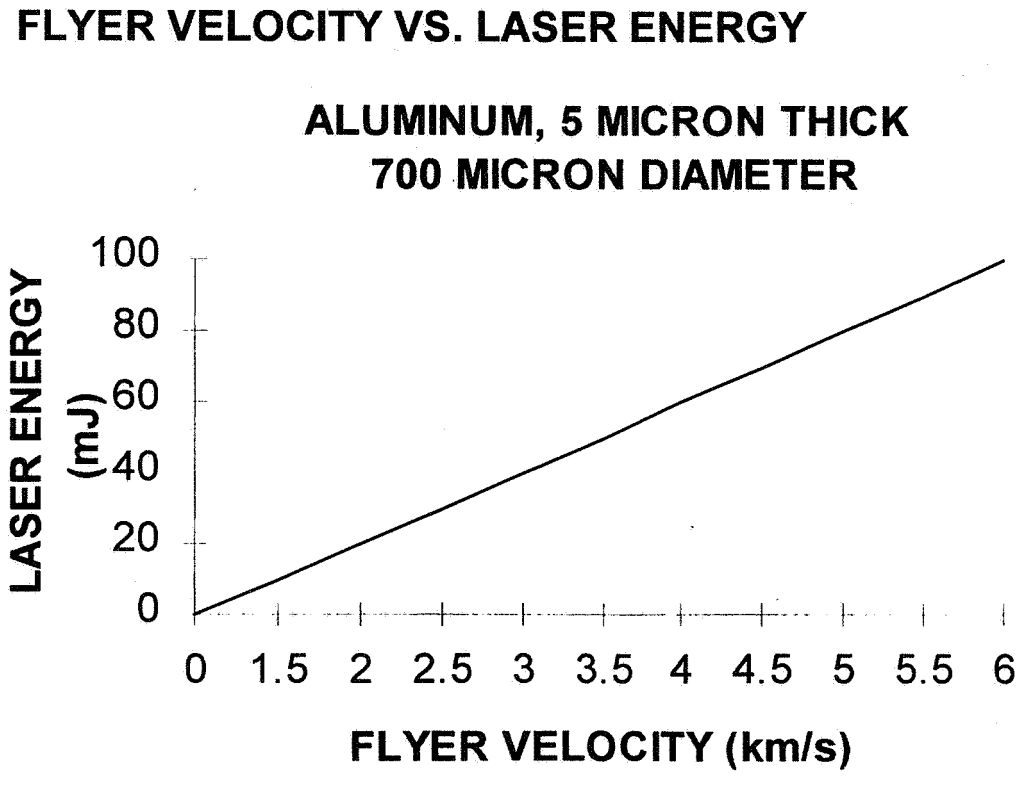


FIGURE 6. CALIBRATION CURVE GENERATED FROM VISAR MEASUREMENT

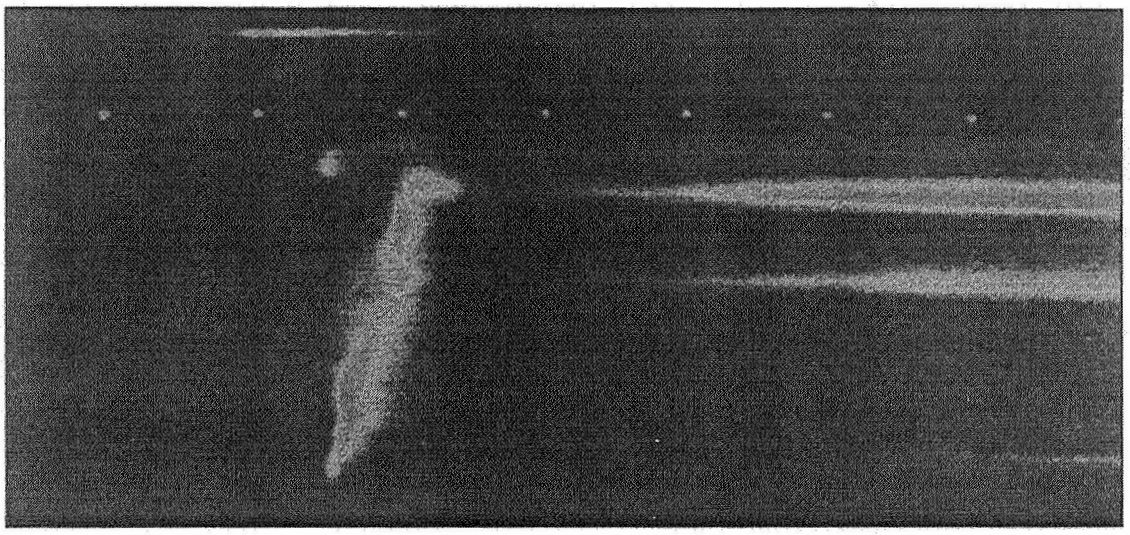


FIGURE 7. STREAK CAMERA IMAGE OF LASER DRIVEN FLYER

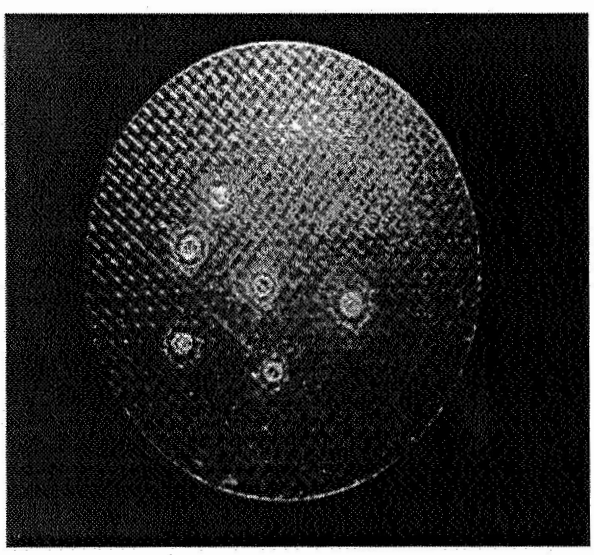
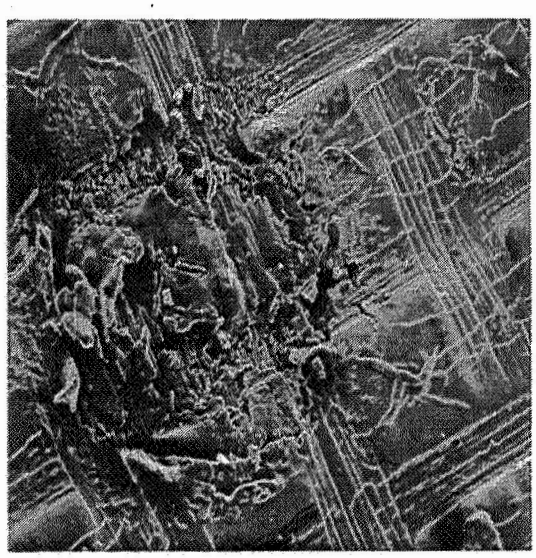


FIGURE 8. IMPACTS ON G/PS COMPOSITE



ALUMINUM FLYER, 1mm DIAMETER, 5 micron THICK, 7.5 km/s

FIGURE 9. IMPACT ON G/PS COMPOSITE

300X

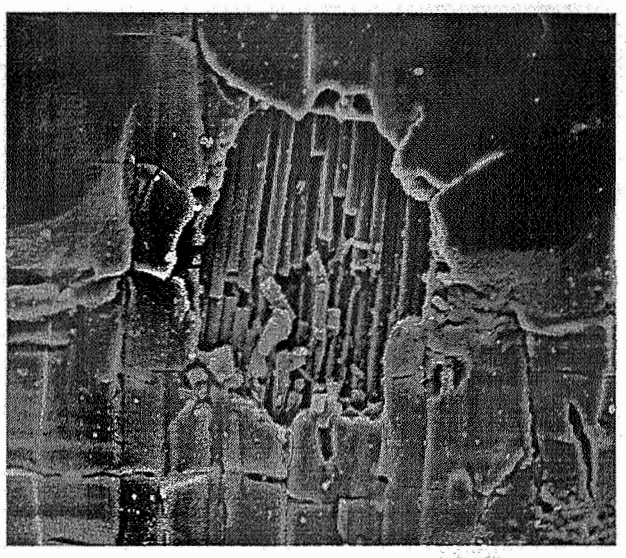


FIGURE 10. G/PS IMPACT FIBER BREAKAGE

350X

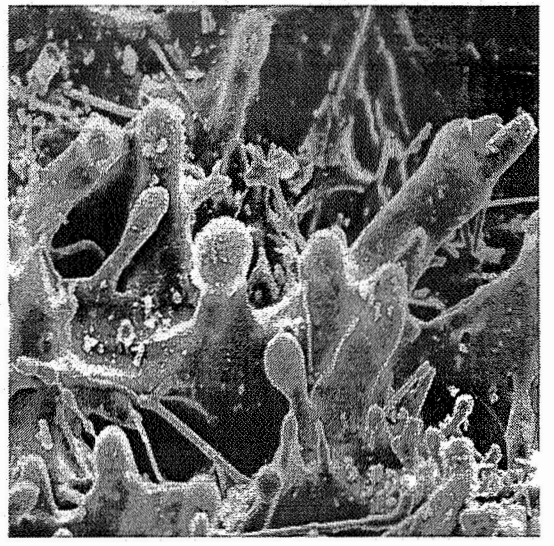
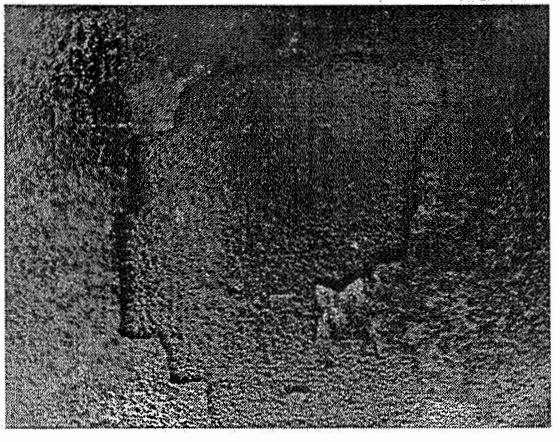


FIGURE 11. G/PS IMPACT MELT

ALUMINUM FLYER, 1mm DIAMETER, 5 micron THICK, 7.5 km/s

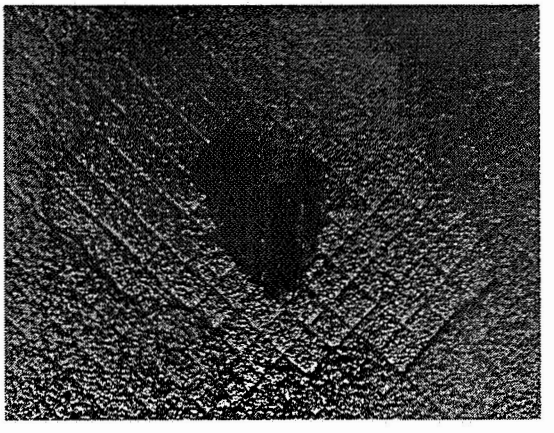
IMPACT DAMAGE, 3mm DIAMETER,

25 MICRON THICK, APPROX. 4 km/s



FRONT

FIGURE 12. FRONT SURFACE DAMAGE



BACK

FIGURE 13. BACK SURFACE DAMAGE.

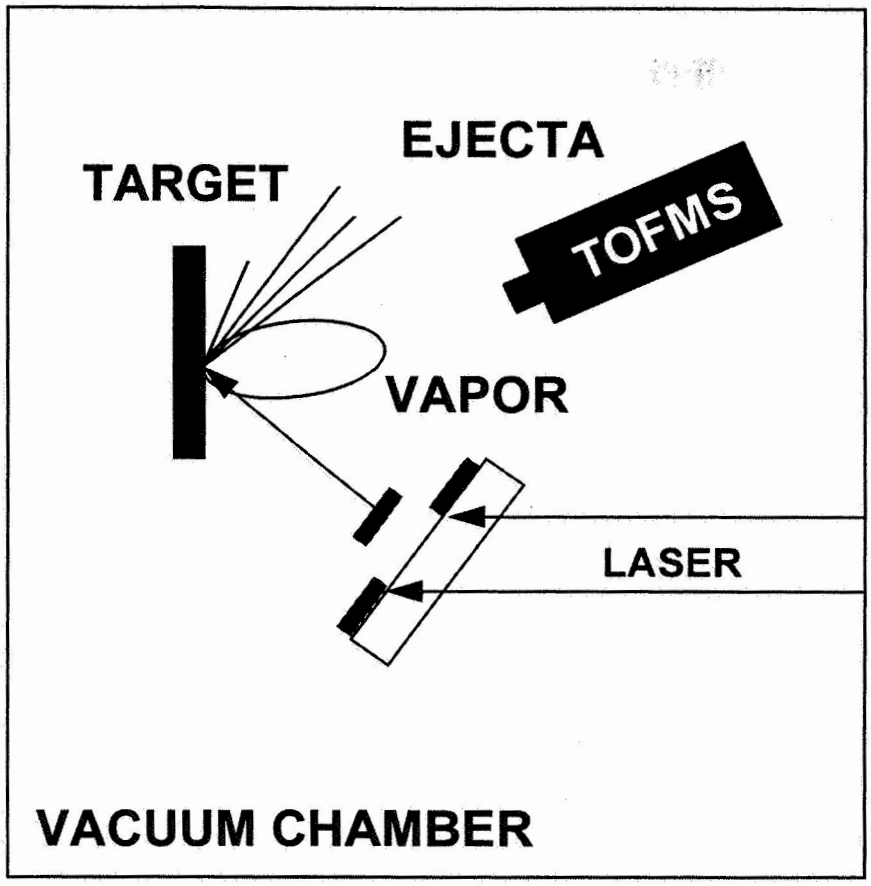


FIGURE 14. EXPERIMENTAL CONFIGURATION USED TO STUDY CHEMISTRY OF IMPACT

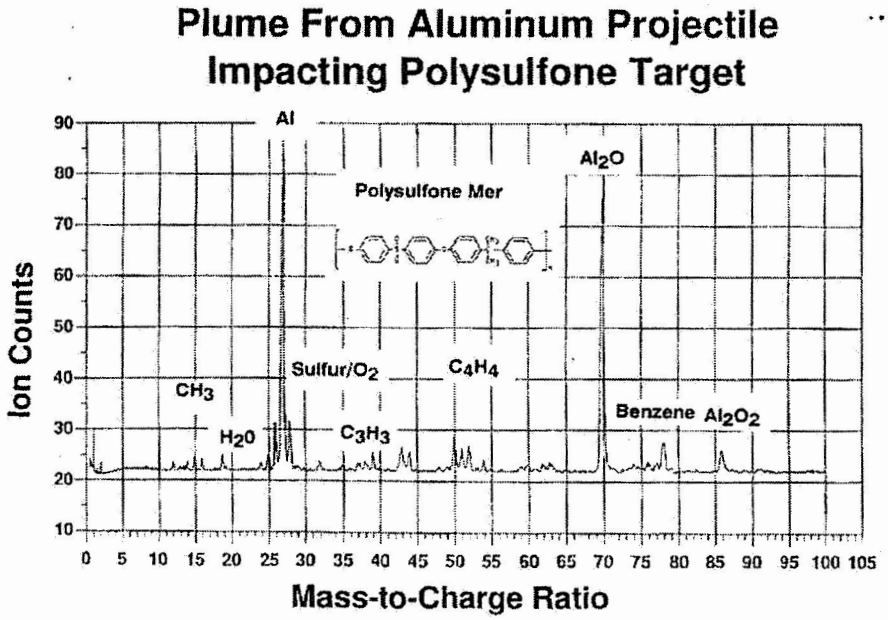


FIGURE 15. TYPICAL TOFMS SPECTRA GENERATED BY IMPACT

8P
S26-18
021468
269707

ASSESSING METEOROID AND SPACE DEBRIS RISKS

Aleck L. Lee*
Lockheed Martin Missiles & Space
Sunnyvale, CA 94088

ABSTRACT

The probability of collisions with micrometeoroid and space debris is a safety and reliability concern to spacecraft designers. Prediction of the number of hits depends on: the solar activity intensity, altitude of the spacecraft, date and time of operation, and particle size. An expert system has been developed to answer the questions concerning the fluxes of micrometeoroid and debris. The database for solar activity forecast is built into the expert system, which extends to the next two solar cycles. Since the mass flux of space debris grows with time, the space debris trend becomes a real-time dependent function. This has been taken into consideration as an integrated part of the expert system. The probability of collision with micrometeoroid is higher when the particles size is less than 1mm, while the probability of collision with space debris is higher when the particle is larger than 1mm. In the expert system, the probability of collision with either source is calculated separately and added up together. Published analytical mass flux prediction models have been used in the expert system and the data gathered with the LDEF program have been used to validate the results. The expert system is interactive, versatile, and user-friendly. It has been applied to support various spacecraft programs.

INTRODUCTION

Collision with micrometeoroid and space debris is a safety and reliability concern to spacecraft designers. The recovered components from spacecraft on orbit show pits and craters on the surfaces. This is evidenced by examining the retrieved solar array in the First Service Mission (SM-1) of the Hubble Space Telescope (HST)[1] and the Long Duration Exposure Facility (LDEF).[2]

The impact particles come from both the natural source, i.e., the micrometeoroids and the meteoroids, and the manmade origins, i.e., the space debris. Studies and retrievable experiments flown in low Earth orbits have been carried out to determine the mass fraction of each source.[3] The identification is achieved by chemical analysis of particle remnants in and around the crater. The analysis of a number of craters on various experimental surfaces allows a statistical evaluation of the relative proportion of meteoroids and orbital debris. However, the interpretation of impact craters is complicated by the large variety of particles in terms of their composition, shapes, orbits, and velocities. A significant portion of the pits remain unidentified yet.

Because of the distinct originalities, the population of meteoroid hits and debris hits behave differently. The meteoroid population is primarily a function of size and altitude. The space debris, on the other hand, depends on additional factors, such as the solar activity index, date and year, inclination angle, and the growth rate of mass in orbit. The process of predicting the total number of hits for a long-life spacecraft becomes very slow and tedious because of the large number of parameters involved.

* AIAA, Associate Fellow
IES, Senior Member

To predict the number of hits, the calculation depends on these parameters: the solar activity intensity indicated by F10.7 index, altitude of the spacecraft, date and time of operation, and so on. A versatile analytical model to answer the questions concerning the micrometeoroid and debris hits has now been developed, based on the concept of an expert system. The database for solar activity forecast is built into the model, which covers up to the next two solar cycles. Since the total mass of space debris grows with time, the space debris trend becomes a real-time dependent function. This has been taken into consideration as an integrated part of the model. The probability of collision with micrometeoroid is higher when the particles size is less than 1mm, while the probability of collision with space debris is higher when the particle is larger than 1mm. In the expert system, the probability of collision with either source is calculated separately and summed together. Published analytical mass flux predictions have been used in the model and the data gathered with the LDEF program are used to validate the results. The model is interactive, versatile, and user-friendly and can be easily applied to obtain quick results to support various LEO spacecraft programs.

METHOD OF SOLUTIONS

The questions often asked are: What is the probability of collision with a particle greater than certain size during the mission life time? How many hits of particles of all sizes can be expected with a prescribed confident level during a given period of time? What is the predicted surface degradation? What is the probability of a catastrophic collision with a critical component? These question can be answered with the knowledge of particle flux impacting on the surfaces of a spacecraft. To predict the particle flux takes tedious and yet routine calculations, based on models and data collected from experiments for micrometeoroid and space debris hits in low earth orbits. An automated process, such as an expert system, would not only expedite the solution for the particle flux, but also impart some insights to the user.

An Expert System

An expert system is a knowledge-based program that mimics experts in a specific field. There are many reasons why an expert system is desirable, such as automation of tasks, productivity multiplied by replicating the expertise of human experts, providing a corporate memory for the knowledge held, ability to interact intelligently with users, and its high efficiency and low operating costs. The problem of predicting particle fluxes impinging on spacecraft surfaces requires a large knowledge base, repeated application of neutral atmospheric models, and interpretation of the impingement effects. These characteristics indicate the advantageous application of an expert system.

The meteoroid-debris expert (MDX) system has been designed to integrate the steps in the process into a user-friendly package and to emulate the way this problem is approached by a human expert. The mass flux impacting on spacecraft surfaces comes from two sources: the meteoroid and the space debris. The flux is treated separately according to its source. The results are summed up to reach the predicted number of hits. In the MDX, both of the time-averaged surface flux, F_r, and the cross-sectional flux, F_c, are given in the output to facilitate analysis. They are related by the formula,[4] $F_c = 4 F_r$.

The MDX would require the date and year along the mission life of the spacecraft and the corresponding natural environment in terms of solar activity index. A similar expert system has been developed for computation of atomic oxygen (AO) flux, where the solar activity index is updated for each month of the mission life for the computation.[5] The MDX shares the knowledge

base with the AO expert system. The following sections discuss the assessment of each type of the mass flux.

Meteoroid Environment Assessment

The mass flux from meteoroid is a function of particle size (or particle mass) and the altitude. The basic formula to compute the integral flux in particles/m2-yr for the size d or greater at 1 AU has been described in the orbital environment guidelines.[4] However, for a spacecraft with a long mission life, the altitude is not constant. This is evidenced in HST, LDEF, and other LEO spacecraft. The MDX considers the altitude changes from beginning of life (BOL) to the end of life (EOL) at one month interval. The predicted value is integrated over the period. Computed in this manner, the MDX renders a mathematically more accurate prediction.

Space Debris Environment Assessment

The prediction of space debris flux involves several more parameters, such as the 13-month smoothed solar radio flux, F10.7 index, for the (t-1) year, inclination angle of the orbit, and the annual growth rate of mass in orbit.[4] MDX handles these parameters with a double integration. A set of particle bin sizes group the particles according to their size. Computation is carried out for the flux of particles in each size range. For each particle size bin, an integration over time from BOL to EOL is carried out, while the real-time F10.7 index and altitude are used in the process. The computation interval is one month. The exact number of days in a month is used, including the month of February in a leap year.

This process would produce a more precise result than that produced by assuming constant values for the parameters from the stand point of the flux models. The MDX is so designed that it is also amenable to the study of effects of any input parameter on the particle flux.

VALIDATION OF THE MODEL

The MDX expert system has been developed based on the published meteoroid and space debris models. The F10.7 index data were stored in a knowledge database, which is to be updated periodically with the solar activity forecast released by NASA-Marshall Space Flight Center. The expert system, like a human expert who learns continuously, needs to update and expand when new data and new application become available.

The first step in the validation is to compare MDX-predicted results to existing results. A set of existing meteoroid and orbital debris fluxes are found.[4] The data show the particle fluxes for the year of 1995 at a constant altitude of 500km with 28.5° inclination. The solar radio index is a constant 97. Figure 1 shows the data, in the format of the number of particles greater than the indicated size per square meter per year versus the particle size. The solid lines represents the meteoroid flux; the dashed line represents the orbital debris flux.

The data predicted with MDX are shown on the same figure. The solid circles represent the predicted meteoroid flux and the triangles represent the debris. The data show good agreement. There are some slight discrepancies, such as the meteoroid flux at 0.01cm and the debris flux for particle size greater 2cm. The differences are approximately 10% or less at these discrepancies.

Since the underlying models are identical, the discrepancies can only stem from the input parameters. The MDX uses the real-time orbit parameters, and the results it produced would be more truthful to the underlying model.

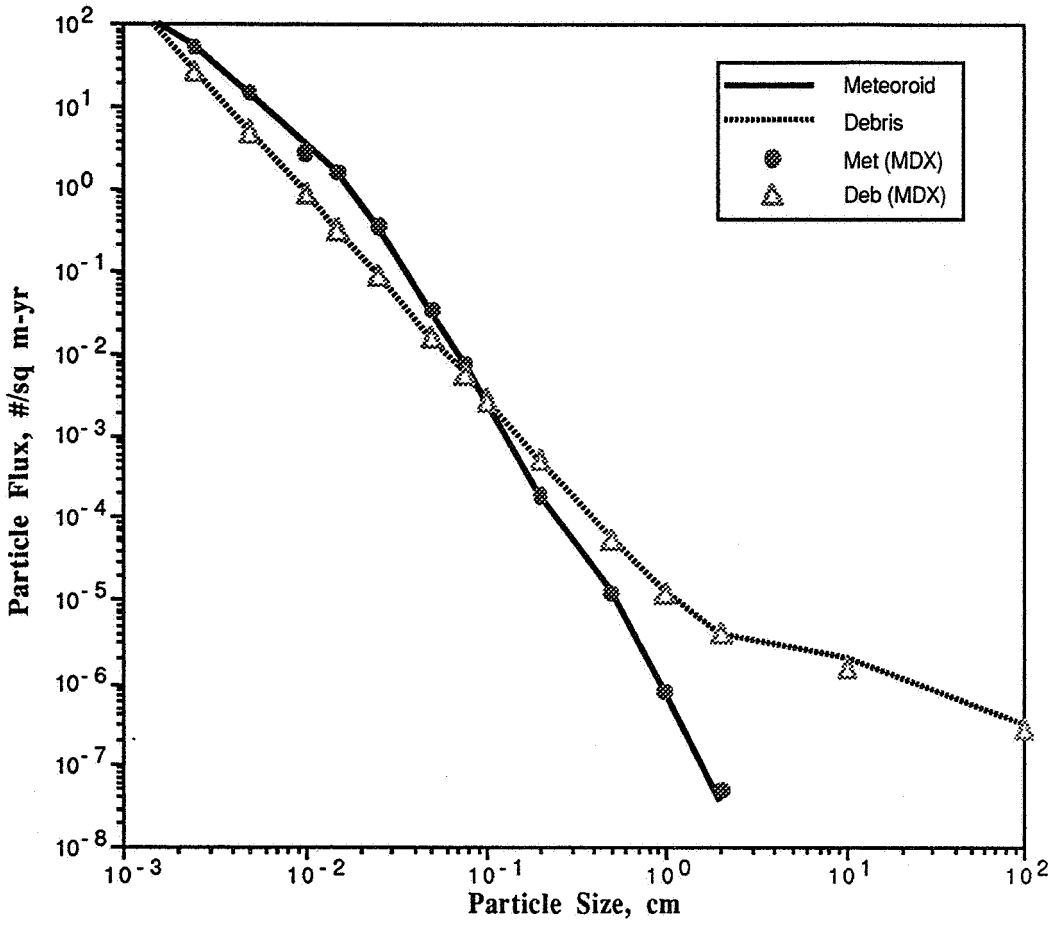


Fig. 1 Comparison of MDX predictions to the flux models in Ref. 4.

Prediction for HST

The HST was launched on the Shuttle Discovery (STS-31) on the 24th April 1990. It was released into a near-circular 28.5° inclination orbit with an initial 620km altitude. During first service mission, SM-1, the Shuttle Endeavour (STS-61) retrieved the -V2 solar array on the 5th December 1993 from a 575km orbit. The total exposure time of the solar array was about 1322 days (3.62 years). The solar radio index, F10.7, ranges from 207 to 95 during this time. The accumulated meteoroid and debris fluxes have been predicted with MDX. The results are tabulated in the last two columns of Table 1.

The number of particle impacts on HST was predicted with an ESABASE/DEBRIS tool.[6] In the calculation, the year of 1992 with a constant F10.7 index equal to 200 and a constant altitude of 600km was used. The results are listed in the middle of Table 1.

A comparison of these results shows that these two predictions agree with each other in general. The differences, which are approximately 50% of the particle flux, are probably caused by the value of the parameters.

Table 1 Comparison of the fluxes predicted by a model and by MDX

	ESABASE predicted flux		MDX predicted flux	
Size, cm	Meteoroid	Debris	Meteoroid	Debris
0.001	690.0	550.0	660.0	810.0
0.005	74.5	9.8	55.6	14.5
0.01	15.1	1.7	10.5	2.6
0.05	0.10	3.1E-2	0.12	4.6E-2
0.1	7.9E-3	5.5E-3	9.5E-3	8.1E-3
0.5	1.5E-5	9.8E-5	4.6E-5	1.6E-4

Prediction for LDEF

The LDEF was deployed by the STS-41C on April 7, 1984. It was placed in a near-circular orbit with an apogee of 480km, a perigee of 474km, and an inclination of 28.5°. By the time it was recovered by the STS-32 crew on January 12, 1990, it had fallen to an altitude of 331km.[7] The total exposure time of the LDEF is 2107 days (5.77 years).

The LDEF impact data have been extensively analyzed to determine the origin of the particle by examination of the size and the chemical composition of the craters. The crater numbers measured on LDEF's various surfaces represent a flux on a flat plate with fixed orientation. This flux is then converted to the cross-sectional area flux. Figure 2 shows the results of conversion of craters greater than 100μm, 200μm, and 500μm to orbital debris and meteoroid fluxes.[8] The meteoroid flux is shown in solid line segments and the debris flux is shown in dash line segments. An average flux has been obtained for the period over the 5.77 years, so that the fluxes shown in the figure are in number of impacts per square meter per year.

The results predicted by MDX at selected particle sizes are also shown in Fig. 2. The solid circles represent the flux that comes from the contribution of meteoroids. The triangles represent the flux of space debris. A comparison of these two results shows good agreement in general, but there are some discrepancies on the order of 20%. Uncertainties exist in the conversion from crater to particle sizes and the estimated percentage of orbital debris versus meteoroids in the LDEF data,[7] and may contribute to the discrepancies.

APPLICATION OF THE MDX EXPERT SYSTEM

Surface Degradation Effects

The surface degradation can be measured by the percent of damaged surface area. The crater size is related to the particle size as a function of velocity. When the number of hits within a size range is known, this percent area coverage (PAC) can be calculated by summing up the contribution of each size range.[9] The MDX provides this function with the assumption that the crater size is the same as the particle size. The expert system can easily accommodate other crater to particle size ratio.

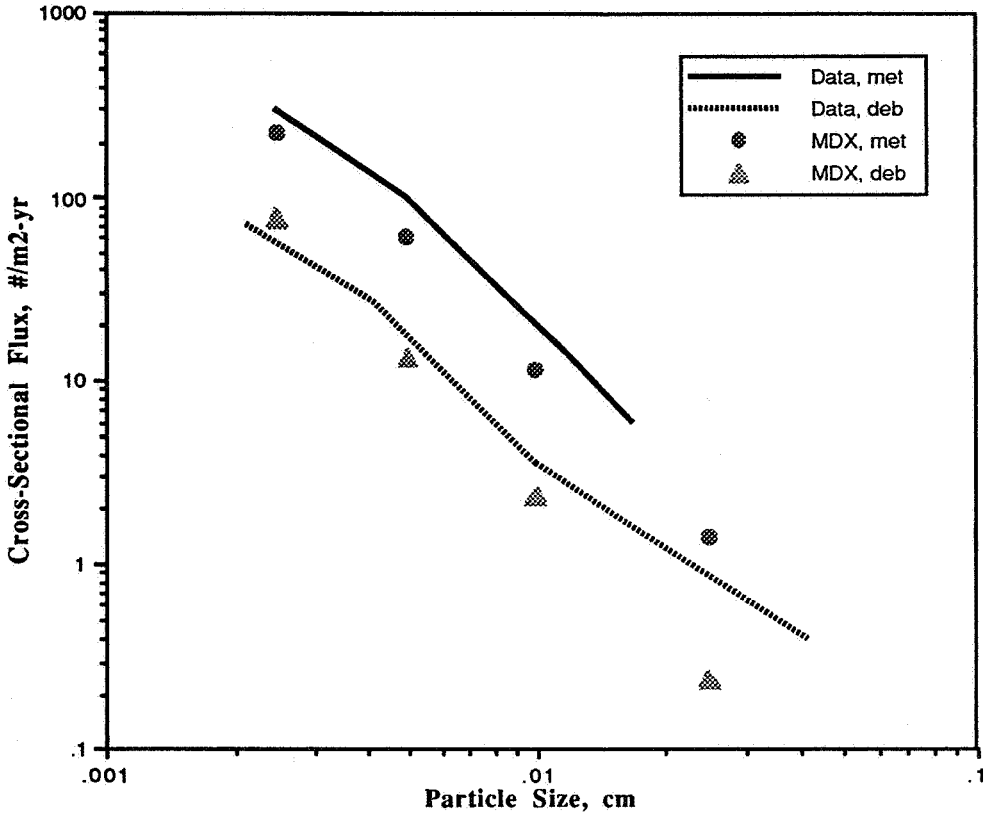


Fig. 2 Comparison of MDX predicted flux to the data correlated in Ref. 8.

Changes of Solar Absorptance

The solar absorptance, α_S, is an important property for a thermal control surface. The α_S change was determined by measurements. An empirical formula was derived for $\Delta\alpha_S$.[10] The formula requires the solar absorptance of the substrate and the particle, and the percent area coverage. The MDX is able to provide quick prediction of the total number of impacts from meteoroids and debris, from which the PAC is derived. The $\Delta\alpha_S$ of the surface can be calculated with the empirical formula while the solar absorptance of the particle and the substrate would have the same value. This is a quick way to assess a first-cut estimate of the changes of solar absorptance due to meteoroid and debris impacts.

Probability of Hits

The probability of exactly n impacts occurring on a surface by particles equal or greater than size d in the corresponding time interval is found from Poisson statistics. If P_n represents the probability of exactly n hits, and N is the total number of hits on the surface during the time interval, the probability can be expressed as the following.

$$P_n = \frac{N^n}{n!} \cdot e^{-N} \quad (1)$$

The probability P, of any number of hits, i.e. $n \geq 1$, can be calculated as $(1 - P_0)$, where P_0 is the probability of no hit. This is obtained by letting n equal to 0 in Eq. (1).

$$P = 1 - e^{-N} \quad (2)$$

Once the total number of hits, N, is known with the application of MDX, the probability of hits can be readily calculated with Eq. (2).

CONCLUSIONS

The MDX expert system based on well-accepted meteoroid and space debris models has been developed. The expert system simplifies the process of predicting the particle flux impinging on spacecraft surfaces during the mission life. The predicted flux is used to assess the effects of the impacts, such as the surface degradation, changes of solar absorptance, and the probabilities of hits and penetrations. The MDX has been validated using the flight data from LDEF and other predicted results for HST. The comparisons show good agreements.

REFERENCES

1. *Hubble Space Telescope Solar-Array Workshop*, ESA WPP-77, 1995.
2. *LDEF-69 Months in Space*, The Third Post-Retrieval Symposium, NASA CP 3275, 1993.
3. Berthoud, L., Mandeville, J., Durin, Christian, and Borg, J., "Debris and Meteoroid Proportions Deduced from Impact Crater Residue Analysis", NASA CP 3275, 1993, pp.431-444.
4. Anderson, J. and Smith, R. E., *Natural Orbital Environment Guidelines for Use in Aerospace Vehicle Development*, NASA TM 4527, June 1994.
5. Lee, A. L., "An Expert System for Atomic Oxygen Effect Analysis", SAE Technical Paper 901410, July 1990.
6. Drolshagen, G., "HST Meteoroid and Debris Impact Analysis: Overview", ESA WPP-77, May 1995, pp.295-300.
7. Humes, D. H., "Small Craters on the Meteoroid and Space Debris Impact Experiment", NASA CP 3275, November 1993, pp.287-322.
8. Zhang, J. and Kessler, D. J., "Orbital Debris and Meteoroid Population as Estimated from LDEF Impact Data", NASA CP 2175, November 1993, pp.373-384.
9. Ma, P. T., Fong, M. C., and Lee, A. L., "Surface Particle Obscuration and BRDF Predictions", SPIE Proceedings, Vol. 1165, August 1989, pp.381-391.
10. Benninghoven, K. A., "Effects of Particulate Contamination on Optical Solar Reflectors", SPIE Proceedings, Vol. 777, May 1987, pp.91-96.

S27-25
021469 10p
369430

A COMPARISON OF ATOMIC OXYGEN DEGRADATION IN LOW EARTH ORBIT AND IN A PLASMA ETCHER

*Jacqueline A. Townsend
Gloria Park
Materials Engineering Branch
NASA Goddard Space Flight Center

ABSTRACT

In low Earth orbit (LEO) significant degradation of certain materials occurs from exposure to atomic oxygen (AO). Orbital opportunities to study this degradation for specific materials are limited and expensive. While plasma etchers are commonly used in ground-based studies because of their low cost and convenience, the environment produced in an etcher chamber differs greatly from the LEO environment. Because of the differences in environment, the validity of using etcher data has remained an open question. In this paper, degradation data for 22 materials from the orbital experiment Evaluation of Oxygen Interaction with Materials (EOIM-III) are compared with data from EOIM-III control specimens exposed in a typical plasma etcher. This comparison indicates that, when carefully considered, plasma etcher results can produce order-of-magnitude estimates of orbital degradation. This allows the etcher to be used to screen unacceptable materials from further, more expensive tests.

INTRODUCTION

When the early shuttle missions returned from low Earth orbit (LEO), it was discovered that certain materials were damaged. The surface morphology and chemical composition of many exposed materials changed, and some paints and coatings eroded away completely. Researchers determined that atomic oxygen (AO), which exists in LEO, had degraded these materials. This degradation has the potential to compromise the performance and lifetime of missions with significant time in LEO. Orbital studies of AO degradation are limited by opportunity, expense, and difficulty in monitoring specimens. Over the last decade, significant progress has been made in producing an environment on the ground that simulates the LEO environment.

Early in the search for ground AO simulations, researchers turned to commercially available plasma etchers because of their low cost and convenience. However, the environment produced in a plasma etcher is very different from the environment in LEO. These differences raise the question of whether the data collected in an etcher can be used in any way to determine how a material will behave in orbit. This paper addresses that question.

The Materials Engineering Branch at Goddard Space Flight Center (GSFC) participated in Evaluation of Oxygen Interaction with Materials (EOIM-III), an orbital experiment that flew aboard the shuttle Atlantis STS-46 in July 1992. Thirty-two of the 82 specimens that flew were submitted and evaluated upon return by the Materials Engineering Branch. Participation in this experiment provided the Branch with a unique opportunity to explore the relationship between orbital and etcher results. In April 1995, the previously unexposed control specimens for these thirty-two materials were tested in an SPI PlasmaPrep X, parallel-plate plasma etcher.

The results of the orbital and etcher exposures were analyzed and compared, and the appropriate use for etcher results was defined.

BACKGROUND

AO Degradation in LEO and Plasma Etcher

A spacecraft traveling at an altitude between 200 and 600 km has a velocity of roughly 8 km/sec. At this altitude, ultraviolet radiation separates the normally diatomic oxygen molecule into two highly reactive oxygen atoms. Although the density and proportions vary, for an average LEO (~275 km) mission the atmosphere is approximately 80% AO. The high velocity of the spacecraft yields an average AO impact energy for ram-oriented surfaces of 5 eV. This energy is sufficient to break chemical bonds and oxidize materials. Many materials have volatile oxidation products which, in LEO, results in mass loss and potential contamination problems for the rest of the spacecraft. Often there are also changes to the thermal and specular properties of the material.

A linear etcher, like the PlasmaPrep X, can be described as a large, parallel plate capacitor enclosed in a vacuum chamber. Low pressure molecular oxygen is fed into the etcher chamber. As with a capacitor, opposite charges are placed on two parallel plates, setting up an electromagnetic field between them. When the molecules enter the field, they become polarized and are attracted to one of the plates. The charges on the plates are quickly reversed, so that the molecule becomes attracted to the opposite plate. The charges are reversed at 13.56 MHz. This is so fast that the resulting vibration of the oxygen separates the molecule and excites the gas into a plasma.

By nature, a plasma consists of many different species. In addition to atomic oxygen, the etcher chamber has molecular, ionic and anionic oxygen at various excited states. There is also a significant density of free electrons. As these species excite and de-excite they emit UV radiation. When the AO collides with a specimen in the etcher chamber the average impact energy is only 0.05 eV.

Table 1 summarizes the differences between the average LEO (ram-oriented) and average etcher environments. Given all these differences, it seems quite reasonable to question whether etcher degradation rates are at all useful in predicting orbital degradation.

Table 1: Comparison of Orbital and Etcher Environments (ref. 1)

Property	(units)	Etcher	LEO (~200 km)
Oxygen Atom Flux	(atoms/cm^2·sec)	10^{19} - 10^{20}	10^{15}
Oxygen Atom Energy	(eV)	0.04 - 0.06	5
Oxygen Molecule Flux	(mol/cm^2·sec)	10^{21}	10^{13}
Oxygen Molecule Energy	(eV)	0.05	10
Electron Density	(cm^{-3})	10^{10}	10^{15}
Electron Energy	(eV)	5	0.1
UV Flux	(cm^{-2}·sec^{-1})	10^{13}	4×10^{11}
UV Wavelength	(nm)	at 130	at 121.6

Reported Results

Orbital degradation is reported as the reaction efficiency (R_e). R_e is defined as:

$$R_e\ (cm^3/atom) = \frac{\Delta V}{\#\ O\ atoms} \qquad (1)$$

where ΔV is the volume-loss and # O atoms is the number of oxygen atoms that collided with the specimen.

The volume loss is usually found from measured mass-loss (Δm_s) and the known density of the material (ρ_s). Since atomic oxygen degradation is a surface interaction, the mass-loss is normalized to mass-loss-per-unit-area. Thus, equation 1 becomes

$$R_e\,(cm^3/atom) = \frac{\Delta m_s}{A_s \cdot \rho_s \cdot F} \qquad (2)$$

where A_s is the exposed area of the specimen, and the fluence (F) is the number of atoms that collided with each square centimeter of the specimen.

There are several ways to determine the number of oxygen atoms to which a specimen was exposed. One method is to measure the mass loss of a control specimen of Kapton that was exposed to the environment along with the test specimen. The R_e of Kapton has been determined in numerous orbital experiments, and it has proven consistent enough that the mass- or volume-loss-per-unit-area of Kapton can be used to estimate the fluence (F) of exposures. Rearranging terms from (1) and (2) yields:

$$F\ (atoms/cm^2) = \frac{\Delta V_{ko}}{A_k \cdot R_{ek}} \qquad (3)$$

where ΔV_{ko} is the volume-loss of Kapton in orbit, A_k is the exposed surface area of the Kapton, and R_{ek} is the reaction efficiency of Kapton (3.0×10^{-24} cm^3/atom, see ref. 5).

There are no adequate models or instruments to measure the fluence inside an etcher directly. Instead, the known R_{ek} and the control specimen volume-loss following an etcher exposure (ΔV_{ke}) are used to calculate the etcher effective fluence (F_f).

$$F_f\ (atoms/cm^2) = \frac{\Delta V_{ke}}{A_k \cdot R_{ek}} \qquad (4)$$

F_f is not the actual AO fluence in the etcher chamber. It is defined as the *orbital* fluence that would cause the volume loss the Kapton control specimen experienced in the etcher experiment.

Finally, the F_f is used to calculate the reaction efficiency of the specimen material (R_{es}).

$$R_{es}\,(cm^3/atom) = \frac{\Delta V_s}{A_s \cdot F_f} \qquad (5)$$

R_{es} is defined as the volume-loss-per-unit-area of the test specimen, ($\Delta V_s/A_s$), divided by the effective fluence (F_f from equation 4). Again, the volume-loss of the material is usually determined from the mass-loss (Δm_s) and the known density (ρ_s) of the material. Thus, equation 5 becomes

$$R_e\,(cm^3/atom) = \frac{\Delta m_s}{A_s \cdot \rho_s \cdot F_f} \qquad (6)$$

EXPERIMENTAL

Evaluation of Oxygen Interaction with Materials (EOIM-III)

Most of the specimens used in the EOIM-III orbital experiment were layered. Each material specimen was placed on an aluminum substrate disk with a layer of M-69 polyester film, double-sided with acrylic adhesive. Many of the material specimens consisted of a material (e.g., Teflon) with a

protective coating (e.g., SiO_x). During the orbital experiment, an aluminum plate with standardized openings (specimen cover) held the flight coupons to prevent degradation along the sides of the specimens (see Figure 1). Therefore, the top layer was considered to be the test material for each specimen.

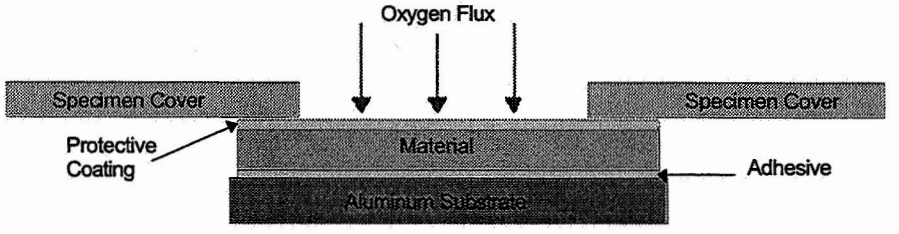


Figure 1
Illustration of EOIM-III specimen layers (ref. 2)

Six coupons were assembled for each specimen material. The flight coupons and the five control coupons were subjected to identical conditions until the flight coupons were tested in orbit. Prior to flight, all the specimens were vacuum baked and then weighed (ref. 2).

The exposed area of the flight coupons was 0.8107 cm^2, dictated by the size of the openings in the specimen cover. They were exposed for 58 hours, for a total AO fluence of 2.07×10^{20} atoms/cm^2 (ref. 2). Following orbital exposure, the flight samples were exposed to vacuum at room temperature, to remove any contaminants that may have accumulated during re-entry or transportation back to Goddard, and then weighed again. Since the density of the exposed surface was unavailable for most specimens, the reaction efficiencies were reported in g/atom (equation 7).

$$R_e(g/atom) = \frac{\Delta m_s}{A_s \cdot \text{fluence}} \qquad (7)$$

In addition to the mass measurements, many other tests were performed before and after the orbital exposure. These tests included surface analysis using an M-Probe ESCA to determine elemental composition and chemical bonding states in the first 100 Å of the surface of each specimen (ref. 2).

Plasma Etcher Tests

The Materials Engineering Branch tested one complete set of the EOIM-III control specimens in a PlasmaPrep X, parallel-plate plasma etcher. The samples were removed from the sealed packages and placed in a desiccator for one month. Then, one at a time, the specimens were tested according to the following procedure.

1. Test specimen was analyzed in the ESCA
2. Test specimen and Kapton control specimen were weighed on a Mettler digital balance.
3. Test specimen and Kapton control specimen were exposed simultaneously in the etcher for 5 hours with the following settings:
 O_2 feed gas 0.3 mbar;
 forward power 120 watts, reflected power 10 to 14 watts;
 average effective fluence (from Kapton erosion) = $2.5 \pm 0.7 \times 10^{20}$ atom/cm^2.
4. Test and Kapton control specimens were re-weighed.
5. Test specimen was analyzed in the ESCA and changes in surface composition were noted.
6. Mass loss and reaction efficiency were calculated (equation 7).

This procedure was completed for each of the 32 specimens. During etching, all specimens rested on an alumina plate to minimize charging or shielding effects from contact with the lower etcher plate. A second plate of alumina with three specimen holes was placed over the specimens to standardize the exposed area and to minimize edge erosion. The area of each of the three holes was 5.067 ± 0.008 cm^2.

RESULTS AND DISCUSSION

Data

From the original set of 32 specimens, 10 were removed from consideration for this paper. The reasons for their removal are discussed in detail later, and a table summarizing the data for all the specimens tested can be found in the Appendix. The following table (Table 2) summarizes the data from both the orbital (ref. 2) and etcher tests for the materials that were used for this paper. The estimated uncertainty (σ) in etcher reaction efficiency comes from propagated errors in weight and area measurements of both the test and control specimens. In Table 2, the specimens are listed in order of orbital reaction efficiency. Note that the order would be different if they were listed in order of etcher reaction efficiency.

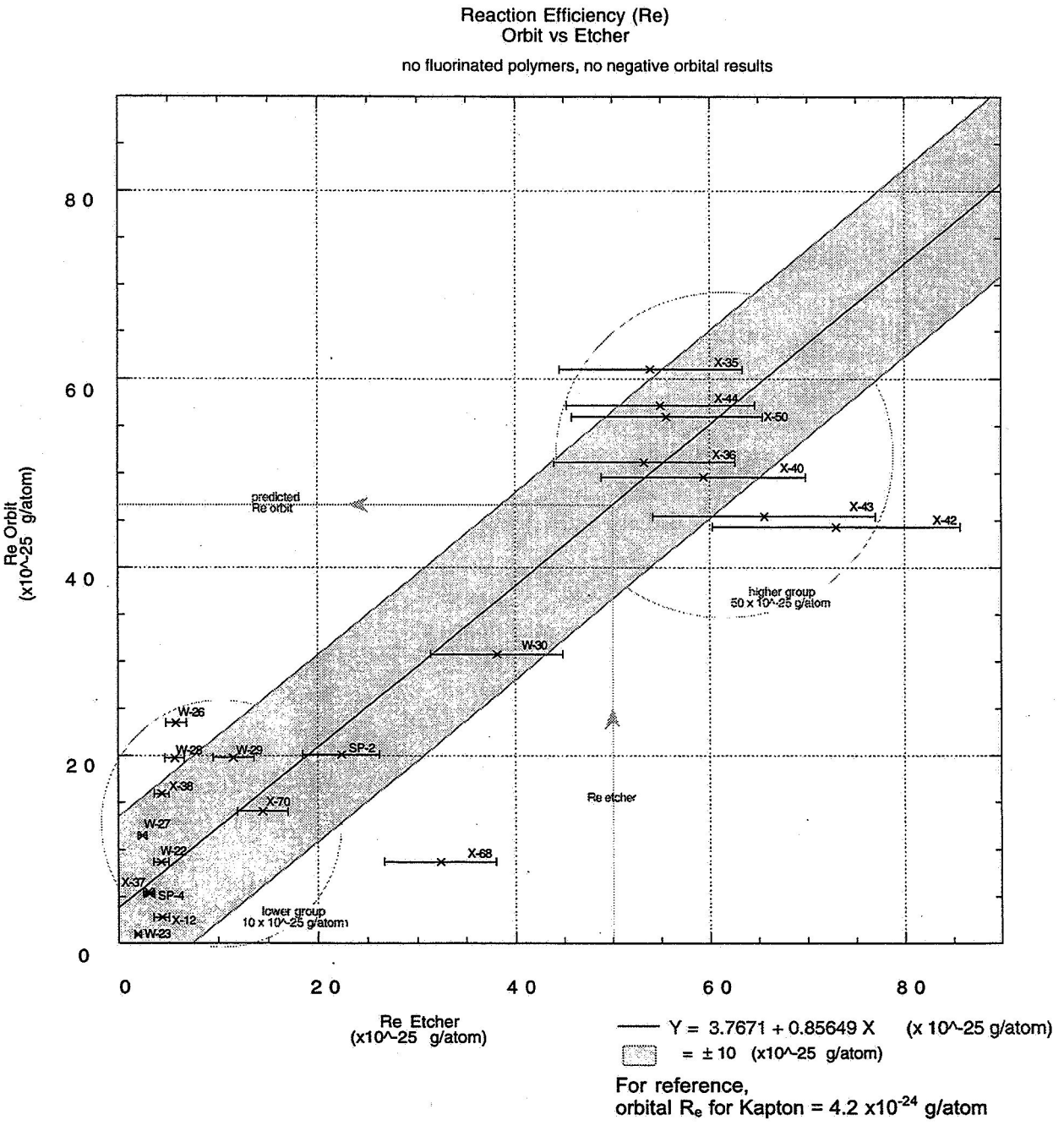
Table 2: Orbital and Etcher results

Speci-men	Material	Reaction Efficiency (g/atom)		
		Orbit	Etcher	
		Re	Re	σ
W23	CV-2500 on Silver Teflon, Ag up	1.00E-25	1.90E-25	3.3E-26
X12	CV-1144-0 on X389-7 Aluminized Beta Cloth	2.79E-25	4.29E-25	7.9E-26
SP4	G11 Epoxy Fiberglass, Selfextinguishing	5.27E-25	3.03E-25	5.3E-26
X37	SiOx on Tefzel, SiOx up	5.48E-25	2.96E-25	5.1E-26
W22	CV-1144-0 on Silver Teflon, Ag up	8.70E-25	4.24E-25	7.7E-26
X68	828/140/TiO2	8.70E-25	3.23E-24	5.6E-25
W27	CV1142	1.15E-24	2.37E-25	4.2E-26
X70	Ni coating on Llumalloy, Ni up	1.41E-24	1.44E-24	2.5E-25
X38	CV-2500 on Kapton	1.60E-24	4.33E-25	7.6E-26
W28	CV-1500 Black Silicone	1.98E-24	5.65E-25	9.9E-26
W29	CV-2566 Silicone	1.98E-24	1.15E-24	2.0E-25
SP2	CV-2500 on Delrin II 900 NC10	2.01E-24	2.23E-24	3.9E-25
W26	CV-1144-0 on Kapton	2.35E-24	5.79E-25	1.0E-25
W30	Kapton 200XC, 2 mil	3.08E-24	3.81E-24	6.7E-25
X42	TPX	4.43E-24	7.30E-24	1.3E-24
X43	Cryovac Film	4.54E-24	6.56E-24	1.1E-24
X40	Victrex PES 4800 G	4.96E-24	5.94E-24	1.0E-24
X36	PEEK 450G	5.12E-24	5.33E-24	9.3E-25
X50	3M Tape #5	5.60E-24	5.56E-24	9.8E-25
X44	Llumalloy	5.72E-24	5.50E-24	9.7E-25
X35	ULTEM 1000	6.10E-24	5.40E-24	9.4E-25
SP3	Delrin II 900 NC10	1.58E-23	1.64E-23	2.8E-24

Numerical Analysis

The orbital and etcher results were compared using Figure 2. The x-axis is etcher R_e in the units 10^{-25} g/atom, and the y-axis is orbital R_e in the same units. Each data point represents one specimen, where the x-coordinate is the etcher reaction efficiency and the y-coordinate is the orbital reaction efficiency. The horizontal error bars correspond to the etcher estimated uncertainty values (σ) in Table 2. The uncertainties of the orbital reaction efficiency measurements were not reported.

Figure 2



A linear regression was performed on the data, and the resulting equation is recorded at the bottom of the graph. The uncertainty of the linear regression (i.e., average uncertainty in the predicted orbital reaction efficiency) is represented on Figure 2 by the gray area surrounding the regression line. It is the average of the difference between the predicted R_{eo} and experimental R_{eo} from all the specimens.

The equation resulting from the linear regression in Figure 2, with estimated uncertainty is

$$Y = 3.7671 + 0.856\,X, \quad \pm 10 \quad (\times 10^{-25}\ g/atom) \tag{8}$$

where Y is the predicted orbital reaction efficiency based on etcher reaction efficiency, and X is the reaction efficiency of the material in the etcher.

Ideally, equation 8 could be used to predict orbital degradation. A material would be tested in the etcher, and the resulting etcher reaction efficiency would be entered as X in equation 8. The calculation would then give a predicted orbital reaction efficiency. Unfortunately, the uncertainty is too large for this to be meaningful.

A simple and useful interpretation of the graph is that it shows data in two sets: one in the range of 50×10^{-25} g/atom in orbit, and one at roughly 10×10^{-25} g/atom in orbit. Although the line from the fit of the data does pass through these two groups, within each of these groups the trend of the data does not follow the linear regression. Therefore, equation 8 cannot be used to predict in orbit where a specimen will fall with respect to the other materials within its group.

The magnitude of the uncertainty illustrates this weakness in the linear regression. An etcher reaction efficiency can indicate in which of the two groups a specimen falls, but it can not indicate whether that material will perform better or worse than other materials within its group in orbit. For instance, in the higher group, an etcher efficiency of 50×10^{-25} g/atom yields a predicted orbital efficiency of $47 \pm 10 \times 10^{-25}$ g/atom. Given this uncertainty, it is not really reasonable to assume that a specimen with an etcher efficiency of 50×10^{-25} g/atom would indicate an orbital efficiency greater than another specimen with an etcher efficiency of 45×10^{-25} g/atom. Instead, it can only be concluded that the material is much more reactive in orbit than a material with an etcher efficiency of roughly 10×10^{-25} g/atom.

These conclusions are useful because knowing to which "grouping" a material belongs can, in some cases, limit the number of materials that need to be tested in a better, more expensive simulation. In other cases this rough estimate can eliminate completely the need for a better simulation. This allows the etcher to be used as a screening device.

An examination of the chemical composition of the two groups yields some useful information (see Table 3). Of the twelve specimens in the lower group ($R_{eo} \sim 10 \times 10^{-25}$ g/atom) nine are silicones, one is SiO_x (X-37), one is nickel sputtered (X-70), and one is an epoxy (SP-4). There is no obvious relationship between the ranking of the materials within this group and type of material. While the lower group consists mostly of silicon-containing materials, there are no silicon-containing materials in the higher group ($R_{eo} \sim 50 \times 10^{-25}$ g/atom). Instead, the higher group contains a variety of organic polymers without silicon. Of the seven specimens in the higher group, five contain oxygen in the normal (i.e., pre-exposure) polymer chain, and the remaining two (X-42, X-43) do not. It should be noted that three specimens do not fall into either of the groups. The reaction efficiencies of SP-3 (Delrin) in LEO and in the etcher were much higher than the other specimens, so it is not displayed on the graph. The other two outlier specimens are W-30 (Kapton 200XC) and X-68 (TiO_2).

Table 3: Summary of Material Classes vs. R_e Groups

Low R_e Group	High R_e Group	Outliers
9 silicones	No silicon-containing specimens	1 Delrin (high R_e)
1 SiO_x	5 organic polymers w/ oxygen	1 Kapton 200XC
1 epoxy	2 organic polymers no oxygen	1 TiO_2
1 Ni sputter		

Exclusion of Specimens

The fact that 10 out of 32 specimens had to be excluded from the study illustrates the difficulty in using the etcher even as a screening device. The reasons for removing the specimens fall into two groups: specimen configuration problems and type of material problems.

The samples X-67, X-68, X-69, SP-1, and SP-5 were eliminated due to configuration problems that made it impossible to compare etcher and orbital results. The most common problems were from protective coatings that did not cover the substrate completely. In the etcher, when the alumina specimen cover was placed over them some of the substrate was still exposed at the edge. The specimen cover in orbit had smaller openings so that no substrate was exposed. This meant that in the etcher the substrate could lose mass, but in orbit only the coating could lose mass. Thus, a comparison between etcher and orbital results could not be made.

A second set of specimens (W-24, W-25, X-11, X-31, and X-32) was excluded because their exposed surfaces contained fluorine. Historically, fluorinated materials have had inconsistent reaction efficiencies both in orbit and in simulations. For orbital results these inconsistencies are slowly being traced to synergistic effects from other orbital conditions (e.g., ultraviolet radiation). These orbital conditions are impossible to mimic with a plasma etcher, but there is more to the problem.

In many tests, etcher reaction efficiencies for fluorinated polymers have been three or four times higher than those attained in orbital tests. A recent study suggests the higher pressure and closed system of the etcher chamber as the cause (see ref. 4). When a fluorinated polymer reacts with AO, fluorine is often released by the oxidation process. In the etcher, this fluorine is excited into a plasma by the same conditions that create the oxygen plasma, and the resulting atomic fluorine degrades materials even more readily than the atomic oxygen does. In orbit, the low pressure and high impact energy carry the fluorine away before it can react significantly with the rest of the material. The conditions in the etcher allow the fluorine to remain in close contact with the material, causing degradation that would not occur in orbit. This means that in the etcher fluorinated compounds degrade much more rapidly than in orbit, and through a process different from what occurs in orbit (ref. 4). For this reason the fluorinated polymers were removed from the study.

ESCA analysis of the specimens after etcher exposure confirms this theory. On the surface of several of the fluorinated polymers some of the carbon-fluorine (- CF_2 -) bonds were converted to carbon-hydrogen (- CFH -), suggesting the release of some fluorine. In addition, following the etching of a fluorinated material, fluorine was found on several subsequent specimens with fluorine concentration decreasing from one run to the next. It seems likely that the atomic fluorine reacts with the etcher chamber and remains in the etcher after the fluorinated specimen is removed. Therefore, the fluorine can be transferred to the next several test specimens.

CONCLUSIONS AND SUMMARY

For many materials, atomic oxygen degradation in low Earth orbit causes mass loss, changes in material properties, and contamination problems. Such degradation can compromise the performance and lifetime of missions with any significant duration in LEO. Plasma etchers are commonly used to

study this degradation, and the results of this paper indicate that when the results are carefully considered there is still value in such experiments.

Etcher results can be used to predict orbital reaction efficiencies with an average uncertainty of 10×10^{-25} g/atom. For some applications, this order-of-magnitude estimate is adequate. When greater precision is necessary, etchers can be used to limit the number of specimens that must be sent for better analysis (e.g., materials with predicted orbital reaction efficiencies greater than 40×10^{-25} g/atom could be excluded). Since etcher tests are significantly less expensive than better simulations, the etcher can be a valuable screening tool for predicting the performance of materials in LEO.

This study also shows that not every material is appropriate for etcher testing. Fluorinated compounds should not be tested in an etcher because evidence indicates degradation of these materials occurs through a process that is significantly different from what occurs in orbit. In addition, fluorine released during the oxidation process can contaminate the chamber and be transferred to the surface of future specimens. These problems with oxidation products may not be unique to fluorinated compounds; therefore, the likely oxidation products of every specimen should be considered before it is tested in an etcher.

REFERENCES

1. Koontz, S.L., K. Albyn, L. Leger, "Materials Selection for Long Life in Low Earth Orbit, A Critical Evaluation of Atomic Oxygen Testing with Thermal Atom System," *Journal of the IES*, March/April 1990.

2. Scialdone, J., C. Clatterbuck, M. Ayres-Treusdell, G. Park, D. Kolos, "Evaluation of Certain Material Films Flown on the Space Shuttle Mission 46, EOIM III Experiment," *NASA Technical Memorandum 104621*, NASA Goddard, September 1995.

3. Taylor, John R., An Introduction to Error Analysis: The Study of Uncertainties in Physical Measurements, University Science Books, Oxford University Press, 1982.

4. Hung, Ching-cheh, G. Cantrell, "Reaction and Protection of Electrical Wire Insulators in Atomic-Oxygen Environments," NASA TM-106767, November 1994.

5. Banks, Bruce A., S. Rutledge, J. Brady, J. Merrow, "Atomic Oxygen Effects on Materials," *NASA Conference Publication 3035*, June 1988.

6. Dever, Joyce, K. de Groh, C. Stidham, T. Stueber, T. Dever, E. Rodriguez, J. Terlep, "Simulation of the Synergistic Low Earth Orbit Effects of Vacuum Thermal Cycling, Vacuum UV Radiation and Atomic Oxygen," *NASA Conference Publication 3831*, November 1993.

7. Pippin, H. Gary, "Analysis of Silverized Teflon Thermal Control Material Flown on the Long Duration Exposure Facility," *NASA Contractor Report 4663*, July 1995.

APPENDIX

The following table summarizes the data from both the orbital and etcher tests.

Specimen	Material	Reaction Efficiency (g/atom) Orbit Re	Etcher Re	σ	
SP5	**G-11, Non-selfextinguishing**	**-3.62E-24**	**3.32E-24**	**5.8E-25**	
X69	**X389-7 Aluminized Beta Cloth, Al up**	**-6.33E-26**	**3.61E-25**	**6.3E-26**	
W23	CV-2500 on Silver Teflon, Ag up	1.00E-25	1.90E-25	3.3E-26	
X11	**X-389-7 Aluminized Beta Cloth, Beta up**	**1.37E-25**	**3.06E-24**	**5.5E-25**	*
W24	**Silver Teflon, Teflon up**	**2.42E-25**	**8.53E-24**	**1.5E-24**	*
X67	**Uralane 5753LV A/B**	**2.53E-25**	**4.94E-24**	**8.6E-25**	
X12	CV-1144-0 on X389-7 Aluminized Beta Cloth	2.79E-25	4.29E-25	7.9E-26	
SP4	G11 Epoxy Fiberglass, Selfextinguishing	5.27E-25	3.03E-25	5.3E-26	
X37	SiOx on Tefzel, SiOx up	5.48E-25	2.96E-25	5.1E-26	
X66	**Uralane 5750LV A/B**	**7.80E-25**	**4.80E-24**	**8.5E-25**	
W22	CV-1144-0 on Silver Teflon, Ag up	8.70E-25	4.24E-25	7.7E-26	
X68	828/140/TiO2	8.70E-25	3.23E-24	5.6E-25	
W27	CV1142	1.15E-24	2.37E-25	4.2E-26	
X70	Ni coating on Llumalloy, Ni up	1.41E-24	1.44E-24	2.5E-25	
X38	Kapton w/ CV-2500	1.60E-24	4.33E-25	7.6E-26	
X32	**Tefzel 500LZ**	**1.74E-24**	**6.24E-24**	**1.1E-24**	*
W28	CV-1500 Black Silicone	1.98E-24	5.65E-25	9.9E-26	
W29	CV-2566 Silicone	1.98E-24	1.15E-24	2.0E-25	
SP2	CV-2500 on Delrin II 900 NC10	2.01E-24	2.23E-24	3.9E-25	
W26	CV-1144-0 on Kapton	2.35E-24	5.79E-25	1.0E-25	
X31	**Aclar 22C, 5 mil**	**2.84E-24**	**1.03E-23**	**1.8E-24**	*
W30	Kapton 200XC, 2 mil	3.08E-24	3.81E-24	6.7E-25	
SP1	**CV-1144-0 on Delrin II900 NC10**	**3.85E-24**	**6.58E-24**	**1.2E-24**	
X42	TPX	4.43E-24	7.30E-24	1.3E-24	
X43	Cryovac Film	4.54E-24	6.56E-24	1.1E-24	
X40	Victrex PES 4800 G	4.96E-24	5.94E-24	1.0E-24	
X36	PEEK 450G	5.12E-24	5.33E-24	9.3E-25	
X50	3M Tape #5	5.60E-24	5.56E-24	9.8E-25	
X44	Llumalloy	5.72E-24	5.50E-24	9.7E-25	
X35	ULTEM 1000	6.10E-24	5.40E-24	9.4E-25	
W25	**Silver Teflon w/hole**	**1.05E-23**	**3.16E-25**	**5.6E-26**	*
SP3	Delrin II 900 NC10	1.58E-23	1.64E-23	2.8E-24	

The specimens in bold were removed from consideration for the paper.
* fluorinated compound

S28-27
021470
10P

COMBINED EFFECTS OF FLUXES OF ATOMIC OXYGEN AND ELECTRONS ON CHEMICAL REACTIONS WITH POLYMERIC MATERIALS.

069432

Jon Shively
CIAM Department, California State University at Northridge

Thomas King, Charles Miglionico, Robert Robertson, Steven Davis, Charles Stein, and Warren Wilson
Space Environment Interactions Branch, Air Force Phillips Laboratory

James Baird
Chemistry Department, University of Alabama at Huntsville

ABSTRACT

Understanding the phenomenology of the interaction of the space environment with organic-composite spacecraft surfaces is both interesting science and important to the longevity of our space assets. The importance of this understanding has been made even more critical by the desire to use new organic composite materials whose lower weight and higher stiffness will make it possible to orbit larger payloads. Inconsistencies between ground simulation and space test data clearly indicate that our understanding of the interaction phenomenology is inadequate. This paper describes the test equipment, designed by Phillips Laboratory, to subject materials to a simulated low-earth-orbit (LEO) environment, consisting of simultaneous fluxes of hyperthermal neutral oxygen atoms (AO), energetic electrons, vacuum-ultraviolet light, and hypervelocity-particle impacts characteristic of space debris and micrometeoroids. Preliminary results of studies of the combined effects of fluxes of AO and electrons on polysulfone resins and composites are presented. The chemical species generated by chemical reactions were monitored using a mass spectrometer, and the results indicate that the primary effect of electrons on AO reactions is through electric fields induced by charging the material surface.

INTRODUCTION

The space environment is complex (1,2), and its replication in ground test facilities presents considerable difficulties. Spacecraft surfaces LEO are exposed to simultaneous bombardment by atomic oxygen (AO), energetic charged particles (primarily electrons), and solar radiation, and are subjected to hypervelocity impacts of micrometeoroids and debris. The AO has a translational energy determined by the spacecraft orbital velocity, about 8 km/s, and a thermal- energy distribution corresponding to a temperature of about 1000 K. The energetic charged-particle environment (primarily electrons and protons) is both complex and variable (affected by solar storms, for example), and particle energies extend from below 1 keV up to 10^{19} eV or more (although most of the electrons have energies below 100 keV, and most of the protons lie below 10 MeV).

It is clearly difficult to reproduce the space environment in a ground simulation facility, and most ground-based testing has been conducted with greatly-simplified environments. In the case of nonmetallic materials, one often finds that the results of space testing do not agree with results obtained in ground-based tests (3-9); the fact that the ground tests do not impose the same environment as space makes it difficult to isolate the reasons for the discrepancies. A major difference between space and ground testing is that the components of the space environment are often applied sequentially in the latter, whereas they are simultaneously present in the former. A material will be exposed to UV, then to electrons, and finally to AO in a ground test, for example, whereas all three components are simultaneously present in a space test. A facility is under development at the Air Force Phillips Laboratory, that will be capable of simultaneous exposure to all components of the space environment. The facility and its associated target diagnostics, are briefly described in the next section.

TEST FACILITY

The test facility under development at the Phillips Laboratory has a bakeable vacuum chamber with metallic seals; an oil-free pumping system provides a vacuum of 10^{-8} torr or better. Monoenergetic electrons, having an energy that can be set to any value in the range from about 1 kV to 20 kV, are provided by an electron gun; UV and visible light is provided by a high-pressure Xe arc lamp, and VUV radiation is provided by a deuterium lamp, with a MgF_2 window. Narrowband UV and VUV radiation can be provided by a monochromator. The AO source (10) has very small O^+ ion and O_2 contamination, and can provide 10^{13} to 10^{14} O atoms/cm^2/sec into a 2cm-diameter spot about 15 cm distant from the source. A laser-driven microflyer launcher can be mounted to the vacuum chamber, to provide small (3 mm or less in diameter) hypervelocity (up to about 10 km/s) impacts on targets in the chamber.

A time-of-flight mass spectrometer is provided, to measure species emitted from the target surface, and laser-stimulated desorption can be used to study species bound on the target surface. Future plans include use of laser-induced fluorescence, Raman spectroscopy, spectroscopic ellipsometry, and PIXE to study changes in the target surface. Post-exposure scanning-electron microscopy (with EDX) and optical microscopy can also be performed; a target-transfer capability will in future allow us to perform post-exposure analyses without breaking vacuum.

PRELIMINARY RESULTS: AO + ELECTRONS ON POLYSULFONE

In the work to be discussed below, we seek to improve understanding of the response of polymeric materials used in spacecraft, to simultaneous exposure to AO, UV and electrons. Preliminary measurements that we have made, using the JPL crossed-beam AO facility (11), suggest that charging of the spacecraft surface can alter the total reaction rate of AO with the polymer. The test facility is sketched in figure 1. The AO source is PSI-type (12) laser-plasma source, driven by a pulsed laser delivering 1.7 pulses per second. Ion s comprised less that 0.1% of the beam, however there was a significant amount of O_2 in the beam.

In our experiments, polysulfone resin and polysulfone/graphite composite targets were bombarded with AO, either alone or with simultaneous exposure to UV and/or 10-20 keV electrons. The AO beam was pulsed, and had a mean energy of 5 eV and an energy spread of ±2eV. The incident beam energy spectrum is shown in figure 2. The velocity spectrum of AO elastically scattered from the target surface, through an angle of 95 degrees, is shown in figure 3. In this and subsequent plots, the number of counts are normalized to 200 source pulses on target. The elastic scattering spectrum has a complex structure, indicating that a number of different scattering centers and scattering mechanisms may be important.

The mass and velocity distributions of reaction products evolved from the surface were measured using a quadrupole mass spectrometer (QMS), operated in time-of-flight mode to obtain velocity information. When the target was bombarded by electrons alone, with no AO beam present, no counts above background were observed when the QMS was set to observe CO, CO_2, SO, or SO_2, which were the primary reaction products studied. We conclude that radiochemical processes were not important mechanisms for producing the observed species. OH and H_2O were not studied because of the background from adsorbed water.

When the target was bombarded with AO plus UV from the plasma in the AO source, no change in count rates was observed when the UV from the AO source was chopped out, so that AO reached the target without the simultaneous presence of UV. Thus, photochemical processes do not influence the production of the observed species, by AO.

In our first experiments a graphite/polysulfone target was used, electrically isolated from the vacuum chamber. We observed that the count rate in the QMS, at an angle of 95 degrees with respect to the incident beam, for a given reaction product from AO bombardment, increased when the target was simultaneously bombarded with electrons, when the current on target exceeded a threshold value. Time-of-flight spectra obtained for CO_2 generated by simultaneous bombardment of the target with AO and electrons are shown in figure 4. We found that the current on target had to be at least 3 μA before there was an observable increase in count rate. The presence or absence of UV made no observable difference. The shape of the velocity spectrum changed slightly when AO and electrons were simultaneously present.

For the second series of experiments, a target consisting of a 5 μm-thick polysulfone resin layer spin-cast onto a semiconducting silicon substrate was prepared. This was done to eliminate possible effects from the carbon fibers in the composite material. The resin thickness was insufficient to stop 10 keV electrons, so the electrons came to rest in the Si substrate. Most of the mass spectra that were taken were for CO_2, because of the greater reaction cross-section for producing it, leading to better counting statistics. With the substrate grounded, simultaneous electron and AO bombardment produced no increase in the count rate of the QMS; when the substrate was electrically isolated from the vacuum chamber ground, the increased count rates seen in the first series of experiments were again observed. In both cases, the presence or absence of UV had no observable effect on the count rates. This suggested that target charging effects, rather than the usual radiation-chemical or photochemical effects, were responsible for the observed changes in count rates. We therefore used a power supply to vary the potential of the target with respect to the chamber ground, and observed a dependence of the QMS count rate on applied voltage. Data obtained for positive bias voltage are plotted in figure 5, and data for negative bias are plotted in figure 6. Both signs of the bias voltage result in a reaction cross section that increases with the magnitude of the bias voltage.

Our preliminary experiments have demonstrated how the rate of erosion of polysulfone can be increased by simultaneous exposure to atomic oxygen and electrons. Furthermore, the effect appears to be due to the presence of electric fields on the target surface. While the results presented here are for the production of CO_2, similar results were observed in other exit channels, such as CO. The relevant observations are summarized in Table 1.

REFERENCES

1. Anderson, B.J., and Smith, R.E., "Natural Orbital Environment Guidelines for Use in Aerospace Vehicle Development", NASA TM 4527, June, 1995

2. Jursa, A.S., ed., *Handbook of Geophysics and the Space Environment*, Air Force Geophysics Laboratory, 1985 NTIS ADA 167000

3. Levine, A.S., ed., *LDEF 69 Months in Space, Third Post-Retrieval Symposium*, NASA Conference Publication 3275, part 3, Nov. 8-12, 1003

4. *Sixth International Symposium on Materials in a Space Environment*, European Space Agency, ESA SP-368, November, 1994

5. Tennyson, R.C., "Atomic Oxygen and its Effect on Materials, *The Behavior of Systems in the Space Environment*, NATO ASI Series E, vol. 245, R. N. DeWitt, et al., eds. Kluwer Academic Publishers, Dordrecht, 1993

6. *Materials Degradation in Low Earth Orbit (LEO)*, V. Srinivasan and B. Banks, eds., TMS, Warrendale, PA, 1990

7. George, P.E., and Dursch, H.W., "Low-Earth Orbit Effects on Organic Composites Flown on the Long Duration Exposure Facility", J. Adv. Mat. 25 (April, 1995), 10

8. Koontz, S., Leger, L., Albyn, K., and Cross, J., "Vacuum Ultraviolet Radiation/Atomic Oxygen Synergism in Materials Reactivity", J. Spacecraft 27 (May-June, 1990), 346

9. Dever, J.A., "Low-Earth Orbital Atomic Oxygen and Ultraviolet Radiation Effects on Polymers", NASA Technical Memorandum 103711 (N91-19294), Feb. 1991

10. Outlaw, R.A. and Davidson, M.R., "Small Ultrahigh Vacuum Compatible Hyperthermal Oxygen Atom Generator", J. Vac. Sci. Technol. A12 (1994), 854

11. Brinza, D.E., et al., "A Facility for Studies of Atomic Oxygen Interactions with Materials", Proc. 3rd International SAMPE Electronics Conf. (1989), p. 646

12. Caledonia, G.E., Krech, R., and Green, B.D., "A High Flux Source of Energetic Oxygen Atoms for Material Degradation Studies", AIAA J. 25 (1987), 59

TABLE 1

Summary of Results

Target Voltage	Electron Beam	Target Response
Target floating	OFF	Baseline rate; no fast peak
	ON	Increased rate, once current threshold exceeded; fast peak
Target grounded	OFF	Baseline; no fast peak
	ON	Baseline; no fast peak
Positive bias	OFF	Increased rate, once voltage threshold is exceeded; no fast peak
	ON	Same as beam OFF.
Negative bias	OFF	Increased rate, once voltage threshold is exceeded; fast peak
	ON	Same as beam OFF

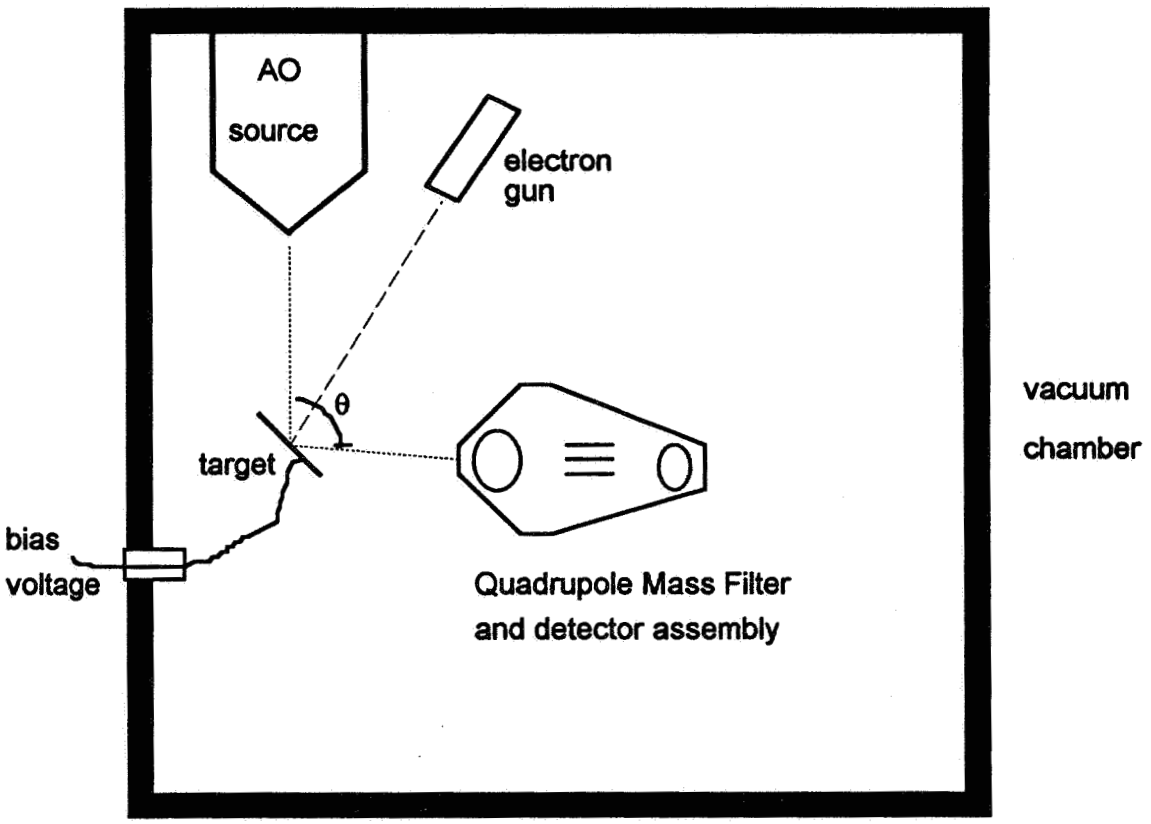


Figure 1. Plan view of JPL AO apparatus. The target was rotated so that the AO beam was incident at an angle of 45^{o}, and the detector was almost always placed so that its line of sight made an angel of 50^{o}, with respect to the normal to the target surface. Thus, most observations were made at an angle of 95^{o} with respect to the incident beam direction; this kept specularly-reflected radiation from the source from reaching sensitive areas of the detector. The ionizer/quadrupole mass filter/detector assembly was enclosed in a metal shield, connected to the vacuum chamber ground, in order to minimize the effects of stray fields. The target was mounted on a ceramic rod, fitted with a brass target holder which could be connected to an external power supply. Both the AO beam and the electron beam had an area of about 1 cm^2 on the target.

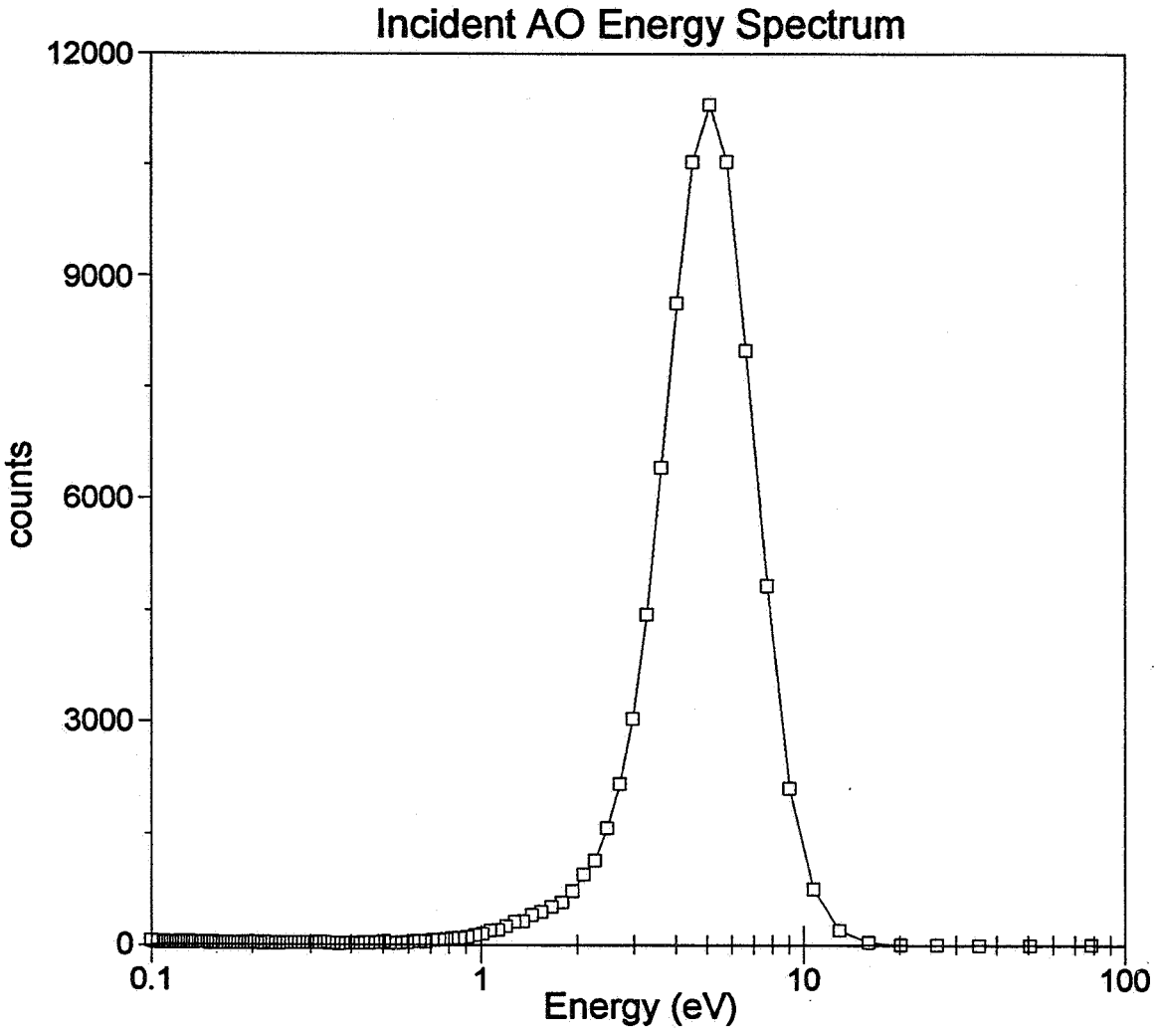


Figure 2. Incident AO beam energy spectrum.

Number of counts is normalized to 200 source pulses.

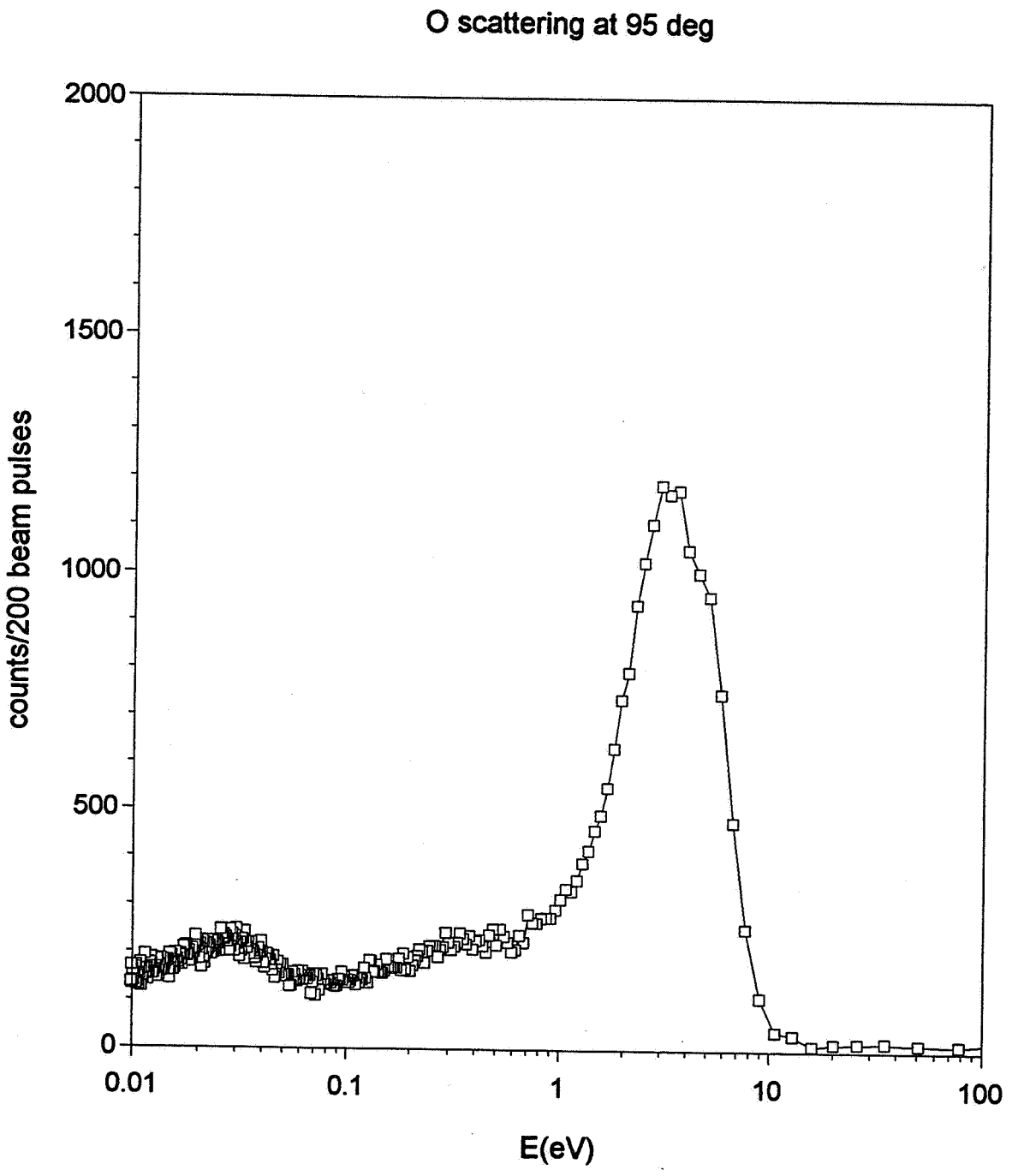


Figure 3. Elastically scattered AO.

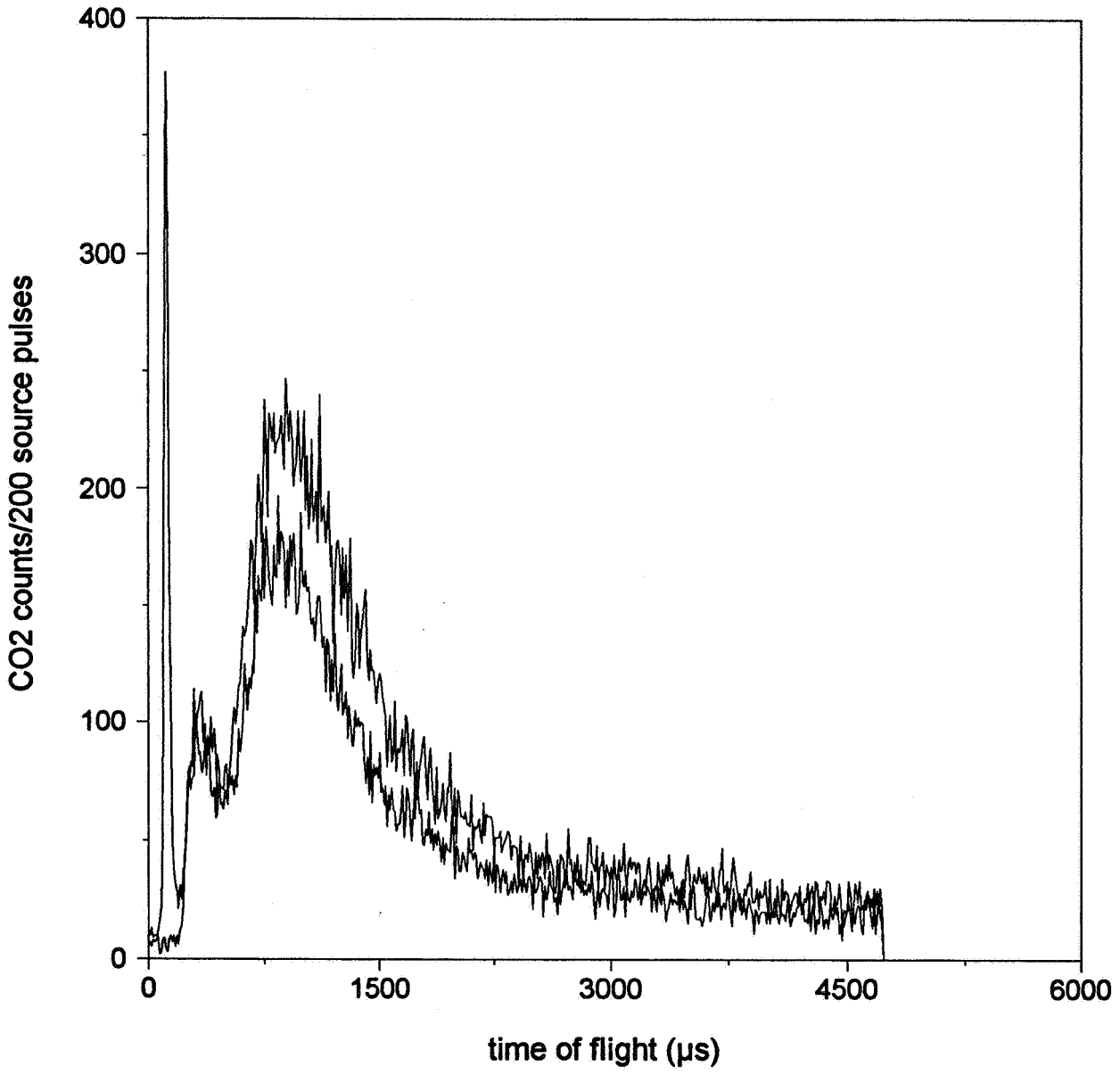


Figure 4. CO2 yield versus electron beam current, target floating.
Top curve is for i = 3 μA/cm2; bottom is for i = 0.

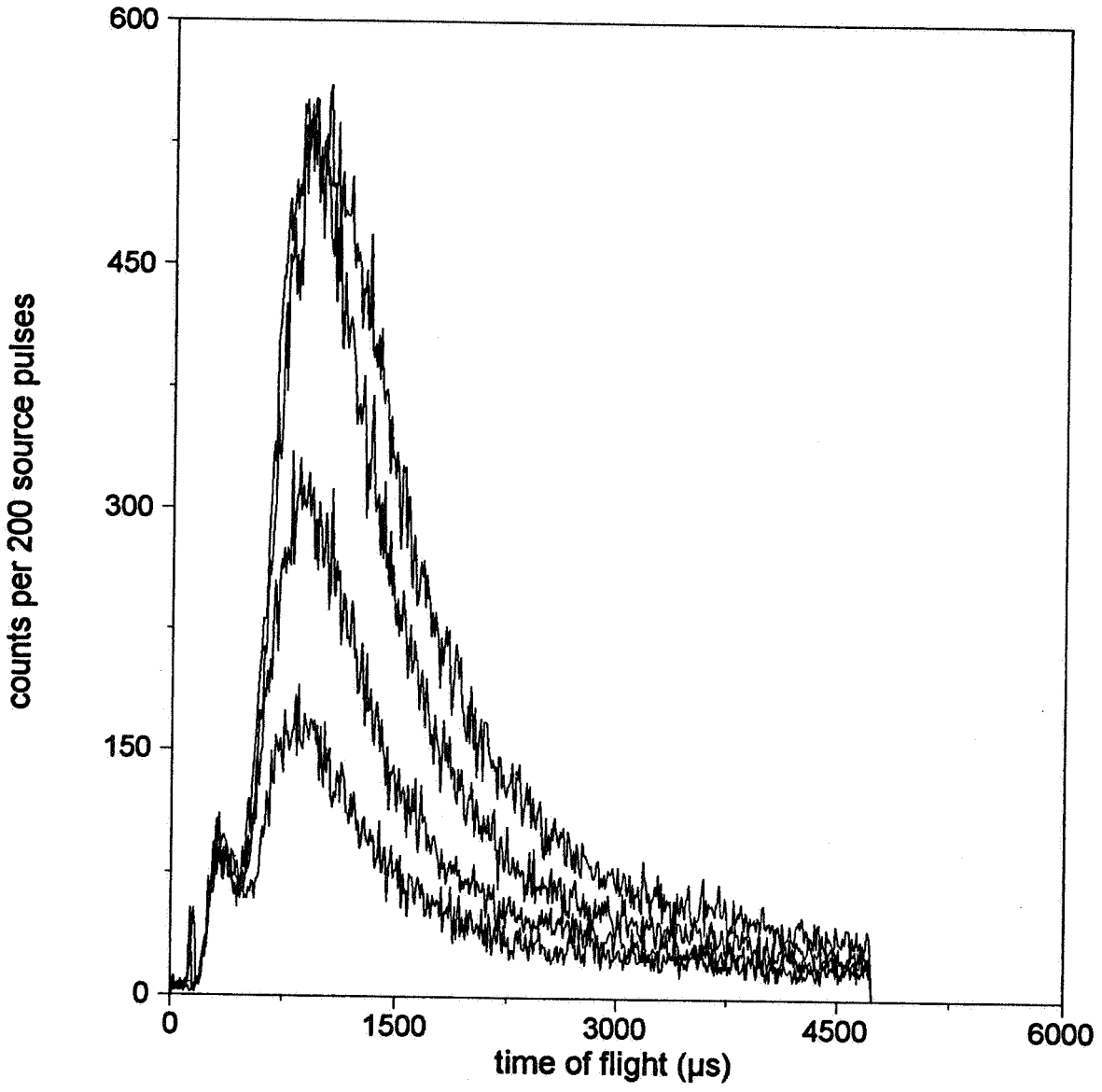


Figure 5. CO2 time-of flight spectrum. Yield for various bias voltages.

Top curve: V=1000V

Next curve: V=300 V

Next-to-bottom curve: V=100V

Bottom curve: V=0 (target grounded)

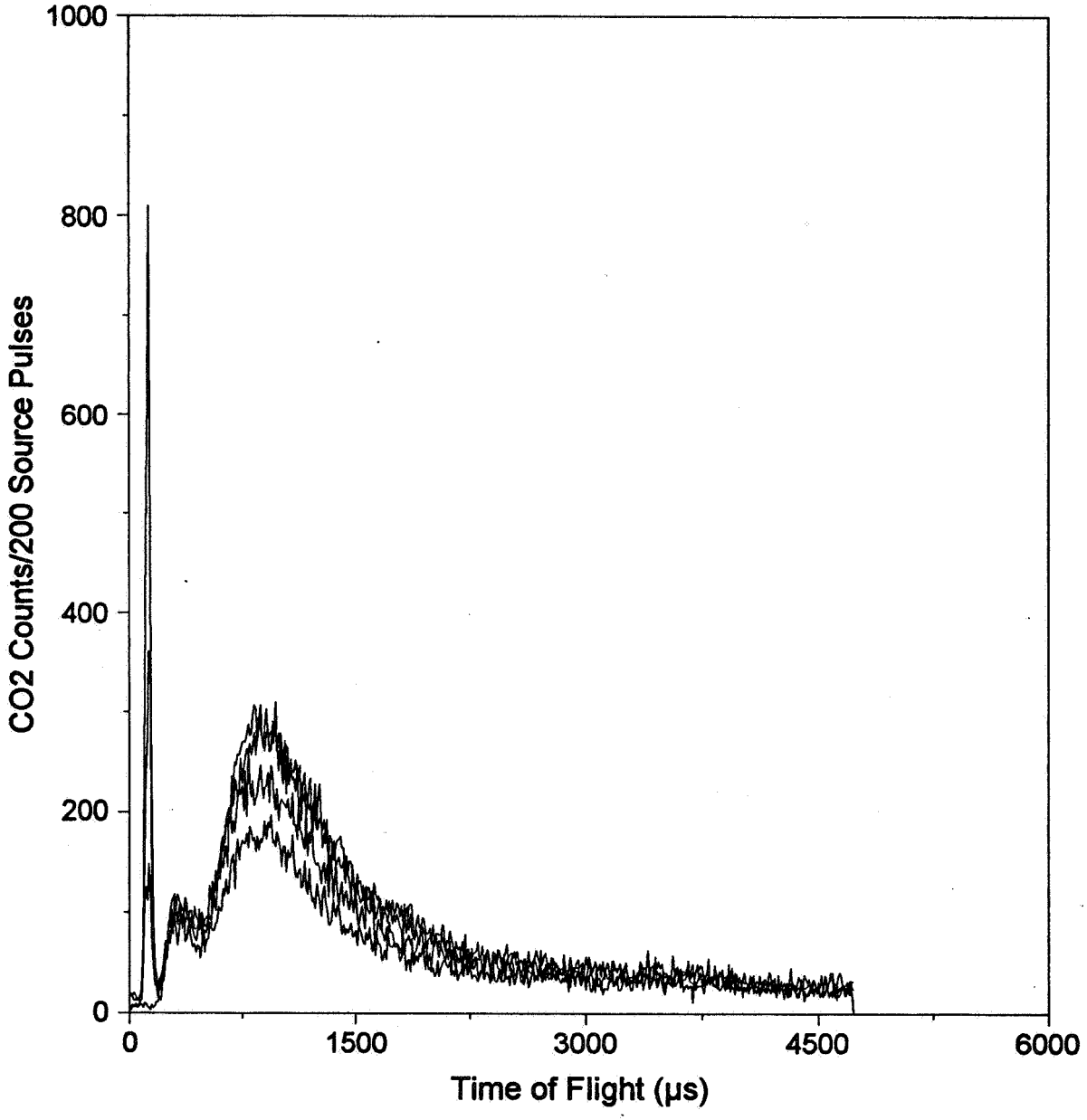


Figure 6. Variation of yield of CO2 with target bias, for negative bias.
The top two curves, for V=-1200 and -1500V, overlay one another;
The middle curve is for V=-900V;
The bottom curve is for V=0 (target grounded).
Note that both the structure and the variation with bias amplitude differ from what is obtained for positive bias.

S29-25
02147N
18P
069600

THE OXIDATION OF REFRACTORY ELEMENTS AND COMPOUNDS IN AN ATOMIC OXYGEN ENVIRONMENT*

Mark M. Opeka
Naval Surface Warfare Center, Dahlgren Division

Robert A. Rapp
Ohio State University, Department of Materials Science

Manfred Wuttig
University of Maryland, Department of Materials and Nuclear Engineering

ABSTRACT

An analytical methodology was developed to predict the behavior of elements and compounds in atomic oxygen (AO) environments. Thermodynamic condensed and vapor phase equilibria were calculated in order to compare the responses to AO and to O_2 of a broad range of materials. The materials included Cu, Ag, Au, Pd, Pt, Rh, Ir, Ru, Os, Re, Cr, Mo, W, Al, Si, Be, C, B, Ti, TiC, TiN, and TiB_2. An experimental apparatus was constructed in order to evaluate the AO-oxidation behavior of selected materials. AO was produced by an N_2 dissociation/NO titration technique to yield thermal AO. AO-response experiments at a P_O (O-atom pressure) of 10^{-5} atm (1 atm = 101.3 kPa) and at temperatures of up to 675 K were conducted with Au, Ru, Ti, TiC, and TiB_2.

The condensed phase equilibria calculations indicated that four metals -- Ag, Au, Ru, and Cr -- form different condensed oxides in AO ($P_O = 10^{-7}$ atm) than in air at 300 K, suggesting that oxidation rates will differ. The vapor phase equilibria calculations indicated that seven metals -- Os, Ru, Ir, Pt, Re, Cr, and Mo -- may exhibit significant vaporization rates in AO ($P_O = 10^{-7}$ atm) at low temperatures (300 K to 1000 K, depending on the metal). Using a vaporization model which includes O-atom supply limitations, the predicted vaporization rates for Os, Ir, Re, and Cr correlate well with published measurements. Experimentally, Au and Ru did not oxidize according to AO-based thermodynamics. The results suggest that high O-to-O_2 recombination coefficients for these metals significantly decreased P_O at the surface. TiC exhibited logarithmic kinetics in AO at 675 K, in qualitative agreement with published O_2 oxidation results for Ti and TiC.

The thermodynamic prediction methodology developed in this research provides the first systematic framework to understand and predict the response of elements and compounds to AO. It has been found to be a powerful tool for understanding AO-oxidation behavior and for predicting the temperature dependence of vaporization rates.

INTRODUCTION

The initial space shuttle flights in the early 1980s provided the surprising observation that a variety of materials exhibit rapid oxidation effects in the low earth orbit (LEO) environment (Ref. 1). Carbon, in all forms including diamond, and Os exhibited substantial mass losses in 1 to 2 days of LEO exposure at room temperature. The mass losses for C and Os were relatively quickly attributed to reactions with ambient atomic oxygen (AO) with attendant formation of volatile oxides (Refs. 2,3). AO is the dominant species in the LEO altitude range of 200 to 600 km, as shown in Figure 1. A systematic assessment of AO effects on elemental metals is motivated by the desire to identify AO-vulnerable metals for satellite designers.

No systematic, analytical survey of the AO-response of metals is known, although significant experimental research has been conducted. Dickens and co-workers identified trends in AO oxide scaling kinetics up to 975 K through studies with Ni, Co, Fe, Cu, Ag, Au, Pd, Pt, Zr, Al, Ta, Sn, Zn and Cd (Ref. 4). Rosner and Allendorf investigated augmented

*This research was supported by John Sedriks and Lewis Sloter of the Office of Naval Research.

metal vaporization in AO versus O_2 up to 3275 K for W, Mo, Re, C, SiC, B, and BN (Refs. 5-10). Fryburg quantified AO-enhanced vaporization for Pt and Cr and also provided the only known correlations with thermodynamics-based (hereafter referred to as "thermo-based") calculations (Refs. 11-15). More recently, NASA and the Strategic Defense Initiative Organization (SDIO) have sponsored research to experimentally survey the AO vulnerability of a wide range of materials (Refs. 16-19).

THERMODYNAMICS-BASED OXIDATION MODEL

A maximum reasonable P_O was selected as a basis for the calculations by assuming a very low orbit altitude of 200 km (Ref. 20). Although the ambient pressure at 200 km altitude is approximately 10^{-9} atm (ref. 21), the high spacecraft velocity increases the O-atom flux (and P_O) on a forward facing surface. The O-atom pressure was estimated from:

$$P_O = J_O \cdot \Delta(mv) \tag{1}$$

where J_O is the O-atom flux, m and v are the mass and velocity, respectively, of an O-atom. The O-atom flux is the O-atom density times the spacecraft velocity. With the spacecraft velocity taken to be 8 km/sec (Ref. 7), and the O-atom density taken to be $5 \cdot 10^9/cm^3$ at 200 km altitude (Ref. 21), P_O was computed to be $1.68 \cdot 10^{-7}$ atm. For the thermo-based calculations, P_O of 10^{-7} atm was assumed.

Although metal evaporation rates at room temperature were of primary interest, rates at temperatures up to 1000 K were calculated to identify the temperature dependence. The thermodynamics model assumed that metal vaporization (as metal and/or metal oxide vapor species) proceeds from the condensed phase in equilibrium with the environment at a given temperature and P_O. The calculations of stable condensed and vapor phase equilibria were carried out using the thermodynamic relationship for the Gibbs Free Energy change for a chemical reaction involving non-standard state conditions:

$$\Delta G = \Delta G^\circ + RT\ln Q \tag{2}$$

where the superscript 0 refers to standard state, R is the gas constant, T is temperature, and Q is the activity quotient. At equilibrium, ΔG is zero and the equation reduces to:

$$\Delta G^\circ = -RT\ln K \tag{3}$$

where K is the equilibrium constant. Free energy reference data from JANAF (Ref. 23), Schick (Ref. 24), Pankratz (Ref. 25), Knacke (Ref. 26), and other sources (Refs. 27-28) were linearized (300 K to 1000 K) for calculation purposes. The magnitude of the error in linearizing the free energy data was below 800 joules/mol, which was significantly less than the error associated with the tabulated values in the respective compilations.

Application of equation (3) for the reaction:

$$O_2 \rightleftharpoons 2O \tag{4}$$

provides an understanding of the highly oxidizing potential of an AO environment. Although the ambient LEO environment pressure is low, P_O of 10^{-7} atm corresponds thermodynamically to approximately 10^{67} atm of O_2 at 300 K and to 435,000 atm of O_2 at 1000 K, as shown in Figure 2.

The computed equilibria for the response of Cr provide an example of the calculation procedure. The condensed phase equilibrium diagram for the Cr-O system, shown in Figure 3, was calculated by applying equation (2) to each possible condensed phase equilibrium reaction:

$$2Cr(c) + 3O(v) \rightleftharpoons Cr_2O_3(c) \tag{5}$$
$$Cr_2O_3(c) + O(v) \rightleftharpoons 2CrO_2(c) \tag{6}$$
$$CrO_2(c) + O(v) \rightleftharpoons CrO_3(c) \tag{7}$$
$$CrO_3(c) \rightleftharpoons CrO_3(l) \tag{8}$$
$$CrO_2(c) + O(v) \rightleftharpoons CrO_3(l) \tag{9}$$

$$Cr_2O_3(c) + 3O(v) \rightarrow 2CrO_3(l) \quad (10)$$

Unit activity was assumed for all condensed phases. Each line in Figure 3 corresponds to one of the previous equilibrium reactions. The diagram shows regions where Cr and Cr oxide phases exist in thermodynamic equilibrium at the respective temperature and P_O conditions. Repeating the calculations using O_2 as the oxidant provided the Cr-O_2 equilibrium diagram shown in Figure 4. Shown on the diagrams are the respective ambient conditions on earth (T = 300 K, Po_2 = 0.2 atm) and at the 200 km altitude in LEO (T = 300 K, $P_O = 10^{-7}$ atm). It is noted that the stable condensed phases at the two ambient conditions are different, which suggests that oxidation and/or vaporization behavior may also differ.

Vapor phase equilibria were also computed utilizing equation (2) and the previous condensed phase equilibria. Two types of diagrams were calculated for each oxidant (AO or O_2). The first type provides the pressures of all vapor species as a function of oxidant activity (or pressure) at a fixed temperature. The Cr-O equilibrium diagram for 1000 K is shown in Figure 5. The second type of vapor phase diagram provides the pressures of all vapor species as a function of temperature at a given oxidant pressure. The Cr-O equilibrium diagram at $P_O = 10^{-7}$ atm is shown in Figure 6. By calculating the Cr-O_2 equilibrium diagram at Po_2 = 0.2 atm and superimposing the results onto the previous Cr-O diagram, a comparison of CrO_x vapor pressures for the two ambient environments is gained, and is shown in Figure 7. It is noted that the vapor pressures for the LEO environment are substantially higher than those in the earth ambient up to approximately 1350 K, suggesting that vaporization of Cr could be significantly more rapid in LEO than on earth in that temperature range.

In order to compare vapor pressure calculations with experimental mass loss and recession data, predicted mass loss rates were calculated from the vapor pressures via the atom fluxes provided by the Hertz-Langmuir equation:

$$J_i = P_i \cdot (2\pi m_i kT)^{-1/2} \quad (11)$$

where J_i, P_i, and m_i are the atom flux, pressure, and mass of the molecule species i arriving to/departing from the surface, and k is the Boltzmann constant.

The predicted mass loss rates were modified by calculating maximum possible mass loss values based on O-atom arrival limitations, using the known O-atom flux at the LEO condition. It is known that under non-equilibrium oxidation conditions, vapor pressures of gaseous oxide species are proportional to equilibrium vapor pressures (observed for W, Mo, and C)[29]. Therefore, non-equilibrium vapor pressures and mass fluxes were computed using the known O-atom supply rate by assuming vapor pressures proportional to equilibrium values.

THERMODYNAMICS CALCULATIONS

Equilibrium condensed-phase equilibria at 300 K were computed for Cu, Ag, Au, Pd, Pt, Rh, Ir, Ru, Os, Re, Cr, Mo, W, VC, NbC, Ti, TiB_2, TiC, TiN, and Sc (Ref. 30) to compare the stable phases in AO ($P_O = 10^{-7}$ atm) and those in air (Po_2 = 0.2 atm) environments. Four elements -- Ag, Au, Ru, and Cr -- were identified which exhibited different condensed phases between the AO environment -- Ag_2O_2, Au_2O_3, RuO_4, and CrO_3 -- and the air environment -- AgO, Au, RuO_2, and CrO_2. As stated previously, oxidation kinetics for these elements may differ significantly in the two environments since different condensed phase oxides are predicted to form.

The known rapid mass loss of Os in LEO environments suggests that Pt-group metals are vulnerable to low-temperature vaporization. Figure 8 provides the thermodynamically predicted vapor pressures versus temperature for the dominant Pt-group metal vapor species at $P_O = 10^{-7}$ atm. It is observed that in addition to Os, three other metals -- Ru, Ir, and Pt -- are predicted to exhibit high vapor pressures at relatively low temperatures.

The results of similar vapor pressure calculations for four of the group VIa and VIIa transition metals are shown in Figure 9. It is noted that Re and Cr, and to a lesser degree Mo, exhibit high vapor pressures at modestly elevated temperatures.

The group VA transition metals are not believed to exhibit enhanced vapor pressures in AO environments versus O_2 environments through consideration of the reaction sequences. The VA metals have not been observed to form a gaseous pentoxide phase. Thus, the gaseous oxides (monoxides and dioxides) form by the rejection of an O-atom from the

condensed phase, as shown in the following equations:

$$M_2O_5(c,l) \rightleftharpoons 2MO(v) + O \quad (12)$$
$$M_2O_5(c,l) \rightleftharpoons 2MO_2(v) + O \quad (13)$$

Under the relatively high P_O of LEO, the previous reactions would be driven to the left, implying that the condensed pentoxide phases would be stabilized by the environment. The previous reactions can be written with O_2 as the oxidant product; in this case, the reactions would be driven to the right by the vacuum environment and low Po_2 of LEO. However, this situation is equivalent to vacuum vaporization and not O-atom-augmented vaporization.

Similarly, the group IVA, IIIA, and IIA metals and Si are also not believed to exhibit enhanced vapor pressures in AO environments versus O_2 environments through consideration of the reaction sequences. These elements form gaseous oxides which possess the same or lower metal valence as the condensed oxides. Thus, the presence of O is not believed to augment vaporization.

Considering the structural elements C, B, and Al, it is noted that all form one or more gaseous oxide phases with a higher valence (on C, B, and Al) than the condensed oxide phase. Carbon forms no condensed oxide phase in the temperature range of interest, while B and Al form the higher valence oxide phases BO_2 and AlO_2. The presence of O drives the following reactions to the right:

$$C(c) + O \rightleftharpoons CO(v) \quad (14)$$
$$C(c) + 2O \rightleftharpoons CO_2(v) \quad (15)$$

$$B_2O_3(c,l) + O \rightleftharpoons 2BO_2(v) \quad (16)$$

$$Al_2O_3(c,l) + O \rightleftharpoons 2AlO_2(v) \quad (17)$$

The calculated gaseous oxide pressures for C, B, and Al at $P_O = 10^{-7}$ atm as functions of temperature are shown in Figure 10. For B and Al, the dioxide vapor species exhibit the highest vapor pressures of the respective vapor species, yet are extremely low from room temperature to approximately 1000 K. For C, the vapor pressures of the gaseous oxides are extremely high; significant mass losses are thermodynamically possible down to low temperatures, and vaporization rates would likely be limited by O-atom transport to the C surface.

The volatile nature of CO_x species suggests that oxidation kinetics of TiC may significantly differ in the two environments. The condensed phase equilibrium diagram for the Ti-C-O/O_2 system at 1000 K is shown in Figure 11. A computation of P_{CO} at the TiC/Ti_3O_5 interface, where the peak P_{CO} is expected due to the maximum value of $a_c = 1$, the results of which are provided in Figure 12, shows that P_{CO} for TiC oxidation is much lower than that for pure C. The computed P_{CO} is negligibly low up to a temperature of approximately 1000 K, which is significantly different from the behavior of pure C.

EVALUATION OF CALCULATIONS WITH MEASUREMENTS

Experimental results, both performed by the author and taken from published research, were utilized to evaluate the thermo-based calculations. Experiments were performed by the author with Au, Ru, Ti, TiC, and TiB_2 samples (Ref. 30). Atomic oxygen was generated using an apparatus very similar to that constructed by Neely (Ref. 31). Nitrogen was partially dissociated via microwave dissociation (2.45 GHz):

$$N_2 + h\nu \Rightarrow N_2 + N(\sim 1\%) \quad (18)$$

This was followed by titration with NO:

$$N_2 + N(\sim 1\%) + NO \Rightarrow N_2 + O(\sim 1\%) \quad (19)$$

resulting in a 1% stream of ground-state $O(^3P)$ in a carrier gas of N_2 (Ref. 32). Typical system operating pressure was 1 torr; thus, P_O was of the order of 10^{-2} torr.

A schematic view of the apparatus is shown in Figure 13. High-purity N_2 (research grade) and NO gases were metered using electronic flow controllers (MKS model 1259 units controlled with MKS 247C power supply)(items A and B). The N_2 flow controller was a 500 sccm unit, while the NO was metered with 10- or 20-sccm units. The primary gas-flow leg (items E, F, G, and H) was constructed from 25mm pyrex tubing. A 760-liter/minute mechanical pump (Leybold Trivac D30A) was used to maintain the desired gas velocity in the system. Pump oil backstreaming was controlled with a dry ice trap (item K). Dissociation of the N_2 was accomplished with an Opthos MPG-4 Microwave Power Generator and a McCarroll cavity. Specimen heating and entry were enabled through a side leg (item G) with a Vycor holder (items O and Q) which enclosed a Nichrome heater element (item R). Sample temperatures up to 675 K could be achieved. A quartz-enclosed type-K thermocouple (not shown) measured the sample temperature continuously. The digital temperature display was an Omega DP116. The system pressure immediately downstream of the sample was measured using an MKS 122AA Barotron (100 torr full-scale)(item I). System pressure near the pump (not shown) was monitored with a Granville-Phillips Model 275 Convectron gauge.

Samples were analyzed using X-ray Photoelectron Spectroscopy (XPS) and Rutherford Backscattering Spectrometry (RBS). XPS analysis was used to identify the valence states of constituent elements, particularly for the TiC samples. The analysis was performed using a Physical Electronics 5400 X-ray Photoelectron Spectrometer using the monochromatized Al Kα line (1486.6eV) and equipped with a concentric, hemispherical analyzer and an ion sputtering gun. Photoelectron takeoff angle was 45°, and the analysis area was 1 mm in diameter. For survey and high resolution scans, the pass energies were 179 eV and 36 eV, respectively. Samples were sputtered using 3 KeV Ar^+.

RBS analysis was used to provide elemental composition information as a function of depth and was performed using a 3 MeV positive-ion tandem accelerator. Scattered particles were detected with a standard surface barrier detector. In general, a 2.0 MeV $^4He^+$ beam was utilized, since it provided high resolution for the detection of oxygen. A 10 MeV $^{28}Si^{4+}$ beam was also used for analysis of the Au samples. Operation was accomplished with an ND 6600 multichannel analysis computer system. RBS spectra were analyzed using a fitting routine. Layer thicknesses and elemental proportions were assumed until a satisfactory fit was achieved between assumed and measured RBS spectra.

Experiments were conducted on Au, Ru, Ti, TiC, and TiB_2. Gold foil (0.25 mm thickness) of 99.95% purity (metals basis) was procured from Johnson-Matthey Alfa. Ruthenium samples were prepared by electron discharge machining (EDM) of samples from an arc-melted button. Ruthenium -20 mesh sponge of 99.95% purity (metals basis) was obtained from Johnson-Matthey Alfa. Surfaces were wet sanded with SiC papers down to 600 grit size. Titanium samples were cut from 0.89-mm thick foil of 99.7% purity procured from Johnson-Matthey Alfa. Vanadium and chromium were the primary impurities, identified via RBS analysis of virgin and oxidized samples. Titanium carbide and titanium diboride samples were diamond sawn from bulk TiC and TiB_2 bars which had been hot-pressed to near-theoretical density by Cercom, Inc. RBS analysis revealed the presence of approximately 0.1 at% W impurity in both compounds.

Nominal sample size was 2.5 x 3.5 x 0.5 mm. In general, samples were diamond machined, diamond polished down to 3μ surface finish, and ultrasonically (US) cleaned in isopropanol and acetone.

Gold was found to exhibit no visible or measurable oxidation after 1 hour at 675 K. RBS analysis ($^{28}Si^{4+}$ beam) of control and AO-exposed Au samples revealed no measurable oxide film, which would have been detectable at thicknesses down to approximately 100Å.

Ruthenium was also found to exhibit no visible oxidation or measurable mass loss. Sample weights of approximately 0.9 gm (weighed to ±0.0001 gm) were unchanged after 1 hour of testing at 325 K and 675 K.

Experiments using the TiC samples revealed visible oxidation (blue color) in 2 hours at 475 K and 675 K, but no detectable change at room temperature. Exposures of ½, 1, 2, 6, and 10 hours duration were then carried out to gain oxidation kinetics at 675 K. Sample color ranged from deep purple for the shortest run, through deep blue, to blue with yellow patches for the longest exposure.

In order to rule out other factors for the observed TiC sample changes, three experiments with TiC were performed for 2 hours at 675 K using other gases. The first test utilized air. The second effectively provided atomic N by flowing and (partly) dissociating the N_2 as usual, but not titrating with NO. The third test provided an NO test environment by running the N_2 and NO with the microwave cavity not operating. In all three experiments, no visible changes in the sample

were observed. RBS analysis also did not detect measurable oxidation in any of the three samples tested in the alternate gases.

Two-hour, 675 K AO tests were also performed with Ti and TiB_2 samples. The Ti sample turned deep gold, while the TiB_2 sample gained a barely perceptible yellow haze which implied that both samples oxidized less than the TiC sample.

Since N_2 is present as the carrier gas, chemically bound N, as in TiN for example (which is gold in color), is a possible reaction product. XPS analyses, however, revealed no chemically bound or gaseous N in any of the samples.

XPS analysis has also shown that TiO_2 is the condensed surface species for the TiC samples exposed to AO at 675 K for ½, 1, 2, and 10 hours. The energy spectra were characteristic of TiO_2 and the atomic concentrations of Ti and O were consistent with TiO_2, correcting for the preferential loss of O during sputtering (Ref. 33). The TiC samples were also depth profiled to provide Ti, C, and O concentrations as a function of sputtering time.

RBS analysis was performed to quantify oxygen content for Ti, TiC, and TiB_2 samples. The total O content for the TiC samples was plotted to provide a kinetic weight gain curve and is shown in Figure 14. The error bars represent the 2σ deviations from the mean values from two independe'nt tests. Silicon was detected on the 10 hour exposed sample. It is believed to have originated from an inadvertent contact of the sample, or sample holder, to a silicone lubricant. The Si was assumed to exist as SiO_2, and the oxygen uptake for the TiC sample was reduced accordingly. The weight gains for the Ti and TiB_2 samples subjected to two-hour test times are also shown in Figure 14. At the two hour test time, both the Ti and TiB_2 samples showed lower weight pickup from oxygen than did the TiC sample.

Experimental results from published research were also utilized to evaluate the thermo-based calculations (Ref. 30). Mass loss information from LEO experiments has been reported for Os, Ir (Ref. 34), and C (Ref. 35). Similar mass loss information from laboratory AO experiments has been reported for Cr (Ref. 14) and Re (Ref. 8). Using the Hertz-Langmuir equation and knowledge of the expected gaseous oxide species, the experimental mass loss data were converted to pressures in order to compare with the predicted thermo-based pressures. Using O-atom arrival rates published with the mass loss data, a third gaseous oxide pressure was computed. For example, it is predicted from thermodynamics that Os vaporizes in AO to form OsO_4 as the dominant species (at 300K, P_i for $OsO_4(v)$ exceeds that of $OsO_3(v)$ by a factor of 10^{46}). Taking $OsO_4(v)$ as the dominant species, three pressures were computed: (1) thermo-based prediction, (2) measured mass-loss-based value, and (3) O-atom arrival limited value. These three pressures were computed for Os, Ir, Re, Cr, and C, and are shown in Figures 15 and 16. It is noted that, although the thermo-based pressures considerably exceed the measurement-based values, the O-atom limited pressures overpredict the measurement-based values by only a factor of 10, in general, and by a maximum of 1000 for Cr.

DISCUSSION

The thermo-based calculations provide a framework for understanding AO-induced mass loss by vaporization. As was shown in Figures 8 and 9, the calculations provided a basis for identifying elements which are vulnerable to significant, low-temperature mass loss by vaporization. If discussion is limited to vaporization at 300 K, vapor pressures for the noble and refractory metal oxides spanned the range of 10^{25} atm for $PtO_3(v)$ to 10^{-72} atm for $(WO_3)_3(v)$. Thus, at 300 K, W, Pd, and Rh were not predicted to exhibit enhanced vaporization from the presence of AO, while Pt, Os, Ru, and Ir, were predicted to exhibit enhanced vaporization in an AO-bearing environment (for the case of $P_O = 10^{-7}$ atm). While no mass loss data for W or Rh in AO at 300 K are known (measurements for W are reported for the range 1400 K to 2600 K (Ref. 7), oxidation scaling experiments up to 775 K have been reported for Pd (Ref. 4). Enhanced vaporization of Pd was not reported, at least suggesting that Pd is not susceptible to low temperature vaporization in AO, in agreement with the thermo-based predictions. Relatively high mass loss rates were predicted for Os and Ir at 300 K (and for Re and Cr at higher temperatures); these results were confirmed by measurements. It was shown in Figures 15 and 16 that the thermo-based mass loss rates must be reduced by the O-atom arrival rates. If C, B, and Al are considered, high mass loss rates were predicted for C, and have been confirmed by experiment. Low mass loss rates were predicted for B and Al. Although no data are known for B, experimental data for Al do not indicate any significant mass loss, which affirms the thermo-based model.

The available mass loss data for Pt and Ru do not show agreement with the thermo-based predictions. The mass loss

of both metals was significantly lower than that predicted by the thermodynamics. For Ru, it is suggested that the recombination coefficient of O to O_2 is sufficiently high that Ru behavior is more accurately modelled by O_2-based thermodynamics. The low measured mass loss rates for Pt relative to thermo-based predictions may also be due to a high recombination coefficient, but could also be due to incomplete thermodynamic data. The existence of condensed "surface states" PtO_3 and PtO_4 have been reported. The calculations reported here utilized thermodynamics data for PtO_2(c) and PtO_3(v) species as the highest oxidation states in the condensed and vapor phase, respectively. The existence of higher oxidation states in the condensed phase would result in significantly lower vapor pressures for PtO_3(v) in the AO envirnment. It was noted that the thermo-based predictions for both Ru and Pt overpredict the mass loss rate, thus, are conservative. No element was found for which a high mass loss rate in AO has been observed, but not predicted by thermodynamics. Thus, thermo-based calculations are a conservative starting point for the understanding of AO-based augmented vaporization effects. Thermodynamics-based calculations bound the problem, which is highly useful.

Despite the high mass loss rate of C in AO environments, TiC was not predicted to be vulnerable to rapid, low-temperature mass loss effects. The calculation of P_{CO} at the TiC/Ti_3O_5 interface showed that the response of TiC is fundamentally different than that of C. Oxidation experiments in AO confirmed the significant difference in AO-response.

CONCLUSIONS

● A thermodynamics-based mass-loss model provides a conservative methodology (ie., always overpredicts mass-loss) for identifying elements which are vulnerable to low-temperature, AO-enhanced mass-loss effects. AO-Vulnerable elements at 500 K and below include C and selected group VIA (Cr), VIIA (Re), and VIIIA (Os, Ir) metals.

● Modifying the thermo-based mass-loss calculations with an O-atom arrival rate limitation yields mass-loss predictions which agree with measurements to within a factor of 10 for Os, Ir, Re, and C and to within factors of 100 to 1000 for Cr.

● A high recombination coefficient (of O to O_2) is believed to significantly reduce the effective P_O on a Ru or Pt surface. Incomplete thermodynamics data is also believed to contribute to mass loss overpredictions for Pt.

● Enhanced low-temperature mass-loss rates are not predicted or expected for B, Al, and group IIA, IIIA, IVA, and VA metals.

● The low-temperature vulnerability of C to AO effects is not observed with TiC. TiC is not rapidly attacked in AO, but exhibits logarithmic kinetics, in qualitative agreement with published results for Ti and TiC oxidation in O_2 environments.

● Only four metals -- Ag, Au, Ru, and Cr -- form different stable, condensed oxide phases in the AO ($P_O = 10^{-7}$ atm) compared with the air environment at 300 K out of the following elements: Cu, Ag, Au, Pd, Pt, Rh, Ir, Ru, Os, Re, Cr, Mo, W, V, Nb, Ti, Sc, Be, B, Al, C, and Si.

● Gold did not measurably or visibly oxidize in a 1 hour AO exposure ($P_O \sim 10^{-5}$ atm) at 675 K.

REFERENCES

1. Dauphin, J., "Atomic Oxygen - A Low Orbit Plague," in *Looking Ahead for Materials and Processes*, de Bossu, J., et al, Eds., Elsevier, Amsterdam, 1987, pp. 345-367.

2. Leger, L.J., et al., "Review of LEO Flight Experiments," in *Proceedings of the NASA Workshop on Atomic Oxygen Effects*, D.E. Brinza, Ed., JPL Pub. 87-14, NASA, 1 Jun 1987, pp. 1-10.

3. Leger, L.J., et al., "Selected Materials Issues Associated with Space Station," *SAMPE Quarterly*, (18) 2, Jan 1987, pp. 48-54.

4. Dickens, P.G., et al., "Oxidation of Metals and Alloys. Part 2. Oxidation of Metals by Atomic and Molecular Oxygen," *Trans. Faraday Society*, (65) 8, 1969, pp. 2235-2247.

5. Rosner, D.E. and Allendorf, H.D., in *Proc. Third Intl Symposium on High Temperature Technology*, Butterworths, London, 1968.

6. Rosner, D.E. and Allendorf, H.D., "Comparative Studies of the Attack of Pyrolytic and Isotropic Graphite by Atomic and Molecular Oxygen at High Temperatures," *AIAA Journal* (6) 4, pp. 650-654.

7. Rosner, D.E. and Allendorf, H.D., "Kinetics of the Attack of High Temperature Molybdenum and Tungsten by Atomic Oxygen," *J. Electrochemical Society* (114) 4, pp. 305-314.

8. Rosner, D.E. and Allendorf, H.D., "Kinetics of the Attack of High Temperature Rhenium by Atomic Oxygen," *J. Chem. Phys.* (49), 1968, pp. 5553f.

9. Rosner, D.E. and Allendorf, H.D., "High Temperature Kinetics of the Oxidation and Nitridation of Pyrolytic Silicon Carbide in Dissociated Gases," *J. Physical Chemistry* (74) 9, 1970, pp. 1829-1839.

10. Rosner, D.E. and Allendorf, H.D., "Kinetics of the Attack of Refractory Materials by Dissociated Gases," in *Heterogeneous Kinetics at Elevated Temperatures*, Belton, G.R.and Worrell, W.L., Eds., Plenum Press, New York, 1970, pp. 231-251.

11. Fryburg, G.C., "Enhanced Oxidation of Platinum in Activated Oxygen," *J. Chem Phys.*, (24) 2, Feb. 1956, pp. 175-180.

12. Fryburg, G.C. and Petrus, H.M., "Variation with Temperature of the Recombination of Oxygen Atoms on a Platinum Surface," *J. Chem Phys.*, (32) 2, Feb. 1960, pp. 622-623.

13. Fryburg, G.C., "Enhanced Oxidation of Platinum in Activated Oxygen. II. Identity of Active Species and Oxide Formed," *J. Chem Phys.*, (42) 11, 1 June 1965, pp. 4051-4052.

14. Fryburg, G. C., et al., *Enhancement of Oxidative Vaporization of Chromium (III) Oxide and Chromium by Oxygen Atoms*, NASA TN D-7629, May 1974.

15. Kohl, F. J., et al., *Thermochemical Analyses of the Oxidative Vaporization of Metals and Oxides by Oxygen Molecules and Atoms*, NASA TM X-73682, May 1977.

16. Banks, B. A., et al., "Atomic Oxygen Effects on Materials," in *NASA/SDIO Space Environmental Effects on Materials Workshop*, Teichman, L.A., and Stein, B.A., Eds., NASA CP-3035, Part I, 1989, pp. 197-239.
(Note: Corrected version of this paper was later released.)

17. Srinivasan, V., and Banks, B.A., Eds., *Materials Degradation in Low Earth Orbit (LEO)*, The Minerals, Metals, and Materials Society, 1990.

18. Levine, A.S., Ed., *LDEF-- 69 Months in Space, First Post-Retrieval Symposium*, NASA CP-3134, Parts 1, 2, and 3, 1991.

19. Levine, A.S., Ed., *LDEF-- 69 Months in Space, Second Post-Retrieval Symposium*, NASA CP-3194, Parts 1, 2, 3, and 4, 1993.

20. Peplinski, D.R., et al., "Introduction to: Simulation of Upper Atmosphere Oxygen, and Satellite Exposure to Atomic Oxygen in Low Earth Orbit," in *13th Space Simulation Conference*, Stecher, J., Ed., NASA CP-2340, 1984, pp. 133-145.

21. _____, *U. S. Standard Atmosphere, 1962*, NASA/USAF/US Weather Bureau, December, 1962.

22. Banks, B. A., et al., "Atomic Oxygen Effects on Materials," in *NASA/SDIO Space Environmental Effects on Materials Workshop*, Teichman, L.A., and Stein, B.A., Eds., NASA CP-3035, Part I, 1989, pp. 197-239. (Note: Corrected version of

this paper was later released.)

23. Stull, D.R., and Prophet, H., Eds., *JANAF Thermochemical Tables*, 2nd Ed., NSRDS-NBS 37, U.S. Govt. Printing Office, Wash. D.C., June 1971.

24. Schick, H.L., *Thermodynamics of Certain Refractory Compounds*, Academic Press, New York, 1966.

25. Pankratz, L.B., *Thermodynamic Properties of Elements and Oxides*, U.S. Bureau of Mines Bulletin 672, U.S. Govt. Printing Office, Wash. D.C., 1982.

26. Knacke, O., et al., Eds., *Thermochemical Properties of Inorganic Substances*, 2nd Ed., Springer-Verlag, Berlin, 1991.

27. Turkdogan, E.T., *Physical Chemistry of High Temperature Technology*, Academic Press, New York, 1980.

28. Ondracek, G., and Wedemeyer, H., "Freie Bildungsenthalpien und Metall-Keramik-Wechselwirkungen," *Sprechsaal*, 108. Jahrg., Nr. 3-4, pp. 75-64.

29. Batty, J.C., and Stickney, R.E., "Quasiequilibrium Treatment of Gas-Solid Reactions. I. Evaporation Rates of Volatile Species Formed in the Reaction of O_2 with W, Mo, and C," *J. Chem Physics*, 51 (10), 15 Nov 1969, pp. 4475-4484.

30. Opeka, M. M., *The Oxidation of Refractory Elements and Compounds in an Atomic Oxygen Environment*, PhD Thesis, U. of MD., Dec. 1995.

31. Neely, W.C., et al., "Production of Ground State Atomic Oxygen in a Multifactor Stress Environment," SPIE vol. 871 *Space Structures, Power, and Power Conditioning*, 1988, pp. 313-316.

32. Kistiakowsky, G.B., and Volpi, G.G., "Reactions of Nitrogen Atoms. I. Oxygen and Oxides of Nitrogen," *J. Chem. Phys.* 27 (5), Nov. 1957, pp. 1141-1149.

33. Betz, G., and Wehner, G., "Sputtering of Multicomponent Materials," In *Sputtering by Particle Bombardment 2*, pp. 11-90. Edited by R. Behrisch. Springer-Verlag, 1983.

34. Gregory, J.C., "Interaction of Hyperthermal Atoms on Surfaces in Orbit: The University of Alabama Experiment," in *Proceedings of the NASA Workshop on Atomic Oxygen Effects*, D.E. Brinza, ed., NASA JPL Pub. 87-14, 1 Jun 1987, pp. 29-36.

35. Triolo, J.J., et al., "Results from Contamination Monitor Package on the STS-8 Mission," Atomic Oxygen Working Group Meeting, Wash. D.C., 23 Jan 1984.

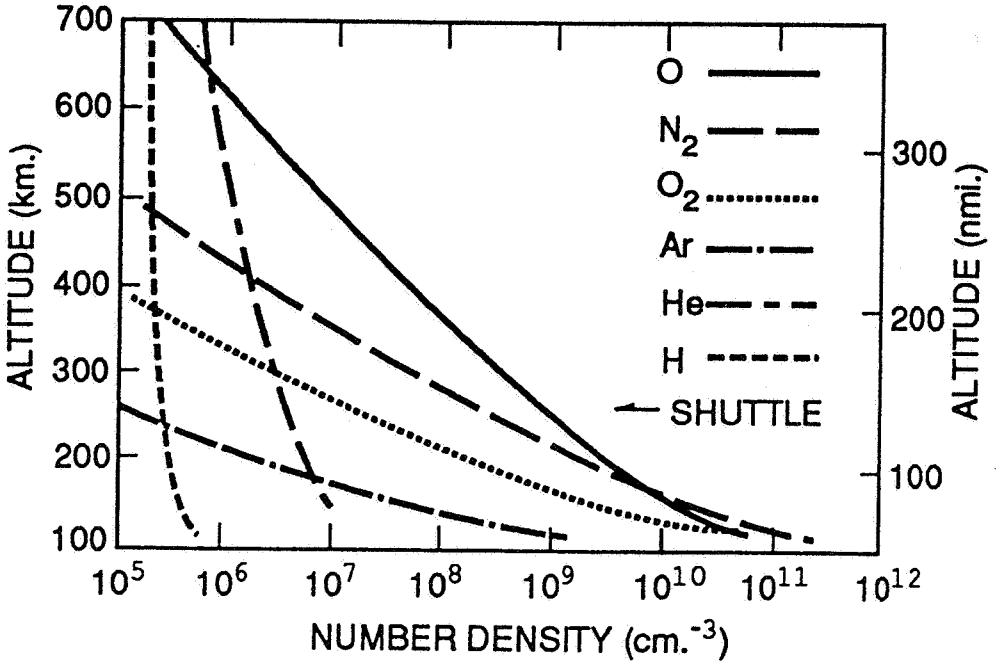


Figure 1 : Atmospheric Composition in Low Earth Orbit from Reference 20

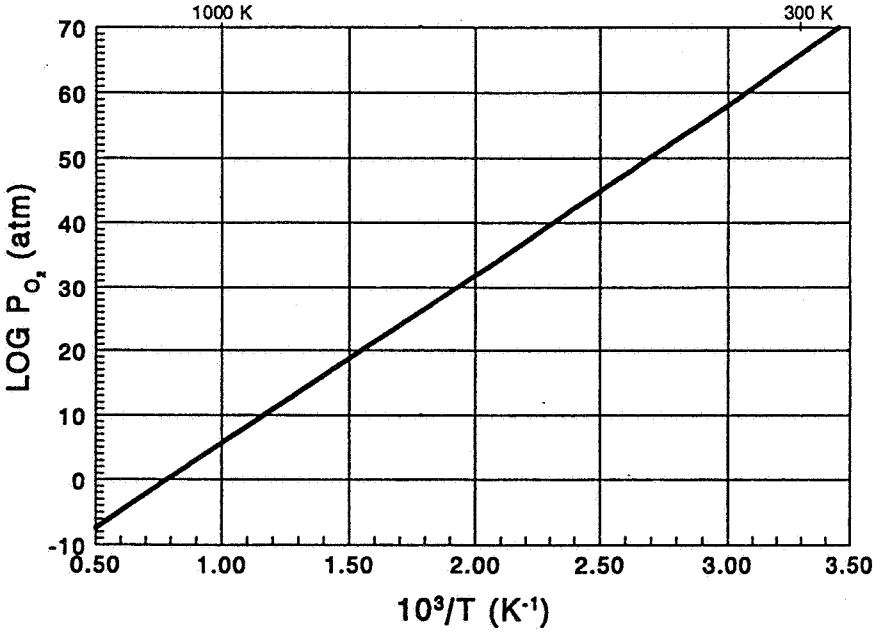


Figure 2 : Equivalent Po_2 Versus Temperature for $P_o = 10^{-7}$ atm.

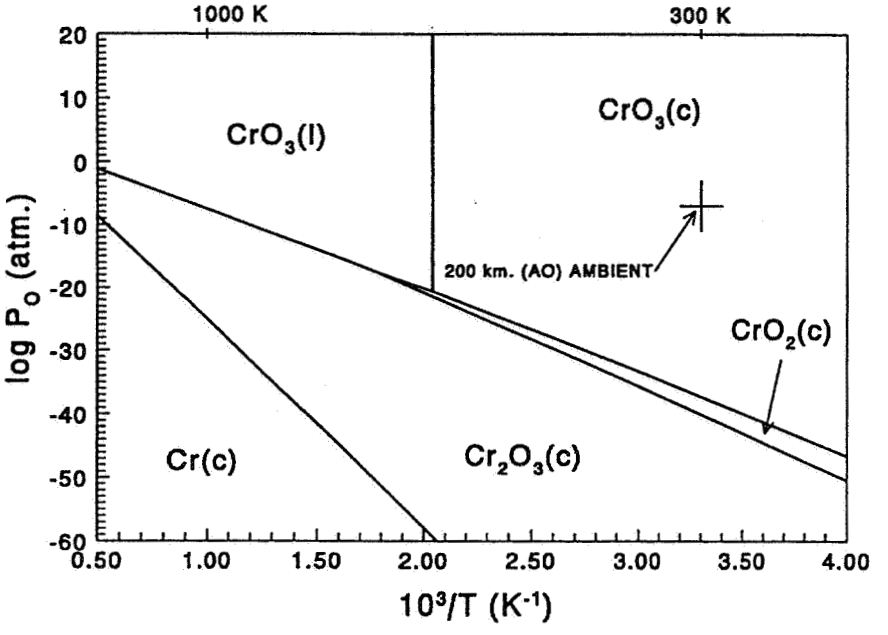


Figure 3 : Chromium-AO Condensed Phase Equilibrium Diagram

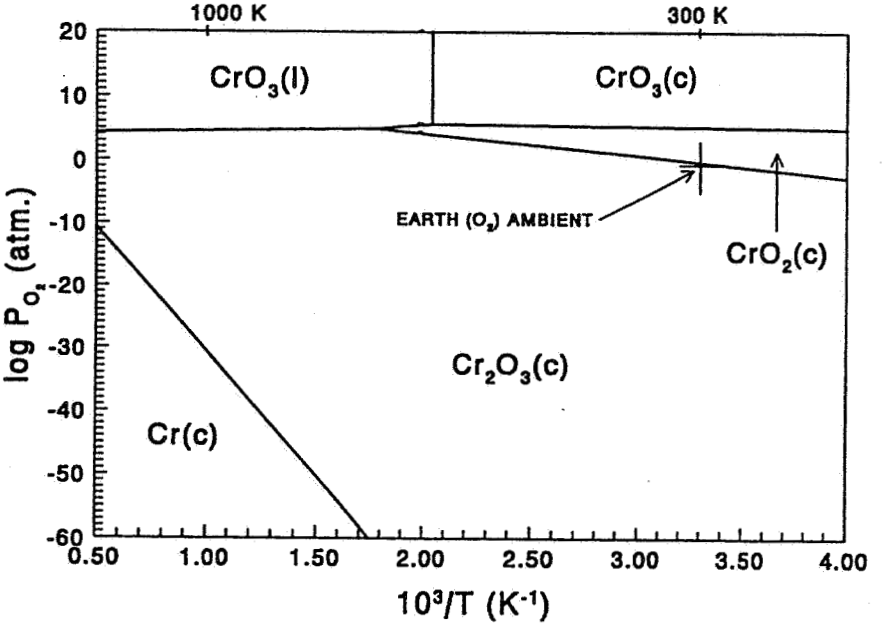


Figure 4 : Chromium-O_2 Condensed Phase Equilibrium Diagram

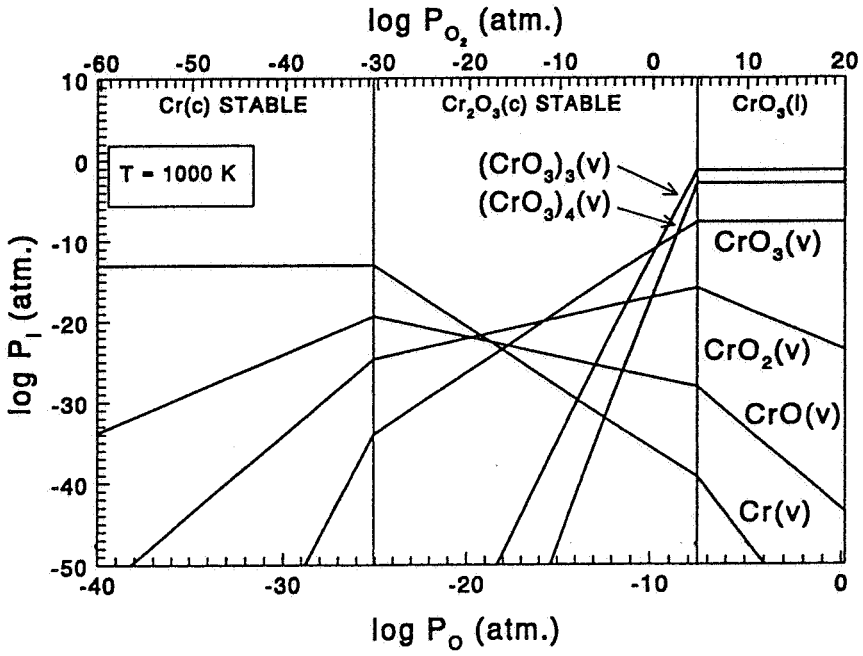


Figure 5 : CrO_x(v) Pressures Versus Oxidant Pressure at 1000 K

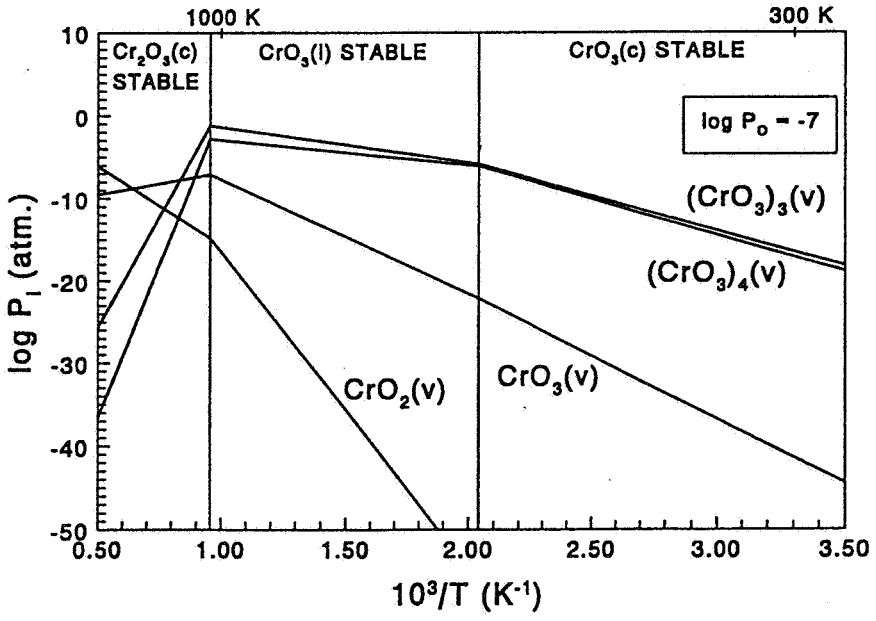


Figure 6 : CrO_x(v) Pressures Versus Temperature at $P_O = 10^{-7}$ atm.

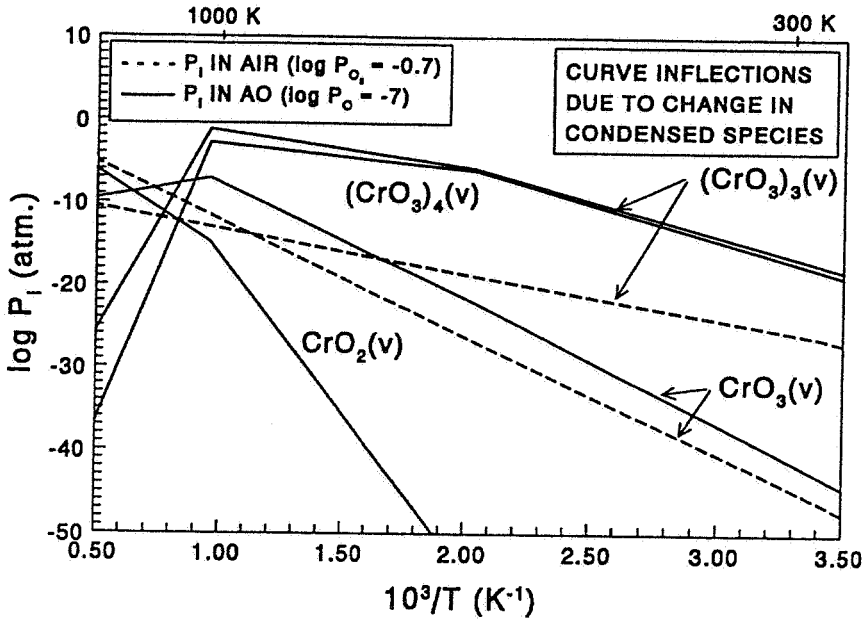


Figure 7 : CrO_x(v) Pressures Versus Temperature; Comparison for $P_O = 10^{-7}$ atm. and $Po_2 = 0.2$ atm.

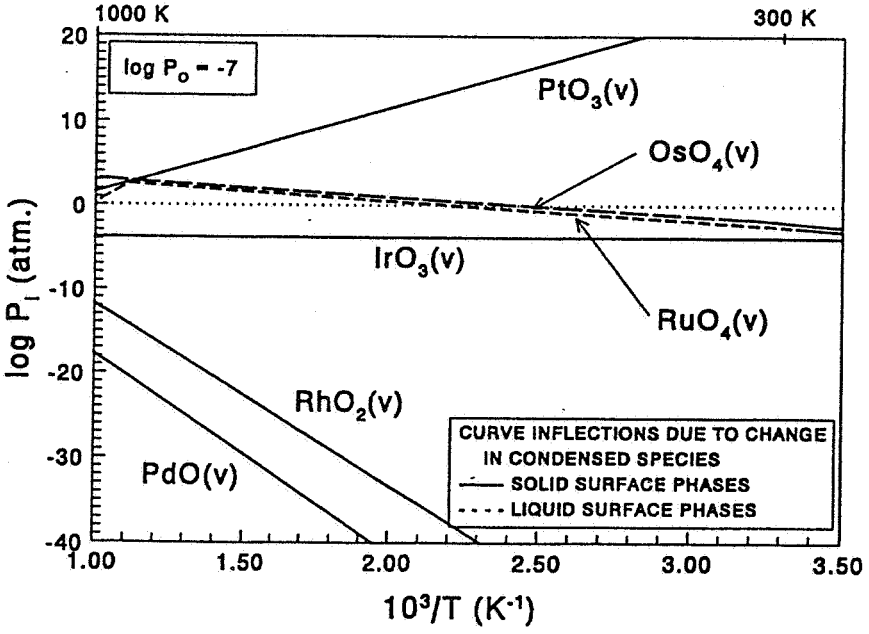


Figure 8 : Pt-Group Metal Oxide Vapor Pressures Versus Temperature at $P_O = 10^{-7}$ atm.

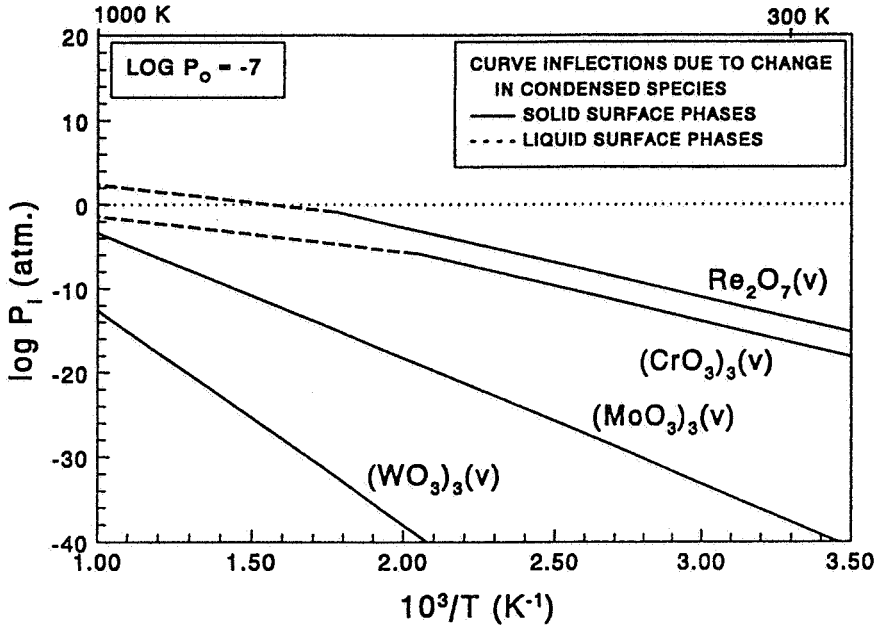


Figure 9 : Refractory Metal Oxide Vapor Pressures Versus Temperature at $P_O = 10^{-7}$ atm.

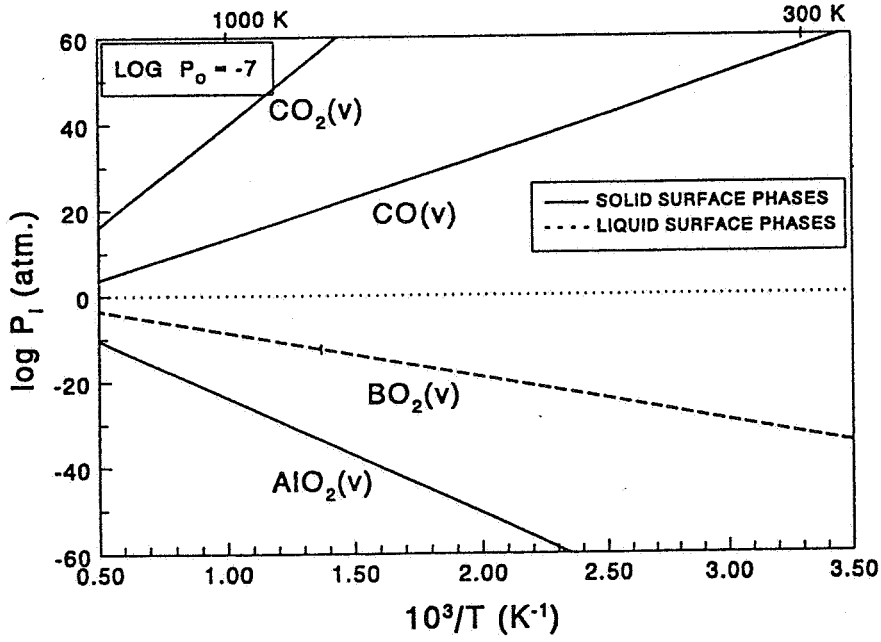


Figure 10 : $AlO_x(v)$, $BO_x(v)$, and $CO_x(v)$ Pressures Versus Temperature at $P_O = 10^{-7}$ atm.

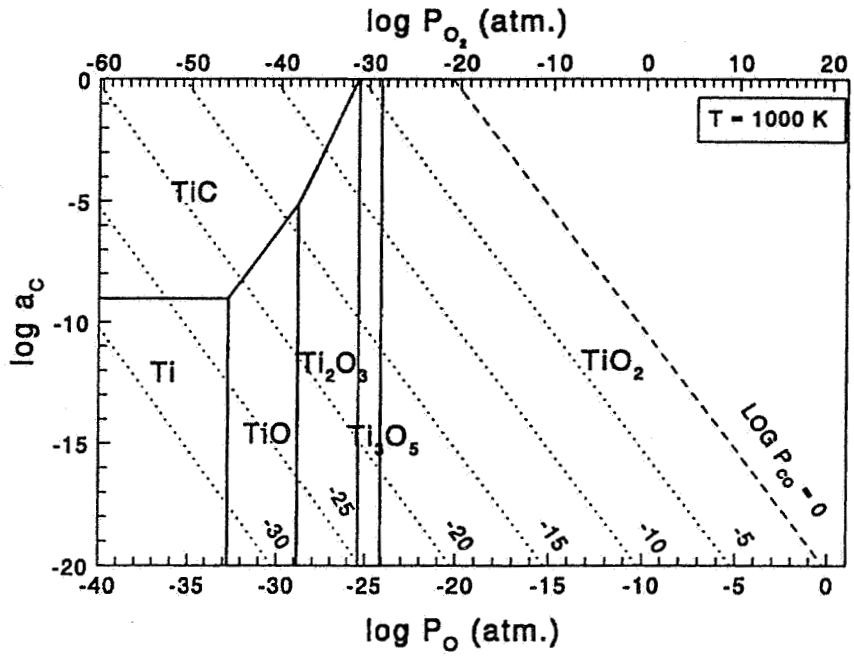


Figure 11 : Titanium-Carbon-Oxygen Condensed Phase Equilibrium Diagram at 1000 K

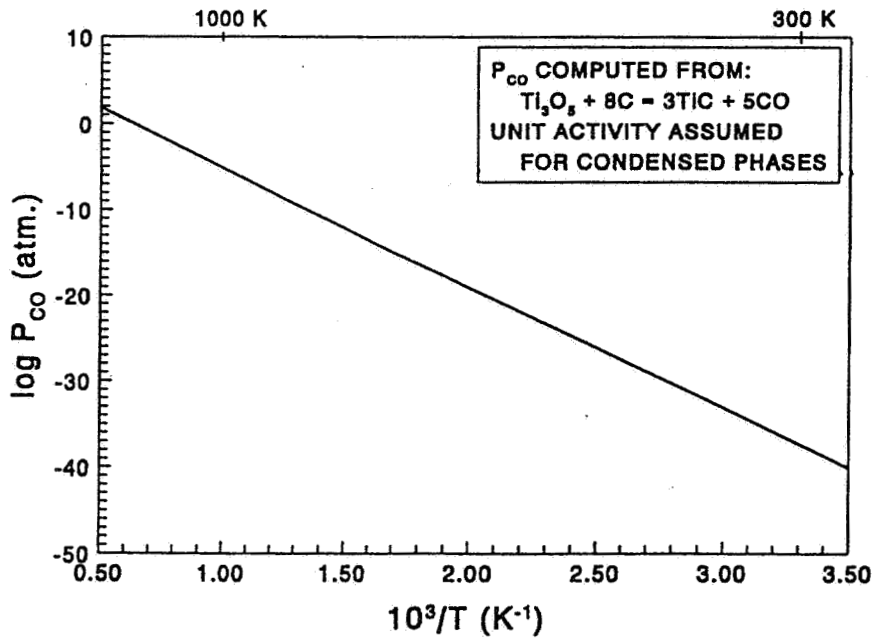


Figure 12 : CO(v) Pressure Versus Temperature at TiC(c)-Ti_3O_5(c) Interface

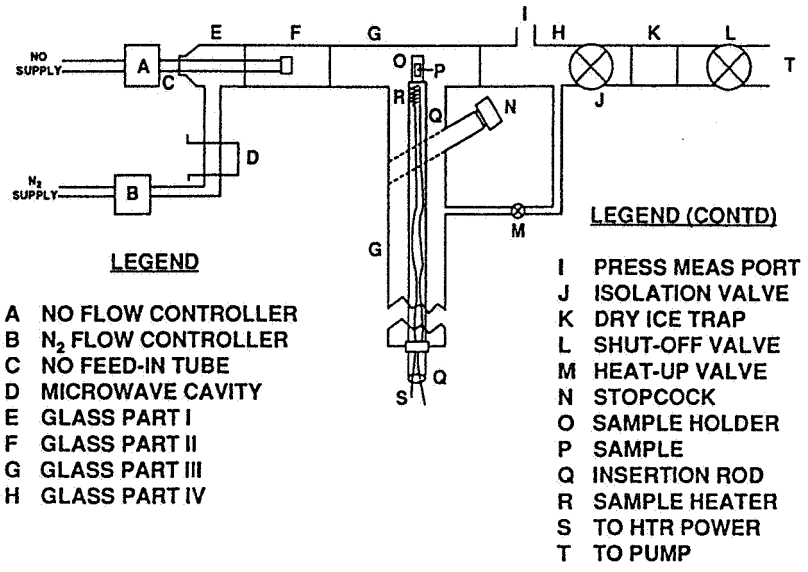


Figure 13 : Atomic Oxygen Testing Apparatus Schematic

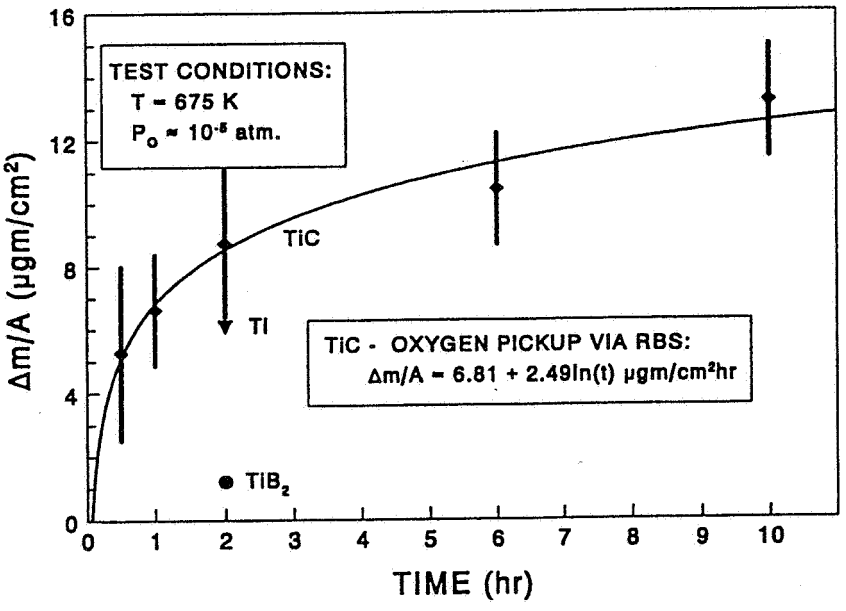


Figure 14 : Oxygen Uptake for TiC, Ti , and TiB_2 in AO

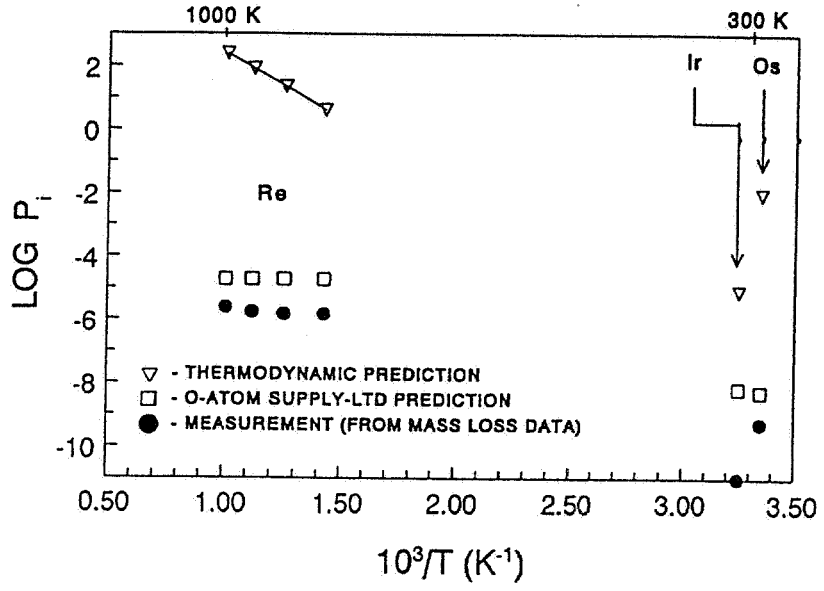


Figure 15 : O-Atom Vaporization Rates for Re, Os, and Ir

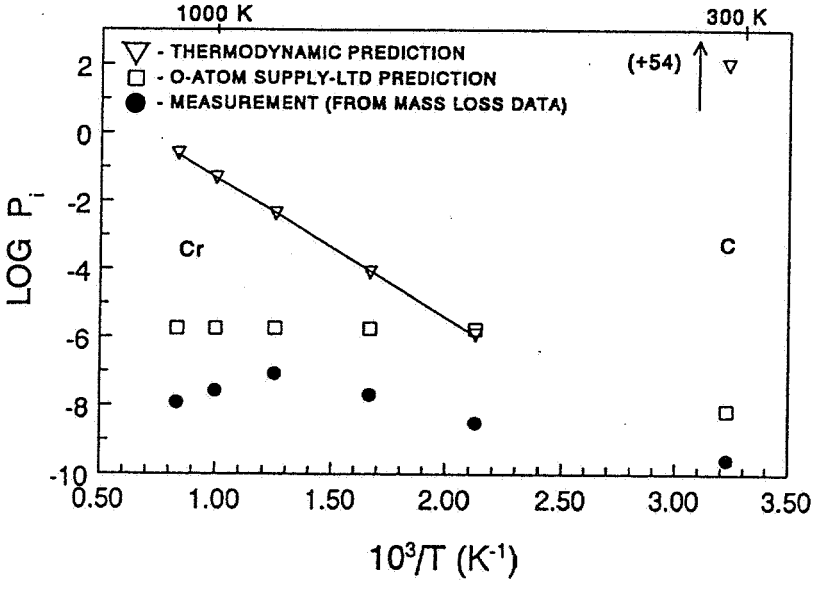


Figure 16 : O-Atom Vaporization Rates for Cr and C

S30-27
ABS ONLY
031472

Abstract for the 19th Space Simulation Conference
Baltimore 28-31 October 1996

Oxygen and VUV Irradiation of Polymers: Atomic Force Microscopy (AFM) and Complementary Studies

1P.
369601

E. Grossman, Y. Noter and Y. Lifshitz
Soreq NRC, Yavne, Israel 81800

Materials in low earth orbit (LEO) are exposed to the various constituents of the space environment, including atomic oxygen (ATOX) and solar UV radiation. While their separate interactions with a variety of materials are frequently well understood, the synergistic interactions are much less so. The present study investigate the effects of oxygen and vacuum UV (VUV) irradiation on two types of polymers commonly used for space applications: fluorocarbons (such as Teflon FEP, Tefzel or Tedlar, having different C/F ratio) and polyimides (Kapton H). As a VUV source we employed a deuterium lamp with a magnesium fluoride window that provided radiation between 115 and 300 nm. The oxygen source was a Kaufman source ion beam. Various fluences of oxygen and VUV were used. The applied radiation schemes were: i) oxygen, ii) VUV, iii) oxygen followed by VUV, iv) VUV followed by oxygen, and v) simultaneous oxygen and VUV.

Atomic Force Microscopy (AFM) was found to be very powerful in detecting the surface degradation from the very early stage. Very low oxygen or VUV fluxes effects which are not detectable using any other surface sensitive technique were observed by the AFM. Complementary techniques included mass loss measurements, changes in surface composition (by XPS) and analysis of the released gases by Residual Gas Analyzer (RGA).

Teflon FEP and Kapton H were found to exhibit different behavior. While Teflon FEP demonstrated VUV sensitivity and an appreciable synergistic effect, Kapton H showed high oxygen reactivity and less significant synergistic effect. These effects will be demonstrated by comparing the results of samples exposed to the different radiation schemes.

S31-14
031473
069603 20P

THERMAL SYSTEM UPGRADE OF THE SPACE ENVIRONMENT SIMULATION TEST CHAMBER

Ashok B. Desai
Environmental Test Engineering and Integration Branch
Engineering Services Division
Goddard Space Flight Center
Greenbelt, MD.

ABSTRACT

The paper deals with the refurbishing and upgrade of the thermal system for the existing thermal vacuum test facility, the Space Environment Simulator, at NASA's Goddard Space Flight Center. The chamber is the largest such facility at the center. This upgrade is the third phase of the long range upgrade of the chamber that has been underway for last few years. The first phase dealt with its vacuum system, the second phase involved the GHe subsystem.

The paper describes the considerations of design philosophy options for the thermal system; approaches taken and methodology applied, in the evaluation of the remaining "life" in the chamber shrouds and related equipment by conducting special tests and studies; feasibility and extent of automation, using computer interfaces and Programmable Logic Controllers in the control system and finally, matching the old components to the new ones into an integrated, highly reliable and cost effective thermal system for the facility. This is a multi-year project just started and the paper deals mainly with the plans and approaches to implement the project successfully within schedule and costs.

INTRODUCTION

The current test facility has been in operation ever since it was commissioned about 35 years ago. The design, fabrication and installation of all its sub-systems, main components and controls, are almost that old. Besides the older technology of the systems and components, its operational and maintenance costs have been quite large. It has needed a relatively large number of operators; the controls being fully manual have required very close monitoring by highly trained and experienced technicians; most of the components are in constant need of preventive and corrective maintenance. Observatory level tests have required large number of technicians at the two floor levels, adding to the costs. The LN_2 consumption cost is also a large portion of running a test in the chamber.

The chamber shrouds in similar facilities and of same age at other locations have had structural failures and have been replaced with new ones. The shroud panels undergo large deflections. The panel to cross-over tubing interface welds were suspected to be the most stressed areas and vulnerable. The GN_2 flows through the various circuits are not balanced and difficult to tune.

The thermal system upgrade would reduce, if not eliminate, many of these costs, improve reliability, more accurate cost estimates, efficiency, and with PLC based control system, reduce operational costs with lesser number of technicians.

EXISTING FACILITY

The test facility is a vertical chamber, about 30 ft. in diameter and 40 ft. high, shown in Fig. 1. The thermal and vacuum system components are distributed from the basement to second floor of the building. It is equipped with eight cryopumps and a turbo-molecular pump, to achieve ultra-high vacuum. The thermal environment variations are provided through a cylindrical side shroud, a bottom shroud and a combination of a frustum and disc type top shrouds. Computer data terminals, with packaged software routines, are used to monitor the payload temperatures. Fig. 2 shows a typical thermal system control panel with manual valves and Fig. 3 shows the PLC based control system panel that was part of the vacuum system upgrade.

The original chamber had diffusion pumps with LN_2 cooled elbows. This system was upgraded recently by replacing the old diffusion pumps and LN_2 cooled elbows with new cryopumps and sliding main valves. A programmable logic controller (PLC)-based interface panel was installed that gives access to and helps monitor chamber pressure, cryopumps and its mechanical pump health, any fault or operator warnings and alarms. All the information is available to the operators through a color graphics display. This capability was included with a view to potential remote/automatic operation of the chamber, for simpler tests, with the vacuum system and the new thermal system, fully integrated.

Thermal System

The thermal shrouds are of aluminum tube-in-sheet arrangement, with both liquid and gaseous nitrogen flow through the tubing. The three main shroud circuits of the current thermal system are operated from a central thermal skid. The GN_2 is made in the main vaporizer and forced through the tubing by a central GN_2 compressor. Separate pumps circulate the LN_2 when called for to flood the shrouds. The tubing had been formed by forging two flat panels together and passing through high pressure rollers. The panels are attached to mechanical supports off the chamber shell. The tubing run vertically through the full height of the chamber. The two rows of panels stacked vertically are connected by interconnecting tubing. The ends of the tubing are connected by welding separate tubes and elbows. This makes for a long tube runs for GN_2/LN_2,

resulting in large temperature gradients and pressure drops. Fig. 4 is an interior view showing the vertical panels of the side shrouds and GN_2 tubings.

Thermal Shrouds

Top Shrouds: These are made up of 36 separate panels in frustum shape. There are two parallel LN_2 and four parallel GN_2 circuits. It is designed for a thermal load of 72 watts/sq. ft. The top of the frustum end up in the dome of the chamber which currently has solar lamps-and-lens assemblies, forming the old, decommissioned solar simulator.

Side Shrouds-- A total of 36 separate panels make up the side shroud into a vertical cylinder of about 28 ft. inside dia. and about 38 ft. height. There are six LN_2 and twelve GN_2 parallel circuits.

Bottom Shrouds-- A 30 ft. dia. disc made from five separate panels form the bottom shrouds. There are five parallel circuits, designed for a maximum of 275 watts/sq. ft. thermal load.

LN_2 Subcooler

A subcooler provides a single-phase LN_2 to the shrouds. Its current capacity is to handle 200-KW thermal load through the circulating LN_2. It has two 20-hp, 150 gpm LN_2 pumps; vacuum jacketed heat exchangers, control valve box and electrical control panel.

Warm GN_2 System

The warm GN_2 system heats or cools the chamber shrouds between the temperature range of -65 ^{0}C to +85 ^{0}C. The system consists of four heat exchangers, a compressor and a refrigeration system, control valve box and electrical control panel. A 125-hp compressor circulates GN_2 with a pressure range of 115 to 180 psia. The R-22 refrigeration system, with a cooling capacity of 10 tons at -80 ^{0}C. cools the GN_2 prior to circulation.

The chamber also has a GHe refrigerator to provide gaseous helium at 15 K. The refrigerator has a capacity to handle 1-kw thermal load at 20 K. The system is skid mounted and was upgraded in 1994.

THERMAL SYSTEM DESIGN

The new thermal system design has two main aims, namely, to increase the existing temperature range along with the overall thermal capacity and to include a control system to enable remote, and for simple tests, automatic operation.

The main design requirements will be, temperature Ramp rates of,

- 40 ^{0}C/Hr. over -185 ^{0}C to +20 ^{0}C,
- 34 ^{0}C/Hr. over +20 ^{0}C to +150 ^{0}C for heating and
- 30 ^{0}C/Hr. over +20 ^{0}C to -130 ^{0}C for cooling.
 And
- Maintain stability of $\pm$ 2 ^{0}C at any temperature between -130 ^{0}C to +150 ^{0}C,
- Shroud temperature uniformity of 10 ^{0}C over the full range.

The design will focus on the following basic features:

- Skid mounted, modular assemblies.
- Handle the top, the side and the bottom shrouds as the three main zones and provide thermal conditioning to the zones.
- Utilize the existing vacuum jacketed lines.
- Utilize the existing GN_2 compressor.
- Use available plant steam as the heat source.
- Use a PLC based control system, compatible with the existing one for the vacuum system.
- System to be capable of remote operation from other control consoles through appropriate instrumentation and feedback loops.
- With new LN_2 pumps, LN_2 mode will be activated by the control system automatically to provide sub-cooled LN_2 to the three shroud zones, with the shroud temperatures less than -180 ^{0}C.
- A 50 kW of payload heat dissipation to be handled.

UPGRADE OPTIONS

Some of the driving factors that affected the design considerations were: overall cost of the upgrade, technically efficient and reliable system, PLC based control system to be integrated with the vacuum and GHe subsystems, minimum downtime for demolition and installation of new components, schedule of on-going test activities and available funding over the life of the project.

Two options were considered to achieve a balance of the above factors:

Multiple TCUs with Zones

The shrouds to be divided into various zones and supplied with multiple and portable thermal conditioning units (TCUs). A sub-option was to have three sets of TCUs, each for the top, the bottom and the side shrouds. The units could be similar in capacities and design and thus be interchangeable. The side shrouds could be further divided in an upper and a lower half circuits, even a few vertical zones, supplied from

separate TCUs. Thus zoned and valved, the top shroud can be moved so as to utilize the lower half of the side shrouds and accommodate smaller test payloads.

Centralized Thermal System

The second option was to replicate the old central system with central heat exchanger and a central GN_2 compressor, with using either the old shrouds in their current configurations or modified in various zones, as discussed above. The system would have new heat exchanger, related piping, control valves and control panels, using the existing heat source and LN_2 supply.

The first option could reduce consumption costs and increase efficiency. High pressure, high density units can be portable enough in size and be economical in design and fabrication costs, being identical units. The units can be interchangeable and replace a unit that suffered a failure. It can provide considerable flexibility and high efficiency. However, the concept would necessitate the shrouds to be modified with extensive manifolds for piping and isolation valves. A lot of cutting and welding of tubing and feeders inside the chamber would be needed to ensure balanced flows and suitable pressure drops for blower type system. It also would require new chamber penetrations for the extra inlet and return piping and valves for each zone. Added to this would be external piping and valves to interface with the sub-cooled LN_2 subsystem.

The second option could reduce equipment and installation costs, as a large single unit would cost less than a multiple units adding up to the same large capacity. This would also be more compatible with the existing shroud configuration. This option would be less flexible and need to be run fully even for a small payload. The zoning of shroud would not make economic sense and reduce the flexibility and efficiency further.

To facilitate the choice between the options, two sets of calculations were carried out to evaluate the required heating/cooling capacities needed, the maximum temperature ramp rates achieved, the required gas flows and related pressure drops and thus the needed capacities and physical dimensions of units for each option.

The results indicated that the size and number of TCUs needed were much larger than reasonable for the space, power and utility requirements around the facility. The associated pressure drops in the long tubing would be too large for the blowers in the TCUs to handle. The consensus opinion was to go for the central system. One more critical decision required for choosing the centralized system was that of determining the potential "life" left in the present shrouds.

APPROACHES TO SHROUD LIFE EVALUATION

As a consideration for a full "turnkey" project to replace the thermal system, the chamber shroud replacement was also a major factor. The existing shrouds pose some problems, namely, they are 35 years old, had leakage problems earlier, limit flexibility in

the design of the new thermal system and the old paint on the shrouds limit higher operating temperatures.

The actual number of thermal cycles imposed on the shrouds were estimated, based on the test history, to be no more than 400 to 450 over its 35 year operation. A surefire indication of shroud components failing is large and small leaks under vacuum. Welded joints between the tubing, under fatigue induced by thermal cycling were the most obvious points of scrutiny. Any extra loads imposed on adjacent panels and tubing due to mechanical restraints, asymmetrical flows and warping of the whole shroud cylinder moving under thermal expansions and contractions, were also planned to be investigated.

A large chamber, at another location, was earlier tested very extensively and critical components analyzed through finite-element techniques, for investigation of the weld joint cracks in the shroud tubing. Ref. 4 describes this study. This precedent allowed the development of a test evaluation plan.

Two outside consultants were contracted to develop detail test methods, procedures and carry out the tests. The analyses and review of the gathered data resulted in conclusion and recommendations for low cost modifications to extend the potential "life" in the thermal shrouds.

Phase 1: Nondestructive Testing:

Eddy current and/or dye-penetration testing of the welds in the cross-over connections in the top, center and bottom panels. Fatigue type indications in the toe and heat affected areas were to be inspected in the welds. The indications, such as porosity, high frequency burns and cold lapping, were judged to be related to the welding process.

Radiographic inspection of the welds in the crossovers, using x-rays, for internal flaws that may be propagating to the surfaces. Radiographic examination showed some crack development in the top crossover tubes at the weld joint with the panel. However, the cracks appeared not be propagating across the tube wall or the weld material. The depths were no more than 10% of the wall thickness and of random occurrence.

Thermograph images of the welds, crossovers and the shroud panels under temperature gradients to record the thermal profiles and effects of flow rates. The thermal imaging of the panels indicated the flow of GN_2 between panels is not uniform and the feed from the manifold is not balanced. This is creating binding and jamming of panels. This is a major factor in inducing inter-panel stresses.

Determination of actual strains and stresses in the areas of the shrouds, under actual, normal thermal cycles. A series of strain gauges and thermocouples were installed on the areas of selected panels and cross-over tubing. Stress/strain measurements under

thermal cycling indicated large loads on the feed and the return pipes. Fig. 5 shows the strain gauges and thermocouple locations on the tubes and panels. This was one of the panels selected for investigation. Figures 6, 7 and 8 show the plotted results at the top, middle and the bottom inlet locations of the tubes. The microstrain values measured by respective strain gauges and temperatures by the thermocouple are plotted together. The strain values closely follow the temperatures through the hot and cold cycle in Fig. 6, the weld joint between top tube and the panel. The difference between the two progressively increases from top through middle to the bottom areas of the test coupon. It was concluded that the thermal strain was being countered by large strains of opposite directions, by external mechanical constraints on the tubes and especially the inlet feeders off the manifolds. Upon inspection, some of the U-bolt type supports on the feeders were found to have sheared off or severely distorted. The adjacent panels were also appeared to be binding at the sides and contributing further. These mechanical fatigue loads are more detrimental to the weld joints.

Phase 2: Destructive Testing:

Determination of the fatigue strength of the material of the panels, tubing and welds and thereby, the life expectancy. A set of test coupons were cut out of the shroud panels, with a section of the cross-over tubing included. One set of panels were set up with external sources of LN_2 and warm GN_2. The setup was then subjected to almost 1110 cycles between LN_2 and GN_2 at about +85 C. The pieces of tubes and panel weld joints were inspected with a scanning electron microscope which revealed series of ridges that indicated effects of progressive incremental fatigue corresponding to the thermal cycles. Fig. 9 through 12 show the sample piece, the crack propagation, its width and the effects of thermal fatigue. The crack was estimated to develop and propagate after almost 900 cycles. This appears to be almost more than twice the actual cycles, the shrouds have undergone in real time. This indicated that the thermal fatigue, as suspected at the start was not the main destructive factor. Another set of panels were configured to be subjected only to mechanical strain loads, representative of the actual measured loads on the shroud assembly.

Performing thermal stress analyses using finite-element based math models of the suspect areas and geometry of the shroud panels was an additional tool available for use. These analyses can establish maximum strain conditions in the structure and only peak strain areas would be analyzed further in detail. To reduce cost and fit the schedule, this option was not pursued.

The cost estimates for the full test evaluation were less than 5% of the total projected cost of a new shroud system. That appeared to be a prudent investment to be able to quantify the potential problems, causes and required modification to extend the life expectancy of the shrouds.

Modifications and Repairs

Top Shrouds

The removal of Solar Cell feedthroughs, purge system and lens assemblies, associated with the old solar reflector subsystem, in the chamber top dome necessitated replacing the top shroud to provide shielding of the payload from the dome walls.

In the first phase of the project, a 29-ft. diameter flat disc top shroud will replace all the 127 panels and the frustum shaped old shroud. The frustum does not add to the working volume of the chamber, as the dome slides out on a pair of rails for loading and unloading of the test articles. It would need only one of the thermal circuits and smaller number of connections. this will eliminate extra feedthroughs and circuits, reducing capacity requirements on the compressor and the thermal system; also ensuring operational and consumption cost savings.

Side Shrouds

The feed and return piping supports, imposing the mechanical loads against the panel movements, will be redesigned with sufficient clearances and Teflon coated pads. The panel interlocks will also be repaired with bolts to take up shear and edges with clearances to relieve the binding of the panels. The feeder manifold and the piping will be modified to balance the flows as much as possible.

AUTOMATION IN CONTROL SYSTEM

The old electro-mechanical relays based manual control system with complex logic and interlock circuitry, has been replaced with PLC based system for the vacuum system of the chamber, as mentioned earlier.

The two control systems will be connected together and integrated into a Local-Area-Network that will also include other chambers in the labs. The goal is to use the Man-Machine-Interface (MMI) software package to automate the controls. The system would be flexible enough to access, set, control and operate from remote operator consoles also. The network is planned to be further integrated with the data acquisition system to provide real time payload and facility system parameters from various PC based access points.

It will be possible to program a bakeout temperature profile with ramp rates, bakeout soak setpoints, contamination monitoring and feedback to terminate or change soak temperature setpoints and finally to bring the thermal system to ambient at the end of the bakeout.

The PLCs are highly flexible, modular and expandable. The programs can be changed and revised as the needs change. The upgraded thermal system is planned to have a similar PLC based control system.

The basic elements of such a system are:

1. The main application or the process to be controlled
2. Input devices
3. Input modules providing signal conversion and protective interface
4. Programmable Logic Controller (PLC)
5. Control logic program for the application process
6. Output modules providing signal conversion and protective interface
7. Output devices such as lights, solenoids and motor controls
8. Man-Machine-Interface software for control and monitoring of the application process

The PLC itself includes these main components:

- Central Processing Unit (CPU)
- Memory
- Control logic program stored in the memory
- Power Supply

FUNDING PLANS, TASK PRIORITIES AND SCHEDULE

Multi-year funding

The Project for the upgrade, as planned, has a four year timeline. All the tasks of project definition, development of design philosophy, specifications, procurement process and demolition of old components and installation of new ones have been planned to correspond to the total funds committed for each of the four years. A multi-year spending plan, in the current overall budget environment becomes a challenge in itself. Detailed spending plans have been developed, based on assumptions about the availability of annual portions of the total funds.

Task Priorities

The various tasks have been prioritized, divided and spread over the fours years to correspond to the funding for those years and the planned and future test schedules. The goal has been to minimize the down time, protect existing subsystems and components from demolition and installation activities and preserve the cleanliness integrity, as much as possible.

CONCLUSION

The series of tests on shroud material, tube welds and piping were a key element in quantifying the potential life of the shrouds and helped in deciding not to replace the shrouds and piping. This provided a major component of savings in cost and time to the project. That also helped avoid the potential problems of welding new piping, fittings and feedthroughs with a new shroud, leakage and extensive cleaning.

The goals of reducing operational costs, increasing efficiency of LN_2 consumption, accurate and predictable controls and test cost estimates can be achieved with PLC based control system and corresponding algorithm sophistication. This requires compatible valves and other process control devices and mechanical and thermal components. The environmental testing lab at Goddard center already has upgraded another chamber with PLC based control system. The advantages of efficiency, wider temperature ranges and reliability in this thermal system has been a foundation on which the SES upgrade was undertaken.

Fully integrated thermal and vacuum chamber under such control system is the way to establishing a state-of-the-art environmental facility for the new, highly complex and sensitive flight hardware for future spacecraft and instruments.

REFERENCES

1. *Operating Procedure for the Space Environment Simulator, Facility 290*, NSI-26-01-198,

2. *Systems Analysis for the Vacuum and Cryogenic Systems*, F. J. Stokes corporation, Philadelphia, PA, and CryoVac, Inc. Columbus, OH; NASA contract No. 5-1333

3. *Preliminary Design Report for the Modification of the Facility 290 Thermal System*, A. Webb and J. Sushon, NSI Technology Services Corporation, NSI-26-09-280, August, 1996.

4. *Fatigue Induced Cracking in Aluminum LN2 Shroud of 39-Foot Vacuum Chamber,* Arthur E. Edwards, Ford Aerospace and Communication Corporation, Palo Alto, CA. Presented at the 13th Space Simulation Conference by Institute of Environmental Sciences; Orlando, FL, 1984.

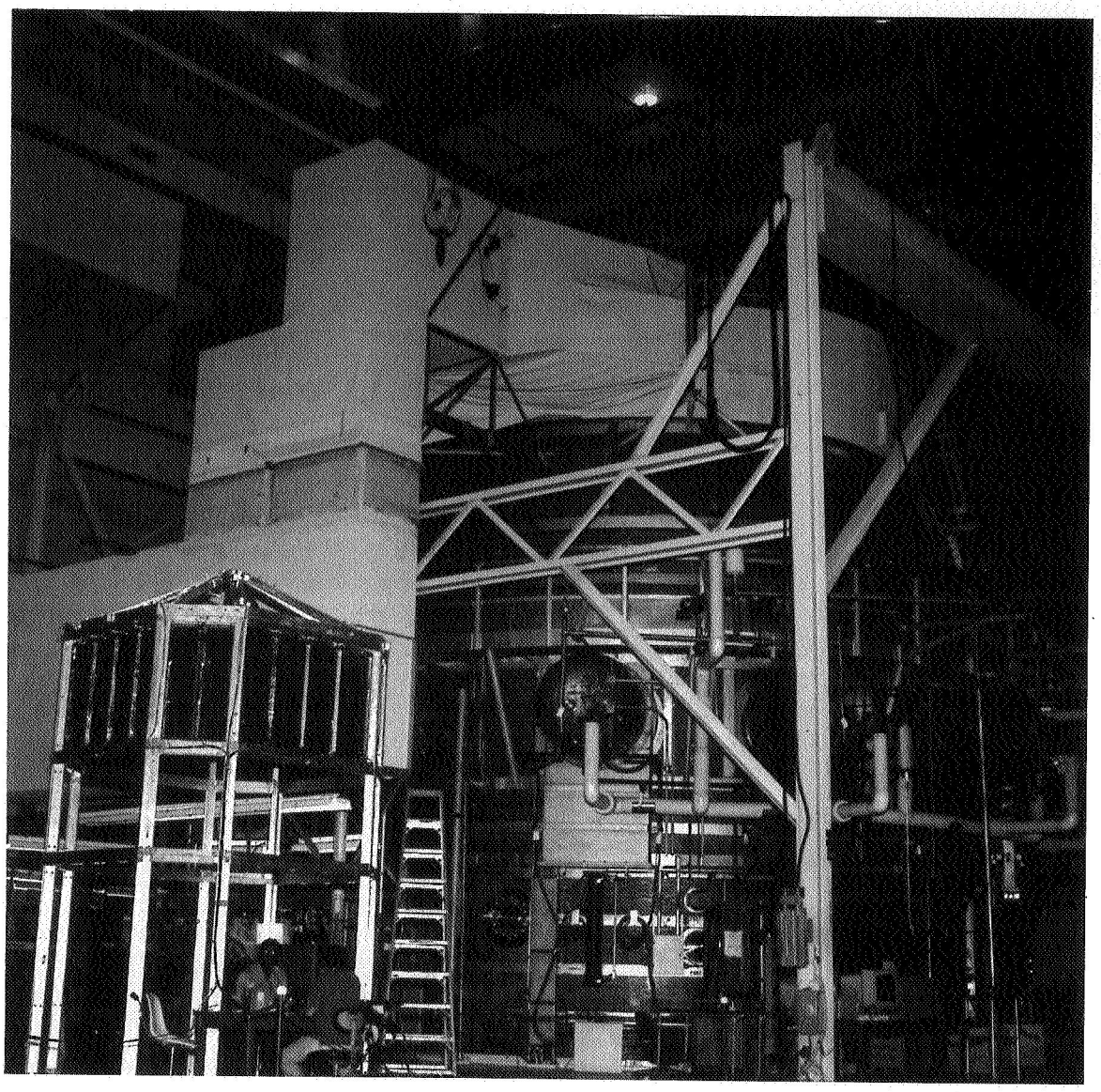


Figure 1. The Space Simulation Environment Chamber

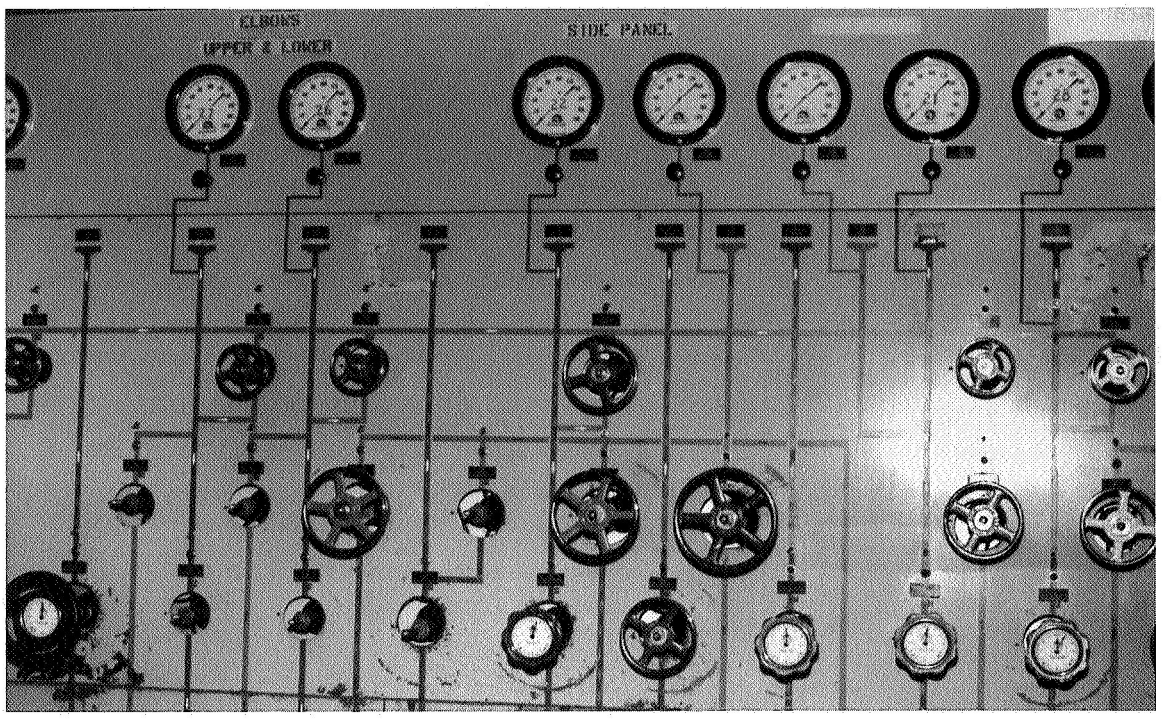


Figure 2. Typical Old Thermal System Control Panel with Manual Valves

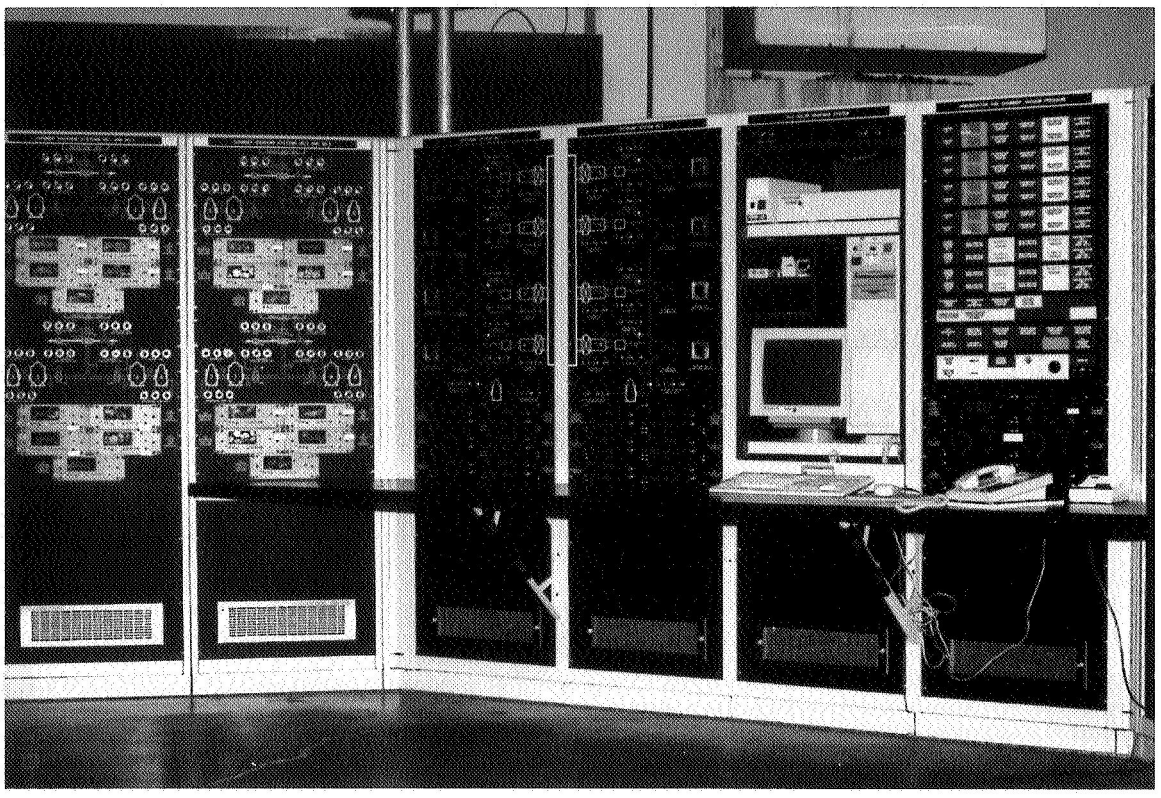


Figure 3. New PLC Based Vacuum System Control Panel

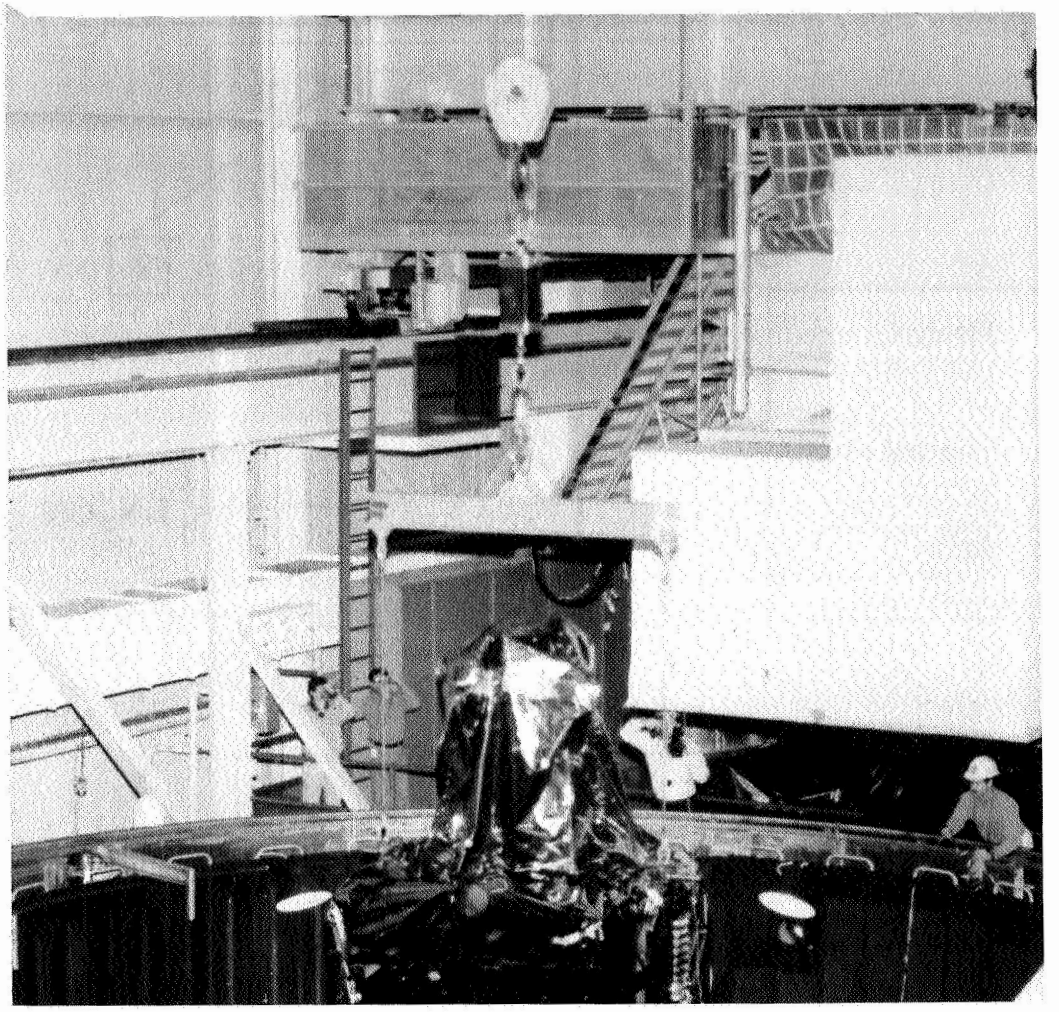
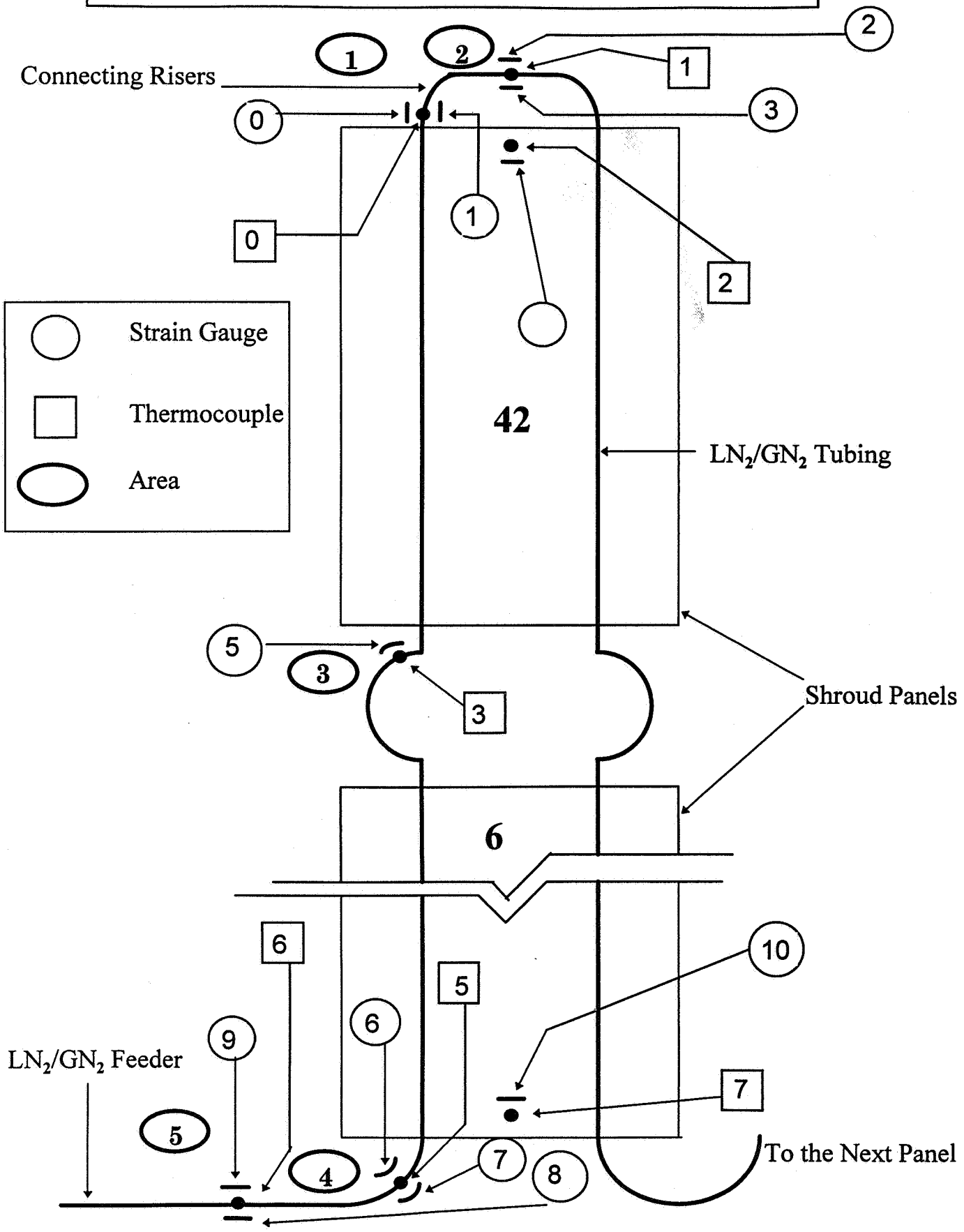


Figure 4. Side Shroud Panels with Integral GN_2 Tubes

Fig. 5. Strain Measurements Under Thermal Cycling



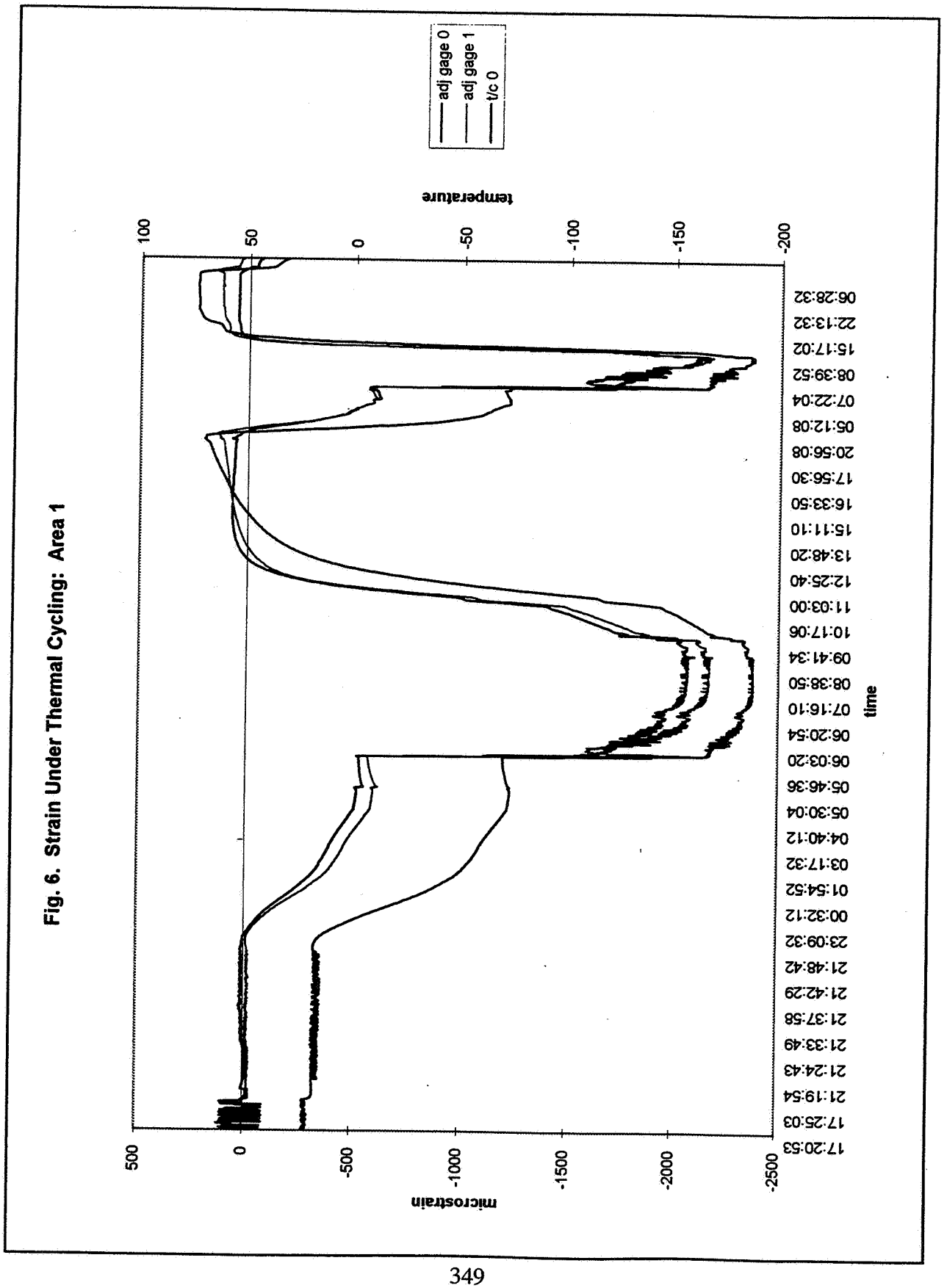


Fig. 6. Strain Under Thermal Cycling: Area 1

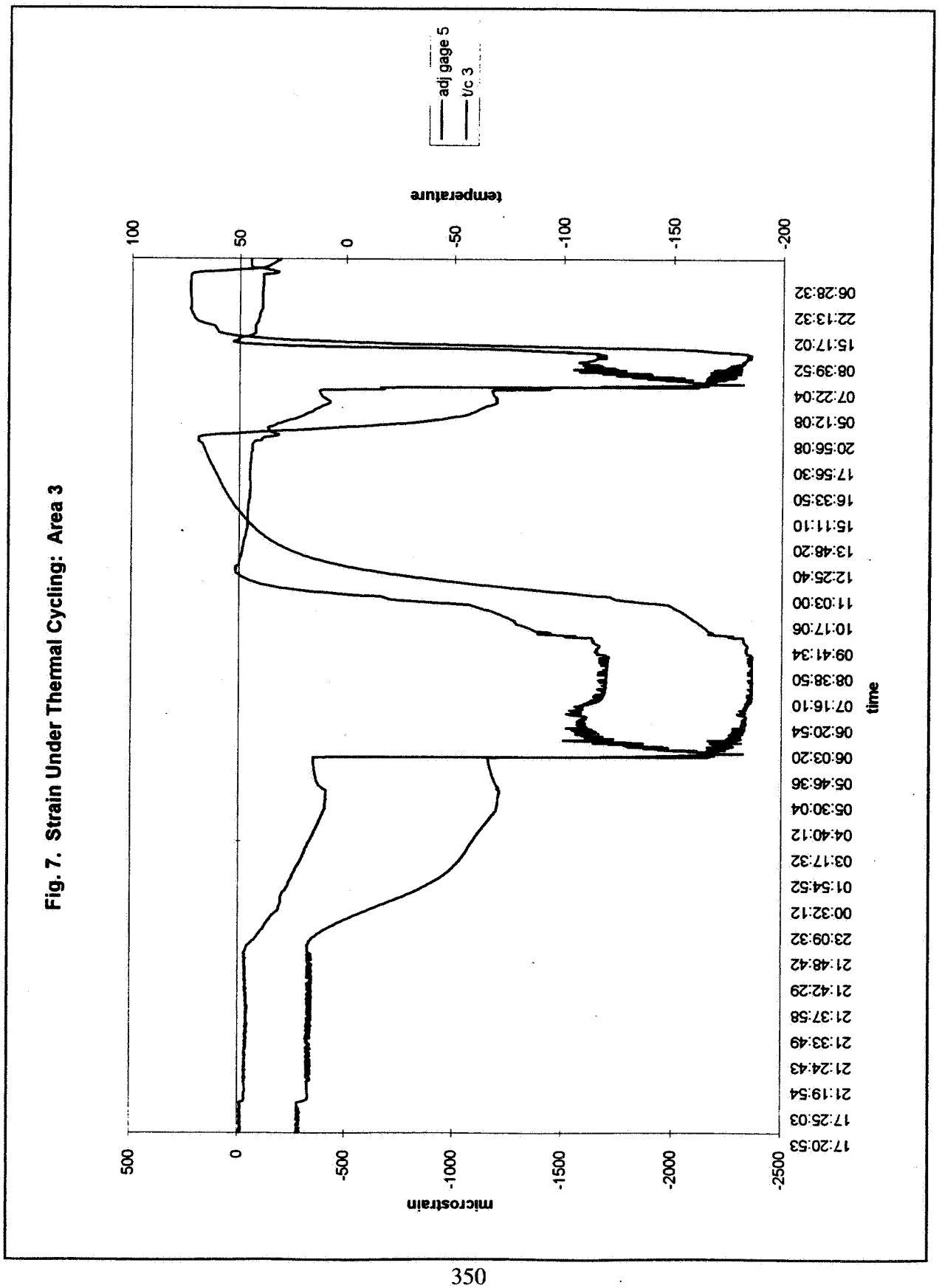


Fig. 7. Strain Under Thermal Cycling: Area 3

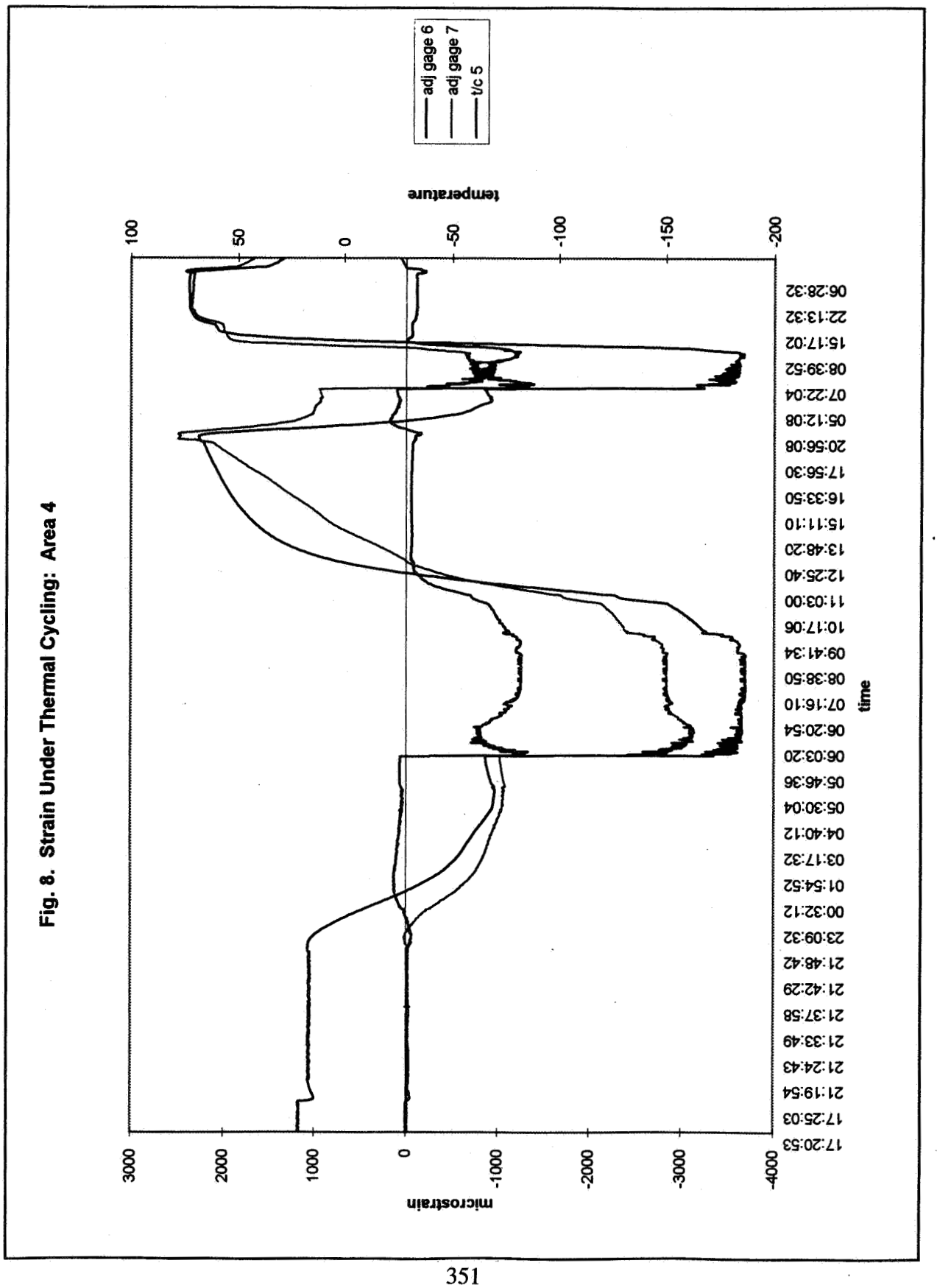


Fig. 8. Strain Under Thermal Cycling: Area 4

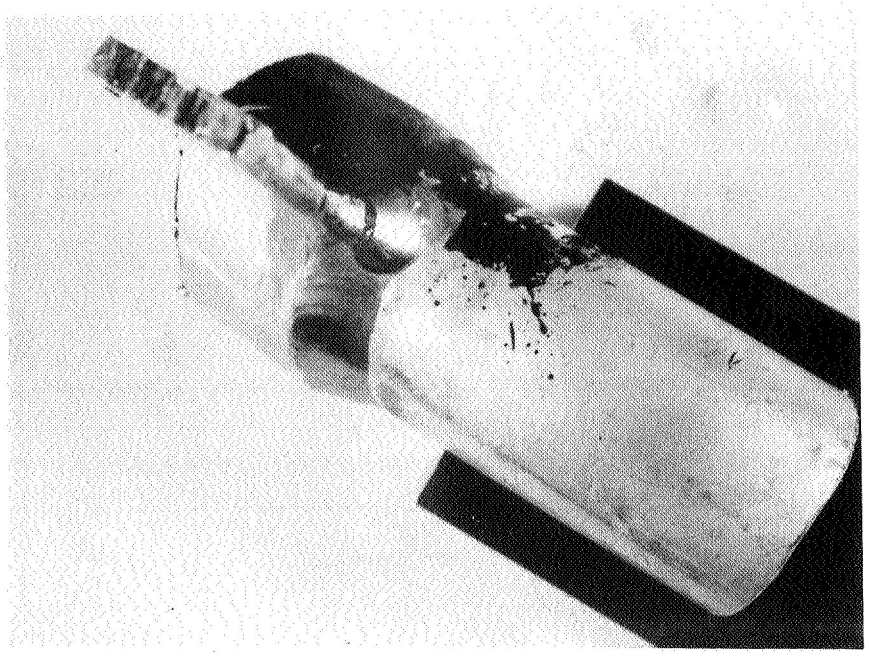


Figure 9. Weld Joint Sample with Crack

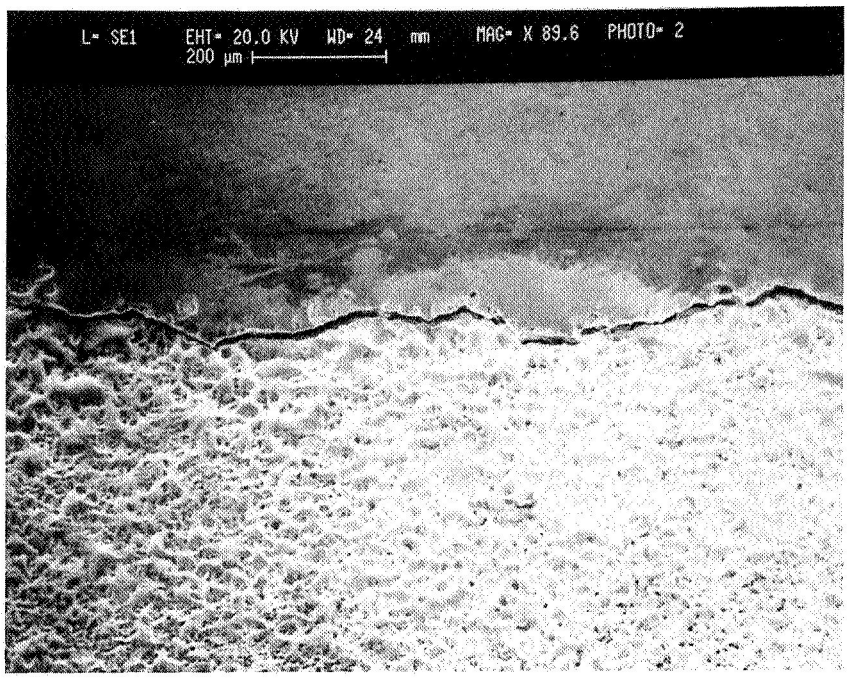


Figure 10. Crack Propagation along the Weld Joint

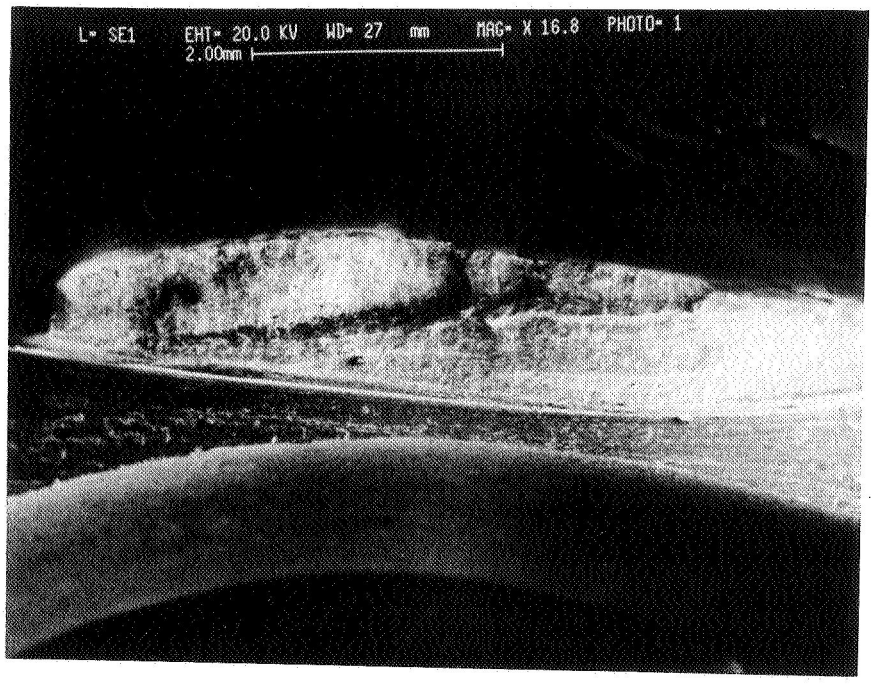


Figure 11. Width of the Developed Crack

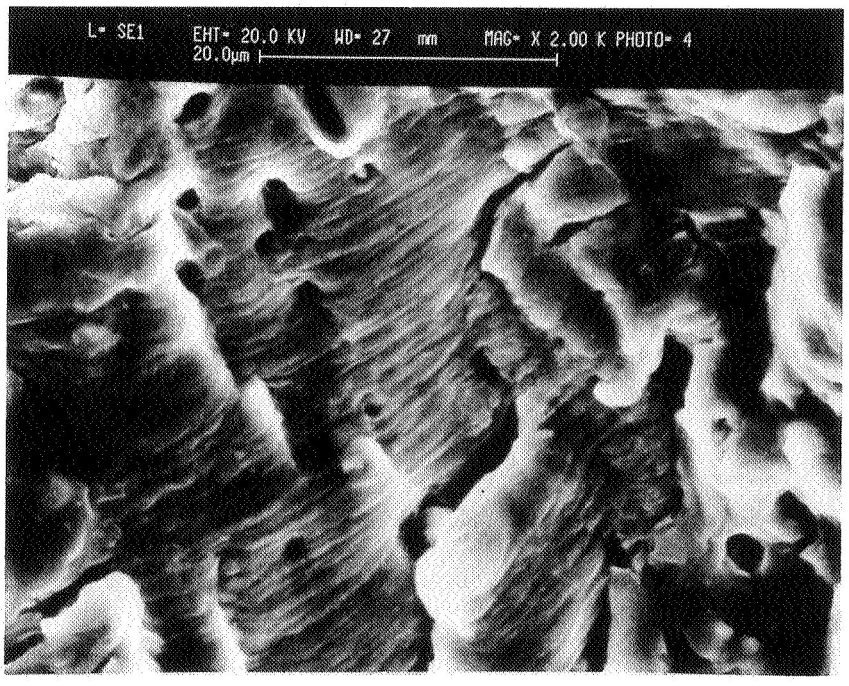


Figure 12. Accumulated Effects of the Fatigue Cycles

532-25
021474

GRAPHIC THREE-AXES PRESENTATION OF RESIDUAL GAS ANALYZER DATA

Kenneth R. Johnson, Jet Propulsion Laboratory, California Institute of Technology
Alejandro G. Levi, OAO Corporation

269605

ABSTRACT

Residual gas analyzers (RGA) are commonly used to measure the composition of residual gases in thermal-vacuum test chambers. Measurements from RGA's are often used to identify and quantify outgassing contaminants from a test article during thermal-vacuum testing. RGA data is typically displayed as snapshots in time, showing instantaneous concentrations of ions from ionized residual gas molecules at different atomic masses. This ion concentration information can be interpreted to be representative of the composition of the residual gas in the chamber at the instant of analysis. Typically, test personnel are most interested in tracking the time history of changes in the composition of chamber residual gas to determine the relative cleanliness and the clean-up rate of the test article under vacuum. However, displays of instantaneous RGA data cannot provide test personnel with the preferred time history information. In order to gain an understanding of gas composition trends, a series of plots of individual data snapshots must be analyzed. This analysis is cumbersome and still does not provide a very satisfactory view of residual gas composition trends. A method was devised by the authors to present RGA data in a three-axis format, plotting Atomic Mass Unit (AMU), the Ionization Signal Response (ISR) as amps/torr as a function of AMU, and Time, to provide a clear graphic visualization of trends of changes in ISR with respect to time and AMU (representative of residual gas composition). This graphic visualization method provides a valuable analytical tool to interpret test article outgassing rates during thermal vacuum tests.

Raw RGA data was extracted from a series of delimited ASCII files and then converted to a data array in a spreadsheet. Consequently, using the 3-D plotting functionality provided by the spreadsheet program, 3-D plots were produced. After devising the data format conversion process, the authors began developing a program to provide real-time 3-D plotting of RGA data. The intent of this program is to automate the RGA data acquisition process and to generate up-to-the-minute time history 3-D displays of stored RGA data (development of this program was not complete at the time of this writing). This paper provides a brief description of the data format conversion process and presents results from a recent test to illustrate the usefulness of this 3-D RGA data plotting technique.

INTRODUCTION

An RGA is an instrument used in nearly every major thermal vacuum test that is conducted at the Jet Propulsion Laboratory (JPL) as well as at many other space simulation facilities. The RGA sensor, which is exposed to the chamber vacuum environment, ionizes some of the gas molecules in a sample, separates the resultant ions into their respective masses (or atomic mass units, AMU), and measures and displays the ISR at each mass. RGA data is used to track the residual gas composition in a vacuum chamber as a test progresses. Displayed RGA data provide the operations personnel important information which helps them to determine the effectiveness or completion of a bakeout of a test article, to detect the presence of a small leak in the chamber, or to assess the composition of molecular components which are outgassing from a test article during a test.

However, the RGA's which are used at JPL provide only sequential snapshots, one at a time, of the ISRs over a range of AMUs. Historically, JPL thermal-vacuum test operators have programmed the RGAs to print a copy of the display to collect printed ISRs data nominally once each hour. At the end of the test, there is a stack of computer paper presenting a series of plots which, while providing the desired residual gas composition data, yields the data in a format that is very cumbersome to interpret.

The RGA data presentation method described in this paper was developed at the Jet Propulsion Laboratory, California Institute of Technology, under a contract with the National Aeronautics and Space Administration.

The authors sought a better way to present RGA data so that interpretation would be made more convenient. As a result, the authors developed a method for presenting the RGA data in a format which would clearly illustrate the time rates of change of various constituents. In this paper, several 3-D plots are presented which show how this method can be used effectively to interpret outgassing responses to various test events. These plots have been generated from RGA data from a single bakeout test. Standard RGA printouts are also presented as a reference for comparison with 3-D plots containing the same data.

METHOD DESCRIPTION

The RGA system transmits its periodic sampling/analysis data from its sensor head to a computer where the transmitted signals are read as a data set and are converted to a string of delimited ASCII-formatted values. For example, one such data set includes values for: 1) File Name; 2) File Time; 3) Total Pressure; 4) Emult; 5) Mode; 6) Scan; 7) Gain; 8) Width; 9) Center Mass; 10) the ISR for the first referenced AMU; 11) the ISR for the second referenced AMU; etc. The RGA software uses these values to display the data in a variety of formats on the computer's monitor screen. One of these data displays shows ISR as a function of AMU.

The RGA software also has a data storage function which saves data sets as a series of sequential ASCII files. When a test has been completed, data is extracted from the series of ASCII files and is converted into a data array from which 3-D plotting functions are used to generate 3-D plots. This simple technique yields dramatic results as will be seen in the figures presented in the example below.

EXAMPLE ILLUSTRATING USE OF THE 3-D RGA DATA PLOTTING METHOD

Figures 1, 2, and 3 present three sequential hourly printouts in the ISR vs. AMU display format. These printouts are actual data taken from a test involving the bakeout of a material which was subsequently used as part of the sun shade for the test set-up for the Mars Pathfinder cruise stage solar thermal vacuum test (MPF-STV-1). Review of figures 1 and 2 reveals that there is an apparent significant difference between the ISR at 05:07 and that at 06:08 on 3/20/96. However, a review of figures 2 and 3 shows that between 06:08 and 07:08, the ISR returned to approximately the same values that were measured at 5:07. These hourly RGA data printouts do not provide an intuitive understanding of what may have happened during this two hour test period. For instance, perhaps the 7:08 data may have been caused by a temporary spurious RGA anomaly. Further information is needed to more fully understand this RGA data.

Figure 4 presents a plot of the temperature of the sun shade (blanket) material throughout the full duration of the test. A GN2 blower seal failure occurred at about 13:00 on 3/18 and the shroud heating was immediately stopped until the blower seal was fixed. By 06:30 on 3/19 the blower seal had been fixed and by 08:00 the bakeout temperature of 140°C was achieved. Temperature control at 140°C was stable until about 05:30 on 3/20 when the shroud temperature-controller high heat switch got stuck in the on position for no apparent reason. The operator on duty cycled the heater switch on and off several times until the high heat switch finally went off and the temperature-controller began to control shroud temperature properly once again. Since this bakeout test had been devised quickly, and since no flight hardware was involved, no overtemperature failsafe protection had been specified or installed. So, when the high heat switch got stuck in the on position, the temperature continued to rise quickly until the operator was successful in switching it off. It can be seen that at the time the 6:08 RGA data snapshot printout was taken, the shroud temperatures were near the high temperature point. Certainly then, the RGA data printout at 6:08 did give indications of actual residual gas compositions which were significantly different than those from data taken one hour earlier.

Figure 5 shows a 3-D plot of hourly RGA data taken over the entire duration of this test. This plot gives a complete overview of the various ISRs throughout the test. A review of the period following the pumpdown shows that the ISR indicative of water content (AMU=18) quickly drops to a low value. Also, the beginning of the bakeout is clearly evidenced by a water spike at about 08:00 on 3/19. The water content then recedes as the bakeout continues, until at about 05:30 on 3/20 another water spike appears. This additional water spike is a

point of interest and warrants a closer look. Since the data which generated this plot are available in an array in spreadsheet format, a smaller data sample, at this point of interest, may yield insights into details of the test at that time.

Figure 6 shows a 3-D plot of hourly RGA data taken over the morning hours of 3/20. This plot very dramatically illustrates a series of steeple-like spikes occurring throughout the 1 to 200 AMU range during the 06:00 time period. This plot also gives the viewer a good general understanding of the effect that the overtemperature condition had on the gas composition inside the chamber.

Figure 7 is a plot of yet a smaller data sample. The figure 7 plot shows data from the same time period as that in figure 6, but only for mass values in the 1 to 100 AMU range. The figure 8 plot stretches out the detail of figure 6 to present the viewer with a more detailed zoom of the lower mass range. Likewise, figure 8 shows a detailed zoom of the 100-150 AMU range for the same time period as figure 6. However, the mass composition scale in figure 8 is different than that of figure 6, providing the viewer even additional insight into the outgassing of the higher AMU constituents during the overtemperature period.

GRANULARITY OF RGA DATA

The RGA software JPL uses to acquire and display RGA data provides for scan rates as frequent as once every 20 seconds or as slow as once every 2 minutes. The slower scan rates tend to yield a better, more accurate sampling throughout the scanned AMU range. The data storage rates can be set at a maximum frequency of once each scan to some lower frequency. By selecting a more frequent data storage rate, RGA plots with finer time scale granularity can be generated. The RGA software that JPL uses allows up to 999 separate ASCII files (data sets) to be stored per each DOS data file name. If the operator wishes to change the data storage rate, he may do so anytime during the test. However, to extend the number of data sets beyond 999, the operator must stop the data storage function temporarily, create a new and unique data file name, then proceed loading data into ASCII files under this new file name. Each separate data file group can then can be analyzed separately with the 3-D plotting function.

CONCLUSIONS

A method for the presentation of RGA in a useful 3-D format has been devised and has been demonstrated to be helpful in easing the interpretation of RGA data. The authors are developing a method to automate the generation of real-time 3-D RGA data plots for display on a monitor screen. This method will provide operators and test personnel a much better tool than is now available for the display and analysis of RGA data trends. It is the authors' intent to have this automated system operating in 1997.

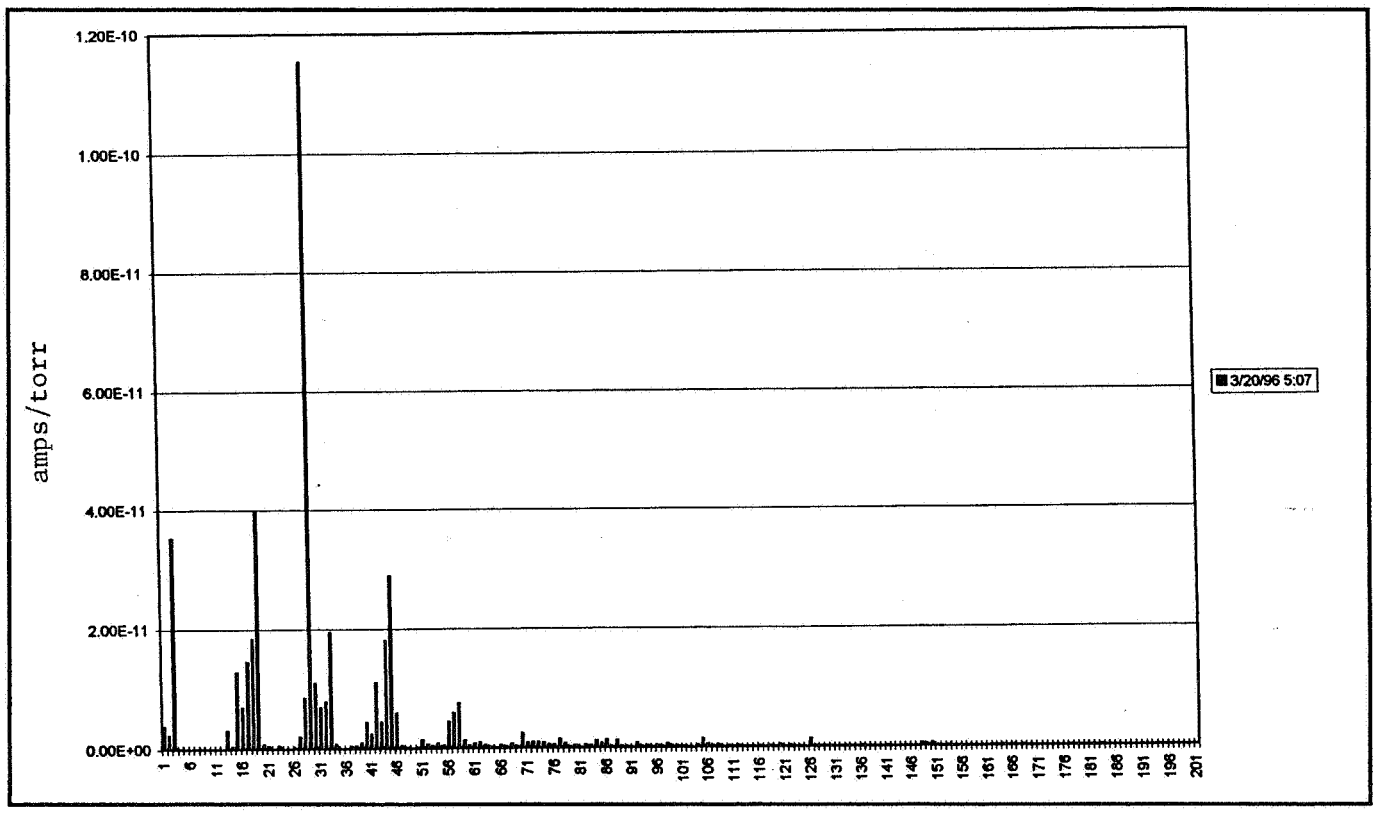


Figure 1. Standard RGA Plot made at 05:07 on 3/20/96

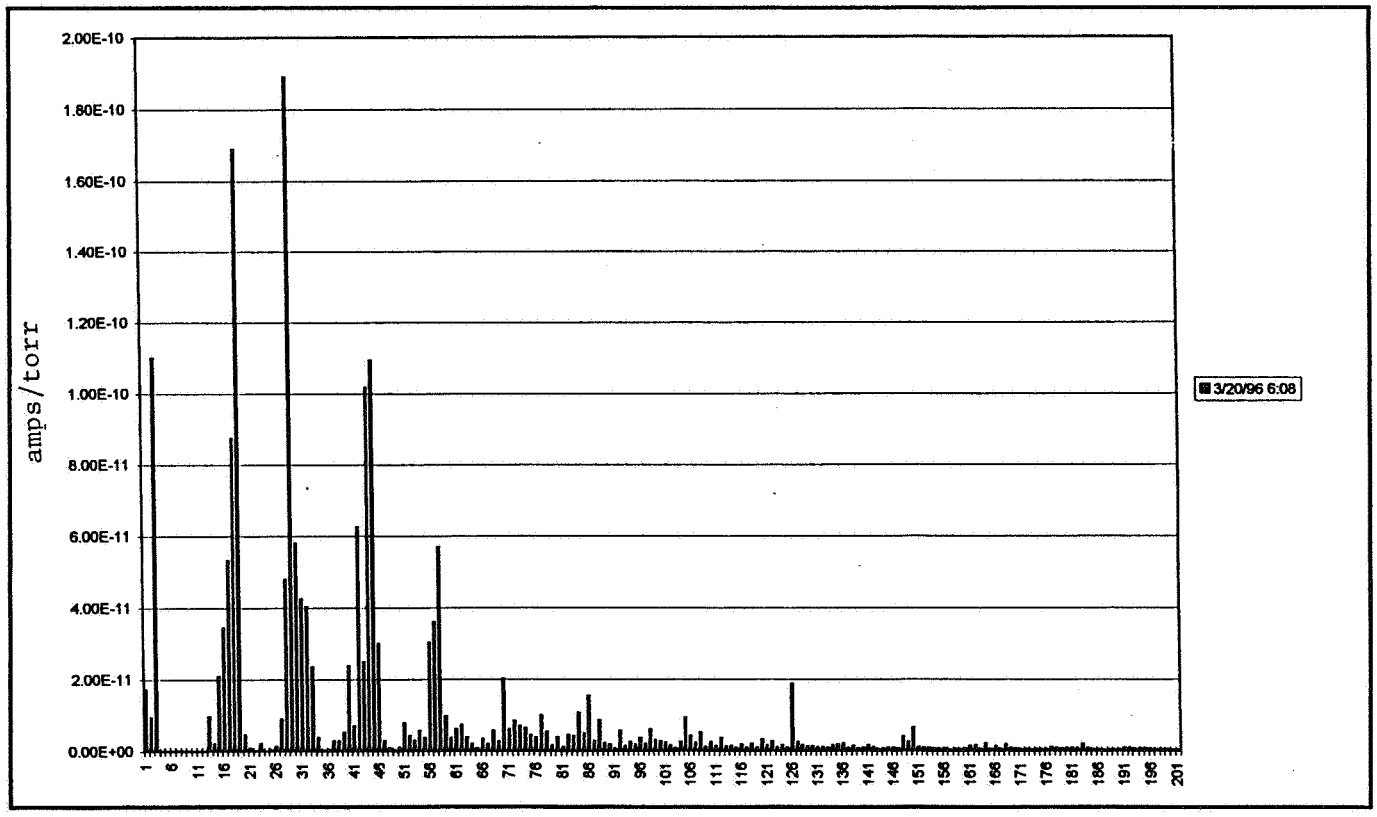


Figure 2. Standard RGA Plot made at 06:08 on 3/20/96

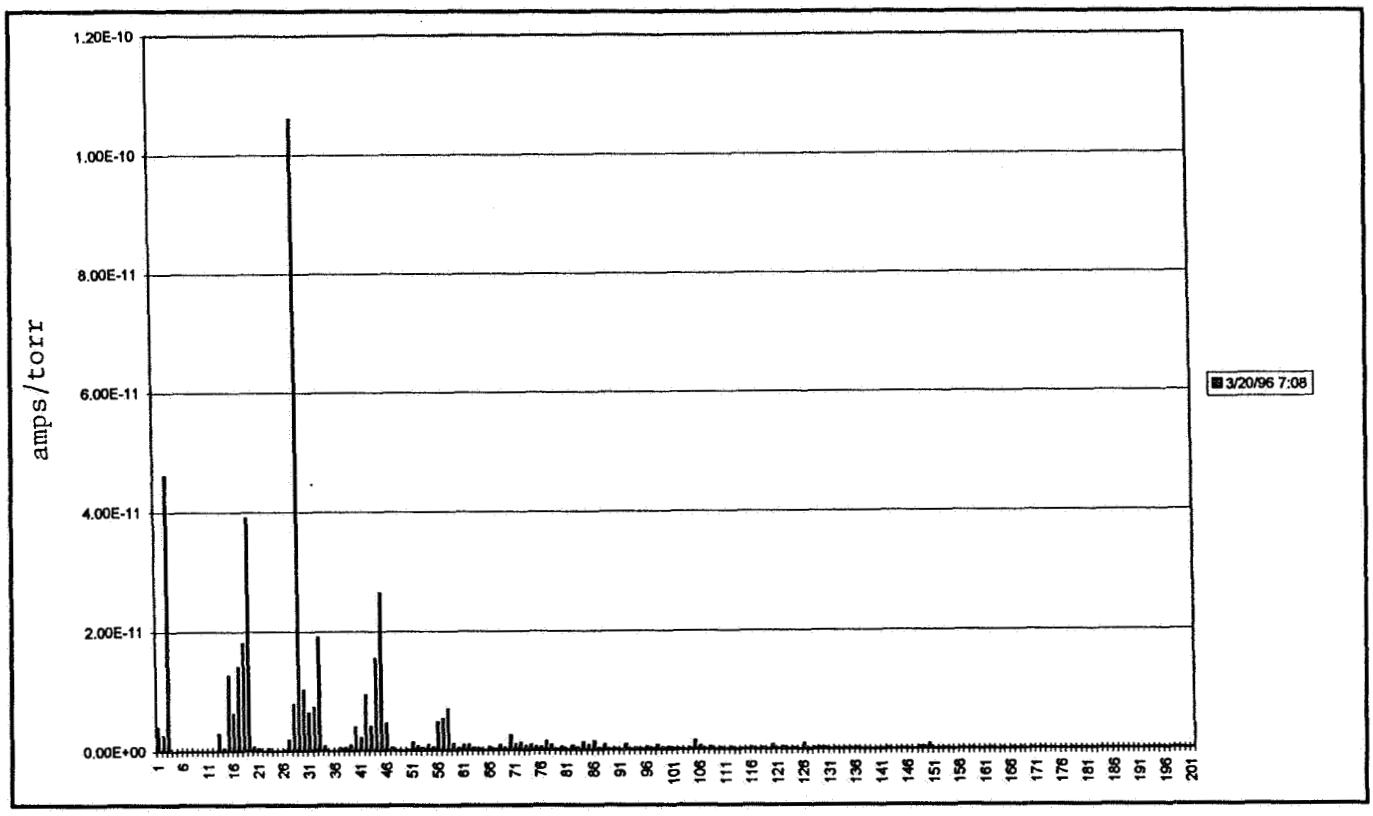


Figure 3. Standard RGA Plot made at 07:08 on 3/20/96

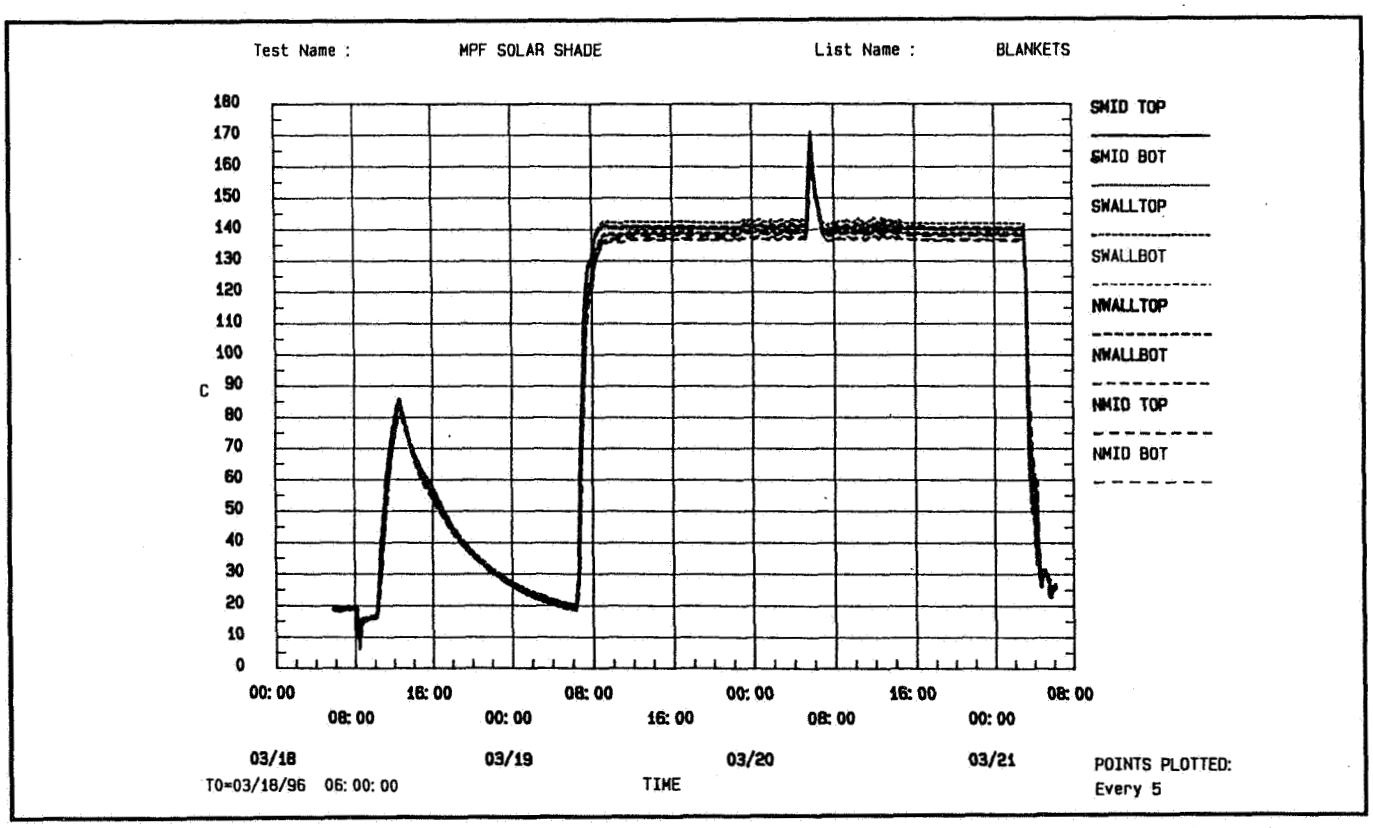


Figure 4. Plot of the Sunshade Material Temperature Throughout the Full Duration of the Sunshade Bakeout Test

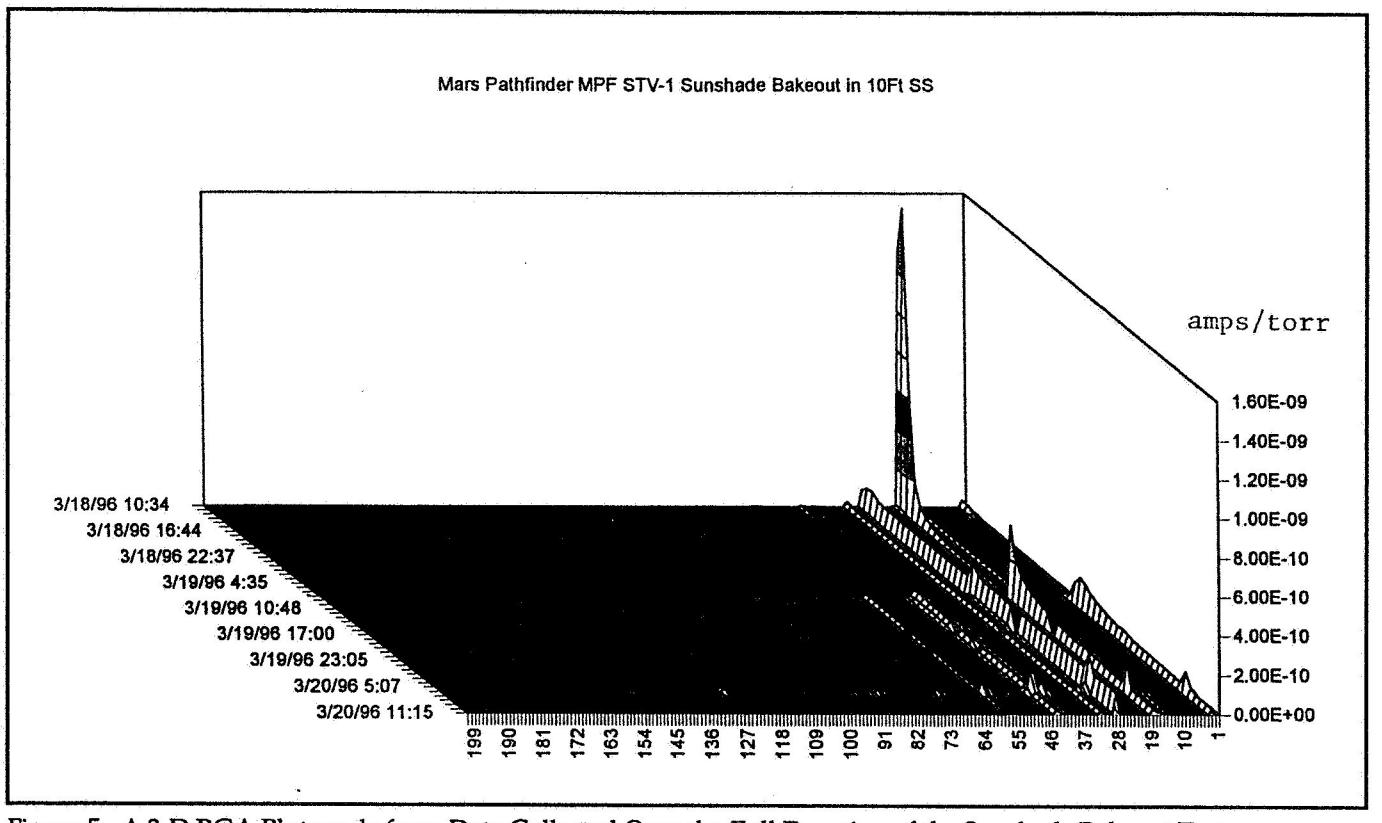


Figure 5. A 3-D RGA Plot made from Data Collected Over the Full Duration of the Sunshade Bakeout Test

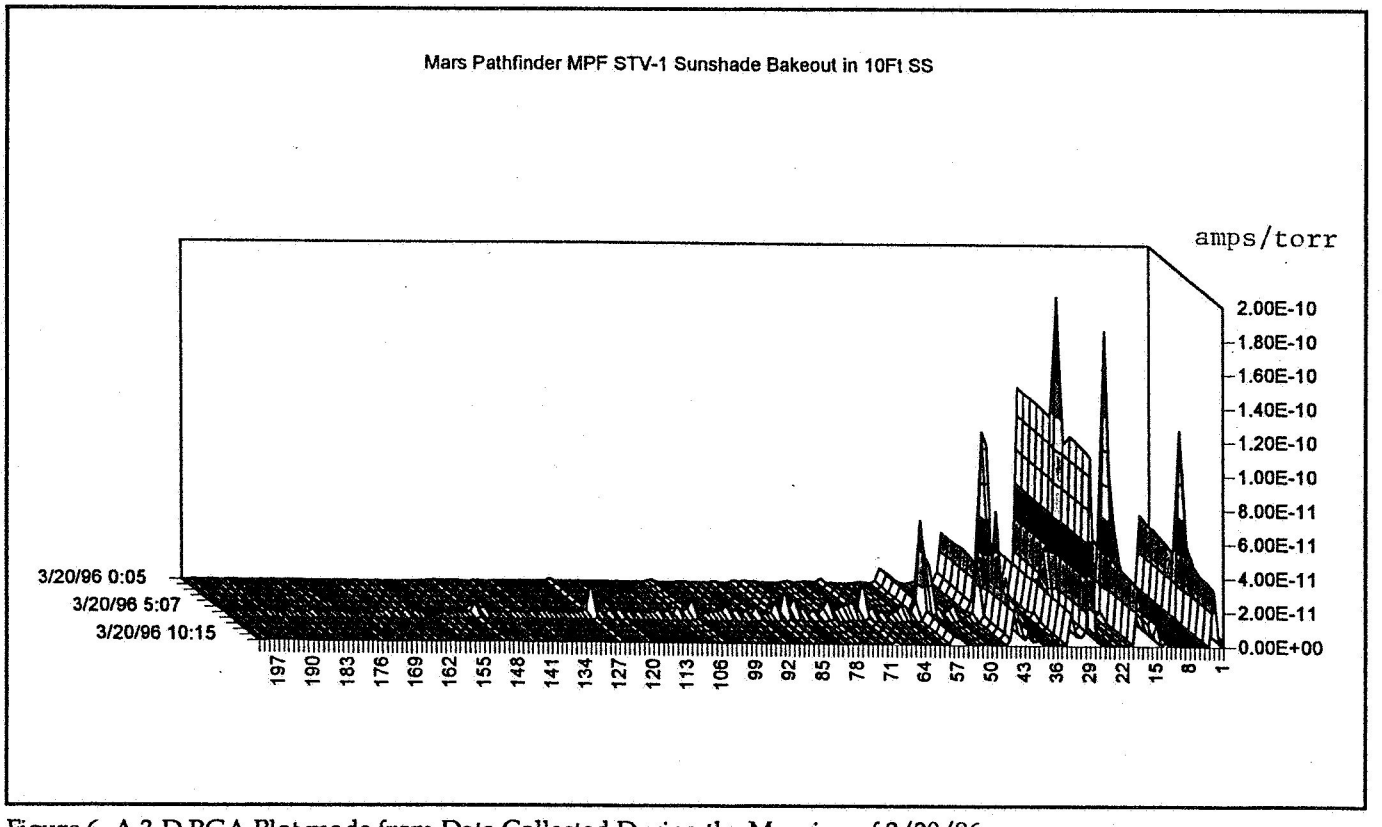


Figure 6. A 3-D RGA Plot made from Data Collected During the Morning of 3/20/96

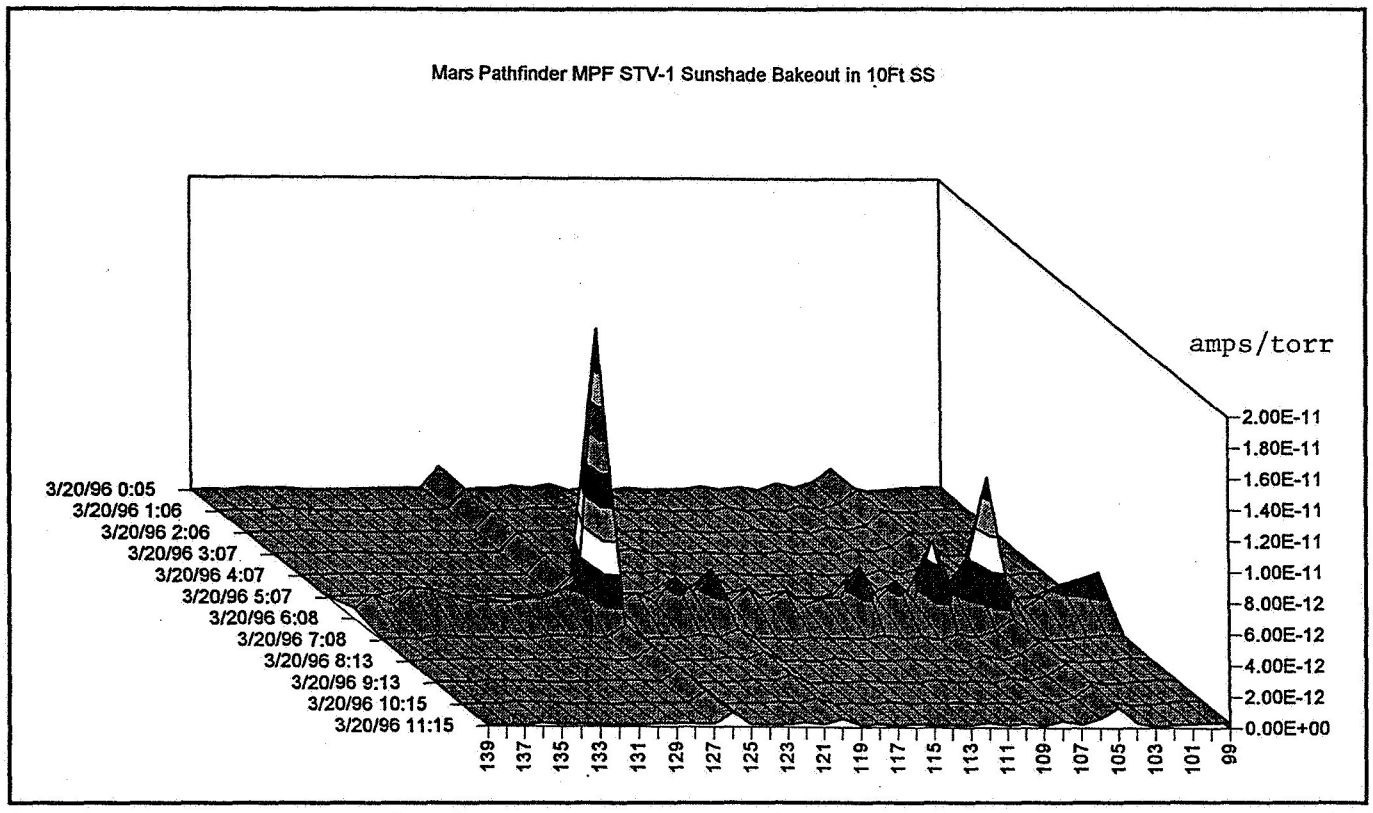


Figure 7. A 3-D RGA Plot made from Data Collected During the Morning of 3/20/96; 1-100 AMU Range

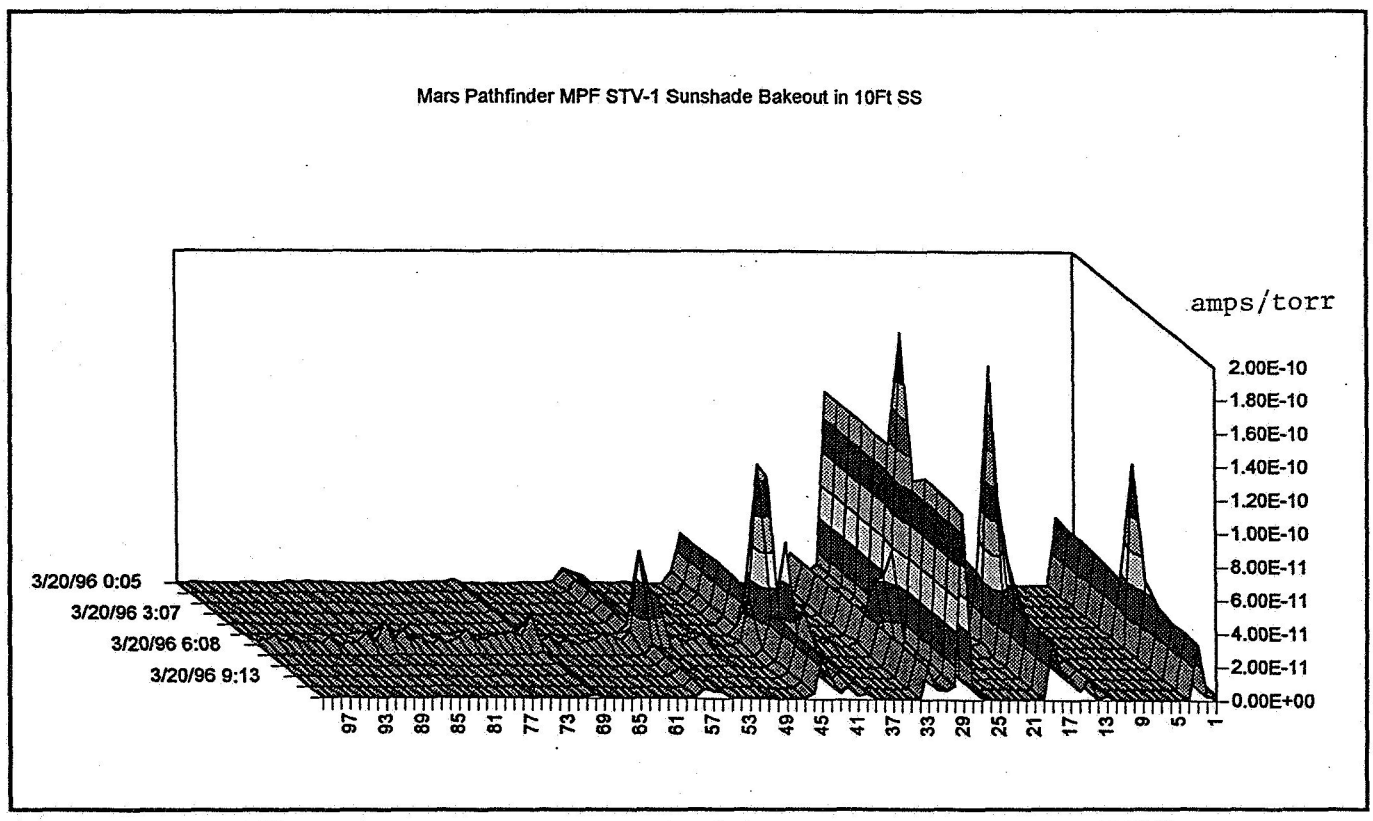


Figure 8. A 3-D RGA Plot made from Data Collected During the Morning of 3/20/96; 100-150 AMU Range

New Generation Deployment Rigs for Solar Arrays

Aad P. Eggers and Robin Kaal
Henk J. Cruijssen
Roderik F. Kolthof

Fokker Space B.V.
Leiden, The Netherlands

S33-14
021475
BP
269615

ABSTRACT

A solar array deployment rig is used to simulate the space zero gravity conditions for ground testing and integration purposes (see figure 1). The quality of the rig is determined by its ability to minimize disturbance forces (static and dynamic) which cause deviation from the space zero gravity environment. These disturbance forces are:

- Weight components acting along the path of the trolley movements
- Friction forces (static and dynamic) from trolley wheels
- Forces resulting from the trolley accelerations (added mass)
- Forces resulting from stiffness and weight of air supply hoses (air bearing trolleys only)

In the conventional deployment rig, which uses wheels with low-friction ball bearings the disturbance forces are dominated by the friction (static and dynamic) in the wheels. Moreover the lubricants of the low-friction ball bearings are sensitive for pollution and aging. Consequently the ball bearings require a lot of maintenance.

At this moment a new generation deployment rig is in use and partially still under development at Fokker Space. This rig uses air-bearings to solve the friction and maintenance problems.

New developments are: an air bearing trolley for partial deployment and an improved air supply system to reduce the disturbance forces introduced by the air supply hoses.

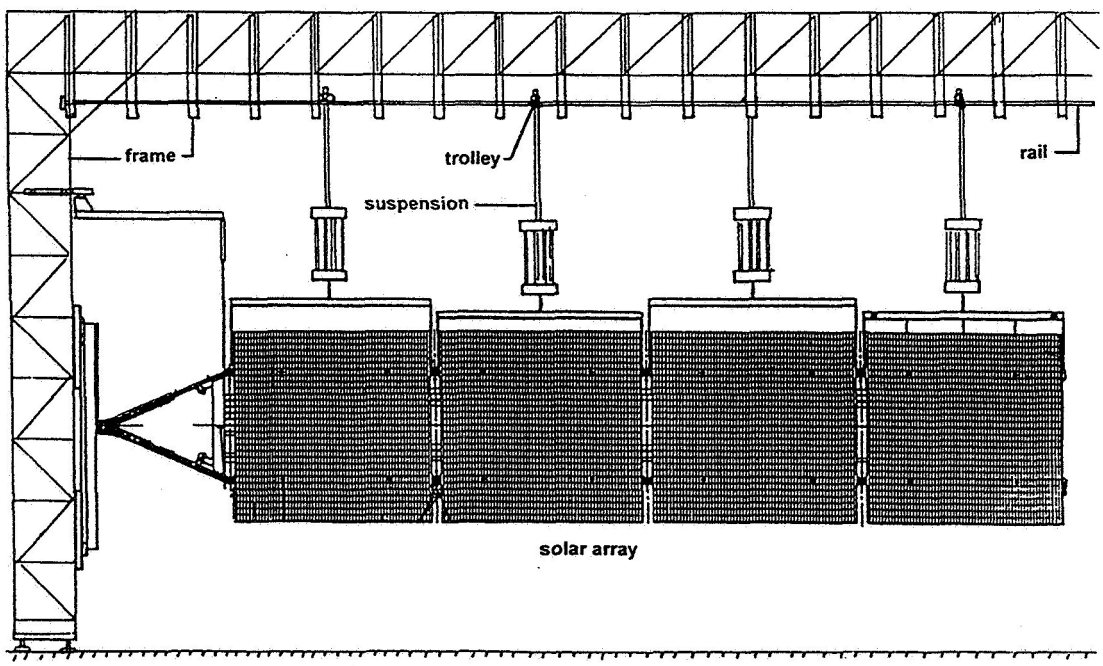


Figure 1: Deployment rig overall view

INTRODUCTION

At Fokker Space the need for deployment rigs exists since Fokker started building rigged solar panel arrays, some 20 years ago. The original design as made by Dick van der Vegt and Jan Webber (see figure 2) has been used ever since, with only minor changes.

A solar array deployment rig is used for support of a solar array in a simulated zero gravity environment. Its purpose is to allow integration, deployment and test of the solar array while the influence of the gravitation forces and gravitation induced forces is reduced to a minimum.

As the power demand on solar arrays becomes larger, the required panel size and size of the complete array grows. Larger solar arrays means that both the length of the arms on which the disturbance forces act and the disturbances forces themselves increase.

Low disturbance torque's are needed because the results of the tests have to be correlated with the mathematical models of the arrays (e.g. the deployment shock model and the deployed stiffness model). As a rule of thumb, the disturbance torque's should be smaller then 10% of the hinge drive torque's.

Another disadvantage of the conventional deployment rig is the amount of maintenance required to keep the disturbance forces generated by the trolleys reasonably low. This is caused by degradation of the ball bearings in the trolley wheels.

The increased disturbance torque's and the amount of maintenance required by the trolley bearings have led to the need of an improved trolley design.

The tests which are done in a deployment rig are:

- Deployment test (functional testing of release, locking, deployment time, etc.)
- Energy surplus test (measurement of the excess in torque of the deploy springs)
- Stiffness test (stiffness of deployed array in lateral directions as input for spacecraft attitude control)
- Deployment shock test (worst case latch-up shock to test integrity of hinges and structures)
- Alignment test (deployed array alignment measurements for adjustments and checks on changes caused by environmental testing)

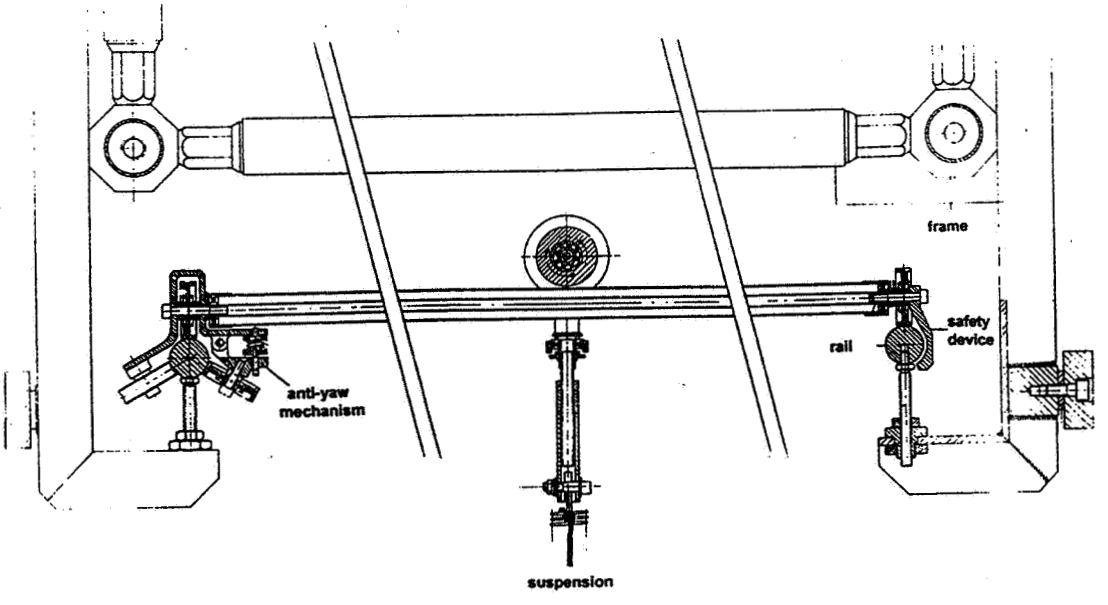


Figure 2: The conventional deployment rig trolley.

THE CONVENTIONAL DEPLOYMENT RIG

The conventional deployment rig as used by Fokker Space consists of two main parts: the deployment rig structure and the trolleys. The deployment rig structure consists of a steel frame which supports two "rails" (grinded rods) in such a way that they are parallel in a horizontal plane. The distance between both rails is 1m. The trolleys support the wing (one trolley per panel) and can travel along these rails. Each trolley consists of four sub-assemblies (see figure 2):

- a single wheel running on one rail with a safety device to prevent separation of the wheel from the rail
- a wheel assembly which runs on the other rail and contains four wheels. These four wheels fix the orientation of the trolley relative to the rails
- a round tube connecting these two parts. The tube can rotate about its axis to allow wiggling of the single wheel running on it
- a single wheel running on this tube; this wheel supports the panel and its suspension (spring and light weight yoke) and allows freedom of movement in between the rails

The wheels of the trolley are equipped with low friction ball bearings. These appeared to be very vulnerable and sensitive to pollution. Friction in the trolley wheels can be compensated for by tilting the complete rig structure. This only accounts for the dynamic friction of the wheels running on the two longitudinal rails and can not be used to compensate for static friction in these wheels or friction in the wheel running on the tube.

The dimension of the trolleys in the longitudinal direction of the rails is limited to the pitch of the solar array panels of the folded wing. This also limits the diameter and stiffness of the transverse tube. Tube deflection is an other source of disturbance forces in the transverse direction of the rig.

TOP LEVEL REQUIREMENTS

For the development of the new deployment rig the following set of top level requirements has been derived:

1. The functionality of the old rig shall at least be covered by the new design
2. The existing rig structure can be used with only minor modifications
3. The trolley disturbance force in the transverse direction of the rig shall be less then 0.01N at a trolley load of 100N (0.1‰)
4. The trolley disturbance force in the longitudinal direction of the rig shall be less then 0.1N at a trolley load of 100N (1‰)
5. The trolleys shall be light weighted to keep dynamic disturbance forces low
6. The deployment rig impact on the clean room environment shall be minimized
7. The maintenance required by the rig shall be minimized
8. The procurement costs of a trolley shall not exceed that of the conventional trolley

DESIGN OPTIONS

At Fokker Space quite some experience is available with the application of air-bearings in test facilities. This experience has been gathered during the design of the primary deployment rig for the OLYMPUS solar arrays and the development of the ERA Integration and Test Facility (EITF).

During the EITF development the first contacts were made with the Catholic University of Leuven (CUL), which eventually led to the design and production of the EITF air-bearings by the CUL. Because of the good cooperation of the CUL and Fokker Space it was obvious to consider the EITF air-bearings as candidates for the design options. The following design options have been evaluated:

1. Deployment rig with flat air-bearings as used in EITF
2. Deployment rig with cylindrical air-bearings (derivative of EITF air-bearings)
3. Flat floor with flat air-bearings as used in EITF
4. Flat ceiling with hanging air-bearings (new CUL development)
5. Water tank with submerged floats
6. Deployment rig with air-bearings which have an air supply through the rails
7. Deployment rig with magnetic bearings

TRADE OFF

It is beyond the scope of this paper to discuss the design options, only the results of the trade off in the form of a trade table are presented here.

Trade factors ⇒	*R 1*	*R 2*	*R 3*	*R 4*	*R 5*	*R 6*	*R 7*	*R 8*	*Total*
Weight ⇒	*5*	*5*	*4*	*4*	*2*	*3*	*5*	*4*	*score*
Deployment rig with flat air-bearings	+			+			+		46
Deployment rig with cylindrical air-bearings	+	+		+			+	+	55
Flat floor with flat air-bearings		-	+	+	+	-	+	+	43
Flat ceiling with hanging air-bearings	-	-		+			+		31
Water tank with submerged floats	-	-			-	-	+	+	26
Deployment rig with air- rails	-		-	+			+		32
Deployment rig with magnetic bearings	-				-	+		-	24

+ = 2; = 1; - = 0

NEW GENERATION DEPLOYMENT RIG

Trolley design (see figure 3)

In the design of the air bearing deployment rig, parts of the conventional rig design were copied to keep the cost of the development acceptable and the financial risk low. The trolleys were completely redesigned, while the rig structure remained unchanged. The main components of the new trolley are:

- the air-bearings
- the anti yaw mechanism
- the transversal rail of the trolley
- the aluminium alloy structural parts
- the air supply hoses

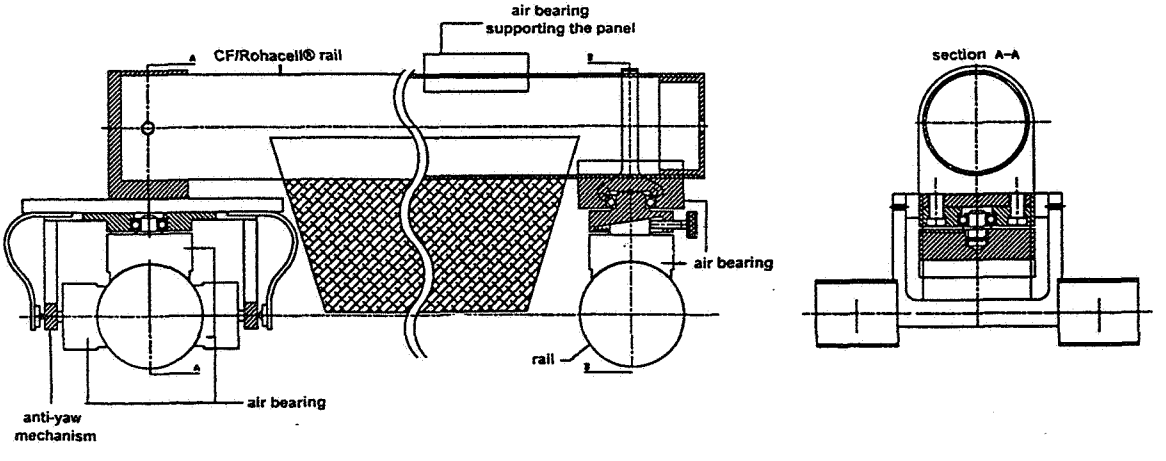


Figure 3: Trolley construction

The air-bearings are self aligning cylindrical pads with a conical air gap, as developed at the CUL. These have an improved stiffness and load capacity compared with bearings with a constant air-gap. Two bearing sizes are incorporated in the trolley design: 30 x 40 mm bearings to support the primary loads and 25 x 30 mm bearings to take the yaw loads resulting from trolley accelerations.

The anti yaw mechanism serves to counteract the torque's about the vertical, which are caused by the trolley acceleration when the trolley is pulled along with the panel, which it is supporting. The amount of torque depends on the acceleration, the trolley mass and the horizontal distance between the support point and the trolley center of gravity. The mechanism provides the pre-load on the anti yaw bearings and transfers the yaw torque from the trolley to one of the longitudinal rig rails.

The transversal rail forms a cylindrical support surface for the single bearing, from which the solar panel is suspended. The rail (see figure 4) is designed to be light weighted and yet have a very high bending stiffness in the vertical plane. This is crucial to the trolley design, because rail tilt is the main cause of disturbance forces, once friction is made negligible by the use of air-bearings. The stiffness is obtained by the use of a CFRP tube which is reinforced by a sandwich of CFRP face sheets and structural foam. The design process has been supported by a FEM model in which local deformations due to air-bearing loads have been investigated (see figure 5).

The brackets and rail end caps, which complete the trolley structure, are made of aluminum 7075 compound. Parts are bonded together with cold setting epoxy.

A special problem of the new trolley design is the air-supply to the trolleys. In the present design the air-supply hoses are the major remaining source of disturbance forces in the longitudinal direction of the rig. In the transversal direction a thin hose can be used, because only one bearing has to be fed. The hose which feeds the trolley has to be much longer and thicker, because it has to cover the complete trolley travel and has to feed all 7 air-bearings of a trolley.

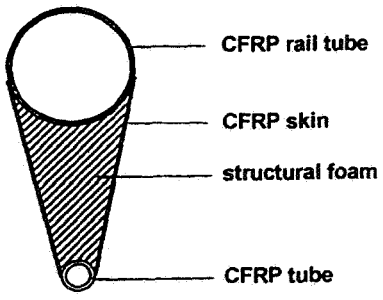


Figure 4: Transversal rail construction

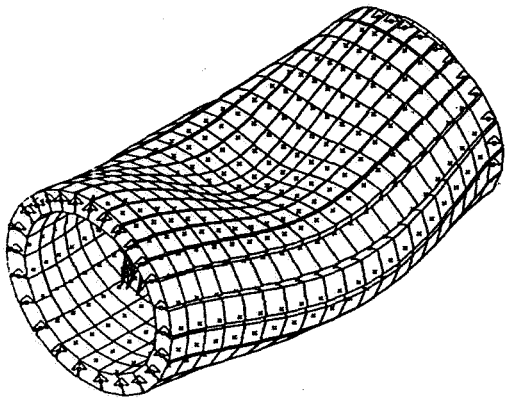


Figure 5: Transversal rail FEM model

Disturbance forces

The major design driver of the trolleys is to keep disturbance forces low. Disturbance forces are defined here as those forces which will not be present in the space zero gravity environment. Disturbance forces are considered to be caused by:

- Friction from the air-bearings (negligible)
- Weight, stiffness and hysteresis in the air supply hoses.
- Tilt of the plane through the longitudinal rails caused by rail deflection under panel and trolley loads.
- Tilt of trolley transversal rail about the rig longitudinal axis caused by rail deflection under the panel load.
- Tilt of trolley transversal rail about the rig longitudinal axis caused by an improper adjustment of the trolley.

In principal it is possible to compensate for the disturbance forces, caused by the weight of the air supply hoses, by applying position dependent tilt to the longitudinal rails. This will only work perfectly if all supply hoses are connected to the same supply manifold, all have the same length and all trolleys carry the same load.

Development approach of the new trolley

To reduce development risks the development was done in a number of steps. First a single bearing was made to test its behavior in conjunction with the existing grinded steel rails. After this had shown to work successfully a prototype trolley has been build to prove the concept feasibility. Finally a series of four trolleys was made to replace a complete set of conventional trolleys.

In the first development step the load capacity of the air bearings was tested and its ability to "ride over" the rail joints. The tests demonstrated the maximum load capacity of 250N of the 1200 mm^2 support bearing. It also showed that with the 100N nominal load the bearing could move over a rail joint without jamming.

In the second development step the functional performance of the prototype trolley has been tested and evaluated.
Test objectives were:

- Determination of disturbance forces from air supply hoses
- Determination of disturbance forces from deflections of the trolley structure
- Determination of trolley behavior at rail joints
- Determination of maintainability

The proper functioning of the anti yaw mechanism has been demonstrated, and the functioning of the whole system was checked out.

A problem appeared to be the rail joints. The air-bearing design has been changed to solve this problem. All findings and lessons learned of the integration and tests were incorporated and a retest was done successfully.

The tests demonstrated the feasibility of the trolley concept and consequently the last development step was taken. Besides the feasibility of the concept the testing revealed some areas for further developments. These possible developments are:

- a trolley for partial deployment of the first solar array panel based on air-bearings. This trolley allows the first panel suspension to move outside the boundary of the two rails (see figure 6 for the hybrid partial deployment trolley)
- a servo driven air-supply system to reduce the disturbance forces from the air supply hoses

Development of the partial deployment trolley

Since the first panel deploys in such a way that it needs more space in the direction perpendicular to the rails than presently available (approximately 1 m), a special trolley was designed. The center of gravity position of the solar panel, hanging on this trolley will be out of the plane in between the grinded rods during a part of the deployment sequence. This causes a tilt moment resulting in a force upwards on one of the trolley sides. A temporary solution for this problem was to use the anti yaw system of a conventional trolley to cope with these forces. The result is a hybrid system using conventional ball bearings in the direction of the grinded rods, and an air-bearing running over a 2m CFRP transversal rail, see figure 6

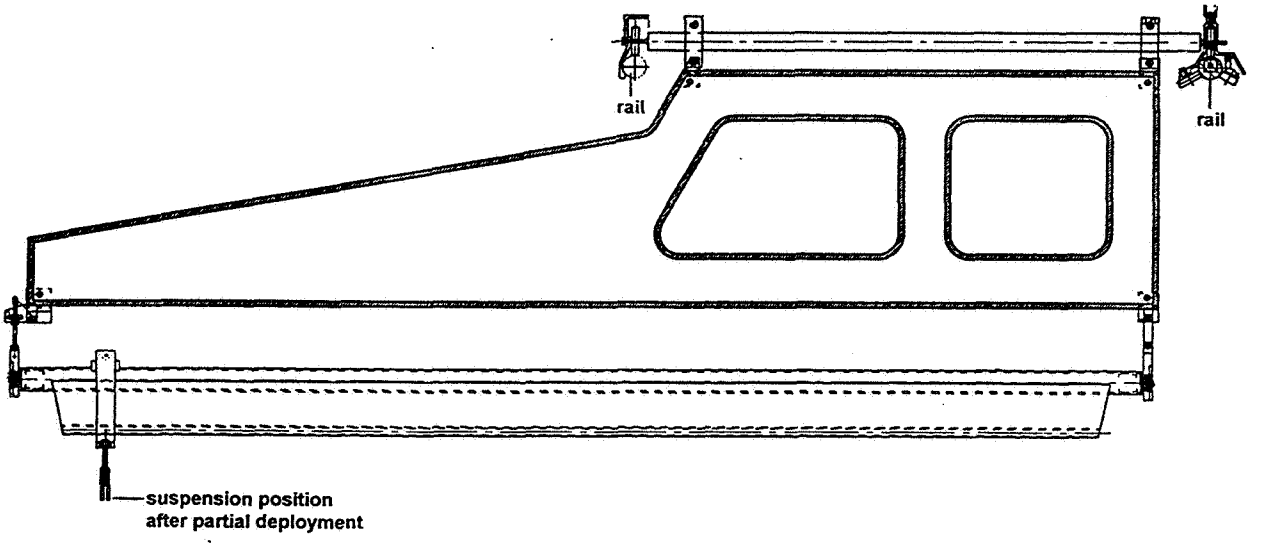


Figure 6: The partial deployment trolley

Actual use in solar array test programs

The air-bearing based, new generation deployment rig is now used in four deployment systems at Fokker Space and one at Matra Marconi Espace.

Properties of the deployment rig

- Mass trolley: 1.6 kg
- Measured disturbance force on proto-trolley
 - Transversal direction: < 0.08N over 0.8 m and < 0.01N over 0.05 m
 - Longitudinal direction: < 0.1N over 10 m rig compensated, < 0.3N without
- Maximum allowed weight on a trolley: 25 kg
- Air consumption: 0.150 Nm^3/min at 8 baro supply pressure
- Maintenance cleaning of rails before major test

Future developments

Now the partial deployment trolley has ball-bearings/wheels in the direction of the rails. These wheels have problems with the rail joints. Another problem is that the rig can not be adjusted for the disturbance forces introduced by the air supply hoses in the direction of the rails, since a hybrid solution is used here now.

A new design of the partial deployment trolley with only air-bearings is expected to be developed in the near future.

269616
S34-14
HRS ONLY
021476
VP

The GSFC 6-Axis Hydraulic Shaker System

Donald Hershfeld

A six degree of freedom, hydraulic shaker system has been installed in the vibration laboratory at Goddard Space Flight Center. This facility will be used to support research and development projects to investigate the feasibility of direct measurement of the multi-degree of freedom interface impedance matrix, the ability to control a multi-degree of freedom vibration environment and the effect of multi-degree of freedom testing on the response of aerospace structures. This paper will present the design characteristics of the shaker and demonstrate its operational performance.

S35-14
021477
14P
069617

Upgrade of a 10-foot Diameter by 15-foot Long Thermal Vacuum Chamber

Andrew T. Webb and Janet Sushon
MANTECH-NSI Technology Services Corporation
Goddard Space Flight Center

Leon McCrary
DynaVac Corporation

ABSTRACT

An extensive upgrade to a 10-foot diameter by 15-long thermal vacuum chamber located at Goddard Space Flight Center (GSFC) commenced in the fall of 1992 and was completed in the summer of 1995. The facility was completely dismantled removing three 35-inch diffusion pumps, other vacuum system components, the 200 horsepower thermal system blower, thermal shrouds, and all interconnecting piping. The intent of the upgrade was to replace the diffusion pumps with clean pumping and backfill systems, to install a new, efficient thermal system and shrouds, and to place the entire control system on a programmable logic controller. Many enhancements were made in the vacuum and thermal systems with provisions made into the design and the programming to provide the capability for any future automation task.

The entire vacuum system was designed and integrated using in-house personnel on a non-interfering basis to other flight related tasks. The thermal system was a competitively bid "turn-key" system. Preparation of a thorough specification, pre-bid conferences with vendors, and good communications with the turn-key contractor resulted in an efficient, flexible, and uniform thermal system. The control system, based on a distributed I/O programmable logic controller (PLC) system, was developed, installed, and programmed by in-house personnel for both the vacuum and the thermal systems.

Application of several different cleaning techniques, attention to cleanliness, pre-cured optical paint, and ability to operate the thermal system at 150°C resulted in the facility exceeding the GSFC contamination requirements by a factor of 10 within several days of bakeout and virtually eliminated any background contamination from the old diffusion pumps.

INTRODUCTION

In the Spring of 1992, NSI was commissioned with developing a preliminary design report (PDR) to define a complete refurbishment of a thermal vacuum chamber at GSFC known as Facility 225. This chamber was built in 1962 by Bethlehem Steel Corporation and was used in another building at GSFC. It originally had an off-axis solar simulator and a thermal system capable of dissipating 1.5 suns. The chamber was installed in building 7 at GSFC in 1988 and set up for use as a thermal vacuum test chamber in the Space Simulation Test Engineering section. There were many inherent problems with using the facility.

Increasing sensitivity of payloads to molecular hydrocarbon and silicone contamination was the primary reason for upgrading the vacuum system. The high vacuum pumping system consisted of three 35-inch diffusion pumps with liquid nitrogen (LN_2) cold traps above them but no main isolation valves. The diffusion pumps used Monsanto Company SantoVac 5 oil which is a low vapor pressure oil. Even with the LN_2 cold traps, the chamber's cold finger chromatography analyses always revealed the presence of this oil. The inherent danger of molecular contamination was a major deterrent for testing many payloads in this facility. An extreme example of this occurred early in 1991 when the shaft on the roots-type blower backing the diffusion pump broke sending an air pulse back through the diffusion pumps and spraying oil into the chamber.[1]

The primary reason for upgrading the thermal system was LN_2 consumption. The facility consumed liquid nitrogen (LN_2) at high rates to overcome the heat input to the recirculating gaseous nitrogen (GN_2) from the 200 horsepower canned blower. There was no need for heaters in this system. Another drawback was the need for LN_2 pumps that were not very operator friendly.

The facility was completely refurbished. The major improvements are listed below: 1) oil-free high vacuum pumping systems, 2) energy efficient thermal system, 3) gravity LN_2 flood system, 4) vacuum-jacketed (VJ) LN_2 supply and vent lines, 5) hinge for door, 6) cryogenic rotary unions for door thermal system piping, 7) vastly improved payload loading system, and 8) integrated PLC control system with many automation features included. Refer to figures 1 and 2 for pictorial representation of this facility.

VACUUM SYSTEM

Due to the nature of the funding for this task, all of the large vacuum components were procured during the summer of 1992. Most of the vendors selected in these procurements agreed to extend the warranty period such that it would not start until the installation of that component and would be good for one year after that time. These first procurements included: two (2) 35-inch cryopumps, two (2) 35-inch side actuated gate valves, one (1) 10-inch turbomolecular pump, one (1) 8-inch booster pump skid, and the vacuum instrumentation.

The design of the vacuum system occurred during the first year. The object was to create an efficient, high performance, vacuum system. This required introducing technologies new to the facilities at GSFC such as crossover to high vacuum using the turbomolecular pump, actively pumped electrical regeneration of the cryopumps, automatic regeneration of the cryopumps, refrigerated cold traps capable of probe temperatures down to -130°C, and more.

Design versus Actual Performance

The sizing of the vacuum system was completed during the PDR phase and was accomplished using theoretical and empirical equations. The equations were entered into spreadsheet format and the curve plotted. The pumping speeds for air were taken from manufacturers published data. Outgassing rates for the chamber materials and shroud materials were approximated using published and empirical data. Refer to Figure 3 for the theoretical versus actual evacuation rates for an "Unbaked" chamber.

The ultimate vacuum achieved in this chamber is on the 10^{-9} torr range when the shrouds are flooded following a 150°C bakeout. The normal unbaked operating pressure range is in the 10^{-7} torr range. The chamber was originally constructed utilizing flanges that sealed with indium. Due to the high cost of indium and availability of better metal sealed flange technology, many of the indium flanges were cut off and replaced with Conflat® style flanges.

Turbomolecular Pump Capabilities

The turbomolecular pump chosen was a heavy duty, horizontal, dual flow, 10-inch throat diameter, turbomolecular pump. The decision was reached in the early stages to procure a turbomolecular pump that was sturdy and could be used for more heavily contaminated payloads. The turbomolecular pump was procured with its own bakeout jacket for quicker cleanups following a test.

The turbomolecular pump was designed into the system for several purposes: 1) to provide helium and hydrogen pumping speed which is not supplied by the cryopumps, 2) to allow the turbopump to perform bakeouts on contaminated payloads and avoid pumping heavy molecular weight hydrocarbons into the cryopumps, 3) to allow clean pumping in the 10-2 torr range using a throttle plate, 4) to be used to crossover to high vacuum thereby increasing capacity in the cryopumps for test duration, and 5) to facilitate chamber leak testing prior to starting a test.

Helium gas, common to many payload tests in a thermal vacuum chamber, pumped by cryopumps will quickly saturate the activated charcoal second stage array (sail) of the cryopump. This occurrence will require the regeneration of the cryopump and possible delay of the test. The presence of a turbomolecular pump as an integral part of the high vacuum pumping system will compliment the cryopumps by actively pumping any helium or hydrogen present in the chamber.

Performing preliminary bakeouts of heavily contaminated payloads at higher chamber pressures (10^{-4} to 10^{-3} torr ranges) using the turbomolecular pump is just as effective at removing bulk condensable contamination as for performing them at lower pressures. Once the majority of these vapors have been released, the cryopumps can be brought on-line and the bakeout continues. This practice will add years to the life of the cryopump by not pumping the condensable, high

molecular weight vapors into the cryopump where they will condense and remain until the cryopump is dismantled and thoroughly cleaned or even replaced.

Crossover to high vacuum with cryopumps will use less than one percent of the cryopumps' theoretical capacity when following the manufacturers' recommendations for crossover mass. The probability is high, however, that during the crossover, when pressures in the cryopump suddenly rise, that heavier vapors normally cryopumped on the first stage array will contact the activated carbon on the second stage array. The potential problem is that heavy molecular weight vapors will not get sufficient energy during a bakeout to leave the activated carbon and will present a loss of air pumping speed over time.

Cryopump Regeneration Techniques / Automation

Large cryopumps release large quantities of water vapor during the regeneration process, especially when these pumps are used for component bakeouts. Traditional methods used on larger cryopumps utilize the "soup" technique where the cryopump vessel is backfilled to atmosphere and the internal pumping surfaces are warmed either with the purge gas or internal heaters or both. This allows the water and other vapors to become a mixture inside the vessel and coat all of the surfaces including the second stage array. This water vapor does not usually get enough energy to leave these sites. Therefore the next time the cryopump is cooled down, the water vapor freezes to the second stage array and reduces the pumps capacity for the lighter gases.

A technique used by manufacturers of smaller cryopumps for the semiconductor industry uses internal electric heaters for regeneration. Internal electrical regeneration entails the use of heaters attached to both the first stage and the second stage arrays. The heaters are controlled by separate thermocouples and control loops during regeneration.

The cryopumps purchased for this upgrade were specified to have heaters installed on the each array with separate controls for each array temperature. Precision micro metering valves were procured to establish a repeatable sweep purge rate. The automatic sequence (see figure 7 for the flow chart) was developed to regenerate one or more cryopumps by shutting off the LN_2, turning off the compressors, enabling both array heaters, starting a sweep purge, and starting the roughing system to pump on the cryopump vessel(s). In this fashion, the cryo sorbed gases and vapors are sublimed or released directly into the roughing system. The cryopump vessel is maintained with the sweep purge at 2 torr. The roughing system contains a refrigerated cold trap that operates at -130°C. This trap effectively cryopumps the evolved vapors and prevents these vapors from damaging the rotary vane vacuum pump. The cold trap also acts an efficient oil trap to prevent any potential backstreaming. The sweep purge dilutes the vapors, acts a ballast for the rotary vane pump, and keeps the pump at a good temperature for removing any vapors that might want to become trapped in the second stage of the rotary vane cycle. This regeneration technique is extremely effective. The rate or rise over a five minute period following this regeneration is less than 2 millitorr for a 35-inch cryopump. The typical acceptable rate of rise for a 35-inch cryopump is less than 15 millitorr per minute or 75 millitorr in 5 minutes.

In addition to this method of automatic regeneration, the cryopump may be put through a "soft" regeneration cycle. "Soft" regeneration is a technique used to quickly remove light gases from the sail and restore pumping capacity by maintaining the first stage (77°K) array cold, heating the second stage (12°K) array, and pumping the released gases away through a clean roughing system. This technique restores capacity for pumping light gases within an hour as opposed to 6 to 8 hours for a normal regeneration.

The use of internal electrical regeneration with sweep purging drastically improves the effectiveness of the regeneration and provides maximum capacity for high vacuum pumping during a test. In addition, crossover with the turbopump maintains full capacity in the cryopump for light gases.

THERMAL SYSTEM

Due to the nature of the modifications required to the chamber, differences in design approaches, and cost control measures, the thermal system was procured as a "turn-key" system. The only exception was that the control code would be written at GSFC while the contractor provided the control theory. The reason for this exception was for consistency in the control panels and control code. A thorough specification package was developed and competitively bid between several

different interested contractors. Some of the key items in this specification package were: 1) design the system and shrouds to dissipate 1.5 suns directed at the door shroud panel in the LN_2 flooded mode, 2) design the thermal system to operate at constant density using house pressure LN_2 (25 psig) for cooling (i.e. use heat exchanger), 3) design the shrouds for atmospheric boiling LN_2 for flooded mode operation, 4) design the shrouds for ease of installation and removal to facilitate cleaning operations, 5) provide a shroud installation/removal fixture, 6) hinge the chamber door and provide thermal system connections that do not require removal in order to open the door, 7) provide access to the chamber pumping header to facilitate working on the chamber, and 8) provide a vacuum jacketed LN_2 piping manifold and supply lines.

LN_2 and GN_2 Cooled Shroud

A new shroud was installed into the refurbished chamber capable of being cooled to LN_2 temperature with atmospheric boiling LN_2 or temperature controlled from -150°C to +150°C. The shroud was constructed of D-tube on sheet with rear end fully covered in a stepped chevron baffle for maximum conductance to the high vacuum pumps. The door shroud is attached to the hinged door and supplied thermal conditioning using a rotary cryogenic union. The D-tube, headers, and manifold sizes were selected to achieve the required operating parameters:

Operating temperature:	LN_2 temperature or -150°C to +150°C
Control of setpoint:	± 2°C or better over the full range
Shroud Uniformity:	± 2°C or better over the full range
Transition Rates:	from +20°C to +100°C within 2 hours (no load)
	from +20°C to -140°C within 4 hours (15 Kw load)
	from -140°C to +25°C within 5 hours (no load)

Gaseous Nitrogen Thermal System

Gaseous nitrogen (GN_2) is used as a heat transfer fluid to achieve the temperature control of the shroud. There are several major advantages for using GN_2 thermal conditioning systems for space simulation chambers. The most common factor is the elimination of potential contamination from other heat transfer fluids such as freons, oils, or brines.

A wide temperature range can be achieved; i.e., -150°C to +150°C as illustrated in figure 4. Ramp rates of -150°C/hour cooling and +80 to +110°C/hour heating were achieved. With a properly designed system, excellent temperature uniformity can be maintained as shown in figure 5.

Design Tradeoffs

To achieve the required temperature uniformity of ± 5°C and the temperature ramp rates of -40°C/hour cooling and 33°C/hour heating using recirculating GN_2, detailed calculations must be made for the required mass flow, the pressure drop through the entire system, and the heat transfer coefficient.

The blower must be designed or selected to achieve the required mass flow and static head required by the system design. If the mass flow is too low, the required temperature ramp rate can not be achieved. If the velocity of the gas in the tubes in the shroud is too low, the Reynolds number and the heat transfer coefficient will be too low to achieve sufficient heat transfer for the required temperature uniformity. If the velocity is too high, the pressure drop becomes greater than the blowers' static head.

Thermal System Operation

The circulating GN_2 is maintained at a constant density of 0.3 lb/ft^3 regardless of the system temperature. This provides a predictable, controllable heat transfer fluid. Without this constant density, heat transfer would be erratic and system control would be much more difficult. From -150°C to +150°C, the system pressure will vary over a range of 12 to 75 psig. Since nitrogen gas closely obeys the ideal gas law, one only needs to regulate the ratio of absolute temperature to absolute pressure in order to maintain a constant density (see equation (1) in the "Control" section). The pressure is automatically controlled, but is inherently stable since this is a closed system.

Blower Design

A new blower was designed to achieve the required mass flow, static pressure head, and low input power to the gas. The performance curves for the blower are shown in figure 6. The blower is a centrifugal impeller blower specially designed to minimize noise. The motor is totally enclosed in the GN_2 system. Unlike previous blowers of this type, the noise from this design is almost undetectable. In addition, the blower is very reliable since there are no mechanical shaft seals. Mechanical shaft seals have proven to be the weak link in previous centrifugal blower designs .

A variable frequency drive for the 20 hp motor was used to minimize the LN_2 consumption. When the system is being cooled or heated, the blower is operated at the full speed to maximize the temperature excursion rates. When the system is at a steady state temperature, the rpm and therefore the energy into the system from the heat of compression is decreased for efficiency and to minimize LN_2 consumption.

Liquid Nitrogen Heat Exchanger

A tube in shell heat exchanger was designed to achieve the required cool down rate of the shroud using the specifications for the mass flow of the blower and minimizing the pressure drop in the heat exchanger. The heat exchanger has more than sufficient capacity since the shroud was able to be cooled at a rate of -120°C/hour compared to the design criteria of -40°C/hour.

CONTROL SYSTEM

Facility 225 is the second thermal-vacuum chamber at GSFC with PLC-based control system. The first PLC-based control system was installed in 1988, and initially was to run a strictly discrete application. Its control function was later expanded to manage more elaborate control functions such as handling analog data, binary-coded decimal (BCD) signals, temperature sensors, and RS-232C interface.

Programmable Logic Controller (PLC)

The system consists of the Central Processing Unit (CPU) and (7) seven remote input/output (I/O) drops. This type of architecture allows the location of the I/O racks as close to the equipment it controls as possible thus limiting the lengths of control cables and the number of conductors in them. The remote I/O interface uses only a coaxial cable.

Thermal System Control

Traditionally, process controls at Goddard were left to pneumatic controllers/recorders. The PLC, however, has the capability to read analog signals from transducers, transmitters, and sensors and to return calculated values to actuators, heaters, as well as process on/off signals. Therefore, it was decided to create a complete feedback control loop using PLC as the controller.

There are two processes formally controlled by the pneumatic controllers that are now controlled by PLC: density and temperature controls. Density control is accomplished by two solenoid valves - supply and vent. Density is monitored by a shroud pressure transducer, which provides a 4-20 mAmp DC linear signal proportional to 0-200 PSIG. Pressure increase and decrease outputs are time proportional and calculated by PLC. Pressure setpoint is calculated using the following formula:

$$P=0.21*T+41.75 \quad \text{where: } T = \text{temperature (°C)} \qquad (1)$$

Temperature is controlled by two (2) analog outputs: heating output to silicon-controlled rectifier (SCR) and cooling output to a current to pressure (I/P) transducer that operates a proportional VJ control valve.

There was a concern that the PID algorithm will be executed too slowly due to the fact that PLC processor would have to spend the majority of its time scanning I/O's and executing discrete ladder logic instructions. This concern was overcome by the fact that the scan time for the CPU used in the system is in the milliseconds range. It became clear that at such scan rates any delay between control updates will be insignificant compared to the speed of the process. With the processor used, it is possible to utilize a timing utility which allows the user to choose fixed intervals at which the successive

proportional integral derivative (PID) calculations are performed. A uniform update time provides tighter control for the process.

Today, PLC-based PID loops are no longer considered a breakthrough. However, the results of our attempts to limit the overshoot and oscillations that inevitably follow a change in the temperature setpoint are worth mentioning. The system is able to maintain process variable within ±0.2°C (see figure 5). All PID parameters are generated by the ladder logic. The PID parameters loaded at the start of a transition allow for the fastest transitions and would normally cause a great deal of overshooting if they were the only parameters. However, as the process variable approaches setpoint, another set of PID parameters is loaded, which allows to reach steady state practically with no overshoot. At this point another set of parameters is loaded, which allows the system to reject great disturbances during steady state operation. The custom loop control strategy proved to handle setpoint changes and load disturbances very well.

Human-Machine Interface (HMI)

With equipment and instrumentation as complex as ours, it is important to provide the operators with a window into the process. Our colorgraphic system consists of a general purpose personal computer (PC) running a graphics program and communicating to the PLC via a high speed (2 megabits/sec) communication link. Following the principle of creating a truly integrated control system, we prepared a consistent operator interface for all system and process information. The system is expandable and upgradable and allows additional functionality to be added in the future. Currently all instrumentation data is collected and displayed on the screen with equipment status shown as well.

Automation Features and Future Capabilities

Certain subsystems are already automated. Cryopumps can be decontaminated by a single switch actuation. Currently remote control functions are being added to the system to ease our struggle for competitive advantage. Some control features, such as pumpdown and backfilling will be automated. The PLC can also be a partner in maintenance. It can provide traceable field device troubleshooting while linking it to on-line documentation improving manpower utilization, saving time and money. Maintenance documentation including mechanical assembly diagrams, internal stock numbers and locations, as well as the supplier part numbers can be displayed by the colorgraphic system.

Exactly what our laboratory will look like in the future is still anybody's guess. What is certain is that as long as it continues to automate, there will be a need for the PLC's real-time control capabilities in one form or another.

PAYLOAD LOADING SYSTEM

The method by which payloads were moved into this facility was extremely clumsy and time consuming. Facility 225 is a horizontally oriented test facility as depicted in figure 1 which requires that payloads be rolled into the chamber via a rail system and a moveable cart. The old loading system consisted of one set of permanent external rails that had tracks so that the door could roll back. A set of heavy rails then had to be craned on top of the permanent rail deck and secured with bolts. These rails mated to the rails inside the chamber and allowed the internal payload cart to be rolled out of the chamber. There were many drawbacks to this approach: 1) the door severely limited crane access for lifting payloads onto the internal cart, 2) the thermal system connections had to be disconnected every time the door was moved, 3) the external payload rails required two sets of crane operations every time the door was to be opened and closed, 4) the length of the payload was limited not by the length of the chamber but by access to the crane, and 5) the permanent external door occupied significant floor space.

The payload loading system was upgraded in two phases. The first phase was included in the "Turnkey" thermal system contract and consisted of hinging the door and utilizing rotary unions for the thermal system supply and return piping. The second phase consisted of removing the permanent external door rail system and fabricating an external payload cart with payload rails matching the internal chamber rails. The external payload was fabricated using the shroud removal cart (specified in the thermal system contract) as a base structure. The cart was reinforced for the increased loading. Air pads were used as the mechanism for moving the external cart to and away from the chamber. The external payload rail system was fabricated to sit inside the frame of the external cart so that they could be removed and the cart still function as the shroud removal fixture.

CONTAMINATION ISSUES

Contamination, especially molecular, was one of the reasons for this upgrade. The chamber was originally fitted with three 35-inch diffusion pumps without main isolation valves. There was an incident in 1991 where the shaft on the blower that was backing the diffusion pumps broke and sent a shock wave up through the diffusion pumps splashing oil all over the chamber. The bulk of the oil was cleaned then with the old shrouds still in place using Dipropylene glycol monoethyl ether[1].

One of the guide rules established for this upgrade was cleanliness. Following demolition, the chamber internal surfaces were thoroughly cleaned with a good surfactant, followed by steam cleaning, and finally with isopropyl alcohol wash. The chamber internal surfaces were again cleaned following all welding activities.

The shrouds are aluminum and are painted with IIT Research Institutes MH 2200 Optical Absorber Coating (formerly 3M ECP2200). MH 2200 is a high temperature optical coating with an optical absorption of 0.96 that requires curing in air at 202°C for four hours. This paint was chosen because it is a high temperature coating and has very low outgassing properties per NASA Reference Publication 1124, Revision 3[2]. Samples were obtained from the batch of paint procured for the shrouds and tested by William A. Campbell Jr., Code 313.2 GSFC, in accordance with ASTM E-595-90. The batch tested was well within NASA's guidelines for %TML, %CVCM, and %WVR.

The shrouds and all internal piping were thoroughly cleaned prior to installation into the chamber. After initial installation and fit check of the shrouds, the shrouds were removed and all internal surfaces were again cleaned. The first cleaning was steam, followed by three wipes using hexane. The final wipe down was using isopropyl alcohol. The shrouds were re-installed in the chamber and leak tested. A large LN_2 cooled scavenger plate was installed in the chamber. The chamber was evacuated using the roughing system and crossed over to high vacuum using the turbomolecular pump. The thermal system was operated for a period of five days at 150°C with the scavenger plate on and the turbomolecular pump as the high vacuum pump. The chamber was backfilled to atmosphere, the scavenger plate and cold finger contamination samples taken and then cleaned. The chamber was then operated at 150°C for two days without the scavenger plate when the TQCM counts went below the GSFC standard for 100°C. The temperature was lowered to 100°C for obtaining the acceptance data. The TQCM counts were less than 20 Hz/hour (a factor of 15 less than acceptance criteria at 100°C) and the cold finger residue mass had decreased by a factor of 20 when compared to the first bakeout. In addition, diffusion pump oil was in the analysis from the first bakeout. No presence of silicones or diffusion pump oils were found in the final cold finger sample.

CONCLUSIONS

The refurbishment was aimed at creating a clean, high vacuum, test facility, implementing PLC control, decreasing LN_2 consumption, and improving efficiency of manpower operations as well as utilities. All of these objectives were achieved while adding additional capabilities. For example, this facility is the only thermal vacuum facility at GSFC currently capable of operating internal payloads at +150°C. This factor alone can save several days off of a contaminated facility bakeout. Additional manpower savings were obtained by upgrading the payload loading system. This is also the only chamber at GSFC under complete PLC control. The implementation of future automation and remote operation tasks will also be a factor in cost reduction efforts currently in progress at GSFC now.

Many thousands of gallons of LN_2 are saved each test by having a more efficient thermal system designed and installed. Due to development of a new control algorythm on another facility at the GSFC, additional LN_2 savings may be able to be realized in the near future for this facility. Without the use of a PLC, such diversity in control techniques would not be possible.

This facility is the role model at the GSFC for other facilities when they undergo process improvements. Currently in development for this facility are some automation efforts aimed at simplifying the operation of the facility and reducing costs to projects for simple bakeouts.

REFERENCES

[1] Bond, William R., "Cleaning of a Thermal Vacuum Chamber with Shrouds in Place," 17th Space Simulation Conference, NASA CP-3181, 1992. (Session E: Thermal Vacuum Testing II).

[2] Campbell, Jr., W.A. and Scialdone, J.J., "Outgassing Data for Selecting Spacecraft Materials," NASA Reference Publication 1124, Revision 3, 1993. (Section 13, page 129 to 130).

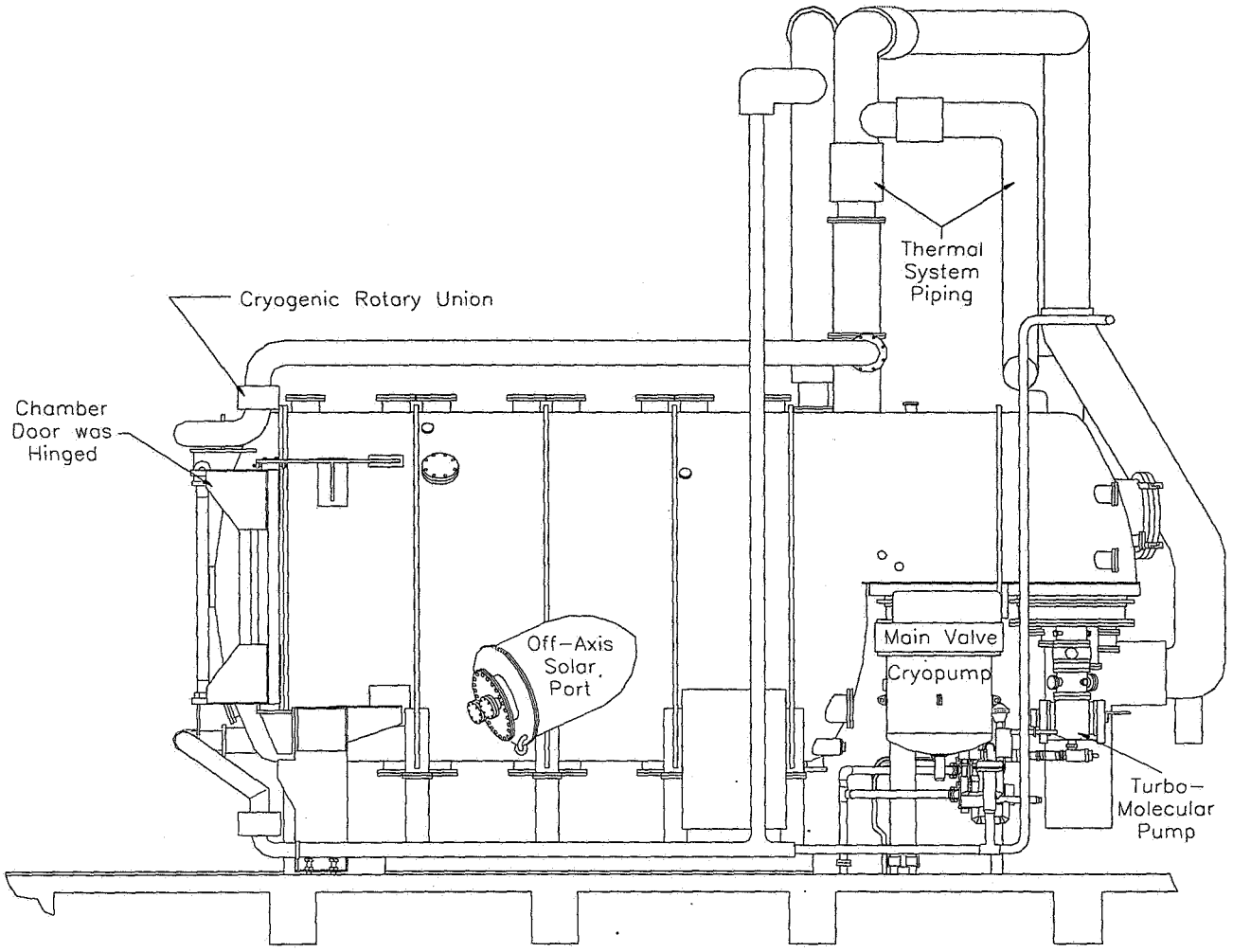


Figure 1: Facility 225 East Elevation

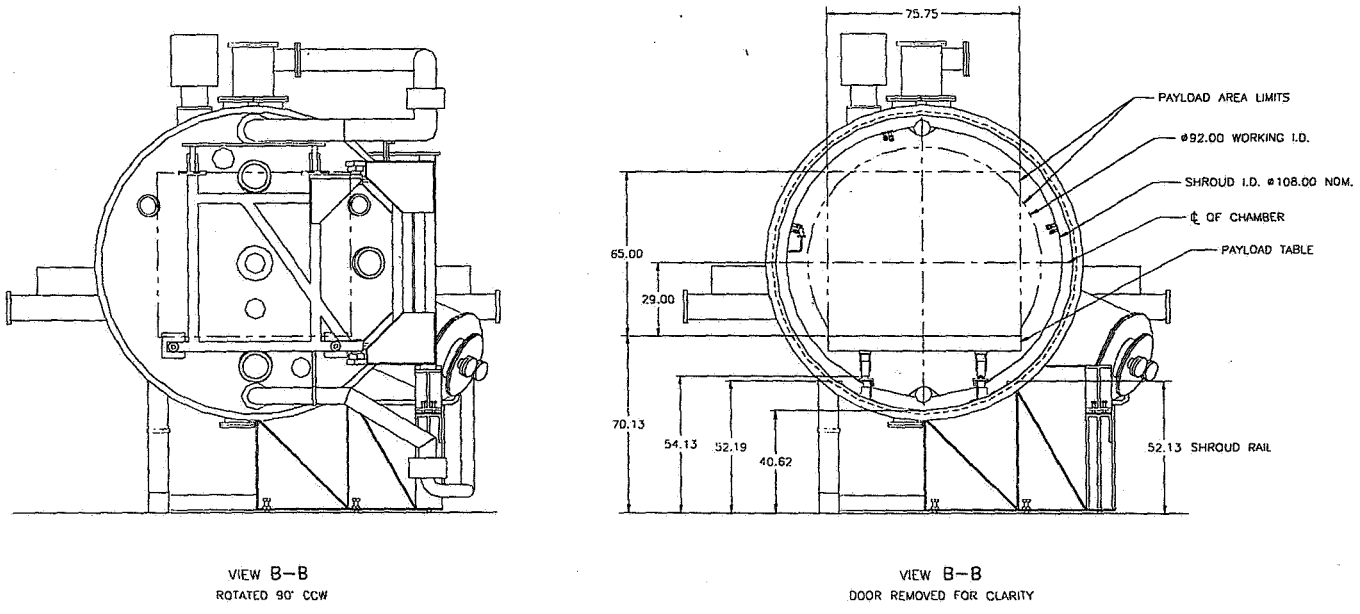


Figure 2: Facility 225 South Elevation

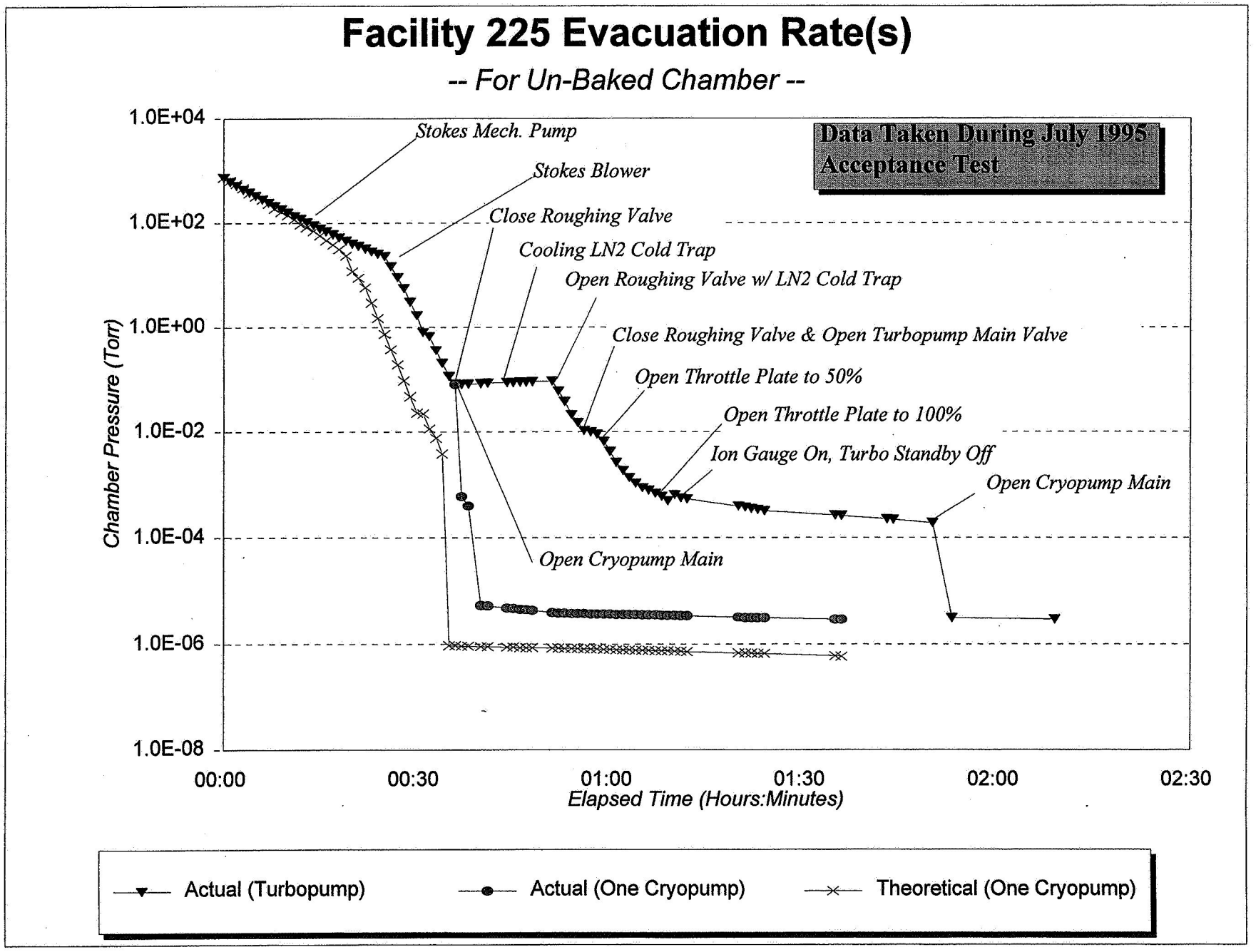


Figure 3: Theoretical versus Actual Vacuum System Performance

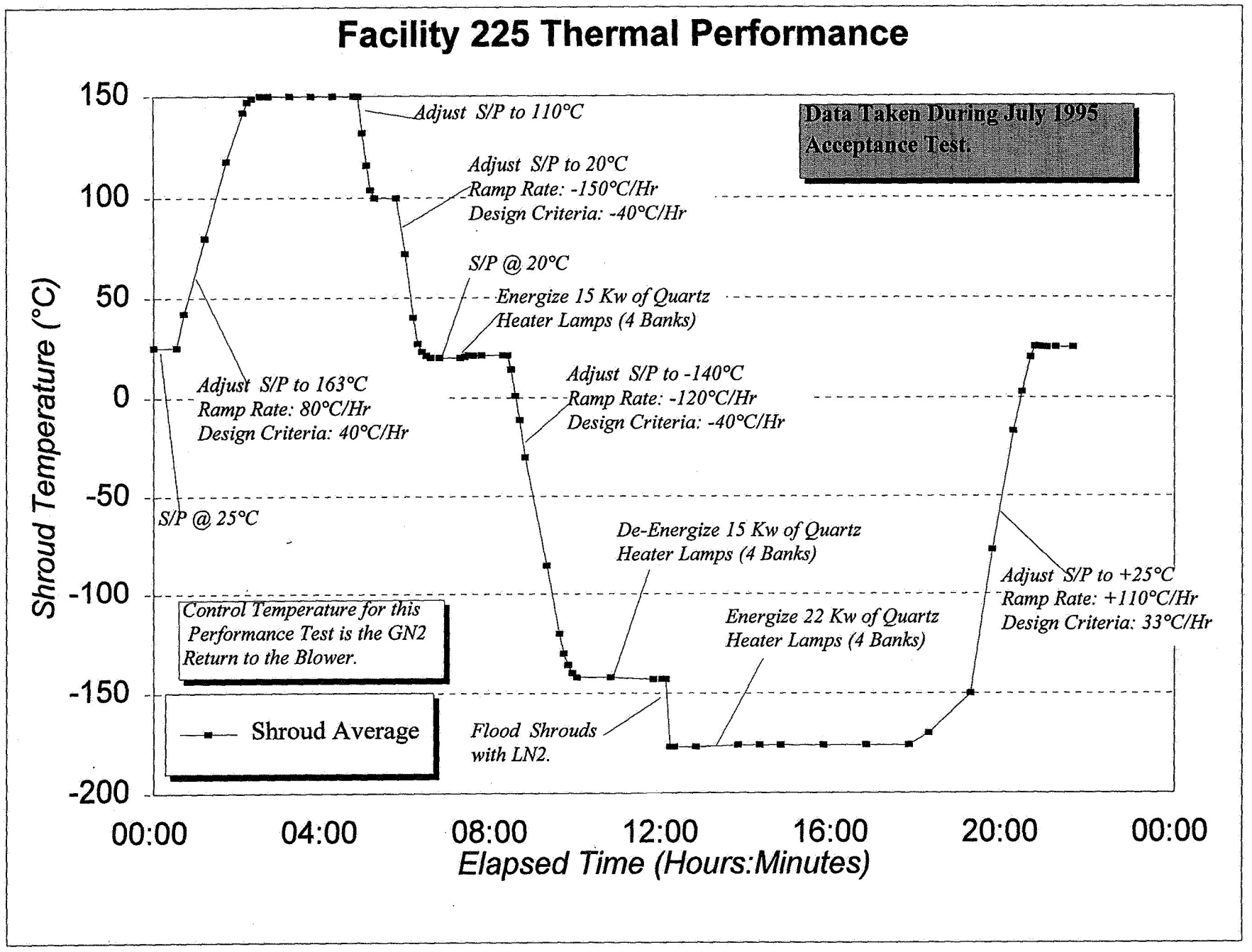


Figure 4: Thermal System Performance

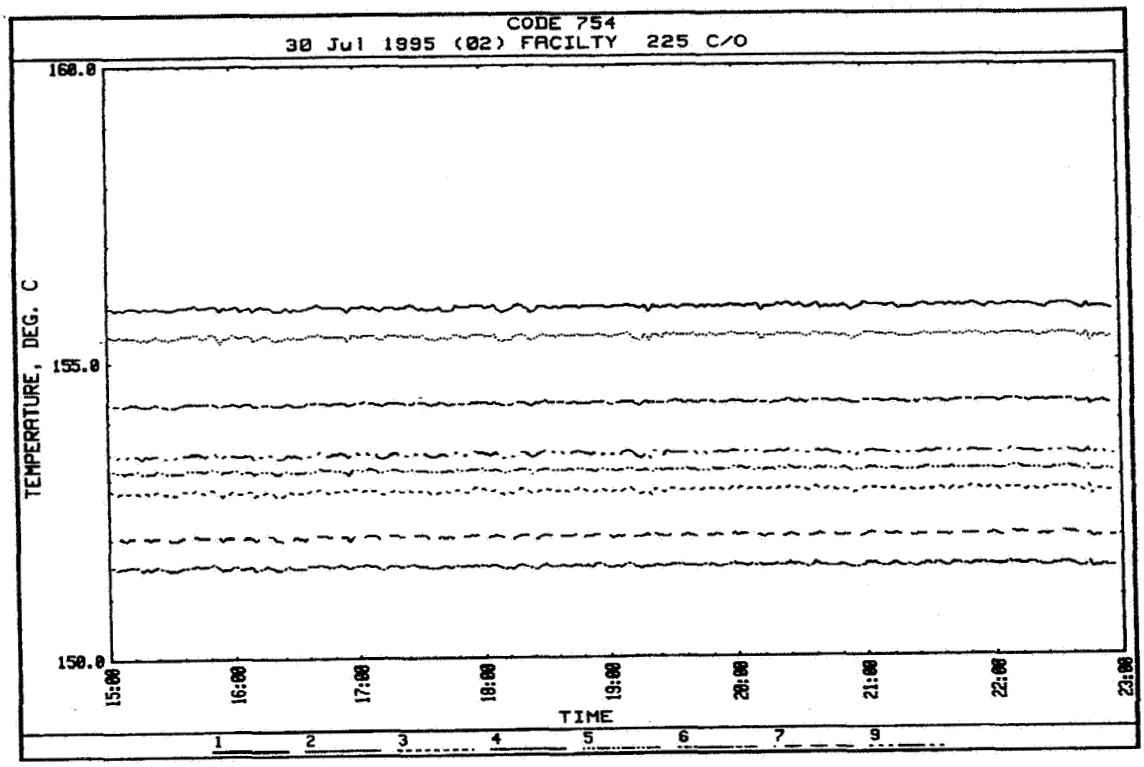


Figure 5: Thermal System Performance at 150°C

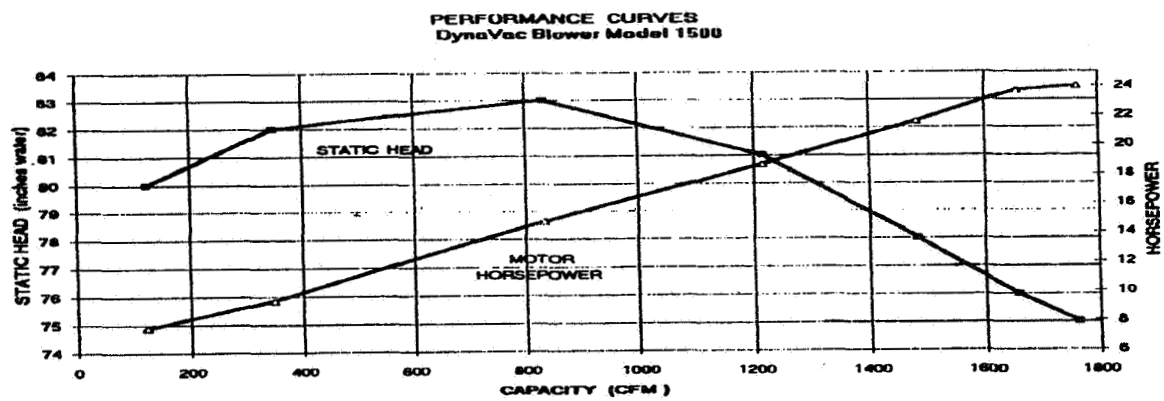


Figure 6: Blower Performance Curve

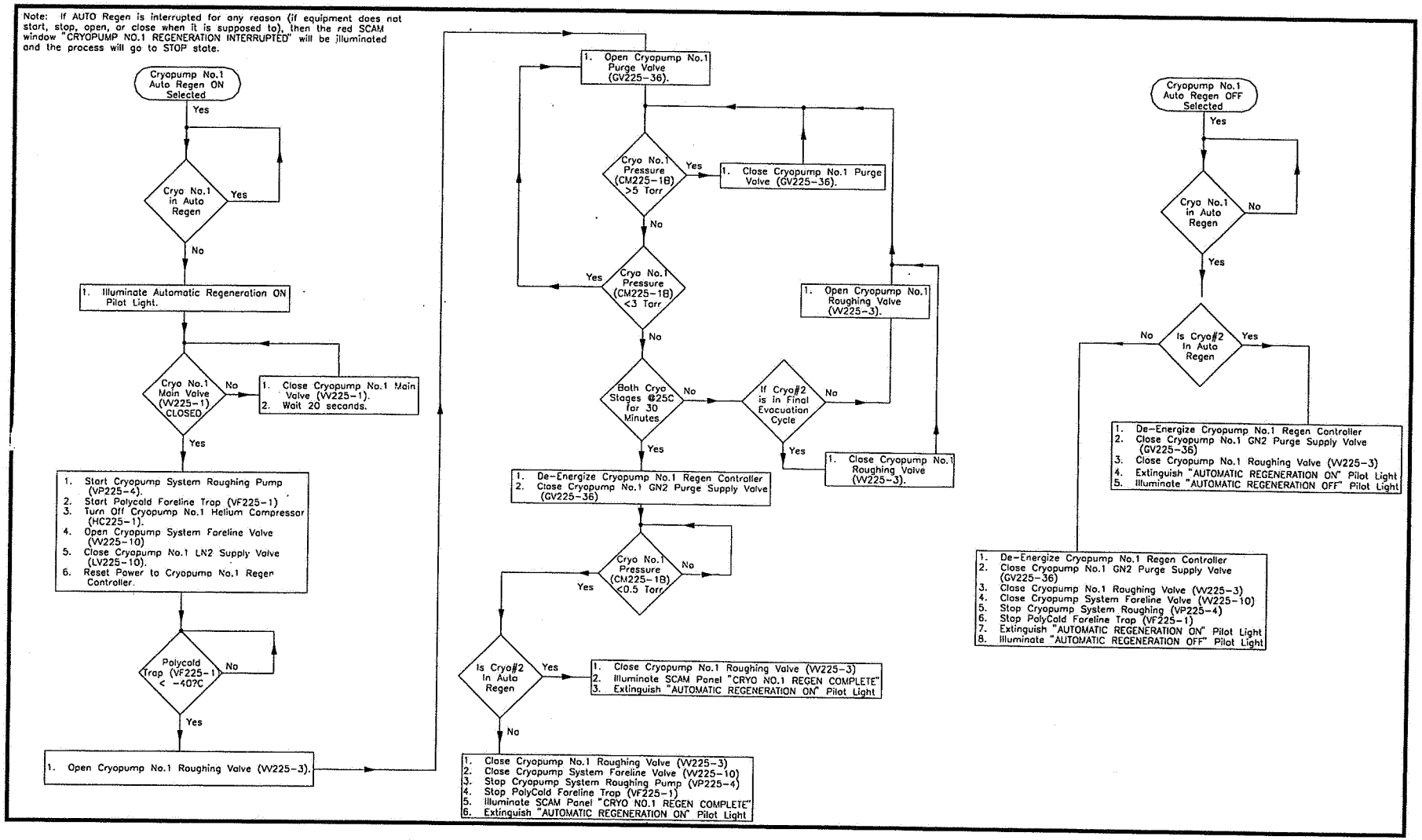


Figure 7: Automatic Cryopump Regeneration Sequence

236-38
021475
14P

AIR COUPLED ULTRASONIC C-SCAN (AIRSCAN) FOR NON DESTRUCTIVE INSPECTION

Ron van der Ven*, Harry Bolks**

*Fokker Space B.V.: Newtonweg 1, 2303 AN, Leiden, The Netherlands
(tel. +31.71.5245767, fax +31.71.5245999)
**Fokker Special Products B.V.: Edisonstraat 1, 7903 AN, Hoogeveen, The Netherlands
(tel. +31.528.285379, fax +31.528.285008)

369618

ABSTRACT

With the objective of Fokker Space and its subcontractors to reduce the cost of its solar arrays, the non destructive inspection (NDI) of the solar panel substrates has been identified as one of the areas of possible cost reduction.

The Fokker Space solar panel substrate design consists of a sandwich construction with Aluminium honeycomb core and CFRP facesheets.

Due to the optimised design of the Fokker Space solar panel substrates with regard to strength versus mass, even small defects can have an impact on the solar panel substrate performance. Therefore a specification has been established for the allowable defect sizes. The NDI test program has to be capable of detecting defects below this allowable defect size.

Fokker Space has performed a market survey to find a fast and inexpensive NDI technique for the inspection of solar panel substrates, which still fulfils all NDI requirements.

In this paper the outcome of the qualification test on solar panel substrate samples is presented. Furthermore the validation and implementation of the Airscan NDI equipment at Fokker Special Products (FSP) are presented.

The Airscan NDI equipment has been purchased at Quality Materials Inspection, Inc. (QMI) USA. Preliminary acceptance of the Airscan equipment occurred at QMI, the final acceptance of the total equipment was at Fokker Special Products.

1. INTRODUCTION

The objective of the Airscan program at Fokker is to reduce the cost and lead time for the non destructive inspection of solar panel substrates.

Required is that all requirements with regard to the detectability of defects are met. Initially, only the detection of skin-to-core defects was evaluated.

The Airscan program at Fokker has been divided in three phases.
In phase 1, the market survey to find a fast, reliable and inexpensive NDI technique for the inspection of solar panel substrates has been conducted. The Airscan NDI technique has been compared to the LTI (USA) Shearography system, the Steinbichler (Germany) Shearography system and the baseline Fokker Laser Holography NDI technique. Automated Airscan NDI technique has been selected as replacement method for Laser Holography.

In phase 2 the Airscan NDI method has been qualified for the detection of skin-to-core defects in ARA (Advanced Rigid Array) solar panels and Flatpack solar panels (e.g. the solar array for Envisat-1).

In phase 3 the validation and implementation of the Airscan equipment at Fokker Special Products has been carried out. The third phase of the Airscan program has been done in the frame of the ESA partnership program.

2. AIRSCAN SYSTEM DESCRIPTION

The Airscan NDI method is an automated ultrasonic inspection method, which is very similar to water jet C-scan. However, the medium for sound transfer is air, not liquid.
Airscan is performed in a through transmission mode, which enables inspection of both sides of a solar panel substrate simultaneously.
The system is complete with a scanning mechanism, control equipment, an image processing system and a printer. The software has the capability to determine the location of the defects on the image. This enables a

quick and easy location of the defect on the actual product.

The Airscan transmitter sends a 400 kHz sound wave through the test object which is received by the receiver. The attenuation of the sound wave is measured. Defects such as delaminations, disbonds etc. will give an increase in attenuation and can be detected by comparison of the attenuation between a good area and a bad area. A NDI calibration sample with the same configuration as the to be scanned product is required to calibrate the Airscan equipment. The Airscan image processing system gives different colours to different attenuation levels. The colours are adjustable with regard to the signal level, this makes it possible to create a threshold amplitude level below which bad areas are indicated with a certain colour.

3. MEASUREMENT PRINCIPLE

The Airscan instrumentation makes use of a toneburst transmitting pulse. This is a wavetrain-like signal and exists of as many as 15 sequential pulses, spaced equally, representing a 400 kHz test frequency. The frequency of this toneburst signal is tuned to the resonance frequency of the transducer in order to obtain a strong acoustic transmitting power. A strong acoustic transmitting power is required because of the extremely high losses of an air coupled system.
The acoustic toneburst will propagate through air and a small portion of the acoustic toneburst signal will pursue further into the part to be inspected. Most of the acoustic energy is reflected at the interface between the air and the part. This is because of the very large difference in acoustic impedance between air and the material which is inspected. The amount of energy transfer into the material is a function of the acoustic impedance values of both the air and the part under test. Also the incident angle of the sound beam effects the strength of the through transmitted signal at the air to part interfaces.
A similar phenomenon exists at the other side (exit side) of the panel. Only a small fraction of the signal will leave the part at the exit side. This small fraction, which is approximately 1/1000 part of the acoustic toneburst input signal, is then divided into 256 different levels for inspection.

The Airscan measurement principle is shown schematically in Appendix A.

For solid materials, the through transmitted signal amplitude may vary as a function of the wall thickness of the sound within the material. As a consequence of the reflections occurring within the part, a reverberation (back and forth bouncing of a toneburst) may occur and as a result this will cause constructive and destructive interference. This phenomena is known as standing waves.

When the wall thickness of the sound within the materials equals for example 1/2 a wavelength, a minimum of sound energy will leave the part. When the wavelength within the material equals 1/4 wavelength (or 3/4, 5/4 or in general any quarter of an odd integer), the maximum amount of energy will exit the part.
To maximise the through transmitted signal amplitude, the effect of standing waves should be realised when using the Airscan system.

A practical way to circumvent such phenomenon is to align the transmitting transducer under a small angle of incidence. When a simple through transmission method is used, this angle is usually in the range of 4 to 14 degrees. At this incident angle, the through transmitted signal is composed of mainly transverse (shear) wave components. The incident signal breaks into the material (Snell's law). At the exit side, the sound beam again will break and propagate in a direction more or less parallel to the incident beam. Since the transverse (or shear) wave is under an inclined angle with the normal to the surface, no standing waves are observed. To find this angle, the transducers are simply aligned to obtain the strongest through transmitted amplitude. In addition to this, a proper beam offset is beneficial to again obtain the maximum through transmitted signal amplitude.

For honeycomb sandwich structures, the sound propagation through the material is based on a different phenomenon. In honeycomb structures there is no evidence of standing waves at the 400 kHz test frequency.
The transducers are aligned perpendicular to the surface, such that at least one focal spot coincides with the surface of the part. The focal spot size at this interface is in the order of 0.8 mm, at a test frequency of 400 kHz and with a given transmitter diameter of 25 mm. At this focal spot size, it becomes feasible to identify individual honeycomb cell walls. In air, longitudinal pressure waves are present. At the interface between air and the facesheet, mode conversion occurs. Within the facesheet both longitudinal and shear waves are generated. Furthermore, mode conversions occur at

the interface between facesheet and honeycomb core material.
At the exit side, the reverse mode conversions will occur. And finally, a longitudinal pressure wave in air is generated. This longitudinal pressure wave in air will propagate towards the receiving transducer.
When a disbond occurs, the through transmitted amplitude is reduced.

Usually, in scanning honeycomb structures the bonding of the skin to the core is inspected. However, the skin areas in between the cell walls of the honeycomb core (the core drums) will be excitated as well. The signal from the core drum is of no interest and needs to be filtered.
In a through transmission mode, the time the signal takes from the upper core drum to the lower core drum is longer (long trip time) than the time the signal needs from the upper skin-to-core joint to the lower skin-to-core joint (short trip time). Note that the transmitter and receiver are located on top of each other and that the signal will follow the shortest path from transmitter to receiver.
It is possible to adjust a gate time domain in the Airscan equipment such that only the short trip time is captured, the response from the long trip time is then excluded. In this way only the signal of interest is obtained.

In figure 1 an example is given of an Airscan image for honeycomb sandwich structures. The image is taken from a holddown solar panel test sample including a dense honeycomb area. Scale 1:3.

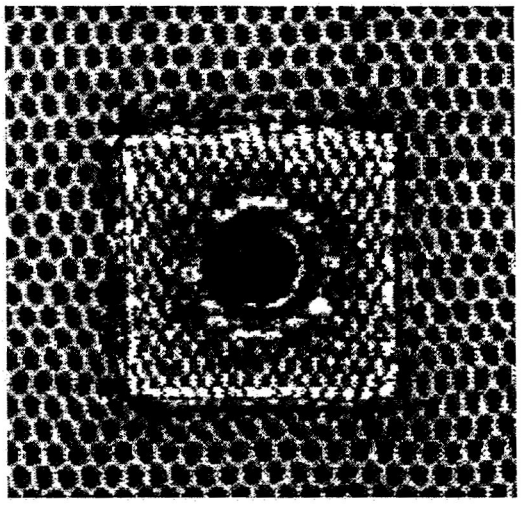


Figure 1: Airscan image for holddown sample

4. QUALIFICATION TEST RESULTS

At Fokker two different solar panel configurations are currently made, one is called ARA which stands for Advanced Rigid Array and the other is called Flatpack. The ARA configuration is used for amongst others commercial geostationary solar arrays; the Flatpack solar array has been developed for the Envisat-1 satellite.

Both solar panel configurations are sandwich constructions with CFRP skins and Aluminium honeycomb core material. One of the CFRP skins is equipped with a co-cured Kapton® foil for insulation between the solar cells and the sandwich construction. Most important difference between ARA and Flatpack type solar panels is the honeycomb core material. ARA solar panels have a 3/8" honeycomb core at a height of 22 mm, Flatpack solar panels have a 1/4" core at a height of 10 mm.
Furthermore the Flatpack solar panels for the Envisat-1 satellite are equipped with a Kapton® TCC foil on the panel rear side for protection against atomic oxygen (ATOX) and for thermal control purposes.

Airscan qualification tests have been performed on both solar panel configurations.
Since the start of the Airscan NDI development, the transducers have been modified and improved a couple of times. The version of transducers is indicated with a date.

Tests on the ARA NDI calibration sample and the ARA M55 qualification panel have been done in December 1992 with the October 1992 version of transducers.

To qualify the Airscan NDI technique for ARA solar panels an ARA NDI calibration sample with programmed defects has been inspected. Inspection has been performed by QMI.
The objective of the Airscan qualification program was to detect all type 3 defects in the ARA NDI calibration sample, and to demonstrate the Airscan capability to detect type 2 defects.
A type 3 defect is defined as a defect where three connecting cell walls of the honeycomb core are not bonded to the facesheet, this results in a defect of a 3 cell size. A type 2 defect is a 2 cell size defect (only 1 cell wall not connected to the facesheet). The definition of defect types is presented in figure 2.

The allowable defect size for ARA solar panels is a 2 cell size defect, providing no two type 2 defects are within a 140 mm radius from each other.

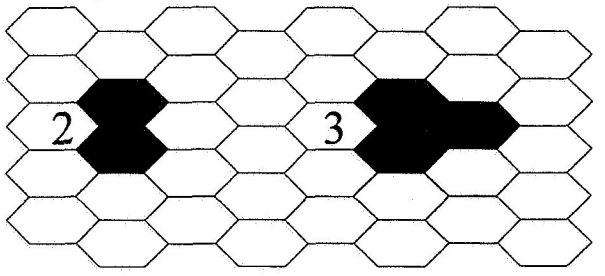


Figure 2: Definition of defect types

The ARA NDI calibration sample has been scanned in the through transmission mode with the CFRP side up. The size of the ARA NDI calibration sample is 610 mm x 409 mm. The ARA NDI calibration sample has a 2 ply and 3 ply facesheet (see figure 3). One of the facesheets is equipped with a co-cured Kapton® foil.

Appendix B shows the Airscan test result image. The test characteristics are as follows:

- Scan direction: length of the sample (24" = 600 mm)
- Index step: 0.020" (distance between scan lines is ± 0.5 mm)
- Scan speed: 6"/s (= 150 mm/s)
- Scan time: ± 1 hour

The defects found in the ARA NDI calibration sample are listed in table 1 and can also be seen on the image of Appendix B.

With Airscan NDI inspection of the ARA NDI calibration sample, both programmed and not programmed defects have been found.
To verify the defects found by Airscan NDI methods in the ARA NDI calibration sample, the sample is examined visually after cross sectional slicing.
One half of the sample has been sliced according to figure 3.
In this figure the locations of the programmed defects are indicated with a marker. The programmed defects are located at the Kapton® side and CFRP side of the calibration sample. The ARA NDI calibration sample contains both programmed type 2 defects and programmed type 3 defects.

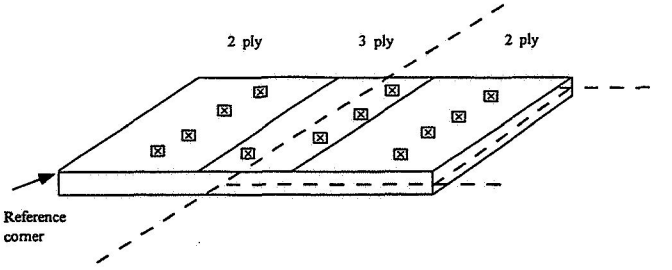


Figure 3: Sliced ARA NDI calibration sample

The sliced part of the ARA NDI calibration sample has been visually inspected for defects by looking in to every single cell. Afterwards the results of visual inspection have been compared with the results obtained by Airscan NDI. The results of this exercise are presented in table 1.

Summarised the Airscan NDI test results are:

- All programmed defects have been confirmed by visual inspection on the sliced part of the sample.
- One defect found by Airscan has been indicated as a possible defect by visual inspection on the sliced part of the sample (there was a hole in the skin laminate filled with adhesive which resulted in less adhesive on the interface of the honeycomb cell wall and the skin).
- All defects found by Airscan have been verified by visual inspection on the sliced part of the ARA NDI calibration sample. The one defect not found by Airscan NDI has been detected by visual inspection. The size of this defect is within the ARA NDI requirements.

The conclusion has been that Airscan NDI meets all objectives of the qualification test program, and therefore Airscan NDI is considered to be qualified for ARA type solar panels.

Full scale Airscan NDI tests have been done on the ARA M55 qualification panel (Telecom 2 solar panel design, dimensions: 2.05 m x 2.12 m).

Due to the large dimensions of the panel and the relatively short arms used for mounting of the transducers, the panel has been scanned in 7 sections. The panel has been scanned with the CFRP side up (transmitter on CFRP side).

The test philosophy has been as follows:

- Scanning of the panel in the through transmission in 7 sections, this will detect possible defects on both sides of the panel.

- When a failure occurs the location of the defect (Kapton® side or the CFRP side) will be determined with an acoustic impedance measurement (QMI bondmaster) or with an ultrasonic pulse-echo measurement.

The ARA M55 qualification panel has been scanned in 7 sections. Scanning of the ARA M55 qualification panel by Airscan took 2 days (lead time), 8-9 hours scanning time.
The total number of defects found by Airscan NDI in the ARA M55 qualification panel is 35, of which 18 are subject to repair.

In a production environment, it has to be decided whether or not it is necessary to determine on which side of the panel the defect is located. For efficiency reasons, it can be decided to repair the defect at both sides of the panel regardless of the exact location of the defect.

To qualify the Airscan NDI technique for Flatpack solar panels a dedicated NDI calibration sample with programmed defects has been made. This sample, identified as the PPF NDI calibration sample, has been made in the frame of the Polar Platform (PPF) solar array program at Fokker. Recently the name of the Polar Platform program has been changed into Enivisat-1.

The PPF NDI calibration sample has been inspected by Airscan NDI at QMI. The programmed skin to core disbonds in the PPF NDI calibration sample are ∅ 8 mm, this is in accordance with the NDI requirements for Flatpack solar panels.
To verify the defects found by Airscan this sample has been inspected by the liquid coupled ultrasonic pulse echo technique qualified within Fokker. Results are presented in table 2.
In addition to the programmed defects 2 other defects are found by both Airscan and ultrasonic NDI.
All defects found by Airscan have been verified by ultrasonic inspection. The Airscan NDI technique is considered to be qualified for Flatpack type solar panels.

Tests on the PPF NDI calibration sample have been done in June 1993 with the same version of transducers.

5. VALIDATION AND IMPLEMENTATION OF AIRSCAN AT FSP

In the beginning of 1995, Fokker had decided to purchase the Airscan NDI equipment.
The purchase of the equipment and the acceptance activities have been part of an ESA partnership program.

The objective of the implementation of Airscan non destructive test equipment at Fokker Special Products is to improve the competitive strength of FSP in the solar array market by reducing manufacturing cost and lead time of the NDI inspection.

A key goal for the Airscan NDI equipment purchased by Fokker is that the performance should be as good or better than the Airscan equipment at QMI on which the qualification tests have been performed.

The acceptance plan for the Airscan NDI facility at Fokker Special Products outlines the implementation and validation approach.
The acceptance plan specifies the deliverable components and documents as well as the requirements which should be fulfilled by the Airscan NDI equipment.

The validation of the Airscan facility at FSP has three objectives:

- To ascertain that the Airscan facility meets the pre-set requirements.

- To ascertain proper functioning of the Airscan equipment in its operational environment.

- To certify the FSP personnel for operation of the equipment.

For the purpose of validation, three dedicated reference samples have been manufactured containing programmed defects. These programmed defects are representative for possible production errors.
Reference samples have been made for ARA Mk2+, ARA Mk3 and Flatpack solar panel configurations.
ARA Mk3 is the current state of the art solar panel design at Fokker for geostationary applications.

The Airscan equipment has been subjected to a pre-acceptance program at QMI (the vendor). For this purpose the three reference samples have been scanned. At final acceptance at FSP, the three reference samples

have been scanned again and the results have been compared to the pre-acceptance test results.
The results of the pre-acceptance testing and the final acceptance testing show good correlation.
To verify the results of the pre-acceptance test and the final acceptance test at FSP, a part of each reference sample has been sliced. The sliced parts have been examined for defects by visual inspection. Again the results of the Airscan inspection show a good correlation with visual inspection after slicing.

FSP personnel has been certified for Airscan operation by a level III instructor from QMI.

Based on the results of the validation phase, the Airscan NDI equipment has been accepted by Fokker Special Products.

The objective of the implementation phase has been to make the Airscan facility operational at FSP.

For the implementation phase the following activities are distinguished.

- Purchasing of the hardware in accordance with the specifications.
- Establishment of the infrastructure and installation at FSP to enable operation.
- Manufacturing of the cradle frame for mounting of solar panels in the Airscan facility.
- Generation of an inspection procedure.

The Airscan facility purchased by Fokker is a vertical panel scanning facility with two scanning towers (see figure 4). The transducers are mounted on the scan tower. Transducers move up and down during the scanning operation. The panel is scanned by moving the cradle with the panel index step wise after every up or down scan movement of the transducers.

The advantages of a vertical scanning facility are the reduction in the required floor space, the elimination of the bending stresses of the part to be scanned and the reduction of repositioning activities.

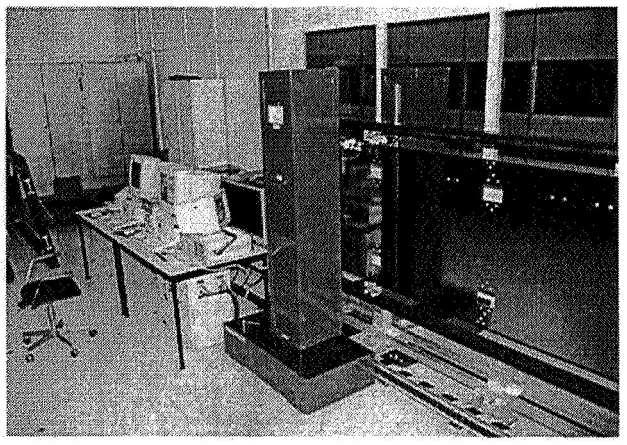


Figure 4: Airscan NDI equipment at FSP

A schematic overview of the Airscan NDI inspection facility as purchased by Fokker is shown in Appendix C.

The software installed for evaluation of the Airscan test results is called WINSPECT. The software has the capability to locate defective areas, to select different colours for different attenuation levels, to measure the attenuation level at any spot, etc. See Appendix D for a typical WINSPECT Airscan image.

An universal cradle frame has been installed for mounting of both ARA and Flatpack solar panel substrates.

A Fokker technical handbook procedure for the NDI inspection using Airscan has been generated. In this inspection procedure the preparation, calibration, inspection and reporting requirements for the inspection of ARA and Flatpack solar panel substrates are outlined.

6. CONCLUSIONS

In phase 2 of the Airscan program, the Airscan NDI method has been qualified for the detection of skin-to-core defects in ARA and Flatpack solar panel sandwich constructions. The resolution of the Airscan NDI method has proven to be better than 5 mm for a skin thickness up to 0.5 mm.
Note: thickness is not considered to be a problem. The attenuation through a thick layer is still small compared to the losses at the interfaces as caused by reflections.

For ARA type solar panels the Airscan NDI method has proved to be capable of detecting production type skin to core defects.

All defects in the ARA NDI calibration sample, except for one small defect (type 2), have been found by Airscan NDI.
All defects found by Airscan NDI have been verified by visual inspection of the sliced part of the sample.

The lead time for the standard Fokker NDI program is 5 days, the reduction in lead time when Airscan NDI is used is about 60%.

The suitability of the Airscan NDI method for Flatpack panels has been evaluated by comparison of the Airscan NDI test results with the results of liquid coupled ultrasonic testing. Ultrasonic testing is a qualified technique at Fokker.

The Airscan NDI method is capable of detecting all programmed skin to core disbonds. All defects found by Airscan NDI have been verified by ultrasonic inspection.

Although both ultrasonic inspection and Airscan are capable of detecting the programmed skin to core disbonds in the PPF NDI calibration sample, manual ultrasonic inspection is not recommended because this method is very time consuming.

Phase 3 of the Airscan program has resulted in a successful validation and implementation of the Airscan NDI equipment at FSP.
After the validation program at Fokker Special Products the following additional conclusions with regard to the Airscan capabilities were drawn.
With Airscan NDI it is possible to detect the presence of foam adhesive at panel areas containing foam (e.g. core splices). However, inspection of the bonding between skin and foam with Airscan is not possible because of air inclusions in the foam. This is inherent to ultrasonic NDI techniques.
Skin-to-edgemember inspection for the presence of disbonds and/or delaminations is also not possible with Airscan. This is due to the fact that there is no path for sound transfer inside the C-channel type edgemember.
For scanning of these areas a Fokker bondtester or an ultrasonic pulse-echo device is required.
For Flatpack type solar panels the Airscan NDI results show good correlation with the visual inspection results after slicing.

Currently, the Airscan NDI activities at FSP for a Flatpack type solar panel (dimensions 5m x 1m) take about 10 hours of lead time and 8 man hours for preparation, calibration, inspection and evaluation of the results. This is a cost reduction of about 60% and a lead time reduction of about 80%, with regard to the previously used NDI methods.

The Airscan NDI technique has been implemented for the inspection of ARA and Flatpack solar panel substrates.

For a proper set-up and calibration of the Airscan equipment it is mandatory to use a NDI calibration sample with the same configuration as the to be inspected product.

For a proper evaluation of the scan results, it is required to have a good knowledge of the panel substrate configuration.

Main advantages of the Airscan method are listed below.

- The Airscan method is a non contact inspection method. This makes it especially interesting for NDI inspection of space products since contamination of the inspected part is not an issue.
- Airscan NDI does not need any special tooling or preparation activities for the part under inspection.
- Airscan is tolerable to rough surface conditions.
- The Airscan NDI method is fully automatic and does not require continuous attention of the operator(s).
- Airscan results can be analysed off line on a personal computer.
- Airscan results can be transferred on paper, floppy disk or modem. This is very useful in case production and engineering facilities are separated. It is also beneficial for configuration control purposes and at the final acceptance of the products.

7. ONGOING ACTIVITIES

Currently, a program has been started to investigate the operating limits of the Airscan NDI facility at FSP and the possibility to replace other NDI techniques by Airscan NDI.

One of the areas currently under investigation is the inspection of curved shaped solar panel sandwich structures. For inspection of curved shaped structures a modification of the cradle frame is needed.

Furthermore, a program has been started to investigate the opportunities to perform Airscan NDI on other products. Possible examples are floor panels for aircraft, antenna structures, printed circuit boards and spacecraft central cylinder structures.
Another possibility is the inspection of prepreg lay-ups prior to cure for the existence of air entrapments. This would enable corrective actions prior to cure which will minimise the risk of scrapping finished parts.

8. REFERENCES

Airscan test facility requirement specification; 95-0187A, February 1995, Fokker Special Products B.V.

Airscan NDI qualification test report; FSS-R-95-0043 issue 1, March 1995, Fokker Space B.V.

Proposal to ESA for the installation of an Airscan test facility for solar array substrates; 95-0188A, March 1995, Fokker Special Products B.V.

Acceptance plan for the acceptance of the ultrasonic C-scan installation; AI-AP-0101, May 1995, Fokker Special Products B.V.

Airscan achievements report; 951217HK, December 1995, Fokker Special Products B.V.

Acceptance test report for the acceptance of the Airscan NDI facility; AI-AR-0102, March 1996, Fokker Special Products B.V.

TABLE 1 - COMPARISON OF AIRSCAN NDI AND DESTRUCTIVE INSPECTION (ARA)

	TYPE OF DEFECT	SIDE	PROGRAMMED DEFECTS	AIRSCAN	CONFIRMED BY SLICING
2 PLY	3	Kapton	(76,51)	(79,50)	N.A.
AREA	3	Kapton	(89,157)	(87,155)	N.A.
AT REF.	2	Kapton	(102,254)	(93,245)	N.A.
CORNER	2	Kapton	(107,356)	(99,348)	N.A.
3 PLY	3	Kapton	(254,58)	(256,55)	N.A.
AREA	3	Kapton	(292,145)	(291,145)	yes "3"
	3	CFRP	(305,249)	(298,238)	yes "3"
	3	CFRP	(305,358)	(301,347)	yes "3"
		Kapton	not programmed	(217,259)	N.A.
2 PLY	3	CFRP	(500,56)	(498,50)	yes "3"
AREA	3	CFRP	(508,140)	(512,136)	yes "3"
	2	CFRP	(508,251)	(508,251)	yes "2"
	2	CFRP	(508,356)	-	yes "2"
		Kapton	not programmed	(457,298)	possible[1)]

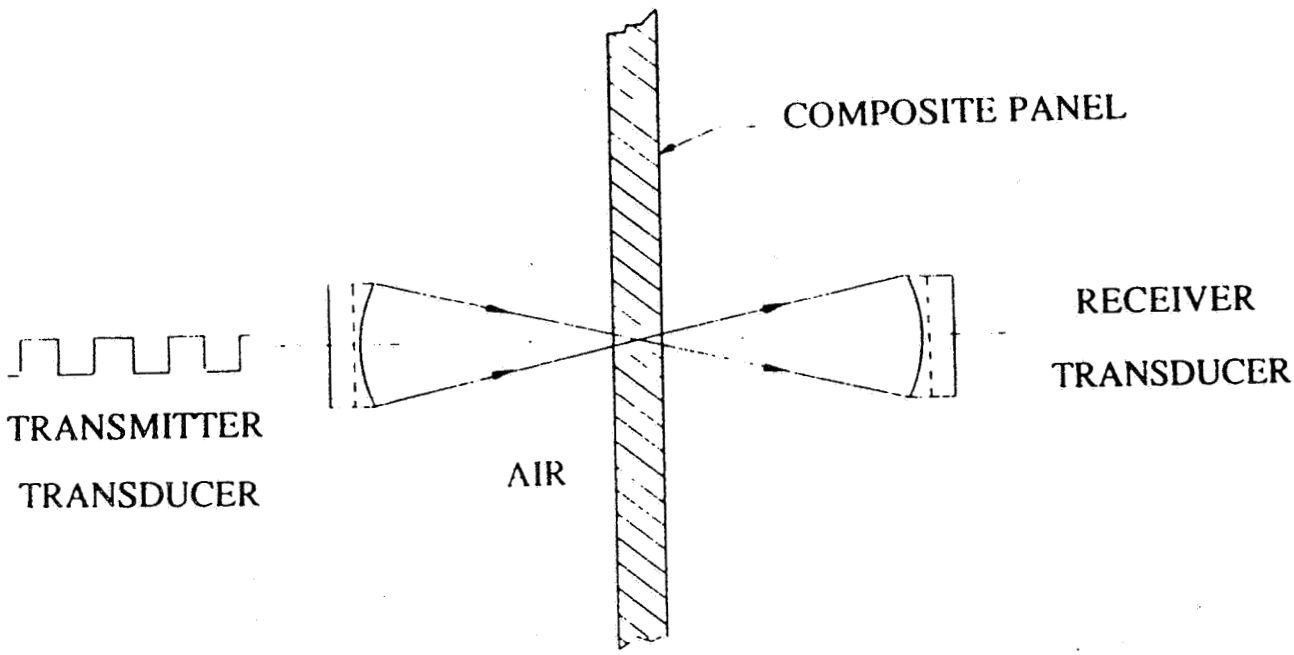
NOTES:
- coordinates taken from the reference corner
- all dimensional readings taken with the CFRP side up
- N.A.: not applicable (i.e. not located in the sliced part of the NDI calibration sample)
- yes "3": defect confirmed by slicing, defect type is 3
- possible 1): a hole in the laminate filled with adhesive resulting in less adhesive on the interface of the honeycomb cell wall and the skin.

TABLE 2 - AIRSCAN NDI, PPF NDI CALIBRATION SAMPLE

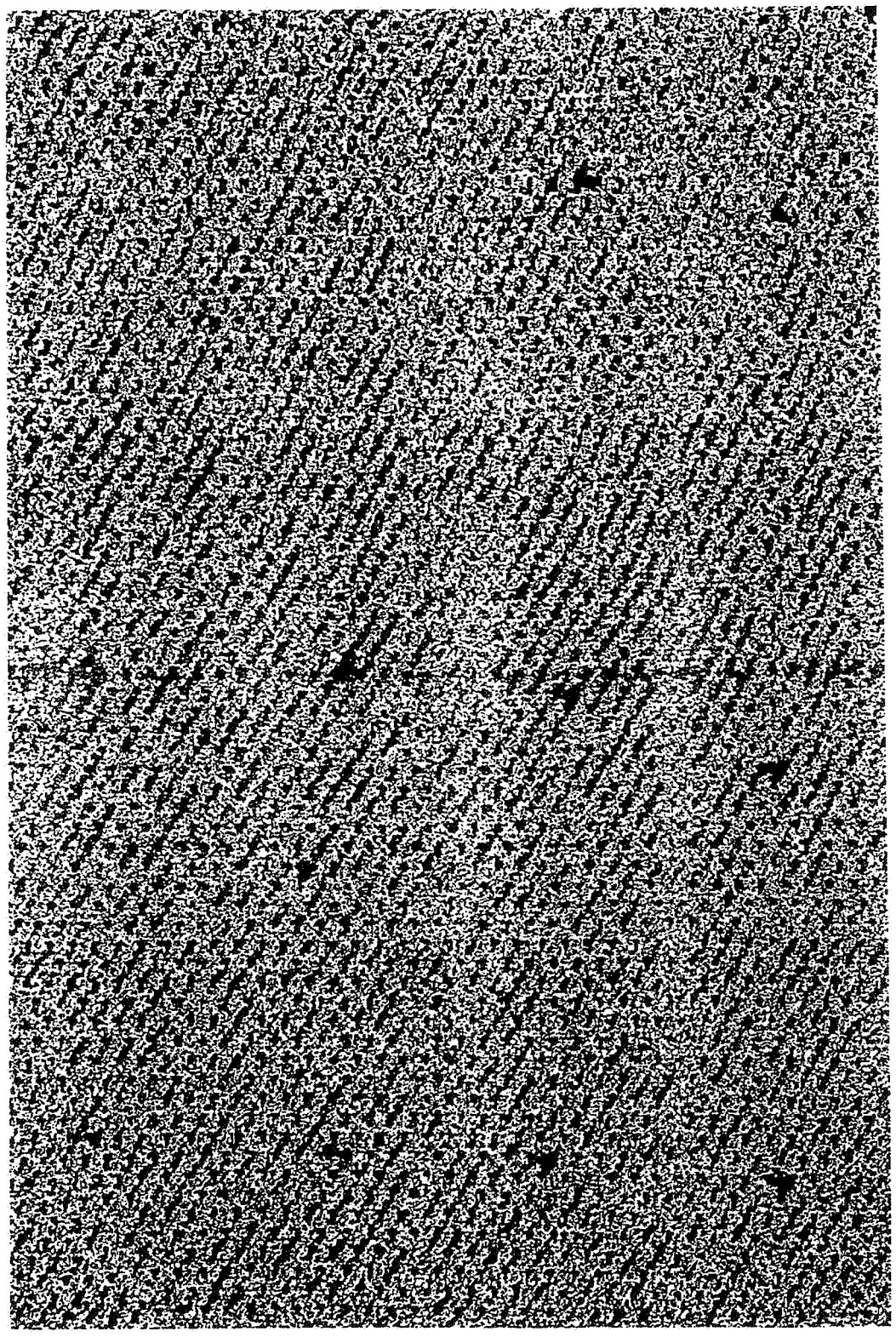
DEFECT NUMBER		SIDE	ULTRASONIC INSPECTION	AIRSCAN
P	1	rear	(50,30)	(30,40)
R	2	rear	(350,30)	(343,52)
O	3	front	(200,60)	(192,67)
G	4	rear	(250,55)	(258,67)
R	5	front	(107,80)	(97,98)
A	6	front	(400,80)	(405,95)
M	7	rear	(50,180)	(38,190)
M	8	rear	(350,180)	(357,190)
E	9	front	(207,210)	(186,213)
D	10	rear	(250,205)	(261,220)
	11	front	(100,230)	(100,235)
	12	front	(400,230)	(412,240)
	13	rear	(50,330)	(36,342)
	14	rear	(350,330)	(360,342)
	15	front	(205,360)	(191,365)
	16	rear	(250,355)	(265,368)
	17	front	(100,380)	(91,390)
	18	front	(400,380)	(413,393)
NOT	a	front	(400,10)	(437,17)
PROGRAMMED	b	front	(410,25)	(442,45)

NOTES: - coordinates of defects may differ because differences in axes definition for Airscan and ultrasonic inspection

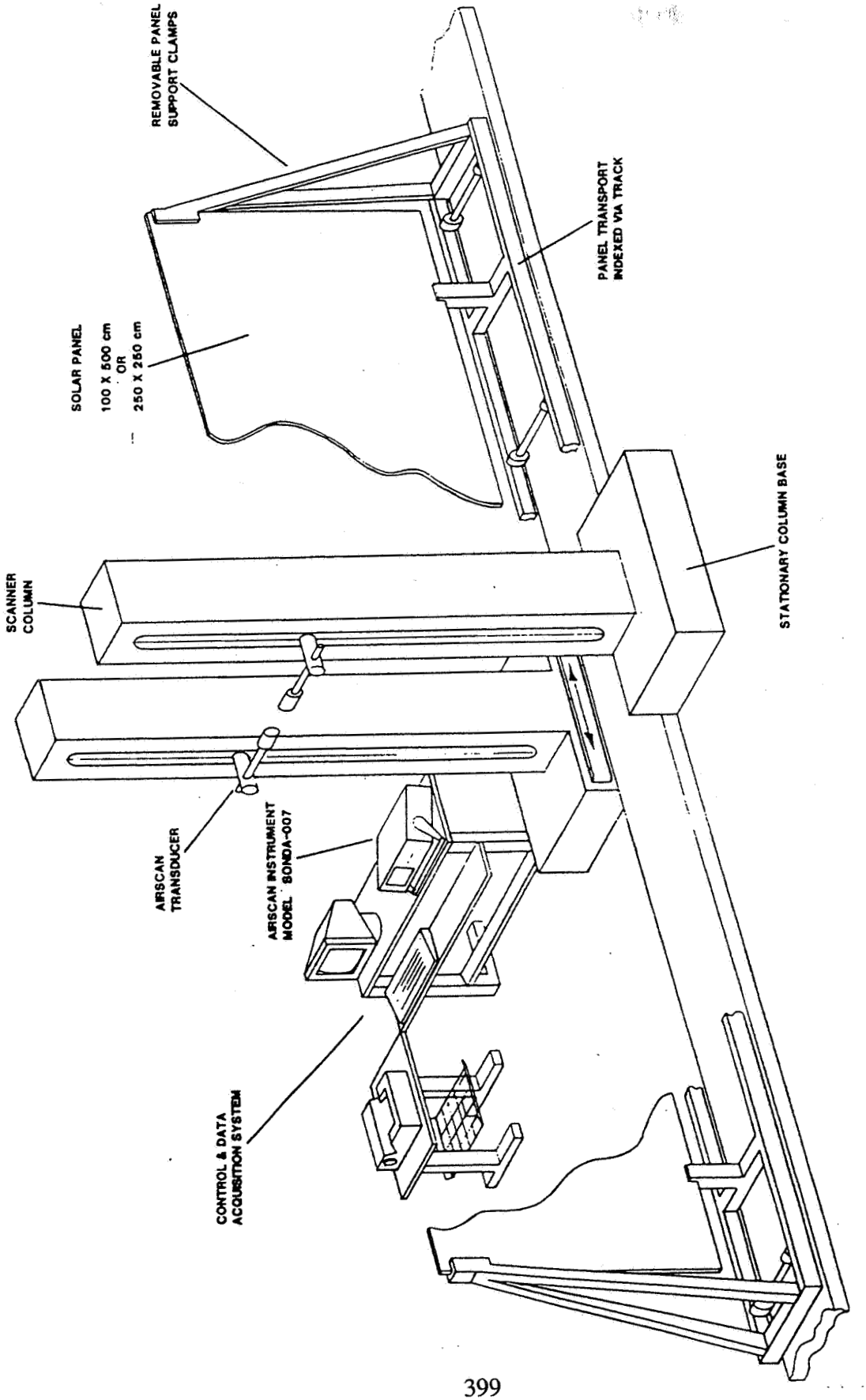
APPENDIX A - AIRSCAN THROUGH TRANSMISSION MEASUREMENT PRINCIPLE



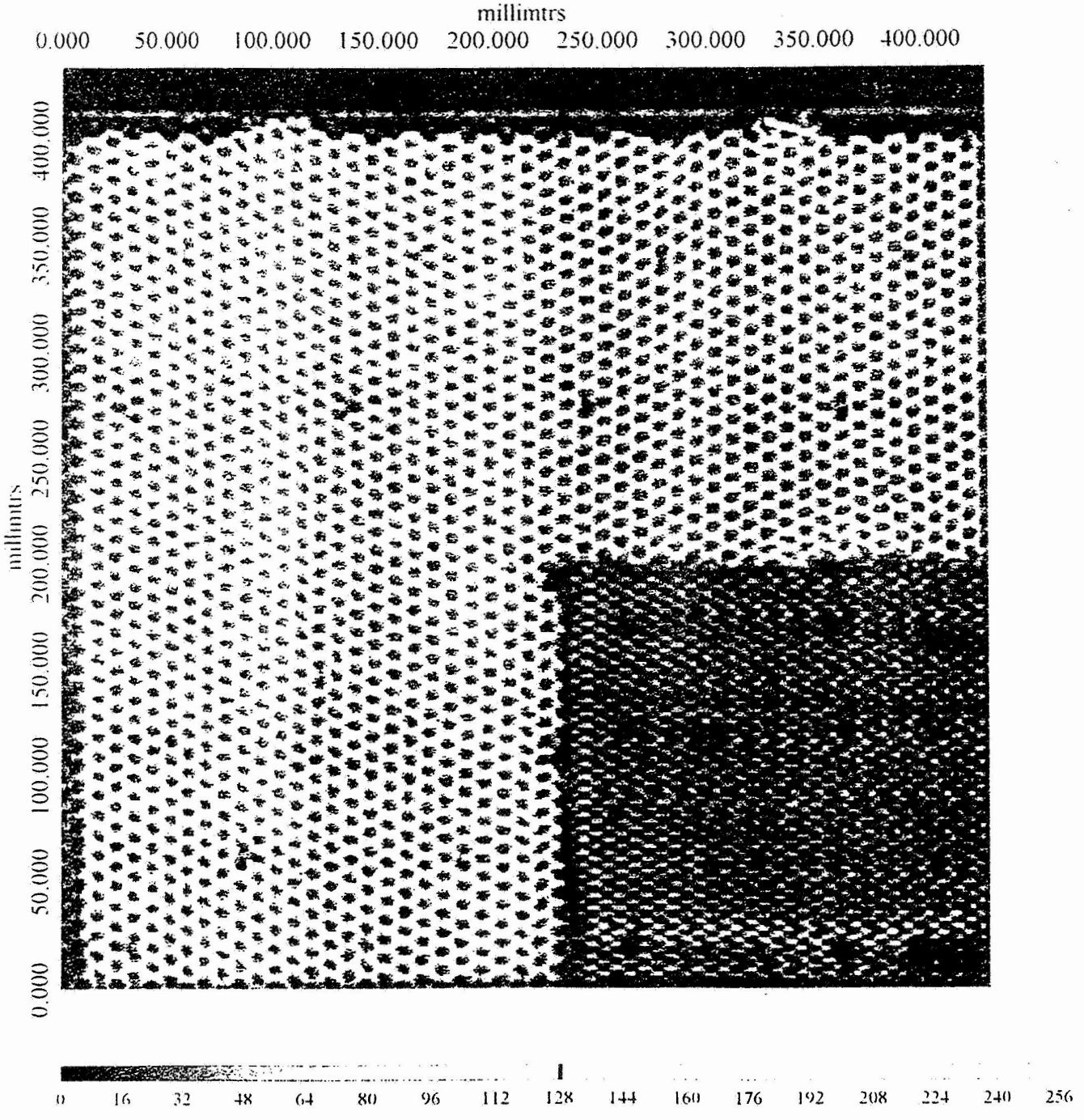
APPENDIX B - AIRSCAN IMAGE OF ARA NDI CALIBRATION SAMPLE



APPENDIX C - AIRSCAN INSPECTION FACILITY AT FOKKER SPECIAL PRODUCTS



APPENDIX D - AIRSCAN IMAGE OF THE ARA MK3 REFERENCE SAMPLE



19
537-35
ABS ONLY
0514480 069620

Low-Pressure Measurement Performance of Capacitance Diaphragm Gages

A.P. Mill and R.W. Hyland

The measurement performance of capacitance diaphragm gages (CDG's) at low pressures is determined primarily by three factors, namely, instabilities in the SDG zero-pressure reading, the effect of thermal transpiration at pressures below 100 Pa, and shifts in the CDG response function or calibration factor with time. A systematic study of 29 CDG's of the type currently being used by calibration laboratories as transfer standards has shown that zero instabilities are strongly correlated with changes in room temperature. The corresponding zero temperature coefficients were found to be generally less than 5 ppm FS/°C for gages with full-scale (FS) ranges of 133, 13.3 amd 133 kPa (10,100 and 1000 torr), but significantly larger (as much as 25 ppm FS/°C) for the 133 Pa (1 torr) gages. A hybrid CDG system has been developed, using a thermoelectric heating/cooling module to regulate the CDG temperature. The data obtained demonstrates that the this approach can improve the zero stability of CDG's and, when control is maintained near room temperature, minimize the effect of thermal transpiration. Repeat calibration data on 72 CDG's accumulated at NIST during the past 17 years have been analyzed. The analysis of nearly 300 calibration records indicated that the shifts in CDG response function with time are highly gage dependent and differ significantly for gages with different full-scale ranges, the largest shifts occuring for gages with the lowest full-scale range.

538-44
021482
12P
369621

Video Aided Inspection of Solar Arrays

Dick van der Vegt and Frits H. Naber
Henk J. Cruijssen

Fokker Space B.V.
Leiden, The Netherlands

ABSTRACT

This paper deals with a new inspection method for solar arrays used in space. A major topic of Full Visual Inspection (FVI) is the detection of possible defects of solar cells such as cracks in solar cells, coverglass cracks, edge- and corner chips. Currently the inspection is carried out by visual observation of each cell with the aid of a stereo microscope.

With the tendency of the increasing dimensions of solar arrays, this method becomes more unworkable and ineffective, with increasing negative safety aspects, both for the hardware and personnel. Although inspection with a stereo microscope is a good method, the inspection results can be questionable because of the working conditions of the inspector and the large amount of cells to be inspected. The method is entirely based on the experience of an inspector. There is no registration of each inspection other then a simple drawing of the defect in case the inspector has found a defect.

A new inspection method was developed and tested at Fokker Space. This inspection method is based on both an Infra Red video system and a visual light Hi-res. video system. The system is capable of digital recording each image of a solar cell. The system offers a reduction in through-put time and provides better ergonomics and improves safety.

INTRODUCTION

Fokker Space is involved in solar arrays for about 20 years now. Every solar array, which leaves the plant is subjected to a rigorous test program. Each rigid panel, covered with solar cells, is subjected to acceptance testing, consisting of at least on-station thermal cycling and other functional acceptance testing.
For newly developed solar arrays, such as the large Envisat solar array Ref (1), the flight wing will also be tested for vibration and acoustic noise on satellite level. Before and after these tests a Full Visual Inspection is carried out on solar array wing level.
The reason for thorough inspection is to check for degradation of the electrical subsystem such as the photovoltaic solar cells, as result of environmental tests. In addition, the individual panels are subjected to "flasher-testing" to prove that the electrical performance of the solar array remains within specification.
The inspections discussed in this paper covers the inspections of a full integrated solar array wing.

The intention of the video inspection feasibility study was to investigate if there were alternative, less time consuming inspection methods, without losing the quality of detecting at least the minimum defects. As the size of the solar panels are growing, the labor involved and the technical risk for such a detailed Full Visual Inspection is growing proportionally. Furthermore, the ergonomic aspects of inspecting on a high scaffold must be considered. For safety reasons it was preferable that a system would be developed allowing automatic inspection including recognition of defects off-line.
The development will be carried out in the following phases:

1 Feasibility study of using video cameras for inspection.
2 Built an inspection system for the Envisat Solar Array with on-line observation by the inspector.
Also off-line inspection is possible by observation of recorded images.

3 Automatic recording of images, with minimal interference of an operator and off-line manual inspection.
4 Automatic recording and off-line automatic recognition of defects by sophisticated software

This paper deals with the first part of the development undertaken at Fokker Space, starting in 1993 up to the expected implementation for the Envisat solar array.

BASELINE REQUIREMENTS

To replace the baseline FVI-method with an alternative method, the following baseline requirements were considered :

1. Cost saving for future projects (if development phase 4 is realized):
 - Time saving / reduction in through put time of FVI
 - Available within the required time frame for the Envisat project (phase 1 and 2)
 - Within the available development budget

2. Safety improvement for Envisat:
 - No additional scaffold for inspection required
 - Labor strain removed as no continuous inspection with microscope / eye is required

3. Inspection method covers the ESA requirements, Ref(2)
 - Original defects still to be found by new method .
 - Qualified by development testing i.e. demonstration to client, that inspection method gives similar results.
 - Covers the Envisat requirements for FVI, Ref(3)

At first, attention was given to the technical requirements. With the support of breadboard testing, a preliminary selection could be made of promising inspection methods. Also, the associated hardware could be reviewed on its technical performance.

PRESENT INSPECTION METHOD

The full visual inspection is done with a stereo microscope. The microscope itself is fixed on a table which can be translated along a frame. The highly trained and qualified person is able to detect specific type of defects in the individual solar cells. These defects and the corresponding criteria for accepting or rejecting the solar cells, which may be damaged as a result of environmental testing, are laid down in stringent ESA-rules: Ref. (2).

When the complete solar array wing is supported by the "zero-g" deployment rig, an inspection rig is placed in front of the panel substrates. The rig allows displacement of the table with the microscope and the light source. Special guide rails allow displacement of the table in vertical direction. All inspection activities are done manually.

In case of detection of defects, it may be required to replace the cells by a new cell. The reason is that the electrical reliability is an important acceptance criteria for the customer, allowing only a certain amount of defects to remain in the solar panels before actual launch.

Firstly a very course inspection is done by the naked eye, concentrating on easy observable defects. These defects can be detected due to the reasonable good reflection characteristics of the cells. Reference is also made to the table 1 below, where the type of defects are outlined. Special light sources are used to illuminate the cells under a shallow angle. Firstly the inspection is carried out with the microscope at a low magnification factor (5x). In case of a defect a closer look can be arrange by zooming to a magnification up to 30x As a light source, typically a ring-form illumination is used. Also special hand carried light sources, using a flexible glassfibre light source, may be used.

Defect type	*Typical defects*	*Defect type*	*Typical defects*
Solar cell defects	hairline cracks broken edge / corners surface nicks edge zone defects finger prints AR-coating voids	Defects on n-contacts	n-bar interruptions n-bar delaminations n-bar voids /pickles/drops
Cover glass defects	hairline cracks broken edge / corners bubbles finger prints AR-coating voids	Defects on p-contacts	contact surface edge delamination bubbles / voids etc. in ontact surface
Cover glass adhesive defects	delamination voids and bubbles discoloration	Inter connector defects	breaks / notches /deformations

Table 1 : Type of defects which need to be inspected on during a full visual inspection (Ref. 1)

ALTERNATIVE INSPECTION METHODS

Various inspection methods were reviewed on their merits. Some companies were asked for assistance as they were specialists in optics. Fokker Space supplied these companies with some solar cell samples which contained already "hidden" defects (on purpose). As a reference, the stereo microscope was used to detect any difference from the baseline FVI (i.e. accepted by the customer as being a qualified detection method). Various test set-ups were made to investigate the performance in detection of defects. The inspection methods which were reviewed were:

1. Microscope (original baseline) : Cell-by-cell inspection with a (stereo-) zoom microscope
2. Unaided eye : Global visual inspection with the unaided eye
3. Standard video : Visible-light video camera. Standard image resolution. Large field of view (~ 60x80 mm)
4. Standard video (zoomed -in) : Same as 3, but higher magnification: small field of view (~ 6x8mm)
5. Infra Red video : IR video camera. Wavelength region 1000 - 1800 nm. Large field of view (~ 60x80 mm)
6. Infra Red video (zoomed-in) : Same as 5, but higher magnification: small field of view (~ 6x8 mm)
7. High Resolution video : Hi-Res (visible light) video system with good image optimization features. Large field of view (~ 60x80 mm)
8. High Resolution video (zoomed-in) Same as 7, but higher magnification: small field of view (~ 6x8 mm)

TRADE OFF

A trade-off was initiated containing the results of all these bread-board testing. Important was that the defects which could be found by the microscope were also possible to be detected by the alternative method i.e. no loss of important data. The following inspection points were considered of importance:

1. Solar cell defects
2. Cover glass defects
3. Inter connector defects

Table 2 shows *how* the inspection methods were rated in relation to the critical inspection points. It must be noted that only a relative "rating" has been made. It was found that the only method which competes with the microscope is the "high-resolution" video. The "zooming-in" was tested to investigate the level of details, which were possible to detect.

	Inspection tool / method	solar cell defects	cover glass defects	Interconnector defects	
1	Microscope (original baseline)	no use(*)	no use(*)	++	
2	Unaided eye	o	o	o	
3	Standard video (VIS)	o/-	o/+	-	
4	Standard video (zoomed -in mode)	no use(#)	no use(#)	+	
5	Infra Red video	++	-/o	-/o	OK
6	Infra Red video (zoomed-in mode)	no use(#)	no use(#)	o/+	option
7	High Resolution video (VIS)	+	+	+	OK
8	High Resolution video (zoomed-in mode)	no use(#)	no use(#)	++	option

Table 2: Appreciation of various inspection methods

Valuation scale:

--	: no results	no use(*):	Too long process time
-	: poor results		
o	: some usable results	:no use(#):	only for local detailed
+	: good results		inspection at relative small
++	: very good results		number of locations

Important aspects supporting the previous trade-off table are mentioned below:

1. Original inspection method i.e. the stereo microscope gave still gave the best results. The original method however would require about 6 weeks (!) for a full visual inspection of a Envisat solar array. Considering the required through-put time and the earlier mentioned human and safety aspects, this was considered unacceptable. It is questionable if the man/microscope method still giving the best results, considering the human aspects, when the 23000 cells of the Envisat solar array have to be inspected.
2. When the Hi-Resolution (Hi-Res) camera was used in a "zoomed-in" mode, defects could be found with the same accuracy as with the stereo-microscope. However, for the Envisat-solar array, which has panel dimensions of 1000 mm x 5000 mm and a total number of 14 panels, this would mean about 20 weeks (!) of inspection time. With a camera-field of only 8x6 mm, the number of locations to be inspected are: 1000/8 x 5000/6 x 14 = 1.5 million locations in 2 seconds (minimum). Hence, this inspection method was disregarded to be of any use for overall inspections. This method can however still be used for few local detailed inspections in case of doubts. In order to save time during the inspection (i.e. one of the primary goals), it should be prevented as much as possible that "zooming-in" would be required
3. Method 4,6 and 8 as mentioned in the previous table 2 resulted in good detection methods, but did not fulfill the original requirements concerning process-time. Method 5 and 7 were considered the most economic inspection method.
4. The IR-camera gave surprising good results in detecting hairline cracks in solar cells with a large field of view. It was found that cracks which are much smaller then the camera resolution, still can be seen due to the contrast between the crack and the crack surrounding.

DETAILED RESULTS OF ENGINEERING / BREADBOARD TESTS

Light Sources

The sensitivity for detection of defects is very dependent of *how* the light source was applied. Engineering tests done with laser light, UV-light and even X-ray gave negative results and were therefore deleted from further testing. Concentration was given on Visual (VIS) and IR-light sources. For instance, "soft" light (from a diffuse light source with large surface) or "hard " light (unidirectional light from a small source) gave completely different results. A special test set-up was made in which different light sources were applied. Several engineering tests were done in the visible light spectral range and in the infrared range (wavelength 1000-1800nm) to detect the differences in detection performance.

Visual wavelength range

Large cracks in cover glasses can already be observed with the naked eye when looking at the solar cells under angles of ~45° if correctly illuminated. The cracks in the bare cell cannot be detected, unless the crack is that big that the cell bond line becomes visible (i.e. bonding material is RTV= red). When looking through a microscope or the proposed video camera the following test results were achieved:

1. When the light source is oriented *perpendicular* to the surface of the solar cells, the Silicon solar cells show a very rough moon surface type view. because of the multiple reflections from the cell surface, obstructing the correct inspection. Hence, cracks in the cell or coverglasses were hardly noticeable.

2. Illumination under an *oblique angle* such that the light is not directly reflected in the camera (so called: "dark field" illumination) gave good results. Refer to figure 1.

3. Hairline cracks, especially those in coverglasses, were good observable in case of vertical orientation of the video camera or the microscope and oblique illumination. Refer to figure 2.

4. Illumination from one side only detects cracks which run *perpendicular* to the light source. Typical angles are 40 to 50 degrees. In case the cracks are "running" at an angle over the surface of the cells or in case of very irregular cracks, the defects can be detected by rotation of either the sample or the light source. Depending on the crack orientations, it is recommended that a multiple light source (say maximum of: 4) is used. The light source can be switched on simultaneously or individually.

5. Tests were done to tilt the complete video camera under an angle, but keeping the light source perpendicular to the cell surface. This did *not* give the required results because when inspecting at large magnification factor only part of the image field could be focused on instead of the complete surface. However, for very detailed inspections it provided the best results. It was concluded that the line of sight had to be perpendicular to the specimen under test. Hairline cracks, especially those in cover glasses, were best observed in case of vertical orientation of the video camera or the microscope.

6. Polaroid glasses were tested to avoid unwanted reflections. This did not give the expected results as not only the reflections were eliminated but also the original defects were " faded" away. Also, color video helps to detect the defects in coverglasses or cells.

7. The way the light source is applied is of utmost importance in finding the defects and the level of detail. The best method can be achieved by the "dark-field" illumination method. Illumination by a circular light source (e.g. a TL-tube in ring form) gave the best results for the overall inspection. For lower magnifications, the angle of incidence of the light source had to be somewhat larger than as used in the stereo microscope.

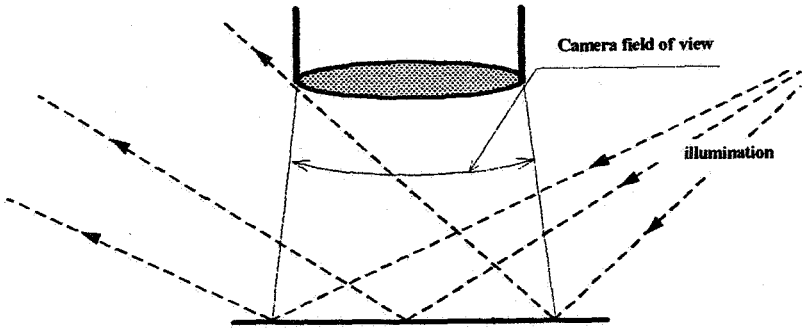


Figure1 : Dark field illumination ; all reflections are outside the field of view of view of the video camera

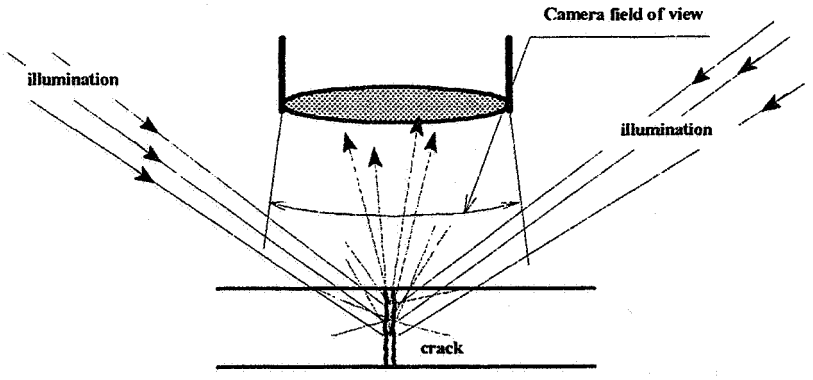


Figure 2 : Reflections in case of a crack. Only light reflected by the crack falls in the field of view of the camera. Dark field illumination from both sides (typical angle ~ 40 degr.)

Infrared wavelength range

Crack in cells and (to a lesser extent) in cover glasses can very well be made visible using an infrared video camera (near infrared, wavelength range 1000-1800 nm). In this case, the requirement on the light source are quite different from the above given conditions for the visible light illumination. The radiating surface of the light source has to be relatively large and should radiate uniformly over its entire surface. Tungsten light sources are required in order to have sufficient radiation in the near infrared spectral range. The position of the light source relative to the panel substrate is not critical. The only condition is that the position of the light source and the IR-camera must be such, that the reflected light enters the camera directly. This condition is met, when the mirror image of the light source covers the complete image field of the camera. Figure 3 shows the schematic picture. The light source has to be a diffuse radiator in order to obtain equal brightness over its surface, when observed by the camera since the camera has always a tilted position with respect to the light source due to the relative large dimensions of the light source.

Remarks:

1. Cell cracks could be detected when the camera was tilted under an angle such that the mirror image of the lamp covered the field of view of the IR-camera. Figure 4 and Figure 5 show typical examples achieved during testing this in more detail.

2. Defects in the cover glasses were more difficult to find since the angular position of the camera, relative to, the direction of the cover glass crack is more critical than for cracks in the solar cells. The level of detail was slightly less. It turned out now, in contrast with the visual camera, that in this case the complete camera required to be reoriented under an oblique angle. Typical angles of 10-20 degrees gave the best results. Figure 6 and figure 7 show the images as found during the tests.

3. Tests done in the infrared wavelength range showed that defects could be detected, even with a relative large field-of-view. However the amount of details was slightly less (See figure 8 and figure 9). Also, it turned out that the cell *type* gave different results, caused by the roughness of the bare cell structure. For instance, a "rough" cell structure gave less crack details due to scatter effects compared to a "smooth" cell.

4. Silicon type solar cells become transparent for wavelengths > 1000nm. The IR video camera is sensitive for wavelengths in the visible range up to 1800 nm. A filter in front of the camera lens blocks the visible light from the light sources, providing better images. This allows inspection of the n-and the p-busbars of the solar cells. In addition, the interconnectors including their spot-welding points can be inspected for this wavelength.

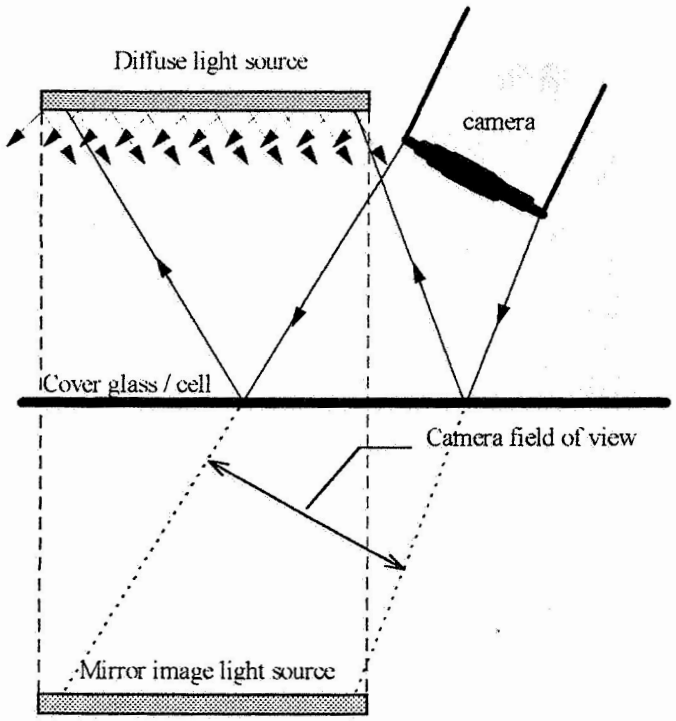


Figure 3: *Schematic picture of the IR-camera and the light source orientation w.r.t. the sample*

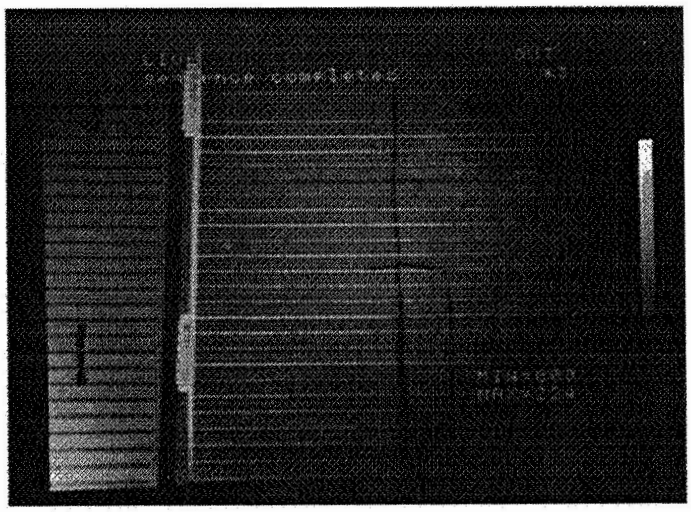


Figure 4: *Results of IR inspection method (view angle: 0 degrees)*

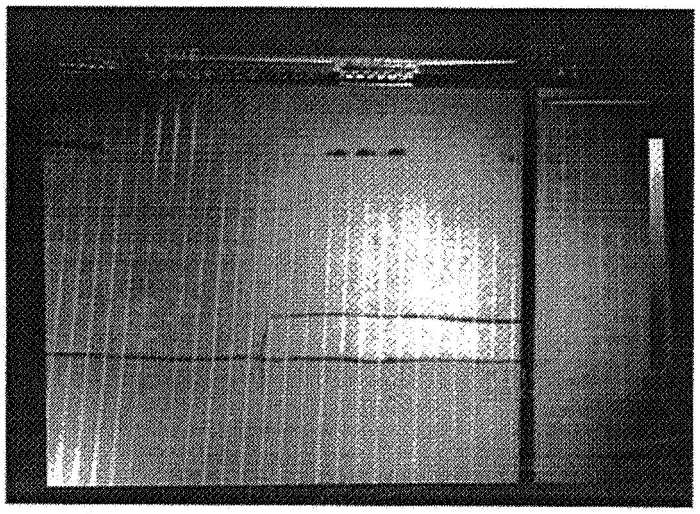


Figure 5: Results of IR inspection method (view angle: 90 degrees)

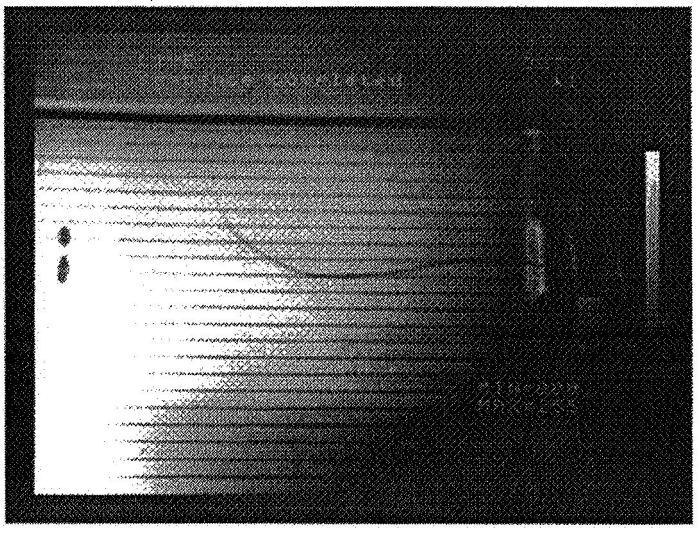


Figure 6: Results of IR inspection method cracks in coverglass (0 degrees)

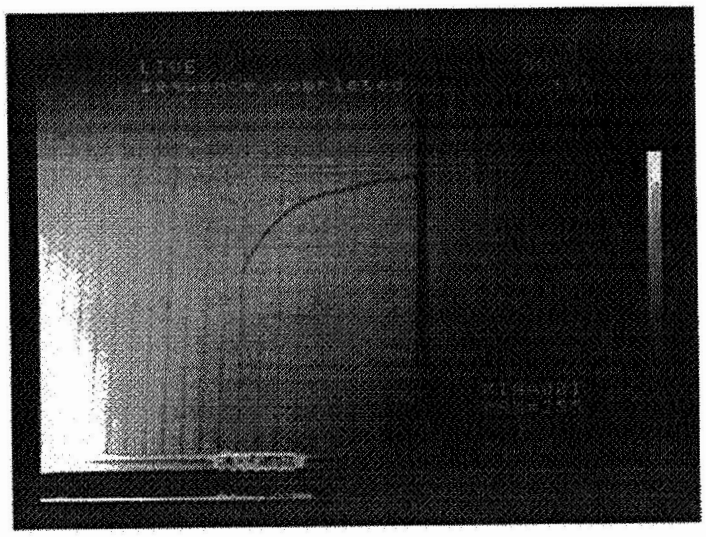


Figure 7: *Results of IR inspection method ; cracks in coverglass (90 degrees rotated)*

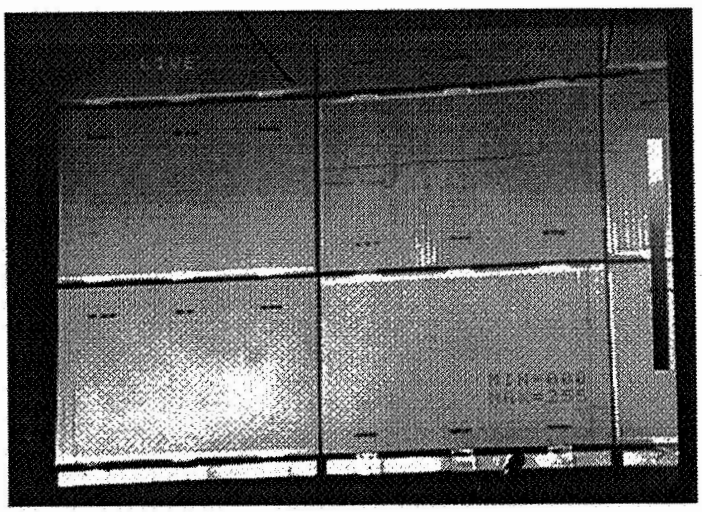


Figure 8: *Results of IR inspection method with large field of view*

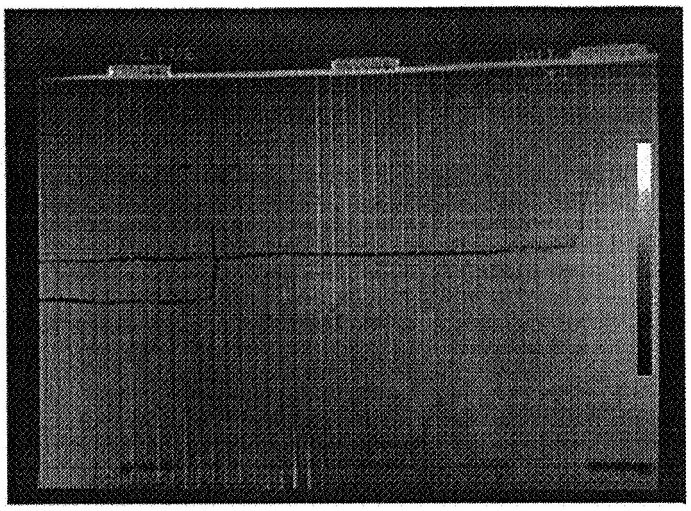


Figure 9: Results of IR inspection method with small field of view

ADDITIONAL TESTING

One of the interesting aspects was, that the original set of inspection criteria for FVI (Ref. 1) had to be relaxed. This process is still not yet finished. The original criteria were in fact considered valid for production of these cells with the coverglasses (so called :CIC's = Cell Integrated Circuit's) and *not* for the final cell bonded to the panel substrate. For the Envisat solar array, it has been agreed that the revised criteria (ref3) for acceptance of the FVI-method would be subject to review, provided that this new inspection method gave reliable data and test results. The video inspection system is ready now for the Envisat solar array. The acceptance test of the system will carried out in Sept/Okt. 1996. ESA will supply tests samples with known solar cell defects in cell and coverglass for this acceptance test. An earlier carried out test, with an ESA provided test sample, was successful tested. The IR camera detected more defects then the defects listed in the reference inspection.

Envisat camera configuration

When using a Hi-Res camera (visible light) another type of light source was needed, requiring that the light bundle is oriented under an angle of about 45 degrees with the surface. Taking into account that both the IR-camera and the Hi-Res camera had to be installed in the same inspection rig and on the same movable x-y trolley table, this could *not* be done without compromising other requirements. The visual system could not be combined with the IR as this system required large surfaces with a special diffuse light source. The compromise is that the inspection rig is optimized for the IR camera/light source inspection. The high resolution camera is also fitted but uses the same light source as the IR camera, which is not the ideal light source.

FINAL TEST RESULTS

It must be concluded that a "one-to-one" replacement of the original FVI- cannot be fulfilled method (see: Baseline Requirements; point 3). For detection of the minimum defects, the best technical method is still using a stereo microscope in combination with highly trained personnel. However, our expectations are that this is true for a relative small solar array, but not for a large array as the Envisat taking also into account that we have limited trained inspectors. However, within the other constraints mentioned under point 1 and point 2 of the Baseline Requirements, it has been found by these tests that a new inspection method could fulfill the requirements of saving time and money but also provide a safe and ergonomic solution. Of importance is also that with the new method inspection results, of each cell, can be recorded as an digital image.

Various bread board tests were done to find an acceptable FVI-method, which gave a similar level of detail of defects to be found. Extra tests were done to "fine-tune" the observations and to get improvements of the first test results by implementing special design features in the test set-up. The following results were obtained:

1. To detect cracks in the bare cells : IR-video
2. To detect cracks in the cover glasses : IR-video
3. To inspect the inter connectors, busbars, etc. : Hi-Res camera being used in a "zoomed-in" mode , only be used for a limited number of suspected points after the course (naked eye) inspections

The identification whether a crack is in the, cover-glass, cell or both can be seen, in most cases, from the characteristics of the crack. When it is doubtful, the specific cell can be inspected with the stereo microscope.

With the IR camera the field of view is increased with a factor 10 (relative to the microscope) (i.e. 80x60 mm); the net inspection time reduces to about 2 weeks.

FUTURE DEVELOPMENTS

The next step is to implement the results of the bread board tests into full-scale testing. At present, such a test is being prepared in the large Cleanroom 16 at Fokker Space. At this time the Qualification solar array wing is available for checking out the inspection system. (see Figure 10). This model has only a small amount of real solar cells.

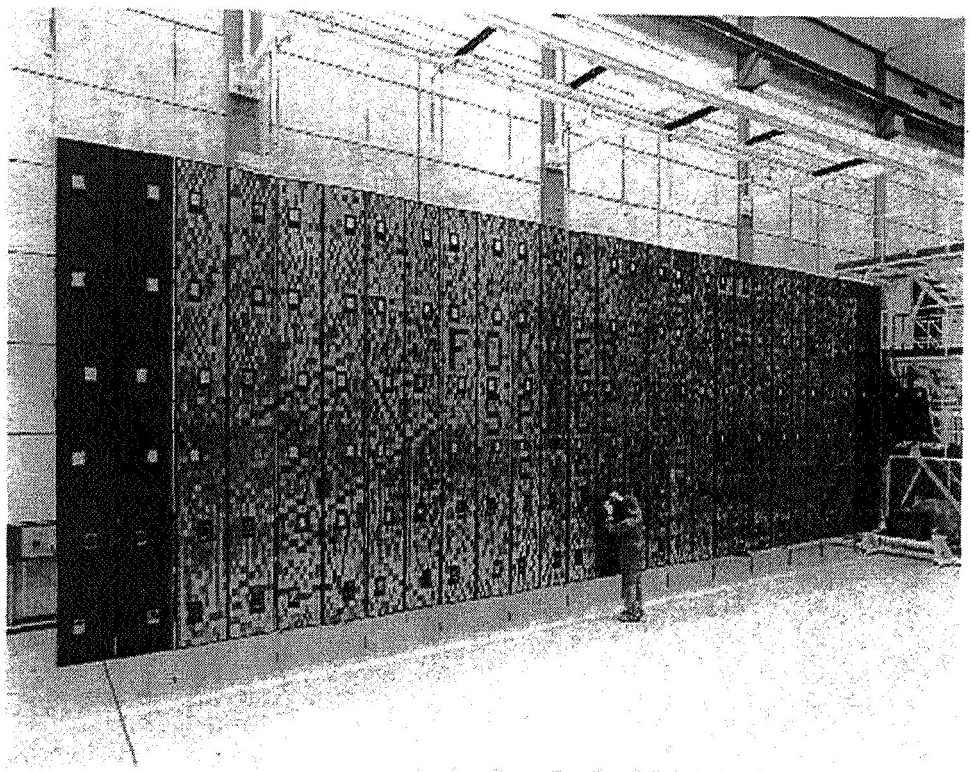


Figure .10 : Envisat solar array in the fully deployed configuration

The test set-up consists of a large (and stiff) rig, which allows X- and Y-translation of the camera. The camera platform can be moved in Z-direction for focusing purposes. (See: figure 11).

The actual Envisat Flight Solar Array inspection will take place in May 1997. All images will be recorded on magnetic tape. The actual inspection will be done on-line via the computer screen.

The next phase will be to see whether the faulty cells (if any) images on tape, can be recognized by software, in order to reduce the number of images which needs visual inspection. This is an off-line activity.

The future gaols are:

-Automatic recording of solar cell images, if possible without an operator, on a continous schedule to shorten the through-put time of the solar array hardware as much as possible.
-Development of software for detecting defects in solar cells by off-line analysis of the magnetic tape.
-Improvement of camera capabilities. Here we are dependent of commercial available hardware.

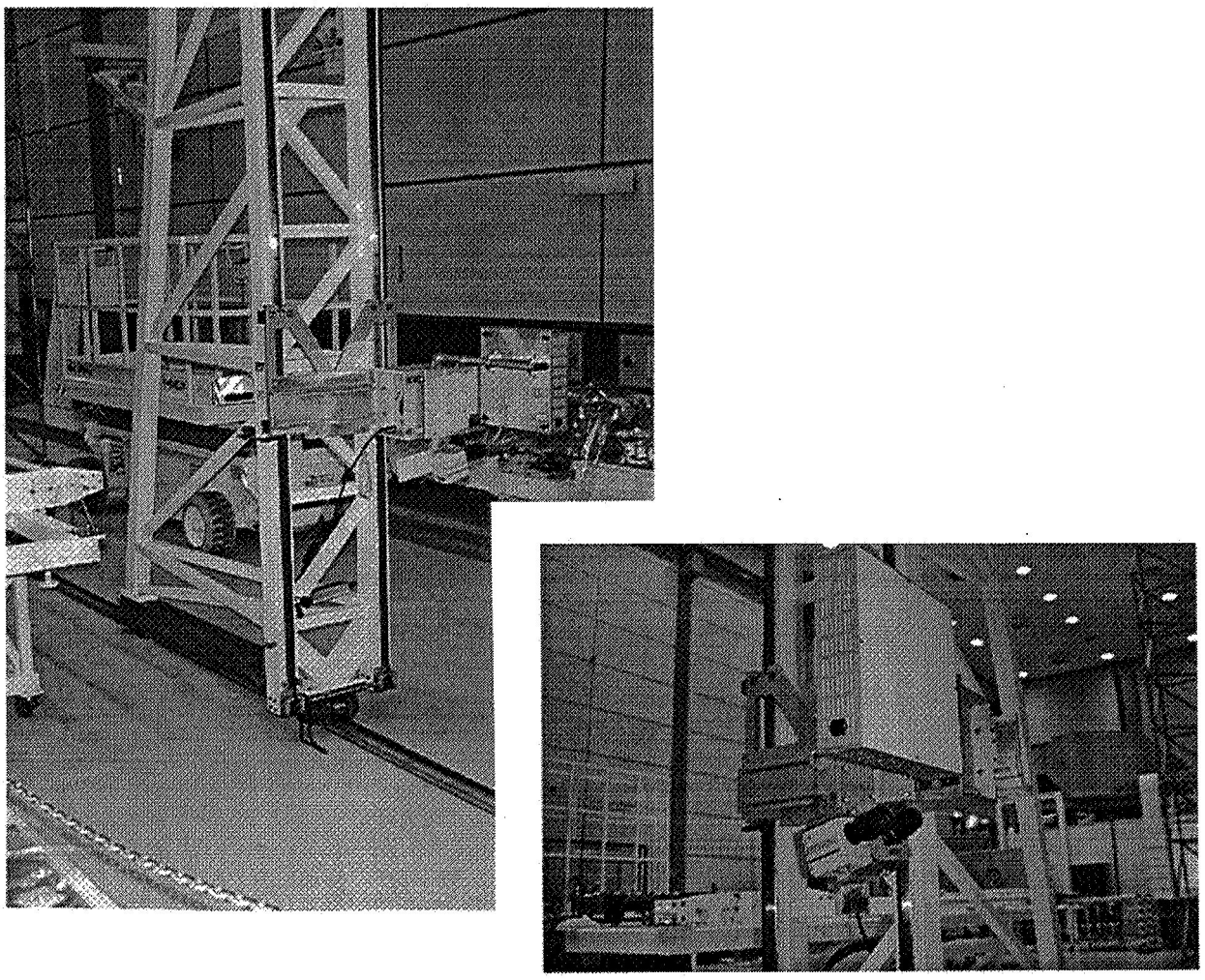


Figure 11: Inspection Rig for Envisat type of solar array.

REFERENCES

(1)	ESA-SP-369	The qualification test programme of the Envisat Solar Array Proceedings of the fourth European Space Power Conference 1995
(2)	ESA-PSS-01-604	Visual Inspection Requirements for solar cells
(3)	PPF-FO-SA-SPE-007	Visual Inpection Specification - PPF-SA panel / PVA Assembly

539-44
021483
6P
369628

AMBIENT PRESSURE THERMAL CYCLING TEST FACILITY FOR SOLAR PANELS *

Jan Ch. Geerse and Jos H. Mertens
Fokker Space BV
Leiden, the Netherlands

ABSTRACT

The acceptance test of solar panels for spacecraft was formerly performed in vacuum to find workmanship failures. Fokker Space BV, in cooperation with ESTEC, has developed an alternative which is cheaper and faster: the Ambient Pressure Thermal Cycling (APTC) test.
This paper describes the validation of this test approach for acceptance testing of solar panels. Further it describes the construction and performance of the test facility and its cost and time effectiveness.

INTRODUCTION

Fokker Space BV is Europe's leading solar array manufacturers for spacecraft. The solar array program ranges from telecommunication and science to earth observation applications.
The Fokker Space solar arrays are based on the Advanced Rigid Array and on the Flatpack solar array design.
A customary step in the acceptance test sequence of space solar panels is the performance of about 10 thermal cycles under vacuum conditions. This test is called the "On Station Thermal Cycling" (OSTC) test. Historically the vacuum environment has been preferred as more realistic and more likely to show possible mechanical effects related to voids in the panel structure, in particular in the adhesive underneath the solar cells. Vacuum thermal cycling is however a time consuming and costly process. The radiative heat transfer at low temperatures is slow and this increases the test duration.
In connection with the market demand for reduction of cost and throughput time Fokker Space some years ago reviewed the total design-, manufacturing-, integration- and testing process of solar arrays. As a result Fokker Space investigated the feasibility of "Ambient Pressure Thermal Cycling" (APTC) in a test facility under direct management. The APTC test is meant to replace the time consuming and expensive OSTC test for the proto-flight and acceptance test program of solar arrays. The purpose of this test is workmanship verification.
The OSTC test is still part of the qualification program of solar arrays.

Ambient pressure thermal cycling uses the faster forced convection thermal exchange which allows in principle a quick and comparatively cheaper simulation of thermally induced stresses in the solar panel structure. However, it provides only a thermal test, somewhat different thermal gradients and no exposure to vacuum before flight. APTC can therefore be envisaged only if two important conditions are met:

1. The panel design has been thoroughly qualified with respect to vacuum effects.
2. The equivalence of OSTC and APTC in detecting workmanship failures has been clearly demonstrated for the qualified panel design.

An APTC - validation program was started. Our main commercial customers and ESA were involved in the validation of this test method and the acceptance of APTC as alternative for OSTC.
This program intended and did lead to the realization of a Fokker Space facility to perform the thermal acceptance tests on solar panels.

* Funding: ESA-Industry Telecommunication Partnership Program

VALIDATION OF THE APTC TEST METHOD

The thermal cycling tests on flight panels after the qualification of the panel design is performed to find workmanship failures. At first workmanship failures in the substrate will be detected with the NDI methods like visual inspection, bond testing, airscan, A-scan, X-ray or holography.
The "Ambient Pressure Thermal Cycling" (APTC) test is a substitution for the "On Station Thermal Cycling" (OSTC) test on flight panels.
APTC is considered to be a valid test method that can replace the OSTC test as part of the proto-flight and acceptance test program for solar panels:

IF APTC does not imply thermal or mechanical loads on the panels in such a way that the structural integrity or lifetime of the solar panels is endangered.

AND APTC provides the same detection capability with respect to workmanship failures as OSTC

OR Workmanship failures for which the above condition cannot be met, will be detected by other means than OSTC (e.g. detection by NDI)

An APTC validation program was started with the cooperation of ESA-ESTEC. As a result of a vacuum mechanical stress analysis, samples were manufactured containing voids under solar cells of different sizes. The voids were the built-in workmanship failures to be detected. Voids in combination with vacuum cause mechanical stresses which can result in solar cell cracks or cover glass cracks. Improper curing of adhesive was also implemented in the samples. The samples were representative for the baseline ARA solar panels for both GEO and LEO missions, as well as for the Flatpack solar panels for Polar Platform.
One sample was subjected to OSTC and the other to APTC testing.
The result of this program showed that the solar panel design is not critical on vacuum related workmanship failures. The voids didn't cause solar cells or cover glass cracks. Only after the extension of the test one solar cell crack occurred.
Based on the results of the APTC validation test, Fokker and ESTEC jointly concluded that

1. APTC is a valid test method that can replace the OSTC test in the frame of proto-flight and acceptance testing of current ARA and Flatpack solar panels.
2. In case of changes to the design, materials or production process, the validity of APTC shall be reviewed.

APTC TEST FACILITY

In 1994 the APTC test facility was built. APTC has to accommodate solar panels like PPF's which means a test volume of several cubic meters. It was therefore realized from the beginning that the problem of internal pressure control, linked to the large temperature changes, would be an important design driver. On the other hand, customers would certainly require from APTC a quality of samples temperature control at least as good as that provided by OSTC. Both problems are obviously linked as the thermal exchange relies on forced convection. This "force" itself, that is the nitrogen gas flow speed, has to be kept at a level which does not exert unacceptable aerodynamic stresses on the tested panels.
The above test chamber design principles and the requirements to ensure a complete sample and personnel safety have led to a rather complex control system. This provides the desired chamber temperature cycle profile and uniformity with the best thermal efficiency. At the same time, it controls the internal atmosphere, for instance the internal pressure, the low oxygen level or the absence of nitrogen droplets. Again for safety reasons, the tested samples temperature is monitored by a completely independent system.
The construction of the facility is a test volume with recirculation channels. The test volume can accommodate 4 panels in test. Two fans circulate the heat transfer medium dry nitrogen gas in the facility. Electrical heaters are the heat source and liquid nitrogen is used for cooling. Liquid nitrogen is stored in a 37.000 liter tank outside the cleanroom. The heating and cooling power is in excess of 300 kW.

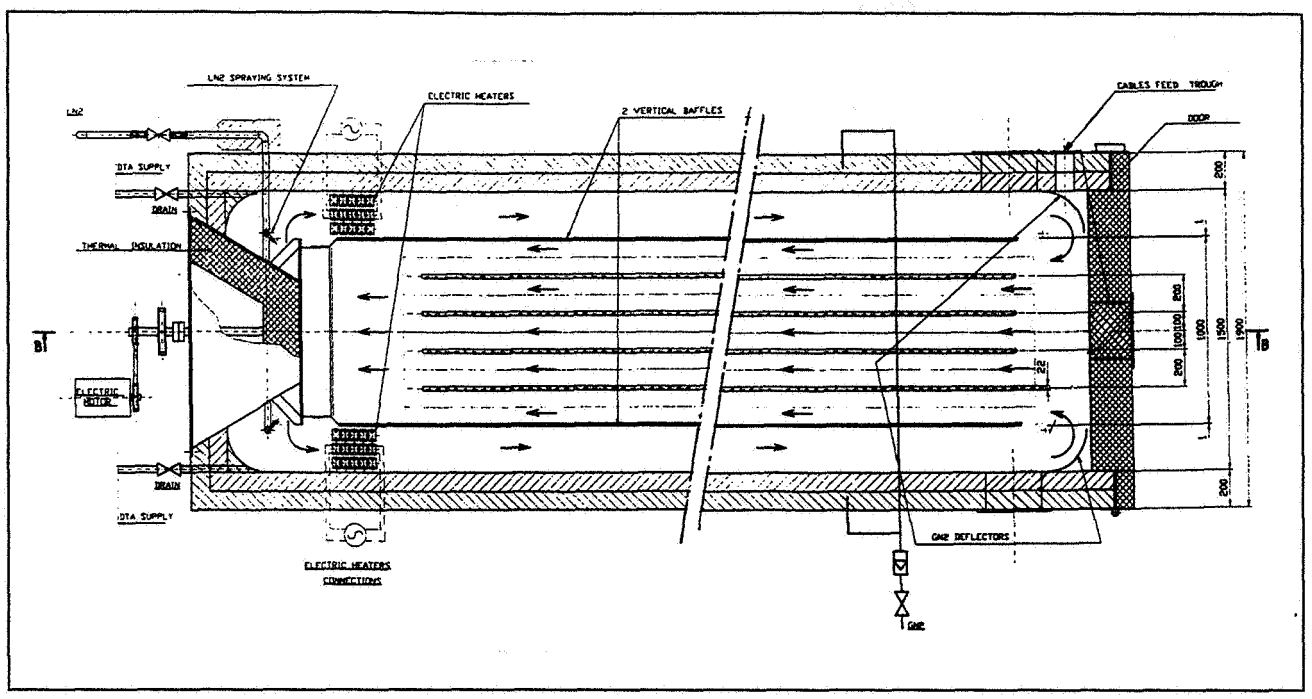


Fig 1: APTC Test Facility, principle sketch top view

The APTC facility has the following characteristics:

- Test volume: 5.2m length x 1m width x 3m height to accommodate up to four solar panels placed in a guidance rail-system
- Temperature range minimum -175 °C and maximum +175 °C
- Temperature rate of change of the gas is controllable between zero and 20 °C/minute for heat-up and cooldown over the complete temperature range
- The facility is placed in a cleanroom class 100.000 This is in the same area were the integration and testing of the solar panels and arrays take place
- The facility-control is completely automatic by a given required project temperature profile.
- The gas flow velocity is computer controlled between 2 and 5 meters per second to maintain a constant dynamic pressure at all temperatures.

The outside dimensions of the facility are 8.5m length x 3m width x 4m height.
The facility is provided with a number of safety features. The facility automatically regulates to a save operation condition when:

- Hot or cold facility temperature extremes are exceeded
- Hot or cold panel temperature extremes are exceeded
- Oxygen level is above 4 %
- Overpressure in the facility is measured

At the start of the test a nitrogen purge drives out the humid air. At the end of the test the door can only be opened when the temperature is ambient and the oxygen level is above 19%.
The facility has a large number of feedthroughs for signals and power leads and also for thermocouples.

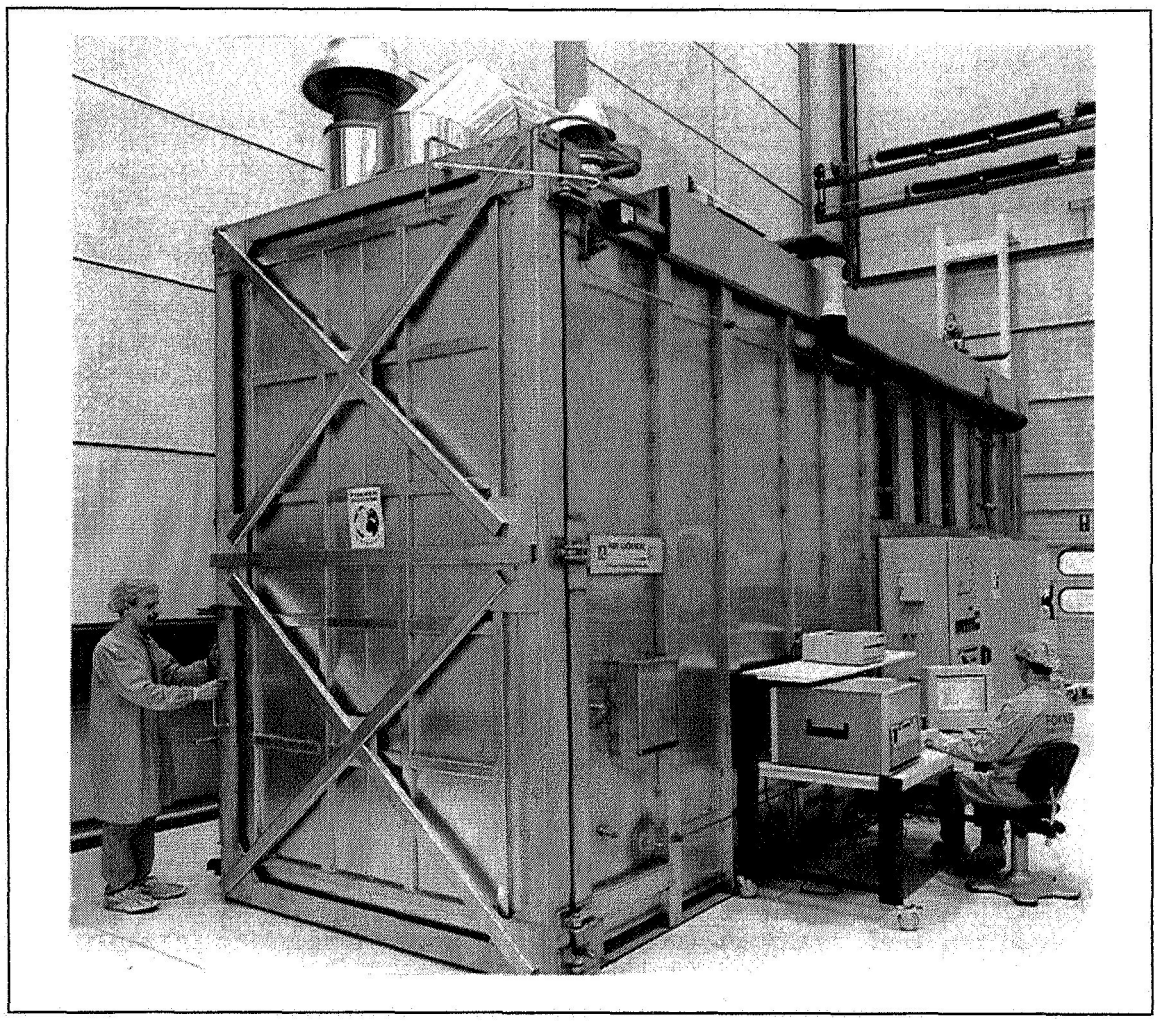


Fig 2: Fokker Space APTC test facility in a cleanroom environment

TEST RESULTS

After the installation of the facility at the Schiphol site of Fokker Space in early 1995, acceptance tests have been performed. Much attention had to be paid to the temperature control of the facility. Temperature overshoots and a non-stable temperature behavior during the dwell occurred. The internal mass of the facility, which also participates in the thermal cycling, influences the temperature control. By finding the right control parameters and adapting the temperature profile of the gas, the panels experience the required temperature profile.
The panel-temperature uniformity is within ±2 °C from the required temperature.
The vibration loads on the panels and the strain in the panels due to the forced flow were measured. Analyses of the data showed that an APTC test has a negligible effect on the fatigue life of the panels and the mechanical stresses are very low.
In figure 3 the panel temperatures are given as measured during a typical APTC test.

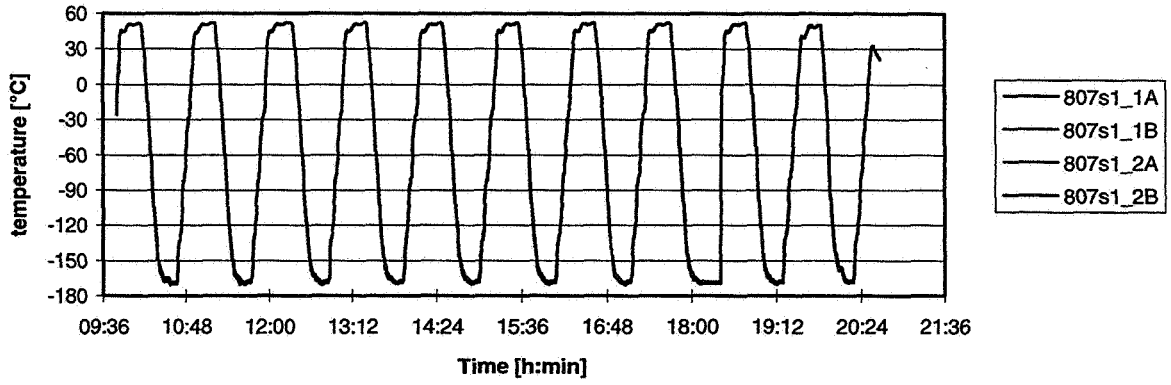


Fig 3: Panel temperatures during a typical APTC test

COST EFFECTIVE TESTING

At present the APTC test facility is operational and has been used in solar panel acceptance testing for Telecom 2, Skynet, Hotbird 3 and will be used for Hotbird 4 and the Polar Platform panels.
The advantages of the APTC facility:

	OSTC	**Improvement APTC**
throughput time	2 weeks per wing (2 panels per test)	3 - 5 days per wing (4 panels per test)
costs including all necessary inspections before and after test	_	50 % of OSTC-test costs
performance	vacuum temp. range -163°C / +130 °C	dry nitrogen temp. range -175°C / +175 °C

Fokker Space has the APTC test facility under direct management. This creates flexibility in the scheduling of thermal tests, which is a great advantage.

The APTC is even more profitable when other articles then solar panels are tested. The APTC has been used for the thermal cycling of spacecraft instruments and for the accelerated curing of bonded assemblies.
The facility can also be used for the thermal cycling of antennae and spacecraft panels.

540-14
021484
BP
369629

ELECTRON OMNI-DIRECTIONAL IRRADIATOR SYSTEM FOR SPACE PACKAGE TESTING

Vincent G. Adams and Walter J. Chappas
Department of Materials and Nuclear Engineering
A. James Clark School of Engineering
Glenn L. Martin Institute of Technology
University of Maryland

ABSTRACT

The University of Maryland operates an integrated radiation testing and space simulation facility that includes a Cobalt-60 room source, a 250 kW TRIGA nuclear reactor / neutron source, and a 1-8 MeV electron linear accelerator. At the center of the facility is a unique test chamber that permits the 2π, in vacuo, electron irradiation of electronic packages. Recent programs include radiation transport, shielding, and dielectric breakdown studies within individual electronic devices, electronic packages, and electronic packaging materials. This paper describes the facilities and the applications for space package testing.

INTRODUCTION

In 1960, the University of Maryland's first nuclear reactor / neutron source went critical, and with its availability, the University's Department of Materials and Nuclear Engineering began working in the fields of radiation effects. Over the past 35 years, the Department's Radiation Facilities have grown to include UV, electron, neutron, and gamma radiation sources and the Department has grown to include a diverse faculty with a world-class experimental and computational capabilities.

However, one of the Radiation Facility's most successful areas of research, is for the evaluation of the degradation of electronic packages exposed to the high energy electron environment of space. Although the general topic has been studied for many years, there has been no practical experimental facility available for simulating these effects on circuit board size electronic packages. This is of critical importance, since many of the electron induced failures can only be observed when devices are assembled into larger packages. In larger geometries, electric fields created by electron induced charge trapping can produce surface effects that lead to device, system, and mission failures.

For the past 20 years, the University of Maryland's radiation test facilities have supported government and commercial space electronics vendors with real-time evaluations of electronic packages designed for use in the near earth electron radiation space environment. The results have been used to characterize shielding, charge build-up, material damage, and other package and mission failures. In addition, radiation transport through circuit board assemblies, and other complex geometries, have been complied and compared to three dimensional computer models. These kind of studies make it possible for satellite designers to identify otherwise undetectable failure modes or take advantage of low dose-rate locations in the package to protect sensitive package elements.

ELECTRON TEST FACILITY

The Department's first high energy electron linear accelerator was installed in 1975. This Applied Radiation Corporation (ARCO) linac, originally part of NASA's Space Radiation Effects Laboratory (Newport News, VA), was an L-band device designed to operate at 10 MeV and 1 mA of beam current. In 1987, the ARCO linac was replaced by a modified S-band clinical accelerator (manufactured by Varian and modified into a research configuration by JM Company).

The new linac can produce micro-second pulses with peak currents up to 500 mA, with electron energies up to 9 MeV. It can be operated in a single pulse mode or it can deliver a continuous train of pulses up to 360 Hz. Pulse radiolysis equipment is also available for optical measurements of radiation induced transient species which absorb in the wave-length region between 215 and 800 nm. Radiation induced conductivity can be measured in single pulse or continuous mode. It can also be used in experiments to determine dose distributions in complex absorbers as well as long term effects on the

electrical properties of semiconductors devices or the mechanical properties of plastics. Performance specifications for the 1-9 MeV device can be found in Table 1)

OMNI-DIRECTIONAL IRRADIATOR

Shortly after the installation of the electron linac in 1975, a specialized irradiation chamber, designed by the National Security Agency and operated at the National Institute of Standards and Technology, was transferred to the University of Maryland. This omni-directional irradiator (ODI), when operating in conjunction with NIST's 3 MeV electron van de Graaff, controlled the orientation during the irradiation of electronic packages commonly found in communication satellites.

Upon its transfer to the University of Maryland, the ODI was modified with an extended drift section and attached to one of the electron linac's two parallel beam lines (Figure 1). The accelerator and ODI section are separated by a thin plastic membrane. The experimental test chamber is able to accept electronic packages, up to 12 inches (30 cm) x 12 inches (30 cm) x 6 inches (15 cm) then under vacuum conditions, control the irradiation so that a package receives a predetermined total electron fluence (or dose) for a specified electron energy and angular distribution. This omni-directional irradiator, or ODI, scans the linac's electron beam in two dimensions then transports the diverging beam down a 2 ft. (.61 m) diameter x 25 ft. (7.6 m) long beam line to the package test chamber. Access to the test chamber is though a single 1 ft (0.3m) x 2 ft (0.61 m) panel. Inside the test chamber, test packages can be quickly and easily affixed to a flexible mounting plate that can be remotely rotated so as to permit package irradiation with any predetermined set of incident angels over 2π radians.

In application, users of the ODI typically identify a space environment of interest (usually determined by a satellite's orbit), then by coupling this information to NASA space environment tables and the projected service life of the satellite, the life-time exposure for the satellite can be established. This spectrum, or in combination with other spectra (e.g. a fission spectrum), can be assembled and programmed into the ODI.

The basis mechanical arrangement for moving the target is shown in Figure 2. The ODI uses a body coordinate system fixed on the target at P. The direction of the incoming electrons is Ω, defined by θ and Φ. Since the scanning divergence is only $\pm 4.3°$, θ and Φ effectively define the fluence direction as seen by all points on the target surface. The target is mounted to Plate 1, which in turn is rigidly fastened to Plate 2. This second plate is a large gear which is coupled to the rotation axis motor. Plate 3 is not so much a plate as an annulus. On the back of plate 2 is a series of Delrin bushings with tongues that fit snugly into a groove along the inner circumference of the annulus. This allows the first two plates to rotate freely, thus effecting the roll motion in θ, but to have no other freedom. Plate 3 in turn fastens to the pitch axis permitting the system freedom in the θ direction. The two axes of motion are completely independent of one another. However, while the Φ axis can perform a complete 360 ° rotation, the θ motion is limited to the range of 0° to 90° from the incident beam direction. This is necessarily so, since larger angles would cause the beam to run into the target support structure. Thus, one hemisphere of the target can be irradiated before it must be inverted and the process repeated.

The process is entirely controlled by a computer which turns the electron beam on and off while moving the part through a series of predetermined θ and Φ increments. At the first Φ position, of which there are ten, the target is stepped through twenty Φ positions. At each Φ, the beam is turned on and scanned across the target until the proper fluence for that position has been accumulated. The beam is turned off and the target is moved to the next Φ position. This is repeated through a complete rotation in Φ, whereupon the system is moved to the next θ step and the process continued until one hemisphere of the target has been irradiated. The vacuum chamber is then vented, the target inverted 180° with respect to the beam direction, the chamber evacuated once again, and the entire sequence repeated until the other hemisphere has been covered. Generally speaking, one complete hemispheric irradiation will take 10-20 minutes, depending on the fluence required.

The fluence is monitored with charge collectors placed outside the target cross-section but within the region of the scanned beam. The collectors are cylindrical aluminum plugs, 0.5 in.(1.27 cm) in diameter and 1 in. (2.54 cm) in length. The plugs are mounded flush in larger aluminum slabs approximately 2.5 in.(6.4 cm) square and of the same thickness. The collectors are electrically isolated with dielectric film . The current in the collectors can be monitored individually or in combination to determine uniformity across the scanned area. The plugs are also connected to a current monitor so that the accumulation of the required charge (i.e. fluence) at a given θ and Φ, can be used as the gate signal for automatically shutting off the electron beam.

NEUTRON TEST FACILITY

The University's neutron test facility is licensed to operate at 250 kW. The modified TRIGA reactor, consists of 93, 20% enriched, uranium fuel elements in a rectangular array. Samples can be exposed to neutron and mixed fields at a number of experimental ports and positions. Small samples, up to 0.75" (1.9 cm)diameter and 2" (5 cm)long, can be pneumatically transferred from a nearby laboratory directly into the center of the core while larger samples can be placed into a 6" (15 cm) diameter tube that runs across the face of the core. Beam ports on both the east and west sides of the facility provide a way of transporting neutrons out of the shield for experimental applications. Figure 3 shows a plan view of the neutron source and Table 2 summarizes test parameters at various irradiation positions.

GAMMA TEST FACILITY

The Gamma Test Facility consists of a 26,000 curie (9.6E14 Bq) cobalt-60 source (September 1, 1987). The source consists of ten source pencil rods (0.5"(1.27 cm) diameter and 12" (30.5 cm) long) in the form of a hollow cylinder with a 4.5" (11.4 cm) pitch. The source is stored at the bottom of a 15 ft. (4.5 m) deep water filled well. Prior to use, an 18" (46 cm) thick solid steel door seals the 15 ft. (4.5 m) x 15 ft (4.5 m) room (Figure 4), and the source is raised into the room's center. Samples are placed in the vault at selected positions to receive specific dose rates. The system automatically lowers the source when a predetermined time limit is reached. Dosimetry is performed in accordance with NIST traceable standards. Currently, experiments include radiation damage to electrical components, beneficial modifications of plastics, synthesis of polymers, preservation of food, and sterilization of biomedical devices.

CONCLUSIONS

The University of Maryland's Department of Materials and Nuclear Engineering operates an integrated space radiation test facility for the evaluation of electronics and materials used in space or radiation environments. The facility has, for the past 35 years, supported a wide distribution of users, with efforts that range from the most fundamental aspects of radiation interactions in materials, to the practical and applied pre-flight testing of satellite electronics. Recent work has included studies of high electron dose damage to solar panels, neutron damage to semiconductors operating at elevated temperatures, and the long-term aging of polymer composite materials exposed to high electron and gamma doses.

Table 1. Electron Linac Performance Specifications

Electron Energy (MeV)	Peak Current (mA)
1.1	360
2.0	440
2.5	450
3.0	460
4.0	430
6.0	280
7.0	200
8.0	110
9.0	40
9.5	3

Table 2. Neutron Source Flux Specifications

MUTR FACILITY CHARACTERIZATION		
PNEUMATIC TRANSFER (RABBIT) SYSTEM		
FLUX		AT FULL POWER (250 kW_t)
Thermal	1.6E10 n/cm^2-kW-s	4.0E12 n/cm^2-s
Epithermal	3.0E8 n/cm^2-kW-s	7.5E10 n/cm^2-s
Fast	8.0E9 n/cm^2-kW-s	2. 0E12 n/cm^2-s
1 MeV equivalent Silicon	6.9E9 n/cm^2-kW-s	1.7E12 n/cm^2-s
Gamma dose rate	19 rad/kW-s	4.8 krad-s
THROUGH TUBE		
Thermal	1.6E9 n/cm^2-kW-s	4.0E11 n/cm^2-s
Fast	1.1E9 n/cm^2-kW-s	2.8E11 n/cm^2-s
1 MeV equivalent Silicon	8.6E8 n/cm^2-kW-s	2.2E11 n/cm^2-s
Gamma dose rate	2.1 rad/kW-s	0.5 krad-s

Figure 1 Linear Accelerator with ODI

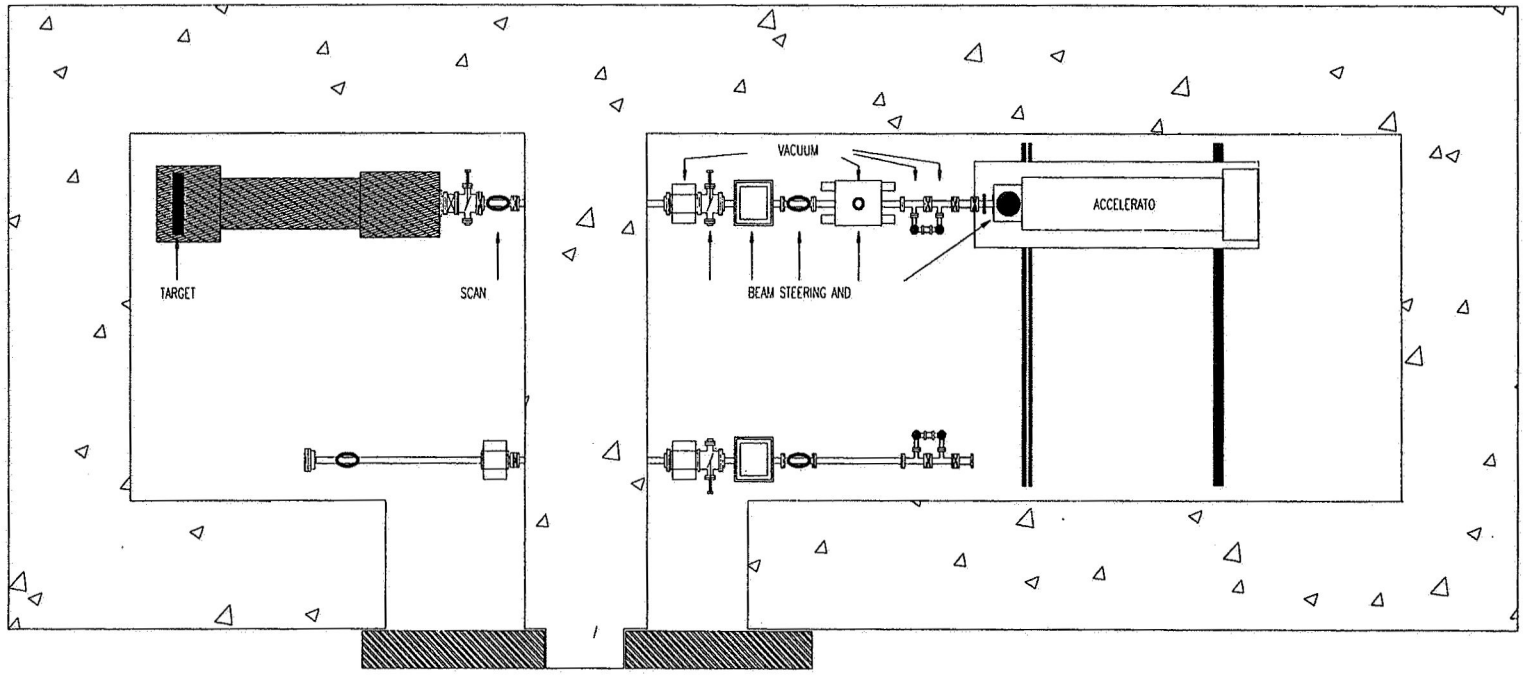


Figure 2 ODI Motion Control System

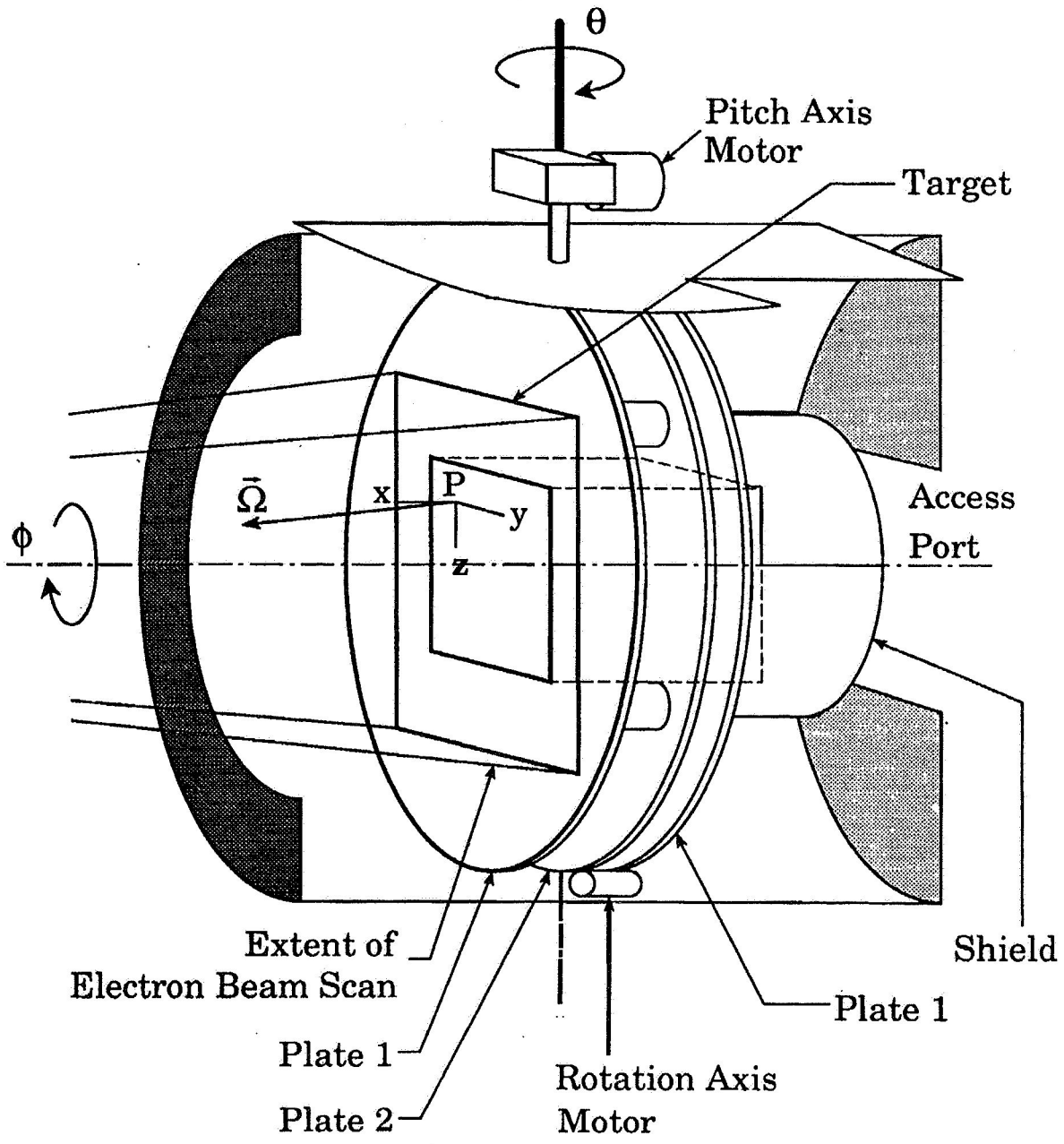


Figure 3 Reactor/Neutron source core diagram

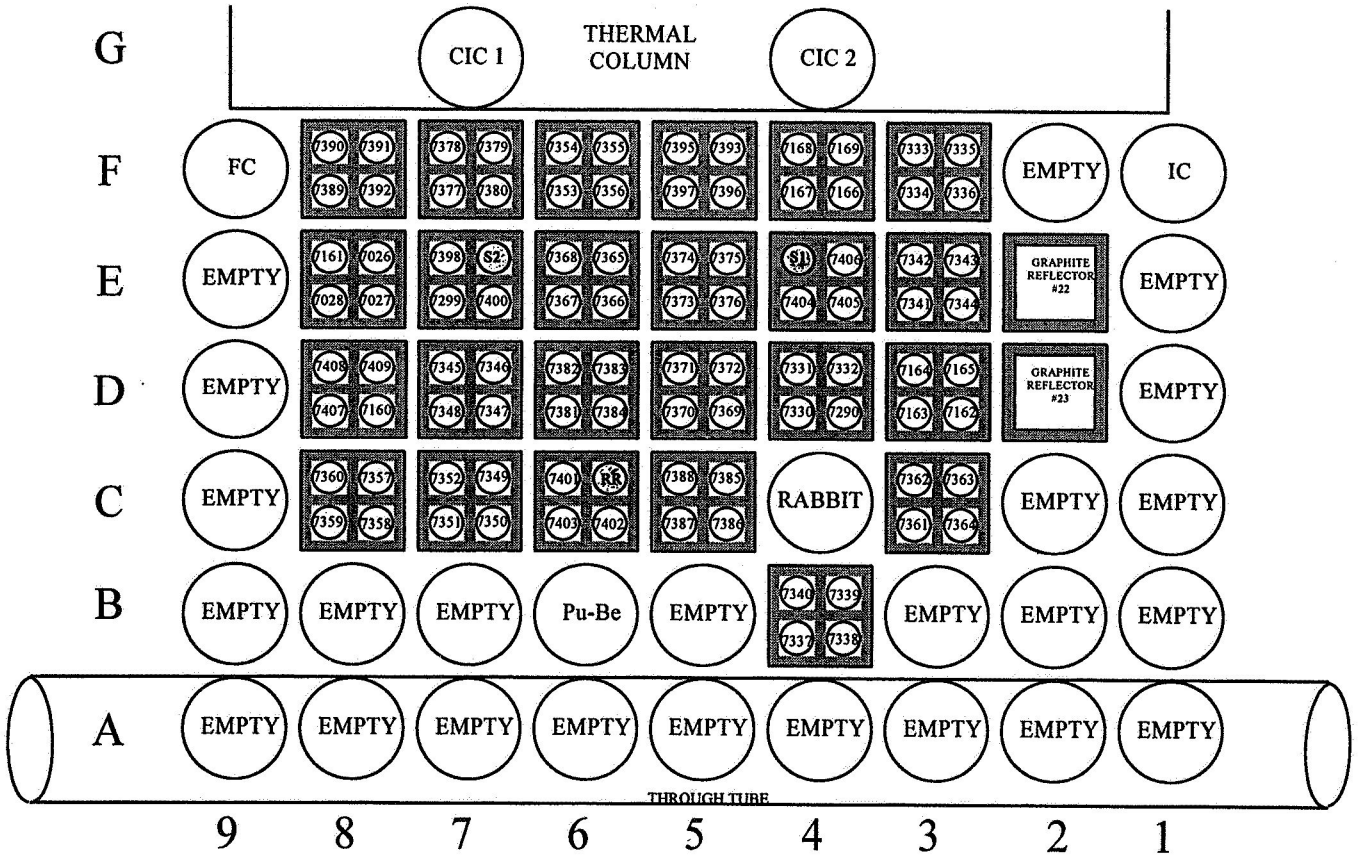
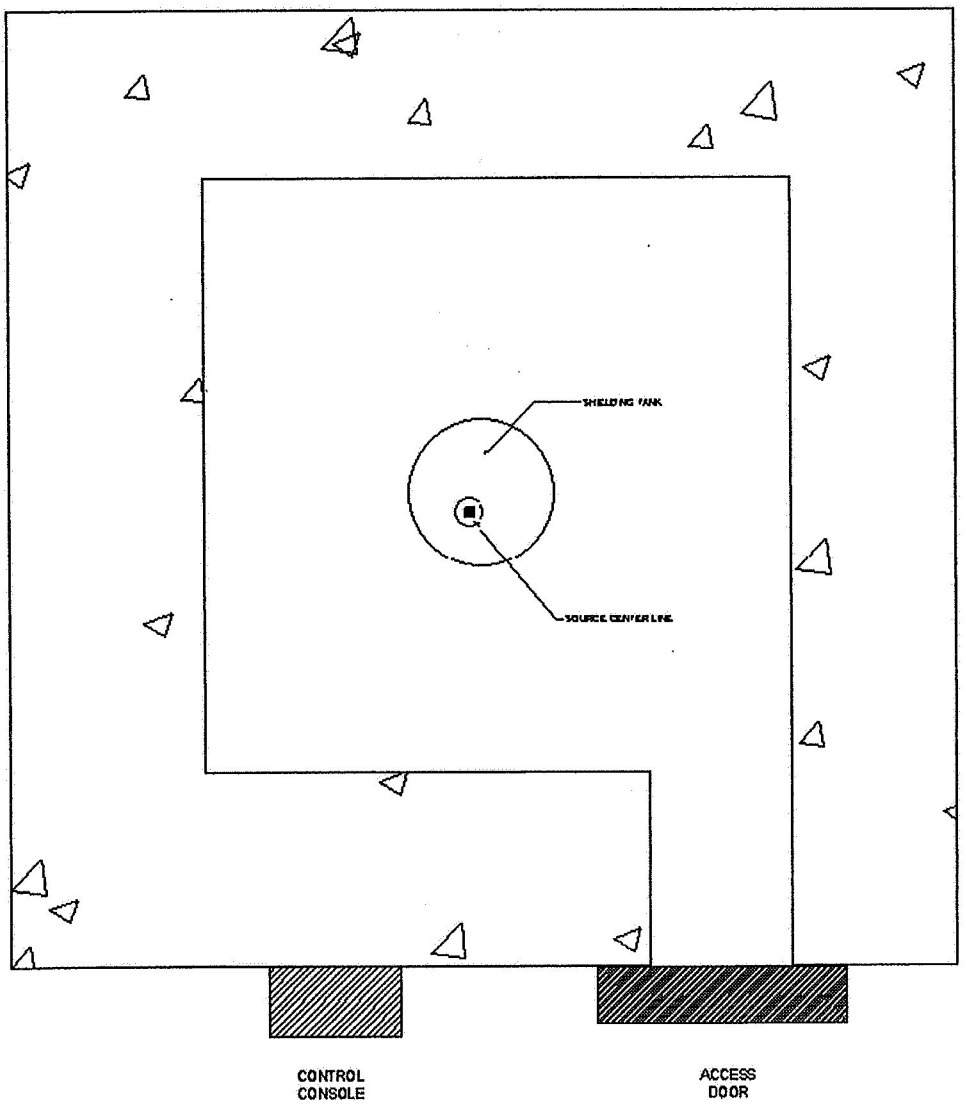


Figure 4 Gamma Facility



269631
541-14
ABS. ONLY
021486
CLOSE
6P

New Facility For Extreme Ultra-Vilet and X-Ray Testing

A. Cucchiaro, I. Domken, P. Jamotton, I. Tychon, and J.P. Tock

Abstract

Since the end of 1994, CSL (Centre Spatial de Liege) has been charged by ESA to develop a new facility in order to proceed to the performance tests of its X-Ray Multi-Mirror Mission (XMM satellite of the long term program for space science).

A veritical facility called FOCAL X (acronym for Facility for Optical Calibration in Liege in the X-ray range) has been built allowing, on the individual Mirror Shells as well as on the Mirror Modules and on the Mirror Assemblies, to determine the main optical characteristics.

To achieve these goals, the facility (vertical vacuum chamber of 4.5m diameter and 12.2 m height) has been equipped with an EUV optical channel (58.4mm), an X-ray collimator channel and an X-ray direct beam channel (1.49 kev and 8.04 kev) with their appropriated detectors. Inside the vacuum chamber a main optical bench coupled with a seismic block supports a tower (7.5m) and an upper optical bench dedicated to the detectors. Associated upper and lower translation and rotation movements complete the needed set-up.

As the handling and the positioning of the speciment are of high constrain, special care has been taken for:
- the long term structural stability of the facility (better than 2 arcsec).
- the reference surface of the optical benches (planarity better than 50 micron).
- the stability of the whole MGSE (better than 2.4 arcsec).

Additionally, the cleanliness aspects being very stringent, special rules have to be followed. The complete results of a first campaign of tests performed on a qualification model of a Mirror Module will be presented.

REPORT DOCUMENTATION PAGE

Form Approved
OMB No. 0704-0188

Public reporting burden for this collection of information is estimated to average 1 hour per response, including the time for reviewing instructions, searching existing data sources, gathering and maintaining the data needed, and completing and reviewing the collection of information. Send comments regarding this burden estimate or any other aspect of this collection of information, including suggestions for reducing this burden, to Washington Headquarters Services, Directorate for Information Operations and Reports, 1215 Jefferson Davis Highway, Suite 1204, Arlington, VA 22202-4302, and to the Office of Management and Budget, Paperwork Reduction Project (0704-0188), Washington, DC 20503.

1. AGENCY USE ONLY *(Leave blank)*	2. REPORT DATE	3. REPORT TYPE AND DATES COVERED
	January 1997	Conference Publication

4. TITLE AND SUBTITLE

Nineteenth Space Simulation Conference
Cost Effective Testing for the 21st Century

5. FUNDING NUMBERS

Code 750

6. AUTHOR(S)

Compiled by Joseph L. Stecher, III

7. PERFORMING ORGANIZATION NAME(S) AND ADDRESS(ES)

Goddard Space Flight Center
Greenbelt, Maryland 20771

8. PERFORMING ORGANIZATION REPORT NUMBER

97A00653

9. SPONSORING/MONITORING AGENCY NAME(S) AND ADDRESS(ES)

NASA Aeronautics and Space Administration
Washington, D.C. 20546-0001

10. SPONSORING/MONITORING AGENCY REPORT NUMBER

CP-3341

11. SUPPLEMENTARY NOTES

Other sponsors: Institute of Environmental Sciences, American Institute for Aeronautics and Aeronautics, American Institute for Aeronautics and Astronautics, American Society for Testing and Materials, and Canadian Space Agency

12a. DISTRIBUTION/AVAILABILITY STATEMENT

Unclassified-Unlimited
Subject Category 18
Report is available from the NASA Center for AeroSpace Information,
800 Elkridge Landing Road, Linthicum Heights, MD 21090; (301) 621-0390.

12b. DISTRIBUTION CODE

13. ABSTRACT *(Maximum 200 words)*

The Institute of Environmental Sciences' Nineteenth Space Simulation Conference, "Cost Effective Testing for the 21st Century" provided participants with a forum to acquire and exchange information on the state-of-the-art in space simulation, test technology, atomic oxygen, program/system testing, dynamics testing, contamination, and materials. The papers presented at this conference and the resulting discussions carried out the conference theme "Cost Effective Testing for the 21st Century."

14. SUBJECT TERMS

Space Simulation, Thermal Simulation, Contamination Control, Dynamic Testing, Spacecraft Materials, New Approaches and Facilities

15. NUMBER OF PAGES

429

16. PRICE CODE

17. SECURITY CLASSIFICATION OF REPORT	18. SECURITY CLASSIFICATION OF THIS PAGE	19. SECURITY CLASSIFICATION OF ABSTRACT	20. LIMITATION OF ABSTRACT
Unclassified	Unclassified	Unclassified	Unlimited